Anhu Li

Double-Prism Multi-mode Scanning: Principles and Technology





Springer Series in Optical Sciences

Volume 216

Founded by

H. K. V. Lotsch

Editor-in-chief

William T. Rhodes, Georgia Institute of Technology, Atlanta, USA

Series editors

Ali Adibi, Georgia Institute of Technology, Atlanta, USA Toshimitsu Asakura, Hokkai-Gakuen University, Sapporo, Japan Theodor W. Hänsch, Max-Planck-Institut für Quantenoptik, Garching, Germany Ferenc Krausz, Ludwig-Maximilians-Universität München, Garching, Germany Barry R. Masters, Cambridge, USA

Katsumi Midorikawa, Saitama, Japan

Bo A. J. Monemar, Department of Physics and Measurement Technology, Linköping University, Linköping, Sweden

Herbert Venghaus, Fraunhofer Institut für Nachrichtentechnik, Berlin, Germany Horst Weber, Technische Universität Berlin, Berlin, Germany Harald Weinfurter, Ludwig-Maximilians-Universität München, München, Germany **Springer Series in Optical Sciences** is led by Editor-in-Chief William T. Rhodes, Georgia Institute of Technology, USA, and provides an expanding selection of research monographs in all major areas of optics:

- lasers and quantum optics
- ultrafast phenomena
- optical spectroscopy techniques
- optoelectronics
- information optics
- applied laser technology
- industrial applications and
- other topics of contemporary interest

With this broad coverage of topics the series is useful to research scientists and engineers who need up-to-date reference books.

More information about this series at http://www.springer.com/series/624

Anhu Li

Double-Prism Multi-mode Scanning: Principles and Technology





Anhu Li School of Mechanical Engineering Tongji University Shanghai, China

ISSN 0342-4111 ISSN 1556-1534 (electronic) Springer Series in Optical Sciences ISBN 978-981-13-1431-5 ISBN 978-981-13-1432-2 (eBook) https://doi.org/10.1007/978-981-13-1432-2

Jointly published with National Defense Industry Press, Beijing, China

The print edition is not for sale in China Mainland. Customers from China Mainland please order the print book from: National Defense Industry Press.

Library of Congress Control Number: 2018952903

© National Defense Industry Press and Springer Nature Singapore Pte Ltd. 2018

This work is subject to copyright. All rights are reserved by the Publishers, whether the whole or part of the material is concerned, specifically the rights of translation, reprinting, reuse of illustrations, recitation, broadcasting, reproduction on microfilms or in any other physical way, and transmission or information storage and retrieval, electronic adaptation, computer software, or by similar or dissimilar methodology now known or hereafter developed.

The use of general descriptive names, registered names, trademarks, service marks, etc. in this publication does not imply, even in the absence of a specific statement, that such names are exempt from the relevant protective laws and regulations and therefore free for general use.

The publishers, the authors and the editors are safe to assume that the advice and information in this book are believed to be true and accurate at the date of publication. Neither the publishers nor the authors or the editors give a warranty, express or implied, with respect to the material contained herein or for any errors or omissions that may have been made. The publishers remains neutral with regard to jurisdictional claims in published maps and institutional affiliations.

This Springer imprint is published by the registered company Springer Nature Singapore Pte Ltd. The registered company address is: 152 Beach Road, #21-01/04 Gateway East, Singapore 189721, Singapore

Preface

With the substantial development of modern optoelectronics, optical scan technology has been increasingly applied in the fields of space laser communication, laser radar, satellite remote sensing, directed-energy application and medical detection. Compared with conventional mechanical beam scan systems such as reflective and gimbaled scan systems, the double-prism beam scan system is advantageous in compact structure, small moment of inertia, superior dynamic performance, great operation reliability and high scan precision. As one significant branch in the optical scan field, the beam steering device based on double prisms can offer a quite potential alternative to common beam scanners used for laser communication, airborne laser radar, microstructure processing, biomedicine and military weapons.

Theoretical research on the double-prism scan system is always confronted with the nonlinear relation between prism motion characteristics and beam pointing direction, which produces inherent difficulties in solving forward problem and inverse problem. Unfortunately, most previous studies on forward and inverse beam scan theories are not comprehensive and systematic enough to satisfy the application requirements in practice. In the book, the double-prism multi-mode beam scan model is proposed to help explore the forward and inverse problems for coarse scanning and fine scanning, and the fine scanning theory based on double prisms is demonstrated to achieve beam scan precision better than microradian order. In particular, the inverse solution algorithms are deeply investigated in order to systematize the inverse beam scan theory. The book will enrich the double-prism multi-mode scan theories and pave the new way to accomplish wide-angle and high-precision scanning, which can offer basic support for further applications.

By far, most double-prism scan systems have been implemented for beam pointing or boresight adjustment applications, such as the lasercom test and evaluation station (LTES) developed by Jet Propulsion Laboratory (JPL) under the support of National Aeronautics and Space Administration (NASA), the step-stare imaging system developed by Defense Research and Development Canada (DRDC), and the infrared countermeasure device developed by Optra Incorporation. However, there is a lack of systematic discussion about the beam

vi Preface

scan technology based on double prisms. In this book, the double-prism multi-mode beam scan technology is well demonstrated on the theoretical basis. Particularly, many innovative achievements are presented with emphasis on the double-prism multi-mode scan strategies, beam scan system design and laboratory test on multi-mode beam scan performance. The beam scan laws and characteristics are also investigated through much detailed computation, testing and analysis, which can help improve the double-prism beam scan technology for more possible applications. In addition, a series of optical scan devices that incorporate rotating, tilting or composite-motion double prisms are contrived, accompanied by further research on their critical techniques and beam scan performance.

The author has been devoted to research on laser scanning and tracking technologies over the past decade and has presented some systematic and complete research achievements, especially on double-prism multi-mode scanning concept. This book is the first monograph intended to generalize double-prism multi-mode scan principle and methods, which has been accomplished by combining previous theories and applications with the author's recent studies. Most significant innovations in this book are summarized as follows. The double-prism multi-mode beam scan theory is established to help demonstrate double-prism beam scan region and high-precision radial scan principle. The theoretical model for tilting double prisms is proposed to achieve micro-radian beam scan precision, which enables high-precision beam deflection based on general mechanical structure. An iterative method is developed to solve the inverse problem of rotating double prisms so that the double-prism system can be successfully applied for passive target tracking operation. Inverse solution methods for tilting double prisms are also developed to enrich the high-precision beam scan theory that can be utilized to track arbitrary target trajectories. Several implementation methods for multi-mode beam scanning are designed to overcome the nonlinear motion control problem by means of specific drive mechanisms for double prisms. The performance verification and accuracy test techniques are both demonstrated for double-prism systems. The kinematics simulation method for a large-aperture rotating prism is proposed, together with synthetic analysis on the prism surface deformation due to dynamic loads. This book features its comprehensive contents, logical descriptions and a variety of cases examples to clarify many crucial and puzzling issues. It has been intended to introduce the latest achievements associated with double-prism multi-mode beam scanning principle and methods, which may enable readers to have a systematic, comprehensive and profound understanding about the double-prism multi-mode beam scan systems.

Most work in this book has been supported by National Natural Science Foundation of China (NSFC) (61675155, 51375347 and 50805107), Key Laboratory of Space Laser Communication and Verification Technology of Chinese Academy of Sciences, and Natural Science Foundation of Shanghai. The author would express sincere gratitude to Mr. Liu Liren, Shanghai Institute of Optics and Fine Mechanics, Chinese Academy of Sciences, for his careful guidance, and thank Researcher Sun Jianfeng, Shen Qiande, and Wang Lijuan for their generous assistance. Thanks to Li Tongbao, academician of Chinese Academy of

Preface vii

Engineering for his kind concerns. Thank Dr. Gao Peng, Chinese Academy of Sciences for his great help. This book has been finished under the support of Prof. Shi Laide, Prof. Bian Yongming, A. P. Liu Guangjun, Prof. Liu Zhao and Dr. Zhong Jidong with Tongji University. During the development of this book, Yi Wanli, Sun Wansong, Zuo Qiyou, Gao Xinjian, Liu Xingsheng, Zhang Yang and other students have paid much hard work. This book excerpts from most research articles published by the author team, and some chapters excerpt from the dissertations of some Master graduates, including Jiang Xuchun, Ding Ye, Wang Wei and Gao Xinjian. Thank Sun Yanbing (editor in chief) and other editors of National Defense Industry Press for their substantial support, and thanks to National Defense Science and Technology Publishing Fund.

This book consists of seven chapters. In Chap. 1, the research status of double-prism beam scan technology is reviewed. In Chap. 2, the theoretical modelling of double-prism multi-mode scan system is performed. Chapter 3 presents a deep investigation on the inverse problem of double prism multi-mode scanning. Chapter 4 concentrates on the beam scan performance for double-prism multi-mode scanning. In Chap. 5, the design principle and methods for some typical double-prism scan systems are demonstrated. In Chap. 6, the performance testing on double-prism multi-mode scan systems is introduced. In Chap. 7, the support design technology for a large-aperture rotating prism is established.

The book can provide significant reference for technical personnel and scientific researchers in the fields of photoelectric tracking, optical scanning and industrial dynamic measurement. It may also attract some teachers, students and potential enthusiasts who are interested in optical machinery or precision instrument.

Shanghai, China Anhu Li

Contents

1	Intr	oduction	1
	1.1	Overview of Beam Scan Technology	1
	1.2	Common Beam Scan Methods	2
		1.2.1 Non-mechanical Beam Scan Method	3
		1.2.2 Micro-Opto-Electro-Mechanical Beam Scan Method	4
		1.2.3 Mechanical Method	5
	1.3	Research Status on Double-Prism Multi-mode Scan System	11
		1.3.1 Theoretical Research	11
		1.3.2 Implementation Methods	17
		1.3.3 Practical Applications	20
	1.4	Problems of Double-Prism Multi-mode Scan System	32
	1.5	Main Work of the Book	35
	Refe	erences	36
2	Dou	ble-Prism Multi-mode Scan Theory	41
	2.1	Introduction	41
	2.2	Basic Principle of Double-Prism Multi-mode Scanning	42
		2.2.1 Approximate Solution for Rotating Scan Model	42
		2.2.2 Basic Solution for Tilting Scan Model	44
	2.3	Theoretical Model of Double-Prism Multi-mode Scan System	46
		2.3.1 Rotating Scan Model	47
		2.3.2 Tilting Scan Model	52
	2.4	Scan Region and Scan Precision of Double-Prism Multi-mode	
		Scanning	56
		2.4.1 Rotating Scan Mode	56
		2.4.2 Tilting Scan Mode	62
	2.5	Coordinate Expressions for Scan Points	64
		2.5.1 Rotating Scan Mode	64
		2.5.2 Tilting Scan Mode	67

x Contents

	2.6	Discus	ssion on Distance Between Two Prisms	69
		2.6.1	Rotating Scan Mode	70
		2.6.2	Tilting Scan Mode	70
	2.7	Doubl	e-Prism Multi-mode Scan Analysis	73
		2.7.1	Blind Zone of Rotating Scan Model	73
		2.7.2	Multi-mode Scan Trajectories of Rotating Scan	
			Model	76
		2.7.3	Scan Region of Tilting Scan Model	76
		2.7.4	Multi-mode Scan Trajectories of Tilting Scan Model	83
	2.8	Multi-	prism Scan Model	85
		2.8.1	Theoretical Model	85
		2.8.2	Coordinate Expressions for Scan Points	86
		2.8.3	Scan Region of Rotating Triple Prisms	88
		2.8.4	Multi-mode Scan Trajectories of Rotating Triple	
			Prisms	90
	2.9	Summ	ary	90
	Refe		·····	93
•				95
3			oblem of Double-Prism Multi-mode Scanning	
	3.1		e Solution for Rotating Double Prisms	95 95
		3.1.1 3.1.2	Two-Step Method	93 104
			Lookup-Table Method	
		3.1.3	Iterative Method	123
	2.0	3.1.4	Damped Least-Squares Iterative Method	132
	3.2		e Solution for Tilting Double Prisms	138
		3.2.1	Analytical Method	138
		3.2.2	Lookup-Table Method	141
		3.2.3	Binary Lookup-Table Method	145
	2.2	3.2.4	Region-Converging Iterative Method	148
	3.3		ary	151
	Refe	erences		151
4	Perf	orman	ce Characterization of Double-Prism Multi-mode	
	Scar	ning .		153
	4.1	Nonlir	nearity Issue	154
	4.2	Singul	arity Issue	158
	4.3	Beam	Distortion	160
		4.3.1	Rotating Scan Mode	160
		4.3.2	Tilting Scan Mode	169
	4.4	Error 1	Modeling for Double-Prism Multi-mode Scanning	171
		4.4.1	Pointing Error Caused by Prism Assembly	172
		4.4.2	Pointing Error Caused by Bearing Assembly	178
	4.5	Summ	ary	181
	Refe			182

Contents xi

5	Desi	gn of E	Oouble-Prism Multi-mode Scan System	183
	5.1	Config	guration	183
	5.2	Motion	n Mechanism	186
		5.2.1	Rotating Double Prisms	186
		5.2.2	Tilting Double Prisms	189
	5.3	Design	of Rotating Double-Prism Scan Device	193
		5.3.1	Design Requirements	193
		5.3.2	Mechanical Structure Design	194
		5.3.3	Control System Design	195
		5.3.4	Assembly Error Analysis	198
		5.3.5	Beam Scan Property and Test	205
	5.4	Design	of Tilting Double-Prism Scan Device	206
		5.4.1	Design Requirements	206
		5.4.2	Motion Law of Two Prisms	206
		5.4.3	Cam-Based Oscillating Mechanism	207
		5.4.4	Mechanical Structure Design	211
		5.4.5	Kinematics Simulation and Analysis	212
		5.4.6	Scan Error Analysis	214
		5.4.7	Influence of Scan Speed on Scan Trajectory	216
	5.5	Design	n of Composite Motion Double-Prism Scan Device	218
		5.5.1	Design Requirements	218
		5.5.2	Layout Scheme of the System	218
		5.5.3	Analysis on the Center of Gravity	219
		5.5.4	Design of Drive Mechanism	222
		5.5.5	Kinematics Simulation and Analysis	225
		5.5.6	Scan Error Analysis	230
	5.6	Summ	ary	234
	Refe	erences		235
6	Perf	ormana	ce Test on Double-Prism Multi-mode Scan System	237
Ů	6.1		uction	237
	6.2		mance Test on Rotating Double Prisms	238
	0.2	6.2.1	Hardware of the Test Platform	238
		6.2.2	Software of the Test Platform	240
		6.2.3	Multi-mode Scan Performance Test	243
		6.2.4	Lookup-Table Method Validation	250
	6.3		mance Test on Tilting Double Prisms	259
	0.5	6.3.1	Test on Tilting Accuracy, Reduction Ratio	237
		3.3.1	and Beam Deflection Range	259
		6.3.2	Test on Beam Deflection Accuracy	262

xii Contents

	6.4	Laser	Coarse-Fine Coupling Tracking Test on Double	
		Rotati	ng Risley-Prism Pairs	265
		6.4.1	Hardware of the Test Platform	266
		6.4.2	Performance Test on Coarse-Fine Coupling Tracking	267
	6.5	Summ	ary	270
	Refe	erences		270
7	Sup	port De	esign Technology of Large-Aperture Prism	271
	7.1	Design	and Analysis of Multi-segmental Support	271
		7.1.1	Radial Multi-segmental Support	272
		7.1.2	Three-Segmental Support Analysis	274
		7.1.3	Multi-segmental Support Analysis	282
		7.1.4	Extension of Multi-segmental Support	284
	7.2	Dynar	nic Performance Analysis	287
		7.2.1	Dynamic Analysis Method	287
		7.2.2	Dynamic Simulation and Analysis of Rotating Prism	288
	7.3	Defon	nation Value Fitting of Prism Surface	295
		7.3.1	Zernike Polynomial Fitting Theory	296
		7.3.2	Surface Fitting	301
	7.4	Summ	ary	310
	Refe	rences		310

About the Author

Anhu Li received Ph.D. in Optical Engineering from Shanghai Institute of Optics and Fine Mechanics, Chinese Academy of Sciences. He is currently a Professor with Tongji University, China. He has led over ten important scientific research projects in the laser tracking fields and also developed many precision optical tracking and test devices. He has published more than 70 articles in several journals including Optics Express, Applied Optics, Optics and Laser Technology, Optical Engineering, Optik, Optica Applicata, Chinese Optics Letters, International Journal of Advanced Manufacturing Technology, Journal of Mechanical Engineering and Proceedings of SPIE. He is an active reviewer for over ten international journals. His research interests include optical scanning, laser tracking, optical test, opto-mechanical integrated design and analysis, and optical instrument.

Chapter 1 Introduction



Abstract An overview of beam scan technology is presented with most emphasis on those common beam scan methods, among which the refractive method using Risley prisms is further investigated. Previous studies on double-prism systems are systematically introduced, which concentrate on the theoretical research and implementation methods required for practical applications such as high-precision beam alignment, multi-mode target tracking and imaging boresight adjustment. Several prevalent problems that need be settled in double-prism systems are clarified, including inverse solutions, beam scan errors, blind zone, control singularity, nonlinearity issue, beam distortion and chromatic aberration. Accordingly, the framework of this book is well organized.

1.1 Overview of Beam Scan Technology

Beam scanning is the technology to change the location of laser beam on the scanned surface according to a desired propagation path, which can be accomplished by the use of mirrors, prisms, lenses, rotating diffraction gratings or by changing the refractive index of transmitted medium. The beam scan device is an integrated system of optics, mechanics, electronics, automation, sensing, detection and communication. It has been increasingly applied for space communication, infrared countermeasures, search and rescue, microscopic observation, industrial measurement, automation equipment and machine vision [1–3]. With the substantial development of industrial technologies, more advanced application requirements motive the improvement of beam scan performance, such as scan coverage, scan precision and dynamic characteristics.

In the fields of free-space laser communication, infrared countermeasures, laser radar, space observation and industrial automation, the beam scan technology has shown great application potential for high-precision dynamic scanning, target tracking and imaging boresight adjustment [4–6]. The common beam steering approaches can be divided into three types of gimbaled mirror, reflective rotating mirrors and refractive rotating mirrors, including mechanical mirror-based gimbals, beam

director units, polygonal mirror mechanisms, Risley prisms, phased-array optics, and micro-electro-mechanical systems (MEMS) using micro-mirrors. Because of the large moment of inertia and poor dynamics, a gimbaled mirror cannot offer the optimal choice to meet those high-precision control requirements. In contrast, reflective rotating mirrors are usually coupled with motors or driven by piezoelectric ceramics (namely voice coil motors) to accomplish beam scan function. For example, Physik Instrumente and Ball Aerospace have applied a series of tracking mirrors for coarse-fine tracking operation in laser communication systems and for wavefront curvature compensation in space telescopes [7, 8]. However, the beam deflection angle is twice as much as the rotation angle of a reflective mirror, and the mirror-based system requires too much working space to achieve large optical aperture.

Compared with the above conventional beam scan mechanisms, the scan mechanism based on refraction theorem can offer not only the outstanding capability of beam steering and boresight adjustment but also the superior dynamic performance. A typical refractive beam scanner consists of rotating double prisms which can perform coaxial and independent rotation to change the beam propagation path for beam pointing applications [9]. Such a beam scanner has the advantageous of compact structure, high accuracy, rapid response, low optical consumption and low cost. In principle, the use of refractive prisms can reduce the sensitivity of beam deviation angle relative to each prism orientation. Therefore, the mechanical transmission errors should have relatively less impacts on the beam scan precision. Refractive prisms are especially suitable for those high-precision scan applications using monochromatic beam, where several important issues to be solved include beam steering mechanism, beam scan mode and prism rotation control.

By far, the beam scan technology is always confronted with the following technical difficulties. The first difficulty lies in wide-range and high-precision beam scan technique, which requires both global beam scanning over wide range and local beam scanning with high precision. The second difficulty involves dynamic time-varying target tracking technique that explains how to control the beam scan operation to track a transient target under complicated environment. The third difficulty is about high-precision spatial orientation technique, where the beam scan mechanism and control method should be innovated in principle to achieve directional beam scanning with better precision than those conventional technologies. Any breakthrough for the above difficulties can significantly promote the development of photoelectric scanning and tracking technology, which will account for the progress in national defense, industrial equipment and other related fields [10].

1.2 Common Beam Scan Methods

Basically, a beam scan device is composed of laser source, optical modulator, beam scanner, optical receiver and controller. The beam scanner, also called beam deflector, is the most important component in a beam scan device.

There are various beam deflectors based on different beam steering principle and methods, such as acousto-optic deflectors, electro-optic deflectors, micro-opto-electro-mechanical deflectors, polyhedral reflectors, rotating prisms and tilting prisms. In general, these beam scan methods fall under three categories, namely non-mechanical method, micro-opto-electro-mechanical method and mechanical method [10].

1.2.1 Non-mechanical Beam Scan Method

1. Acousto-Optic Beam Scan Method

Acousto-optic beam deflector is based on the principle of acousto-optic deflection. The drive source is used to input a radio-frequency power signal into the transducer, where the electric signal can be converted to an ultrasonic signal and transmitted into acousto-optic medium. The ultrasonic grating in the medium is then generated from the elastic-optic effects due to mechanical stress wave, thereby leading to the diffraction of incident laser beams.

In 1967, Dixon developed an acousto-optic tunable filter based on acousto-optic interaction in the anisotropic medium [11]. In 1992, Lincoln Laboratory firstly explored the beam control method using non-mechanical devices and applied an acousto-optic deflector for laser beam tracking [12]. Brimrose Corp. proposed the TeO₂-based acousto-optic deflector that could achieve about 50 μ s response time and only 0.5 W power to perform beam scanning across a 40 mrad range [13]. In 2006, Wen implemented beam scanning operation for 42 resolvable spots over a 9.048 mrad range [14]. In 2012, China Electronics Technology Group Corp. employed ZnO piezoelectric films to achieve the maximum beam steering angle of 5.7° [15].

Without mechanical motion components, the acousto-optic beam scan device can feature small volume, light weight, low driving power, good compatibility with computers and automatic control. However, there are inevitable shortcomings such as low beam transmittance, small clear aperture, limited scan coverage and low diffraction efficiency. In addition, most existing models for acousto-optic scan analysis have never considered the influence of ultrasonic absorption, uneven ultrasonic distribution and other factors on the diffracted beam.

2. Electro-Optic Beam Scan Method

Electro-optic beam deflector can steer the laser beam on the basis of electro-optic effect. At present, the main methods to perform electro-optic beam deflection rely on the optical-phased-array (OPA) technology, which was firstly proposed in 1971. Meyer developed a one-dimensional OPA device using the lithium tantalite phase modulator, which could operate in a 0.5 mm period and a spectral region within 800 times the optical wavelength in order to perform beam deflections across a 0.073° range. Compared to mechanical beam scan methods, the OPA technology is advantageous in random access, high resolution, high accuracy and rapid positioning. The

working principle of OPA is mainly in the constructive and destructive interference for light waves, where the phase modulation can be accomplished by means of liquid crystals, optical waveguide arrays, electro-optic crystals, electro-optic ceramics and electro-humidity transducers [16].

In addition, magneto-optic deflector can be utilized for beam deflection due to the impacts of beam polarization state and additional magnetic field. It is evident that the magneto-optic effect will result in the same disadvantages as the electro-optic effect, such as poor beam transmission quality and insufficient clear aperture [15]. Also, there are some immature technologies that require further investigation.

Generally, the non-mechanical beam scan device can offer the benefits of compact structure, sensitive response, light weight, low power consumption, no moment of inertia, nanosecond scan speed and random access. Such a beam scan device should remove many limitations of mechanical beam control methods and further improve the performance of optical system, including agile beam control, programmable beam scanning, multi-beam generation and electron lensing. Therefore, the breakthroughs in non-mechanical beam scan technologies have produced significant impacts on the development of high-performance laser radars and photoelectric sensors.

1.2.2 Micro-Opto-Electro-Mechanical Beam Scan Method

The core idea of beam scan method based on micro-opto-electro-mechanical system (MOEMS), namely using an array of actuators to change the shape of a mirror, dates back to the second century A.D., when Archimedes planned to destroy enemy ships using solar heat. In his description, the shaped mirror incorporated an array of polished metal plates, and the actuators were a group of Greek citizens to simultaneously adjust their mirrors such that the cumulative reflected sunlight could converge to a common focal point on the enemy ship, setting it aflame [17]. Modern MOEMS beam scan technology has been flourishing since 1980s. In 1982, Petersen [18] proposed a silicon-based MOEMS for beam scanning, according to his in-depth investigation on the mechanical and electronic properties of silicon material. Compared with traditional beam scan systems, the MOEMS beam scanner is particularly prominent in dynamic response and power consumption. In addition, the MOEMS is attractive due to compact size, low cost, great potential for mass production, as well as superior optical and mechanical properties. With the substantial development of manufacturing process, the MOEMS beam scan technology has been applied for barcode scanning, high-resolution imaging, and laser confocal microscopy. Now available MOEMS products include optical switch, optical attenuator, optical scanner and optical display based on digital micro-mirror device.

There are different drive methods used for MOEMS beam scanning, such as electrostatic drive, electromagnetic drive and thermal drive. The electrostatic drive method is usually accomplished by means of plate capacitors, which features simple principle and strong operability. For a MOEMS beam scan device using electrostatic drive method, the common electrode attached to the substrate surface and a

plurality of regularly arranged electrostatic driving membranes can function as two electrodes of plate capacitor, respectively. Once the control voltage is applied to a mirror unit, there will be concave deformation on the corresponding membrane due to electrostatic attraction, which leads to downward movement of the mirror unit. Independent movements of multiple mirror units can result in the entire deformation of a deformable mirror, thereby enabling beam deflection within a small angular range [19].

Earlier developed MOEMS reflector arrays can only perform one-dimensional beam scanning with relatively poor accuracy but cannot accomplish phase control function. Two one-dimensional MOEMS are required to achieve beam scanning in horizontal and vertical directions, respectively, which accounts for the system with large physical dimensions, complicated drive programs and low scan speed. Recently, the two-dimensional MOEMS scan mirror has been proposed for horizontal and vertical beam scanning, which can avoid the coupling effects among optical components to improve beam scan speed. For example, Wu et al. [20] reported a 4×4 phased array of micro mirrors based on piston-tip-tilt MEMS using electrothermal drive, where each mirror had $0.5 \, \text{mm} \times 0.5 \, \text{mm}$ clear aperture. Under $5 \, \text{V}$ DC voltage, this system could achieve two-dimensional beam scanning across a range of over 30° .

Since the MOEMS beam scan technology is advantageous in its capability of accurate beam control in time and space, compact structure and low power consumption, it can offer a promising beam scan approach for optical communication, military photoelectric reconnaissance, autonomous space rendezvous, laser rangefinder, laser guidance, warning and monitoring system and spacecraft miniaturization. However, there are several complications that may prevent the MOEMS beam scan technology from further applications, including the shortage of fundamental research on MOEMS, the difficulties in micro fabrication and packaging processes, the lack of system-level performance testing methods, the low testing efficiency and inconsistent evaluation standards.

1.2.3 Mechanical Method

1. Gimbaled Method

For a gimbaled beam scanner, the laser source should be mounted on a rotary gimbal to achieve two-dimensional scanning across a wide range [15]. In many applications where the scanner has large volume and heavy weight, the drive mechanism is required with relatively large power. Moreover, there are inherent problems such as coupling motion, coupling inertia, and wire-wound moment interference that may limit the dynamic performance of a gimbaled scanner [21, 22].

Figure 1.1 shows two typical gimbaled beam scanners. Figure 1.1a gives a threedimensional model of coarse tracking turntable for the scan telescope applied in laser communication terminal at a long link distance. Such a scan telescope is viable to

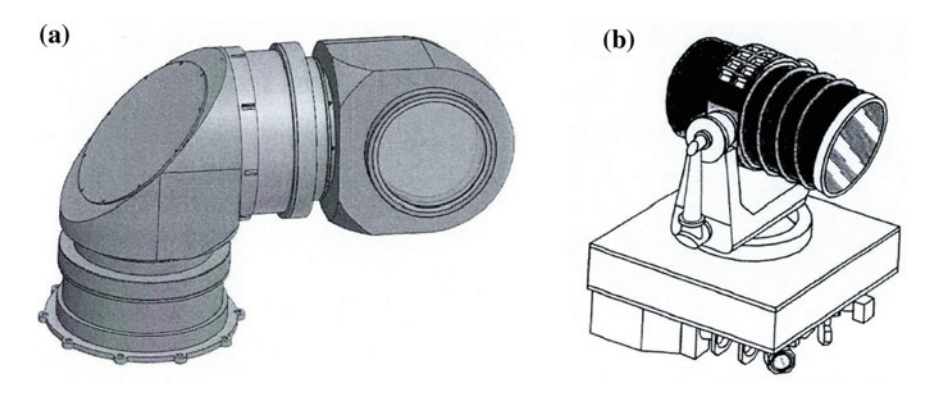


Fig. 1.1 Two gimbaled beam scanners. a coarse tracking turntable in scan telescope; b LCT structure diagram

scan and point within a hemisphere or even a larger three-dimensional space. Usually, the terminal is installed on a satellite platform and the base of turntable is fixed to the satellite. The pitch axis of the turntable is parallel to the equator plane, while the azimuth axis is perpendicular to the equator plane. Beacon light from another communication terminal can be captured through two-dimensional scan motion of the turntable. The captured beacon light will be reflected into the optical system by a mirror. The mirror should rotate according to the target missing distance reported by the optical system such that the reflected light beam is irradiated into the fine tracking field of view (FOV) and stabilized at the FOV center as much as possible. If the optical axis for communication is deviated due to the mutual movement of two terminals, the telescope system can perform active adjustment according to the change of target missing distance. Figure 1.1b presents the Laser Communication Transceiver (LCT) system for laser communication on the space station, developed by Goddard Space Flight Center (GSFC). This system is based on a Cassegrain-structure telescope, where the primary mirror is a concave mirror with large diameter, and the secondary mirror is a convex mirror of small size. The third plane mirror is used to guide the beam from the gap of horizontal axis. The beam is then reflected downwards by another plane mirror and turns into a parallel beam that propagates to the optical base station. The optical path transmitted in the servo turntable, named Coude path, is common for transmission and reception. The remaining parts of the system has been integrated inside the base station, including laser transmitter, capture detector, tracking detector and laser receiver [23].

2. Reflective Method

For reflective method, the beam path is deflected by rotating a mirror mounted in front of the laser source. The mirror can be a plane mirror, a spherical mirror or a polyhedral mirror [15].

Beam canners must have two degrees of freedom to implement two-dimensional scan function. It is possible to realize two-dimensional beam scanning with only one

mirror, which features simple structure, poor flexibility and coupling effects at high scan speed. As shown in Fig. 1.2, the addition of mirrors can offer more freedom and improve the flexibility of the system, but the system control will become more complicated as a result. Since a scanner composed of one or two mirrors changes the optical axis of the system, three or four mirrors should be used to keep the optical axis unchanged, as shown in Fig. 1.2b and c [21].

As shown in Fig. 1.3a, a viable reflective scan system is employed to measure the diameter of an aerial cable [24]. The device incorporates a planar mirror, a spherical mirror and a polygonal mirror. Figure 1.3b offers a beam scan example using two-axis rotating mirror and f- θ scan objective lens. As the scan mirror is controlled to rotate at a specific angular speed, the scan beam will generate a trajectory in terms of a certain functional relation. A combination of more scan mirrors can lead to much richer beam scan trajectories. But the coupling effects among these scan mirrors maybe occur at high scan speed [15].

Figure 1.4 shows a typical laser scan imaging system using a rotating polygonal mirror [25]. The spatial direction of a modulated beam is changed with high-speed rotation of the polyhedron mirror. The beam converges through the lens to form a one-dimensional or two-dimensional scanned image on the imaging plane. Usually, the system can produce a telecentric beam path to guarantee the axial parallelism of emergent beam. In an ideal case, each reflection surface of the polygonal mirror can steer the beam across an angular range of $4\pi/N$, where N denotes the number of polygonal reflection surfaces. The rotating polygonal beam scanner is advantageous in high scan speed, wide scan range and motion stability. For an imaging system using the polygonal beam scanner, the polygonal mirror is often placed in front of the imaging objective lens such that the modulated beam can form a scan pattern or image on the imaging plane after transmitting through polyhedral mirror and objective lens. Now that beam scan operation is performed before objective lens, this system can realize linear beam scan function by means of objective lens design [25].

Reflective beam scan method requires simple structure and easy implementation to enable its widespread applications. However, the beam scan precision is rather sensitive to mechanical errors and rotation angle errors because the angle between incident beam and reflected beam is twice as much as the incidence angle of beam path, which may confine high-precision beam control to some extent. Due to the structure layout of reflective scanner, there should be a long distance between the scanner and the measured target, which claims more severe requirements for the clear

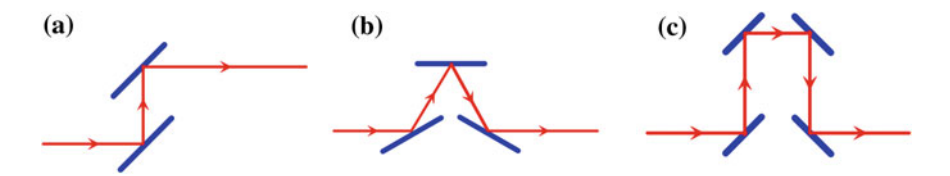


Fig. 1.2 Different mirror combinations. a two-mirror combination; b three-mirror combination; c four-mirror combination

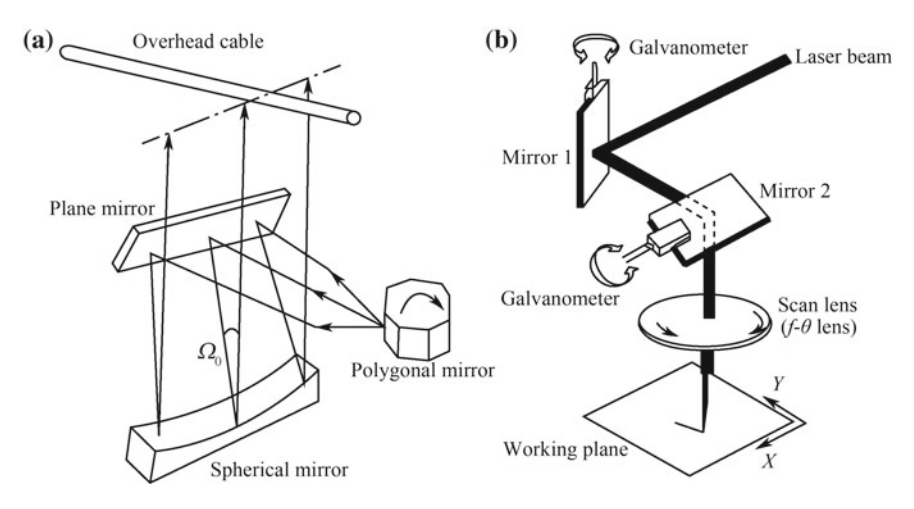
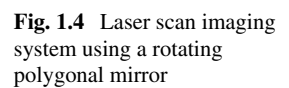
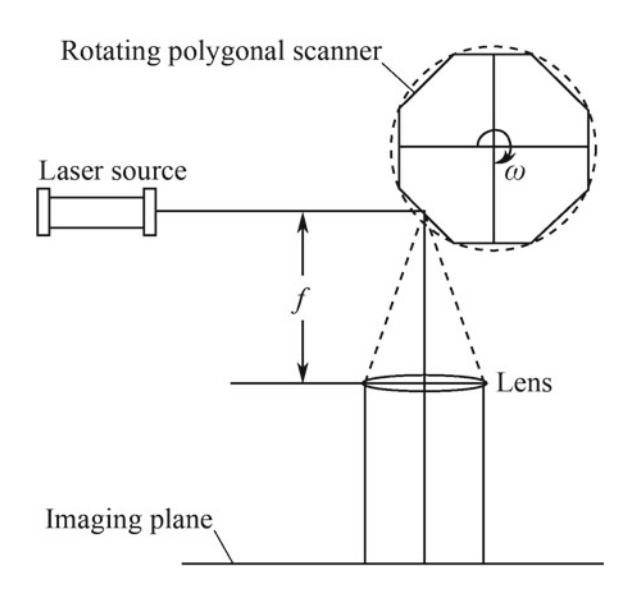


Fig. 1.3 Reflective beam scan system. a scan system using spherical mirror; b two-axis system using f- θ scan objective





aperture of optical elements. Therefore, the reflective method is suitable for some specific applications where small clear aperture is required.

3. Compound Axis System

In the Pointing-Acquisition-Tracking (PAT) system for inter-satellite laser communication, the PAT performance is generally controlled with a compound axis system, which incorporates a coarse aiming mechanism, a fine aiming mechanism and a

pre-aiming mechanism. The beam deflection is mainly accomplished by two-axis or three-axis gimbaled frame, Cassegrain telescope and fast tilting mirror mechanism.

In the coarse aiming mechanism, a transponder antenna (Cassegrain telescope) is mounted on an inner gimbaled frame, and two motors on the gimbaled frame are used to drive the rotation of pitch axis and azimuth axis to achieve beam scan function. One advantage of this method is that a large field of view can be obtained through smart control. Unfortunately, there are some significant shortcomings for this method, such as relatively poor dynamics, great power consumption and large size of drive mechanism. In addition, the bearing friction induced by coarse aiming mechanism is one of the primary factors that affect beam scan performance and target tracking accuracy.

The fine aiming mechanism is mainly composed of a two-axis or three-axis fast tilting mirror, a piezoelectric ceramic actuator (or voice coil motor), a tracking sensor and a position sensor. The fast tilting mirror in a closed control loop can track the incident beacon light according to the error signal from fine tracking detector, thereby forming a loop for fine tracking. This fine tracking loop can determine the accuracy of the overall system and thus require wide bandwidth. The pre-aiming mechanism can also perform beam deflection using a tilting mirror, which should be planned to pre-deflect the emergent beam with an angle corresponding to the incident beam. Figure 1.5 shows the structure of a fast tilting mirror. The mirror can be driven by two piezoelectric ceramics distributed on the rotating axes, each of which consists of a flexible hinge mechanism. Once a piezoelectric ceramic outputs a displacement signal, the fast tilting mirror will produce a certain beam deflection. Different from traditional tracking systems with large inertia and low bandwidth, the two-axis fast tilting mirror offers smooth motion, no gap, no mechanical friction and high displacement resolution. The beam deflection range can be up to milliradian level, the beam deflection accuracy can reach microradian level, and the response frequency is of kilohertz order. That is, the available bandwidth and tracking accuracy have been greatly improved [15].

4. Refractive Method

The refractive method can be performed through rotating or tilting optical elements to change the beam pointing. For example, Fig. 1.6 presents three common beam scan schemes using one or two refractive prisms [15]. Figure 1.6a is a layout diagram of rotating single prism, Fig. 1.6b is a layout diagram of tilting double prisms around two parallel axes, and Fig. 1.6c is a layout diagram of rotating double prisms.

The presented double-prism multi-mode scan system in the book is a typical refractive beam steering system, which usually consists of two wedge prisms, namely Risley prisms. Based on the refraction theorem, two prisms can change the direction of transmitting beam through their rotating or tilting motion, which enable two-dimensional beam scanning across a certain angular range. The rotating double-prism beam scan system can change the beam propagation path by the coaxial and independent rotation of two prisms. Thus, the beam deviation or boresight adjustment is performed within a large cone region. The tilting double-prism scan system can achieve beam deviation within a smaller range by tilting two prisms in an orthogonal

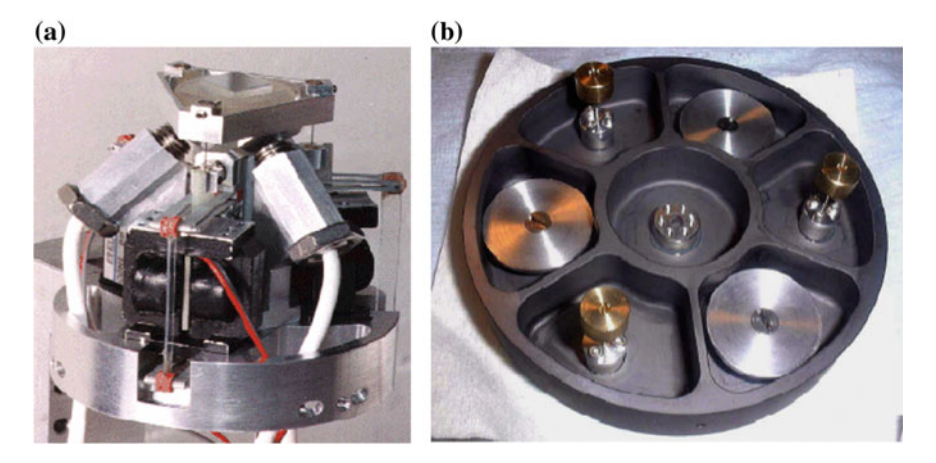


Fig. 1.5 Two-axis fast tilting mirror. a piezoelectric ceramic structure; b back view of tilting mirror



Fig. 1.6 Common refractive beam scan schemes using a rotating single prism, b tilting double prism and c rotating double prisms

configuration. Due to a large reduction ratio from the tilting angle of each prism to the beam deviation angle, it is possible to accomplish high-precision beam scanning with general mechanical setup [10, 26].

Another type of refractive beam scanner is based on the equivalent prism composed of a flat-concave lens and a convex-flat lens with the same radius of curvature [27, 28]. As shown in Fig. 1.7a, the combination of two lenses do not change the beam propagation path when the flat surfaces of two lenses are placed parallel to each other. In Fig. 1.7b or c, the first lens is kept stationary, and the second lens rotates about its center of curvature. Therefore, the two lenses can be equivalent to a prism with adjustable wedge angle and principal cross section. If each lens is of cylinder shape, one scanner can only steer the beam in one direction, and two scanners are required to perform two-dimensional beam scanning. In addition, a beam scanning composed of two spherical lenses can also achieve two-dimensional beam scanning.

The advantage of the above scheme is that the rotation angle of the lens is linear with respect to the beam deviation angle. But for automatic beam scan applications, the mechanical structure is complicated and the beam scan range is relatively small. Furthermore, it is difficult to fabricate a lens with cylindrical or spherical surface, and the fabrication accuracy may be limited.

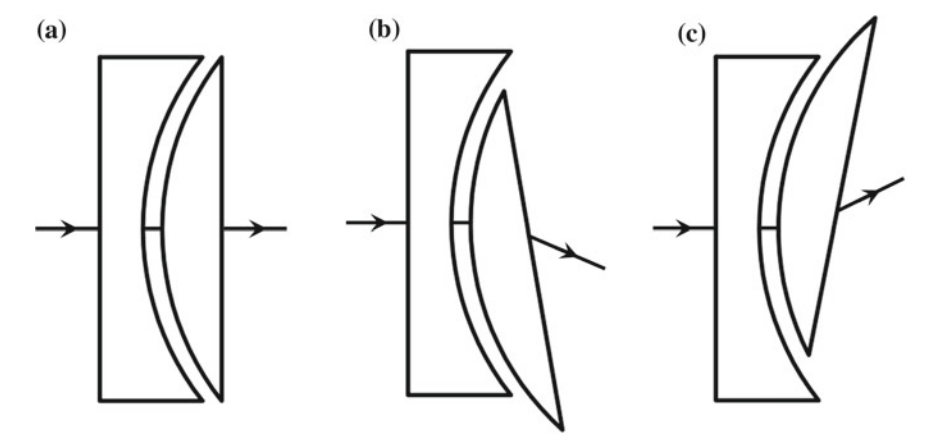


Fig. 1.7 Beam scan principle using adjustable prism, where **a** the prism is at the initial orientation, **b** the prism rotates counterclockwise, and **c** the prism rotates clockwise

1.3 Research Status on Double-Prism Multi-mode Scan System

1.3.1 Theoretical Research

Rotating double-prism system is an extension of the Risley-prism-based scan technique [29, 30]. The original Risley prisms refer to a pair of wedge prisms that can only deflect laser beam within a small angular range. Nowadays, rotating double prisms can achieve wide-angle beam pointing and scanning due to the rapid progress of prism processing technique. The beam deflection resolution and accuracy of rotating double prisms are further improved with the substantial development of precision machinery and control algorithms [31]. Consequently, the theoretical research on rotating double-prism system has mainly focused on beam steering mechanism, beam scan mode and beam scan performance.

1. Forward and Inverse Solutions

The study of beam steering mechanism relies on the relation between the orientations of two prisms and the pointing direction of emergent beam or the target position. There are two essential problems encountered in the discussion about beam steering mechanism, called forward problem and inverse problem [10, 32, 33]. The forward problem is about how to determine the pointing direction of emergent beam and the target position according to the given motion laws of two prisms, namely how to deduce the pitch angle and azimuth angle of emergent beam as well as the target coordinates from the rotation or tilting angles of two prisms. Contrarily, the inverse problem requires the motion state of two prisms for the desired beam pointing direction or target position. In other words, the rotation or tilting angles of two prisms

need be obtained with the prior knowledge of the pitch angle and azimuth angle of emergent beam or the target coordinates. Exact solution to the forward problem is beneficial to explore the beam steering mechanism based on double prisms, which can provide the prerequisite and foundation for beam pointing applications. As the reverse process of forward solution, the solution to the inverse problem plays a significant role in optical scanning and target tracking applications.

In 1985, Amirault and DiMarzio [34] firstly presented a two-step method to solve the inverse problem of rotating double prisms, which can simplify the variables involved with inverse solution and reduce the complexity of computation.

In 1995, Boisset et al. [35] used first-order paraxial theory to derive the approximate expression for the pointing direction of emergent beam. An iterative method was then proposed to find out the inverse solution, which can determine prism orientations according to the measurement information in a closed-loop system. Unfortunately, this iterative method may fail in many practical applications owing to its dependence on the measurement data from detector.

In 2002, Degnan [36] employed paraxial ray matrices to describe the beam propagation through Risley prisms. He further developed an analytic method that can solve the inverse problem without any iterative algorithm. This method is still based on the first-order paraxial approximation, which may generate great errors when used for wide-angle beam deviation. Therefore, the method works only when each prism has quite small wedge angle or refractive index.

In 2007, Tao and Cho [37] performed rigorous ray tracing procedure through rotating double prisms to obtain the exact expression for target position, where the influence of all system parameters was under consideration. As for inverse solution, a numerical iteration algorithm based on the damped least-squares method was thoroughly presented regardless of its much complicated computation.

In 2008, Yang [32] also applied the non-paraxial ray tracing method for the analytical formulae that can be used to calculate the pointing direction of emergent beam from the given orientations of two prisms. Such a forward solution requires tedious computation and is usually accomplished by computer programming in practice. Using an explicit Jacobian matrix, Yang implemented the trust region method and original Newton method to solve the inverse problem through numerical iteration. The simulation results for a specified rotating double-prism system have indicated that the Newton method can achieve higher convergence rate and greater robustness than the trust region method.

In 2009, Tirabassi and Rothberg [38] suggested a vector description of Snell' law to enable the concise expression for the exiting point of emergent beam as well as the beam scan point.

In 2011, Jeon [39] generalized a first-order formula approximate to the forward solution, which was obtained by representing the beam deviation due to double prisms with the product of rotation matrices. It turns out that the first-order approximation can generate high-precision scan patterns in good agreement with the exact solution obtained from Snell's law. Using the series expansion of the product of rotation matrices, this method can also be applied to the system comprising an arbitrary number of Risley prisms.

In the same year, Li [40] expanded the exact forward solution for emergent beam into a power series to help perform numerical comparison among the prediction results of first-order, second-order and third-order approximations. On the basis of the most accurate third-order approximation, an inverse solution was further derived with greatly improved solving accuracy. Moreover, Li [41] presented non-paraxial vector expressions for the emergent beam from rotating double prisms under four different configurations. Then the two-step method was demonstrated in detail to formulate the inverse solution, accompanied by an example of determining two prisms' orientations according to the given target trajectory. Even though this method requires rather simplified computation to obtain the analytical inverse solution, it cannot offer exact solution to the inverse problem under any near-filed condition, where the beam exiting position from the system has significant impact on the beam scan position.

In 2013, Zhou et al. [6] applied the first-order approximation method and the non-paraxial ray tracing method to solve the forward problem of rotating double prisms. The comparison results have shown that the non-paraxial ray tracing method can well describe the beam steering mechanism of the system, while the conventional first-order approximation method may generate forward solution that disagrees with the experiment data. Generally, the difference between first-order approximation and experiment data becomes more obvious as the beam deviation angle increases. For any wide-angle beam steering system based on rotating double prisms, the non-paraxial ray tracing method offers a more effective and accurate approach to develop the forward solution.

2. Beam Scan Mode

In order to explore Risley-prism-based beam scan modes, it is necessary to reveal the intrinsic connection of the beam scan trajectory with the structural parameters and motion characteristics of the system. Also, the beam scan error requires comprehensive analysis to provide available guidance for the mechanical setup and motion control scheme [33, 42].

In 1999, Marshall [43] presented systematical research on the beam scan modes originated from rotating double prisms, using the first-order paraxial approximation method. By selecting particular values for the individual wedge angles, angular velocities and initial orientations of two prisms, any specific beam scan pattern may be produced as required in practical applications. However, the first-order approximation can only generate approximate scan patterns without considering the influence of all system parameters, such as the spatial distances among two prisms and the receiving screen.

In 2011, Li [40, 41] applied the non-paraxial ray tracing method to derive the general expression for beam scan pattern. The third-order theory for beam scan mode was then established on the series expansion of beam pointing expression. Further comparison between the approximation of different orders and the exact forward solution has been performed in both near field and far field. It turns out that (i) the difference between the beam pointing angle obtained by approximation and the one obtained by exact solution is relatively small but cannot be ignored in near field, (ii) the beam scan error resulting from third-order approximation is rather less than

the one resulting from first-order approximation, and (iii) there will be larger errors in both first-order and third-order approximation as the wedge angle of either prism increases.

In the same year, Jeon [39] constructed rotation matrices to help simulate the beam scan patterns under different ratios of angular velocities and different rotary directions of two prisms. The beam scan mode was also demonstrated for the combination of an arbitrary number of prism elements, as exemplified by the four-element Risley prism system shown in Fig. 1.8. Nevertheless, this method is still based on the first-order approximation which accounts for an inevitable beam scan error.

In 2012, Horng and Li [44] investigated the most prevalent error sources, from component errors to misalignment errors, and their impacts on the beam scan precision of rotating double prisms. It has been found that some slight errors in the structure and motion parameters of each prism can lead to significant changes in beam scan mode. Furthermore, the misalignment error of the rotation axis of any component with respect to the optical axis of the system may result in a severe decrease of beam pointing accuracy.

In 2013, Schitea et al. [45] modeled rotating double-prism system in Catia V5R20 and generated a variety of beam scan patterns upon introducing difference to the angular velocities and geometrical parameters of two prisms. Such beam scan patterns are useful for the parameter selection of rotating double prisms in practice.

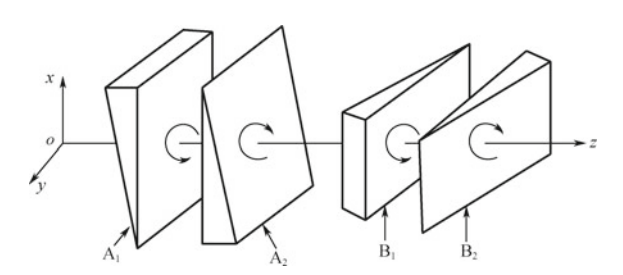
3. Beam Scan Performance

Based on the above forward and inverse solutions, many researchers have further studied beam scan performance of the double-prism multi-mode scan system, mainly including beam distortion, image deformation, chromatic aberration and its calibration.

In 2005, Schwarze et al. [31] investigated the beam compression effect produced by rotating double prisms, which was quantified with a compression factor in roughly inverse proportion to the cosine of the angle between the emergent beam and the emergent surface normal. Without compensation, the compression effect would lead to lower power density in an infrared countermeasure system and smaller signal-to noise ratio in a laser communication system.

In the same year, Sun et al. [46] also discussed the distortion of beam shape by means of the vector refraction theorem. It has been elucidated that the emergent beam distortion depends on the relative rotation angle of two prisms. In most cases, the beam shape is compressed in some directions but stretched in other directions.

Fig. 1.8 Four-element Risley prism system



However, the beam is purely compressed in one direction when two prisms are at the same orientation, and there is no beam distortion when the relative rotation angle of two prisms is 180° .

In 2007, Lavigne and Ricard [47] applied a 3D refraction model to help characterize the image deformation resulting from rotating double prisms. Since the light beam may enter the imaging field of view in different directions, the beam deviation is not uniform over all image pixels and then contribute to prismatic-like image distortion. In order to take the beam deviation at each pixel into account, the 3D refraction model was utilized to modify the linear homographic transformation. Experimental results have confirmed that the modified transformation can well improve the real-time calibration method for distorted images.

In 2012, Ostaszewski et al. [29] presented several pictures of the transmitted beam profile at 0°, 45° and 60° deviation angle, which indicated that the beam could be more distorted at a larger deviation angle. Moreover, it has been clarified that the beam distortion will introduce uneven distribution of the light intensity at a distant terminal, which cannot be avoided for any refractive beam scanner with planar optics.

In 1999, Curatu et al. [48] suggested that the achromatic prisms made of different materials could offer compensation for the chromatic aberration induced by a rotating prism. An achromatic Si–Ge combination was firstly considered to correct chromatic aberration in the 3–5 μm spectral region. In order to reduce the secondary spectrum resulting from two-prism doublet, a three-prism triplet was further proposed on the basis of the apochromatic CaF2–ZnSe–Ge combination. The chromatic focal shifts of a single Ge prism, an achromatic Si–Ge prism and an apochromatic CaF2–ZnSe–Ge prism were respectively 300, 1.43 and 0.7 μm for the demanded beam deviation. In addition, the achromatic prisms operating in the 8–9.5 μm spectral region were developed and optimized with a commercial software [49]. The final design adopted one pair of achromatic prisms based on the Ge–ZnS combination, which could produce a chromatic blur of only 2.9 μm in the focal plane.

In 2000, Sasian [50] derived a compact set of formulae that could be used for quick estimation of the wave aberrations from a prism and a plane diffraction grating. Four conditions for the absence of wave aberrations were further described as the theoretical basis to eliminate aberration.

In the same year, Weber et al. [51] proposed a ZnSe Risley prism pair where diffractive gratings were etched into the prism surfaces to correct chromatic aberration. Test results in the 4.4–5 μm wavelength band indicated that the correction offered by diffractive gratings could roughly double the imaging resolution of the system over the uncorrected case. Moreover, it was concluded that the diffractively corrected prisms could form an alternative lightweight scanner in missile seekers.

In 2003, Duncan et al. [52] presented the achromatic doublet prisms for infrared countermeasure applications. Sixteen materials in 120 different combinations were examined to help investigate the optimum infrared material characteristics. For midwave infrared applications across the 2–5 μ m spectral region, it has been shown that LiF–ZnS doublet prisms can achieve the minimum chromatic dispersion as low as 1.7816 mrad at a maximum beam deviation angle of 45° on average. In 2007, Bos et al. [53] introduced another prism to overcome the singularity problem of two-prism

achromatic design. Comparative analysis has indicated that the three-prism system composed of AMTIR-1-Ge doublet prisms can minimize the secondary dispersion of a two-prism design to 0.79 mrad.

In 2007, Chen [54] contrived beam steering devices based on one pair of counterrotating Grisms, similar to one pair of Risley prisms, in order to achieve the largest allowable beam deviation angle of 45° . As a combination of prism and grating, Grism was presented as the integrated diffractive-refractive optics instead of those refractive optics to minimize the residual chromatic aberration. For example, the worst residual chromatic aberration was about $100~\mu rad$ in the apochromatic system.

In 2011, Florea et al. [55] proposed chalcogenide-based Risley prisms for the minimal spectral dispersion and improved thermal performance in infrared radiation applications. Evaluation results have shown that the spectral dispersion in the 2–5 μ m region for LiF–As₂S₃ doublet prisms should be three times smaller than that for LiF–ZnS doublet prisms, and the dispersion in the 8–12 μ m region for ZnSe–As₂Se₃ combination should be twice smaller than that for ZnS–Ge combination.

4. High-Precision Beam Scan Theory

Currently, the theoretical research on Risley prisms has concentrated mostly on rotating double prisms but rarely on tilting double prisms. Earlier in 2006, Li et al. [56] developed a geometric method to formulate the hundredfold-order reduction ratio from the tilting angles of two prisms to the beam deviation angle. It has been verified in principle that tilting double prisms should achieve beam scan precision of submicroradian order, which facilitates the design of mechanical structure and control system for high-accuracy beam steering operation.

In the same year, Li et al. [57] demonstrated the vertical filed angle and horizontal field angle of the emergent beam to help describe the amount of beam deviation for tilting double prisms. Comparative analysis was also performed to reveal the influence of different prism parameters on the beam deviation angle. Providing the incident beam within the same angular range, it was found that two prisms with larger wedge angle could achieve beam deviation within a wider angular range. However, the change rate of beam deviation angle would increase as a result, which led to a certain decrease of beam steering accuracy.

On the above basis, Li et al. [58] further investigated the primary error sources and their impacts on beam steering accuracy. It has been clarified that the beam steering accuracy is mainly associated with those possible errors in tilting angles of two prisms, wedge angle, the homogeneity of refractive index, the incidence angle of the beam relative to the X-axis, and the perpendicularity between the principal sections of two prisms. Given the total error converted on prism orientation as 12.72'', the resultant error in beam deviation angle was about $0.365 \,\mu$ rad on average, which could meet the requirement of beam steering accuracy superior to $0.8 \,\mu$ rad (1σ) .

In 2014, Li et al. [59] applied the variable separation method to derive an analytic inverse solution for tilting double prisms. For example, the tilting angles of two prisms were deduced from the desired vertical and horizontal angles of emergent

beam to generate an arbitrary target trajectory. Considering the influence of all system parameters on the beam exiting position, the lookup-table method was also proposed to obtain a numerical inverse solution for target tracking in near field.

1.3.2 Implementation Methods

The double-prism multi-mode scan system offers a potential alternative to conventional beam scanners in optical scanning, tracking and positioning applications. To promote or improve system implementation in practice, many relevant studies have been presented with emphasis on the opto-mechanical design based on Risley prisms, the support techniques for large-aperture rotating prism as well as the motion control algorithms for rotating or tilting double prisms.

1. Opto-Mechanical Design

Based on rotating double prisms, Zu et al. [60] introduced an optical device to simulate satellite trajectories, where the prism rotation was accomplished with gear sets driven by servo motors. Sun [21] devised a rotating double-prism device with worm and gear drive mechanism, which had large transmission ratio to enable highprecision prism rotation over a slight angular displacement. Specifically, the hybrid stepper motor was adopted to actuate the worm and gear mechanism joined to each prism cell, the angle encoder was equipped to acquire angular position feedback for the real-time compensation of tangential synthetic error, and the self-locking worm and gear mechanism could contribute to the enhanced stability and robustness of the whole system. In 2013, Li and Gao [61] proposed a rotating prism device driven by synchronous belt mechanism, which could offer the advantages of smooth transmission, little noise and no slip to achieve the precise control of prism rotation. Besides, Ostaszewski et al. [29] have applied torque motors to directly drive a Risley prism beam pointer, as shown in Fig. 1.9. Although the direct drive scheme allows compact structure and easy control of the system, it may suffer from the torque fluctuation and cogging effects induced by torque motors, which can affect the angular accuracy of prism rotation. Another shortcoming is that a large-aperture rotating prism need be accommodated with special customization and addition cost for torque motor.

As for tilting double prisms, Li et al. invented a sophisticated beam steering mechanism using two optical wedges in 2006 [62, 63] and an orthogonal tilting double-prism beam scanner in 2010 [64]. For this beam scanner, the joint bearings were employed to transform the horizontal motion of linear motors to the small-angle tilting motion of prism cells, and the displacement or angle sensors were involved in the closed-loop control of high-precision tilting motion. However, the use of joint bearings will generate motion clearance that has adverse impacts on beam scan precision. In 2012, Li et al. [65] presented a tilting prism assembly which applied cam-based drive mechanism to realize the small-amplitude oscillation of prism cell. The cam was connected to the driving motor through synchronous belt in order to achieve greater stability and lower noise.

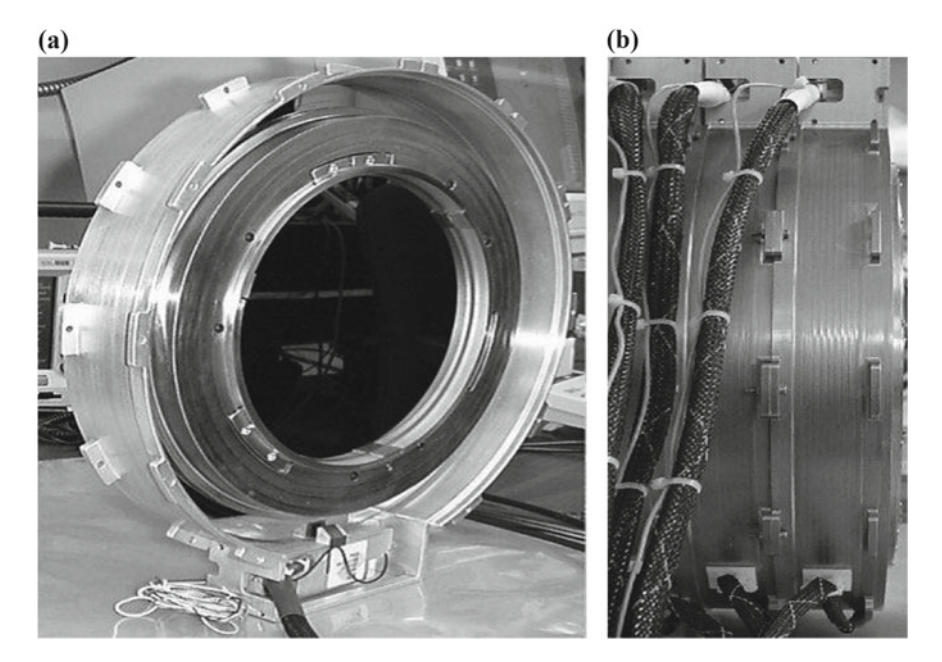


Fig. 1.9 Prism assembly driven by torque motor. a single-prism system; b lateral view of three-prism system

Regarding large-aperture rotating double-prism scan device, the simulation, analysis and test on mechanical support are crucial techniques to mitigate or overcome the influence of prism weight and different surroundings on the prism deformation. Fortunately, there are plenty of achievements about optimizing the support structure of large-aperture optics to enhance its static rigidity, dynamic rigidity and temperature insensitivity. The integrated simulation and analysis on optical-mechanical-thermal performance has been performed in many applications, which can be helpful and instructive to improve the existing support methods.

Dynamic performance analysis is a significant branch of the investigation on optomechanical systems. Currently, it is popular to study the dynamic characteristics of a specific system or analyze the response of static structure to any external load, but much less interest has been placed on what impacts the force produced by system motion have on the optical components. In fact, both external dynamic loads and internal motion loads should be taken into account for the accurate prediction of dynamic characteristics. Chapter 7 will expound more details about the support techniques for large-aperture rotating prism and the dynamic performance analysis on opto-mechanical systems.

2. Motion Control Algorithms

In practice, the beam scan operation based on Risley prisms are required with high precision, rapid response, superior reliability and great controllability. However, the

motion control of Risley prisms may suffer from some certain difficulties because the rotating or tilting angle of each prism is nonlinear with respect to the beam deviation angle [42]. That explains why a lot of motion control algorithms have been proposed to overcome those difficulties.

In 1995, Boisset et al. [35] developed a closed-loop control system for rotating double prisms to perform active alignment between beam spot and quadrant detector. The quadrant detector was used to detect the misalignment error between the center of beam spot and the center of the detector itself. Given the error signal, an active alignment algorithm was applied to calculate the required rotation angles of two prisms to align the beam spot with the center of quadrant detector. The algorithm can work only when the initial prism orientations are known, and it may fail once the beam spot position exceeds the detectable range of quadrant detector. In addition, the required rotation angles of two prisms are obtained from an approximate inverse solution, which should limit the active alignment accuracy to some extent.

In 2004, Sun et al. [66] employed the Proportion-Integral-Derivative (PID) controller to plan the rotation of driving motors according to the difference between each prism orientation obtained from lookup-table method and the one measured with angle encoder. The genetic algorithm was used to optimize the control parameters so that the PID controller could offer excellent performance.

In 2006, Sánchez and Gutow [67] proposed a three-element Risley prism system to eliminate the blind spots and control singularities that were problematic in traditional Risley-prism systems. But the proposed system was under-constrained and could produce infinite sets of inverse solutions for the prism orientations. A control law was then presented to solve these problems, where the proposed system had been separated into a single prism and a coupled prism pair. In this law, the individual prism orientation should be calculated from the desired pitch angle and azimuth angle of emergent beam, and the orientations of other two prisms should be determined using the difference between the desired beam deviation and the beam deflection imparted by the single prism. The control law could generate smooth and continuous motion profiles for three prisms while tracking any arbitrary target trajectory, and the required angular velocities of three prisms were minimized across the field of view. Nevertheless, it is evident that the proposed system requires larger hardware cost and more complicated software design.

In 2007, García-Torales et al. [68] implemented an electronic servomotor system for rotating double prisms by means of PID control based on an Adaline Neural Network Algorithm (NNA). Different from traditional PID control methods, the Adaline NNA involved learning algorithms to simplify the automatic tuning process for PID control parameters. It was asserted that NNA should increase the coincidence between the actual values and the preset values of prism motion parameters, such as angular displacement, angular velocity and angular acceleration. Furthermore, NNA could improve the anti-interference performance of the system.

In 2010, Liu [69] established a mathematic transfer function model for the control loop of the coarse-fine composite axis beam steering device based on rotating double prisms. Simulation results indicated that a composite axis system with greater band-

width ratio could have more robust capacity to resist the satellite vibration noise and intrinsic torque disturbance.

Since 2014, Li et al. has been engaged in the development and optimization of a new control strategy, exemplified by the tilting double-prism scanner driven by cam-based mechanism [70]. Given any specific beam scan trajectory, the complicated and nonlinear control problem can be transferred to the more operative cam profile design. As long as the cam profile has been properly designed to linearize the control of cam rotation, the high-precision tilting motion of two prisms is simply accomplished by the uniform rotation of driving motors. This method paves a new way to improve motion control algorithms for Risley prisms, which will facilitate any further application based on rotating or tilting double prisms.

1.3.3 Practical Applications

The double-prism multi-mode scan system is advantageous in compact structure, high accuracy, rapid response, large deviation coverage, great dynamic performance and superior environmental adaptability. As a rather potential technology for wide-angle beam pointing or boresight adjustment, the double-prism system has been increasingly applied in the fields of laser communication, space observation, infrared countermeasure, target search and rescue, machining, biomedical and military equipment [10, 33, 71–74].

Generally, the above applications fall under three categories: (i) high-precision beam pointing and alignment, (ii) multi-mode target search, recognition and tracking, and (iii) imaging boresight adjustment and observation.

1. High-Precision Beam Pointing and Alignment

(1) Laser Communication and Laser Radar

Free-space optical interconnection is one of the most promising approaches to overcome the technical difficulties in optical communication, originated from high-density connections among all electronic subsystems. While operating in the extremely hostile industrial environment, the optical interconnected devices are supposed to maintain the alignment of optical transmitter and receiver for a long time. Usually, the boresight alignment is accomplished through either passive methods or active methods [36, 75, 76]. The passive methods should require a set of strict equipment for long-time and stable alignment, where some pre-alignment components are equipped to reduce the effective degrees of freedom of the system. In contrast, the active methods should be accommodated with detectors to measure the misalignment error between any two optical devices, which can be fed back to the tuning mechanism for real-time alignment. For example, an active alignment method for free-space optical interconnection has been reported on the basis of rotating double prisms [21, 36]. In this method, a closed-loop control system can be implemented with one quadrant detector, two stepping motors, optical components and one control

computer, as shown in Fig. 1.10. The quadrant detector is utilized to detect the misalignment error of optical axis, according to which the computer controls stepping motors to adjust rotating double prisms until the optical axis is well aligned with the center of the detector.

For free-space laser communication, OPTRA Inc. has developed various rotating double-prism beam steering devices to perform target tracking operation, as shown in Fig. 1.11. Figure 1.11a and b present four Risley Prism Assembly (RPA) systems named RP-25F, RP-25S, RP-50F and RP-50S, which offer large torque or high beam steering rate [77]. Figure 1.11d and e display the rotating double-prism beam steering devices used for airborne lasercom terminal and compact beam steering, respectively [78, 79]. Technical specifications listed in Table 1.1 indicate that these devices have not only impressive advantages in compact structure and low power consumption but also outstanding performance of beam pointing accuracy and beam scan coverage [31].

For space flight, the beam pointing device is significantly constrained by its physical envelope and available power, and a power-off hold function is also required. Accordingly, Lockheed Martin Advanced Technology Center designed the Miniature Risley Mechanism (MRM) based on rotating double prisms with 0.75° wedge angle, as shown in Fig. 1.11f. The MRM that featured a closed-loop control system and a fail-safe flexure-type break assembly was successfully tested to verify its performance requirements for space flight [80].

International Telephone and Telegraph Corporation (ITT) contrived the rotating double-prism beam steering device for simultaneous manipulation of infrared optical and radio frequency beams, as shown in Fig. 1.11g. This method of hybridizing sensor and communication payloads into one device opens new possibilities for instrumentation [81].

Degnan et al. [82] managed to implement a double-prism beam steering device for transmitter compensation in NASA's Next-Generation Satellite Laser Ranging (NGSLR) System. Test results indicated that the system could produce an accept-

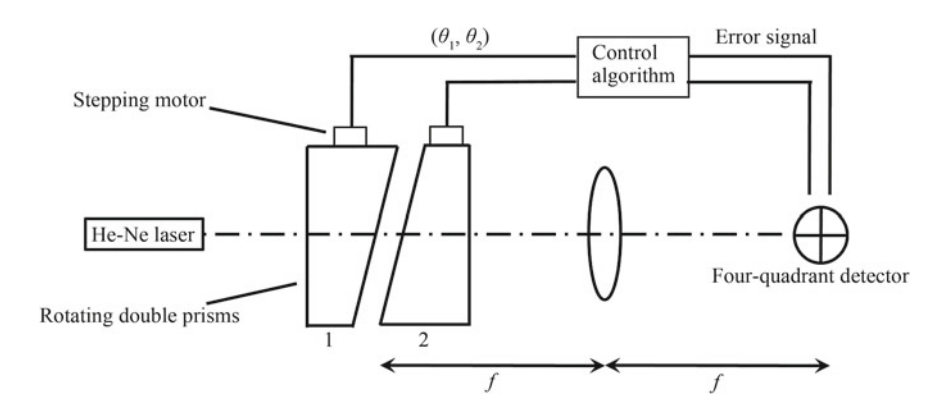


Fig. 1.10 Schematic diagram of active alignment

Table 1.1 Technical specifications of several rotating double-prism products

lable I.1 le	chnical specind	Table 1.1 Technical specifications of several rotating double-prism products	ral rotating do	uble-prism pro	ducts					
No.	1	2	3	4	5	9	7	8	6	10
Type/name	RP-25F	RP-25S	RP-50S	RP-50F	Infrared	Airborne	Compact laser	Minimature	Conformal	Three-prism
					counteraction system	lasercom terminal	steering system	Risley assembly	beam pointer	beam pointer
i										
Firm	OPTRA	OPTRA	OPTRA	OPTRA	OPTRA	OPTRA	OPTRA	Lockheed Martin Advanced	ITT-AES	Ball Aerospace & Technology Corporation
								Technology Center		
Application	Optical	Beam scanning	Beam pointing	Beam scanning		Airborne laser	Beam steering	Beam	Infrared and	Target tracking
	avoidance				counteraction	communica- tion		alignment and boresight adjustment	RF beam steering	
Aperture	25 mm	25 mm	50 mm	50 mm	10 mm	4″	1"	19 mm	115 mm	4"
Scan coverage	120°	120°	120°	120°	110°	120°	120°	1	120°	144°
Pointing precision	≤1 mrad	≤1 mrad	≤1 mrad	≤1 mrad	1 mrad	0.7 mrad	1 mrad	0.025 mrad	ı	0.1 mrad
Wavelength range	UV-LWIR	UV-LWIR	UV-LWIR	UV-LWIR	2–5 µm	1.54–1.57 µm	2.0-4.7 µm	I	1.55 µm	1.55 µm
Response time	≤175 ms	<275 ms	≤250 ms	≥350 ms	110 ms	500 ms	100 ms	1	400 ms	ı
Max rotation speed	3000 RPM	6000 RPM	500 RPM	4000 RPM	I	I	ı	I	ı	
Bandwidth	≥75 Hz	≥40 Hz	≥75 Hz	≥40 Hz	50 Hz	50 Hz	50 Hz	37 Hz	ı	23 Hz
Physical size	Diameter	Diameter	Diameter	Diameter	Diameter 3.2",	Diameter	Diameter 2.3",	Length 64 mm,	Diameter	ı
	50 mm	76 mm	length 116 mm	length 116 mm		8.7" sengui	Icugui 3.3	Height 58 mm	l / 3 mm, length 100 mm	
Mass	1.0 kg	1.3 kg	2.8 kg	2.8 kg	3.5 lb	52.4 lb	2.3 lb	ı	5.5-6.5 kg	ı

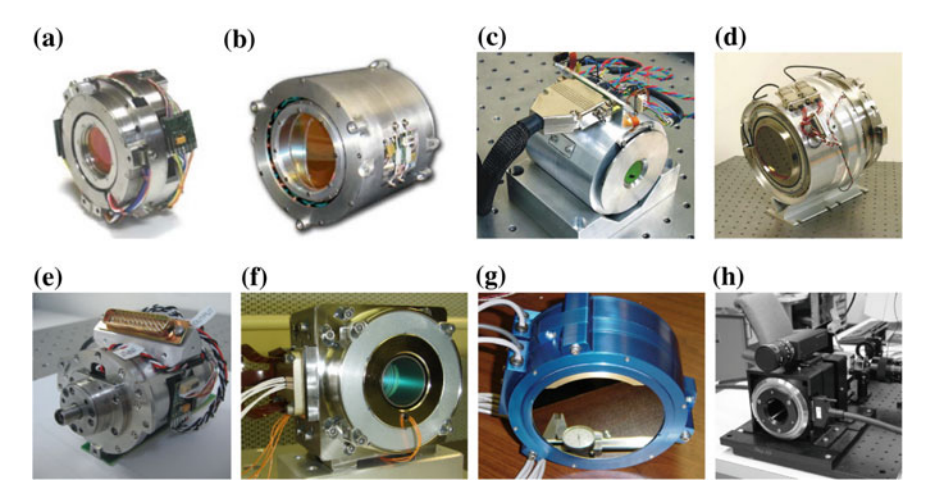


Fig. 1.11 Several types of rotating double-prism products. a No. 1 and No. 2 devices; b No. 3 and No. 4 devices; c-h No. 5-No. 10 devices

able transmitter pointing error of sub-arcsec order. Furthermore, it was reported that rotating double prisms had also been integrated into the boresight adjustment mechanism (BAM) for Geoscience Laser Altimeter System (GLAS) launched in 2003 [83], where the BAM was capable of precisely steering laser beam over the range of ± 300 arcsec.

Tame and Stutzke [84] proposed the Risley-prism-based beam antenna that could be applied on a wide variety of mobile platforms for signal transmission. Generally, Risley prism antennas are compact, cheap and reliable enough to offer a promising alternative to traditional dish antennas. Li et al. [56] and Sun et al. [85] constructed an optical tracking, acquisition and tracking (PAT) test-bed to verify the working performance of inter-satellite laser communication terminals. In this PAT test-bed, rotating double prisms were employed to simulate satellite motion trajectories across a range of 360° azimuth and $\pm 15^\circ$ elevation, where the random accuracy in simulation should be 50–200 μrad . Additionally, tilting double prisms were involved for fine beam scanning within a range of over 500 μrad , where the fine tuning accuracy could reach 0.5 μrad .

Laser beam steering technology based on rotating double prisms has been further developed to accomplish beam scanning, target aiming and tracking operations that are required in the fields of laser radars, laser guidance, laser weapons and laser beam directors [6]. For laser radar systems where the physical dimensions and beam scan precision are specially conditioned, rotating double prisms serve as an appropriate approach to perform high-precision beam scanning. Earlier in 1981, NASA built a germanium Risley prism scanner for the CO₂ Doppler lidar mounted on CV-990 aircraft for meteorological research, as shown in Fig. 1.12 [34]. The scanner went through a severe flight test on that aircraft, and it was demonstrated that the scanner could successfully position a laser beam used for vector wind velocity measurements.

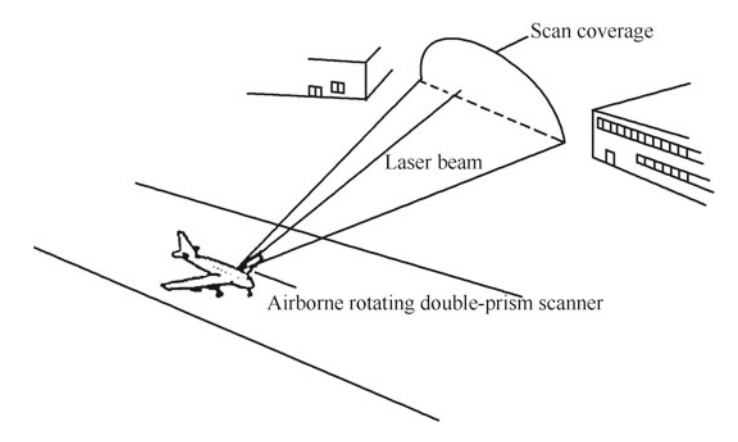
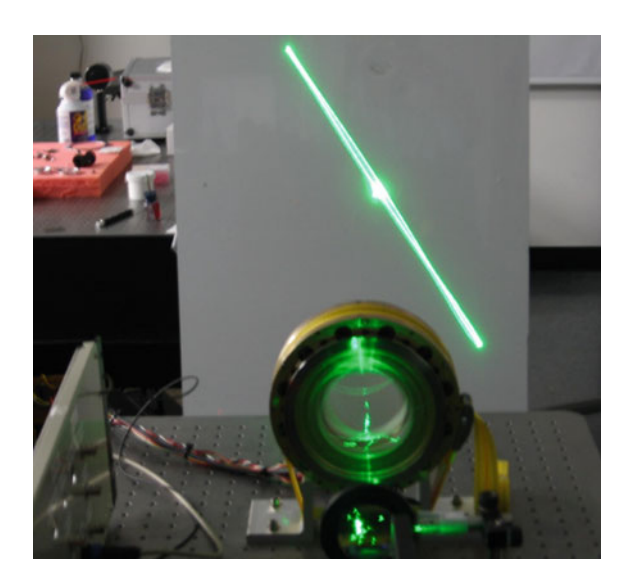


Fig. 1.12 Rotating double-prism beam scanner in airborne lidar

Fig. 1.13 Second generation of airborne 3D imaging lidars



In 2007, Harris Corporation and MIT Lincoln Laboratory proposed a Jigsaw three-dimensional imaging laser radar which introduced rotating double prisms to actualize beam scanning in real time and expand the imaging field of view [86]. Results from the ground integration and test indicated that the system was capable of high-precision beam scanning over a $\pm 20^{\circ}$ conical region. Results from the flight test on a UH-1 helicopter have verified that the laser radar could easily recognize various military targets under the camouflaged scenes. In the same year, Sigma Space Corporation succeeded in both rooftop testing and flight testing of the second generation airborne three-dimensional imaging laser radar shown in Fig. 1.13, where the rotating double-prism system was used as a laser beam scanner to cover a 28° conical region [87].

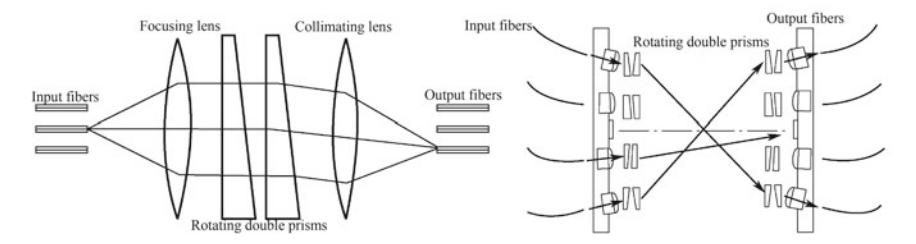


Fig. 1.14 Rotating double-prism mechanism applied in optical fiber switch

(2) Optical Switch and Wavefront Control

The beam steering principle by means of rotating double prisms can be applied to optical switch design for optical fiber laser communication, as illustrated in Fig. 1.14 [75, 88]. Here the beam emitted from the single-mode fiber is coupled into the dedicated information channel after passing through focusing lens, rotating double prisms and collimating lens in sequence. Switching operation between any two channels is accomplished by the independent rotation of two prisms. It is asserted that this optical switch can manipulate broad-band laser beams with an appropriate switching speed, small insertion loss, great working stability and repeatability up to ± 0.012 dB or better. Considering that the beam deviation angle is insensitive to the rotation angles of two prisms, the beam deviation accuracy can be accommodated with common stepping motors. Another benefit is that the optical switch offers superior flexibility for the customization of $M \times N$ optical switch arrays, where a large difference is acceptable between the values of M and N [21].

Rotating double prisms can also function as a wavefront director for interferometry systems, such as the vectorial shearing interferometer used to measure wavefront aberrations. In general, this interferometer accomplishes large and differential wavefront displacements using a high-precision rotation device incorporated in a Mach-Zehnder interferometer. Therefore, Paez and Strojnik [89] and García-Torales et al. [30, 90] developed vectorial shearing interferometers that integrated the rotating double-prism system to deflect a light beam and control the wavefront displacement without changing the image orientation. Since the wavefront tilt and displacement are determined by the relative rotation angle between two prisms, this interferometer enables consecutive adjustment of both shearing direction and shearing displacement in order to test symmetrical or asymmetrical optical elements [21].

(3) Laser Doppler Vibrometry and Microstructure Fabrication

Tirabassi and Rothberg proposed a Risley-prism-based scanning head for Laser Doppler Vibrometry (LDV), as shown in Fig. 1.15 [38, 91]. By far, most popular commercial laser vibrometers incorporate a pair of orthogonally situated galvanometer mirrors to deflect the laser beam in a point-by-point or continuous scan mode. But the mirrors with large inertia can limit the performance of LDV in more specific applications such as circular tracking of high-speed rotors, where the mirrors must oscillate continuously at high rotation speeds. As a perfect alternative solution, the

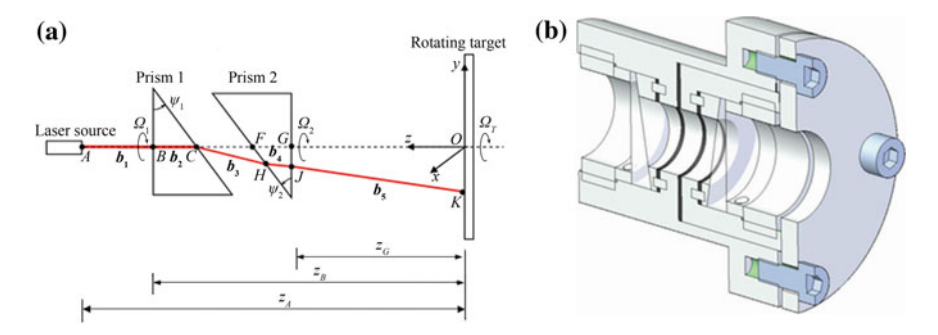


Fig. 1.15 Laser Doppler vibrometer based on rotating double prisms, where **a** is the schematic diagram of a laser tracking system and **b** shows the mechanical model of the system

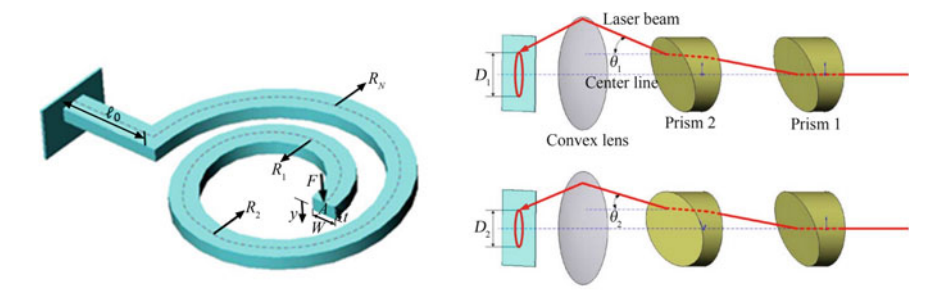
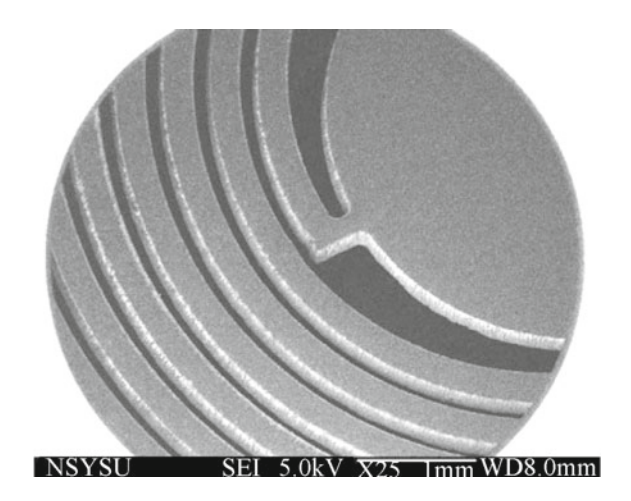


Fig. 1.16 Schematic diagram illustrating the fabrication principle of spiral spring microstructure

proposed LDV scanning head requires the whole-body rotation rather than continuous oscillation of two prisms to steer the laser beam. In order to predict measured velocities in general tracking applications, the direction of incident beam to the LDV must be known, together with an arbitrary known point along the beam path. Experimental data has confirmed that the rotating double-prism tracking system could offer significant advantages over the conventional dual-mirror scanning system, such as low moment of inertia and great dynamic characteristics.

Pan et al. [92] applied a rotating double-prism optical device to fabricate microstructures with high aspect ratio, as shown in Fig. 1.16. Since the spiral spring microstructures used as resonators in micro-electro-mechanical systems (MEMS) should have physical dimensions less than 0.25 mm, any conventional processing technique can hardly achieve the desired accuracy shown in Fig. 1.17. Therefore, rotating double prisms were utilized to enable fast fabrication of spiral microstructures, in which the cutting linewidth could be controlled by adjusting the pointing direction of the final emergent beam. This fabrication method was independent of crystal orientation and capable of rapid prototyping for silicon-based microstructures. Vibration test on spiral microstructures has verified that the measured dynamic characteristics were in good agreement with the simulation results from ANSYS.

Fig. 1.17 Photomicrograph of the spiral spring microstructure produced by laser cutting



2. Multi-mode Target Search, Recognition and Tracking

(1) Infrared Countermeasures

Infrared countermeasure (IRCM) systems based on waveform jamming technology can resist the infrared guided missiles that may impose significant threats to military aircraft flying in hostile surroundings [31]. A typical IRCM system is usually composed of a missile warning sensor, multi-band infrared laser and a two-axis gimbaled beam steering platform. However, two-axis gimbaled platforms suffer from the large dimensions and the necessity to protrude from the aircraft, which may result in increased aircraft drag, larger operation power and slow response rate. In addition, these platforms are highly sensitive to the vibration loads that can produce beam steering errors and reduce jamming power. For next generation IRCM systems, the rotating double-prism scanner can offer a more compact, agile and robust alternative to the conventional gimbaled platform to adjust the imaging boresight for target search, recognition and tracking applications. The IRCM systems based on rotating double prisms are especially suitable for airborne, ship-borne or space-borne laser communication where the installation space is poorly limited. By far, it has already been reported that rotating double prisms can be applied for optoelectronic countermeasure, missile seekers and security cameras.

Schwarz et al. [31] developed an IRCM system based on rotating double prisms to achieve beam steering accuracy better than 1 milliradian over a 110° field of view. Yuan et al. [93] invented an airborne infrared scanning and observing device for photoelectric reconnaissance, which featured light weight, compact structure and insensitivity to vibration. This device incorporated two prisms having individual wedge angles of 10.3° and 3.5° to deflect the sighting axis with a maximum angle up to 31°.

(2) Image Acquisition

In target search, recognition, rescue and surveillance applications, the target search operation need be accommodated with large imaging field of view (FOV), while the target recognition requires high image resolution. To accomplish these two opposed concepts, it is necessary to acquire images with both wide FOV and high resolution using an opto-mechanical device of finite dimensions. A popular solution to the above dilemma is to alternate between one imaging system with wide FOV and low resolution and the other one with narrow FOV and high resolution. However, such a solution leads to the loss of situation awareness in a narrow FOV and the decrease of recognition capability in a wide FOV.

Lavigne and Ricard [94] demonstrated an image acquisition strategy based on the step-stare imaging system which incorporated a pair of achromatic Riley prisms, as shown in Fig. 1.18. Rotating double prisms were used to deflect the narrow FOV of a high-resolution camera towards a sequence of pre-calculated best positions across the desired wide FOV. The high-resolution mosaic images taken at those sequential positions were assembled together to provide a global image with wide FOV and high resolution. Characterized by small volume, light weight and low cost, the step-stare imaging system can achieve perfect combination of wide FOV and high resolution, which offers a promising approach to facilitate target search and rescue or ground surveillance on unmanned aircrafts.

(3) Target Tracking

Aiming for smooth tracking of arbitrary target trajectories, Ball Aerospace & Technologies Corporation contrived a three-element Risley prism beam steering system instead of the traditional double-prism system to eliminate control singularities. A prototype of the three-element system has been presented in Fig. 1.11h, together with its performance parameters in Table 1.1 [29, 67].

To accomplish multi-target tracking for motion capturing, Souvestre et al. developed the laser tracking system based on a digital micro-mirror device (DMD) and

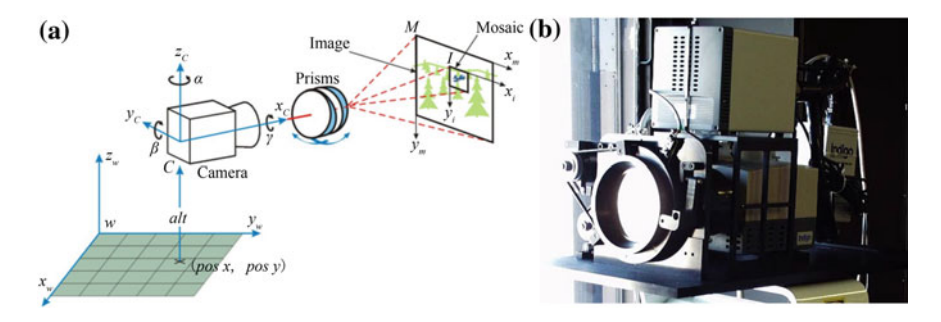


Fig. 1.18 Step-stare imaging system, where a illustrates the step-stare image acquisition strategy and b shows a physical prototype of the system

rotating double prisms [95, 96]. Conceptually, the laser tracking system was separated into a DMD-based local scanner to generate fully reconfigurable laser patterns and a Risley-prism-based global scanner to enlarge the scan field of view, as shown in Fig. 1.19. The photo detector could measure the numbers, positions and shapes of reconfigurable laser patterns in order to determine the relative position between each laser pattern and target center. According to this relative position, the local scanner and global scanner should be controlled to steer laser beam for target tracking function.

In the proposed system, two Risley prisms with 50.8 mm clear aperture and 10° wedge angle were used to perform beam scanning within a 20.4° conical region. Each prism rotation was driven by a DC motor, and the angular position was measured with a 2000 pts magnetic encoder. Through the closed control loop using PID controller, the reduction ratio from DC motor to prism was set to 3 for an angular resolution of 0.03 and a theoretical maximum speed of 3000 rpm. Despite the power loss due to diffraction, the proposed system can offer advantages such as wide field of view, high resolution and fully reconfigurable pattern at high refresh rate. In addition, the system can easily achieve sub-centimeter tracking accuracy at much more effective cost than traditional fast steering mirrors. Targeted applications of the system include multitarget tracking, tank reconnaissance and other possibilities where the cooperative lighting condition is absent or where a hemispheric field of view is required.

3. Imaging Boresight Adjustment and Observation

As a versatile approach to adjust the imaging boresight and enlarge the imaging field of view, optical instruments based on rotating double prisms have been successfully applied in the fields of microscopic observation, biomedical imaging, microassembly and micromanipulation.

(1) Biomedical Observation

Fountain and Knopp [97] invented a scan imaging system for surgical operation, where Risley prisms were coaxially mounted on separate rotating stages. A surgical

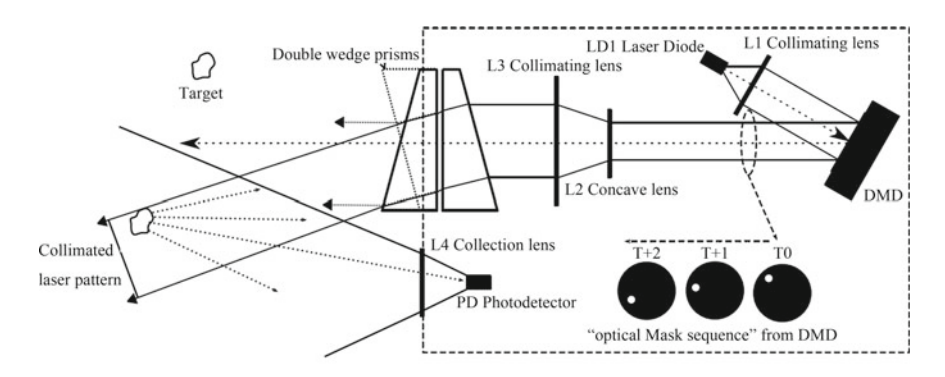


Fig. 1.19 Principle of multi-target tracking system for motion capturing

laser beam could be steered and scanned along any arbitrary trajectory by adjusting the rotation angles of two prisms. Synchronous rotation of the prisms would produce a circular scan pattern dependent on the relative rotation angle of two prisms, whereas counter rotation of the prisms at equal speeds and in opposite directions would lead to a diametric straight scan pattern. Kim et al. [98] developed a novel robotic endoscope composed of rotating double prisms, an auto-zooming system, a rigid endoscope, a CCD camera, two sleeves, two driving motors and an encoder, as shown in Fig. 1.20. The driving motors were used to rotate two separate sleeves in which the prisms had been inserted, and the encoder was applied to read the actual orientations of two prisms. Scattered light from the target should transmit through two prisms, rigid endoscope and auto-zooming system in turn, which was eventually captured by CCD camera. Upon placing Risley prisms in front the conventional endoscope, it became feasible to acquire high-quality images across a wide field of view (up to 40°) without moving the overall system.

Warger II et al. [99] demonstrated a confocal reflectance microscopy for imaging skin lesions, which incorporated rotating double-prism scanner, avalanche photodiode, telescope, spectroscope, quarter-wave plate and objective lens. It has been verified that rotating double-prism scanner would enable high-resolution image without missing pixels as long as the scan frequency was chosen in a proper manner.

(2) Microassembly and Micromanipulation

Insufficient vision information owing to occlusion, low resolution and small field of view has been a prevalent problem for microassembly and micromanipulation. Therefore, Tao and Cho [37, Tao et al. 100] proposed a variable view imaging system (VVIS) based on the integration of optics and robotics technologies. The VVIS included optical components such as rotating double prisms, steering mirror, deformable mirror and imaging lenses. Through appropriate motion control of both rotating double prisms and steering mirror, the proposed system could achieve variable observation views of micro objects to provide sufficient vision information, as illustrated in Fig. 1.21.

The capability of VVIS has been demonstrated in microassembly simulation and experiment to perform micro peg-in-hole insertion task, where the 450 μ m \times 400 μ m \times 300 μ m micro peg was held by a micro manipulator [37, 100]. At the first

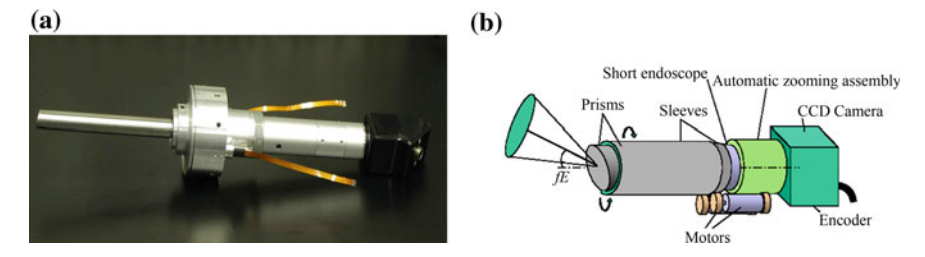


Fig. 1.20 Endoscope with a wide field of view, where \mathbf{a} show a prototype for test and \mathbf{b} is a schematic diagram of the overall system

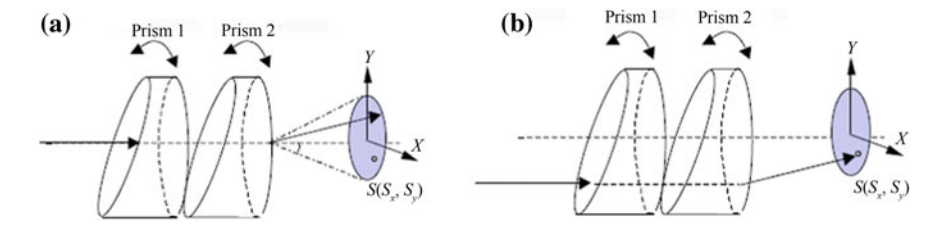


Fig. 1.21 Operation of variable view imaging system, where ${\bf a}$ shows the first step and ${\bf b}$ shows the second step

step, a vertical view was obtained from the VVIS to provide vision information that could guide the peg towards the top of a selected hole. At the second step, the orientations of rotating double prisms and steering mirror were adjusted to obtain a tilted view from the VVIS so that the peg bottom could be observed. According to the vision information in the tilted view, the micro manipulator was then controlled to insert the peg into the selected hole. This successful experiment has verified that the rotating double-prism scanner can be widely applied for vision-based microassembly.

(3) Gun Sight Compensation and Other Applications

Strong [101] proposed a range compensator for gun sight based on rotating double prisms. As a result of gravity and crosswind factors, any projectile may depart from its desired flight path in both vertical and lateral directions. For the purpose that the projectile strikes target, the common solution is to re-aim target using the vertical and lateral compensation from a reliable experience table, where the influence of target distance and shooting surroundings has been taken into account. However, the proposed compensator incorporates rotating double prisms to deviate the gun sight for departure compensation, which allows the shooter to simply maintain the target centered with the gun sight.

In pinhole imaging systems used for concealed optical surveillance, rotating double prisms can function as a bidirectional tilting mechanism to expand the observation field of view. The rotating double-prism system can also offer an effective boresight adjustment approach to accomplish image stabilization. As for large-scale astronomical telescopes, the rotating double-prism system is often employed to atmospheric scattering. Furthermore, the combination of rotating double prisms and other optical elements can be applied to correct the dynamic aberrations originated from conformal domes [102]. Characterized by the insensitivity of beam deviation angle relative to prism orientations, the rotating double-prism system is particularly suitable for those applications required with high beam scan precision, such as a boresight alignment device in the laser altimeter designed for Mars Observer [103].

1.4 Problems of Double-Prism Multi-mode Scan System

Regarding double-prism beam scan technology, most researchers are interested in solutions to forward and inverse problems, beam scan mode, beam scan performance, opto-mechanical setup or motion control method. Double-prism scan systems have been successfully applied in the fields of laser communication, laser radar, mechanical processing, biomedicine, military weapons and so on. However, there are several essential problems remaining to be solved for further applications based on double prisms.

1. Exact Solutions to the Inverse Problem

It is a common choice to use first-order paraxial approximation and non-paraxial ray tracing method to solve the forward problem of a double-prism system. But no ideal exact solution has been presented for the inverse problem, which results from two possible reasons. First, there are many difficulties in the inverse derivation of multiple beam refractions. Second, the beam exiting position from the second prism depart from the optical axis of the system owing to the influence of structural parameters such as prism thickness. Therefore, the exact inverse solution for two prism orientations are still not available on the basis of the desired beam pointing or the target coordinates.

The two-step method offers a simplified procedure for the inverse derivation of beam path. Paraxial ray matrices and non-paraxial ray tracing method can also produce effective solution to the inverse problem. Nevertheless, the approximate methods cannot give exact inverse solution and are especially suitable for beam scanning in far field.

Generally, the lookup-table method or numerical iteration algorithm can be applied to enhance the solving accuracy for high-precision beam scanning in near field. However, the huge computation data and certain precision of lookup table will limit the efficiency and accuracy of inverse solution. As for conventional iteration algorithms, the solution accuracy can be improved after more iterations, but the solution efficiency will decrease as a result. Accordingly, these two methods are not suitable for real-time and high-precision beam scan applications.

Aiming at a rotating double-prism system, this book introduces an iterative algorithm which combines two-step method with forward ray tracing method. The algorithm can offer high accuracy, low computation and high efficiency to meet the real-time and high-precision requirements of beam scanning and tracking operation on dynamic targets.

2. Scan Errors

Actually, beam scan errors can cause the decrease of scan stability in various application fields. Therefore, it is difficult but essential to analyze the error sources and their impacts on system performance, as well as the methods of error elimination or reduction. Actual scan errors which depend on the comprehensive accuracy of the

system are roughly inducted as follows: (1) solution errors; (2) component errors; (3) assembly errors.

Solution errors come from approximate or numerical iterative solutions of the forward and inverse problems. Correspondingly, researchers have made efforts into these aspects. One hand is to investigate effective and exact solutions of the forward or inverse problems. The other hand lies in optimizing those solutions, which means consideration about seeking a good tradeoff between accuracy and speed so as to accomplish requirements for real-time performance and lower errors of dynamic scanning.

Practically, inevitable errors of refractive index or structural parameters like wedge angle and thickness are existent in the prism manufacture. The popular research on these errors is conducted with theoretical analysis or simulation, such as the ray tracing method and Zemax modeling method, etc. To reduce those errors, new processing and detecting techniques are indispensable for the promotion of prism accuracy and surface quality. Besides, considering environmental factors into the system design can be another valid approach to reduce errors in the application.

Assembly errors regularly refer to the installation errors of prisms and bearings, and the mechanical transmission errors that can be equivalent to the rotating or tilting errors of prisms. In this book, a three-dimensional assembly error model of the double-prism scan system will be constructed and the effects of those types of errors on beam pointing precision will be investigated. According to the given demand for pointing precision, it is significant to calculate the permissible assembly errors for the design of double-prism multi-mode scan systems.

3. Blind Zone

Sometimes, the beam scan device is supposed to scan globally within a certain range. However, the unavoidable blind zone caused by structural parameters prevents rotating double-prism systems from some probable applications, especially of the near-field scanning, as the blind zone of pointing covers a range up to several hundred micro-radians around the optical axis. Taking practical tracking or searching for instance, the blind zone may lead to the target loss. Therefore, it is necessary to clarify the formation law of blind zone in order to explore its shape, position and dimension as well as the influential factors, which may help reduce or eliminate the blind zone.

Similar to one pair of Risley prisms with different wedge angles or refractive indices, adding a new prism to the double-prism system can effectively mitigate and even eliminate the scan blind zone [29]. However, it brings new problems such as complicated solving process and infinite reverse solutions, which make it more difficult to design the scanning device and the control algorithm.

This book demonstrates deeply why the blind zone forms in rotating double prisms and how different system parameters have an impact on the blind zone.

4. Singularity Problem

Another puzzle to be resolved is the singularity problem in the control process of rotating double prisms. In other words, the rotation angles of two prisms will make

an instantaneous change when the beam points towards the direction parallel to the optical axis or the direction of maximum deflection angle (or when the scan target approaches to the center or edge of scan region in a specific trajectory). That requests for infinite rotation speeds of prisms theoretically, challenging the drive and control of servo motors. Though few references reported the phenomenon [53, 67], no one has seriously analyzed the underlying causes and inherent laws of singularity, which will be discussed later in this book. The addition of another prism, mentioned previously, enables the smooth and continuous scanning, but the method shows similar shortcomings to the solution of blind zone.

5. Nonlinear Control Problem

The governing equations that describe the correlation between rotating or tilting angles of prisms and beam pointing are both nonlinear. Currently, most inverse solutions employ two-step method or lookup-table method, however, their deficiency on solving accuracy and time complexity may hinder the real-time tracking of uncertain targets. In this book, an iteration method is provided to solve the inverse problem, which avoids complicated nonlinear solutions. Besides, the nonlinear scan control problem is transformed to the design of motion mechanisms, which reduces the difficulty in real-time control and opens a new avenue for the inverse tracking applications of double-prism system.

6. Beam Distortion Problem

In previous research, the distortion of beam shape in double-prism system has been proven to be slighter with the decrease of wedge angle. Conversely in the wide-field scan occasion, the beam is poorly distorted which leads to inhomogeneous distribution of energy intensity. These may pose negative effects on the double-prism system, such as lowering the energy intensity in infrared counter measures (IRCM) and reducing signal-to-noise ratio of laser communication system. Thus, the influential factors of beam distortion, the quantitative relationship between the distortion degree and each system parameter, and the compensation or counteraction of the distortion are attached great importance to the applications of rotating double prisms. Since the beam distortion properties are investigated in the aspects of the structure parameters of prisms at arbitrary incident angles, the book can positively provide a reference for the design of double-prism scan systems.

7. Chromatic Aberration Problem

Chromatic aberration, as a serious defect in prism imaging, is seldom taken into consideration in application fields of monochromatic beam such as satellite laser communication. However, optical imaging systems usually employ white light or polychromatic light, so chromatic aberration cannot be neglected when double prisms are used for wide-angle adjustment of the imaging visual axis. Currently, there are two chief achromatic methods for prisms including prism combination method and grating element method. Prism combination method is to glue prisms with different dispersion properties together to achieve the chromatic aberration correction. The

prisms are known as positive-negative glued prism, for instance, Si–Ge prism and CaF_2 –ZnSe–Ge prism; while grating element method etches diffractive gratings on the prism or applies grism [54] in order for calibration. As an integrated component of prism and grating, the grism replicates the transmission grating onto the bevel edge of right-angle prism which combines optical performances of the both elements. The dispersion magnitude of the grism depends on the structural parameters such as incident angle, the grating constant and wedge angle of the prism. In consequence, the chromatic aberration can be calibrated with the regulating of dispersion by adjusting those above parameters in analytical formulae.

1.5 Main Work of the Book

It is a comprehensive book to introduce the double-prism multi-mode beam scan principle and methods. The emphasis of this book is placed on double Risley-prism multi-mode beam scan models, effective methods and critical techniques applied in multi-mode optical scanning and target tracking fields. It is also the first systematic book which demonstrates both fundamental multi-mode beam scan theory and practical implementation techniques based on double Risley prisms.

This book contains rigorous modeling of double Risley-prism multi-mode scan system, high-efficiency solution algorithms for inverse problem, abundant illustrative examples and scan error analysis, along with design guidance and performance test on specific beam scan devices. The book presents the latest research results on forward beam scan models, inverse target tracking algorithms, sub-microradian fine scan system based on tilting Risley prisms, nonlinear motion control strategy for double prisms, calibration and experiment techniques for various double-prism layouts, as well as opto-mechanical system design and analysis. Characterized by rigorous theoretical derivation illustrated with rich implementation cases and original beam scanners, the book may offer valuable reference for the further development of multi-mode beam scan technology used in the photoelectric scanning and tracking systems.

There are two meanings of multi-mode beam scanning based on double prisms, explained as follows.

The first meaning refers to multi-mode scan motion of double prisms, since each prism can operate at rotating, tilting and composite motion mode. The scan mode with rotating double prisms is suitable for wide-range beam scanning, and the scan mode with tilting double prisms features high precision owing to the reduction ratio from the tilting angle of each prism to the beam deviation angle. As for the composite scan mode, the multi-degree-of-freedom motion of two prisms allows more abundant scan scales and scan patterns.

The second meaning lies in multi-mode beam scan trajectory, since the size and shape of any scan trajectory can be changed under different motion modes of two prisms. In other words, a beam scan trajectory with arbitrary size and shape, such as straight line, circle, ellipse and hyperbola, can be produced by adjusting the motion

parameters of two prisms and the spatial distances among all optical elements. Multimode beam scan trajectory is often used in constant or time-varying beam scan applications where the target trajectory may be complicated.

Actually, the above two meanings are complementary with respect to each other. A variety of beam scan modes can be generated under different motion modes of two prisms or under different prism speed ratios at the same motion mode. For some specific double-prism scan devices, much richer multi-mode beam scan scales and scan trajectories are available by introducing difference to the combination of system parameters or the amount of prism pairs.

This book can provide basic support for technical researchers and engineers, especially those who work in the fields of beam scanning, target tracking, optical test, opto-mechanical design and optical instrument. It can also serve the potential enthusiasts in universities, scientific institutions and enterprises.

References

- Liu LR, Wang LJ, Luan Z et al (2006) Physical basis and corresponding instruments for PAT performance testing of inter-satellite laser communication terminals. Proc SPIE, 63040C-63040C-11
- Ma HJ, Zhu XL (2005) The latest progress of free space laser communications. Laser Optoelectron Prog 42(3):7–10
- Li AH, Li ZZ (2013) Dual-view variable-focus three-dimensional measuring system: CN, 201310039374.X, 5 June 2013
- 4. Sui B, Du D, Chen Q et al (2003) Path accuracy measurement of industrial robot based on binocular vision. Chin J Mech Eng 39(5):88–91
- Liu LR (2007) Laser communications in space I optical link and terminal technology. Chin J Lasers 34(1):3–20
- Zhou Y, Lu YF, Mo Hei et al (2013) Analytical inverse solutions for rotational double prism beam steering. Opt Precis Eng 21(7):1693–1700
- Marth H, Donat M, Pohlhammer CF (1992) Latest experience in design of piezoelectric-driven fine-steering mirrors. Proc SPIE 1543:248–261
- 8. Xu FF, Ji M, Zhao CS (2010) Status of fast steering mirror. J Appl Opt 31(5):847–850
- 9. Rosell FA (1960) Prism scanners. J Opt Soc Am 50:521–526
- Ding Y (2014) Mathematical modeling and simulation analysis of double-prism scanning system. Tongji University, Shanghai
- Shuai YB, Si L, Ma YX (2003) New progress of beam scanning technology. Chin J Lasers 26(3):287–294
- 12. Xue LS, Wang Y (2003) Development and outlook of optical space communication. J Electron Devices
- 13. Wen T, Wei JB, Ma DT et al (2005) A novel method of increase acousto-optic deflector spatial resolution. Chin J Lasers 32(12):1631–1635
- 14. Wen T (2006) Study on the key techniques of an acquisition tracking and pointing system in wireless laser communication. National University of Defense Technology, Changsha
- Li AH (2007) Research on large-aperture high-accuracy optical beam scanner. Shanghai Institute of Optics and Fine Mechanics, the Chinese Academy of Sciences, Shanghai
- Yan Z, Xu J (2013) Research development of beam scanning technology. Electro-Optic Technol Appl 4:1–9
- 17. Bifano T (2010) Adaptive imaging: MEMS deformable mirrors. Nat Photonics 5(1):21–23

References 37

- 18. Peterson KE (1982) Silicon as a mechanical material. Proc IEEE 70(5):420-457
- Corrigan R, Cook R, Favotte O (2001) Grating light valve technology brief [EB/OL]. Sunnyvale California: Silicon Light Machines. 13 Oct 2016. http://www.siliconlight.com/wp-content/themes/siliconlight/pdf/glv-opcom-ver.pdf
- Wu L, Maley SB, Dooley SR et al (2010) A large-aperture, piston-tip-tilt micromirror for optical phase array applications. J Microelectromech Syst 19(6):1450–1461
- Sun JF (2005) Research on the satellite trajectory optical simulator. Shanghai Institute of Optics and Fine Mechanics, Chinese Academy of Sciences, Shanghai
- 22. Li AH, Li ZZ, Zhang Q et al (2012) Combined driving micro-displacement regulation device: CN, 201110340632.9, 11 Apr 2012
- Sun HY (2012) Research on coarse tracking turntable for Leo satellite laser communications.
 Changehun University of Science and Technology, Changehun
- 24. Yang GG (1977) Optical measuring technology. Zhejiang University Press, Hangzhou
- Xu M, Hu JS (2008) Analysis and calculation of rotating polygonal scanner in laser scanning imaging system. Chin J Lasers 35(5):782–787
- Li AH, Liu LR, Sun JF et al (2009) Large-aperture high-accuracy optical scanner. J Mech Eng 45(1):200–204
- 27. Griffith P, Mitchell P (2013) Where's the beam. Photonics Spectra, 110-114
- 28. Juhala RE, Dube G (2004) Refractive beam steering. Proc SPIE 5528:282-292
- Ostaszewski M, Harford S, Doughty N et al (2006) Risley prism beam pointer. Proc SPIE 6304:630406-630406-10
- 30. García-Torales G, Strojnik M, Paez G (2002) Risley prisms to control wave-front tilt and displacement in a vectorial shearing interferometer. Appl Opt 41(7):1380–1384
- 31. Schwarze CR, Vaillancourt R, Carlson D et al (2005) Risley-prism based compact laser beam steering for IRCM, laser communications, and laser radar [EB/OL]. Optra Inc, Tospfield, MA. 13 Oct 2016. http://www.optra.com/images/TP-Compact_Beam_Steering.pdf
- Yang YG (2008) Analytic solution of free space optical beam steering using Risley prisms. J Lightwave Technol 26(21):3576–3583
- Gao XJ (2015) Research on rotating double-prism dynamic tracking. Tongji University, Shanghai
- Amirault CT, DiMarzio CA (1985) Precision pointing using a dual-wedge scanner. Appl Opt 24(9):1302–1308
- Boisset GC, Robertson B, Hinton HS (1995) Design and construction of an active alignment demonstrator for a free-space optical interconnect. IEEE Photonics Technol Lett 7(6):676–678
- Degnan JJ (2016) Ray matrix approach for the real time control of SLR2000 optical elements [EB/OL]. Sigma Space Corporation, Lanham, MD. 13 Oct 2016. http://cddis.nasa.gov/lw14/ docs/papers/autl_jdm.pdf
- Tao XD, Cho H (2007) Variable view imaging system and its application in vision based microassembly. Proc SPIE 6719: 67190L–67190L-12
- Tirabassi M, Rothberg SJ (2009) Scanning LDV using wedge prisms. Opt Lasers Eng 47(3-4):454–460
- Jeon Y (2011) Generalization of the first-order formula for analysis of scan patterns of Risley prisms. Opt Eng 50(11):113002–113002-7
- Li YJ (2011) Third-order theory of the Risley-prism-based beam steering system. Appl Opt 50(5):679–686
- Li YJ (2011) Closed form analytical inverse solutions for Risley-prism-based beam steering systems in different configurations. Appl Opt 50(22):4302–4309
- 42. Jiang XC (2012) Research on the coarse-fine coupling scanning device based on double-prism. Tongji University, Shanghai
- 43. Marshall GF (1999) Risley prism scan patterns. Proc SPIE 3787:74-86
- 44. Horng JS, Li YJ (2012) Error sources and their impact on the performance of dual-wedge beam steering systems. Appl Opt 51(18):4168–4175
- 45. Schitea A, Tuef M, Duma VF et al (2013) Modeling of Risley prisms devices for exact scan patterns. Proc SPIE 8789:878912–878912-11

46. Sun JF, Liu LR, Yun MJ et al (2005) The effect of the rotating double-prism wide-angle laser beam scanner on the beam shape. Optik 116(12):553–556

- 47. Lavigne V, Ricard B (2007) Fast Risley prisms camera steering system: calibration and image distortions correction through the use of a three-dimensional refraction model. Opt Eng 46(4):043201–043201-10
- 48. Curatu E, Chevrette P, St-Germain D (1999) Rotating prisms scanning system to equip a NFOV camera lens. Proc SPIE 3779:154–164
- 49. Lacoursière J, Douceta M, Curatua E et al (2002) Large-deviation achromatic Risley prisms pointing systems. Proc SPIE 4773:123–131
- 50. Sasian JM (2000) Aberrations from a prism and a grating. Appl Opt 39(1):34–39
- Weber DC, Trolinger JD, Nichols RG et al (2000) Diffractively corrected Risley prism for infrared imaging. Proc SPIE 4025:79–86
- 52. Duncan BD, Bos PJ, Sergan V (2003) Wide-angle achromatic prism beam steering for infrared countermeasure applications. Opt Eng 42(4):1038–1047
- 53. Bos PJ, Garcia H, Sergan V (2007) Wide-angle achromatic prism beam steering for infrared countermeasures and imaging applications: solving the singularity problem in the two-prism design. Opt Eng 46(11):113001–113001-5
- 54. Chen CB (2007) Beam steering and pointing with counter-rotating grisms. Proc SPIE 6714:671409-671409-9
- 55. Florea C, Sanghera J, Aggarwal I (2011) Broadband beam steering using chalcogenide-based Risley prisms. Opt Eng 50(3):033001–033001-5
- 56. Li AH, Liu LR, Sun JF et al (2006) Research on a scanner for tilting orthogonal double prisms. Appl Opt 45(31):8063–8069
- Li AH, Sun JF, Liu LR et al (2006) Design principle of performance testing device for laser beam microradian pointing and tracking in intersatellite laser communications. Acta Optica Sinica 26(7):975–979
- 58. Li AH, Sun JF, Liu LR et al (2006) Design and analysis of high accuracy beam deflection device. Acta Optica Sinica 35(9):1379–1383
- 59. Li AH, Ding Y, Bian YM et al (2014) Inverse solutions for tilting orthogonal double prism. Appl Opt 53(17):3712–3722
- Zu JF, Liu LR, Yun MJ et al (2003) Satellite trajectory optical simulation device: CN, 03129234.8, 24 Dec 2003
- Li AH, Gao XJ (2013) Rotary prism device driven by synchronous belt: CN, 201310072421.0, 12 June 2013
- 62. Sun JF, Liu LR, Yun MJ et al (2005) Intersatellite laser communication terminal high-precision static and dynamic measuring device: CN, 200410024986.2, 23 Feb 2005
- Li AH, Liu LR, Sun JF et al (2005) Double wedge beam deflection mechanism: CN, 200510026553.5, 28 Dec 2005
- Li AH, Li ZZ, Jiang XC (2011) A tilting optical wedge scanning device: CN, 201010588924.X, 18 May 2011
- Li AH, Wang W, Ding Y et al (2013) Cam-driven tilting prism mechanism: CN, 201210375722.6, 16 Jan 2013
- Sun JF, Liu LR, Yun MJ et al (2004) Double prisms for two-dimensional optical satellite relative-trajectory simulator. Proc SPIE 5550:411–418
- 67. Sánchez M, Gutow D (2006) Control laws for a 3-element Risley prism optical beam pointer. Proc SPIE 6304:630403–630403-7
- García-Torales G, Flores JL, Muñoz RX (2007) High precision prism scanning system. Proc SPIE 6422:64220X–64220X-8
- 69. Lu W, Liu LR, Sun JF et al (2010) Control loop analysis of the complex axis in satellite laser communications. Proc SPIE 7814:781410–781410-11
- Li AH, Yi WL, Sun WS et al (2015) Tilting double-prism scanner driven by cam-based mechanism. Appl Opt 54(16):5788–5796
- Oka K, Kaneko T (2003) Compact complete imaging polarimeter using birefringent wedge prisms. Opt Express 11(13):1510–1519

References 39

 Duma VF (2007) Double-prisms neutral density filters: a comparative approach. Proc SPIE, 67851W-67851W-9

- Warger WC II, DiMarzio CA (2007) Dual-wedge scanning confocal reflectance microscope. Opt Lett 32(15):2140–2142
- 74. Tao XD, Cho H, Janabi-Sharifi F (2010) Optical design of a variable view imaging system with the combination of a telecentric scanner and double wedge prisms. Appl Opt 49(2):239–246
- 75. William CS (2005) Optical switch using Risley prisms: US, US6859120B2, 22 Feb 2005
- 76. James JS, Single C (2001) M × N optical fiber switch: US, US2001/0046345A1, 29 Nov 2001
- RPA Compact Beam Steering Device. Optra Inc, Topsfield, MA. 13 Oct 2016. http://www.optra.com/images/PS_RPA_Datasheet_R2.pdf
- 78. Schwarze C (2006) A new look at Risley prisms. Photonics Spectra 40(6):67–70
- Schundler E, Carlson D, Vaillancourt R et al (2011) Compact, wide field DRS explosive detector. Proc SPIE 8018:801810–801810-12
- 80. Clark CS, Gentile S (2009) Flight miniature Risley prism mechanism. Proc SPIE 7429:74290G–74290G-8
- 81. Winsor R, Braunstein M (2006) Conformal beam steering apparatus for simultaneous manipulation of optical and radio frequency signals. Proc SPIE 6215:62150G–62150G-10
- Degnan J, Mcgarry J, Zagwordzki T et al (2008) Transmitter point-ahead using dual Risley prisms: theory and experiment. In: Proceedings of the 16th international workshop on laser ranging, pp 332–338
- 83. Hakun C, Budinoff J, Brown G et al (2004) A boresight adjustment mechanism for use on laser altimeters. In: Proceedings of the 37th aerospace mechanisms symposium, pp 45–58
- 84. Tame BJ, Stutzke NA (2010) Steerable Risley prism antennas with low side lobes in the Ka band. In: IEEE international conference on wireless information technology and systems (ICWITS), pp 1–4
- Sun JF, Liu LR, Yun MJ et al (2005) The design and fabrication of the satellite relative-movement trajectory simulator for inter-satellite laser communications. Proc SPIE 5892:58921J–58921J-8
- Vaidyanathan M, Blask S, Higgins T et al (2007) Jigsaw phase III: a miniaturized airborne
 Jimaging laser radar with photon-counting sensitivity for foliage penetration. Proc SPIE 6550:65500N–65500N-12
- 87. Degnan J, Wells D, Machan R et al (2006) Second generation 3D imaging lidars based on photon counting. Proc SPIE 6771:67710N–67710N-7
- 88. Snyder JJ, Kwiatkowski SL (2003) Single channel M×N optical fiber: US Patent, US6636664B2, 21 Oct 2003
- 89. Paez G, Strojnik M (2002) Versatility of the vectorial shearing interferometer. Proc SPIE 4486:513–522
- 90. García-Torales G, Flores JL (2007) Vectorial shearing interferometer with a high resolution phase shifter. Proc SPIE 6723:672330–672330-8
- 91. Rothberg SJ, Tirabassi M (2013) Development of a scanning head for laser Doppler vibrometry (LDV) using dual optical wedges. Rev Sci Instrum 84(12):121704–121704-10
- Pan CT, Hwang YM, Hsieh CW (2005) Dynamic characterization of silicon-based microstructure of high aspect ratio by dual-prism UV laser system. Sens Actuators, A 122(1):45–54
- 93. Yuan PP, Tao Z, Luan YD et al (2011) Airborne infrared scanning observation device realized by double optical wedge: CN, 201010291427.3, 13 Apr 2011
- 94. Lavigne V, Ricard B (2005) Step-stare image gathering for high-resolution targeting. In: Meeting proceedings RTO-MP-SET-092, pp 17-1-17-14
- Souvestre F, Hafez M, Regnier S (2009) A novel laser-based tracking approach for wide field of view for robotics applications. In: International symposium on optomechatronic technologie, pp 328–333
- 96. Souvestre F, Hafez M, Regnier S (2010) DMD-based multi-target laser tracking for motion capturing. Proc SPIE 7596:75960B–75960B-9
- 97. Fountain WD, Knopp CF (1992) System for scanning a surgical laser beam: International, WO92/03187, 5 Mar 1992

98. Kim K, Kim D, Matsumiya K et al (2005) Wide FOV wedge prism endoscope. In: Proceedings of the 2005 IEEE engineering in medicine and biology society 27th annual conference, pp 5758–5761

- 99. Warger II WC, Guerrera SA, Eastman Z et al (2009) Efficient confocal microscopy with a dual-wedge scanner. Proc SPIE 7184:71840M-71840M-11
- Tao XD, Cho H, Janabi-Sharifi F (2008) Active optical system for variable view imaging of micro objects with emphasis on kinematic analysis. Appl Opt 47(22):4121–4132
- 101. Strong G (2005) Gun sight compensator: US, US2005/0039370A1, 24 Feb 2005
- 102. Li Y, Li L, Huang Y (2008) Conformal optical design using counterrotating wedges and Zernike fringe sag surfaces. Proc SPIE 7133:713340–713340-8
- Chu C (2004) Double Risley prism pairs for optical beam steering and alignment. US, US20040057656A1, 25 Mar 2004

Chapter 2 Double-Prism Multi-mode Scan Theory



Abstract The multi-mode beam scan model is firstly established on the basis of double Risley prisms. Theoretical modelling of double prisms at rotating or tilting scan mode is performed with both vector refraction method and geometric method. Several essential issues concerned with beam scan performance are thoroughly investigated, including multi-mode parameter selection, multi-mode scan trajectories, scan coverage, blind zone and scan precision. Tilting double prisms are specially explored to achieve sub-microradian scan precision within smaller scan range in both vertical and horizontal directions. The multi-prism combination model is also demonstrated for larger beam scan region, within which multi-mode scan trajectories can be generated.

2.1 Introduction

It is fundamental to establish the beam steering mechanism for developing multimode scan theories and techniques based on double Risley prisms, that is, to find the internal relation between the emergent beam pointing and the corresponding prism orientations. There are two basic problems encountered in the beam steering applications of Risley-prism systems that have to be addressed, namely the forward problem and the inverse one [1]. The former focuses on how to determine the deviation angle of the beam emerging from the system according to the given orientations of two prisms. The latter is about how to inversely solve the orientations of two prisms according to the given deviation angle of the final emergent beam.

Through forward and inverse solution models, the relation between the beam pointing position and the corresponding prisms' orientations can be established in any double Risley-prism-based system. The beam propagation model based on paraxial approximation can serve as an effective tool to investigate the double-prism beam scan mechanism. But in practice, the structural and layout parameters of a double-prism system will influence the beam steering position at all prism surfaces, and further, the beam scan position on the target [2]. Therefore, it is essential to establish

a rigorous mathematical model of the beam propagation through two prisms and explore the effects of different structural and layout parameters on the beam scan position, which can help reveal the beam steering mechanism and beam scan law.

2.2 Basic Principle of Double-Prism Multi-mode Scanning

2.2.1 Approximate Solution for Rotating Scan Model

In 1960, Rosell historically adopted a pair of rotating Risley prisms to produce various beam scan patterns, and derived the beam deviation expressions for both thin prism and thick prism [3]. Since then, rotating double prisms have been applied in more and more technical fields.

Conceptually, the rotating double-prism beam steering system is composed of two coaxial and sequential prisms, which usually have the same wedge angle and refractive index. Both prisms are capable of independent rotation around the common axis. As shown in Fig. 2.1, the beam is incident parallel to the optical axis of the system and refracted by prism 1 and prism 2 in order. With different combinations of prism orientations, the beam can be steered to any position within a certain angular range [4]. The pitch angle ρ and azimuth angle φ of the emergent beam can be further determined according to the rotation angles θ_{r1} and θ_{r2} of two prisms.

If the wedge angle of each prism is relatively small, there are approximate formulae as follows [3]:

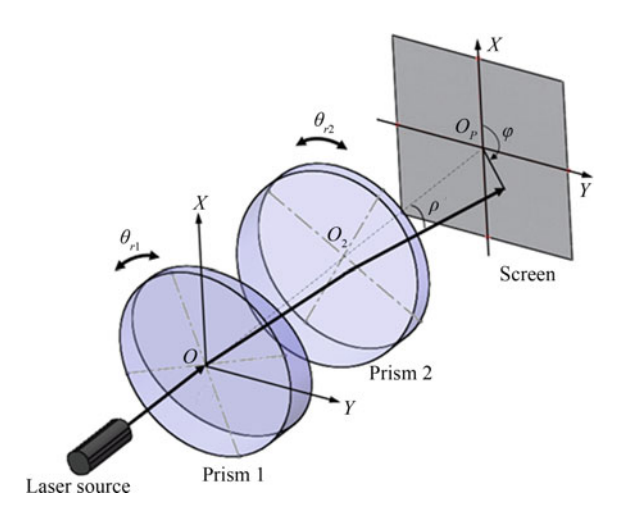


Fig. 2.1 Schematic diagram illustrating the beam deviation by rotating double prisms

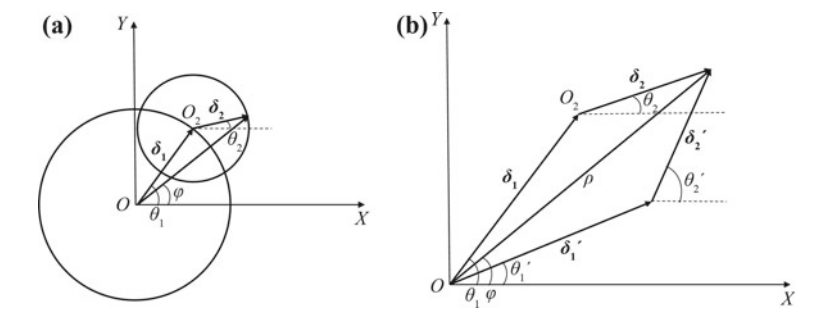


Fig. 2.2 First-order approximation to the beam deviations imparted by double prisms, where a describes the beam pointing direction, and b indicates two sets of inverse solutions

$$\begin{cases} \varphi = \frac{\theta_{r_1} + \theta_{r_2}}{2} \\ \rho = 2\alpha(n-1)\cos\frac{\theta_{r_1} - \theta_{r_2}}{2} \end{cases}$$
 (2.1)

where θ_{r1} and θ_{r2} denote the individual rotation angles of two prisms, φ and ρ are, respectively, the azimuth angle and the pitch angle, n and α represent the refractive index and wedge angle of each prism.

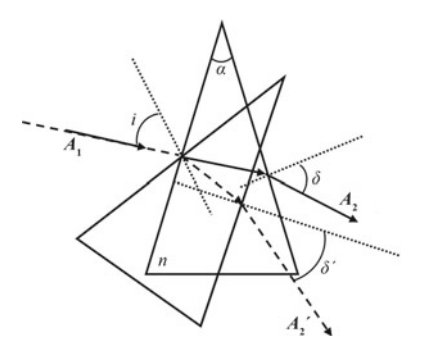
However, as the wedge angle gets larger, the solving accuracy of the above formulae decreases to some extent, which cannot be accepted in some practical applications.

A first-order approximation method has ever been proposed in reference [4], where each of two prisms is regarded with relatively small wedge angle. The magnitude of beam deviation depends only on the wedge angle and the refractive index. Thus, the emergent beam is always steered towards the thickest end of the principal section of each prism, despite the prism orientation and the pointing direction of incident beam. As shown in Fig. 2.2a, the beam deviations imparted by two prisms can be described by a pair of vectors δ_1 and δ_2 . The beam is firstly steered to one circle centered at the beginning of δ_1 and taking the length of δ_1 as radius, and then steered to the other circle centered at the beginning of δ_2 and taking the length of δ_2 as radius. Consequently, the vector ρ for the total beam deviation is considered as the sum of δ_1 and δ_2 . According to the parallelogram law indicated in Fig. 2.2b, there are two possible solutions of prism orientations to steer the final emergent beam in a certain direction.

For a double-prism system composed of thick prisms, the incident beam to prism 2 is actually non-paraxial, and the incidence angle of the beam to prism 2 varies with the relative rotation angle of two prisms, which results in a non-circular field of view [5]. Nevertheless, the simplified model based on thin prisms can remove the complication of calculating optical path to provide prediction results, which help clarify the beam deviation laws in any rotating double-prism scanner.

On the previous basis, Li [6] obtained one general forward solution for the beam transmitting through two thick prisms. The solution was then expanded into a power series to deduce the third-order approximation with greatly enhanced accu-

Fig. 2.3 Beam steering principle by tilting a single prism



racy. Unfortunately, this method involves the first-order or third-order non-paraxial approximation, which can only be utilized to investigate the beam steering issues over a small angular range.

Therefore, the non-paraxial ray tracing method or the geometric method should be applied to establish an accurate beam propagation model for the double-prism multimode scan system. The former based on Snell's law can trace the beam propagation path in order to obtain a precise forward solution, while the latter can be performed through the coordinate transformation of beam vectors.

2.2.2 Basic Solution for Tilting Scan Model

The tilting prism used for beam steering has been reported in an earlier optics literature [7]. Figure 2.3 illustrates the principle of beam steering by tilting one single prism, where n and α denote the refractive index and wedge angle of the prism, respectively. The incident beam is specified by the vector A_1 with an incidence angle i, and the emergent beam is described by the vector A_2 , of which the deviation angle is δ . Besides, the incidence angle is prescribed to be positive when the incident beam is counterclockwise with respect to the prism surface normal, and the beam deviation angle is prescribed to be positive when the acute angle between the emergent beam and the incident beam is clockwise. Seen from Fig. 2.3, the emergent beam vector is A_2 with a deviation angle δ if the prism keeps stationary, and it turns to A_2 with a deviation angle δ once the prism tilts with an angle i.

According to Snell's law, the final beam deviation angle can be expressed as

$$\delta = i + \arcsin(\sin \alpha \sqrt{n^2 - \sin^2 i} - \cos \alpha \sin i) - \alpha$$
 (2.2)

Given small wedge angle α and small incidence angle i, (2.2) can be simplified as

$$\delta \approx (n-1)\left(1 + \frac{n+1}{2n}i^2\right)\alpha \approx (n-1)\alpha$$
 (2.3)

α/(°)	Max δ_1 /mrad	Min δ_1 /mrad	Range δ_1 /mrad	Max $\partial \delta_1/\partial i/(\text{rad}/(^\circ))$	Min $\partial \delta_1/\partial i/(\text{rad}/(^\circ))$	Mean $\partial \delta_1/\partial i/(\text{rad}/(^\circ))$
2	18.245	18.050	0.1954	9.800×10^{-6}	-1.900×10^{-5}	-4.518×10^{-6}
3	27.448	27.082	0.3666	1.133×10^{-5}	-3.209×10^{-5}	-1.019×10^{-5}
4	36.720	36.121	0.5990	1.063×10^{-5}	-4.768×10^{-5}	-1.818×10^{-5}
5	46.073	45.171	0.9014	7.708×10^{-6}	-6.587×10^{-5}	-2.854×10^{-5}
6	55.519	54.235	1.284	2.528×10^{-6}	-8.677×10^{-5}	-4.134×10^{-5}
7	65.071	63.315	1.756	-4.933×10^{-6}	-1.105×10^{-4}	-5.665×10^{-5}
8	74.744	72.433	2.312	-1.472×10^{-5}	-1.373×10^{-4}	-7.457×10^{-5}

Table 2.1 Beam deviation angle δ_1 and change rate $\partial \delta_1/\partial i$ corresponding to different wedge angle

Differentiating (2.2) with respect to i, we can obtain the change rate of the beam deviation angle relative to the incidence angle:

$$\frac{\partial \delta}{\partial i} = 1 + \frac{(-\cos i \cos \alpha - \frac{\sin \alpha \sin i \cos i}{\sqrt{n^2 - \sin^2 i}})}{\sqrt{1 - (\sin \alpha \sqrt{n^2 - \sin^2 i} - \sin i \cos \alpha)^2}}$$
(2.4)

Table 2.1 indicates the dependence of δ on α when the incidence angle of the incident beam ranges from -5° to 5° .

Providing the incidence angle i within the same range, the beam deviation angle together with the absolute value of the change rate of beam deviation angle will vary within a larger range as the wedge angle increases, as shown in Table 2.1. That is, the beam steering accuracy becomes lower and lower. Consequently, the magnitude of wedge angle must be synthetically optimized according to the requirements of both beam scan range and beam scan precision.

It is also inferred from Table 2.1 that, if the wedge angle is as small as 5°, the tilting motion of the prism within a narrow angular range can be equivalent to the continuous variation of the beam incidence angle, which enables precise deviation of the emergent beam.

Reference [8] has provided the accurate and approximate expressions for the deviation angle of the beam passing through a single prism. When $\alpha = 5^{\circ}$ and $i = -30^{\circ}$ to 30° , the beam deviation range is plotted in Fig. 2.4a. The accurate and approximate solutions of beam deviation in Fig. 2.4a are obtained from (2.2) and (2.3), respectively. It was also validated in reference [8] that there could be a hundredfold-order reduction ratio from the tilting angle of one prism to the consequent beam deviation angle, as shown in Fig. 2.4b.

Furthermore, the beam deviation angle is non-monotonic when the prism orientation θ ranges within -30° to 30° . In order to facilitate the control of beam scanning, the tilting angle must be limited on either side of the value that results in the minimum

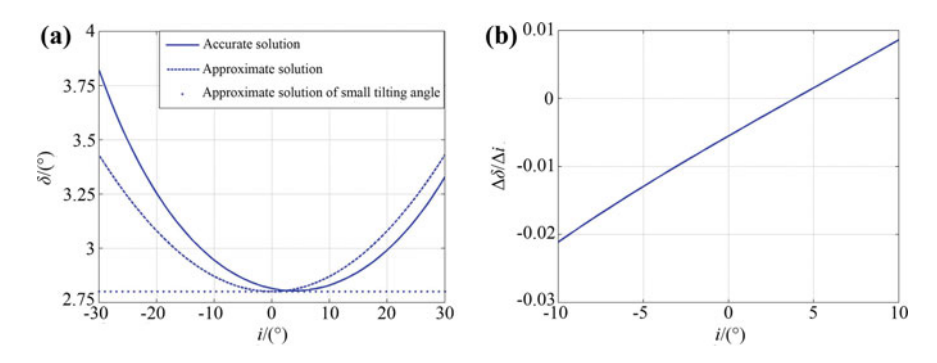


Fig. 2.4 Beam deviation angle associated with the incidence angle, where a shows the variation of the deviation angle with the incidence angle, and b depicts the change rate of the deviation angle relative to the incidence angle

Table 2.2 Influence of wedge angle on minimum beam deviation angle and the required tilting angle range

α/(°)	3	4	5	6	7
$\delta_{\min}/(^{\circ})$	1.5496	2.0668	2.5846	3.1032	3.6227
<i>i</i> /(°)	-2.4333	-3.0613	-3.7097	-4.5806	-5.2903
$\theta_{\min}/(^{\circ})$	-2.4333	-3.0613	-3.7092	-4.5806	-5.2903
θ _{max} /(°)	7.1111	5.1111	2.8889	2.2222	0.88889

beam deviation angle. For a refractive prism, the minimum beam deviation angle can be determined from

$$\delta_{\min} = 2\arcsin(n) \cdot \sin\frac{\alpha}{2} - \alpha$$
 (2.5)

Corresponding to different values of the wedge angle α , Table 2.2 lists the minimum beam deviation angles δ_{\min} , the incidence angle i of the beam, as well as the minimum tilting angle range $\theta_{\min} - \theta_{\max}$ required to achieve the beam scan range of 600 μ rad.

2.3 Theoretical Model of Double-Prism Multi-mode Scan System

The beam scan mode depends on the motion form of double prisms. There are diverse motion forms of double prisms, including coaxial rotation, orthogonal tilting motion and their combination, which can generate multiple scan modes and enhance the versatility of the system in different scan applications. Generally, the double-prism system at rotating scan mode is able to perform high-accuracy radial scanning within

a wide scan coverage, and the one at tilting scan mode will achieve higher directional scan accuracy as a result of the much larger reduction ratio from prism orientation to beam deviation angle. Moreover, the system at composite scan mode has more motion degrees of freedom to produce variable-scale and multi-mode scan patterns. This section mainly expounds the theoretical modelling of rotating and tilting double-prism systems, and the composite system can be modelled in a similar fashion.

2.3.1 Rotating Scan Model

Under the Cartesian coordinate system OXYZ defined in Fig. 2.5, the rotating scan model is composed of two identical prisms [9], named prism 1 and prism 2 sequentially in the positive Z-direction. The prisms have the same wedge angle α , refractive index n and thinnest-end thickness d_0 . The incident surface 11 of prism 1 is a plane perpendicular to the Z-axis, and the emergent surface of prism 1 is a wedged plane 12. Oppositely, the incident surface of prism 2 is a wedged plane 21, and the emergent surface 22 of prism 2 is perpendicular to the Z-axis. For simplicity, the coordinate origin O(0, 0, 0) is fixed at the center of prism surface 11, the centers of prism surfaces 21 and 22 are labeled with O' and O_2 , respectively, and the distance between points O and O_2 is denoted by O1. Both prisms are able to rotate around the O2-axis, and the counterclockwise rotation angle is defined as positive angle. In addition, the rotation angular velocities of prism 1 and prism 2 are, respectively, represented by O2-axis, and O3-axis, and O4-axis, and O5-axis, are applied to O5-axis, and O6-axis, and O7-axis, and O8-axis, and O9-axis, and O9-axis, and O9-axis, and axis, ax

Initially, the principal section of each prism is located in the XOZ plane, with its thinnest end pointing towards the positive X-direction. The rotation angles of two prisms are given by $\theta_{r1} = \theta_{r2} = 0^{\circ}$, which act as time-dependent variables denoted by $\theta_{r1}(t)$ for prism 1 and $\theta_{r2}(t)$ for prism 2. Assuming that the laser beam is firstly incident on the incident surface of prism 1, the angle of the incident beam relative to the positive Y-direction is denoted by β_{r1} , and that between the beam projection in the XOZ plane and the positive Z-direction is denoted by γ_{r1} . In principle, β_{r1} and γ_{r1} are taken within 0° to 180° and -90° to 90° , respectively, but their actual ranges should be properly modified under the consideration of total internal reflection. After refracted by rotating double prisms, the beam path eventually reaches the screen P in the XO_PY plane, which locates away from the emergent surface center O_2 of prism 2 with a distance O_2 . Furthermore, ρ stands for the deviation angle of the emergent beam with respect to the positive Z-direction, and φ represents the angle between the emergent beam projection in the XO_PY plane and the positive X-direction.

1. Based on Vector Refraction Theorem

According to the vector refraction theorem [10], if the beam transmits through two homogeneous media, the incident and refracted beam vectors can be expressed as

$$n_1 A_1 \times \mathbf{N} = n_2 A_2 \times N$$

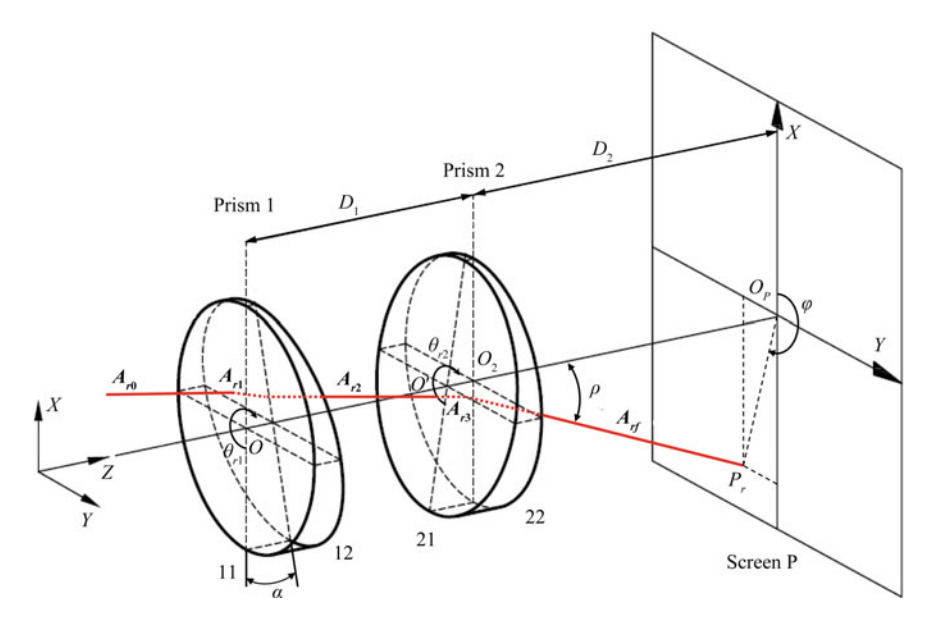


Fig. 2.5 Schematic diagram illustrating rotating double-prism scan model

$$A_2 = \frac{n_1}{n_2} A_1 + \left\{ \sqrt{1 - \left(\frac{n_1}{n_2}\right)^2 \left[1 - (A_1 \cdot N)^2\right]} - \frac{n_1}{n_2} (A_1 \cdot N) \right\} N$$

where A_1 and A_2 are unit vectors for the incident and emergent beams, respectively, N denotes the normal vector to the refractive surface, pointing from medium 1 towards medium 2, and the two media have different refractive indices n_1 and n_2 .

Each of the above equations can be used to describe the propagation path of the refracted beam.

The normal vectors to the incident and emergent surfaces of prism 1, denoted by N_{11} and N_{12} , along with the ones to the incident and emergent surfaces of prism 2, denoted by N_{21} and N_{22} , are obtained from

$$N_{11} = (0, 0, 1)^{\mathrm{T}} \tag{2.6a}$$

$$N_{12} = (\cos \theta_{r1} \sin \alpha, \sin \theta_{r1} \sin \alpha, \cos \alpha)^{\mathrm{T}}$$
 (2.6b)

$$N_{21} = (-\cos \theta_{r2} \sin \alpha, -\sin \theta_{r2} \sin \alpha, \cos \alpha)^{\mathrm{T}}$$
 (2.6c)

$$N_{22} = (0, 0, 1)^{\mathrm{T}} \tag{2.6d}$$

The incident beam vector to prism 1, the refracted beam vector at the incident surface of prism 1, and the emergent beam vector from prism 1 are written as A_{r0} , A_{r1} and A_{r2} in sequence. A_{r2} is also the incident beam vector to the incident surface of prism 2. The refracted beam vector at the incident surface of prism 2 and the emergent

beam vector from prism 2 are, respectively, denoted by A_{r3} and A_{rf} . According to the vector refraction theorem, we have

$$A_{r0} = (\sin \beta_{r1} \sin \gamma_{r1}, \cos \beta_{r1}, \sin \beta_{r1} \cos \gamma_{r1})^{T} = (x_{r0}, y_{r0}, z_{r0})^{T}$$

$$(2.7a)$$

$$A_{r1} = \frac{1}{n} A_{r0} + \left\{ \sqrt{1 - \left(\frac{1}{n}\right)^{2} \cdot [1 - (A_{r0} \cdot N_{11})^{2}]} - \frac{1}{n} A_{r0} \cdot N_{11} \right\} \cdot N_{11}$$

$$= (x_{r1}, y_{r1}, z_{r1})^{T}$$

$$(2.7b)$$

$$A_{r2} = n A_{r1} + \left\{ \sqrt{1 - n^{2} \cdot [1 - (A_{r1} \cdot N_{12})^{2}]} - n A_{r1} \cdot N_{12} \right\} \cdot N_{12}$$

$$= (x_{r2}, y_{r2}, z_{r2})^{T}$$

$$(2.7c)$$

$$A_{r3} = \frac{1}{n} A_{r2} + \left\{ \sqrt{1 - \left(\frac{1}{n}\right)^{2} \cdot [1 - (A_{r2} \cdot N_{21})^{2}]} - \frac{1}{n} A_{r2} \cdot N_{21} \right\} \cdot N_{21}$$

$$= (x_{r3}, y_{r3}, z_{r3})^{T}$$

$$(2.7d)$$

$$A_{rf} = n A_{r3} + \left\{ \sqrt{1 - n^{2} \cdot [1 - (A_{r3} \cdot N_{22})^{2}]} - n A_{r3} \cdot N_{22} \right\} \cdot N_{22}$$

$$= (x_{rf}, y_{rf}, z_{rf})^{T}$$

$$(2.7e)$$

All the refracted beam vectors can be further specified by substituting (2.6) into (2.7). The final expression for the emergent beam pointing is omitted here owing to the fussy derivation.

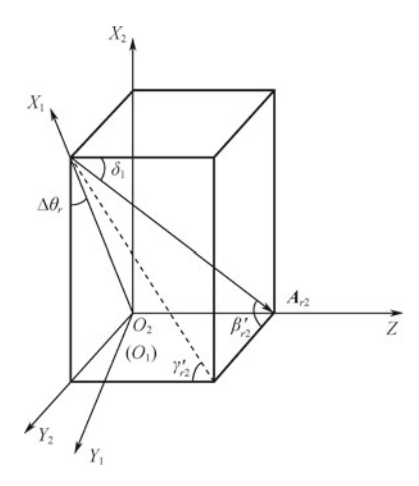
2. Based on Geometric Method

Two Cartesian coordinate systems, $O_1X_1Y_1Z$ and $O_2X_2Y_2Z$, are defined as shown in Fig. 2.6. The coordinate system $O_1X_1Y_1Z$ can rotate at the same speed as prism 1, where the X_1O_1Z plane is specified by the principal section of prism 1 and the positive X_1 -direction points towards the thinnest end of prism 1. Similarly, $O_2X_2Y_2Z$ is a coordinate system rotating at the same speed as prism 2, where the X_2O_2Z plane is specified by the principal section of prism 2 and the positive X_1 -direction points towards the thinnest end of prism 2. The X_1O_1Z plane can also be determined in terms of the emergent beam vector A_{r2} from prism 1 and the beam projection in the $X_2O_2Y_2$ plane, because the incident beam is purely deflected within the principal section while propagating through prism 1.

Under the global coordinate system OXYZ, the incident beam vector to prism 1 is given by $A_{r0} = (\sin \beta_{r1} \sin \gamma_{r1}, \cos \beta_{r1}, \sin \beta_{r1} \cos \gamma_{r1})^T$. Since the coordinate system $O_1X_1Y_1Z$ can be obtained by rotating the coordinate system OXYZ counterclockwise around the Z-axis with an angle θ_{r1} , the incident beam vector is expressed as follows under the coordinate system $O_1X_1Y_1Z$:

$$A'_{r0} = A_{r0} \text{Rot}(Z, \theta_{r1}) = (x'_{r0}, y'_{r0}, z'_{r0})^{\text{T}}$$
 (2.8a)

Fig. 2.6 Definition of angles under two dynamic coordinate systems



Where
$$\mathbf{Rot}(Z, \theta_{r1}) = \begin{pmatrix} \cos \theta_{r1} & \sin \theta_{r1} & 0 \\ -\sin \theta_{r1} & \cos \theta_{r1} & 0 \\ 0 & 0 & 1 \end{pmatrix}$$
.

Under the coordinate system $O_1X_1Y_1Z$, the emergent beam vector from prism 1 is written as

$$A'_{r2} = \left(\sin \beta'_{r1} \sin(\gamma'_{r1} - \delta_1), \cos \beta'_{r1}, \sin \beta'_{r1} \cos(\gamma'_{r1} - \delta_1)\right)^{\mathrm{T}}$$
(2.8b)

The deviation angle of the emergent beam from prism 1 with respect to the incident beam can be deduced from

$$\delta_1 = i_1 - \arcsin(\sin i_1 \cos \alpha - \sin \alpha \sqrt{\overline{n_1^2 - \sin^2 i_1}}) - \alpha \tag{2.8c}$$

where β'_{r1} denotes the angle of A'_{r0} relative to the Y_1 -axis under the coordinate system $O_1X_1Y_1Z$, given by $\beta'_{r1} = \arccos(y'_{r0}); \gamma'_{r1}$ is the angle between the projection of A'_{r0} in the X_1O_1Z plane and the Z-axis, given by $\gamma'_{r1} = \arctan(x'_{r0}/z'_{r0}); i_1$ represents the incidence angle of the beam to prism 1, given by $i_1 = \gamma'_{r1}$; and \overline{n}_1 is the equivalent refractive index of prism 1, given by $\overline{n}_1 = \sqrt{n^2 + (n^2 - 1)\cot^2\beta'_{r1}}$.

After rotating clockwise around the Z-axis with an angle θ_{r1} , the emergent beam vector from prism 1 can be transformed as follows under the coordinate system OXYZ:

$$A_{r2} = A'_{r2} \mathbf{Rot}(Z, -\theta_{r1}) = (x_{r2}, y_{r2}, z_{r2})^{\mathrm{T}}$$
 (2.8d)

By rotating the coordinate system $O_1X_1Y_1Z$ counterclockwise around the Z-axis with an angle $\theta_{r2} - \theta_{r1}$, the coordinate system $O_2X_2Y_2Z$ is also specified. Under

the coordinate system $O_2X_2Y_2Z$, the emergent beam vector from prism 1 can be expressed as

$$A_{r2}'' = A_{r2}' \text{Rot}(Z, \theta_{r2} - \theta_{r1}) = (x_{r2}'', y_{r2}'', z_{r2}'')^{\text{T}}$$
(2.9a)

The emergent beam vector from prism 2 is expressed as follows under the coordinate system $O_2X_2Y_2Z$:

$$A'_{rf} = \left(\sin \beta'_{r2} \sin(\gamma'_{r2} - \delta_2), \cos \beta'_{r2}, \sin \beta'_{r2} \cos(\gamma'_{r2} - \delta_2)\right)^{\mathrm{T}}$$
(2.9b)

The deviation angle of the emergent beam from prism 2 with respect to the incident beam can be obtained from

$$\delta_2 = i_2 - \arcsin(\sin i_2 \cos \alpha - \sin \alpha \sqrt{\overline{n_2^2 - \sin^2 i_2}}) - \alpha \tag{2.9c}$$

where β'_{r1} denotes the angle of A''_{r2} relative to the Y_2 -axis under the coordinate system $O_2X_2Y_2Z$, given by $\beta'_{r2} = \arccos(y''_{r2}), \gamma'_{r2}$ is the angle between the projection of A''_{r2} in the X_2O_2Z plane and the Z-axis, given by $\gamma'_{r2} = \arctan(x''_{r2}/z''_{r2}); i_2$ represents the angle of the incident beam to prism 2, given by $i_2 = \gamma'_{r2} + \alpha$; and \bar{n}_2 is the equivalent refractive index of prism 2, given by $\overline{n_2} = \sqrt{n^2 + (n^2 - 1)\cot^2\beta'_{r2}}$.

After rotating clockwise around the Z-axis with an angle θ_{r2} , the emergent beam vector from prism 2 can be transformed as follows under the coordinate system OXYZ:

$$A_{rf} = A'_{rf} Rot(Z, -\theta_{r2}) = \left(x_{rf}, y_{rf}, z_{rf}\right)^{\mathrm{T}}$$
(2.9d)

Providing the incident beam perpendicular to the incident surface of prism 1, namely $\beta_{r1} = 90^{\circ}$ and $\gamma_{r1} = 0^{\circ}$, the emergent beam vector from prism 2 is determined by

$$\begin{pmatrix} x_{rf} \\ y_{rf} \\ z_{rf} \end{pmatrix} = \begin{pmatrix} -\cos\theta_{r2}(\sin\delta_{1}\cos\delta_{2}\cos\Delta\theta_{r} + \cos\delta_{1}\sin\delta_{2}) + \sin\theta_{r2}\sin\delta_{1}\sin\Delta\theta_{r} \\ -\sin\theta_{r2}(\sin\delta_{1}\cos\delta_{2}\cos\Delta\theta_{r} + \cos\delta_{1}\sin\delta_{2}) - \cos\theta_{r2}\sin\delta_{1}\sin\Delta\theta_{r} \\ \cos\delta_{1}\cos\delta_{2} - \sin\delta_{1}\sin\delta_{2}\cos\Delta\theta_{r} \end{pmatrix}$$
(2.10a)

where

$$\delta_1 = \arcsin(n \sin \alpha) - \alpha \tag{2.10b}$$

$$\delta_2 = i_2 - \arcsin\left(\sin i_2 \cos \alpha - \sin \alpha \sqrt{\overline{n_2}^2 - \sin^2 i_2}\right) - \alpha \tag{2.10c}$$

$$i_2 = -\arctan(\tan \delta_1 \cos \Delta \theta_r) + \alpha$$
 (2.10d)

$$\overline{n_2} = \sqrt{n^2 + (n^2 - 1)\cot^2 \beta'_{r2}}$$
 (2.10e)

$$\beta'_{r2} = \arccos(\sin \delta_1 \sin \Delta \theta_r)$$
 (2.10f)

$$\Delta \theta_r = \theta_{r1} - \theta_{r2} \tag{2.10g}$$

The angle of the emergent beam relative to the Z-axis is defined as pitch angle ρ , given by

$$\rho = \arccos(z_{rf}) = \arccos[\cos \delta_1 \cos \delta_2 - \sin \delta_1 \sin \delta_2 \cos \Delta \theta_r]$$
 (2.11a)

The angle between the emergent beam projection in the *XOY* plane and the positive *X*-direction is defined as azimuth angle φ , given by

$$\varphi = \begin{cases} \arccos\left(\frac{x_{rf}}{\sqrt{x_{rf}^2 + y_{rf}^2}}\right), y_{rf} \ge 0\\ 2\pi - \arccos\left(\frac{x_{rf}}{\sqrt{x_{rf}^2 + y_{rf}^2}}\right), y_{rf} < 0 \end{cases}$$
(2.11b)

2.3.2 Tilting Scan Model

Under the Cartesian coordinate system OXYZ established in Fig. 2.7, the tilting scan model [1] consists of two identical prisms, named prism 1 and prism 2 sequentially in the positive Z-direction. The prisms have the same wedge angle α and refractive index n. Initially, the incident surface 11 of prism 1 is perpendicular to the Z-axis, and the emergent surface 12 is the wedged plane with an angle α . Oppositely, the incident surface 21 of prism 2 is the wedged plane with an angle α , and the emergent surface 22 is perpendicular to the Z-axis. For simplicity, the coordinate origin O(0, 0, 0) coincides with the center of prism surface 11, the centers of prism surfaces 21 and 22 are marked as O' and O_2 , respectively, and the distance between points O and O_2 is denoted by O1. The principal section of prism 1 is located in the XOZ plane with its thinnest end towards the positive X-direction, whereas the one of prism 2 is located in the YOZ plane with its thinnest end towards the positive Y-direction.

Prism 1 can tilt around the axis which keeps perpendicular to its principal section and passes the center point O, at an angular velocity denoted by ω_{t1} , while prism 2 is able to tilt around the axis perpendicular to the principal section and passing the center point O_2 , at an angular velocity denoted by ω_{t2} . The tilting angles of prism 1 and prism 2 are, respectively, initialized by $\theta_{t1} = \theta_{t2} = 0^{\circ}$ and act as time-dependent variables denoted by $\theta_{t1}(t)$ and $\theta_{t2}(t)$. Here the counterclockwise tilting angle is prescribed to be positive, and thus, the clockwise tilting angle is prescribed to be negative.

Assuming that the laser beam is firstly incident on the incident surface of prism 1, the angle of the incident beam relative to the positive *Y*-direction is denoted by β_{t1} , and the angle between the incident beam projection in the *XOZ* plane and the positive

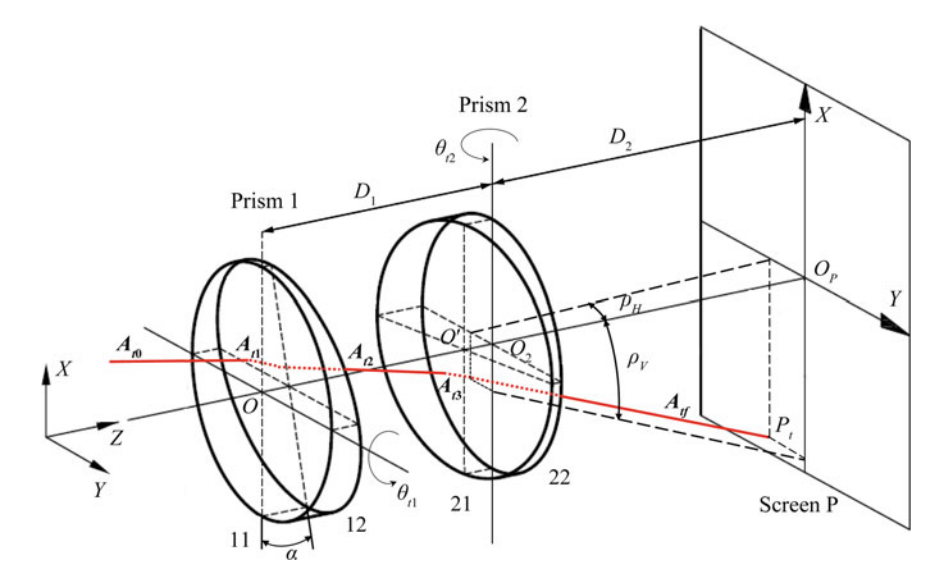


Fig. 2.7 Schematic diagram illustrating tilting double-prism scan model

Z-direction is denoted by γ_{t1} . β_{t1} and γ_{t1} are taken within 0° to 180° and -90° to 90°, respectively, but their actual ranges need be modified under the consideration of total internal reflection. After refracted by two tilting prisms, the beam finally arrives at the screen P, which is placed away from the emergent surface of prism 2 with a distance D_2 .

1. Based on Vector Refraction Theorem

The normal vectors to the incident and emergent surfaces of prism 1, denoted by N_{11} and N_{12} , along with those to the incident and emergent surfaces of prism 2, denoted by N_{21} and N_{22} , are obtained from

$$N_{11} = (\sin \theta_{t1}, 0, \cos \theta_{t1})^{\mathrm{T}}$$
 (2.12a)

$$N_{12} = (\sin(\alpha + \theta_{t1}), 0, \cos(\alpha + \theta_{t1}))^{\mathrm{T}}$$
 (2.12b)

$$N_{21} = (0, -\sin(\alpha + \theta_{t2}), \cos(\alpha + \theta_{t2}))^{\mathrm{T}}$$
 (2.12c)

$$N_{22} = (0, -\sin\theta_{t2}, \cos\theta_{t2})^{\mathrm{T}}$$
 (2.12d)

The incident beam vector to prism 1, the refracted beam vector at the incident surface of prism 1, and the emergent beam vector from prism 1 are written as A_{t0} , A_{t1} and A_{t2} in sequence. A_{t2} is also the incident beam vector to the incident surface of prism 2. The refracted beam vector at the incident surface of prism 2 and the

emergent beam vector from prism 2 are, respectively, denoted by A_{t3} and A_{tf} . From the vector refraction theorem, we have

$$A_{t0} = (\sin \beta_{t1} \sin \gamma_{t1}, \cos \beta_{t1}, \sin \beta_{t1} \cos \gamma_{t1})^{T}$$

$$= (x_{t0}, y_{t0}, z_{t0})^{T}$$

$$(2.13a)$$

$$A_{t1} = \frac{1}{n} A_{t0} + \left\{ \sqrt{1 - \left(\frac{1}{n}\right)^{2} \cdot \left[1 - (A_{t0} \cdot N_{11})^{2}\right] - \frac{1}{n} A_{t0} \cdot N_{11}} \right\} \cdot N_{11}$$

$$= (x_{t1}, y_{t1}, z_{t1})^{T}$$

$$(2.13b)$$

$$A_{t2} = n A_{t1} + \left\{ \sqrt{1 - n^{2} \cdot \left[1 - (A_{t1} \cdot N_{12})^{2}\right] - n A_{t1} \cdot N_{12}} \right\} \cdot N_{12}$$

$$= (x_{t2}, y_{t2}, z_{t2})^{T}$$

$$(2.13c)$$

$$A_{t3} = \frac{1}{n} A_{t2} + \left\{ \sqrt{1 - \left(\frac{1}{n}\right)^{2} \cdot \left[1 - (A_{t2} \cdot N_{21})^{2}\right] - \frac{1}{n} A_{t2} \cdot N_{21}} \right\} \cdot N_{21}$$

$$= (x_{t3}, y_{t3}, z_{t3})^{T}$$

$$(2.13d)$$

$$A_{tf} = n A_{t3} + \left\{ \sqrt{1 - n^{2} \cdot \left[1 - (A_{t3} \cdot N_{22})^{2}\right] - n A_{t3} \cdot N_{22}} \right\} \cdot N_{22}$$

$$= (x_{tf}, y_{tf}, z_{tf})^{T}$$

$$(2.13e)$$

Substituting (2.12) into (2.13), all the refracted beam vectors can be determined. The final expression for the emergent beam pointing is not provided here.

2. Based on Geometric Method

The incident beam to prism 1, specified by $A_{t0} = (\sin \beta_{t1} \sin \gamma_{t1}, \cos \beta_{t1}, \sin \beta_{t1} \cos \gamma_{t1})^{T}$, is merely refracted within the *XOZ* plane while propagating through prism 1. Hence, the emergent beam vector from prism 1 is written as [11]

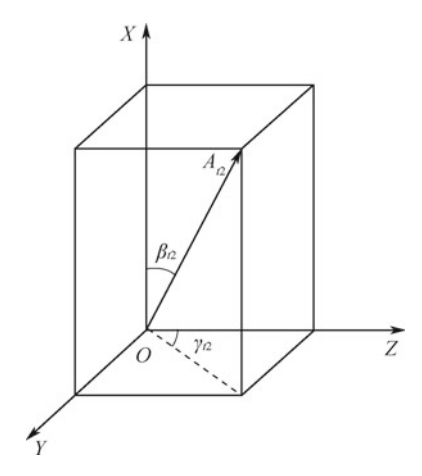
$$A_{t2} = (\sin \beta_{t1} \cos \theta_{11}, \cos \beta_{t1}, \sin \beta_{t1} \sin \theta_{11})^{\mathrm{T}}$$
 (2.14a)

The deviation angle of the emergent beam from prism 1 with respect to the incident beam can be obtained from

$$\delta_1 = i_1 - \arcsin(\sin i_1 \cos \alpha - \sin \alpha \sqrt{\overline{n_1}^2 - \sin^2 i_1}) - \alpha \tag{2.14b}$$

where θ_{11} is the angle between the emergent beam projection in the *XOZ* plane and the positive *X*-direction, given by $\theta_{11} = \pi/2 - \gamma_{t1} + \delta_1$; i_1 is the incidence angle of the beam to prism 1, given by $i_1 = \gamma_{t1} - \theta_{11}$; and \overline{n}_1 is the equivalent refractive index of prism 1, given by $\overline{n}_1 = \sqrt{n^2 + (n^2 - 1) \cot^2 \beta_{t1}}$.

Fig. 2.8 Definition of the angles of the incident beam to prism 2 with respect to the coordinate axes



Similarly, while propagating through prism 2, the beam is only refracted within the *YOZ* plane. The beam incident to prism 2 is exactly the one emerging from prism 1, which can also be expressed as [11]

$$A_{t2} = (\cos \beta_{t2}, \sin \beta_{t2} \sin \gamma_{t2}, \sin \beta_{t2} \cos \gamma_{t2})^{\mathrm{T}}$$
 (2.15a)

where β_{t2} is the angle of A_{t2} relative to the positive X-direction, given by $\beta_{t2} = \arccos(\sin \beta_{t1} \cos \theta_{11})$; and γ_{t2} is the angle between the projection of A_{t2} in the YOZ plane and the positive Z-direction, given by $\gamma_{t2} = \arctan(\cot \beta_{t1}/\sin \theta_{11})$ (Fig. 2.8).

The emergent beam vector from prism 2 is determined by [11].

$$A_{tf} = (\cos \beta_{t2}, \sin \beta_{t2} \sin(\gamma_{t2} - \delta_2), \sin \beta_{t2} \cos(\gamma_{t2} - \delta_2))^{\mathrm{T}} = (x_{tf}, y_{tf}, z_{tf})^{\mathrm{T}}$$
(2.15b)

The deviation angle between the incident and emergent beams for prism 2 is available from

$$\delta_2 = i_2 - \arcsin\left(\sin i_2 \cos \alpha - \sin \alpha \sqrt{\overline{n}_2^2 - \sin^2 i_2}\right) - \alpha \tag{2.15c}$$

where i_2 denotes the incidence angle of the beam to prism 2, given by $i_2 = \gamma_{t2} + \alpha + \theta_{t2}$, and \overline{n}_2 is the equivalent refractive index of prism 2, given by $\overline{n}_2 = \sqrt{n^2 + (n^2 - 1)\cot^2\beta_{t2}}$.

The vertical field angle ρ_V is defined by the angle of the emergent beam projection in the *XOZ* plane relative to the *Z*-axis, expressed as

$$\rho_{V} = \arctan(\frac{x_{tf}}{z_{tf}}) = \arctan\frac{\cot \beta_{t2}}{\cos(\gamma_{t2} - \delta_{2})}$$
 (2.16a)

The horizontal field angle $\rho_{\rm H}$ is defined by the angle between the emergent beam projection in the YOZ plane and the Z-axis, expressed as

$$\rho_{\rm H} = \arctan(\frac{y_{tf}}{z_{tf}}) = \gamma_{t2} - \delta_2 \tag{2.16b}$$

Without any special statement, the incident beam to each double-prism scan model is supposed to propagate along the optical axis in the subsequent chapters, namely $A_{r0} = A_{t0} = (0, 0, 1)^{T}$. However, the proposed methods are also helpful to investigate the general situation where the beam is incident with an arbitrary angle.

2.4 Scan Region and Scan Precision of Double-Prism Multi-mode Scanning

2.4.1 Rotating Scan Mode

1. Beam Scan Region

Based on the rotating scan model in Sect. 2.3.1, the pitch angle of the emergent beam can be obtained as follows when the incident beam is along the optical axis of the system:

$$\rho = \arccos[\cos \delta_1 \cos \delta_2 - \sin \delta_1 \sin \delta_2 \cos \Delta \theta_r] \tag{2.17}$$

It can be found that the pitch angle ρ is concerned with the beam deviation angle δ_1 induced by prism 1, δ_2 induced by prism 2 and the relative rotation angle $\Delta\theta_r$ of double prisms, which accounts for the functional relation expressed as $\rho=f$ ($\Delta\theta_r$, α , n). Since the wedge angle α and refractive index n are both constants in a specific rotating double-prism system, the beam deviation angle δ_1 is kept unchanged while δ_2 is only dependent on the relative rotation angle $\Delta\theta_r$. Therefore, the expression for the pitch angle can be simplified as a function associated with $\Delta\theta_r$, namely $\rho=f$ ($\Delta\theta_r$). It is further clarified that f ($-\Delta\theta_r$) = f ($\Delta\theta_r$) when $\Delta\theta_r$ 1 varies within -180° to 180° , which confirms $\rho=f$ ($\Delta\theta_r$) as an even function. Providing that $\alpha=10^\circ$, n=1.517 and $\Delta\theta_r$ ranges within -180° to 180° , the relation of the pitch angle ρ with respect to $\Delta\theta_r$ can be determined as shown in Fig. 2.9.

Obviously, the correlation curve in Fig. 2.9 is symmetric about $\Delta\theta_r = 0^\circ$, and the pitch angle ρ decreases with the increment of the absolute value $|\Delta\theta_r|$. The maximum value of the pitch angle is $\rho_{\text{max}} = 10.480^\circ$ when $|\Delta\theta_r| = 0^\circ$, and the minimum value is $\rho_{\text{min}} = 0^\circ$ when $|\Delta\theta_r| = 180^\circ$, which correspond to the conditions illustrated in Fig. 2.10a, b, respectively. With the knowledge of $|\Delta\theta_r| = 0^\circ$ in Fig. 2.10a, the pitch angle is simplified as $\rho = \arccos[\cos\delta_1\cos\delta_2 - \sin\delta_1\sin\delta_2] = \delta_1 + \delta_2$, namely the sum of beam deviation angles induced by prism 1 and prism 2. Given $|\Delta\theta_r| = 180^\circ$ in Fig. 2.10b, the pitch angle becomes $\rho = \arccos[\cos\delta_1\cos\delta_2 + \sin\delta_1\sin\delta_2] =$

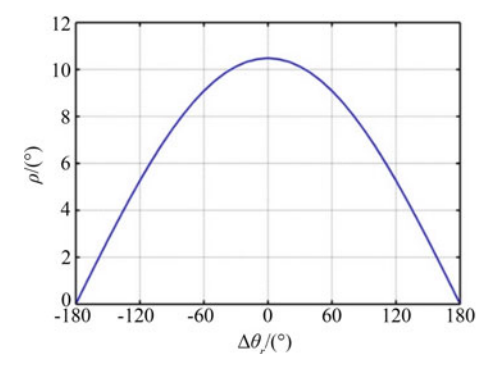


Fig. 2.9 Variation of the pitch angle ρ with the relative rotation angle $\Delta\theta_r$ of double prisms

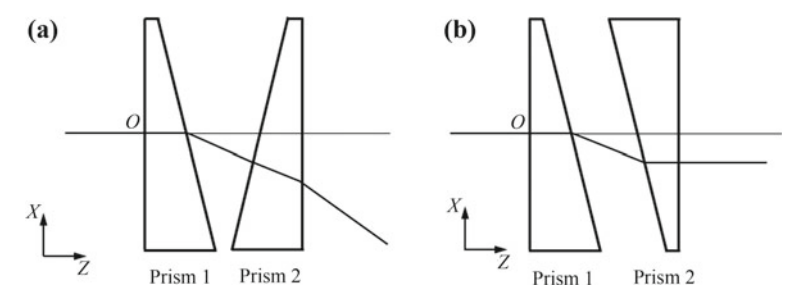


Fig. 2.10 Conditions for the extreme values of the pitch angle ρ , where **a** is for the maximum pitch angle, and **b** is for the minimum pitch angle

 $\delta_1 - \delta_2$. Here $\delta_1 = \delta_2$, which indicates that the beam deviation effects due to prism 1 and prism 2 are canceled by each other, so the final emergent beam propagates parallel to the incident beam. Moreover, the pitch angle is always taken from 0° to $\delta_1 + \delta_2$ as long as $|\Delta\theta_r|$ varies within 0° to 180° .

Upon rotating prism 1 with an angle C_1 while keeping prism 2 stationary, the relative rotation angle of two prisms is given by $\Delta\theta_r=C_1$. The two prisms are then rotated at the same speed, with the relative rotation angle $\Delta\theta_r$ held constant. Consequently, the emergent beam can produce a circular trajectory on the screen located at a distance of D_2 . The radius of the circular trajectory is $r=D_2\cdot \tan\rho$, where $\rho=f(C_1)$. It has been mentioned before that the pitch angle $\rho=f(\Delta\theta_r)$ is an even function symmetric about $\Delta\theta_r=0^\circ$. Thus, we only consider the situation of $C_1 \geq 0^\circ$, and the situation of $C_1 < 0^\circ$ can be discussed in the same approach. When $\Delta\theta_r=C_1$ takes $0^\circ, 45^\circ, 90^\circ, 135^\circ$ and 180° in turn, the far-field scan trajectories produced by the emergent beam are plotted in Fig. 2.11. Note that the scan trajectories are observed in the positive Z-direction, and the distance D_2 is set to 1 mm for simplicity. Seen from Fig. 2.11, the circular trajectory with the maximum radius of $r_{\rm max}=0.185$ mm is obtained when $\Delta\theta_r=0^\circ$, while the one with the radius of 0, namely a point, is

Fig. 2.11 Scan trajectories under constant $\Delta\theta_r$

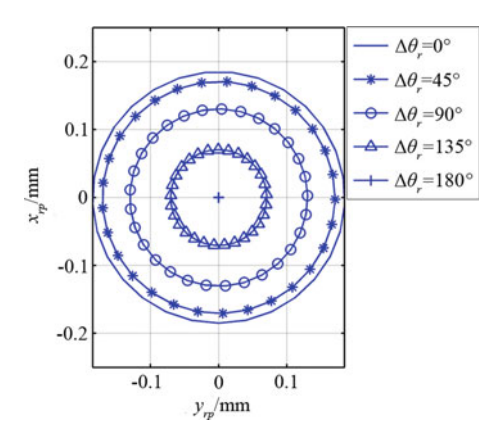
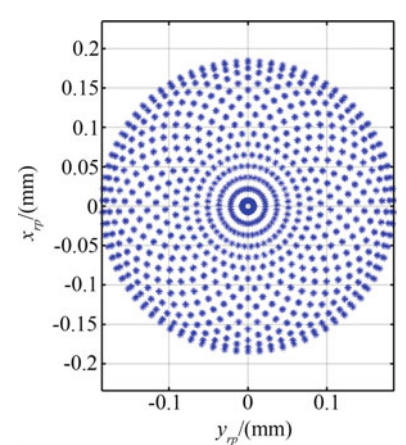


Fig. 2.12 Scan region of rotating double-prism system



obtained when $\Delta\theta_r=180^\circ$. In general, the radius of beam scan trajectory decreases as $\Delta\theta_r$ increases from 0° to 180° .

The pitch angle $\rho=f\left(\Delta\theta_r\right)$ has proven a continuous function associated with the relative rotation angle $\Delta\theta_r$ of two prisms. Thus, the radius of circular scan trajectory is taken from $r_{\rm max}$ to 0 when $\Delta\theta_r$ varies within 0° to 180°. By changing $\Delta\theta_r$, the emergent beam can be steered to any position within a cone area, specified by the radius $r_{\rm max}$ of bottom surface and the height D_2 . Figure 2.12 shows the beam scan trajectory under various combinations of prism orientations, namely the double-prism beam scan region on the screen located at a distance of $D_2=1$ mm.

The above analysis indicates that a conical scan region can be formed for any rotating double-prism system, the volume of which depends on the pitch angle range. Usually, the pitch angle takes 0° at minimum and reaches its maximum value when the relative rotation angle of two prisms is 0° . To investigate the beam scan region under far-field condition, we should only discuss the maximum value ρ_{max} of the pitch angle.

Fig. 2.13 Relation of ρ_{max} relative to α

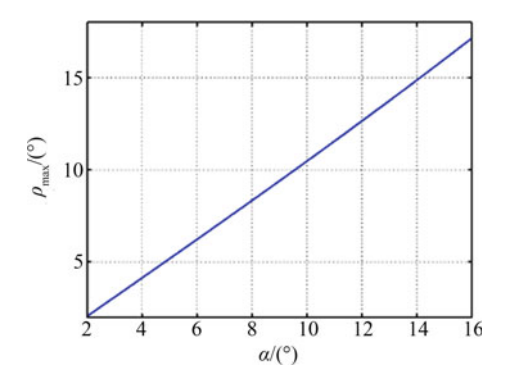


Fig. 2.14 Relation of ρ_{max} relative to n

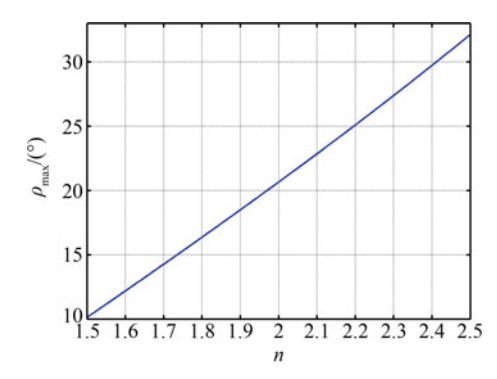


Figure 2.13 illustrates the relation of the scan region relative to the wedge angle α , where the refractive index n is constant at 1.517. Similarly, the relation between the scan region and the refractive index n is presented in Fig. 2.14, where the wedge angle $\alpha = 10^{\circ}$. It is evident that the beam scan region of a rotating double-prism system will be enlarged with the increment of wedge angle α or refractive index n.

2. Radial Scan Precision of Emergent Beam

The error analysis model for the pitch angle of emergent beam can be expressed as

$$\delta_{\rho} = \left| \frac{\partial \rho}{\partial \Delta \theta_r} \right| \delta_{\Delta \theta_r} + \left| \frac{\partial \rho}{\partial \alpha} \right| \delta_{\alpha} + \left| \frac{\partial \rho}{\partial n} \right| \delta_n \tag{2.18}$$

where $\delta_{\Delta\theta_r}$, δ_{α} and δ_n are, respectively, the absolute errors of $\Delta\theta_r$, α and n.

The wedge angle error δ_{α} and refractive index error δ_n are both classified as systematic errors, except the random error $\delta_{\Delta\theta_r}$ in the relative rotation angle of two prisms. With regard to any specific Risley-prism system, $\delta_{\Delta\theta_r}$ occurs as the unique factor that affects the pitch angle error δ_{ρ} .

The impacts of δ_{α} , δ_{n} and $\delta_{\Delta\theta_{r}}$ on δ_{ρ} are separately clarified in Fig. 2.15a, b, c. As shown in Fig. 2.15a, b, the correlation curves of $|\partial \rho/\partial \alpha|$ and $|\partial \rho/\partial n|$ with respect to $\Delta\theta_{r}$ have some essential similarities, such as the symmetric distribution

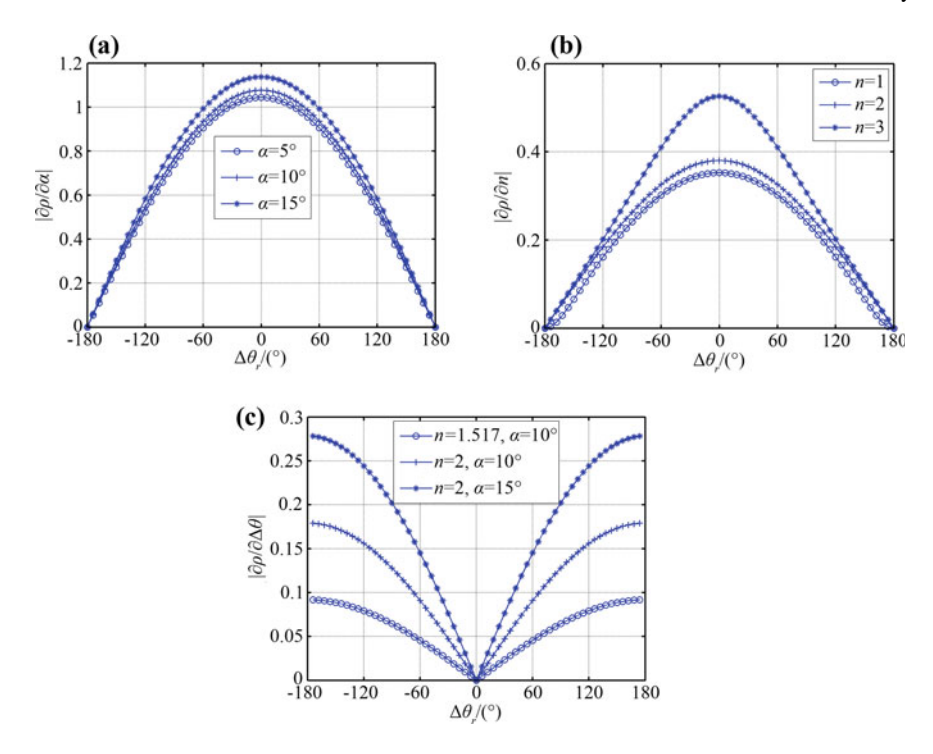


Fig. 2.15 The impacts of $\Delta\theta_r$ on the partial derivatives of pitch angle, including $\mathbf{a} \; |\partial \rho/\partial \alpha|$, $\mathbf{b} \; |\partial \rho/\partial n|$ and $\mathbf{c} \; |\partial \rho/\partial \Delta\theta_r|$

about $\Delta\theta_r=0^\circ$ and the gradual increment with $\Delta\theta_r$ varying from -180° to 0° . Meanwhile, the increment of wedge angle α or refractive index n will give rise to a larger δ_ρ corresponding to δ_α or δ_n . It is somewhat different in Fig. 2.15c that the correlation curves of $|\partial \rho/\partial \Delta\theta_r|$ relative to $\Delta\theta_r$ are also symmetric about $\Delta\theta_r=0^\circ$, but they decrease monotonically as $\Delta\theta_r$ varies from -180° to 0° . Anyway, the δ_ρ corresponding to $\delta_{\Delta\theta_r}$ increases as a result of the increasing α or n. The larger α or n becomes, the worse the impact of each error source on the radial scan precision gets, which contributes to a larger scan region on the other hand. In practice, we should make a good balance between scan region and scan precision while selecting the material and structural parameters of each prism.

Specifically, if the wedge angle $\alpha=10^\circ$, the refractive index n=1.517 and the relative rotation angle $\Delta\theta_r$ ranges from -180° to 180° , the maximum values of $|\partial\rho/\partial\alpha|$ and $|\partial\rho/\partial n|$ are 1.077 and 0.358 when $\Delta\theta_r=0^\circ$, whereas $|\partial\rho/\partial\Delta\theta_r|$ takes its maximum value 0.092 when $\Delta\theta_r=180^\circ$. Assume that the manufacture error of wedge angle δ_α approximates to 1", the refractive index error δ_n resulting from inhomogeneous optical glass is up to $\pm 1 \times 10^{-5}$, and the relative rotation angle error of two prisms $\delta_{\Delta\theta_r}$ achieves 0.01°. It can be calculated that the maximum values of δ_ρ induced by each independent factor among δ_α , δ_n and $\delta_{\Delta\theta_r}$ are about 5.22, 3.58

and $16.06 \mu rad$, respectively. In principle, the radial scan precision can be superior owing to the large reduction ratio from the relative rotation angle error of two prisms to the pitch angle error, which reaches hundredfold order for this example.

3. Circumferential Scan Precision of Emergent Beam

To help evaluate the circumferential scan precision of rotating double prisms, the change rate of azimuth angle is investigated when the system produces a circular scan trajectory on the screen during one revolution of two prisms.

The relative rotation angle $\Delta\theta_r$ of two prisms is held constant so that the azimuth angle depends only on the rotation angle θ_{r2} of prism 2.

Given that $\Delta\theta_r$ is the unique influential factor of beam deviation angles δ_1 and δ_2 , we can find $A = \sin\delta_1\cos\delta_2\cos\Delta\theta_r + \cos\delta_1\sin\delta_2$ and $B = \sin\delta_1\sin\Delta\Delta\theta_r$ both constants. Resolving the emergent beam vector into two components given by $x_{rf} = -A\cos\theta_{r2} + B\sin\theta_{r2}$ and $y_{rf} = -A\sin\theta_{r2} - B\cos\theta_{r2}$, we have

$$\cos \varphi = \frac{x_{rf}}{\sqrt{x_{rf}^2 + y_{rf}^2}} = \frac{-A \cos \theta_{r2} + B \sin \theta_{r2}}{\sqrt{A^2 + B^2}}$$
(2.19)

The azimuth angle φ has proven a function associated with the rotation angle θ_{r2} , expressed as $\varphi = f(\theta_{r2})$. Thus, the azimuth angle error δ_{φ} can be calculated from

$$\delta_{\varphi} = \left| \frac{\mathrm{d}\varphi}{\mathrm{d}\theta_{r2}} \right| \delta_{\theta_{r2}} \tag{2.20}$$

If $y_{rf} \ge 0$, the change rate $d\varphi/d\theta_{r2}$ of the azimuth angle is determined by

$$\frac{d\varphi}{d\theta_{r2}} = -\frac{1}{\frac{-A\cos\theta_{r2} - B\sin\theta_{r2}}{\sqrt{A^2 + B^2}}} \cdot \frac{A\sin\theta_{r2} + B\cos\theta_{r2}}{\sqrt{A^2 + B^2}} = 1$$
 (2.21a)

Otherwise $y_{rf} < 0$, the change rate becomes

$$\frac{d\varphi}{d\theta_{r2}} = \frac{1}{\frac{A\cos\theta_{r2} + B\sin\theta_{r2}}{\sqrt{A^2 + B^2}}} \cdot \frac{A\sin\theta_{r2} + B\cos\theta_{r2}}{\sqrt{A^2 + B^2}} = 1$$
 (2.21b)

It is worth mentioning that the change rate of azimuth angle is constant at 1 because the relative rotation angle of two prisms remains unchanged, which accounts for equal variation of the azimuth angle and each prism orientation. For rotating double prisms, the circumferential scan precision is always consistent with the rotation angle precision of each prism.

2.4.2 Tilting Scan Mode

1. Beam Scan Region

Providing the incident beam along the optical axis, the vertical field angle ρ_V of the emergent beam is expressed as

$$\rho_{V} = \arctan\left(\frac{x_{tf}}{z_{tf}}\right) = \arctan\frac{\cot \beta_{t2}}{\cos(\gamma_{t2} - \delta_{2})} = \arctan\frac{-\tan \delta_{1}}{\cos \delta_{2}}$$
(2.22a)

The horizontal field angle $\rho_{\rm H}$ is given by

$$\rho_{\rm H} = \arctan\left(\frac{y_{tf}}{z_{tf}}\right) = \gamma_{t2} - \delta_2 = -\delta_2 \tag{2.22b}$$

Obviously, the vertical field angle $\rho_{\rm V}$ and horizontal field angle $\rho_{\rm H}$ are both functions concerned with the tilting angles of two prisms, denoted by θ_{t1} for prism 1 and θ_{t2} for prism 2. Figure 2.16 shows the change laws of vertical and horizontal field angles, where the wedge angle $\alpha=10^\circ$, the refractive index n=1.517 and each tilting angle varies within -45° to 45° . It turns out that the tilting angle of prism 1 mainly affects the vertical field angle rather than the horizontal field angle, while the tilting angle of prism 2 has most effects on the horizontal field angle instead of the vertical field angle.

If the tilting angle θ_{t2} of prism 2 is kept unchanged, the vertical field angle ρ_V acts as a non-monotonous function dependent on the tilting angle θ_{t1} of prism 1. ρ_V firstly increases and then decreases with the increment of θ_{t1} within -45° to 45° . Similarly, if θ_{t1} is held constant, the horizontal field angle ρ_H is a non-monotonous function relative to θ_{t2} . ρ_H firstly increases and then decreases as θ_{t2} increases within -45° to 45° . It is interesting to find that the maximum values of ρ_V and ρ_H , namely -5.22° and -5.23° , are both obtained when $\theta_{t1} = -7.56^\circ$ and $\theta_{t2} = -2.34^\circ$. To facilitate the beam steering control of tilting double prisms and to avoid multiple sets

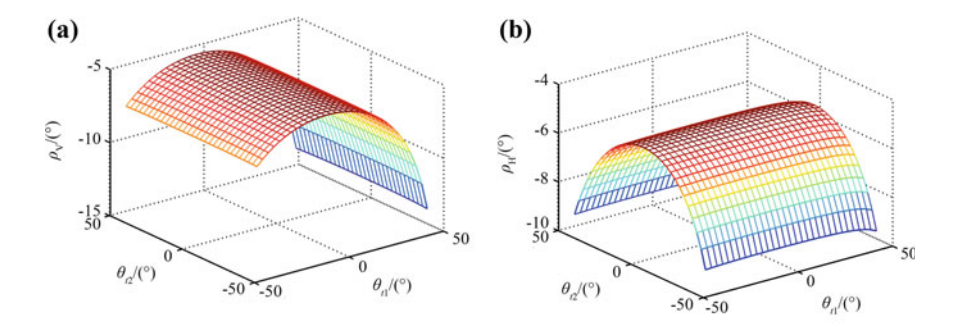


Fig. 2.16 The change laws of a vertical field angle ρ_V and b horizontal field angle ρ_H

of inverse solutions, the tilting angle range of each prism should be narrowed from -45° to 45° to 45° , where ρ_{V} and ρ_{H} are both monotonic functions.

2. Beam Scan Precision

The beam scan error model contains error terms induced by tilting angle error, wedge angle error and refractive index error of each prism, which can be resolved in the vertical and horizontal directions as follows

$$\delta_{V} = \left| \frac{\partial \rho_{V}}{\partial \theta_{t1}} \right| \delta_{\theta_{t1}} + \left| \frac{\partial \rho_{V}}{\partial \theta_{t2}} \right| \delta_{\theta_{t2}} + \left| \frac{\partial \rho_{V}}{\partial \alpha} \right| \delta_{\alpha} + \left| \frac{\partial \rho_{V}}{\partial n} \right| \delta_{n}$$
 (2.23a)

$$\delta_{H} = \left| \frac{\partial \rho_{H}}{\partial \theta_{t1}} \right| \delta_{\theta_{t1}} + \left| \frac{\partial \rho_{H}}{\partial \theta_{t2}} \right| \delta_{\theta_{t2}} + \left| \frac{\partial \rho_{H}}{\partial \alpha} \right| \delta_{\alpha} + \left| \frac{\partial \rho_{H}}{\partial n} \right| \delta_{n}$$
 (2.23b)

Assuming that $\alpha=10^\circ$ and n=1.517, the correlation curves of the emergent beam pointing with respect to prism orientations are plotted in Fig. 2.17. Figures 2.17a, b indicate the change laws of the partial derivatives expressed as $\partial \rho_V/\partial \Delta \theta_{t1}$ and $\partial \rho_H/\partial \Delta \theta_{t1}$ when prism 2 remains stationary. Similarly, Fig. 2.17c, d display the variation of the partial derivatives expressed as $\partial \rho_V/\partial \Delta \theta_{t2}$ and $\partial \rho_H/\partial \Delta \theta_{t2}$ when prism 1 is kept stationary.

It can be concluded from Figs. 2.16 and 2.17 that, the deviation range of the emergent beam is enlarged as the tilting angle of each prism increases. However, the absolute value of the change rate of either vertical or horizontal field angle increases as well, which may produce adverse effects on the beam scan precision. Specially, the scan precision will be drastically reduced when θ_{t1} or θ_{t2} increases within 20° to 45°. In order to facilitate the motion control for high-precision beam scanning, the tilting angles θ_{t1} and θ_{t2} are both limited within 0° to 10°, where the vertical field angle ranges from -5.66° to -5.29° and the horizontal field angle ranges from -5.44° to -5.24° .

Once the tilting angle of each prism is limited, $|\partial \rho_V/\partial \alpha|$ reaches its maximum value 0.621 and $|\partial \rho_H/\partial \alpha|$ reaches its maximum value 0.567 when $\theta_{t1}=10^\circ$ and $\theta_{t2}=10^\circ$. Providing the manufacturing error of wedge angle α up to 1", the resultant errors of ρ_V and ρ_H are, respectively, 3.01 and 2.75 μ rad. It is also found that $|\partial \rho_V/\partial n|$ and $|\partial \rho_H/\partial n|$ reaches their individual maximum values of 0.196 and 0.182 μ rad when $\theta_{t1}=\theta_{t2}=10^\circ$. Given the refractive index error due to inhomogeneous optical glass as $\pm 1 \times 10^{-5}$, the resultant errors of ρ_V and ρ_H are, respectively, 1.960 and 1.820 μ rad. Both the wedge angle error and refractive index error are classified as systematic errors, which can be corrected using optical calibration techniques. Therefore, the random errors in each tilting mechanism remains to be the primary error sources of vertical and horizontal field angles.

When $\theta_{t1} = \theta_{t2} = 10^\circ$, the partial derivatives $|\partial \rho_V/\partial \theta_{t1}|$, $|\partial \rho_V/\partial \theta_{t2}|$, $|\partial \rho_H/\partial \theta_{t1}|$, and $|\partial \rho_H/\partial \theta_{t2}|$ reach their maximum values 5.42×10^{-2} , 3.17×10^{-4} , 8.22×10^{-4} and 0.339×10^{-2} , respectively. Therefore, the maximum error in the vertical field angle can be determined by adding 0.0542 times the tilting angle error of prism 1 to 3.17×10^{-4} times the tilting angle error of prism 2, whereas the maximum error

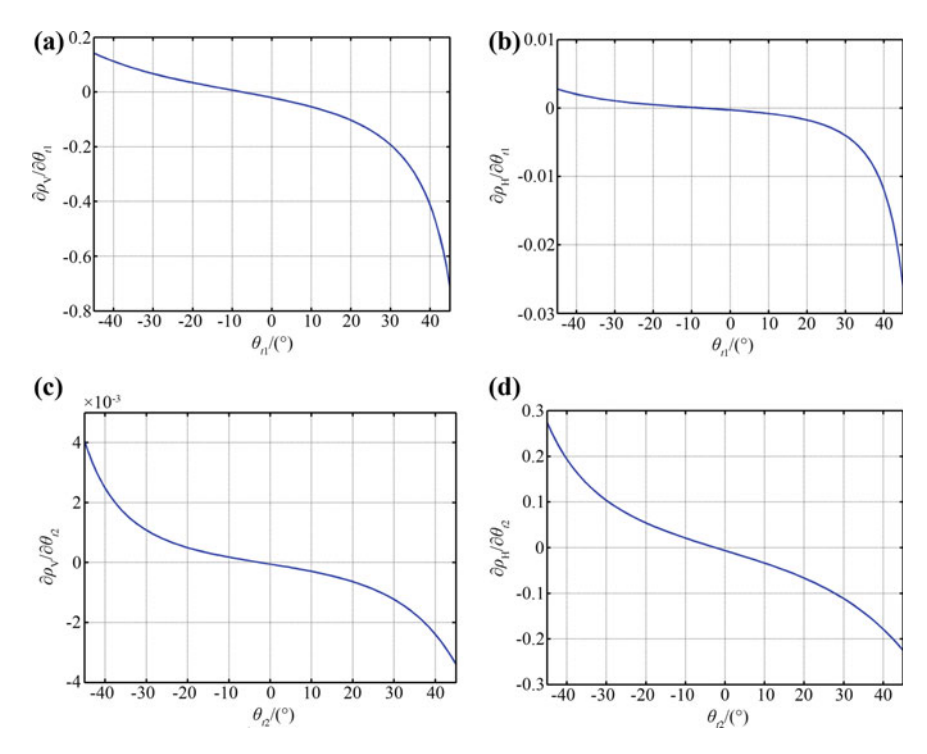


Fig. 2.17 The change laws of the partial derivatives of field angles with respect to prism orientations, where **a** and **b** show the effects of θ_{t1} on $\frac{\partial \rho_{V}}{\partial \theta_{t1}}$ and $\frac{\partial \rho_{H}}{\partial \theta_{t1}}$, **c** and **d** shows the effects of θ_{t2} on $\frac{\partial \rho_{V}}{\partial \theta_{t2}}$ and $\frac{\partial \rho_{H}}{\partial \theta_{t2}}$

in the horizontal field angle is the sum of 8.22×10^{-4} times the tilting angle error of prism 1 and 0.0339 times the tilting angle error of prism 2. These results account for the fact that the tilting double-prism system can achieve higher scan precision in both vertical and horizontal directions.

It is noteworthy that the beam scan precision is also relevant to the wedge angle of each prism. For any single prism, the influence of wedge angle on the beam scan precision can be considered as in Sect. 2.2.2.

2.5 Coordinate Expressions for Scan Points

2.5.1 Rotating Scan Mode

1. Equations for Incident and Emergent Surfaces of Rotating Double Prisms

Figure 2.18 shows a schematic diagram that illustrates the beam propagation through the rotating double-prism scanner [9], where the central-axis thickness of each prism

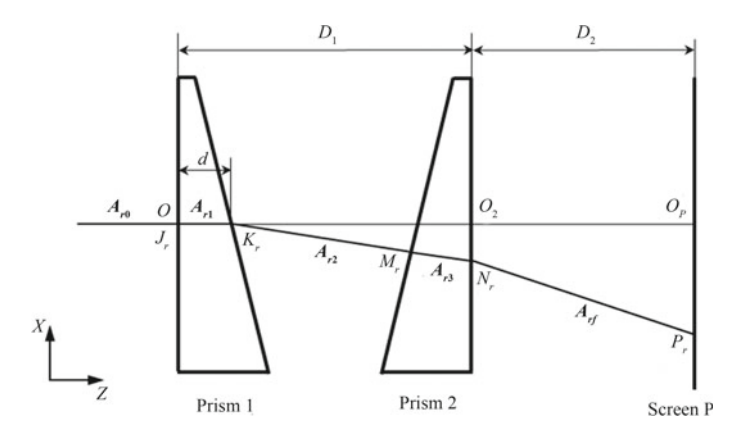


Fig. 2.18 Schematic diagram illustrating the beam propagation through rotating double prisms

is denoted by d. Given the normal vector $N_{11} = (0, 0, 1)^{T}$ passing the known point O(0, 0, 0), the equation for the incident surface of prism 1 is expressed as

$$z = 0 \tag{2.24a}$$

According to the normal vector $N_{12} = (\cos \theta_{r1} \sin \alpha, \sin \theta_{r1} \sin \alpha, \cos \alpha)^{T}$ passing the known point (0, 0, d), the equation for the emergent surface of prism 1 can be expressed as

$$\cos \theta_{r1} \sin \alpha \cdot x + \sin \theta_{r1} \sin \alpha \cdot y + \cos \alpha \cdot (z - d) = 0$$
 (2.24b)

Similarly, the equation for the incident surface of prism 2 is expressed in terms of the normal vector $N_{21} = (-\cos\theta_{r2}\sin\alpha, -\sin\theta_{r2}\sin\alpha, \cos\alpha)^{T}$ passing the known point $O'(0, 0, D_{1} - d)$:

$$-\cos\theta_{r2}\sin\alpha \cdot x - \sin\theta_{r2}\sin\alpha \cdot y + \cos\alpha \cdot [z - (D_1 - d)] = 0$$
 (2.24c)

The equation for the emergent surface of prism 2 is expressed in terms of the normal vector $N_{22} = (0, 0, 1)^T$ passing the known point $O_2(0, 0, D_1)$:

$$z = D_1 \tag{2.24d}$$

And the equation for the screen P can be expressed as

$$z = D_1 + D_2 (2.24e)$$

Intersection Coordinates of the Beam and Rotating Double Prisms

Since the incident beam propagates along the vector $A_{r0} = (x_{r0}, y_{r0}, z_{r0})^{T}$ and intersects prism 1 at the point $J_r(x_{rj}, y_{rj}, z_{rj})$, the equation for the incident beam is written as $\frac{x - x_{rj}}{x_{r0}} = \frac{y - y_{rj}}{y_{r0}} = \frac{z - z_{rj}}{z_{r0}} = t_{c0}$, where $t_{c0} = \frac{-z_{rj}}{z_{r0}}$.

Referring to Sect. 2.3.1, the refracted beam at the incident surface of prism 1 is along the vector $A_{r1} = (x_{r1}, y_{r1}, z_{r1})^{\mathrm{T}}$ and passes the point $J_r(x_{rj}, y_{rj}, z_{rj})$. Thus, the equation for the refracted beam is written as $\frac{x - x_{rj}}{x_{r1}} = \frac{y - y_{rj}}{y_{r1}} = \frac{z - z_{rj}}{z_{r1}} = t_{c1}$, and the intersection point $K_r(x_{rk}, y_{rk}, z_{rk})$ of the beam and the emergent surface of prism 1 is given by

$$\begin{cases} x_{rk} = x_{r1} \cdot t_{c1} + x_{rj} \\ y_{rk} = y_{r1} \cdot t_{c1} + y_{rj} \\ z_{rk} = z_{r1} \cdot t_{c1} + z_{rj} \end{cases}$$
(2.25a)

where
$$t_{c1} = \frac{-\cos\theta_{r1}\sin\alpha \cdot x_{rj} - \sin\theta_{r1}\sin\alpha \cdot y_{rj} - \cos\alpha(z_{rj} - d)}{\cos\theta_{r1}\sin\alpha \cdot x_{r1} + \sin\theta_{r1}\sin\alpha \cdot y_{r1} + \cos\alpha \cdot z_{r1}}$$
.

The equation for the refracted beam at each prism surface can be obtained by the same means. Combining these equations with the equations for prism surfaces, we can determine the coordinate values of intersection point between the beam path and each prism surface. Specifically, the point $M_r(x_{rm}, y_{rm}, z_{rm})$ at which the beam intersects the incident surface of prism 2 is given by

$$\begin{cases} x_{rm} = x_{r2} \cdot t_{c2} + x_{rk} \\ y_{rm} = y_{r2} \cdot t_{c2} + y_{rk} \\ z_{rm} = z_{r2} \cdot t_{c2} + z_{rk} \end{cases}$$
(2.25b)

where
$$t_{c2} = \frac{\cos\theta_{r2} \cdot \sin\alpha \cdot x_{rk} + \sin\theta_{r2} \sin\alpha \cdot y_{rk} - \cos\alpha \cdot [z_k - (D_1 - d)]}{-\cos\theta_{r2} \cdot \sin\alpha \cdot x_{r2} - \sin\theta_{r2} \sin\alpha \cdot y_{r2} + \cos\alpha \cdot z_{r2}}$$
.

The point $N_r(x_m, y_m, z_m)$ at which the beam intersects the emergent surface of prism 2 is given by

$$\begin{cases} x_{rn} = x_{r3}t_{c3} + x_{rm} \\ y_{rn} = y_{r3}t_{c3} + y_{rm} \\ z_{rn} = z_{r3}t_{c3} + z_{rm} \end{cases}$$
(2.25c)

where
$$t_{c3} = \frac{D_1 - z_{rm}}{z_{r3}}$$

where $t_{c3} = \frac{D_1 - z_{rm}}{z_{r3}}$. The point at which the emergent beam from prism 2 intersects the screen P, namely the beam scan point $P_r(x_{rp}, y_{rp}, z_{rp})$, is given by

$$\begin{cases} x_{rp} = x_{rf}t_{c4} + x_{rn} \\ y_{rp} = y_{rf}t_{c4} + y_{rn} \\ z_{rp} = z_{rf}t_{c4} + z_{rn} = D_1 + D_2 \end{cases}$$
 (2.25d)

where
$$t_{c4} = \frac{D_1 + D_2 - z_{rn}}{z_{rf}} = \frac{D_2}{z_{rf}}$$
.

2.5.2 Tilting Scan Mode

1. Equations for Incident and Emergent Surfaces of Tilting Double Prisms

Figure 2.19 shows a schematic diagram illustrating the beam propagation through the tilting double-prism scanner, where the central-axis thickness of each prism is still denoted by d. Given the normal vector $N_{11} = (\sin \theta_{t1}, 0, \cos \theta_{t1})^{\text{T}}$ passing the known point O(0, 0, 0), the equation for the incident surface of prism 1 is expressed as

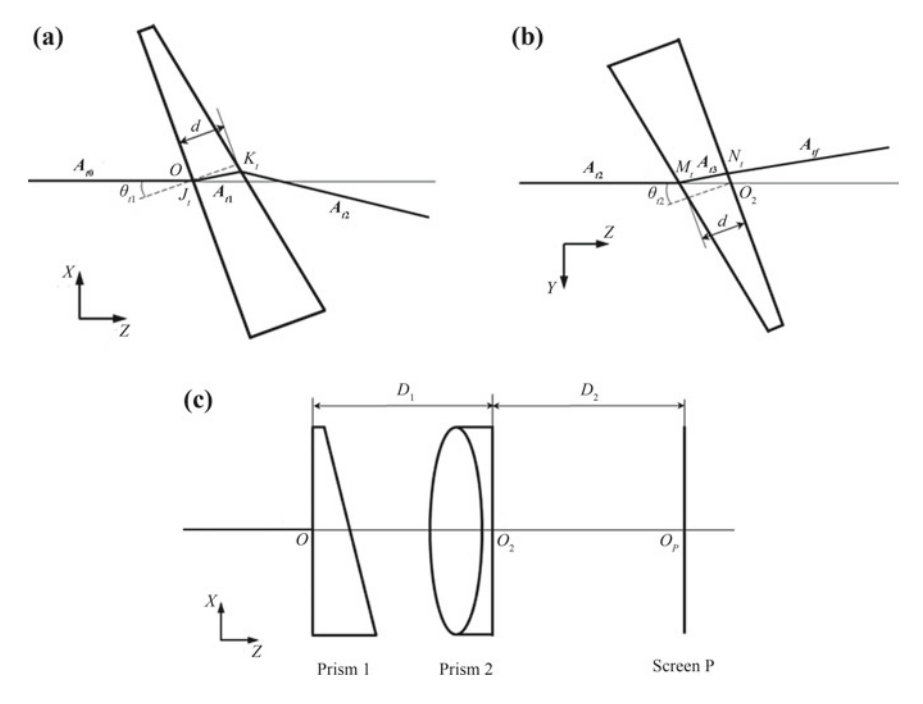


Fig. 2.19 Shematic diagram illustrating the beam propagation through tilting double-prism system, where $\bf a$ and $\bf b$ shows the principal sections of prism 1 and prism 2, respectively, and $\bf c$ shows the system configuration

$$\sin \theta_{t1} \cdot x + \cos \theta_{t1} \cdot z = 0 \tag{2.26a}$$

The equation for the emergent surface of prism 1 is expressed in terms of the normal vector $N_{12} = (\sin(\alpha + \theta_{t1}), 0, \cos(\alpha + \theta_{t1}))^{\mathrm{T}}$ passing the known point $(\sin\theta_{t1} \cdot d, 0, \cos\theta_{t1} \cdot d)$:

$$\sin(\alpha + \theta_{t1}) \cdot (x - \sin \theta_{t1} \cdot d) + \cos(\alpha + \theta_{t1})(z - \cos \theta_{t1} \cdot d) = 0 \tag{2.26b}$$

The equation for the incident surface of prism 2 is expressed in terms of the normal vector $N_{21} = (0, -\sin(\alpha + \theta_{t2}), \cos(\alpha + \theta_{t2}))^T$ passing the known point $(0, \sin\theta_{t2} \cdot d, D_1 - \cos\theta_{t2} \cdot d)$:

$$-\sin(\alpha + \theta_{t2})(y - \sin\theta_{t2} \cdot d) + \cos(\alpha + \theta_{t2})[z - (D_1 - \cos\theta_{t2} \cdot d)] = 0 \quad (2.26c)$$

The equation for the emergent surface of prism 2 is expressed in terms of the normal vector $N_{22} = (0, -\sin\theta_{t2}, \cos\theta_{t2})^{\mathrm{T}}$ passing the known point $O_2(0, 0, D_1)$:

$$-\sin\theta_{t2} \cdot y + \cos\theta_{t2}(z - D_1) = 0 \tag{2.26d}$$

The equation for the screen P can be expressed as $z = D_1 + D_2$.

2. Intersection Coordinates of the Beam and Tilting Double Prisms

It is already known that the incident beam propagates along the vector $A_{t0} = (x_{t0}, y_{t0}, z_{t0})^{T}$ and intersects the incident surface of prism 1 at the point $J_{t}(x_{tj}, y_{tj}, z_{ti})$, where $z_{ti} = -x_{ti} \cdot \tan \theta_{11}$.

Referring to Sect. 2.3.2, the refracted beam at the incident surface of prism 1 is along the vector $A_{t1} = (x_{t1}, y_{t1}, z_{t1})^{\mathrm{T}}$ and passes the point $J_t(x_{tj}, y_{tj}, z_{tj})$. Thus, the equation for the refracted beam is written as $\frac{x - x_{tj}}{x_{t1}} = \frac{y - y_{tj}}{y_{t1}} = \frac{z - z_{tj}}{z_{t1}} = u_{c1}$, and the intersection point $K_t(x_{tk}, y_{tk}, z_{tk})$ of the beam path and the emergent surface of prism 1 is given by

$$\begin{cases} x_{tk} = x_{t1}u_{c1} + x_{tj} \\ y_{tk} = y_{t1}u_{c1} + y_{tj} \\ z_{tk} = z_{t1}u_{c1} + z_{tj} \end{cases}$$
 (2.27a)

where
$$u_{c1} = -\frac{\sin(\alpha+\theta_{t1})\cdot(x_{tj}-\sin\theta_{t1}\cdot d)+\cos(\alpha+\theta_{t1})\cdot(z_{tj}-\cos\theta_{t1}\cdot d)}{\sin(\alpha+\theta_{t1})\cdot x_{t1}+\cos(\alpha+\theta_{t1})\cdot z_{t1}}$$
.

Similarly, the equation for the refracted beam at each prism surface can be obtained. Combining these equations with the equations for prism surfaces, we can determine the coordinate values of intersection point between the beam path and each prism surface. The point $M_t(x_{tm}, y_{tm}, z_{tm})$ at which the beam intersects the incident surface of prism 2 is given by

$$\begin{cases} x_{tm} = x_{t2}u_{c2} + x_{tk} \\ y_{tm} = y_{t2}u_{c2} + y_{tk} \\ z_{tm} = z_{t2}u_{c2} + z_{tk} \end{cases}$$
 (2.27b)

where
$$u_{c2} = \frac{\sin(\alpha + \theta_{t2}) \cdot (y_{tk} - \sin \theta_{t2} \cdot d) - \cos(\alpha + \theta_{t2}) \cdot [z_{tk} - (D_1 - \cos \theta_{t2} \cdot d)]}{-\sin(\alpha + \theta_{t2}) \cdot y_{t2} + \cos(\alpha + \theta_{t2}) \cdot z_{t2}}$$

The point $N_t(x_t, y_t, z_t)$ at which the beam intersects the emergent surface of prism 2 is given by

$$\begin{cases} x_{tn} = x_{t3}u_{c3} + x_{tm} \\ y_{tn} = y_{t3}u_{c3} + y_{tm} \\ z_{tn} = z_{t3}u_{c3} + z_{tm} \end{cases}$$
 (2.27c)

where $u_{c3} = \frac{\sin \theta_{t2} \cdot y_{tm} - \cos \theta_{t2} \cdot (z_{tm} - D_1)}{-\sin \theta_{t2} \cdot y_{t3} + \cos \theta_{t2} \cdot z_{t3}}$. The point at which the emergent beam from prism 2 intersects the screen P, namely the beam scan point $P_t(x_{tp}, y_{tp}, z_{tp})$, is given by

$$\begin{cases} x_{tp} = x_{tf}u_{c4} + x_{tn} \\ y_{tp} = y_{tf}u_{c4} + y_{tn} \\ z_{tp} = z_{tf}u_{c4} + z_{tn} \end{cases}$$
 (2.27d)

where $u_{c4} = \frac{D_1 + D_2 - z_{tn}}{z_{tf}}$.

2.6 Discussion on Distance Between Two Prisms

Two prisms can be placed as close as possible to a critical distance without collision. That is, a minimum distance need be set to avoid the motion interference between two prisms. On the other hand, if two prisms are too far away from each other, the laser beam may propagate beyond the clear aperture of the system, which implies no emergent beam from prism 2. Therefore, the maximum distance between two prisms should meet the requirement of the beam propagation within the clear aperture.

For example, two identical prisms are taken with the wedge angle $\alpha = 10^{\circ}$ and the refractive index n = 1.517. The rotation angle ranges of two prisms are set to 0° to 360° while the tilting angle ranges of two prisms are 0° to 10°. The clear aperture of each prism is $D_p = 80$ mm, and the thinnest-end thickness is $d_0 = 5$ mm. So the central-axis thickness of the prism can be obtained from $d = d_0 + D_p/2 \cdot \tan \alpha$.

2.6.1 Rotating Scan Mode

In the rotating scan mode, the collision is most likely to occur when the two prisms are situated with their thickest ends face to face. The minimum distance between two prisms can be set as two times the thickest-end thickness, given by

$$2 \times (d_0 + D_p \cdot \tan \alpha) = 2 \times (5 + 80 \cdot \tan 10^\circ) = 38 \text{ mm}$$

Actually, considering the size of the frame and other structures, the minimum distance between two prisms must be multiplied by a safety factor λ ($\lambda > 1$).

In order to calculate the maximum distance between two rotating prisms with the clear aperture $D_p=80$ mm, it is necessary to solve the distance D_1 corresponding to the distance of 40 mm between the beam exiting point N_r and the center point O_2 on the emergent surface 22. For rotating double prisms, the radial deviation of the emergent beam depends on the relative rotation angle $\Delta\theta_r$ of two prisms. Supposing that the laser beam passes through the center point O along the incident beam vector $A_{r0}=(0,0,1)^T$, prism 2 should be able to rotate within the range of 0° to 360° while prism 1 is kept stationary. In other words, the relative rotation angle of two prisms varies within 0° to 360° . By employing the one-dimensional search method, we can find that the distance from the beam exiting point N_r to the center point O_2 reaches $|N_rO_2|_{\rm max}=39.939$ mm when the distance between two prisms $D_1=439$ mm, and $|N_rO_2|>40$ mm when $D_1=440$ mm.

The situation when $D_1=439$ mm is further illustrated in Fig. 2.20. It can be seen that the distance $|M_rO'|$ between the intersection point M_r and the center O' at the surface 21 varies with the relative rotation angle $\Delta\theta_r$ of two prisms, as well as the distance $|N_rO_2|$ from the intersection point N_r to the center O_2 at the surface 21. Thus, the maximum distance between two prisms is about $D_1=439$ mm, and the emergent beam will nearly exceed the clear aperture of the system when $\Delta\theta_r=0^\circ$.

In conclusion, the distance D_1 between two prisms is determined within 38–439 mm for the specified rotating double-prism system with $\alpha = 10^{\circ}$, n = 1.517, $D_p = 80$ mm and $d_0 = 5$ mm.

2.6.2 Tilting Scan Mode

At tilting scan mode, the collision is most likely to occur when two prisms tilt simultaneously with their maximum tilting angles. The smallest distance between two round prism surfaces can be measured through the measurement function of 3D design software. Providing the distance between two prisms as $D_1 = 60$ mm and the tilting angle of each prism as 10° , the minimum distance between the opposite surfaces of two prisms is measured to be 10.92 mm and its projection length in the Z-direction is 10.12 mm. Consequently, the minimum distance between two prisms is set to 49.88 mm for reference. Note that the measured distance between two opposite

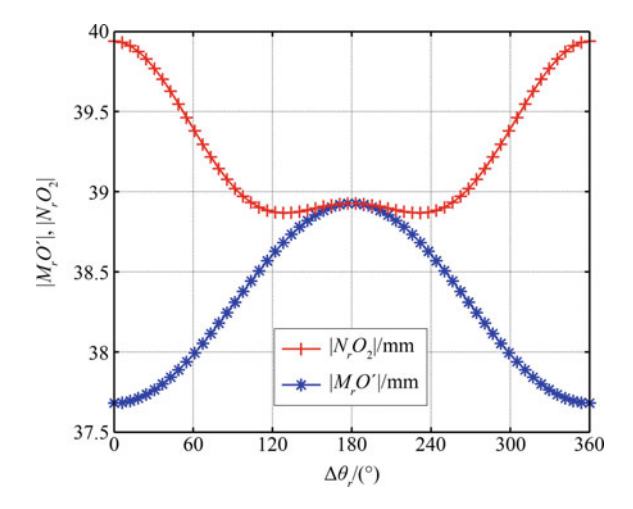


Fig. 2.20 The relation of $|M_rO'|$ and $|N_rO_2|$ with respect to $\Delta\theta_r$

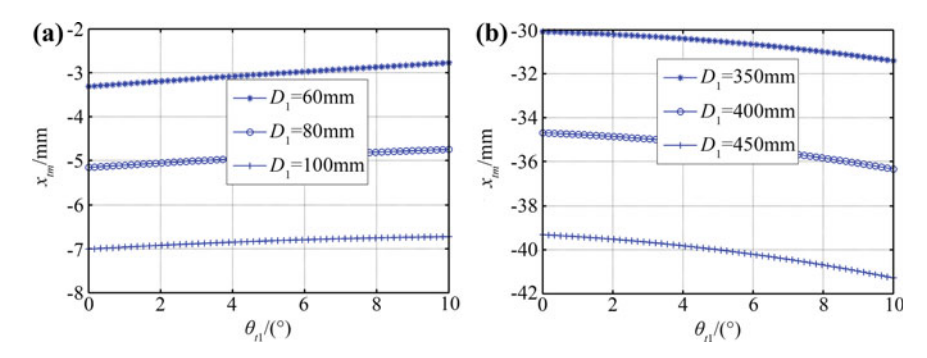


Fig. 2.21 Relation between the x_{lm} and θ_{l1} , when **a** $D_1 = 60$ mm, $D_1 = 80$ mm, $D_1 = 100$ mm and **b** $D_1 = 350$ mm, $D_1 = 400$ mm, $D_1 = 450$ mm

prism surfaces in the 3D model of double prisms is actually the minimum distance between two spatial points, which is shorter than the minimum distance between two round prism surfaces in the Z-direction. Thus, the minimum distance for reference is slightly larger than the theoretical minimum distance between two prisms. Similar to the rotating double-prism system, the minimum distance between tilting double prisms must be multiplied by a safety factor λ ($\lambda > 1$).

Assume that the incident beam propagates along the vector $A_{t0} = (0, 0, 1)^{T}$ and passes the center point O. According to Sect. 2.3.2, when prism 1 tilts from 0° to 10° but prism 2 keeps stationary, the laser beam is merely refracted within the XOZ plane. The emergent beam from prism 1 intersects the incident surface of prism 2 at the point M_t . Specifically, the x_{tm} coordinate of the point M_t varies with the tilting angle of prism 1 as shown in Fig. 2.21, while $y_{tm} = 0$ and $z_{tm} = D_1 - \cos\alpha/\cos(\alpha + \theta_{t2}) \cdot d$.

$\theta_{t1}/(^{\circ})$	x _{tk} /mm	y _{tk} /mm	z _{tk} /mm	x_{t2}	yt2	z_{t2}
0	0.000	0	12.053	-0.092	0	0.996
2	0.144	0	12.105	-0.093	0	0.996
4	0.290	0	12.161	-0.094	0	0.996
6	0.437	0	12.223	-0.095	0	0.995
8	0.587	0	12.290	-0.097	0	0.995
10	0.740	0	12.362	-0.098	0	0.995

Table 2.3 Coordinates (x_{tk}, y_{tk}, z_{tk}) of beam exiting point K_t and emergent beam vector $(x_{t2}, y_{t2}, z_{t2})^T$

Figure 2.21a illustrates three cases with smaller distances between two prisms, i.e. $D_1 = 60$ mm, $D_1 = 80$ mm and $D_1 = 100$ mm. It is found that the point M_t moves in the positive X-direction with the increment of tilting angle θ_{t1} , and the distance $|x_{tm}|$ from M_t to the center point on the prism surface 21 can reach its maximum when $\theta_{t1} = 0^\circ$. In Fig. 2.21b, three cases with larger distances between two prisms are illustrated, i.e. $D_1 = 350$ mm, $D_1 = 400$ mm and $D_1 = 450$ mm. The point M_t moves in the positive X-direction as the tilting angle θ_{t1} increases, and the distance $|x_{tm}|$ can reach its maximum when $\theta_{t1} = 10^\circ$.

Seen from (2.27b), $x_{tm} = x_{t2}u_{c2} + x_{tk}$ mainly depends on three parameters, namely x_{t2} , u_{c2} and x_{tk} . As the tilting angle θ_{t1} of prism 1 varies within 0° to 10°, the consequent cordinates (x_{tk}, y_{tk}, z_{tk}) of the beam exiting point K_t and the emergent beam vector $(x_{t2}, y_{t2}, z_{t2})^T$ from prism 1 are listed in Table 2.3.

It can be concluded from Table 2.3 that the x_{tk} cordinate increases while the x_{t2} value decreases with θ_{t1} increasing within 0° to 10°. When $\theta_{t2} = 0$ °, u_{c2} can be simplified as $u_{c2} = [(D_1 - d) - z_{tk}]/z_{t2}$. Since z_{tk} and z_{t2} are changed slightly during the tilting process, u_{c2} mainly depends on D_1 . Therefore, x_{tm} can be greatly influenced by x_{tk} but hardly by x_{t2} when the distance D_1 is small. That accounts for x_{tm} increasing with θ_{t1} when $D_1 = 60$ mm or $D_1 = 100$ mm. On the opposite, x_{tm} is mainly influenced by x_{t2} but not x_{tk} anymore when the distance D_1 is large. Thus, x_{tm} decreases with the increasing θ_{t1} when $D_1 = 300$ mm or $D_1 = 440$ mm.

We concentrate on the specified double-prism system with the clear aperture $D_p = 80$ mm. The laser beam will exceed the clear aperture of the system when $D_1 = 440$ mm, so the maximum distance between two prisms should be less than 440 mm. According to the change law of x_{tm} , the maximum value of $|x_{tm}|$ will be obtained when $\theta_{t1} = 10^{\circ}$. In other words, the distance from the point M_t to the center point O' reaches its maximum when $\theta_{t1} = 10^{\circ}$.

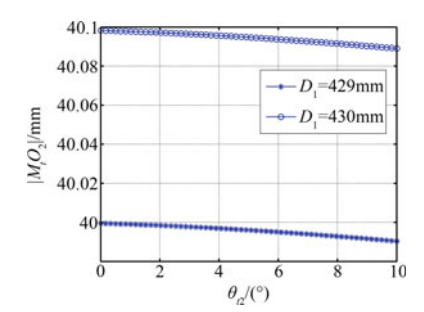
To determine the tilting status of prism 2 when the beam is farthest from the center point of the emergent surface, the tilting angle of prism 1 is set to 10° and that of prism 2 varies from 0° to 10° at a uniform speed. The laser beam is merely refracted in the *YOZ* plane while passing through prism 2, and the consequent values of the refracted beam vector $(x_{t3}, y_{t3}, z_{t3})^{T}$ are listed in Table 2.4.

Seen from Table 2.4, the laser beam is steered away from the optical axis by prism 2 as θ_{12} increases within 0° to 10°. Hence, the beam may propagate beyond

Table 2.4 Sample values of refracted beam vector $(x_{t3}, y_{t3}, z_{t3})^{T}$

$\theta_{t2}/(^{\circ})$	x_{t3}	<i>y</i> _t 3	z_{t3}
0	-0.0648	-0.0600	0.9961
2	-0.0648	-0.0721	0.9953
4	-0.0648	-0.0844	0.9943
6	-0.0648	-0.0967	0.9932
8	-0.0648	-0.1091	0.9919
10	-0.0648	-0.1217	0.9904

Fig. 2.22 Relation between $|N_t O_2|$ and θ_{t2} when $D_1 = 429$ mm and $D_1 = 430$ mm



the clear aperture of the system if the distance D_1 becomes too large. Consequently, the maximum distance between two prisms can be obtained when the maximum value of the distance from the point N_t to the center point O_2 , given by $|N_t O_2| = \sqrt{x_{tn}^2 + y_{tn}^2 + (z_{tn} - D_1)^2}$, is equal to 40 mm.

The relation between $|N_tO_2|$ and θ_{t2} is illustrated in Fig. 2.22. It can be found that $|N_tO_2|_{\rm max}=39.9995$ mm when $D_1=429$ mm and $|N_tO_2|_{\rm max}>40$ mm when $D_1=430$ mm, which indicates that the maximum distance between two prisms is about 429 mm. Under the specific condition of $D_1=429$ mm, $\theta_{t1}=10^\circ$ and $\theta_{t2}=10^\circ$, the laser beam approaches the boundary of the clear aperture of the system.

In conclusion, the distance D_1 between two prisms can range within 50–429 mm for the specified tilting double prism system with $\alpha = 10^{\circ}$, n = 1.517, $D_p = 80$ mm and $d_0 = 5$ mm.

2.7 Double-Prism Multi-mode Scan Analysis

2.7.1 Blind Zone of Rotating Scan Model

Conditioned by the structural parameters of the rotating double-prism system, the scan point of the emergent beam cannot cover the area near the coordinate origin on the screen, which illustrates that a scan blind zone will occur at the center of the whole scan region [12]. In Fig. 2.23, a scan blind zone is viewed in the rotating

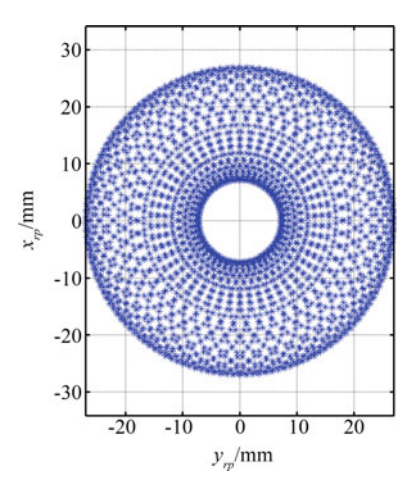


Fig. 2.23 Scan region of rotating double-prism system

double-prism system with $\alpha=10^\circ$, n=1.517, $d_0=10$ mm, Dp=400 mm, D1=400 mm and $D_2=400$ mm.

The scan blind zone probably leads to the target loss during searching and tracking applications. In order to reduce the adverse influence of the scan blind zone on the optical scan applications, the key factors affecting the formation of scan blind zone are investigated as follows.

The beam scan point and the center point on the screen are denoted by P_r and O_P , respectively. As indicated in Fig. 2.24, the distance $|P_rO_P|$ is correlated to the relative rotation angle $|\Delta\theta_r|$ of two prisms, and the minimum of $|P_rO_P|$ is defined as the radius R of the scan blind zone. Upon employing the one-dimensional search method throughout the accessible range of D_1 (i.e., 38–439 mm), a unique minimum value of $|P_rO_P|$ can be determined when D_1 varies from 38 to 315 mm, accompanied by $|\Delta\theta_r| = 180^\circ$. In Fig. 2.24(a), the minimal $|P_rO_P|$ of 7.1207 mm occurs when $D_1 = 100$ mm and $|\Delta\theta_r| = 180^\circ$, and the pitch angle of the emergent beam equals to 0. Moreover, as shown in Fig. 2.25a, the minimal $|P_rO_P|$ remains unchanged as D_2 varies.

Nevertheless, when D_1 varies within [316, 439] mm, the minimal $|P_rO_P|$ is related to the factor D_2 . As shown in Fig. 2.24b, in the case of $D_1=400$ mm and $D_2=1$ mm, the minimal $|P_rO_P|$ is 35.258 mm where $|\Delta\theta_r|=147.69^\circ$ or 212.31°. But in the case of $D_1=400$ mm and $D_2=100$ mm, the unique minimal $|P_rO_P|$ is 35.268 mm where $|\Delta\theta_r|=180^\circ$. Moreover, to present the correlation of D_2 to the minimal $|P_rO_P|$ (namely, the radius of scan blind zone) in Fig. 2.25b, D_1 is thus set to 400 mm as a constant. It is illustrated that with D_2 increasing within the range of (1, 2.37) mm, the minimal $|P_rO_P|$ occurs on two sides of $|\Delta\theta_r|=180^\circ$ and increases from 35.258 to 35.268 mm. In contrast, when $D_2\geq 2.37$ mm, the minimal $|P_rO_P|$ equals to 35.268 mm where $|\Delta\theta_r|=180^\circ$, and there is no change in the radius of blind zone.

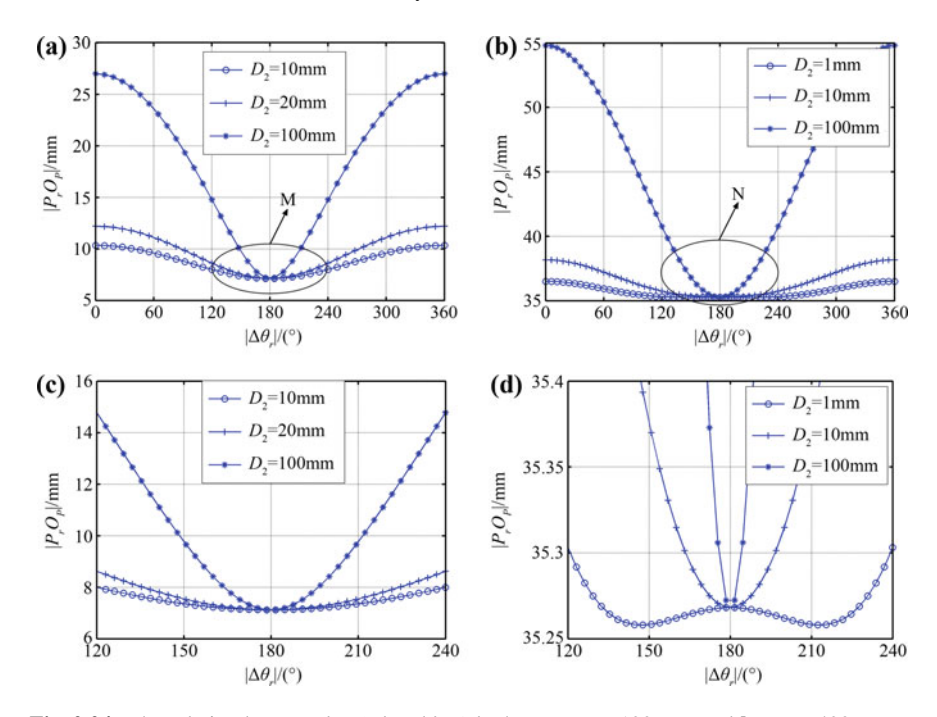


Fig. 2.24 The relation between $|P_rO_P|$ and $|\Delta\theta_r|$ when **a** $D_1 = 100$ mm and **b** $D_1 = 400$ mm, **c** and **d** are the enlarged view of area M and N, respectively

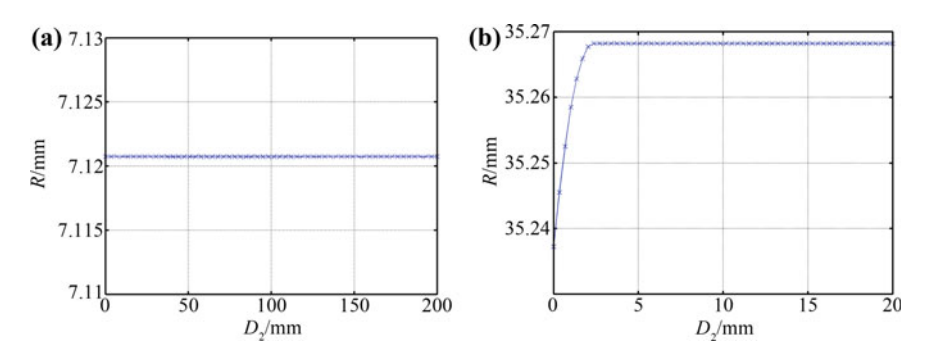


Fig. 2.25 The relation between R and D_2 when $\mathbf{a} D_1 = 100 \text{ mm}$ and $\mathbf{b} D_1 = 400 \text{ mm}$

In general, a beam scan blind zone cannot disappear in a rotating double-prism system. Given the wedge angle α , the refractive index n and the thinnest-end thickness d, the change rules of the blind zone radius can be summarized as follows according to the distance threshold between two prisms and that between prism 2 and the screen, written as D_{1c} and D_{2c} , respectively.

(1) If $D_1 \le D_{1c}$, the blind zone radius is merely dependent on D_1 while independent of D_2 , which can be obtained at $|\Delta \theta r| = 180^{\circ}$;

(2) If $D_1 > D_{1c}$, both D_1 and D_2 have effects on the blind zone radius. When $D2 \le D2c$, the blind zone radius gets enlarged with the increment of D_2 , and the corresponding relative rotation angles are symmetric about $|\Delta\theta_r| = 180^\circ$. When $D_2 > D_{2c}$, the blind zone radius keeps uniform with the variation of D_2 , which can only be found at $|\Delta\theta_r| = 180^\circ$.

2.7.2 Multi-mode Scan Trajectories of Rotating Scan Model

A variety of beam scan trajectories can be generated when two prisms are rotating at different combinations of angular velocities or angular accelerations. The exact coordinates of beam scan point in near field is the sum of the approximate coordinates in far field and the coordinates of the beam exiting point on the emergent surface of prism 2, except for the Z-coordinate. As shown in Fig. 2.26, several beam scan trajectories are simulated under different speed combinations of two prisms and compared with each other in near field and far field, where $\alpha=10^{\circ}$, n=1.517, $D_p=80$ mm, $d_0=5$ mm, $D_1=100$ mm, and $D_2=400$ mm. In Fig. 2.26, the values obtained in far field represents the approximate coordinates, and that in near field represents the exact coordinates. In the subsequent chapters, the meanings of near field and far field are not changed without any special statement.

As shown in Fig. 2.26i, when two prisms are rotating at the same speed but in the opposite directions, the beam scan trajectory in far field is close to a line segment along the X-axis, while it seems like an ellipse symmetric about the origin in near field. Generally, the scan trajectories do not pass the origin any longer when two prisms rotate at different uniform speeds matched in near field. Moreover, the intersection position of the beam path with the emergent surface of prism 2 has significant influence on the final scan trajectory, which should not be ignored.

It is also worth mentioning that much more interesting scan trajectories can be generated by introducing difference to the wedge angles of two prisms. For example, there are several beam scan trajectories simulated in Fig. 2.27. The involved simulation parameters of rotating double prisms are consistent with the aforementioned ones, except for the wedge angle α_2 of prism 2. Obviously, different wedge angles of two prisms can not only increase the diversity of beam scan trajectories, but also offer a possible way to eliminate blind spots in the beam scan region.

2.7.3 Scan Region of Tilting Scan Model

1. Discussion on Structural Parameters of Prisms

According to (2.27d), the beam scan position on the receiving screen is mainly related to the structural parameters, the refractive index and the layout arrangement of two prisms. Taking the laser communication from the earth to the moon for example, the

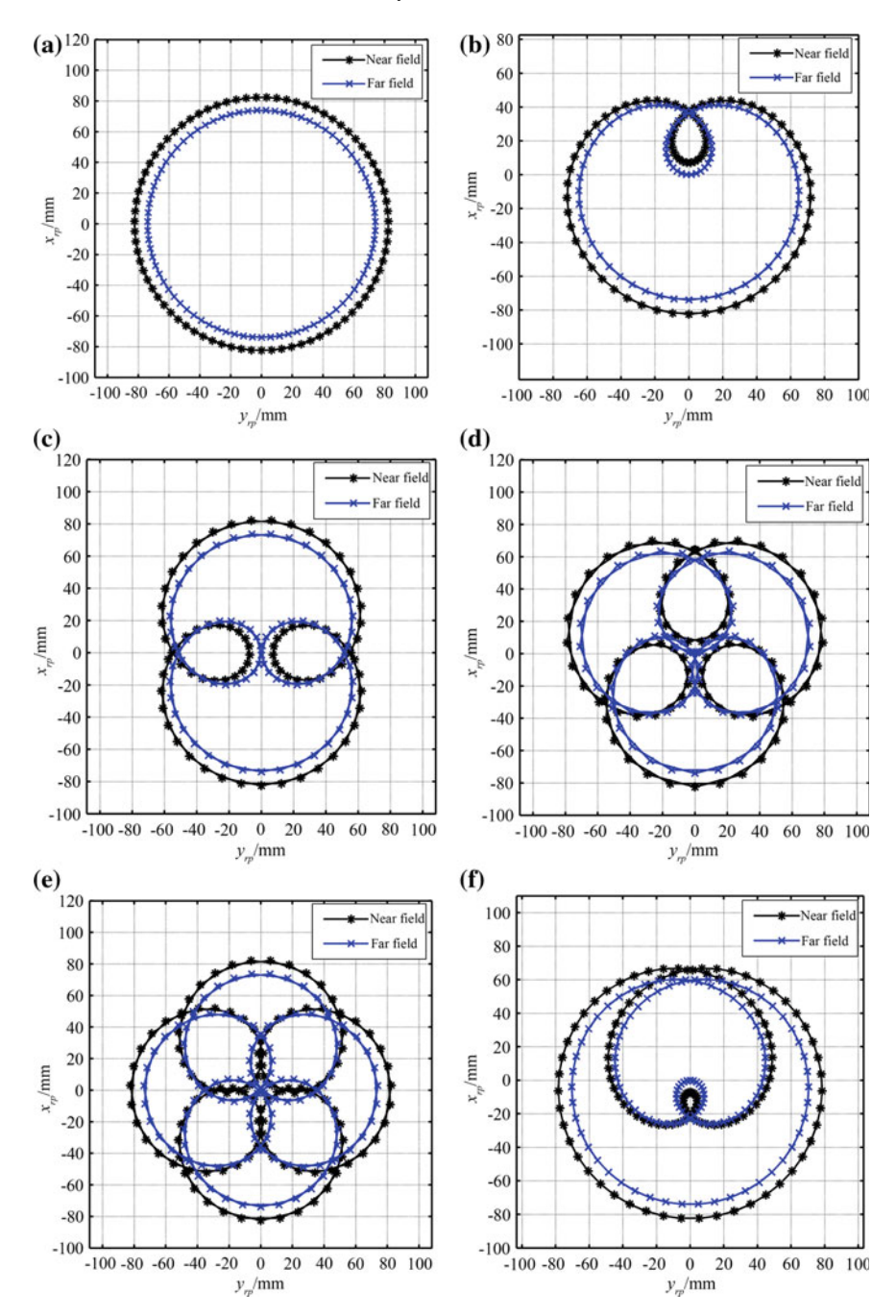


Fig. 2.26 Beam scan trajectories when **a** $\omega_{r2} = \omega_{r1}$; **b** $\omega_{r2} = 2\omega_{r1}$; **c** $\omega_{r2} = 3\omega_{r1}$; **d** $\omega_{r2} = 4\omega_{r1}$; **e** $\omega_{r2} = 5\omega_{r1}$; **f** $\omega_{r2} = 1.5\omega_{r1}$; **g** $\omega_{r2} = 2.5\omega_{r1}$; **h** $\omega_{r2} = 3.5\omega_{r1}$; **i** $\omega_{r2} = -\omega_{r1}$; **j** $\omega_{r2} = -2\omega_{r1}$; **k** $\omega_{r2} = -3\omega_{r1}$; **l** $\omega_{r2} = -4\omega_{r1}$; **m** $\omega_{r2} = -5\omega_{r1}$; **n** $\omega_{r2} = -1.5\omega_{r1}$; **o** $\omega_{r2} = -2.5\omega_{r1}$; **p** $\omega_{r2} = -3.5\omega_{r1}$; **o** $\omega_{r2} = -2.5\omega_{r1}$; **p** $\omega_{r2} = -3.5\omega_{r1}$

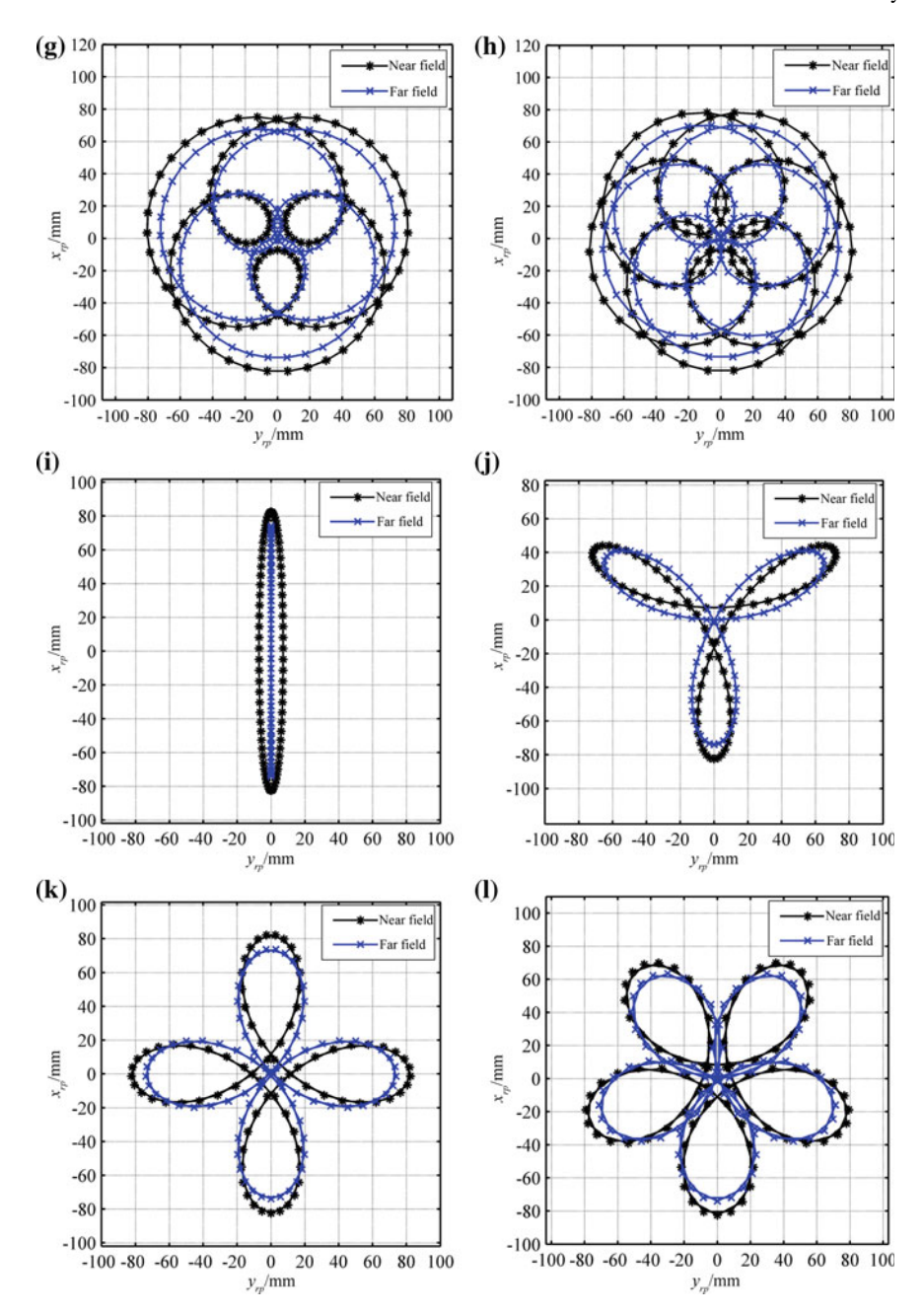


Fig. 2.26 (continued)

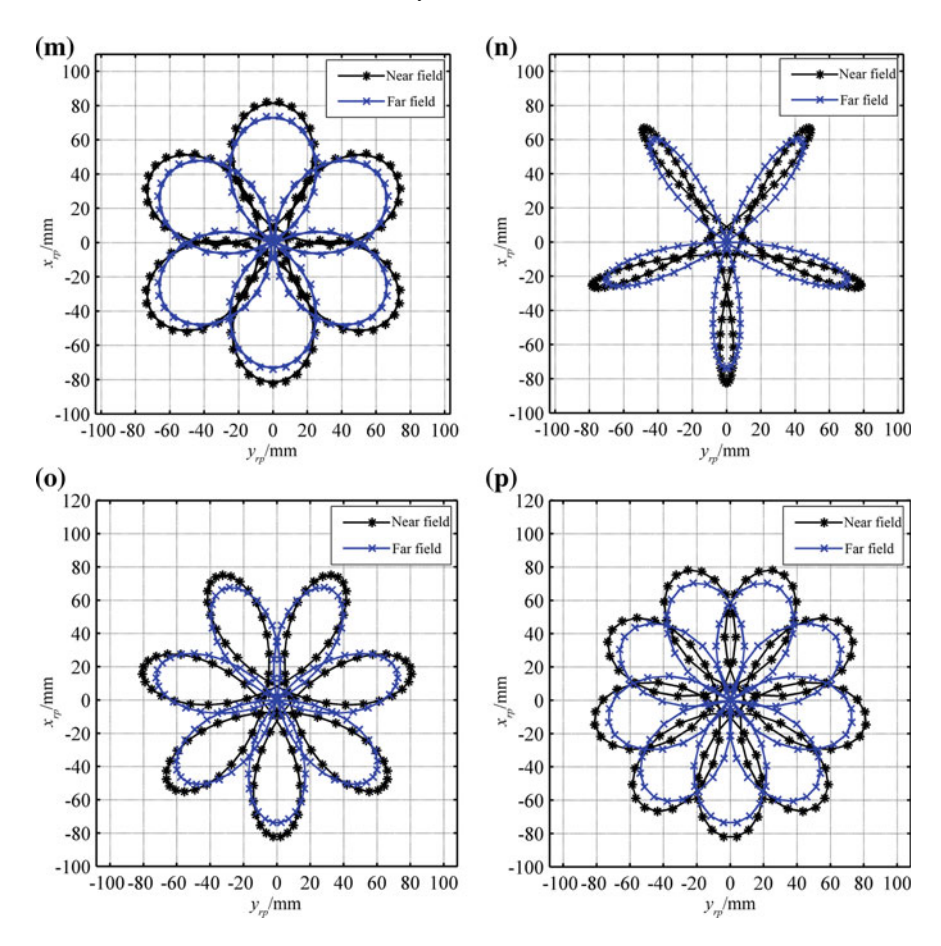


Fig. 2.26 (continued)

exact and approximate coordinates of beam scan point will be compared with regard to a tilting double-prism system with clear aperture of $D_p = 400$ mm. The distance between two prisms is set to $D_1 = 200$ mm and the tilting angles of each prism is limited to vary within 0° to 10° at the same speed.

Table 2.5 has listed the approximate coordinates (x'_{tp}, y'_{tp}) of beam scan points on the screen under the far-field condition and the exact ones (x_{tp}, y_{tp}) under the near-field condition. Under the former condition, D_2 stands for the distance from the earth to the moon, i.e. $D_2 = 3.844 \times 10^{11}$ mm. As a result, the maximum difference in (x'_{tp}, y'_{tp}) and (x_{tp}, y_{tp}) is 13.14 mm, which occurs when the prism orientations are both 0° . In general, the difference is acceptable for any long-distance beam propagation, but it cannot be ignored under the latter condition where $D_2 = 38.44$ mm.

Although we only discuss on the tilting double-prism system with the clear aperture $D_p = 80$ mm, a similar conclusion can be drawn by comparing the far-field

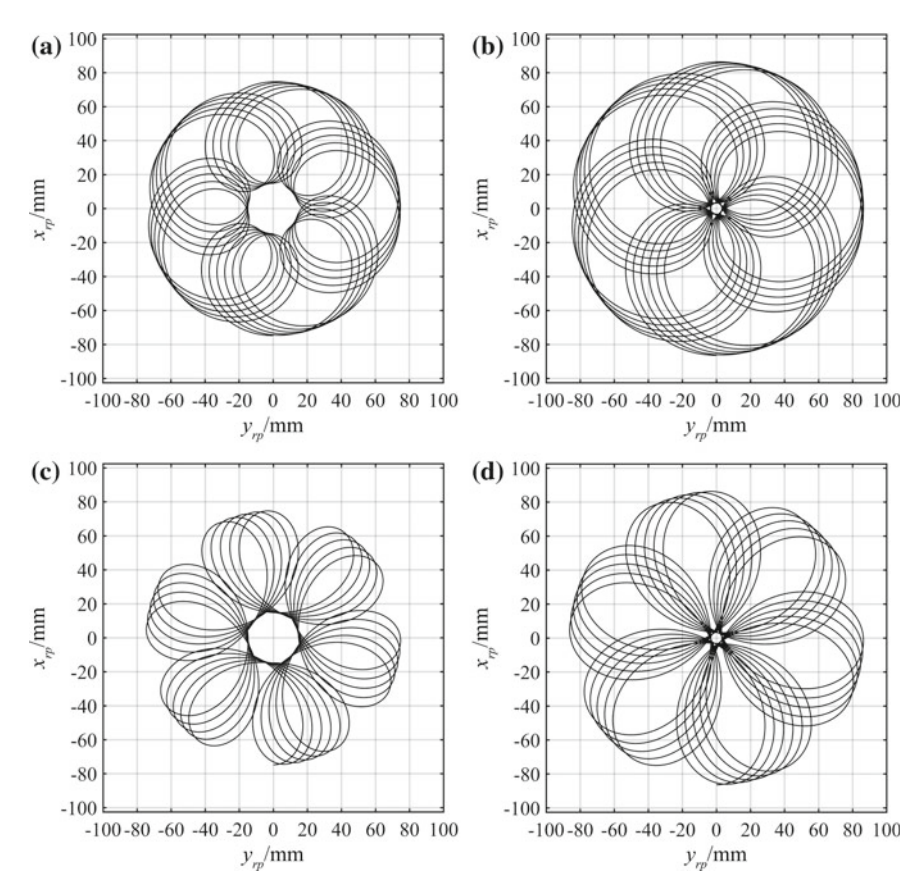


Fig. 2.27 Bean scan trajectories when **a** $\alpha_2 = 8^\circ$, $\omega_{r2} = 6.1\omega_{r1}$; **b** $\alpha_2 = 11^\circ$, $\omega_{r2} = 6.1\omega_{r1}$; **c** $\alpha_2 = 8^\circ$, $\omega_{r2} = -5.1\omega_{r1}$; **d** $\alpha_2 = 11^\circ$, $\omega_{r2} = -5.1\omega_{r1}$

condition with the near-field one. That is, the beam scan error induced by the beam exiting position is negligible in far field, but not in near field.

Scan Region in Near Field

A tilting double-prism system can achieve higher scan precision than a rotating double-prism system with the same structural parameters. But it is also important to obtain appropriate scan region in many optical applications. Therefore, the influence of the system parameters on the scan region should be firstly investigated when the system is designed [13].

Figure 2.28 shows the beam scan region of the model described in Sect. 2.6, with structural parameters of $D_1 = 100$ mm and $D_2 = 400$ mm. The theoretical scan region is a parallelogram-like area with any two adjacent edges that are nearly perpendicular to each other. To facilitate the calculation process, the largest rectangular area in the theoretical scan region can be regarded as the actual scan region. For the following

Table 2.5 Coordinates of beam intersection point on a receiving screen located in near or far field

D_2/mm	$\theta_{t1} = \theta_{t2} I(^{\circ})$	$ x_{tp}/mm $	yıp/mm	x_{tp}' /mm	y_{ip}' /mm
3.844×10^{11}	0	-35,628,217,193	-35,250,932,285	-35,628,217,180	_35,250,932,282
	2	-35,952,738,451	-35,377,324,535	-35,952,738,439	-35,377,324,532
	4	-36,360,173,343	-35,577,318,678	-36,360,173,331	-35,577,318,674
	9	-36,854,859,120	-35,851,982,715	-36,854,859,109	-35,851,982,711
	∞	-37,442,106,314	-36,202,980,864	-37,442,106,303	-36,202,980,859
	10	-38,128,339,349	-36,632,591,740	-38,128,339,339	-36,632,591,734
38.44	0	16.41902483	6.248362113	3.562821718	3.525093228
	2	16.00529619	6.840269794	3.595273844	3.537732453
	4	15.62110683	7.455490354	3.636017333	3.557731867
	9	15.26658961	8.096359930	3.685485911	3.585198271
	∞	14.94224702	8.765478005	3.744210630	3.620298086
	10	14.64900431	9.465736811	3.812833934	3.663259173

Fig. 2.28 Beam scan region of a tilting double-prism system

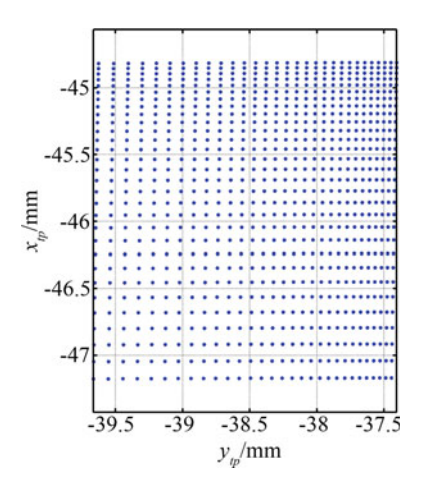


Table 2.6 Primary parameters of beam scan region under different values of D_2

D ₂ /mm	x _{tpmin} /mm	x _{tpmax} /mm	y _{tpmin} /mm	y _{tpmax} /mm	Area of scan region/mm ²	Center of scan region/mm
200	-27.34	-26.28	-20.58	-19.09	$1.06 \times 1.50 = 1.59$	(-26.81, -19.83)
400	-47.17	-44.82	-39.63	-37.44	$2.35 \times 2.18 = 5.13$	(-45.99, -38.53)
800	-86.83	-81.90	-77.71	-74.16	$4.93 \times 3.54 = 17.46$	(-84.37, -75.93)
1600	-166.16	-156.08	-153.87	-147.60	10.08 × 6.27 = 63.19	(-161.12, -150.73)

example, the scan region locates at the specific area where x_{tp} varies within -47.17 to -44.82 mm and y_{tp} varies within -39.63 to -37.44 mm. The scan region has the size of 2.35 mm \times 2.19 mm and the coordinates of its center point are (-45.99, -38.53 mm).

3. Factors Influencing Beam Scan Region

Regarding the tilting double-prism system in Sect. 2.6, Table 2.6 shows primary parameters of the beam scan region when $D_1 = 100$ mm and D_2 takes different values. Obviously, as the receiving screen is placed farther away from the center of the emergent surface, the scan region gets enlarged and the center of scan region locates farther away from the center of the receiving screen.

The primary parameters of beam scan region are viewed in Table 2.7 when D_1 takes different values and $D_2 = 400$ mm. Since D_2 is held constant, the variation of D_1 can only affect the scan range in the X-direction other than the Y-direction. The deviation of the emergent beam in the Y-direction depends mainly on the tilting angle of prism 2, and the beam propagation after prism 1 has nothing to do with D_1 .

D_1 /mm	x _{tpmin} /mm	x_{tpmax} /mm	y _{tpmin} /mm	y _{tpmax} /mm	Area of scan region/mm ²	Center of scan region/mm
50	-42.23	-40.20	-39.63	-37.44	2.03 - 2.18 = 4.42	(-41.22, -38.53)
100	-47.17	-44.82	-39.63	-37.44	2.35 - 2.18 = 5.13	(-45.99, -38.53)
200	-57.04	-54.05	-39.63	-37.44	3.00-2.18 = 6.53	(-55.55, -38.53)
400	-76.79	-72.51	-39.63	-37.44	4.28 - 2.18 = 9.34	(-74.65, -38.53)

Table 2.7 Primary parameters of beam scan region under different values of D_1

Table 2.8 Primary parameters of beam scan region under different values of d_0

d ₀ /mm	x _{tpmin} /mm	x _{tpmax} /mm	y _{tpmin} /mm	y _{tpmax} /mm	Area of scan region/mm ²	Center of scan region/mm
5	-47.17	-44.82	-39.63	-37.44	$2.35 \times 2.18 = 5.13$	(-45.99, -38.53)
10	-46.19	-44.20	-40.27	-37.75	$1.99 \times 2.52 = 5.02$	(-45.19, -39.01)
15	-45.20	-43.58	-40.91	-38.05	$1.63 \times 2.86 = 4.66$	(-44.39, -42.13)

Both the scan range in the X-direction and the total area of scan region increase with the increment of D_1 , and the center of scan region moves in the negative X-direction.

Likewise, Table 2.8 presents the primary parameters of beam scan region when

Likewise, Table 2.8 presents the primary parameters of beam scan region when $D_1 = 100$ mm, $D_2 = 400$ mm and d_0 takes different values. Now that D_1 and D_2 are kept invariant, the scan region is reduced in the X-direction but enlarged in the Y-direction with the increment of d_0 . Correspondingly, the center of scan region has larger X-coordinate but smaller Y-coordinate.

2.7.4 Multi-mode Scan Trajectories of Tilting Scan Model

When two prisms tilt under different combinations of angular velocities, the various beam scan trajectories can be generated. In Fig. 2.29a, the beam scan trajectory is viewed when the tilting angular velocities of prisms are uniform and $\omega_{t2} = 2\omega_{t1}$. The tilting angles of two prisms are given by $\theta_{t1} = -|t-10+10|$ and $\theta_{t2} = -|2t-10|+10$, respectively. It turns out that the trajectory is a closed curve, and the beam scan point moves cyclically along the curve. Similarly, Fig. 2.29b, c display the beam scan trajectories when $\omega_{t2} = 4\omega_{t1}$, and the tilting angles of two prisms are, respectively, given by $\theta_{t1} = -|t-10|+10$ and $\theta_{t2} = -|4t-10|+10$. During the beam scan process, the scan point firstly moves along the path shown in Fig. 2.29b, roughly in the

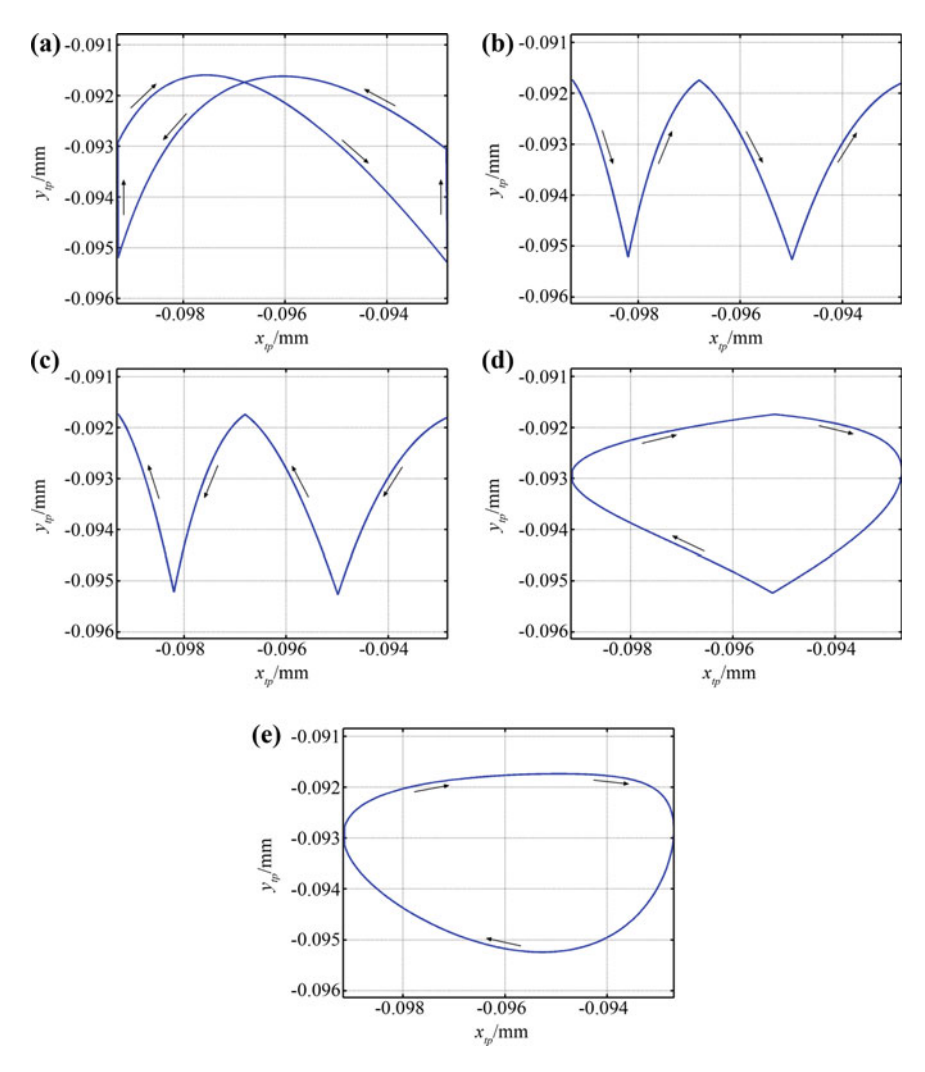


Fig. 2.29 Beam scan trajectories under different tilting angular velocities, where the black arrows show the moving direction of beam scan point. **a** uniform ω_{t1} , uniform ω_{t2} and $\omega_{t2} = 2\omega_{t1}$; **b** and **c** uniform ω_{t1} , uniform ω_{t2} and $\omega_{t2} = 4\omega_{t1}$; **d** sine function for ω_{t1} and uniform ω_{t2} ; **e** sine function for ω_{t1} and cosine function for ω_{t2}

positive *X*-direction, and then returns to the beginning position along the identical path shown in Fig. 2.29c. More beam scan trajectories are simulated under non-uniform angular velocities of two prisms. Providing θ_{t1} as $\theta_{t1} = 5\sin(\pi t/5) + 5$, θ_{t2} is given by $\theta_{t2} = -|2t - 10| + 10$ in Fig. 2.29d and $\theta_{t2} = 5\cos(\pi t/5) + 5$ in Fig. 2.29e. Each of the consequent scan trajectories is a closed curve, and the scan point moves cyclically along the curve. It is noteworthy that there are several sharp points on the former trajectory, while the latter one is relatively smooth due to the sine function

for ω_{t1} and the cosine function for ω_{t2} . In general, the scan trajectories shown in Fig. 2.29 reflect the discontinuous differentiability of tilting angle functions, and the closed trajectory curves indicate the beam scan periodicity induced by different tilting cycles within the limited angle range of 0° to 10° .

2.8 Multi-prism Scan Model

To meet the multi-scale and multi-mode beam scan requirements, there is plenty of multi-prism configurations, such as three prisms, four prisms and other combinations. The multi-prism scan model can expand beam scan region [14], improve beam scan precision and also produce multi-mode scan trajectories. As a result, the scan adaptability and flexibility are greatly enhanced although the structure design and control strategy of a multi-prism system become more complicated than any double-prism system.

2.8.1 Theoretical Model

By way of example, the triple-prism scan model is chosen from many possible combinations. Based on the rotating double-prism model in Fig. 2.5, the third prism is introduced with its plane facet situated outwards, as shown in Fig. 2.30. Another configuration with the plane facet situated inwards can be discussed with the same method [15].

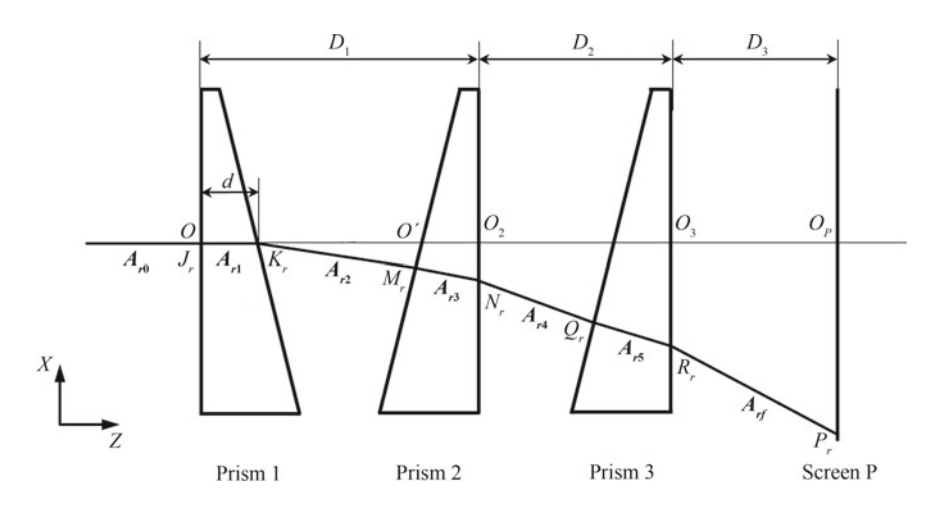


Fig. 2.30 Schematic diagram of beam propagation through rotating triple-prism system

The rotating triple-prism system can be regarded as the combination of a rotating double-prism system and one directional prism. Three prisms have the same wedge angle α and refractive index n. The center points at the emergent surfaces of prism 2 and prism 3 are, respectively, marked as O_2 and O_3 . The distance between O_2 and O_3 is O_2 , and the one between O_3 and the center point O_P on the screen P is O_3 . The rotation angle and angular velocity of prism 3 are denoted by O_3 and O_4 and O_5 , respectively. In addition, the intersection point of the final emergent beam with the receiving screen is defined as O_2 .

The unit normal vectors to the surfaces of prism 1 and prism 2 have been given by (2.6a)–(2.6d) in Sect. 2.3.1. As for prism 3, the normal vectors to the incident and emergent surfaces are expressed as

$$N_{31} = (-\cos\theta_{r3}\sin\alpha, -\sin\theta_{r3}\sin\alpha, \cos\alpha)^{\mathrm{T}}$$
 (2.28a)

$$N_{32} = (0, 0, 1)^{\mathrm{T}}. (2.28b)$$

As shown in Fig. 2.30, A_{r0} is the incident beam vector to prism 1, A_{r1} , A_{r2} , A_{r3} , A_{r4} , A_{r5} and A_{rf} are the refracted beam vectors at all prism surfaces in turn. The expressions for A_{r0} , A_{r1} , A_{r2} , A_{r3} and A_{r4} are available from (2.6) and (2.7). Other vectors A_{r5} and A_{rf} can be obtained as follows according to the vector refraction theorem:

$$A_{r5} = \frac{1}{n} A_{r4} + \left\{ \sqrt{1 - \left(\frac{1}{n}\right)^2 \cdot [1 - (A_{r4} \cdot N_{31})^2]} - \frac{1}{n} A_{r4} \cdot N_{31} \right\} \cdot N_{31}$$

$$= (x_{r5}, y_{r5}, z_{r5})^{\mathrm{T}}$$

$$(2.29a)$$

$$A_{rf} = n A_{r5} + \left\{ \sqrt{1 - n^2 \cdot [1 - (A_{r5} \cdot N_{32})^2]} - n A_{r5} \cdot N_{32} \right\} \cdot N_{32}$$

$$= (x_{rf}, y_{rf}, z_{rf})^{\mathrm{T}}$$

$$(2.29b)$$

The expressions for the refracted beam vectors can be further derived by substituting (2.28) into (2.29), omitted here.

2.8.2 Coordinate Expressions for Scan Points

The intersection coordinates of the beam path through any multi-prism scan model can also be determined as in Sect. 2.5. We still take the triple-prism system for example in this section

1. Equations for Incident and Emergent Surfaces of Rotating Triple Prisms

As shown in Fig. 2.30, the central-axis thickness of each prism is denoted by d. The equations for the surfaces of prism 1 and prism 2 are the same as (2.24a) and (2.24d)

in Sect. 2.5.1, and the equation for the incident surface of prism 3 can be expressed in terms of the normal vector $N_{31} = (-\cos\theta_{r3}\sin\alpha, -\sin\theta_{r3}\sin\alpha, \cos\alpha)^{T}$ passing the known point $(0, 0, D_1 + D_2 - d)$, as follows

$$-\cos\theta_{r3}\sin\alpha \cdot x - \sin\theta_{r3}\sin\alpha \cdot y + \cos\alpha \cdot [z - (D_1 + D_2 - d)] = 0. \quad (2.30a)$$

The equation for the emergent surface of prism 3 is expressed in terms of the normal vector $N_{32} = (0, 0, 1)^{T}$ passing the known point $O_3(0, 0, D_1 + D_2)$:

$$z = D_1 + D_2. (2.30b)$$

Furthermore, the equation for the screen P is expressed as

$$z = D_1 + D_2 + D_3. (2.30c)$$

2. Intersection Coordinates of the Beam and Rotating Triple Prisms

The beam path intersects all surfaces of prism 1 and prism 2 at the points written as $J_r(x_{rj}, y_{rj}, z_{rj})$, $K_r(x_{rk}, y_{rk}, z_{rk})$, $M_r(x_{rm}, y_{rm}, z_{rm})$ and $N_r(x_{rm}, y_{rn}, z_{rm})$ in sequence, which can be deduced from (2.25a)–(2.25c) in Sect. 2.5.1.

Referring to Sect. 2.8.1, the refracted beam at the emergent surface of prism 2 is along the vector $A_{r4} = (x_{r4}, y_{r4}, z_{r4})^{T}$ and passes the point $N_r(x_m, y_m, z_m)$. Thus, the equation for the refracted beam is expressed as $\frac{x - x_{rm}}{x_{r4}} = \frac{y - y_{rm}}{y_{r4}} = \frac{z - z_{rm}}{z_{r4}} = t_{c4}$, and the intersection point $O_r(x_{rq}, y_{rq}, z_{rq})$ of the beam path with the incident surface of prism 3 is given by

$$\begin{cases} x_{rq} = x_{r4} \cdot t_{c4} + x_{rn} \\ y_{rq} = y_{r4} \cdot t_{c4} + y_{rn} \\ z_{rq} = z_{r4} \cdot t_{c4} + z_{rn} \end{cases}$$
(2.31a)

where $t_{c4} = \frac{\cos\theta_{r3}\sin\alpha \cdot x_{rn} + \sin\theta_{r3}\sin\alpha \cdot y_{rn} - \cos\alpha \cdot [z_{rn} - (D_1 + D_2 - d)]}{-\cos\theta_{r3}\sin\alpha \cdot x_{r4} - \sin\theta_{r3}\sin\alpha \cdot y_{r4} + \cos\alpha \cdot z_{r4}}$.

Similarly, the point $R_r(x_{rr}, y_{rr}, z_{rr})$ at which the beam intersects the emergent surface of prism 3 is given by

$$\begin{cases} x_{rr} = x_{r5} \cdot t_{c5} + x_{rq} \\ y_{rr} = y_{r5} \cdot t_{c5} + y_{rq} \\ z_{rr} = z_{r5} \cdot t_{c5} + z_{rq} \end{cases}$$
(2.31b)

where $t_{c5} = \frac{D_1 + D_2 - z_{rq}}{z_{r5}}$.

The point at which the emergent beam from prism 3 intersects the screen, namely the beam scan point $P_r(x_{rp}, y_{rp}, z_{rp})$, is given by

$$\begin{cases} x_{rp} = x_{rf} \cdot t_{c6} + x_{rr} \\ y_{rp} = y_{rf} \cdot t_{c6} + y_{rr} \\ z_{rp} = z_{rf} \cdot t_{c6} + z_{rr} = D_1 + D_2 + D_3 \end{cases}$$
 (2.31c)

where
$$t_{c6} = \frac{D_1 + D_2 + D_3 - z_{rr}}{z_{rf}} = \frac{D_3}{z_{rf}}$$
.

2.8.3 Scan Region of Rotating Triple Prisms

The geometrical parameters of rotating triple prisms are set as follows. Each prism has the wedge angle $\alpha=10^\circ$, the refractive index n=1.517, the clear aperture $D_p=80$ mm and the thinnest-end thickness $d_0=5$ mm. The distance between prism 1 and prism 2 is $D_1=100$ mm and that between prism 2 and prism 3 is $D_2=100$ mm. Two different scan regions are demonstrated in Fig. 2.31a, b, where the distance from prism 3 to the screen takes $D_3=40$ mm and $D_3=100$ mm, respectively.

Seen from Fig. 2.31, the radius of scan blind zone is related to D_3 when D_1 and D_2 are constant. Comparing with Fig. 2.23, it is evident that the blind zone can be eliminated by the third prism. Figure 2.32 illustrates the relation between the size of blind zone and D_3 . When D_3 is relatively small, the radius of blind zone decreases to some extent; and when $D_3 \ge 80$ mm, the blind zone is completely eliminated. That is, the addition of a third prism can narrow or even eliminate the blind zone.

In order to discuss the influence of rotating triple prisms on the beam scan region, the layout parameters are set as follows. The rotating double-prism system has $D_2 = 400$ mm, while the rotating triple-prism system has $D_2 = 100$ mm and $D_3 = 300$ mm. In other words, the distance from prism 2 to the receiving screen is kept consistent

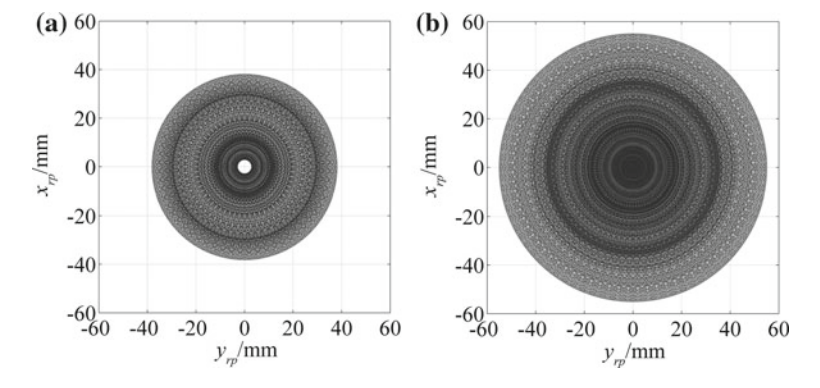


Fig. 2.31 Scan regions of rotating triple prisms when a $D_3 = 40$ mm and b $D_3 = 100$ mm

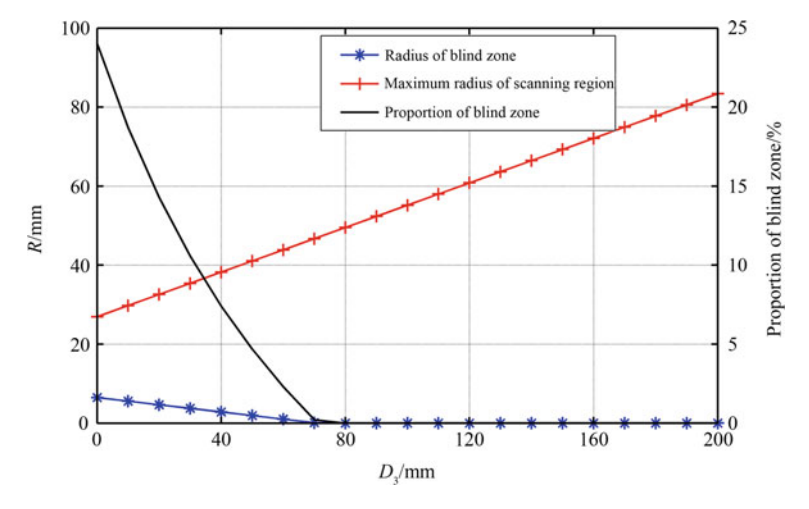


Fig. 2.32 Relation between the size of blind zone and D_3

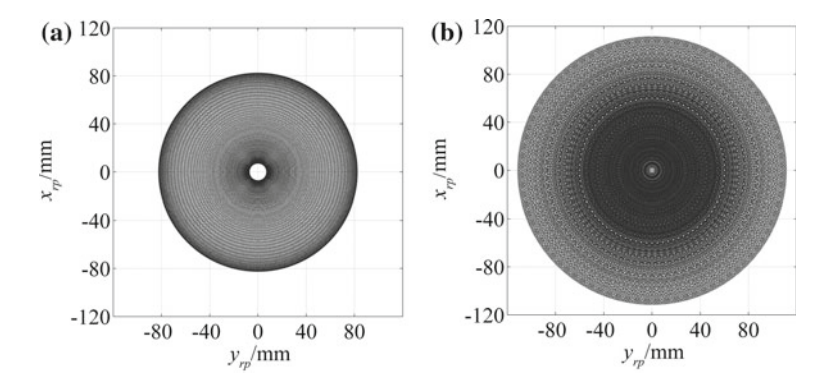


Fig. 2.33 Scan regions of a rotating double-prism system and b rotating triple-prism system

in two systems. Other parameters remain unchanged as before. Figure 2.33a, b separately illustrate beam scan regions of the rotating double-prism system and the rotating triple-prism system. Regarding the double-prism system, the scan region has the radius of 82.4833 mm and there is a scan blind zone with the radius of 7.1207 mm. As for the triple-prism system, the radius of scan region becomes 111.6279 mm and there is no blind zone anymore. In other words, the beam scan region of the triple-prism system can be enlarged by 84.53% over that of the double-prism system.

2.8.4 Multi-mode Scan Trajectories of Rotating Triple Prisms

Taking the rotating triple-prism system for example, the multi-mode beam scan trajectories can be generated under different speed combinations of three prisms, as shown in Fig. 2.34. The system parameters are $\alpha = 10^{\circ}$, n = 1.517, $D_p = 80$ mm, $d_0 = 5$ mm, $D_1 = D_2 = 100$ mm and $D_3 = 300$ mm.

Clearly, rotating triple prisms can generate much richer beam scan patterns. Comparing Fig. 2.26a with Fig. 2.34a, it is also found that rotating triple prisms can cover a larger scan region. Moreover, Fig. 2.34g shows a scan trajectory passing the coordinate origin, which further validates that the blind zone can be eliminated using a third prism.

2.9 Summary

In this chapter, the multi-mode beam scan model is firstly established on the basis of double Risley prisms. Theoretical modelling of double prisms at rotating or tilting scan mode is performed with both vector refraction method and geometric method. Several important beam scan issues are further investigated, including multi-mode scan trajectory, scan region, scan precision, parameter matching and multi-prism scan model. For rotating double-prism scan model, the relation between the pitch angle of emergent beam and the orientations of two prisms are presented to help quantify the influence of system parameters on beam scan range and beam scan precision. The formation mechanism of scan blind zone is revealed in principle. As for tilting double-prism scan model, the relation between the tilting angles of two prisms and the change rate of the vertical or horizontal field angle of emergent beam is thoroughly investigated. It is also clarified that tilting double prisms can achieve higher beam scan precision within smaller scan range in both vertical and horizontal directions. Moreover, the multi-prism combination model, especially the rotating triple-prism model, is introduced to derive the coordinate expressions for the intersection point at each interface of three prisms. The beam scan region of the triple-prism system is further demonstrated, within which the multi-mode beam scan trajectories can be generated.

2.9 Summary 91

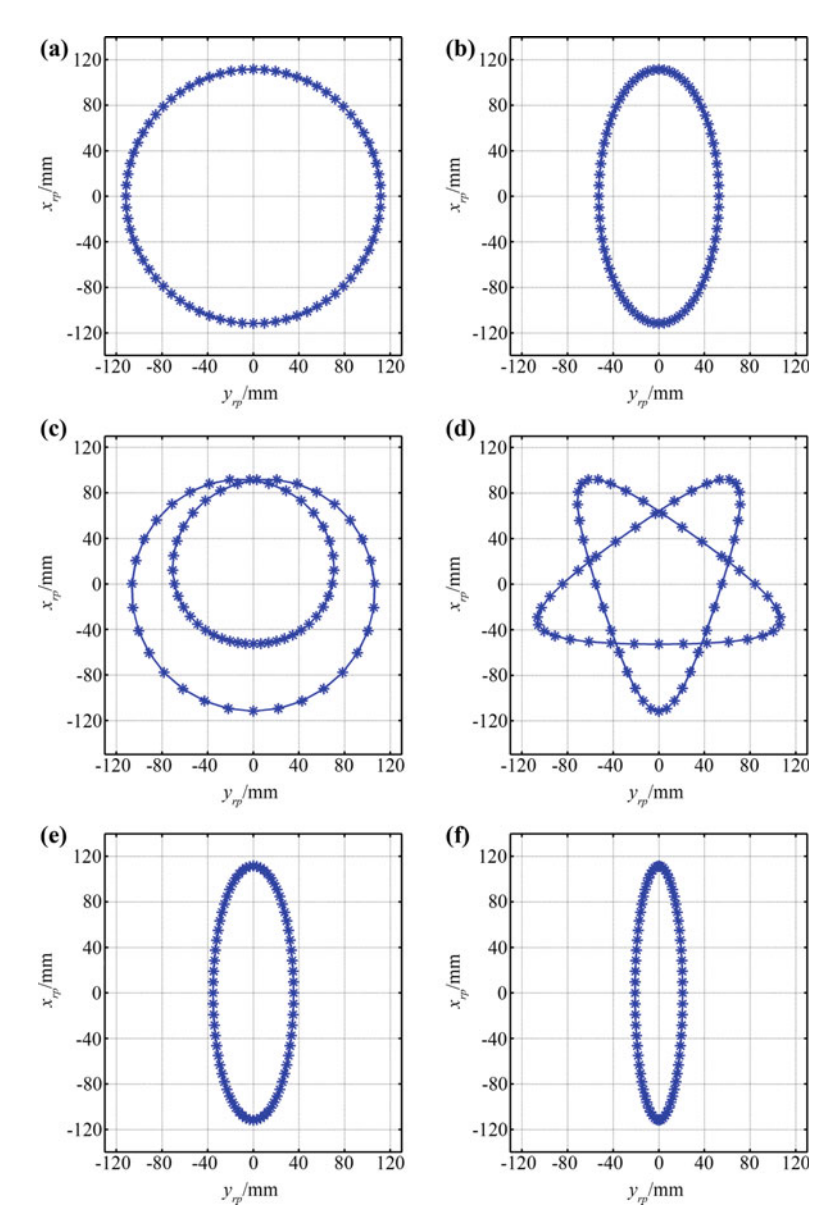


Fig. 2.34 Different scan trajectories of rotating triple prisms with different speed combinations of three prisms, such as $\mathbf{a} \ \omega_{r1}:\omega_{r2}:\omega_{r3}=1:1:1$, $\mathbf{b} \ \omega_{r1}:\omega_{r2}:\omega_{r3}=1:1:-1$, $\mathbf{c} \ \omega_{r1}:\omega_{r2}:\omega_{r3}=1:1:1.5$, $\mathbf{d} \ \omega_{r1}:\omega_{r2}:\omega_{r3}=1:1:-1.5$, $\mathbf{e} \ \omega_{r1}:\omega_{r2}:\omega_{r3}=1:-1:1$, $\mathbf{f} \ \omega_{r1}:\omega_{r2}:\omega_{r3}=1:-1:-1$, $\mathbf{g} \ \omega_{r1}:\omega_{r2}:\omega_{r3}=1:-1:1.5$, $\mathbf{h} \ \omega_{r1}:\omega_{r2}:\omega_{r3}=1:-1:-1.5$, $\mathbf{i} \ \omega_{r1}:\omega_{r2}:\omega_{r3}=1:2:1$, $\mathbf{j} \ \omega_{r1}:\omega_{r2}:\omega_{r3}=1:2:-1$, $\mathbf{k} \ \omega_{r1}:\omega_{r2}:\omega_{r3}=1:2:1.5$, $\mathbf{l} \ \omega_{r1}:\omega_{r2}:\omega_{r3}=1:2:-1.5$, $\mathbf{m} \ \omega_{r1}:\omega_{r2}:\omega_{r3}=1:-2:1$, $\mathbf{n} \ \omega_{r1}:\omega_{r2}:\omega_{r3}=1:-2:-1$, $\mathbf{n} \ \omega_{r1}:\omega_{r2}:\omega_{r3}=1:-2:-1.5$

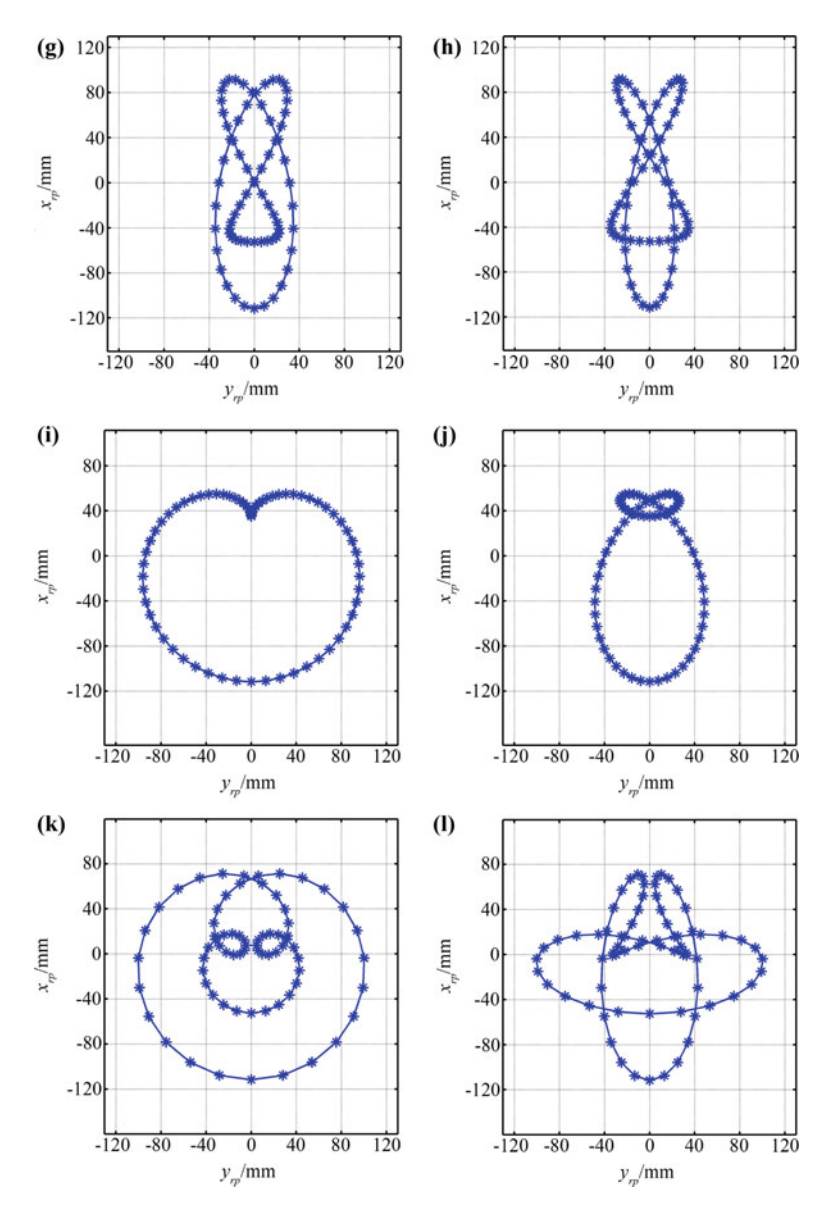


Fig. 2.34 (continued)

References 93

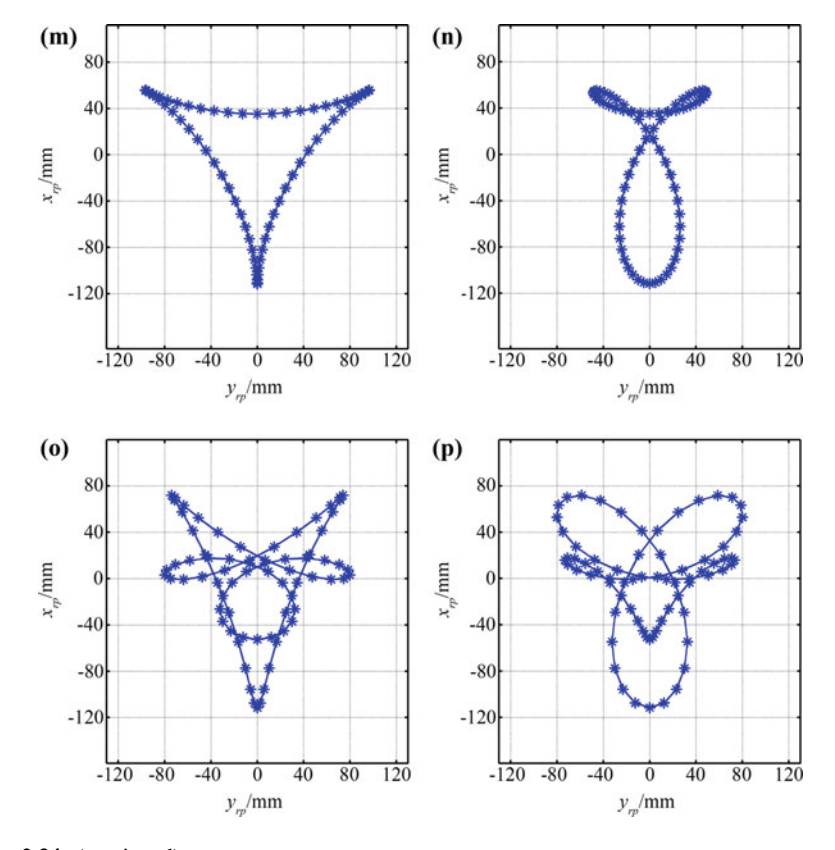


Fig. 2.34 (continued)

References

- Li AH, Ding Y, Bian YM et al (2014) Inverse solutions for tilting orthogonal double prisms. Appl Opt 53(17):3712–3722
- Ding Y (2014) Mathematical modeling and simulation analysis of double-prism scanning system. Tongji University, Shanghai
- 3. Rosell FA (1960) Prism scanners. J Optical Soc America 50:521–526
- 4. Fan DP, Zhou Y, Lu YF et al (2013) Overview of beam steering technology based on rotational double prisms. Chinese Optics 6(2):136-150
- Schwarze CR, Vaillancourt R, Carlson D et al (2005) Risley-prism based compact laser beam steering for IRCM, laser communications, and laser radar [EB/OL]. Optra Inc, Tospfield, MA, 9 [2016-10-13]. http://www.optra.com/images/TP-Compact_Beam_Steering.pdf
- Li YJ (2011) Third-order theory of the Risley-prism-based beam steering system. Appl Opt 50(5):679–686
- 7. Editorial Group of Handbook of Optical Instrument Design (1971) Handbook of optical instrument design (Part I). Nation Defence Industry Press, Beijing
- 8. Senderáková D, Štrba A (2003) Analysis of a wedge prism to perform small-angle beam deviation. Proc. of SPIE 5036:148–151

- Li AH, Gao XJ, Ding Y (2014) Comparison of refractive rotating dual-prism scanner used in near and far field. Proc SPIE 9192:929216–919216-13
- 10. Sun JF (2005) Research on the satellite trajectory optical simulator. Shanghai Institute of Optics and Fine Mechanics, Chinese Academy of Sciences, Shanghai
- 11. Li AH, Liu LR, Sun JF et al (2006) Research on a scanner for tilting orthogonal double prisms. Appl Opt 45(31):8063–8069
- 12. Li AH, Sun WS, Yi WL et al (2016) Investigation of beam steering performances in rotation Risley-prism scanner. Opt Express 24(12):12840–12850
- 13. Li AH, Yi WL, Zuo QY et al (2016) Performance characterization of scanning beam steered by tilting double prisms. Opt Express 24(20):23543–23556
- Sánchez M, Gutow D (2006) Control laws for a 3-element Risley prism optical beam pointer. Proc SPIE 6304:630403–630403-7
- 15. Li AH, Liu XS, Sun WS (2017) Forward and inverse solutions for three-element Risley prism beam scanners. Opt Express 25(7):7677–7688

Chapter 3 Inverse Problem of Double-Prism Multi-mode Scanning



Abstract Several typical methods are presented to solve the inverse problem of rotating or tilting double prisms, accompanied by numerous cases. Regarding rotating double prisms, the two-step method for approximate solutions and the lookuptable method with limited efficiency are both demonstrated. An iterative method combining two-step method with non-paraxial ray tracing is proposed to generate more accurate and efficient inverse solutions. Additionally, the damped least-squares iterative method is introduced for more general applications. As for tilting double prisms, the analytical method and lookup-table method are well implemented to solve the inverse problem. Binary lookup-table method and region-converging iterative method are further developed to improve solving accuracy and solving efficiency.

Based on the forward beam scan model presented in Chap. 2, the inverse problem remains as one crucial issue for the applications of double-prism multi-mode scanning. The inverse problem is about how to solve the orientations of two prisms according to the given beam deviation or target position [1]. Due to the nonlinear relation between the rotation or tilting angles of two prisms and the beam deviation angle [2, 3], it is difficult to obtain any exact inverse solution using analytical expressions. A numerical method is feasible to solve this problem, but the solving efficiency and calculation accuracy should meet the requirements of real-time and high-precision tracking applications. In this chapter, some effective inverse solution methods will be introduced.

3.1 Inverse Solution for Rotating Double Prisms

3.1.1 Two-Step Method

Two-step method has already been proposed in [4] to solve the inverse problem of rotating double prisms. Without considering the impacts of structural parameters on the beam propagation path, two-step method is applicable in some approximate

situations such as far-field target tracking. Both the thickness of each prism and the distance between two prisms are negligible, so the emergent beam is considered to deviate from the center of prism 2 in approximation [5].

1. Two Sets of Inverse Solutions

Given the coordinates of any target point, it is easy to specify the emergent beam by the unit vector $(x_{tf}, y_{tf}, z_{tf})^{T}$ or the combination of pitch angle ρ and azimuth angle φ . For rotating double prisms, the pitch angle ρ is only associated with the relative rotation angle $\Delta\theta_r$ of two prisms, expressed as

$$\rho = \arccos(z_{rf}) = \arccos(\cos \delta_1 \cos \delta_2 - \sin \delta_1 \sin \delta_2 \cos \Delta \theta_r)$$

As indicated by two-step method, the angle $\Delta\theta_r$ is deduced from the desired pitch angle ρ at the first step, and the rotation angles θ_{r1} and θ_{r2} are determined according to the desired azimuth angle φ at the second step.

For simplification, the first step is to keep prism 1 stationary at the initial orientation of $\theta_{0r1}=0$ but rotate prism 2 to the θ_{0r2} orientation. Then $\Delta\theta_r$ can be obtained once θ_{0r2} is deduced from the desired ρ , and the corresponding azimuth angle is calculated to be φ_0 . The second step is to rotate prism 1 and prism 2 synchronously with an angle $\varphi-\varphi_0$ deduced from the desired φ . Thus, the final values of θ_{r1} and θ_{r2} is considered as one set of inverse solution. Similarly, the other set of inverse solution can be determined if prism 2 is kept stationary while prism 1 rotates at the first step.

(1) First Set of Inverse Solution

At the first step, it can be deduced that $\theta_{0r1} = 0$ and $\Delta\theta_r = \theta_{0r1} - \theta_{0r2} = -\theta_{0r2}$. The values are applied to the derivation in Sect. 2.3.1, which can simplify the expression of each beam vector during the beam propagation.

Basically, the normal vectors to prism surfaces are simplified as

$$N_{11} = (0, 0, 1)^{\mathrm{T}} \tag{3.1a}$$

$$N_{12} = (\sin \alpha, 0, \cos \alpha)^{\mathrm{T}} \tag{3.1b}$$

$$N_{21} = (-\sin\alpha\cos\theta_{0r2}, \sin\alpha\sin\theta_{0r2}, \cos\alpha)^{\mathrm{T}}$$
 (3.1c)

$$N_{22} = (0, 0, 1)^{\mathrm{T}} \tag{3.1d}$$

Providing that the incident beam vector A_{r0} to prism 1 travels parallel to the optical axis of the system, the refracted beam vector at the incident surface of prism 1 is written as $A_{r1} = A_{r0} = (0, 0, 1)^{T}$. The dot product of A_{r1} and N_{12} is given by $A_{r1} \cdot N_{12} = \cos \alpha$.

The emergent beam vector from prism 1 is written as

$$A_{r2} = n \begin{pmatrix} 0 \\ 0 \\ 1 \end{pmatrix} + \left\{ \sqrt{1 - n^2 \sin^2 \alpha} - n \cos \alpha \right\} \cdot \begin{pmatrix} \sin \alpha \\ 0 \\ \cos \alpha \end{pmatrix}$$

$$= \begin{pmatrix} \sin \alpha \left(\sqrt{1 - n^2 \sin^2 \alpha} - n \cos \alpha \right) \\ 0 \\ n \sin^2 \alpha + \cos \alpha \sqrt{1 - n^2 \sin^2 \alpha} \end{pmatrix} = \begin{pmatrix} b_1 \\ 0 \\ b_2 \end{pmatrix}$$
(3.2a)

where the intermediate variables b_1 and b_2 are both constants because the wedge angle α and the refractive index n are already known. The dot product of A_{r2} and N_{21} can be obtained from $A_{r2} \cdot N_{21} = -b_1 \sin \alpha \cos \theta_{0r2} + b_2 \cos \alpha$.

The refracted beam vector at the incident surface of prism 2 is written as

$$A_{r3} = \frac{1}{n} \cdot \begin{pmatrix} b_1 \\ 0 \\ b_2 \end{pmatrix} + \left\{ \sqrt{1 - \left(\frac{1}{n}\right)^2 \left[1 - (A_{r2} \cdot N_{21})^2\right]} - \frac{1}{n} (A_{r2} \cdot N_{21}) \right\}$$

$$\cdot \begin{pmatrix} -\sin\alpha\cos\theta_{0r2} \\ \sin\alpha\sin\theta_{0r2} \\ \cos\alpha \end{pmatrix} = \frac{1}{n} \cdot \begin{pmatrix} b_1 \\ 0 \\ b_2 \end{pmatrix} + p_1 \cdot \begin{pmatrix} -\sin\alpha\cos\theta_{0r2} \\ \sin\alpha\sin\theta_{0r2} \\ \cos\alpha \end{pmatrix}$$

$$= \begin{pmatrix} \frac{b_1}{n} - p_1\sin\alpha\cos\theta_{0r2} \\ p_1\sin\alpha\sin\theta_{0r2} \\ \frac{b_2}{n} + p_1\cos\alpha \end{pmatrix} = \begin{pmatrix} q_1 \\ q_2 \\ p_0 \end{pmatrix}$$
(3.2b)

where the intermediate variable p_1 , given by $p_1 = \sqrt{1 - (1 - m^2)/n^2 - m/n}$, is dependent on $m = A_{r2} \cdot N_{21} = -b_1 \sin \alpha \cos \theta_{0r2} + b_2 \cos \alpha$. The dot product of A_{r3} and N_{22} can be expressed as $A_{r3} \cdot N_{22} = p_0 = b_2/n + p_1 \cos \alpha$.

Thus, the emergent beam vector from prism 2 is written as

$$A_{rf} = n \begin{pmatrix} q_1 \\ q_2 \\ p_0 \end{pmatrix} + \left[\sqrt{1 - n^2 (1 - p_0^2)} - n p_0 \right] \cdot \begin{pmatrix} 0 \\ 0 \\ 1 \end{pmatrix}$$

$$= \begin{pmatrix} n q_1 \\ n q_2 \\ \sqrt{1 - n^2 (1 - p_0^2)} \end{pmatrix} = \begin{pmatrix} x_{0rf} \\ y_{0rf} \\ z_{rf} \end{pmatrix}$$
(3.2c)

Since the emergent beam vector is available in the inverse derivation process, the Z-component of the vector is utilized to determine those intermediate variables in inverted sequence.

Obviously, prism 1 remains stationary and prism 2 rotates with an angle θ_{0r2} in order to achieve the desired pitch angle ρ . According to (3.1) and (3.2), the rotation angle θ_{0r2} is written as

$$\theta_{0r2} = 2k\pi \pm \arccos\left(\frac{b_2\cos\alpha - m}{b_1\sin\alpha}\right) \in [0, 2\pi), (k \in \mathbb{Z})$$
 (3.3)

where the variables are given by $b_1 = \sin \alpha \left(\sqrt{1 - n^2 \sin^2 \alpha} - n \cos \alpha \right)$, $b_2 = n \sin^2 \alpha + \cos \alpha \sqrt{1 - n^2 \sin^2 \alpha}$, $m = (n^2 - 1 - n^2 p_1^2)/2np_1$, $p_1 = (p_0 - b_2/n)/\cos \alpha$ and $p_0 = \sqrt{1 - \left(1 - z_{rf}^2\right)/n^2}$, respectively.

Then the relative rotation angle can be obtained from $\Delta\theta_r = -\theta_{0r2}$, and the *X*- and *Y*-components of the emergent beam vector are $x_{0rf} = nq_1 = b_1 - np_1 \sin \alpha \cos \theta_{0r2}$ and $y_{0rf} = nq_2 = np_1 \sin \alpha \sin \theta_{0r2}$, respectively.

The consequent azimuth angle of the emergent beam is expressed as

$$\varphi_{0} = \begin{cases} \arccos\left(\frac{x_{0rf}}{\sqrt{x_{0rf}^{2} + y_{0rf}^{2}}}\right), & y_{0rf} \ge 0\\ 2\pi - \arccos\left(\frac{x_{0rf}}{\sqrt{x_{0rf}^{2} + y_{0rf}^{2}}}\right), & y_{0rf} < 0 \end{cases}$$
(3.4)

At the second step, the relative rotation angle $\Delta\theta_r$ should be kept constant, and two prisms rotate synchronously with an angle $\varphi - \varphi_0$ in order to achieve the desired azimuth angle φ . Therefore, the rotation angle of prism 1 becomes

$$\theta_{r1} = \theta_{0r1} + \varphi - \varphi_0 = \varphi - \varphi_0 \tag{3.5a}$$

And the rotation angle of prism 2 becomes

$$\theta_{r2} = \theta_{0r2} + \varphi - \varphi_0 = \theta_{r1} - \Delta\theta_r = \varphi - \varphi_0 - \Delta\theta_r \tag{3.5b}$$

(2) Second Set of Inverse Solution

Similarly, prism 2 is kept stationary at the first step, namely $\theta'_{0r2} = 0$. It has been illustrated in Chap. 2 that the pitch angle ρ is an even function with respect to the relative rotation angle $\Delta\theta_r$. Hence, the absolute value of $\Delta\theta_r$ should be unchanged in two sets of inverse solutions, which accounts for $\Delta\theta_r = \theta_{0r2}$ and $\theta'_{0r1} = \theta_{0r2}$. The values are also applied to the derivation in Sect. 2.3.1 in order to simplify the expressions of beam vectors.

The normal vectors to prism surfaces are written as

$$N_{11} = (0, 0, 1)^{\mathrm{T}} \tag{3.6a}$$

$$N_{12} = (\sin \alpha \cos \theta_{0r2}, \sin \alpha \sin \theta_{0r2}, \cos \alpha)^{\mathrm{T}}$$
(3.6b)

$$N_{21} = (-\sin\alpha, 0, \cos\alpha)^{\mathrm{T}} \tag{3.6c}$$

$$N_{22} = (0, 0, 1)^{\mathrm{T}} \tag{3.6d}$$

Since the incident and refracted beam vectors at the incident surface of prism 1 are already known as $A_{r1} = A_{r0} = (0, 0, 1)^{T}$, the dot product of A_{r1} and N_{12} is given by $A_{r1} \cdot N_{12} = \cos \alpha$.

The emergent beam vector from prism 1 is written as

$$A_{r2} = n \begin{pmatrix} 0 \\ 0 \\ 1 \end{pmatrix} + \left\{ \sqrt{1 - n^2 \sin^2 \alpha} - n \cos \alpha \right\} \cdot \begin{pmatrix} \sin \alpha \cos \theta_{0r2} \\ \sin \alpha \sin \theta_{0r2} \\ \cos \alpha \end{pmatrix}$$

$$= \begin{pmatrix} \sin \alpha \cos \theta_{0r2} \left(\sqrt{1 - n^2 \sin^2 \alpha} - n \cos \alpha \right) \\ \sin \alpha \sin \theta_{0r2} \left(\sqrt{1 - n^2 \sin^2 \alpha} - n \cos \alpha \right) \\ n \sin^2 \alpha + \cos \alpha \sqrt{1 - n^2 \sin^2 \alpha} \end{pmatrix} = \begin{pmatrix} b_1 \cos \theta_{0r2} \\ b_1 \sin \theta_{0r2} \\ b_2 \end{pmatrix}$$
(3.7a)

With the dot product of A_{r2} and N_{21} given by $A_{r2} \cdot N_{21} = -b_1 \sin \alpha \cos \theta_{0r2} + b_2 \cos \alpha = m$, the refracted beam vector at the incident surface of prism 2 is expressed as

$$A_{r3} = \frac{1}{n} \cdot \begin{pmatrix} b_{1} \cos \theta_{0r2} \\ b_{1} \sin \theta_{0r2} \\ b_{2} \end{pmatrix} + \left\{ \sqrt{1 - \left(\frac{1}{n}\right)^{2} \left[1 - (A_{r2} \cdot N_{21})^{2}\right]} - \frac{1}{n} (A_{r2} \cdot N_{21}) \right\}$$

$$\cdot \begin{pmatrix} -\sin \alpha \\ 0 \\ \cos \alpha \end{pmatrix} = \frac{1}{n} \cdot \begin{pmatrix} b_{1} \cos \theta_{0r2} \\ b_{1} \sin \theta_{0r2} \\ b_{2} \end{pmatrix} + p_{1} \cdot \begin{pmatrix} -\sin \alpha \\ 0 \\ \cos \alpha \end{pmatrix}$$

$$= \begin{pmatrix} \frac{b_{1} \cos \theta_{0r2}}{n} - p_{1} \sin \alpha \\ \frac{b_{1} \sin \theta_{0r2}}{n} \\ \frac{b_{2}}{n} + p_{1} \cos \alpha \end{pmatrix} = \begin{pmatrix} q_{3} \\ q_{4} \\ p_{0} \end{pmatrix}$$
(3.7b)

With the dot product of A_{r3} and N_{22} given by $A_{r3} \cdot N_{22} = p_0 = b_2/n + p_1 \cos \alpha$, the emergent beam vector from prism 2 is expressed as

$$A_{r3} = n \begin{pmatrix} q_3 \\ q_4 \\ p_0 \end{pmatrix} + \left[\sqrt{1 - n^2 (1 - p_0^2)} - n p_0 \right] \cdot \begin{pmatrix} 0 \\ 0 \\ 1 \end{pmatrix}$$

$$= \begin{pmatrix} n q_3 \\ n q_4 \\ \sqrt{1 - n^2 (1 - p_0^2)} \end{pmatrix} = \begin{pmatrix} x'_{0rf} \\ y'_{0rf} \\ z'_{rf} \end{pmatrix}$$
(3.7c)

Then the relative rotation angle can be obtained from $\Delta\theta_r = \theta_{0r2}$, and the *X*- and *Y*-components of the emergent beam vector are $x'_{0rf} = nq_3 = b_1 \cos\theta_{0r2} - np_1 \sin\alpha$ and $y'_{0rf} = nq_4 = b_1 \sin\theta_{0r2}$, respectively.

The consequent azimuth angle of the emergent beam is given by

$$\varphi_0' = \begin{cases} \arccos\left(\frac{x'_{0rf}}{\sqrt{x'_{0rf}^2 + y'_{0rf}^2}}\right), & y'_{0rf} \ge 0\\ 2\pi - \arccos\left(\frac{x'_{0rf}}{\sqrt{x'_{0rf}^2 + y'_{0rf}^2}}\right), & y'_{0rf} < 0 \end{cases}$$
(3.8)

At the second step, two prisms rotate synchronously with an angle $\varphi - \varphi'_0$ to achieve the desired azimuth angle φ , and the relative rotation angle is held constant at $\Delta\theta_r$. Therefore, the rotation angle of prism 1 becomes

$$\theta'_{r1} = \theta_{0r2} + \varphi - \varphi'_0 \tag{3.9a}$$

And the rotation angle of prism 2 becomes

$$\theta_{r2}' = \varphi - \varphi_0' \tag{3.9b}$$

2. Application of Two-Step Method

When rotating double prisms are employed in target tracking applications, it is necessary to inversely solve the rotation angles of two prisms according to the given target position. The inverse solutions are useful to control the motors driving two prisms so that the beam can be steered precisely as soon as possible.

The inverse derivation process has proven that, in far field, only the emergent beam vector is required to determine the corresponding rotation angles of prisms. By adjusting the rotation angle of each prism, the emergent beam can be steered towards any point within scan region to track the target moving along an arbitrary trajectory.

The following simulation presents the inverse solutions that can be applied to track 6 specific target trajectories in far field. In simulation, the structural parameters of each prism are wedge angle $\alpha = 10^{\circ}$, refractive index n = 1.517, clear aperture $D_p = 80$ mm, thinnest-end thickness $d_0 = 5$ mm, the distance between two prisms

is $D_1 = 100$ mm, and the distance from prism 2 to the receiving screen is $D_2 =$ 400 mm. Note that the beam scan period is set to 10 s, and the target trajectories are observed in the positive Z-direction.

Case 1: a linear target trajectory given by $y = 40, x \in [-10, 10]$.

Case 2: a circular target trajectory given by $x^2 + y^2 = 60^2$.

Case 2: a circular target trajectory given by
$$x^2 + y^2 = 60^\circ$$
.
Case 3: an elliptical target trajectory given by $\frac{x^2}{40^2} + \frac{y^2}{60^2} = 1$.
Case 4: an astroid target trajectory given by
$$\begin{cases} x = 60\cos^3\theta \\ y = 60\sin^3\theta \end{cases}, \quad 0 \le \theta \le 2\pi.$$
Case 5: a spiral target trajectory given by
$$\begin{cases} x = 6t\cos t \\ y = 6t\sin t \end{cases}, \quad 0 \le t \le 10.$$

Case 5: a spiral target trajectory given by
$$\begin{cases} x = 6t \cos t \\ y = 6t \sin t \end{cases}, \quad 0 \le t \le 10.$$

Figures 3.1, 3.2, 3.3, 3.4 and 3.5 display the rotation angle curves of two prisms that correspond to linear, circular, elliptical, astroid and spiral target trajectories, respectively. In each of these figures, (a) shows a target trajectory, while (b) and (c) illustrate the time-dependent variation of two inverse solution sets obtained by two-step method, respectively.

Similarly, Fig. 3.6a shows a rose-like target trajectory, while Fig. 3.6b and c illustrate the time-dependent variation of two inverse solution sets obtained by twostep method. As indicated in Fig. 3.6, there are sudden changes in the rotation angle curves, called singularity problem, once the target moves from the 1st quadrant to the 3rd quadrant or from the 2nd quadrant to the 4th quadrant. To obtain continuous rotation angle curves, the first set of inverse solution should be interchanged with the second one wherever a sudden change occurs. Accordingly, the rotation angle curves are improved as shown in Fig. 3.7.

Case 6: a rose-like target trajectory given by
$$\begin{cases} x = 60\cos 4\theta\cos\theta, \\ y = 60\cos 4\theta\sin\theta \end{cases}, \quad 0 \le \theta \le 2\pi.$$

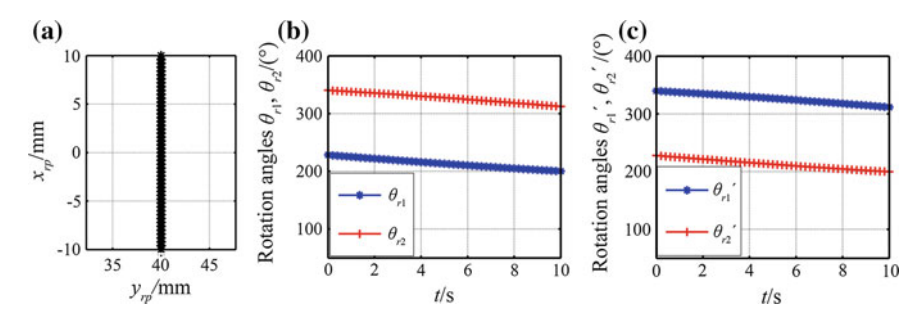


Fig. 3.1 A linear scan case by two-step method, where a shows the linear target trajectory, b is the first set of inverse solution, and c is the second set of inverse solution

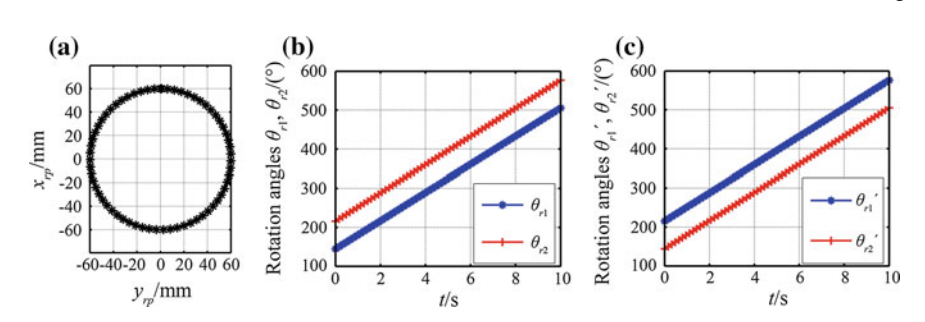


Fig. 3.2 A circular scan case by two-step method, where a shows the circular target trajectory, b is the first set of inverse solution, and c is the second set of inverse solution

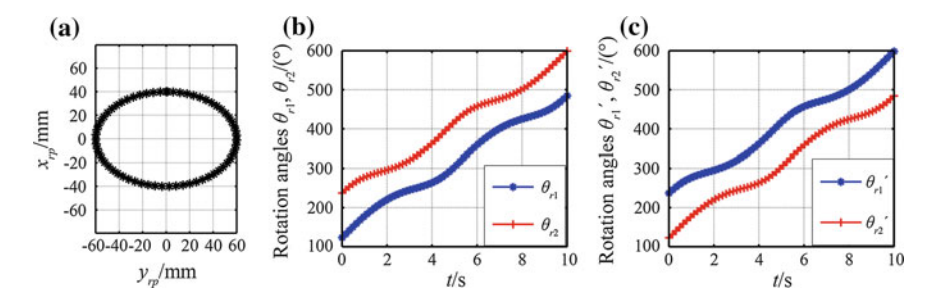


Fig. 3.3 An elliptical scan case by two-step method, where **a** shows the elliptical target trajectory, **b** is the first set of inverse solution, and **c** is the second set of inverse solution

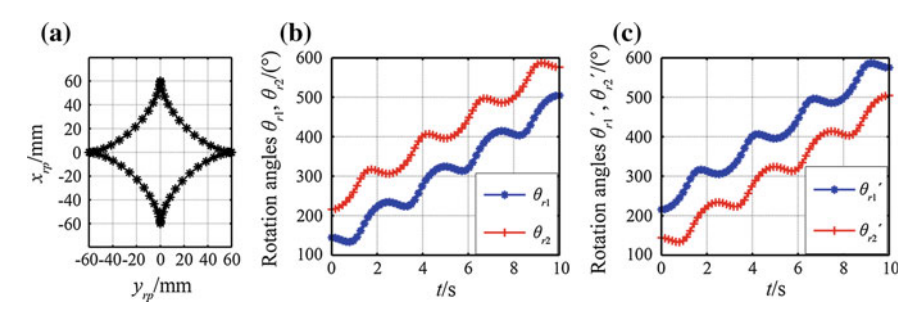


Fig. 3.4 An astroid scan case by two-step method, where $\bf a$ shows the astroid target trajectory, $\bf b$ is the first set of inverse solution, and $\bf c$ is the second set of inverse solution

In conclusion, two-step method has been applied to determine two sets of prism orientations for each of the sample points taken from some target trajectories. This method is well suited for target tracking in far field, without considering the influence of those structural parameters on the emergent beam. However, the method may fail to solve the inverse problem in near field, because the emergent beam vector is much associated with the beam exiting position and cannot be deduced simply from the

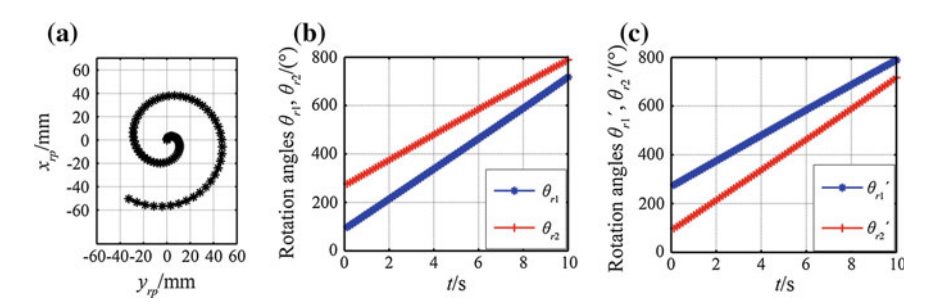


Fig. 3.5 A spiral scan case by two-step method, where a shows the spiral target trajectory, b is the first set of inverse solution, and c is the second set of inverse solution

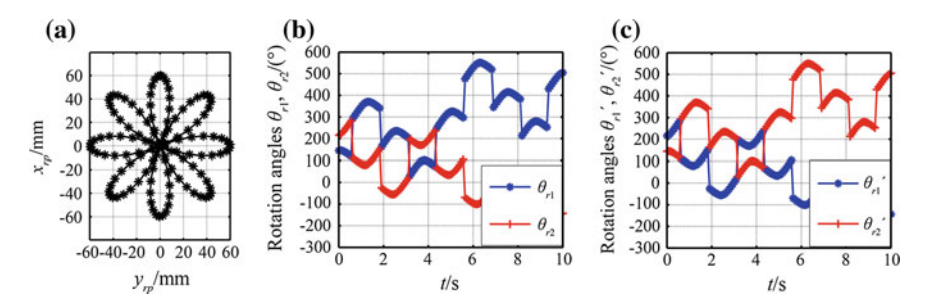


Fig. 3.6 A rose-like scan case by two-step method, where $\bf a$ shows the rose-like target trajectory, $\bf b$ is the first set of inverse solution, and $\bf c$ is the second set of inverse solution

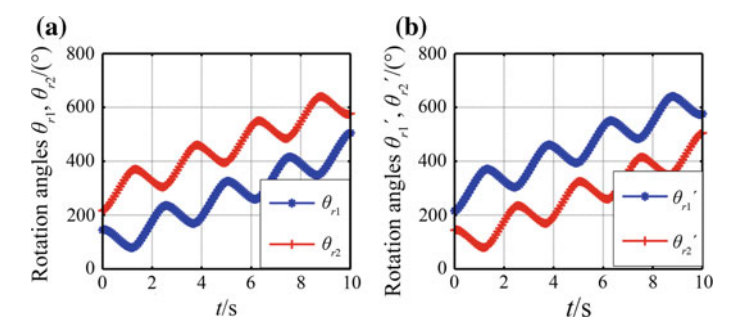


Fig. 3.7 Continuous rotation angle curves obtained by interchanging two sets of inverse solutions, where \mathbf{a} is the first set of rotation angle curves and \mathbf{b} is the second set of rotation angle curves

given target position. Therefore, it is indispensable to find other methods to solve the inverse problem of rotating double prisms employed in near-field applications.

3.1.2 Lookup-Table Method

1. Principle of Lookup-Table Method

The principle of lookup-table method [1, 6] is to establish the mapping relation from the target coordinates to the rotation angles of two prisms by making a lookup table. Generally, the lookup-table method can be summarized as follows.

Firstly, make a lookup table. As mentioned before, the coordinates of a scan point are mainly dependent on the rotation angles θ_{r1} and θ_{r2} , the wedge angle α , the refractive index n, the central-axis thickness d, the distance D_1 between two prisms and D_2 from prism 2 to the screen. Usually, both rotation angles can vary within $0^{\circ}-360^{\circ}$ during one revolution, while other parameters should be selected properly according to the application of rotating double prisms. Every revolution of prism rotation can be further divided into $360^{\circ}/\theta_{tre}$ steps, where θ_{tre} is the rotation step angle decided by beam scan precision. Based on the formulae in Sect. 2.5.1, the coordinates (x_{rp}, y_{rp}, z_{rp}) of the beam scan point on the screen, named the actual point, can be deduced from the rotation angles $(\theta_{r1}, \theta_{r2})$ with a resolution of θ_{tre} . Thus, the numerical values of $(\theta_{r1}, \theta_{r2})$ and (x_{rp}, y_{rp}, z_{rp}) are written to the lookup table in correspondence.

Secondly, search the lookup table. With a target trajectory given by y = f(x), the coordinates (X_{rp}, Y_{rp}, Z_{rp}) of each target point are taken from the trajectory at a certain sampling frequency, where $Z_{rp} = D_1 + D_2$. Then it is necessary to search the lookup table for the actual point closest to each target point, namely to find the coordinates (x_{rp}, y_{rp}, z_{rp}) of the actual point that will minimize the error given by

$$\Delta = \sqrt{(X_{rp} - x_{rp})^2 + (Y_{rp} - y_{rp})^2 + (Z_{rp} - z_{rp})^2}$$
. The coordinates (x_{rp}, y_{rp}, z_{rp}) can be utilized to further determine the related rotation angles $(\theta_{r1}, \theta_{r2})$ in the lookup table, which are approximate to the consequent prism orientations for the target point.

Finally, process data. To establish a continuous function of prism orientations relative to the elapsing time, the function interpolation or curve fitting method is employed to process the discrete rotation angles $(\theta_{r1}, \theta_{r2})$ obtained by lookup-table method.

2. Application of Lookup-Table Method

In simulation, the involved parameters are $\alpha = 10^{\circ}$, n = 1.517, $D_p = 80$ mm, $d_0 = 5$ mm, $D_1 = 100$ mm and $D_2 = 400$ mm. Providing the rotation step angle $\theta_{tre} = 0.1^{\circ}$, the prism rotation can be divided into 3600 steps in one revolution. Additionally, the Z-coordinate of beam scan point is held constant at $Z_{rp} = Z_{rp} = D_1 + D_2 = 500$ mm.

Using the Meshgrid function in Matlab, the rotation angles θ_{r1} and θ_{r2} are combined in random as the element of a 3600×3600 matrix. The values of (x_{rp}, y_{rp}) corresponding to each element of the matrix are deduced from the formulae

in Sect. 2.5.1 and then written to the lookup table. Thus, a completed table contains data with the size of $3600 \times 3600 \times 2 = 2.592 \times 10^7$.

For example, a linear scan case is introduced to demonstrate the application of lookup-table method. There are only 51 sample points shown in simulation results to illustrate the beam scan process. With the target trajectory given by y=40, $x \in [-10, 10]$, the coordinates (X_{rp}, Y_{rp}) of each sample point on the target trajectory can be calculated. Then, the lookup table is searched for the coordinates (x_{rp}, y_{rp}) that will minimize the error given by $\Delta = \sqrt{(X_{rp} - x_{rp})^2 + (Y_{rp} - y_{rp})^2}$, together with the corresponding row number N and column number M in the table. The consequent rotation angles are determined by $\theta_{r1} = \theta_{tre} \times (N-1)$ and $\theta_{r2} = \theta_{tre} \times (M-1)$, which are written in the combined form of $(\theta_{r1}, \theta_{r2})$ to establish a matrix. This matrix comprises a sequence of approximate prism orientations required for the target trajectory. In order to connect those discrete elements of the matrix, the segmented low-order interpolation method is also employed. Therefore, the rotation angle curves of two prisms can be further obtained in approximation.

Given 4 specific target trajectories, the consequent rotation angle curves of two prisms are simulated as follows.

Case 1: a linear target trajectory given by y = 40, $x \in [-10, 10]$.

Clearly, Fig. 3.8a shows a linear target trajectory and Fig. 3.8b illustrates change laws of the rotation angles obtained by lookup-table method. Since this method relies on searching the lookup table for the actual point closest to each target point, the error between these two points is definitely the reason why the prism orientations are approximate. There are 51 sample points taken from the target trajectory. The actual point corresponding to each sample point is listed in Table 3.1, as well as the consequent rotation angles of two prisms. Note that only the first 16 sample points can be found because the complete data is of large size. As the calculation results

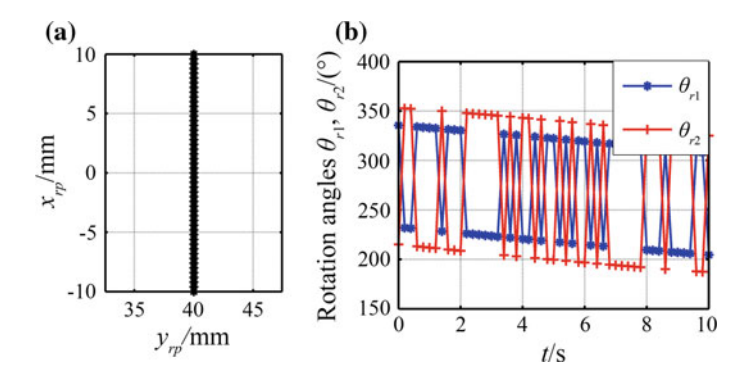


Fig. 3.8 A linear scan case by lookup-table method, where $\bf a$ is the linear target trajectory and $\bf b$ shows the rotation angle curves of two prisms

No.	Target po	oint/mm	Actual poi	nt/mm	Error/mm	Prism orientati	ons/(°)
	X_{rp}	Y_{rp}	x_{rp}	y _{rp}	Δ	θ_{r1}	θ_{r2}
1	-10	40	-10.004	39.984	0.016	335.5	215.0
2	-9.6	40	-9.598	40.021	0.021	232.0	352.6
3	-9.2	40	-9.197	39.989	0.012	231.4	352.2
4	-8.8	40	-8.809	40.013	0.016	334.0	213.1
5	-8.4	40	-8.388	39.978	0.025	333.5	212.4
6	-8	40	-8.004	39.994	0.007	333.0	211.8
7	-7.6	40	-7.621	40.006	0.022	332.5	211.2
8	-7.2	40	-7.234	40.016	0.038	228.5	349.9
9	-6.8	40	-6.785	40.032	0.035	331.4	209.9
10	-6.4	40	-6.403	40.033	0.033	330.9	209.3
11	-6	40	-5.990	39.972	0.030	330.4	208.6
12	-5.6	40	-5.609	40.027	0.029	226.1	347.9
13	-5.2	40	-5.204	40.020	0.020	225.5	347.4
14	-4.8	40	-4.800	40.008	0.008	224.9	346.9
15	-4.4	40	-4.396	39.993	0.008	224.3	346.4
16	-4	40	-3.994	39.973	0.028	223.7	345.9

 Table 3.1 Calculation results in linear scan case by lookup-table method (not complete)

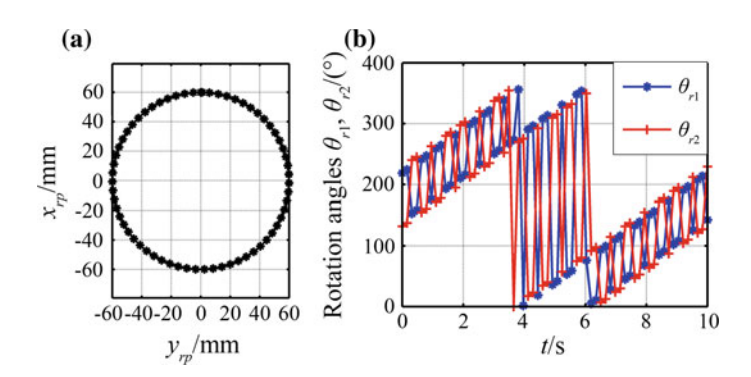


Fig. 3.9 A circular scan case by lookup-table method, where a is the circular target trajectory and b shows the rotation angle curves of two prisms

indicate, the error of the actual point with respect to each target point is within the range of 0.005 mm $\leq \Delta \leq$ 0.038 mm. Besides, it takes 18 s for the whole calculation in a computer configured with Intel(R) Core(TM) i5 CPU and 8 GB memory. If without any special statement, the following calculation tasks are performed under the same computer configuration.

No.	Target po	int/mm	Actual po	oint/mm	Error/mm	Prism orientation	ons/(°)
	X_{rp}	Y _{rp}	x_{rp}	yrp	Δ	θ_{r1}	θ_{r2}
1	60.000	0.000	60.015	0.021	0.025	218.5	131.8
2	59.700	5.990	59.716	5.981	0.018	224.2	137.5
3	58.804	11.920	58.814	11.945	0.027	153.0	239.7
4	57.320	17.731	57.337	17.727	0.017	158.7	245.4
5	55.264	23.365	55.277	23.372	0.015	241.4	154.7
6	52.655	28.766	52.682	28.747	0.033	247.1	160.4
7	49.520	33.879	49.531	33.889	0.015	175.9	262.6
8	45.891	38.653	45.893	38.673	0.020	258.6	171.9
9	41.802	43.041	41.825	43.040	0.023	264.3	177.6
10	37.297	47.000	37.294	47.020	0.021	193.1	279.8
11	32.418	50.488	32.440	50.492	0.022	198.8	285.5
12	27.216	53.472	27.228	53.483	0.016	281.5	194.8
13	21.741	55.922	21.722	55.946	0.030	210.3	297.0
14	16.050	57.813	16.058	57.827	0.015	216.0	302.7
15	10.198	59.127	10.195	59.143	0.016	298.7	212.0
16	4.244	59.850	4.270	59.863	0.029	304.4	217.7

 Table 3.2 Calculation results in circular scan case by lookup-table method (not complete)

Case 2: a circular target trajectory given by $x^2 + y^2 = 60^2$.

Figure 3.9a shows a circular target trajectory and Fig. 3.9b illustrates change laws of the rotation angles obtained by lookup-table method. There are 64 sample points in the circular scan case, among which the first 16 sample points are listed in Table 3.2 together with the related calculation results. It turns out that the error between each pair of actual point and target point is within the range of 0.015 mm $\leq \Delta \leq 0.034$ mm, and the whole calculation takes 23 s.

Case 3: an elliptical target trajectory given by $\frac{x^2}{40^2} + \frac{y^2}{60^2} = 1$.

Figure 3.10a shows an elliptical target trajectory and Fig. 3.10b illustrates change laws of the rotation angles obtained by lookup-table method. Also, 64 sample points are extracted from the target trajectory. The first 16 sample points and the related calculation results are listed in Table 3.3. It can be found that the error between each pair of actual point and target point is limited by 0.004 mm $\leq \Delta \leq$ 0.045 mm, and the whole calculation takes 25 s.

Case 4: an astroid target trajectory given by
$$\begin{cases} x = 60\cos^3\theta \\ y = 60\sin^3\theta \end{cases}, \quad 0 \le \theta \le 2\pi.$$

Similarly, Fig. 3.11a shows an astroid target trajectory and Fig. 3.11b illustrates change laws of the rotation angles obtained by lookup-table method. The first 16 of 64 sample points on the target trajectory are listed in Table 3.4, together with the

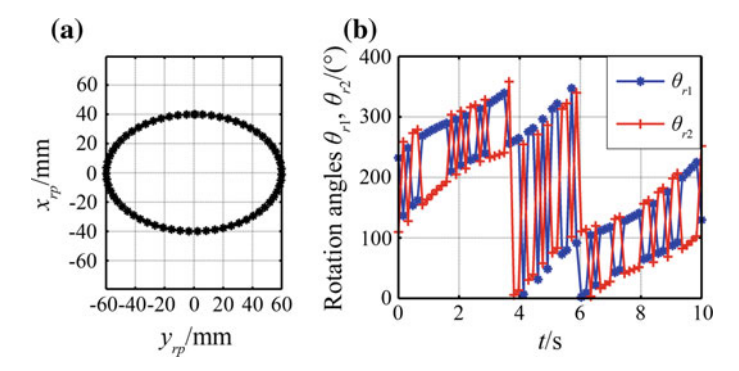


Fig. 3.10 An elliptical scan case by lookup-table method, where a is the elliptical target trajectory and b shows the rotation angle curves of two prisms

Table 3.3 Calculation results of the elliptical scan case by lookup-table method (not complete	hod (not complete)
---	--------------------

No.	Target po	int/mm	Actual po	oint/mm	Error/mm	Prism orientati	ons/(°)
	X_{rp}	Y _{rp}	x_{rp}	y _{rp}	Δ	θ_{r1}	θ_{r2}
1	40.000	0.000	39.987	-0.001	0.013	232.1	109.6
2	39.800	5.990	39.784	5.998	0.018	136.6	258.7
3	39.203	11.920	39.199	11.921	0.004	248.5	127.6
4	38.213	17.731	38.230	17.708	0.028	153.9	272.9
5	36.842	23.365	36.850	23.384	0.021	162.3	278.8
6	35.103	28.766	35.099	28.755	0.011	268.4	154.8
7	33.013	33.879	33.025	33.878	0.011	273.6	163.3
8	30.594	38.653	30.609	38.681	0.032	278.2	171.4
9	27.868	43.041	27.871	43.068	0.027	282.3	179.0
10	24.864	47.000	24.858	47.006	0.009	286.0	186.1
11	21.612	50.488	21.619	50.461	0.028	289.4	192.7
12	18.144	53.472	18.131	53.487	0.019	209.9	303.6
13	14.494	55.922	14.511	55.912	0.020	295.8	204.6
14	10.700	57.813	10.689	57.795	0.022	220.0	309.2
15	6.799	59.127	6.839	59.128	0.040	302.3	214.6
16	2.829	59.850	2.860	59.848	0.031	228.7	315.6

related calculation results. It is found that the error between each pair of actual point and target point is limited by 0.004 mm $\leq \Delta \leq$ 0.040 mm, and the whole calculation takes 28 s.

3. Improvement on Lookup-Table Method

The above four cases indicate that there are sudden changes in the prism orientations obtained by lookup-table method. In other words, there may be much difference in the rotation angles of each prism that correspond to the adjacent sample points on

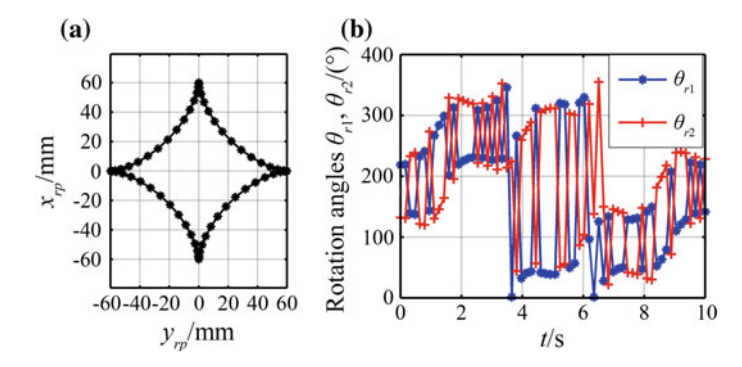


Fig. 3.11 An astroid scan case by lookup-table method, where **a** is the astroid target trajectory and **b** shows the rotation angle curves of two prisms

Table 3.4 Calculation results of the astroid scan case by lookup-	o-table method (not complete	e)
--	------------------------------	----

No.	Target po	int/mm	Actual po	oint/mm	Error/mm	Prism orientation	ons/(°)
	X_{rp}	Y_{rp}	x_{rp}	yrp	Δ	θ_{r1}	θ_{r2}
1	60.000	0.000	60.015	0.021	0.025	218.5	131.8
2	59.105	0.060	59.125	0.071	0.023	219.3	130.8
3	56.483	0.470	56.474	0.468	0.009	139.1	232.8
4	52.314	1.549	52.330	1.520	0.032	137.2	238.6
5	46.883	3.543	46.885	3.563	0.020	232.4	121.6
6	40.552	6.612	40.556	6.628	0.016	240.8	120.1
7	33.732	10.801	33.727	10.801	0.005	143.5	273.3
8	26.845	16.042	26.817	16.047	0.029	266.7	130.4
9	20.291	22.149	20.270	22.146	0.021	283.7	145.5
10	14.411	28.839	14.419	28.812	0.028	298.9	164.1
11	9.464	35.749	9.475	35.760	0.015	201.6	328.9
12	5.600	42.471	5.629	42.489	0.034	313.0	195.2
13	2.855	48.580	2.876	48.555	0.032	219.6	327.6
14	1.148	53.677	1.150	53.704	0.028	225.3	324.2
15	0.295	57.419	0.263	57.405	0.034	229.1	321.0
16	0.021	59.550	0.046	59.572	0.032	231.1	318.7

the target trajectory. Sometimes, such sudden changes may occur repeatedly during beam scanning. In practice, this phenomenon can increase the response time of rotating double prisms, which limits the feasibility of some real-time target tracking applications. The reason for the phenomenon is that the inverse solution for a rotating double-prism system is not unique. For an arbitrary target point, two sets of prism orientations can be found during one revolution.

For example, the lookup-table method is applied to track the target point (50, 40). The error of each actual point in the lookup table with respect to the target point can

0.1

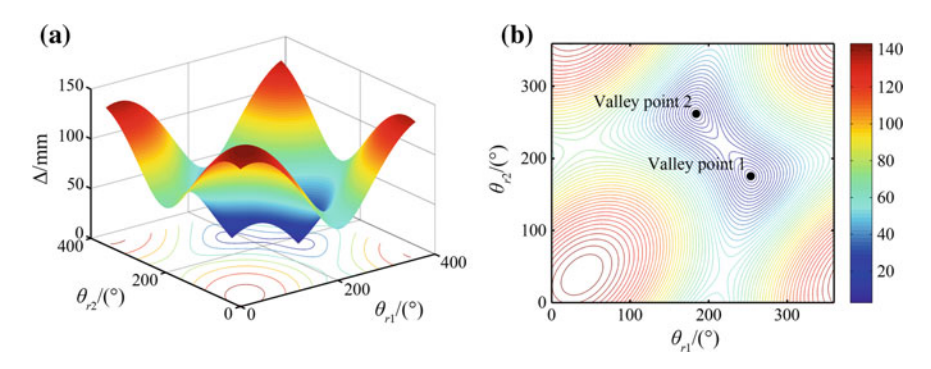


Fig. 3.12 Distribution of the error between actual point and target point, where a display the three-dimensional distribution and b is a contour plot

Table 3.5 Life	1 \(\Delta\) of the target	point (50, 40)			
Step angle/(°)	Size of lookup table	Rotation angles $(\theta_{r1}, \theta_{r2})$ at valley point $1/(^{\circ})$	Valley value 1/mm	Rotation angles $(\theta_{r1}, \theta_{r2})$ at valley point $2/(^{\circ})$	Valley value 2/mm
1	360 × 360	(254, 175)	0.395	(184, 262)	0.174
0.5	720 × 720	(253.5, 175.5)	0.093	(184, 262)	0.174

0.035

(183.8, 262.0)

0.028

(235.5, 175.8)

Table 3.5 Error Δ of the target point (50, 40)

 3600×3600

be calculated from $\Delta = \sqrt{\left(X_{rp} - x_{rp}\right)^2 + \left(Y_{rp} - y_{rp}\right)^2}$, and the relation of the error Δ and the rotation angles $(\theta_{r1}, \theta_{r2})$ is plotted in Fig. 3.12. There are two valley points shown in Fig. 3.12, which validate that the same target point corresponds to two sets of prism orientations $(\theta_{r1}, \theta_{r2})$ during one revolution. Thus, the rotation angles obtained by lookup-table method are prone to switch between two sets of possible solutions in practical applications.

(1) Determinant Conditions

As shown in Table 3.5, the valley values of the error Δ and the consequent rotation angles of two prisms are dependent on the step angle used for searching the lookup table.

It is evident that the minimum error occurs at the valley point 2 when the step angle is set to 1° or 0.1° , but at the valley point 1 when the step angle becomes 0.5° . In other words, the step angle has effects on the error between each pair of actual point and target point as well as the position at which the minimum error is found.

To illustrate the situation where the target position is changed with slight translation, the target point (50, 41) is taken for example. The consequent rotation angles obtained in different lookup tables are listed in Table 3.6, along with the error Δ between the actual and target points.

There is only 1 mm translation in the positive Y-direction from the point (50, 40) to the target point (50, 41). Comparing Table 3.6 with Table 3.5, it is found that both

Step angle/(°)	Size of lookup	Rotation	Valley value	Rotation	Valley value
	table	angles (θ_{r1} , θ_{r2}) at valley point $1/(^{\circ})$	1/mm	angles (θ_{r1} , θ_{r2}) at valley point 2/(°)	2/mm
1	360 × 360	(254, 177)	0.330	(185, 262)	0.103
0.5	720×720	(253.5, 177)	0.121	(185, 262)	0.103
0.1	3600×3600	(253.8, 177.7)	0.022	(184.9, 261)	0.019

Table 3.6 Error Δ of the target point (50, 41)

the minimum error of (50, 40) and that of (50, 41) occur at the valley point 2 when the step angle is set to 1° or 0.1°. When the step angle becomes 0.5°, the minimum error of (50, 40) is found at the valley point 1 where the prism orientations (θ_{r1} , θ_{r2}) = (253.5°, 175.5°), but the minimum error of (50, 41) is still at the valley point 2 where (θ_{r1} , θ_{r2}) = (185°, 262°). Since there are two valley points, the slight translation of target point may result in significant changes in the prism orientations, which can cause the loss of target in real-time target tracking applications.

On the above basis, it is concluded that the rotation angle curves obtained by lookup-table method will not be continuous enough if the determinant condition is only to minimize the error given by $\Delta = \sqrt{(X_{rp} - x_{rp})^2 + (Y_{rp} - y_{rp})^2}$. To overcome such a problem, two sets of valley points are compared for the one with better continuity, namely the improved inverse solution.

(2) Constraint Conditions

In correspondence to each sample point on the target trajectory, two combinations of prism orientations can be determined once the valley points of the error Δ are found by linear search method. The optimal combination of rotation angles for the current target point is taken as the one that has less difference from the rotation angles for the previous target point. That is, the rotation angle of each prism cannot switch in random between the values corresponding to two valley points of the error Δ . Hence, the lookup-table method will lead to two possible sets of inverse solutions for any given target trajectory, as shown in Figs. 3.13, 3.14, 3.15 and 3.16.

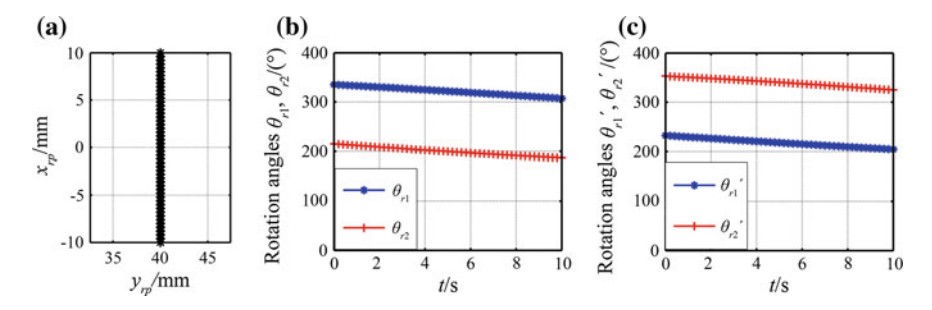


Fig. 3.13 A linear scan case by lookup-table method, where \mathbf{a} shows the linear target trajectory, \mathbf{b} is the first set of inverse solution, and \mathbf{c} is the second set of inverse solution

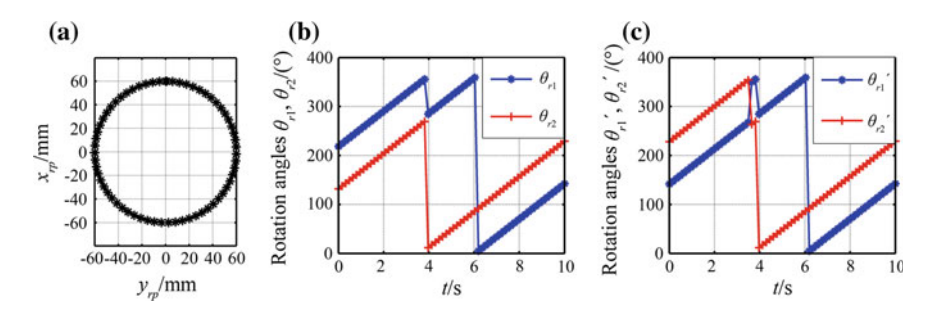


Fig. 3.14 A circular scan case by lookup-table method, where a shows the circular target trajectory, b is the first set of inverse solution, and c is the second set of inverse solution

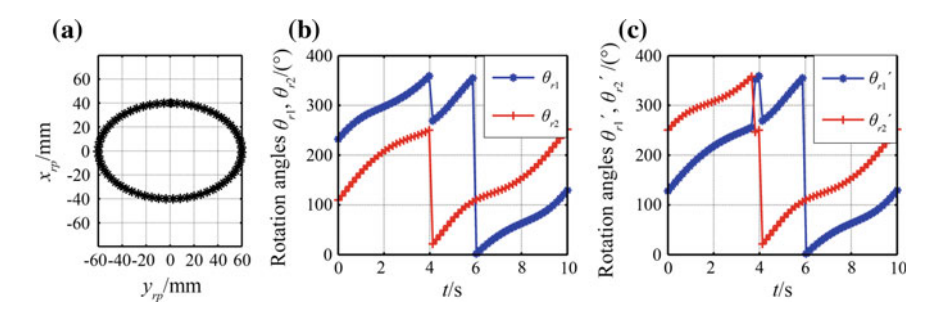


Fig. 3.15 An elliptical scan case by lookup-table method, where a shows the elliptical target trajectory, b is the first set of inverse solution, and c is the second set of inverse solution

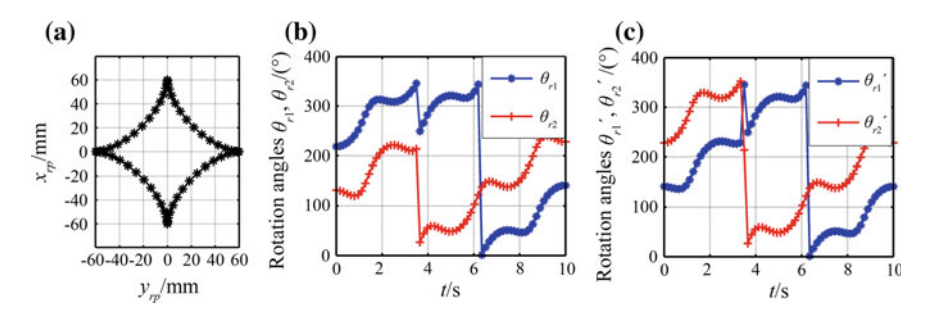


Fig. 3.16 An astroid scan case by lookup-table method, where **a** shows the astroid target trajectory, **b** is the first set of inverse solution, and **c** is the second set of inverse solution

Case 1: a linear target trajectory given by y = 40, $x \in [-10, 10]$.

Clearly, Fig. 3.13a shows a linear target trajectory, while Fig. 3.13b and c manifest two sets of inverse solutions obtained by lookup-table method, respectively. The first 16 of 51 sample points on the target trajectory are listed in Table 3.7, together with the related calculation results. It can be found that the error between each pair of actual point and target point is limited by $0.004 \text{ mm} \le \Delta \le 0.041 \text{ mm}$ in the first set of inverse solution and $0.004 \text{ mm} \le \Delta' \le 0.041 \text{ mm}$ in the second one. The whole calculation takes 222 and 219 s for these two sets of inverse solutions, respectively.

Case 2: a circular target trajectory given by $x^2 + y^2 = 60^2$.

Figure 3.14a shows a linear target trajectory, while Fig. 3.14b and c manifest two sets of inverse solutions obtained by lookup-table method, respectively. The first 16 of 64 sample points on the target trajectory are listed in Table 3.8, together with the related calculation results. It is found that the error between each pair of actual point and target point is limited by 0.0015 mm $\leq \Delta \leq 0.040$ mm in the first set of inverse solution and 0.0015 mm $\leq \Delta' \leq 0.040$ mm in the second one. The whole calculation takes 215 and 216 s for these two sets of inverse solutions, respectively.

Case 3: an elliptical target trajectory given by $\frac{x^2}{40^2} + \frac{y^2}{60^2} = 1$.

Figure 3.15a shows an elliptical target trajectory, while Fig. 3.15b and c manifest two sets of inverse solutions obtained by lookup-table method, respectively. The first 16 of 64 sample points on the target trajectory are listed in Table 3.9, together with the related calculation results. It is found that the error between each pair of actual point and target point is limited by 0.004 mm $\leq \Delta \leq 0.046$ mm in the first set of inverse solution and 0.007 mm $\leq \Delta' \leq 0.046$ mm in the second one. The whole calculation takes 215 s for each set of inverse solution.

Case 4: an astroid target trajectory given by
$$\begin{cases} x = 60\cos^3\theta \\ y = 60\sin^3\theta \end{cases}, \quad 0 \le \theta \le 2\pi.$$

Figure 3.16a shows an astroid target trajectory, while Fig. 3.16b and c manifest two sets of inverse solutions obtained by lookup-table method, respectively. The first 16 of 64 sample points on the target trajectory are listed in Table 3.10, together with the related calculation results. It is found that the error between each pair of actual point and target point is limited by 0.006 mm $\leq \Delta \leq 0.046$ mm in the first set of inverse solution and 0.005 mm $\leq \Delta' \leq 0.046$ mm in the second one. The whole calculation takes 216 and 217 s for these two sets of inverse solutions, respectively.

The last three cases indicate that there are still sudden changes as one of the prism orientations approaches 0° or 360° . Considering the 360° rotation cycle of each prism, the following constraint conditions are placed in the improved lookup-table method.

If
$$\theta_{r1}(i) - \theta_{r1}(i-1) > 180^{\circ}$$
, then $\theta_{r1}(i) = \theta_{r1}(i) - 360^{\circ}$.
If $\theta_{r1}(i) - \theta_{r1}(i-1) < -180^{\circ}$, then $\theta_{r1}(i) = \theta_{r1}(i) + 360^{\circ}$.

(not complete)
sup-table method
by lool
scan case b
in linear
ulation results
Calculati
Table 3.7

No.	Target point	ıt	The first se	The first set of inverse solution	solution			The secon	d set of inve	The second set of inverse solution		
	X_{rp}/mm	Y_{rp} /mm	x _{rp} /mm	y _{rp} /mm	Δ/mm	$\theta_{r1}/(^{\circ})$	$\theta_{r2}/(^{\circ})$	x'_{rp} /mm	y'rp/mm	\\\\\\\\\\\\\\\\\\\\\\\\\\\\\\\\\\\\\\	$ \theta'_{r1}/(^{\circ}) $	$\theta'_{r2}/(^{\circ})$
1	-10.000	40.000	-10.004	39.984	0.016	335.5	215.0	-10.008	39.983	0.019	232.6	353.1
2	-9.600	40.000	-9.617	40.016	0.023	335.0	214.4	-9.598	40.021	0.021	232.0	352.6
3	-9.200	40.000	-9.194	39.989	0.012	334.5	213.7	-9.197	39.989	0.012	231.4	352.2
4	-8.800	40.000	-8.809	40.013	0.016	334.0	213.1	-8.787	40.018	0.022	230.8	351.7
5	-8.400	40.000	-8.388	39.978	0.025	333.5	212.4	-8.388	39.978	0.025	230.2	351.3
9	-8.000	40.000	-8.004	39.994	0.007	333.0	211.8	-7.980	39.999	0.020	229.6	350.8
7	-7.600	40.000	-7.621	40.006	0.022	332.5	211.2	-7.572	40.016	0.032	229.0	350.3
8	-7.200	40.000	-7.238	40.015	0.041	332.0	210.6	-7.234	40.016	0.038	228.5	349.9
6	-6.800	40.000	-6.785	40.032	0.035	331.4	209.9	-6.827	40.025	0.037	227.9	349.4
10	-6.400	40.000	-6.403	40.033	0.033	330.9	209.3	-6.421	40.030	0.036	227.3	348.9
11	-6.000	40.000	-5.990	39.972	0.030	330.4	208.6	-6.014	40.031	0.034	226.7	348.4
12	-5.600	40.000	-5.610	39.965	0.037	329.9	208.0	-5.609	40.027	0.029	226.1	347.9
13	-5.200	40.000	-5.191	40.021	0.023	329.3	207.4	-5.204	40.020	0.020	225.5	347.4
14	-4.800	40.000	-4.812	40.007	0.014	328.8	206.8	-4.800	40.008	0.008	224.9	346.9
15	-4.400	40.000	-4.434	39.988	0.036	328.3	206.2	-4.396	39.993	0.008	224.3	346.4
16	-4.000	40.000	-3.986	39.974	0.030	327.7	205.5	0.046	59.572	0.032	231.1	318.7

Table 3.8 Calculation results in circular scan case by lookup-table method (not complete)

No.	Target point	nt	The first so	The first set of inverse solution	solution			The secon	The second set of inverse solution	rse solution		
	X_{rp}/mm	Y_{rp} /mm	x _{rp} /mm	y _{rp} /mm	Δ/mm	$\theta_{r1}/(^{\circ})$	$\theta_{r2}/(^{\circ})$	x'_{rp} /mm	y' _{rp} /mm	Δ'/mm	$ \theta'_{r1} ^{(\circ)}$	$\theta_{r2}'(^{\circ})$
	000.09	0.000	60.015	0.021	0.025	218.5	131.8	60.015	-0.021	0.025	141.5	228.2
2	59.700	5.990	59.716	5.981	0.018	224.2	137.5	29.667	5.979	0.035	147.2	234.0
8	58.804	11.920	58.767	11.933	0.039	230.0	143.2	58.814	11.945	0.027	153.0	239.7
	57.320	17.731	57.325	17.767	0.036	235.7	149.0	57.337	17.727	0.017	158.7	245.4
100	55.264	23.365	55.277	23.372	0.015	241.4	154.7	55.231	23.355	0.034	164.4	251.2
2	52.655	28.766	52.682	28.747	0.033	247.1	160.4	52.652	28.802	0.037	170.2	256.9
7	49.520	33.879	49.492	33.860	0.034	252.9	166.1	49.531	33.889	0.015	175.9	262.6
8	45.891	38.653	45.893	38.673	0.020	258.6	171.9	45.920	38.641	0.032	181.6	268.3
	41.802	43.041	41.825	43.040	0.023	264.3	177.6	41.789	43.006	0.037	187.3	274.1
01	37.297	47.000	37.266	46.980	0.036	270.1	183.3	37.294	47.020	0.021	193.1	279.8
	32.418	50.488	32.405	50.514	0.029	275.8	189.1	32.440	50.492	0.022	198.8	285.5
12	27.216	53.472	27.228	53.483	0.016	281.5	194.8	27.203	53.440	0.034	204.5	291.3
13	21.741	55.922	21.781	55.923	0.040	287.2	200.5	21.722	55.946	0.030	210.3	297.0
14	16.050	57.813	16.047	57.779	0.035	293.0	206.2	16.058	57.827	0.015	216.0	302.7
15	10.198	59.127	10.195	59.143	0.016	298.7	212.0	10.184	59.095	0.035	221.7	308.5
16	4.244	59.850	4.270	59.863	0.029	304.4	217.7	4.264	59.814	0.041	227.4	314.2

(not complete)
p
meth
je
aþ
lookup-t
by l
scan case
aJ
Ë
ellipt
ts in el
results
ation
Ξ
글
Ű
Table 3.9
ė.
=
\mathbf{z}
-

No.	Target point	nt	The first sa	The first set of inverse solution	solution			The secon	The second set of inverse solution	erse solution		
Y_{rp}	X_{rp}/mm	Y_{rp} /mm	x _{rp} /mm	y _{rp} /mm	Δ/mm	$\theta_{r1}/(^{\circ})$	$\theta_{r2}/(^{\circ})$	x'_{rp} /mm	y' _{rp} /mm	Δ'/mm	$\theta'_{r1}/(^{\circ})$	$\left \theta_{r2}'/(^{\circ}) \right $
	40.000	0.000	39.987	-0.001	0.013	232.1	109.6	39.987	0.001	0.013	127.9	250.4
2	39.800	5.990	39.789	5.965	0.027	240.5	118.4	39.784	5.998	0.018	136.6	258.7
	39.203	11.920	39.199	11.921	0.004	248.5	127.6	39.205	11.900	0.020	145.3	266.2
	38.213	17.731	38.232	17.703	0.034	255.8	136.8	38.230	17.708	0.028	153.9	272.9
	36.842	23.365	36.849	23.387	0.022	262.5	146.0	36.850	23.384	0.021	162.3	278.8
,,	35.103	28.766	35.099	28.755	0.011	268.4	154.8	35.076	28.784	0.033	170.3	283.9
7	33.013	33.879	33.025	33.878	0.011	273.6	163.3	33.002	33.900	0.025	177.9	288.2
8	30.594	38.653	30.609	38.681	0.032	278.2	171.4	30.602	38.687	0.035	185.1	291.9
	27.868	43.041	27.871	43.068	0.027	282.3	179.0	27.859	43.076	0.036	191.9	295.2
10	24.864	47.000	24.858	47.006	0.009	286.0	186.1	24.905	46.981	0.045	198.2	298.1
	21.612	50.488	21.619	50.461	0.028	289.4	192.7	21.602	50.526	0.039	204.3	300.9
12	18.144	53.472	18.176	53.471	0.033	292.6	198.9	18.131	53.487	0.019	209.9	303.6
[3	14.494	55.922	14.511	55.912	0.020	295.8	204.6	14.513	55.911	0.022	215.1	306.3
14	10.700	57.813	10.700	57.844	0.030	299.0	209.9	10.689	57.795	0.022	220.0	309.2
15	6.799	59.127	6:836	59.128	0.040	302.3	214.6	6.795	59.083	0.044	224.5	312.3
16	2.829	59.850	2.785	59.852	0.045	305.9	219.0	2.860	59.848	0.031	228.7	315.6

Table 3.10 Calculation results in astroid scan case by lookup-table method (not complete)

No.	Target point	nt	The first se	The first set of inverse solution	solution			The secon	The second set of inverse solution	rse solution		
	X_{rp}/mm	Y _{rp} /mm	x _{rp} /mm	y _{rp} /mm	Δ/mm	$\theta_{r1}/(^{\circ})$	$\theta_{r2}/(^{\circ})$	x'_{rp} /mm	y'rp/mm	\delta/mm	$\theta'_{r1}/(^{\circ})$	$\theta'_{r2}/(^{\circ})$
	000.09	0.000	60.015	0.021	0.025	218.5	131.8	60.015	-0.021	0.025	141.5	228.2
	59.105	090.0	59.125	0.071	0.023	219.3	130.8	59.075	0.075	0.034	140.8	229.4
	56.483	0.470	56.526	0.460	0.044	221.8	128.2	56.474	0.468	0.009	139.1	232.8
	52.314	1.549	52.328	1.586	0.040	226.2	124.8	52.330	1.520	0.032	137.2	238.6
	46.883	3.543	46.885	3.563	0.020	232.4	121.6	46.884	3.570	0.027	136.3	247.1
	40.552	6.612	40.556	6.628	0.016	240.8	120.1	40.563	6.584	0.030	137.7	258.4
	33.732	10.801	33.730	10.792	0.009	252.0	122.2	33.727	10.801	0.005	143.5	273.3
	26.845	16.042	26.817	16.047	0.029	266.7	130.4	26.815	16.051	0.032	155.1	291.4
	20.291	22.149	20.270	22.146	0.021	283.7	145.5	20.295	22.123	0.027	171.3	309.5
0	14.411	28.839	14.419	28.812	0.028	298.9	164.1	14.383	28.830	0.030	188.0	322.8
_	9.464	35.749	9.488	35.757	0.025	308.7	181.4	9.475	35.760	0.015	201.6	328.9
2	5.600	42.471	5.629	42.489	0.034	313.0	195.2	5.634	42.488	0.039	211.9	329.7
3	2.855	48.580	2.865	48.613	0.035	313.6	205.7	2.876	48.555	0.032	219.6	327.6
41	1.148	53.677	1.136	53.650	0.029	312.3	213.3	1.150	53.704	0.028	225.3	324.2
15	0.295	57.419	0.297	57.456	0.038	310.3	218.5	0.263	57.405	0.034	229.1	321.0
91	0.021	59.550	-0.002	59.522	0.037	308.9	221.2	0.046	59.572	0.032	231.1	318.7

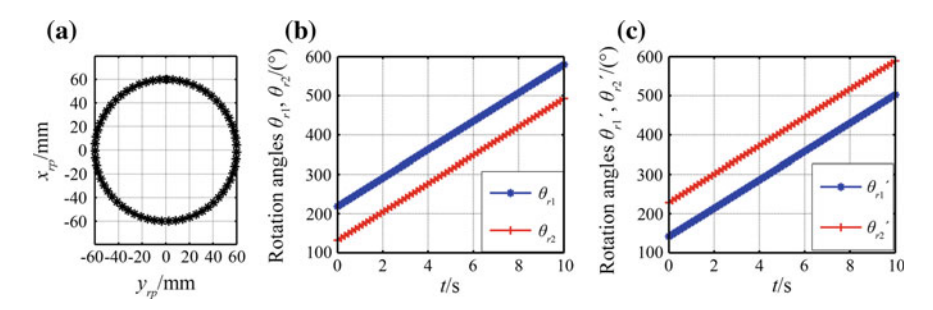


Fig. 3.17 A circular scan case by the improved lookup-table method, where a shows the circular target trajectory, b is the first set of inverse solution, and c is the second set of inverse solution

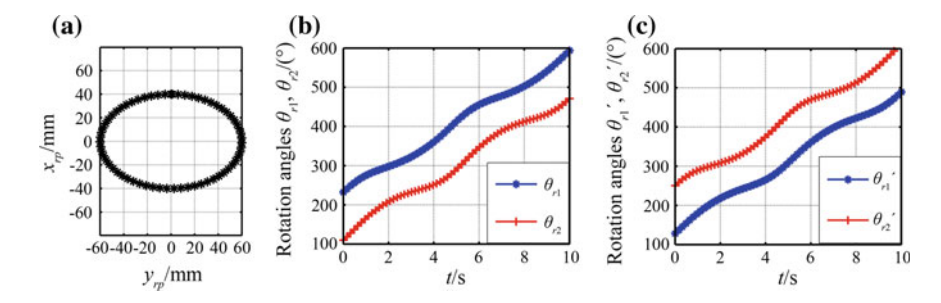


Fig. 3.18 An elliptical scan case by the improved lookup-table method, where \mathbf{a} shows the elliptical target trajectory, \mathbf{b} is the first set of inverse solution, and \mathbf{c} is the second set of inverse solution

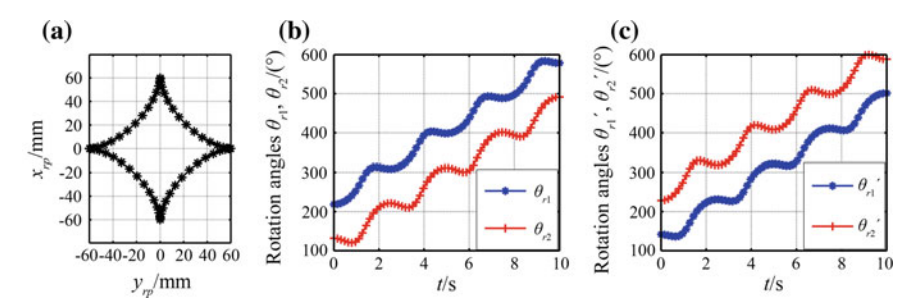


Fig. 3.19 An astroid scan case by the improved lookup-table method, where a shows the astroid target trajectory, b is the first set of inverse solution, and c is the second set of inverse solution

Thus, the rotation angle range of each prism is extended to $-\infty$ to $+\infty$, which can eliminate the phenomenon of sudden changes within 0° –360°. Based on the improved lookup-table method, the circular, elliptical and astroid scan cases are performed as shown in Figs. 3.17, 3.18 and 3.19.

Case 1: a circular target trajectory given by $x^2 + y^2 = 60^2$.

Figure 3.17a shows a circular target trajectory, while Fig. 3.17b and c manifest two sets of inverse solutions obtained by the improved lookup-table method, respectively. The first 16 of 64 sample points on the target trajectory are listed in Table 3.11, together with the related calculation results. It is found that the error between each pair of actual point and target point is limited by 0.015 mm $\leq \Delta \leq 0.041$ mm in the first set of inverse solution and 0.015 mm $\leq \Delta' \leq 0.041$ mm in the second one. The whole calculation takes 216 and 217 s for these two sets of inverse solutions, respectively.

Case 2: an elliptical target trajectory given by $\frac{x^2}{40^2} + \frac{y^2}{60^2} = 1$.

Figure 3.18a shows a circular target trajectory, while Fig. 3.18b and c manifest two sets of inverse solutions obtained by the improved lookup-table method, respectively. The first 16 of 64 sample points on the target trajectory are listed in Table 3.12, together with the related calculation results. It is found that the error between each pair of actual point and target point is limited by 0.004 mm $\leq \Delta \leq 0.046$ mm in the first set of inverse solution and 0.006 mm $\leq \Delta' \leq 0.046$ mm in the second one. The whole calculation takes 238 and 235 s for these two sets of inverse solutions, respectively.

Case 3: an astroid target trajectory given by
$$\begin{cases} x = 60\cos^3\theta \\ y = 60\sin^3\theta \end{cases}, \quad 0 \le \theta \le 2\pi.$$

Figure 3.19a shows a circular target trajectory, while Fig. 3.19b and c manifest two sets of inverse solutions obtained by the improved lookup-table method, respectively. The first 16 of 64 sample points on the target trajectory are listed in Table 3.13, together with the related calculation results. It is found that the error between each pair of actual point and target point is limited by 0.004 mm $\leq \Delta \leq 0.045$ mm in the first set of inverse solution and 0.005 mm $\leq \Delta' \leq 0.046$ mm in the second one. The whole calculation takes 230 and 247 s for these two sets of inverse solutions, respectively.

Despite that the solving accuracy is reduced slightly by the improved lookuptable method, the rotation angle curves prove to be much more continuous, which can facilitate the motion control of two prisms.

By adding some constraint conditions, two sets of continuous inverse solutions are obtained to remove the problem of losing target due to the sudden changes in prism orientations. Nevertheless, the solving accuracy of lookup-table method depends on the size of lookup table. For example, the accuracy of prism orientations can achieve up to 0.1° when the step angle is set to 0.1° , and the consequent target tracking precision is about 0.01 mm. Given an arbitrary target point, the lookup-table method involves searching a 3600×3600 matrix linearly for two valley points, which requires intensive computation. The above cases indicate that it takes about 4 s on average to obtain one set of inverse solution to each target point, which is rather time-consuming for tracking dynamic targets. Therefore, the solving accuracy

_
©
et
협
豆
5
$\ddot{\circ}$
ĭ
2
_
ō
2
Ħ
8
Ξ
<u>e</u>
P
ta
6
'n
Ā
8
\simeq
р
ē
5
Ĕ
\pm
the imp
(D
ĕ
_
Ş
<u></u>
S
cas
\tilde{z}
a
õ
5,
ਫ
Ξ
Ö
-Ξ
2
.⊟
S
Ħ
Su
ě
ī
1
Ξ
а
⊐
2
ď
\circ
7
3
le
<u>_</u>
ľa

No Target point The first set of inverse solution	Target noi	l l	The first of	The first set of inverse solution	colution			The secon	The second set of inverse solution	ree colution		
	raiget point	111	THE HIST S	of of Hivelse	Solution			1110 200011	a set of illive	rise solution		
	X_{rp}/mm	V_{rp} /mm	x _{rp} /mm	y _{rp} /mm	Δ/mm	$\theta_{r1}/(^{\circ})$	$\theta_{r2}/(^{\circ})$	x_{rp}' /mm	y'_{rp} /mm	∆'/mm	$ \theta'_{r1}'(^{\circ}) $	$\theta'_{r2}/(^{\circ})$
-	000.09	0.000	60.015	0.021	0.025	218.5	131.8	60.015	-0.021	0.025	141.5	228.2
2	59.700	5.990	59.716	5.981	0.018	224.2	137.5	29.667	5.979	0.035	147.2	234.0
3	58.804	11.920	58.767	11.933	0.039	230.0	143.2	58.814	11.945	0.027	153.0	239.7
4	57.320	17.731	57.325	17.767	0.036	235.7	149.0	57.337	17.727	0.017	158.7	245.4
5	55.264	23.365	55.277	23.372	0.015	241.4	154.7	55.231	23.355	0.034	164.4	251.2
9	52.655	28.766	52.682	28.747	0.033	247.1	160.4	52.652	28.802	0.037	170.2	256.9
7	49.520	33.879	49.492	33.860	0.034	252.9	166.1	49.531	33.889	0.015	175.9	262.6
8	45.891	38.653	45.893	38.673	0.020	258.6	171.9	45.920	38.641	0.032	181.6	268.3
6	41.802	43.041	41.825	43.040	0.023	264.3	177.6	41.789	43.006	0.037	187.3	274.1
10	37.297	47.000	37.266	46.980	0.036	270.1	183.3	37.294	47.020	0.021	193.1	279.8
11	32.418	50.488	32.405	50.514	0.029	275.8	189.1	32.440	50.492	0.022	198.8	285.5
12	27.216	53.472	27.228	53.483	0.016	281.5	194.8	27.203	53.440	0.034	204.5	291.3
13	21.741	55.922	21.781	55.923	0.040	287.2	200.5	21.722	55.946	0.030	210.3	297.0
14	16.050	57.813	16.047	57.779	0.035	293.0	206.2	16.058	57.827	0.015	216.0	302.7
15	10.198	59.127	10.195	59.143	0.016	298.7	212.0	10.184	59.095	0.035	221.7	308.5
16	4.244	59.850	4.270	59.863	0.029	304.4	217.7	4.264	59.814	0.041	227.4	314.2

Table 3.12 Calculation results in elliptical scan case by the improved lookup-table method (not complete)

Table 3.12	Calculation	n results in e	Table 3.12 Calculation results in elliptical scan case by the improved lookup-table method (not complete)	case by the	improved la	ookup-table	method (not	complete)				
No.	Target point	nt	The first se	The first set of inverse solution	solution			The secon	The second set of inverse solution	rse solution		
	X_{rp}/mm	Y_{rp} /mm	x _{rp} /mm	y _{rp} /mm	Δ/mm	$\theta_{r1}/(^{\circ})$	$\theta_{r2}/(^{\circ})$	x'_{rp} /mm	y'_{rp} /mm	∆'/mm	$\theta'_{r1}/(^{\circ})$	$\theta_{r2}'/(^{\circ})$
-	40.000	0.000	39.987	-0.001	0.013	232.1	109.6	39.987	0.001	0.013	127.9	250.4
2	39.800	5.990	39.789	5.965	0.027	240.5	118.4	39.784	5.998	0.018	136.6	258.7
3	39.203	11.920	39.199	11.921	0.004	248.5	127.6	39.205	11.900	0.020	145.3	266.2
4	38.213	17.731	38.232	17.703	0.034	255.8	136.8	38.230	17.708	0.028	153.9	272.9
5	36.842	23.365	36.849	23.387	0.022	262.5	146.0	36.850	23.384	0.021	162.3	278.8
9	35.103	28.766	35.099	28.755	0.011	268.4	154.8	35.076	28.784	0.033	170.3	283.9
7	33.013	33.879	33.025	33.878	0.011	273.6	163.3	33.002	33.900	0.025	177.9	288.2
∞	30.594	38.653	30.609	38.681	0.032	278.2	171.4	30.602	38.687	0.035	185.1	291.9
6	27.868	43.041	27.871	43.068	0.027	282.3	179.0	27.859	43.076	0.036	191.9	295.2
10	24.864	47.000	24.858	47.006	0.009	286.0	186.1	24.905	46.981	0.045	198.2	298.1
11	21.612	50.488	21.619	50.461	0.028	289.4	192.7	21.602	50.526	0.039	204.3	300.9
12	18.144	53.472	18.176	53.471	0.033	292.6	198.9	18.131	53.487	0.019	209.9	303.6
13	14.494	55.922	14.511	55.912	0.020	295.8	204.6	14.513	55.911	0.022	215.1	306.3
14	10.700	57.813	10.700	57.844	0.030	299.0	209.9	10.689	57.795	0.022	220.0	309.2
15	6.799	59.127	6:839	59.128	0.040	302.3	214.6	6.795	59.083	0.044	224.5	312.3
16	2.829	59.850	2.785	59.852	0.045	305.9	219.0	2.860	59.848	0.031	228.7	315.6

$\overline{}$
£
<u>e</u>
ď
Ħ
8
ب
2
ت
p
2
Ħ
8
Ε.
<u>e</u>
ð
ř
ġ
Ξ
7
Ō
=
ĕ
\geq
ĭ
ద
the im
0
æ
_
Ð.
0
cas
\circ
П
can
Š
р
ō
troi
astroi
n a
s in astroi
n a
n a
n a
n a
n a
n a
n a
n a
n a
alculation results in a
n a
3 Calculation results in a
3 Calculation results in a
3.13 Calculation results in a
3.13 Calculation results in a
ble 3.13 Calculation results in a
3.13 Calculation results in a

				•								
No.	Target point	nt	The first se	The first set of inverse solution	solution			The secon	The second set of inverse solution	rse solution		
	X_{rp}/mm	Y _{rp} /mm	x _{rp} /mm	y_{rp}/mm	Δ/mm	$\theta_{r1}/(^{\circ})$	$\theta_{r2}/(^{\circ})$	x'_{rp} /mm	y' _{rp} /mm	Δ'/mm	(°)/ _{r1} /(°)	$\theta'_{r2}/(^{\circ})$
1	000.09	0.000	60.015	0.021	0.025	218.5	131.8	60.015	-0.021	0.025	141.5	228.2
2	59.105	090.0	59.125	0.071	0.023	219.3	130.8	59.075	0.075	0.034	140.8	229.4
3	56.483	0.470	56.526	0.460	0.044	221.8	128.2	56.474	0.468	0.009	139.1	232.8
4	52.314	1.549	52.328	1.586	0.040	226.2	124.8	52.330	1.520	0.032	137.2	238.6
5	46.883	3.543	46.885	3.563	0.020	232.4	121.6	46.884	3.570	0.027	136.3	247.1
9	40.552	6.612	40.556	6.628	0.016	240.8	120.1	40.563	6.584	0.030	137.7	258.4
7	33.732	10.801	33.730	10.792	0.009	252.0	122.2	33.727	10.801	0.005	143.5	273.3
8	26.845	16.042	26.817	16.047	0.029	266.7	130.4	26.815	16.051	0.032	155.1	291.4
6	20.291	22.149	20.270	22.146	0.021	283.7	145.5	20.295	22.123	0.027	171.3	309.5
10	14.411	28.839	14.419	28.812	0.028	298.9	164.1	14.383	28.830	0.030	188.0	322.8
11	9.464	35.749	9.488	35.757	0.025	308.7	181.4	9.475	35.760	0.015	201.6	328.9
12	5.600	42.471	5.629	42.489	0.034	313.0	195.2	5.634	42.488	0.039	211.9	329.7
13	2.855	48.580	2.865	48.613	0.035	313.6	205.7	2.876	48.555	0.032	219.6	327.6
14	1.148	53.677	1.136	53.650	0.029	312.3	213.3	1.150	53.704	0.028	225.3	324.2
15	0.295	57.419	0.297	57.456	0.038	310.3	218.5	0.263	57.405	0.034	229.1	321.0
16	0.021	59.550	-0.002	59.522	0.037	308.9	221.2	0.046	59.572	0.032	231.1	318.7

can only be enhanced by reducing the step angle, but the amount of calculation will be increased exponentially as a result.

In principle, the lookup-table method relies on the forward solution of rotating double prisms to solve the inverse problem. Consequently, the solving accuracy is uneasy to control and the solving efficiency cannot be satisfactory in real-time target tracking applications.

3.1.3 Iterative Method

1. Principle of Iterative Method

Generally, the exiting point of the emergent beam from prism 2 is transient in the inverse problem of rotating double prisms. Without the determination of beam exiting point, the emergent beam vector cannot be deduced from the given target point on the screen.

As illustrated in Sect. 3.1.1, two-step method can be applied to obtain the rotation angles of two prisms because the emergent beam vector is determined in approximation. Upon neglecting the effects of structural parameters such as the thickness of each prism and the distance between two prisms, the beam exiting point can be assumed at the center of the emergent surface of prism 2, and the emergent beam vector can be further determined according to the given target point. However, the effects of those structural parameters on the beam exiting point are usually significant in practice. The beam exiting point is actually transient but not fixed to the center of the emergent surface of prism 2. Therefore, the emergent beam vector is not available anymore for the implementation of two-step method in many practical applications.

Combining the inverse derivation formulae of two-step method with the forward ray tracing formulae [7], an iterative method [8] is proposed on the basis of beam scan principle in far field and near field. The method can be employed to determine the orientations (θ_{r1} , θ_{r2}) of two prisms with satisfactory precision.

Figure 3.20 illustrates the inverse solving process by the proposed iterative method. At the first iteration, the beam exiting point is assumed at the center $N^0(0,0)$ of the emergent surface of prism 2, as required in far field. Given the target point as $P(X_{rp},Y_{rp})$, the emergent beam vector can be specified by $A_{rf}^0 = \overrightarrow{N^0P}$. Thus, two-step method is applied to obtain the approximate inverse solution $(\theta_{r1}^1,\theta_{r2}^1)$. By substituting $(\theta_{r1}^1,\theta_{r2}^1)$ into the forward ray tracing formulae in near field, the consequent beam scan point $P^1(x_{rp}^1,y_{rp}^1)$ and beam exiting point $N^1(x_{rm}^1,y_{rm}^1)$ are determined. The vector specified by $A_{rf}^1 = \overrightarrow{N^1P}$ is regarded as the emergent beam vector at the second iteration. Also, two-step method is applied to obtain the approximate inverse solution $(\theta_{r1}^2,\theta_{r2}^2)$, which is substituted into the forward formulae to determine the consequent beam scan point $P^2(x_{rp}^2,y_{rp}^2)$ and beam exiting point $N^2(x_{rm}^2,y_{rm}^2)$. Similarly, the vector specified by $A_{rf}^{i-1} = \overrightarrow{N^{i-1}P}$ ($i=3,4\dots n$) is regarded as the emergent

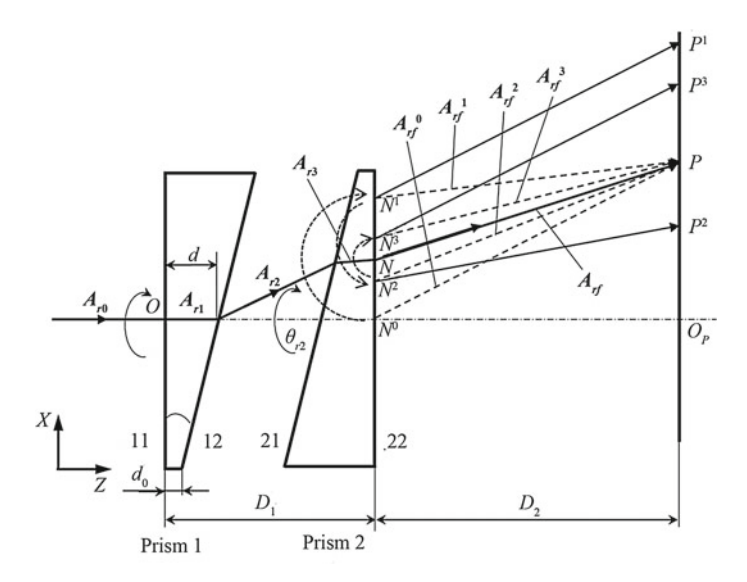


Fig. 3.20 Schematic diagram illustrating the inverse solving process by the iterative method

beam vector at the subsequent iteration, and the above process is repeated to update the beam scan point $P^i\left(x_{rp}^i,y_{rp}^i\right)$ and beam exiting point $N^i\left(x_m^i,y_m^i\right)$. Such an iterative procedure should be stopped as long as the beam scan point P^i approaches the target point P to the extent required by $\Delta = \sqrt{\left(x_{rp}^i - X_{rp}\right)^2 + \left(y_{rp}^i - Y_{rp}\right)^2} < \delta$, where δ denotes the given error threshold.

For example, the iterative method is employed to solve the inverse problem for the target point given by P(0, 20). The error threshold between the beam scan point and the target point is set to $\delta = 0.0001$ mm, and the beam exiting point is assumed as $N^0(0, 0)$ at the first iteration. Consequently, there should be two sets of prism orientations obtained by the iterative method. The iterative process for these inverse solutions are presented in Tables 3.14 and 3.15, respectively.

As shown in the above tables, the iterative method is characterized by rapid convergence while solving the rotation angles of two prisms for the target point P(0, 20). Only 9 iterations are required to obtain each set of inverse solution. In addition, the final error between the beam scan point and the target point is up to $\delta = 0.0001$ mm, and the numerical accuracy of prism orientations achieves better than 0.01° .

The relation of the error Δ between the beam scan point and the target point with respect to the number k of iterations is revealed in Fig. 3.21. It turns out that the iteration error is reduced rapidly as the number of iterations increases, which can

No.	Beam exiting point/mm	ng	Beam scan j	point/mm	Error/mm	Prism orient	tations/(°)
k	x_{rn}	yrn	x_{rp}	Уrp	Δ	θ_{r1}	θ_{r2}
1	6.830350	2.312234	6.830350	22.312234	7.211110	195.936655	344.383475
2	5.609818	4.516284	-1.220532	22.204051	2.519432	216.204930	366.329188
3	5.861903	4.149227	0.252086	19.632943	0.445284	212.988204	367.110193
4	5.807144	4.231077	-0.054760	20.081850	0.098479	213.715934	367.148334
5	5.818955	4.213569	0.011812	19.982491	0.021120	213.560311	367.145861
6	5.816402	4.217359	-0.002553	20.003790	0.004570	213.594012	367.146756
7	5.816954	4.216540	0.000552	19.999181	0.000987	213.586734	367.146578
8	5.816835	4.216717	-0.000119	20.000177	0.000213	213.588307	367.146617
9	5.816861	4.216679	0.000026	19.999962	0.000046	213.587967	367.146608

Table 3.14 Iterative process for the first set of inverse solution to the target point P(0, 20)

Table 3.15 Iterative process for the second set of inverse solution to the target point P(0, 20)

No.	Beam exiting	point/mm	Beam scan po	oint/mm	Error/mm	Prism orienta	tions/(°)
k	x'_{rn}	y'_{rn}	x'_{rp}	y' _{rp}	Δ'	θ'_{r1}	θ'_{r2}
1	-7.162066	-0.566626	-12.978926	15.216695	13.832301	366.874162	213.315592
2	-5.570714	4.605747	1.591352	25.172373	5.411640	323.407555	177.846465
3	-5.869522	4.137182	-0.298808	19.531435	0.555733	327.112376	172.834753
4	-5.805519	4.233487	0.064003	20.096305	0.115633	326.262754	172.852656
5	-5.819306	4.213047	-0.013787	19.979560	0.024655	326.444326	172.854261
6	-5.816327	4.217471	0.002980	20.004424	0.005334	326.404987	172.853221
7	-5.816970	4.216516	-0.000644	19.999045	0.001152	326.413482	172.853428
8	-5.816831	4.216722	0.000139	20.000206	0.000249	326.411647	172.853382
9	-5.816861	4.216678	-0.000030	19.999955	0.000054	326.412043	172.853392

confirm the iterative method with great convergence. In addition, there is much lower complexity of computation for the iterative method. The whole calculation takes 0.3 and 0.06 s for two sets of inverse solutions, respectively. Hence, the iterative method is efficient enough to be used in real-time tracking applications for dynamic targets.

2. Application of Iterative Method

In simulation, the iterative method is applied to solve the inverse problem for those specific target trajectories in Sect. 3.1.1. The error threshold between the beam scan point and each target point is set to $\delta = 0.0001$ mm.

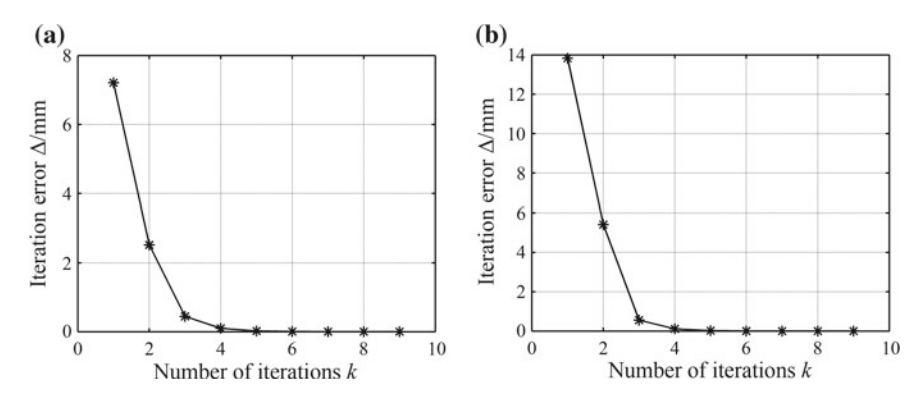


Fig. 3.21 Relation of the iteration error relative to the number of iterations, where \mathbf{a} is for the first set of inverse solution and \mathbf{b} is for the second set of inverse solution

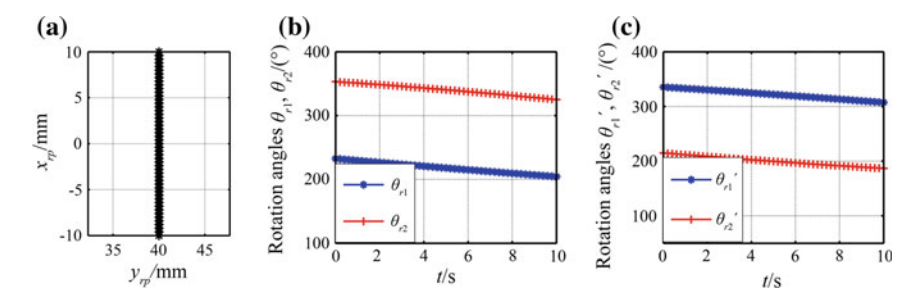


Fig. 3.22 A linear scan case by iterative method, where \mathbf{a} shows the linear target trajectory, \mathbf{b} is the first set of inverse solution, and \mathbf{c} is the second set of inverse solution

Case 1: a linear target trajectory given by y = 40, $x \in [-10, 10]$.

Figure 3.22a shows a linear target trajectory, while Fig. 3.22b and c manifest two sets of inverse solutions obtained by iterative method, respectively. The first 16 of 51 sample points on the target trajectory and the related calculation results are listed in Table 3.16. It is found that the error of the actual point relative to the target point is up to 0.00007 mm in each set of inverse solution. For the first set of inverse solution, the calculation takes 0.104 s in total and 0.0020 s on average for each target point. For the second one, the calculation takes 0.107 s in total and 0.0021 s on average for each target point.

Table 3.16 Calculation results in linear scan case by iterative method (not complete)

Table	tante or calculation less	alation resu.	1 11 21	its in them sean ease of netative interior (not complete)	se of nerm	ve memor	dinos son)	(2)						
No.	Target point	t	The	The first set of inverse solution	rse solution				The s	The second set of inverse solution	nverse solution	uc		
	X _{rp} /mm	Y_{rp}/mm	k	x _{rp} /mm	y ₁ /mm	Δ/mm	$\theta_{r1}/(^{\circ})$	$\theta_{r2}/(^{\circ})$	k	x',/mm	y' _{rp} /mm	Δ'/mm	$\theta'_{r1}/(^{\circ})$	$\theta'_{r2}/(^{\circ})$
_	-10.00000	-10.00000 40.00000	∞	-10.00005	40.0004	0.00007	232.59	353.07	∞	-9.99997	40.00006	0.00007	335.48	215.01
2	-9.60000	40.00000	∞	-9.60005	40.00004	0.00007	232.00	352.63	∞	-9.59997	40.00006	0.00007	334.99	214.36
8	-9.20000	40.00000	∞	-9.20005	40.00004	0.00007	231.41	352.19	∞	-9.19997	40.00006	0.00007	334.50	213.72
4	-8.80000	40.00000	∞	-8.80005	40.00004	0.00007	230.82	351.74	∞	-8.79997	40.00006	0.00007	334.00	213.08
5	-8.40000	40.00000	∞	-8.40005	40.00004	0.00007	230.22	351.28	∞	-8.39997	40.00006	0.00007	333.50	212.44
9	-8.00000	40.00000	∞	-8.00005	40.00004	0.00007	229.63	350.82	∞	-7.99997	40.00006	0.00007	332.99	211.80
7	-7.60000	-7.60000 40.00000	∞	-7.60005	40.00004	0.00007	229.04	350.35	∞	-7.59997	40.00006	0.00007	332.48	211.16
∞	-7.20000	-7.20000 40.00000	∞	-7.20005	40.00005	0.00007	228.45	349.88	∞	-7.19997	40.00006	0.00007	331.96	210.53
6	-6.80000	40.00000	∞	-6.80005	40.00005	0.00007	227.85	349.40	∞	-6.79997	40.00006	0.00007	331.44	209.90
10	-6.40000	-6.40000 40.00000	∞	-6.40005	40.00005	0.00007	227.26	348.91	∞	-6.39997	40.00006	0.00007	330.92	209.27
11	-6.00000	-6.00000 40.00000	∞	-6.00005	40.00005	0.00007	226.67	348.42	∞	-5.99996	40.00006	0.00007	330.39	208.64
12	-5.60000	-5.60000 40.00000	∞	-5.60005	40.00005	0.00007	226.08	347.92	∞	-5.59996	40.00006	0.00007	329.86	208.02
13	-5.20000	-5.20000 40.00000	∞	-5.20005	40.00005	0.00007	225.49	347.42	∞	-5.19996	40.00006	0.00007	329.33	207.39
14	-4.80000	40.00000	∞	-4.80005	40.00005	0.00007	224.90	346.91	∞	-4.79996	40.00006	0.00007	328.79	206.78
15	-4.40000	40.00000	∞	-4.40005	40.00005	0.00007	224.31	346.40	∞	-4.39996	40.00006	0.00007	328.25	206.16
16	-4.00000	-4.00000 40.00000	∞	-4.00005	40.00005	0.00007	223.72	345.87	8	-3.99996	40.00006	0.00007	327.70	205.55

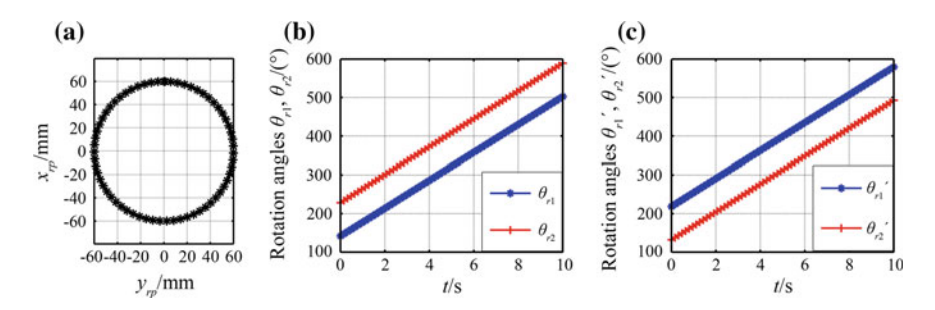


Fig. 3.23 A circular scan case by iterative method, where a shows the circular target trajectory, b is the first set of inverse solution, and c is the second set of inverse solution

Case 2: a circular target trajectory given by $x^2 + y^2 = 60^2$.

Figure 3.23a shows a circular target trajectory, while Fig. 3.23b and c manifest two sets of inverse solutions obtained by iterative method, respectively. The first 16 of 64 sample points on the target trajectory and the related calculation results are listed in Table 3.17. It is found that the error of the actual point relative to the target point is up to 0.00004 mm in each set of inverse solution. For the first set of inverse solution, the calculation takes 0.121 s in total and 0.0019 s on average for each target point. For the second one, the calculation takes 0.167 s in total and 0.0026 s on average for each target point.

Case 3: an elliptical target trajectory given by $\frac{x^2}{40^2} + \frac{y^2}{60^2} = 1$.

Figure 3.24a shows an elliptical target trajectory, while Fig. 3.24b and c manifest two sets of inverse solutions obtained by iterative method, respectively. The first 16 of 64 sample points on the target trajectory and the related calculation results are listed in Table 3.18. It is found that the error of the actual point relative to the target point is up to 0.00009 mm in each set of inverse solution. For the first set of inverse solution, the calculation takes 0.120 s in total and 0.0019 s on average for each target point. For the second one, the calculation takes 0.123 s in total and 0.0019 s on average for each target point.

Case 4: an astroid target trajectory given by
$$\begin{cases} x = 60\cos^3\theta \\ y = 60\sin^3\theta \end{cases}, \quad 0 \le \theta \le 2\pi.$$

Figure 3.25a shows an elliptical target trajectory, while Fig. 3.25b and c manifest two sets of inverse solutions obtained by iterative method, respectively. The first 16 of 64 sample points on the target trajectory and the related calculation results are listed in Table 3.19. It is found that the error of the actual point relative to the target point is up to 0.00010 mm in each set of inverse solution. For the first set of inverse solution, the calculation takes 0.128 s in total and 0.0020 s on average for each target point. For the second one, the calculation takes 0.130 s in total and 0.0021 s on average for each target point.

Table 3.17 Calculation results in circular scan case by iterative method (not complete)

No.	Target point		The	The first set of inverse solution	se solution				The	The second set of inverse solution	nverse solution			
	X _{rp} /mm	Y _{rp} /mm	k	x _{rp} /mm	yrp/mm	∆/mm	$\theta_{r1}/(^{\circ})$	(°)	k	<i>x'</i> _{rp} /mm	<i>y'</i> _{rp} /mm	∆'/mm	(°)/ _{r1} /(°)	(°)
	000000:09	0.00000	∞	59.99997	-0.00004	0.00004	141.51	228.24	∞	59.99997	0.00004	0.00004	218.49	131.76
	59.70025	5.99000	∞	59.70023	5.98997	0.00004	147.24	233.97	∞	59.70022	5.99004	0.00004	224.22	137.49
	58.80399	11.92016	∞	58.80397	11.92012	0.00004	152.97	239.70	∞	58.80396	11.92019	0.00004	229.95	143.22
	57.32019	17.73121	∞	57.32017	17.73117	0.00004	158.70	245.43	∞	57.32015	17.73124	0.00004	235.68	148.95
	55.26366	23.36510	∞	55.26365	23.36506	0.00004	164.43	251.16	∞	55.26362	23.36512	0.00004	241.41	154.68
	52.65495	28.76553	∞	52.65495	28.76549	0.00004	170.15	256.89	∞	52.65491	28.76555	0.00004	247.14	160.41
	49.52014	33.87855	∞	49.52013	33.87850	0.00004	175.88	262.61	∞	49.52009	33.87856	0.00004	252.87	166.14
∞	45.89053	38.65306	∞	45.89053	38.65302	0.00004	181.61	268.34	∞	45.89049	38.65307	0.00004	258.60	171.87
6	41.80240	43.04137	∞	41.80241	43.04132	0.00004	187.34	274.07	∞	41.80236	43.04137	0.00004	264.33	177.60
10	37.29660	46.99961	∞	37.29661	46.99957	0.00004	193.07	279.80	∞	37.29655	46.99961	0.00004	270.06	183.33
1	32.41814	50.48826	∞	32.41815	50.48822	0.00004	198.80	285.53	∞	32.41809	50.48825	0.00004	275.79	189.06
12	27.21577	53.47244	∞	27.21579	53.47240	0.00004	204.53	291.26	∞	27.21572	53.47243	0.00004	281.52	194.79
13	21.74147	55.92235	∞	21.74149	55.92231	0.00004	210.26	296.99	∞	21.74142	55.92233	0.00004	287.25	200.52
14	16.04993	57.81349	∞	16.04996	57.81345	0.00004	215.99	302.72	∞	16.04989	57.81347	0.00004	292.98	206.25
15	10.19803	59.12698	∞	10.19806	59.12695	0.00004	221.72	308.45	∞	10.19799	59.12696	0.00004	298.71	211.98
16	4.24423	59 84970	×	4 24427	50 84067	0,000,0	27.75	217.19	٥	4 24410	50 0 4067	70000	20.4.4.4	11.1.0

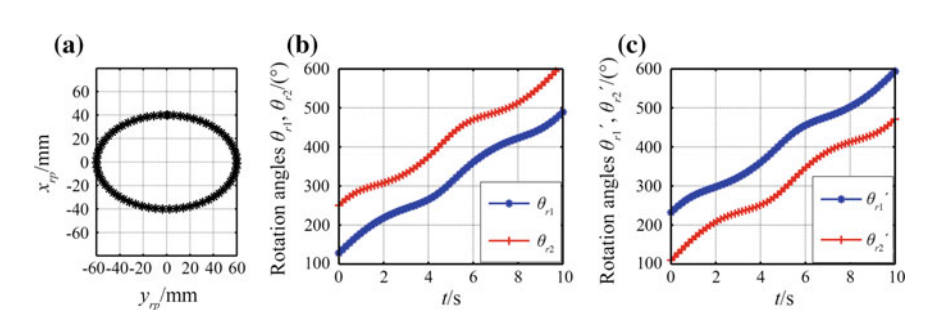


Fig. 3.24 An elliptical scan case by iterative method, where **a** shows the elliptical target trajectory, **b** is the first set of inverse solution, and **c** is the second set of inverse solution

Case 5: a spiral target trajectory given by
$$\begin{cases} x = 6t \cos t \\ y = 6t \sin t \end{cases}, \quad 0 \le t \le 10.$$

Figure 3.26a shows an elliptical target trajectory, while Fig. 3.26b and c manifest two sets of inverse solutions obtained by iterative method, respectively. There are 64 sample points taken from the target trajectory, where the first 9 points are inside a scan blind zone and the consequent prism orientations are not available. Table 3.20 lists the first 16 sample points outside the blind zone and the related calculation results. It is found that the error of the actual point relative to the target point is up to 0.00010 mm in each set of inverse solution. For the first set of inverse solution, the calculation takes 0.159 s in total and 0.0025 s on average for each target point. For the second one, the calculation takes 0.158 s in total and 0.0025 s on average for each target point.

Case 6: a rose-like target trajectory given by
$$\begin{cases} x = 60\cos 4\theta\cos\theta \\ y = 60\cos 4\theta\sin\theta \end{cases}, \quad 0 \le \theta \le 2\pi.$$

Figure 3.27a shows an elliptical target trajectory, where the central circle highlights a scan blind zone. Figures 3.27b and c manifest two sets of inverse solutions obtained by iterative method. The enlarged views of A and B are further displayed in Fig. 3.27d and e, respectively. There are 127 sample points taken from the target trajectory, and the consequent rotation angle curves of two prisms are not continuous due to the blind zone. Table 3.21 lists the first 16 sample points outside the blind zone and the related calculation results. It is found that the error of the actual point relative to the target point is up to 0.00010 mm in each set of inverse solution. For the first set of inverse solution, the calculation takes 0.201 s in total and 0.0016 s on average for each target point. For the second one, the calculation takes 0.204 s in total and 0.0016 s on average for each target point.

According to the above cases, the solving process for each target point requires no more than 9 iterations when the solving accuracy is set to $\delta=0.0001$ mm, and the convergence rate is almost unchanged in two sets of inverse solutions. Compared to lookup-table method, the iterative method is advantageous in less computation and superior solving efficiency. Since the calculation usually takes 0.002 s on average for

Table 3.18 Calculation results in elliptical scan case by iterative method (not complete)

					•	•								
No.	Target point	پ	The 1	The first set of inverse solution	erse solution				The s	The second set of inverse solution	inverse solution	u		
	X _{rp} /mm	Y_{rp}/mm	k	x _{rp} /mm	y ₁ /mm	Δ/mm	$\theta_{r1}/(^{\circ})$	(°)	k	<i>x'</i> _{rp} /mm	y'p/mm	Δ'/mm	$\theta'_{r1}/(^{\circ})$	$\theta_{r2}'/(^{\circ})$
-	40.00000	0.00000	∞	40.00006	0.00005	0.00007	127.91	250.38	∞	40.00006	-0.00005	0.00007	232.09	109.62
2	39.80017	5.99000	∞	39.80022	5.99006	0.00007	136.59	258.67	∞	39.80023	5.98997	0.00007	240.52	118.45
m	39.20266	11.92016	∞	39.20270	11.92022	0.00007	145.33	266.22	∞	39.20272	11.92013	0.00007	248.50	127.60
4	38.21346	17.73121	∞	38.21349	17.73127	9000000	153.94	272.94	∞	38.21352	17.73120	0.00006	255.85	136.84
ď	36.84244	23.36510	∞	36.84245	23.36515	0.00005	162.27	278.80	∞	36.84249	23.36509	0.00005	262.49	145.96
9	35.10330	28.76553	∞	35.10331	28.76557	0.00004	170.27	283.85	∞	35.10334	28.76553	0.00004	268.40	154.82
7	33.01342	33.87855	∞	33.01343	33.87858	0.00003	177.87	288.18	∞	33.01345	33.87855	0.00003	273.62	163.30
∞	30.59369	38.65306	7	30.59370	38.65298	0.00008	185.06	291.92	7	30.59361	38.65305	0.00008	278.22	171.36
6	27.86827	43.04137	7	27.86827	43.04134	0.00003	191.85	295.20	7	27.86824	43.04136	0.00003	282.30	178.96
10	24.86440	46.99961	7	24.86439	46.99964	0.00002	198.25	298.15	7	24.86442	46.99962	0.00002	285.99	186.09
11	21.61209	50.48826	7	21.61206	50.48832	0.00007	204.25	300.91	7	21.61216	50.48828	0.00007	289.40	192.74
12	18.14384	53.47244	∞	18.14386	53.47242	0.00002	209.88	303.59	∞	18.14382	53.47243	0.00002	292.64	198.92
13	14.49431	55.92235	8	14.49433	55.92232	0.00003	215.13	306.31	∞	14.49428	55.92233	0.00003	295.81	204.63
14	10.69995	57.81349	8	10.69998	57.81346	0.00004	220.01	309.17	∞	10.69992	57.81347	0.00004	299.02	209.86
15	69862.9	59.12698	∞	6.79872	59.12695	0.00004	224.54	312.25	∞	6.79865	59.12696	0.00004	302.34	214.63
16	2.82949	59.84970	∞	2.82952	59.84967	0.00004	228.73	315.63	∞	2.82945	59.84967	0.00004	305.86	218.96

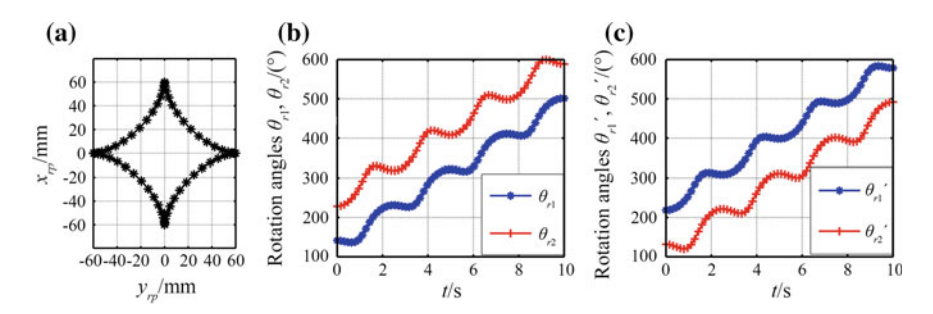


Fig. 3.25 An astroid scan case by iterative method, where $\bf a$ shows the astroid target trajectory, $\bf b$ is the first set of inverse solution, and $\bf c$ is the second set of inverse solution

each target point, the iterative method offers an ideal approach for real-time target tracking applications. Moreover, the solving accuracy of the method depends on the iteration error threshold, which implies that the target tracking accuracy can be controlled in practice.

3.1.4 Damped Least-Squares Iterative Method

The two-step method, lookup-table method and iterative method are all proposed under the assumption that the incident beam propagates along the optical axis of the rotating double-prism system. However, the incident beam can be inclined to the optical axis in some specific applications, where those methods are not feasible anymore. To solve the inverse problem of such a system, the damped least-squares iterative method has been proposed in [3].

1. Principle of the Damped Least-Squares Iterative Method

Considering the nonlinear and complicated relation between prism orientations and the final beam deviation, the coordinates (x_{rp}, y_{rp}) of the beam scan point P_r are both expressed as the functions dependent on the rotation angles θ_{r1} and θ_{r2} :

$$\begin{bmatrix} x_{rp} \\ y_{rp} \end{bmatrix} = \begin{bmatrix} f_x(\theta_{r1}, \theta_{r2}) \\ f_y(\theta_{r1}, \theta_{r2}) \end{bmatrix} = F(\boldsymbol{\theta})$$
 (3.10)

where θ denotes the joint variable of θ_{r1} and θ_{r2} .

The damped least-squares iterative method is then applied to establish the numerical inverse relation for rotating double prisms. Basically, this method involves differentiating the forward relation of (3.10) to obtain a Jacobian matrix given by

Table 3.19 Calculation results in astroid scan case by iterative method (not complete)

No.	Target point		The	The first set of inverse solution	se solution				The	second set of in	The second set of inverse solution			
	X _{rp} /mm	Y _{rp} /mm	k	x _{rp} /mm	yrp/mm	∆/mm	$\theta_{r1}/(^{\circ})$	(°)	k	<i>x'</i> _{rp} /mm	y' _{rp} /mm	∆'/mm	(°)/(°)	(°)
	00000009	0.00000	∞	59.99997	-0.00004	0.00004	141.51	228.24	∞	59.99997	0.00004	0.00004	218.49	131.76
2	59.10523	0.05970	∞	59.10521	0.05967	0.00004	140.81	229.35	∞	59.10521	0.05973	0.00004	219.31	130.77
	56.48303	0.47048	∞	56.48301	0.47046	0.00002	139.11	232.79	∞	56.48301	0.47050	0.00002	221.84	128.16
4	52.31429	1.54851	4	52.31427	1.54855	0.00005	137.22	238.65	4	52.31427	1.54846	0.00005	226.17	124.74
5	46.88311	3.54324	∞	46.88313	3.54326	0.00003	136.27	247.07	∞	46.88314	3.54322	0.00003	232.38	121.57
9	40.55227	6.61172	∞	40.55232	6.61177	0.00007	137.74	258.45	∞	40.55233	6.61169	0.00007	240.78	120.07
7	33.73207	10.80120	6	33.73206	10.80118	0.00002	143.50	273.29	6	33.73205	10.80120	0.00002	252.01	122.22
∞	26.84521	16.04166	6	26.84520	16.04163	0.00003	155.06	291.33	6	26.84518	16.04166	0.00003	266.66	130.39
6	20.29090	22.14908	6	20.29089	22.14905	0.00003	171.34	309.52	6	20.29087	22.14907	0.00003	283.67	145.49
10	14.41137	28.83901	6	14.41137	28.83899	0.00003	187.97	322.74	6	14.41134	28.83900	0.00003	298.93	164.16
1	9.46372	35.74939	∞	9.46368	35.74948	0.00000	201.61	328.93	~	9.46379	35.74945	0.00009	308.74	181.42
12	5.59963	42.47052	∞	5.59960	42.47056	900000	211.93	329.77	∞	5.59967	42.47055	0.00006	313.05	195.21
13	2.85472	48.57957	7	2.85479	48.57949	0.00010	219.64	327.60	7	2.85465	48.57950	0.00010	313.63	205.67
14	1.14846	53.67661	7	1.14844	53.67664	0.00004	225.28	324.23	7	1.14849	53.67663	0.00004	312.27	213.32
15	0.29461	57.41887	∞	0.29463	57.41886	0.00003	229.08	320.95	∞	0.29459	57.41886	0.00003	310.33	218.46
16	0.02124	59.55023	∞	0.02127	59.55020	0.00004	231.11	318.75	∞	0.02120	59.55020	0.00004	308.85	221.21

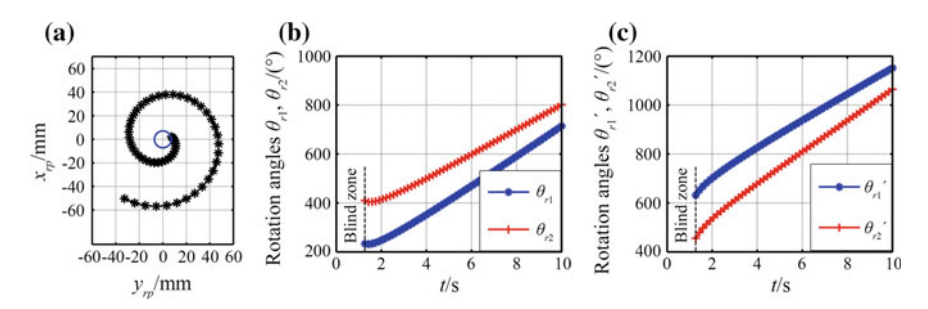


Fig. 3.26 A spiral scan case by iterative method, where a shows the spiral target trajectory, b is the first set of inverse solution, and c is the second set of inverse solution

$$\boldsymbol{J} = \begin{bmatrix} \frac{\partial f_x}{\partial r_1} & \frac{\partial f_x}{\partial r_2} \\ \frac{\partial f_y}{\partial r_1} & \frac{\partial f_y}{\partial r_2} \end{bmatrix}$$
(3.11)

Therefore, the inverse solving process based on the damped least-squares iterative method is summarized as follows [3].

Step 1. The target point is given by $P_d = (x_d, y_d)$.

Step 2. Derive the forward relation as shown in (3.10).

Step 3. Initialize the joint variable θ as $\theta_0 = (\theta_{r10}, \theta_{r20})$.

Step 4. Calculate the Jacobian matrix J when $\theta = \theta_i$ at the *i*th iteration.

Step 5. Update θ_{i+1} using the formula $\theta_{i+1} = \theta_i + \zeta J^+[P_d - F(\theta_i)]$, where ζ denotes a gain factor and $J^+ = J^T (JJ^T + \varepsilon I)^{-1}$. In addition, the damped factor ε can be given by $\varepsilon = \varepsilon_0 (1 - \omega/\omega_0)^2$ if the variable $\omega = \sqrt{\det(JJ^T)}$ is under a threshold ω_0 , otherwise $\varepsilon = 0$.

Step 6. Determine the absolute error Δ between the beam scan point and the target point by the formula $\Delta = |P_d - F(\theta_{i+\infty})|$. If the error Δ is under an error threshold δ , θ_{i+1} should be accepted as the final solution. Otherwise return to Step 4.

2. Improvement on the Damped Least-Squares Iterative Method

The disadvantage of the damped least-squares iterative method is that the iterative process is too lengthy for real-time target tracking applications. Since it is quite time-consuming to find the Jacobian matrix with four partial differentials at each iteration, a numerical differentiation method should be employed to obtain approximate partial differentials with high efficiency [9].

According to this method, an n-order Lagrange interpolation polynomial $L_n(\theta)$ is regarded as the substitution for the forward relation $F(\theta)$ between prism orientations and target coordinates. Thus, it is acceptable that the partial differentiation functions of $F(\theta)$ are approximate to those of $L_n(\theta)$. In this way, the partial differentials of $L_n(\theta)$ relative to the rotation angle θ_{r1} are obtained at a specific node where $\theta_{r1} = \theta_s$.

Table 3.20 Calculation results in spiral scan case by iterative method (not complete)

				(analdman and a man and a	maran Caa		duras sau	(212						
No.	Target point	t t	The	The first set of inverse solution	rse solution				The s	The second set of inverse solution	nverse solutic	uc		
	X _{rp} /mm	Y_{rp}/mm	k	x _{rp} /mm	y ₁ /mm	Δ/mm	$\theta_{r1}/(^{\circ})$	$\theta_{r2}/(^{\circ})$	k	<i>x'</i> _{rp} /mm	y' _{rp} /mm	Δ'/mm	$\theta'_{r1}/(^{\circ})$	$\theta'_{r2}/(^{\circ})$
6	2.25853	7.27660	6	2.25858	7.27657	0.00006	233.75	409.95	6	2.25848	7.27660	7.27660 0.00006	631.76	455.56
10	1.21496	8.48488	6	1.21490	8.48494	0.00008	231.25	404.56	6	1.21504	8.48492	0.00008	652.45	479.15
=	-0.15719	9.52251	6	-0.15724	9.52255	0.00006	233.61	404.73	6	-0.15714	9.52255	0.00006	668.28	497.16
12	-1.82642	10.31575	6	-1.82644	10.31577	0.00003	238.06	407.27	6	-1.82640	10.31577	0.00003	682.02	512.81
13	-3.74620	10.79714	7	-3.74622	10.79715	0.00002	243.73	411.16	7	-3.74618	10.79716 0.00002	0.00002	694.54	527.11
4	-5.85622	10.90837	∞	-5.85630	10.90840	0.00008	250.20	415.96	∞	-5.85621	10.90845 0.00008	0.00008	706.26	540.50
15	-8.08428	10.60293	6	-8.08425	10.60293	0.00003	257.24	421.38	6	-8.08428	10.60291	0.00003	717.41	553.27
16	-10.34850	9.84836	6	-10.34846	9.84836	0.00004	264.71	427.28	6	-10.34849	9.84833 0.00004	0.00004	728.12	565.56
17	-12.56009	8.62808	6	-12.56004	8.62808	0.00004	272.51	433.53	6	-12.56007	8.62804	8.62804 0.00004	738.51	577.49
18	-14.62636	6.94271	6	-14.62631	6.94272	0.00004	280.57	440.07	6	-14.62634	6.94267	6.94267 0.00004	748.64	589.14
19	-16.45399	4.81079	6	-16.45395	4.81080 0.00005	0.00005	288.84	446.84	6	-16.45396	4.81075	4.81075 0.00005	758.56	600.57
20	-17.95242	2.26894	6	-17.95238	2.26896	0.00005	297.28	453.79	6	-17.95239	2.26891	2.26891 0.00005	768.31	611.80
21	-19.03724	-0.62866	6	-19.03720	-0.62863	0.00005	305.87	460.90	6	-19.03720	-0.62868 0.00005	0.00005	777.92	622.89
22	-19.63348	-3.81136	6	-19.63345	-3.81133	0.00005	314.57	468.13	6	-19.63344	-3.81138	0.00005	787.40	633.84
23	-19.67871	-7.19379	6	-19.67868	-7.19376	0.00005	323.38	475.48	6	-19.67867	-7.19380	0.00005	796.78	644.68
24	-19.12580	-10.67813	6	-19.12578	-10.67809	0.00004	332.28	482.92	6	-19.12575	-10.67813	0.00004	806.07	655.43

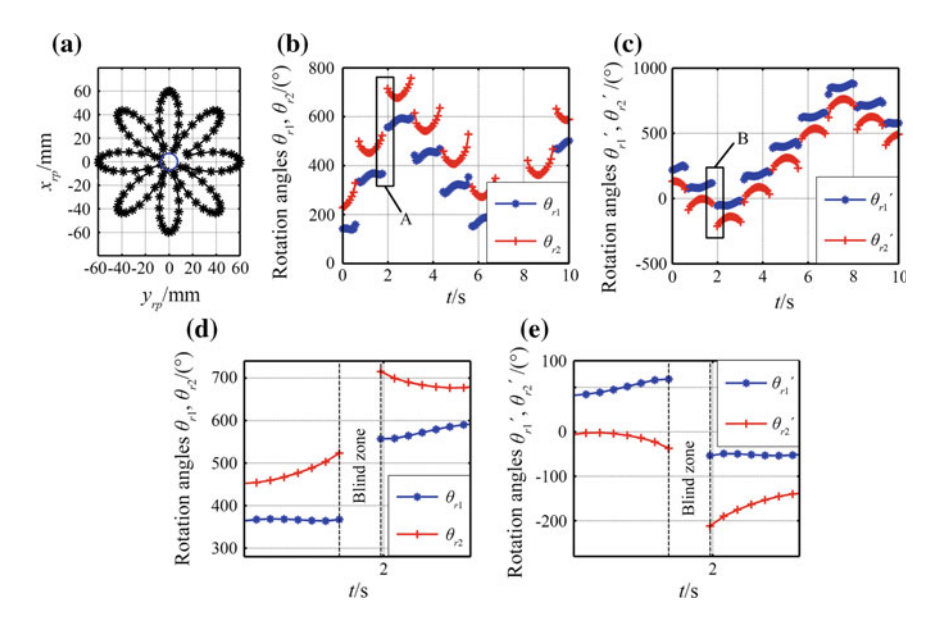


Fig. 3.27 A rose-like scan case by iterative method, where $\bf a$ shows the rose-like target trajectory, $\bf b$ is the first set of inverse solution, $\bf c$ is the second set of inverse solution, $\bf d$ displays the enlarged view of A in the first set of inverse solution, and $\bf e$ displays the enlarged view of B in the second set of inverse solution

A similar approach can be applied to deduce the partial differentials of $L_n(\theta)$ relative to the other rotation angle θ_{r2} , which is omitted here.

The rotation angle θ_{r2} is held constant during the numerical differentiation of $F(\theta)$ relative to θ_{r1} , which accounts for the forward relation transformed as $F(\theta) = g(\theta_{r1})$. For necessity, four more discrete nodes, including $\theta_{s-2} = \theta_s - 2h$, $\theta_{s-1} = \theta_s - h$, $\theta_{s+1} = \theta_s + h$ and $\theta_{s+2} = \theta_s + 2h$, are taken in the neighborhood of the specific node θ_s . Here h denotes the distance between any two adjacent nodes, which depends on the desired solving accuracy. Then a fourth-order Lagrange polynomial can be determined as follows in approximation to the function $g(\theta_{r1})$:

$$L_4(\theta_{r1}) = \sum_{i=s-2}^{s+2} \left[\prod_{j=s-2, j \neq i}^{s+2} \left(\frac{\theta_{r1} - \theta_j}{\theta_i - \theta_j} \right) \cdot g(\theta_i) \right]$$
(3.12)

Note that $g(\theta_i)$ represents the function values of $g(\theta_{r1})$ at the node where $\theta_{r1} = \theta_i$.

By differentiating the interpolation remainder defined as $R_4(\theta_{r1}) = g(\theta_{r1}) - L_4(\theta_{r1})$, the numerical differential of $g(\theta_{r1})$ at the specific node where $\theta_{r1} = \theta_s$ is derived as follows.

$$g'(\theta_s) = \frac{1}{12h} \left[g(\theta_{s-2}) - 8g(\theta_{s-1}) + 8g(\theta_{s+1}) - g(\theta_{s+2}) \right] - \frac{h^4}{30} g^{(5)}(\xi)$$
 (3.13)

Table 3.21 Calculation results in rose-like scan case by iterative method (not complete)

					and Common			(ana.d.						
No.	Target point		The	The first set of inverse solution	rse solution				The s	The second set of inverse solution	rverse solutio	ņ		
	X _{rp} /mm	Y_{rp} /mm	k	x _{rp} /mm	y ₁ /mm	Δ/mm	$\theta_{r1}/(^{\circ})$	θ _{r2} /(°)	k	<i>x'</i> _{rp} /mm	y' _{rp} /mm	Δ'/mm	θ' _{r1} /(°)	$\theta'_{r2}/(^{\circ})$
_	0000009	0.00000	∞	59.99997	-0.00004	0.00004	141.51	228.24	∞	59.99997	0.00004	0.00004	218.49	131.76
2	58.73050	2.93897	∞	58.73048	2.93894	0.00004	143.37	232.51	∞	58.73048	2.93900 0.00004	0.00004	222.36	133.22
8	54.98757	5.51716	7	54.98762	5.51722	0.00008	143.42	239.43	7	54.98763	5.51711	0.00008	228.04	132.03
4	48.96408	7.40020	7	48.96403	7.40014	0.00008	142.17	248.63	7	48.96402	7.40024 0.00008	0.00008	235.02	128.56
5	40.96914	8.30486	∞	40.96918	8.30490	9000000	140.32	259.87	∞	40.96919	8.30483 0.00006	0.00006	242.59	123.05
9	31.41034	8.02038	6	31.41032	8.02036	0.00003	138.91	273.40	6	31.41031	8.02039 0.00003	0.00003	249.74	115.25
7	20.77042	6.42504	6	20.77039	6.42501	0.00004	140.32	291.21	6	20.77037	6.42505 0.00004	0.00004	254.05	103.17
∞	9.57975	3.49688	6	9.57976	3.49692	0.00004	159.28	329.03	6	9.57978	3.49686 0.00004	0.00004	240.83	71.08
10	-12.27501	-5.92950	6	-12.27499	-5.92948	0.00003	335.15	498.79	6	-12.27498	-5.92951	0.00003	76.41	-87.23
11	-21.91219	-11.97069	6	-21.91217	-11.97065	0.00004	331.61	477.56	6	-21.91215	-11.97069 0.00004	0.00004	85.69	-60.26
12	-30.10270	-18.45612	6	-30.10269	-18.45610	0.00002	337.21	467.18	6	-30.10268	-18.45612	0.00002	85.81	-44.15
13	-36.51584	-24.98183	∞	-36.51585	-24.98187	0.00005	344.63	460.13	∞	-36.51588	-24.98182	0.00005	84.13	-31.37
14	-40.92932	-31.11465	7	-40.92931	-31.11462	0.00002	352.11	455.21	7	-40.92929	-31.11465	0.00002	82.37	-20.73
15	-43.23908	-36.41978	∞	-43.23908	-36.41975	0.00002	358.78	452.37	∞	-43.23906	-36.41978	0.00002	81.44	-12.15
16	-43.46199	-40.48904	∞	-43.46199	-40.48899	0.00004	363.97	451.92	∞	-43.46195	-40.48904	0.00004	81.97	-5.97
17	-41.73112	-42.96797	∞	-41.73113	-42.96793	0.00004	367.26	454.20	8	-41.73108	-42.96797 0.00004	0.00004	84.42	-2.52

where the last term is relatively small and can be neglected in approximation.

Thus, it is feasible to establish a Jacobian matrix which contains four numerical differentials at each iteration, given the relation of (3.13). On these basis, the damped least-squares iterative method improved by numerical differentiation is also employed to solve the inverse problem for target trajectories in Sect. 3.1.1. The simulation results indicate that the inverse solutions obtained by this method are always consistent with those generated from the iterative method, as long as the geometrical parameters and the iteration error threshold remains unchanged. Despite the slightly larger time consumption than the iterative method, the damped least-squares iterative method is one of the most fitting approaches for rotating double prisms with an arbitrary incident beam.

3.2 Inverse Solution for Tilting Double Prisms

3.2.1 Analytical Method

1. Principle of Analytical Method

In a tilting double-prism system, the incident beam is usually supposed to propagate along the optical axis of the system, and the tilting angle of each prism is limited within $\theta_{t\min}-\theta_{t\max}$. To derive the analytical inverse solution for tilting double prisms, the emergent beam is specified by the unit vector $(x_{tf}, y_{tf}, z_{tf})^T$ or the combination of vertical field angle ρ_V and horizontal field angle ρ_H , which can be transformed as

$$A_{ff} = (x_{ff}, y_{ff}, z_{ff})^{T}$$

$$= \left(\frac{\tan \rho_{H}}{\sqrt{\tan^{2} \rho_{V} + \tan^{2} \rho_{H} + 1}}, \frac{\tan \rho_{H}}{\sqrt{\tan^{2} \rho_{V} + \tan^{2} \rho_{H} + 1}}, \frac{1}{\sqrt{\tan^{2} \rho_{V} + \tan^{2} \rho_{H} + 1}}\right)^{T}$$
(3.14)

It has been mentioned in Sect. 2.3.1 that the *X*-component of the emergent beam vector is given by $x_{tf} = \cos \beta_{t2}$. Thus, the angle β_{t2} between the incident beam to prism 2 and the positive *Z*-direction is written as $\beta_{t2} = \arccos x_{tf}$. Substituting $i_1 = -\theta_{t1}$ into (2.15), the angle β_{t2} can also be determined by

$$\beta_{t2} = \frac{\pi}{2} + \delta_1 = \frac{\pi}{2} + \arcsin(\sin\theta_{t1}\cos\alpha + \sin\alpha\sqrt{n^2 - \sin^2\theta_{t1}}) - \theta_{t1} - \alpha \quad (3.15)$$

According to (3.15), the angle β_{t2} is only associated with the tilting angle θ_{t1} of prism 1, which accounts for the functional relation expressed as $\beta_{t2} = f(\theta_{t1})$. Then the variable separation method is applied to (3.15) in order to solve the tilting angle θ_{t1} inversely, namely to establish the relation expressed as $\theta_{t1} = f^{-1}(\beta_{t2})$.

Similarly, with the horizontal field angle given by $\rho_H = \arctan(y_{tf}/z_{tf}) = \gamma_{t2} - \delta_2 = -\delta_2$, the beam deviation angle δ_2 due to prism 2 is deduced from $\delta_2 = -\rho_H$. Concerning $i_2 = \gamma_{t2} + \alpha + \theta_{t2} = \alpha + \theta_{t2}$, the angle δ_2 can also be determined by

$$\delta_2 = \theta_{t2} - \arcsin\left[\sin(\alpha + \theta_{t2})\cos\alpha - \sin\alpha\sqrt{\overline{n_2}^2 - \sin^2(\alpha + \theta_{t2})}\right]$$
 (3.16)

According to (3.16), the beam deviation angle δ_2 is merely dependent on the tilting angle θ_{t2} of prism 2, which accounts for the functional relation expressed as $\delta_2 = g(\theta_{t2})$. Then the tilting angle θ_{t2} can be inversely solved by separating the variables in (3.16), expressed as $\theta_{t2} = g^{-1}(\delta_2)$.

Therefore, the tilting angle θ_{t1} of prism 1 is expressed in the analytical form as follows [1]:

$$\theta_{t1} = \frac{1}{2} \left(k_2 \pi + (-1)^{k_2} \arcsin \frac{n^2 - \frac{l_1^2 + l_2^2 + 1}{2}}{\sqrt{(l_1 l_2)^2 + \left(\frac{l_1^2 + 1 - l_2^2}{2}\right)^2}} + k_1 \pi + \arctan \left(\frac{l_1^2 + 1 - l_2^2}{2l_1 l_2}\right) \right)$$
(3.17a)

where $\theta_{t1} \in \left[\theta_{t\min}, \theta_{t\max}\right](k_1, k_2 \in Z), \ l_1 = (\cos m_t - \cos \alpha)/\sin \alpha, \ l_2 = \sin m_t/\sin \alpha, \ m_t = \beta_{t2} + \alpha - \pi/2, \ \text{and} \ \beta_{t2} = \arccos x_{tf} = \arccos\left(\rho_V / \sqrt{\tan^2 \rho_V + \tan^2 \rho_H + 1}\right).$

The tilting angle θ_{t2} of prism 2 is analytically expressed as

$$\theta_{t2} = \frac{1}{2} \left(k_4 \pi + (-1)^{k_4} \arcsin \frac{\frac{\overline{n_2}^2 - \frac{l_3^2 + l_4^2 + 1}{2}}{\sqrt{(l_3 l_4)^2 + \left(\frac{l_3^2 + 1 - l_4^2}{2}\right)^2}} - 2\alpha + k_3 \pi + \arctan \left(\frac{l_3^2 + 1 - l_4^2}{2l_3 l_4}\right) \right)$$
(3.17b)

where $\theta_{t2} \in [\theta_{t\min}, \theta_{t\max}](k_3, k_4 \in Z), l_3 = (\cos \alpha - \cos(\rho_H - \alpha))/\sin \alpha$ and $l_4 = -\sin(\rho_H - \alpha)/\sin \alpha$.

2. Application of Analytical Method

Based on the above derivation, the exact solution to tilting angles of two prisms can be obtained once the emergent beam vector or the combination of vertical and horizontal field angles is known. Accordingly, the emergent beam can be steered by tilting prisms to track any moving target within the scan region.

For example, the analytical method is applied for the tilting angle curves of two prisms that can generate 5 specific target trajectories. Here the influence of the beam exiting point on the beam scan point is neglected in approximation. In simulation, the involved parameters of each prism are wedge angle $\alpha=10^\circ$, refractive index n=1.517 and tilting angle range within $0^\circ-10^\circ$. The distance from prism 2 to the screen is set to $D_2=1$ mm, and the beam scan speed remains uniform throughout a period of 10 s. Note that the target trajectories are observed in the positive Z-direction, and

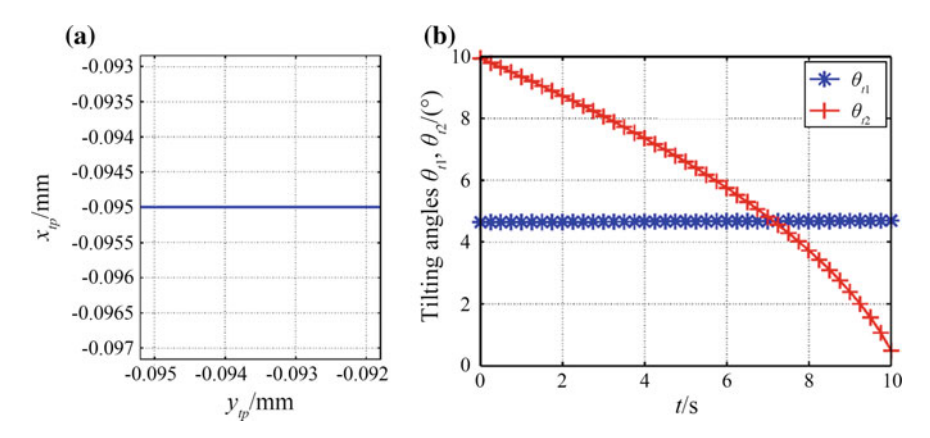


Fig. 3.28 A linear scan case, where **a** shows the linear target trajectory parallel to the *Y*-axis and **b** manifests the inverse solution obtained by analytical method

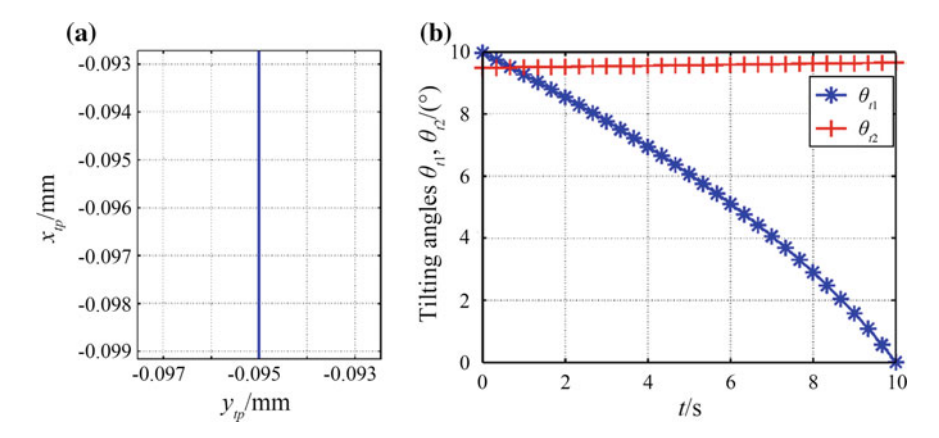


Fig. 3.29 A linear scan case, where **a** shows the linear target trajectory parallel to the *X*-axis and **b** manifests the inverse solution obtained by analytical method

the positive *X*- and *Y*-directions are defined to be upward and rightward, respectively (Figs. 3.28, 3.29, 3.30, 3.31 and 3.32).

Case 1: a linear target trajectory given by x = -0.0950, $y \in [-0.095200, -0.091797]$.

Case 2: a linear target trajectory given by y = -0.0950, $x \in [-0.099157, -0.092715]$.

Case 3: a linear target trajectory given by $y = \frac{x}{2} - 0.0455$, $x \in [-0.099157, -0.092715]$.

Case 4: a parabolic target trajectory given by $y = 300(x + 0.0960)^2 - 0.0950$, $x \in [-0.099157, 0.092715]$.

Case 5: a circular target trajectory given by $(x + 0.0960)^2 + (y + 0.0935)^2 = 0.0015^2$.

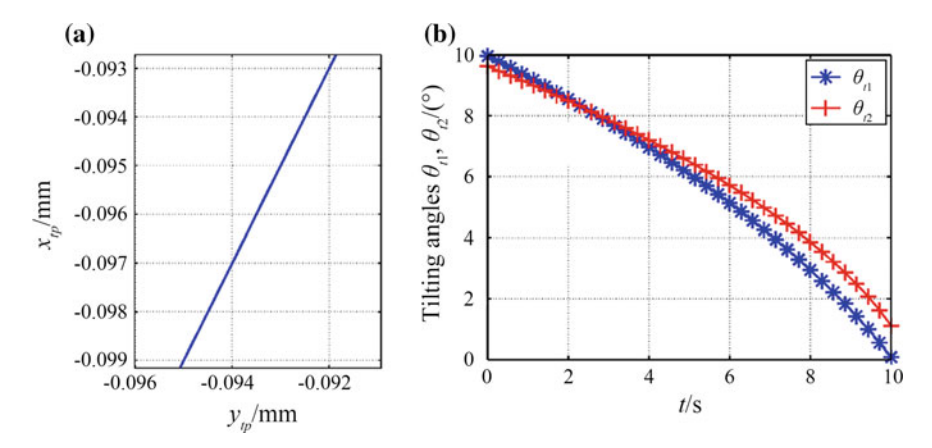


Fig. 3.30 A linear scan case, where a shows the inclined linear target trajectory and b manifests the inverse solution obtained by analytical method

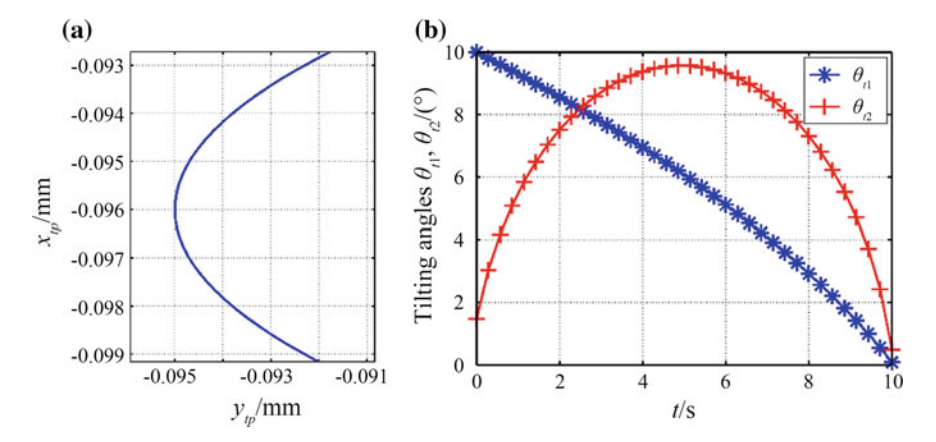


Fig. 3.31 A parabolic scan case, where a shows the parabolic target trajectory and b manifests the inverse solution obtained by analytical method

3.2.2 Lookup-Table Method

1. Principle of Lookup-Table Method

A lookup-table method [1] is introduced in this Section to solve the inverse problem of tilting double prisms in near field. The principle of this method is in the mapping relation from the target coordinates to the tilting angles of two prisms. Without loss of generality, the lookup-table method can be implemented in three steps.

Firstly, establish a lookup table. For tilting double prisms, the beam scan point is associated with the structural and positional parameters, including the tilting angles θ_{t1} and θ_{t2} , the wedge angle α , the central-axis thickness d, the distance D_1 between

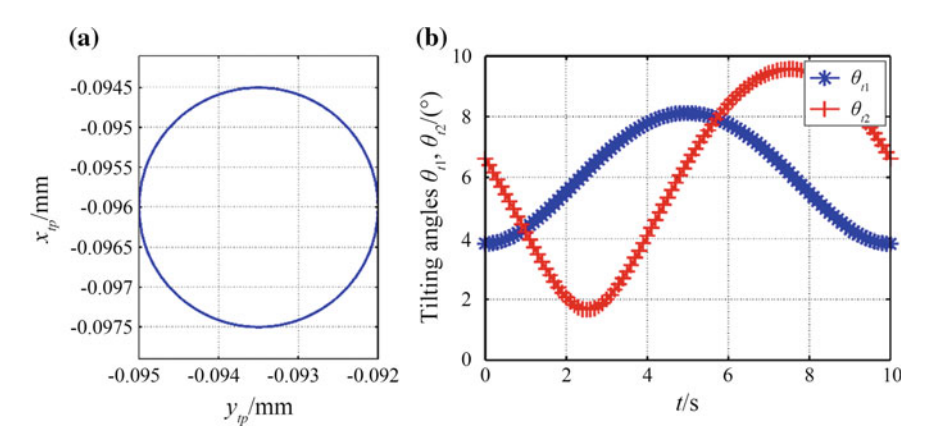


Fig. 3.32 A circular scan case, where a shows the circular target trajectory and b manifests the inverse solution obtained by analytical method

two prisms and the one D_2 from prism 2 to the screen. Those parameters as well as the tilting angle range $\theta_{tmin} - \theta_{tmax}$ are usually specified by the application requirements. For the purpose of discretization, every revolution of tilting motion is further divided into $(\theta_{tmax} - \theta_{tmin})/\theta_{tre}$ steps, where θ_{tre} represents the tilting step angle dependent on the beam scan precision. Using the formulae in Sect. 2.5.2, the coordinates (x_{tp}, y_{tp}, z_{tp}) of beam scan point can be deduced from the combination of tilting angles $(\theta_{t1}, \theta_{t2})$, each of which is limited by $\theta_{tmin} - \theta_{tmax}$ with a resolution of θ_{tre} . The correlated $(\theta_{t1}, \theta_{t2})$ and (x_{tp}, y_{tp}, z_{tp}) are thus written to the lookup table.

Secondly, search the lookup table. With a target trajectory given by y = f(x), a sequence of target points, expressed as (X_{tp}, Y_{tp}, Z_{tp}) , can be taken from the trajectory at a certain sampling frequency, where $Z_{tp} = D_1 + D_2$. Then the lookup table is searched for a known point closest to each target point. In other words, the coordinates (x_{tp}, y_{tp}, z_{tp}) of the known point will minimize the error given by

 $\Delta = \sqrt{(X_{tp} - x_{tp})^2 + (Y_{tp} - y_{tp})^2 + (Z_{tp} - z_{tp})^2}$. According to the coordinates (x_{tp}, y_{tp}, z_{tp}) , it is convenient to find the related tilting angles of two prisms in the lookup table, which are regarded as the inverse solution to the desired target point in approximation.

Finally, process data. The function interpolation or curve fitting operation is performed on the discrete tilting angles (θ_{t1} , θ_{t2}) obtained by lookup-table method, which leads to a continuous and time-dependent function of prism orientations.

2. Application of Lookup-Table Method

In simulation, the involved geometrical parameters are $\alpha=10^{\circ}$, n=1.517, $D_p=80$ mm, $d_0=5$ mm, $D_1=100$ mm and $D_2=400$ mm. The tilting motion of each prism is limited within the angular range of $0^{\circ}-10^{\circ}$, which can be further divided into 2500 steps upon setting the tilting step angle to $\theta_{tre}=0.004^{\circ}$. Note that

the Z-coordinate of beam scan point is constant at $Z_{tp} = z_{tp} = D_1 + D_2 = 500$ mm in such a tilting double-prism system.

The tilting angles θ_{t1} and θ_{t2} can be combined in random with the Meshgrid function in Matlab, and these combinations are utilized to establish a 2500×2500 matrix. The values of (x_{tp}, y_{tp}) that corresponds to each element of the matrix are determined by the formulae in Sect. 2.5.2 and then written to the lookup table. Accordingly, a completed lookup table contains data with the size of $2500 \times 2500 \times 2 = 1.25 \times 10^7$.

A linear scan case parallel to the *Y*-axis is taken for example in order to expound the lookup table process, where the beam scan operation remains uniform throughout a period of 10 s. At the sampling frequency of 40 Hz, there are 400 sample points extracted from the target trajectory. Note that only 40 sample points are displayed in a concise manner. Once the coordinates (X_{tp}, Y_{tp}) of each sample point are deduced from the target trajectory given by x = -45, $y \in [-39.63, -37.44]$, it is required to search the lookup table for the coordinates (x_{tp}, y_{tp}) that will minimize the error given by $\Delta = \sqrt{(X_{tp} - x_{tp})^2 + (Y_{tp} - y_{tp})^2}$, as well as the corresponding row number *N* and column number *M* in the table. The consequent tilting angles are determined by $\theta_{t1} = \theta_{tre} \times (M - 1)$ and $\theta_{t2} = \theta_{tre} \times (N - 1)$, which are written in the combined form of $(\theta_{t1}, \theta_{t2})$ to establish a matrix. This matrix contains a sequence of approximate tilting angles required for the target trajectory. All discrete elements in the matrix can be connected together using a segmented low-order interpolation method. Therefore, the tilting angle curves of two prisms are further obtained in approximation.

By the proposed lookup-table method, the inverse solutions to 5 specific target trajectories are simulated as follows, respectively.

```
Case 1: a linear target trajectory given by x = -45, y \in [-39.63, -37.44].
```

Case 2: a linear target trajectory given by y = -38, $x \in [-47.17, -44.82]$.

Case 3: a linear target trajectory given by $y = \frac{x}{2} - 15.5$, $x \in [-47.17, -44.82]$.

Case 4: a parabolic target trajectory given by $y = (x+45.995)^2 - 39$, $x \in [-47.17, -44.82]$.

Case 5: a circular target trajectory given by $(x + 45.995)^2 + (y + 38.535)^2 = 1$.

Figure 3.33 indicates that the beam scan operation along the linear trajectory parallel to the Y-axis is mainly accomplished by tilting prism 2 within the angular range from 10° to 0.3° . There is a nonlinear relation between the motion profile of prism 2 and the target trajectory. The tilting angle of prism 1 still varies within a certain range of 0.05° due to the slight coupling effect of prism 1 and prism 2. As shown in Fig. 3.34, the tilting angle of prism 1 ranges from 10° to 0° and that of prism 2 varies within a certain range of 0.16° in order to perform the beam scan operation along the linear trajectory parallel to the X-axis.

Figure 3.35 presents the tilting angle curves of prism 1 and prism 2 in correspondence to the inclined linear target trajectory. It is clarified that the difference in the slope of linear trajectory will lead to various tilting angle curves of two prisms. Given the parabolic target trajectory, the inverse solution for tilting prisms is plotted in Fig. 3.36. Since the parabolic trajectory is symmetric about x = -0.096, there is

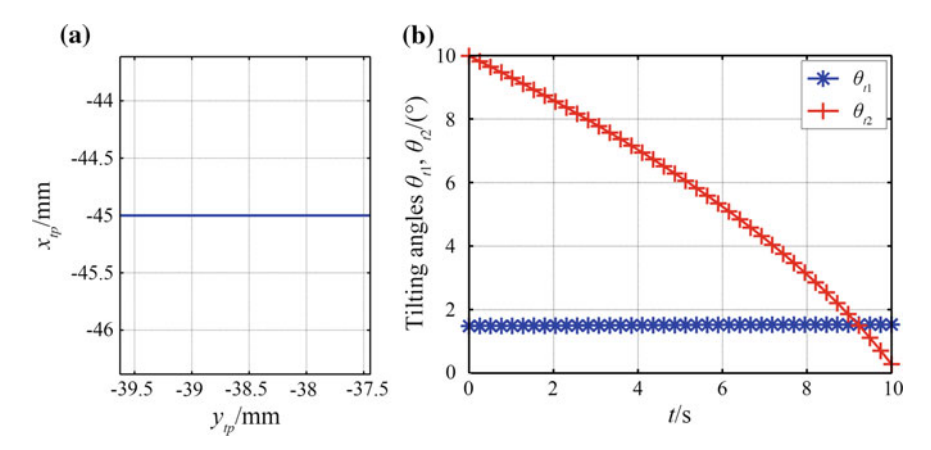


Fig. 3.33 A linear scan case, where **a** shows the linear target trajectory parallel to the *Y*-axis and **b** manifests the inverse solution obtained by lookup-table method

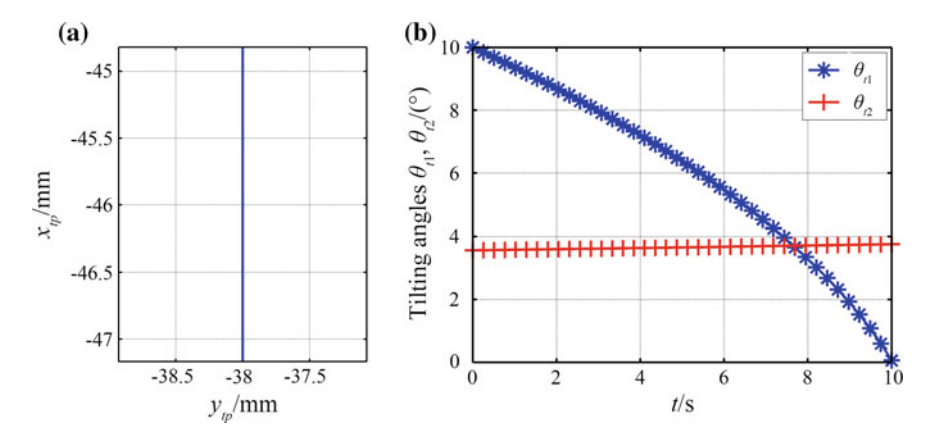


Fig. 3.34 A linear scan case, where **a** shows the linear target trajectory parallel to the *X*-axis and **b** manifests the inverse solution obtained by lookup-table method

approximate symmetry in the tilting angle curve of prism 2, whereas the tilting angle of prism 1 decreases monotonously from 10° to 0° . Similarly in Fig. 3.37, the circular target trajectory is completely symmetric, which accounts for the periodic variation in the tilting angle curves of both prism 1 and prism 2. In addition, each prism should stop tilting motion at its initial orientation because the circular trajectory is in a closed form.

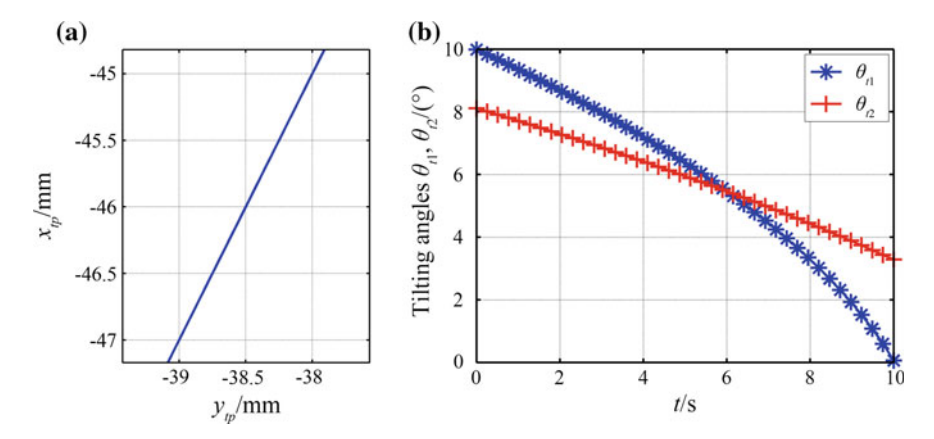


Fig. 3.35 A linear scan case, where a shows the inclined linear target trajectory and b manifests the inverse solution obtained by lookup-table method

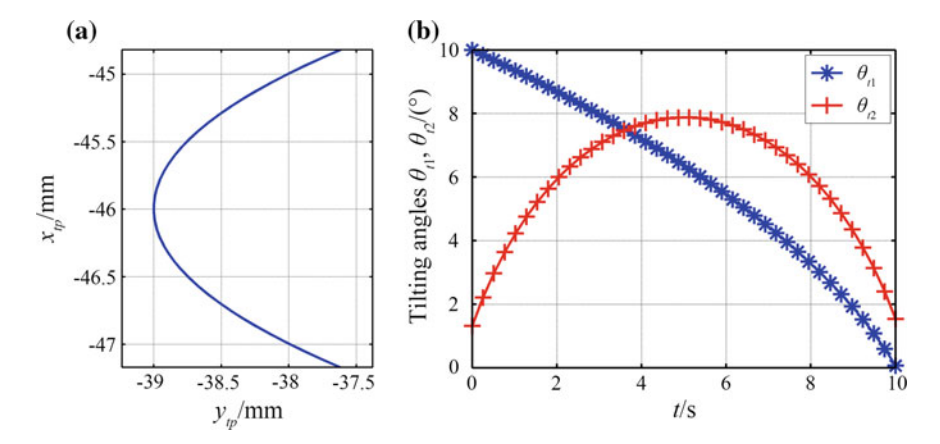


Fig. 3.36 A parabolic scan case, where a shows the parabolic target trajectory and b manifests the inverse solution obtained by lookup-table method

3.2.3 Binary Lookup-Table Method

1. Principle of Binary Lookup-Table Method

It has been previously demonstrated that the tilting angle θ_{t1} of prism 1 has primary impacts on the vertical field angle ρ_V of the emergent beam and the *X*-coordinate of beam scan point, while the tilting angle θ_{t2} of prism 2 mainly influence the horizontal field angle ρ_H of the emergent beam and the *Y*-coordinate of beam scan point. Such a functional relation between the tilting angles of two prisms and the final beam deviation remains monotonous within the angular range of $\theta_{tmin} - \theta_{tmax}$. Therefore, a binary search procedure that can decouple the beam deviation effects of prism 1

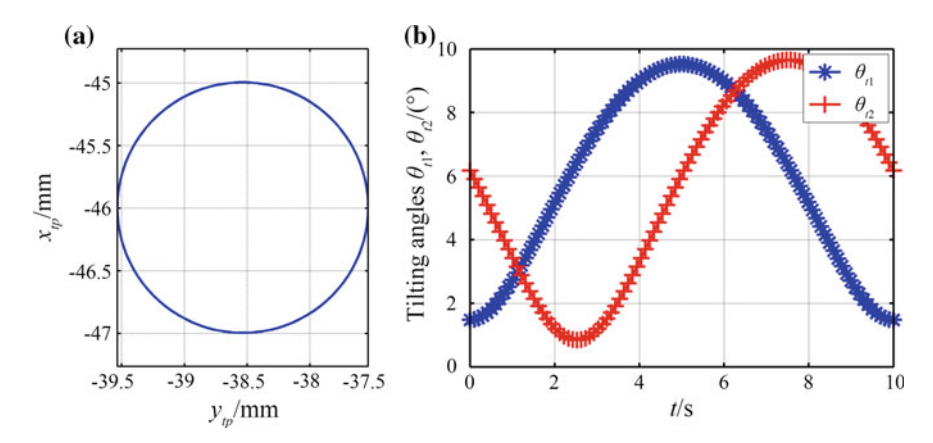


Fig. 3.37 A circular scan case, where a shows the circular target trajectory and b manifests the inverse solution obtained by lookup-table method

and prism 2 is introduced to the lookup-table method. Compared with lookup-table method, the major difference in this binary lookup-table method is that the search procedure can be well optimized to enhance its solving efficiency.

To help elucidate this optimized method, there should be a further description about the binary search procedure. For example, given a monotonous decreasing function, the procedure is feasible to search the definition domain for a specific node corresponding to the desired function value. The initial search range, namely the definition domain, is divided into two equal sections. If the function value at the division node is smaller than the desired one, the search range should be replaced by the former section of the initial search range. Otherwise, the latter section is considered as the new search range. Through a few iterations, the search range is narrowed down in order to approach the specific node to an acceptable extent.

Once the above details are accounted for, the binary lookup-table method is summarized as follows for a given target point. Accordingly, the inverse solution to any target trajectory can be obtained by applying the method to a sequence of sample points on the trajectory.

Firstly, the first actual point at each row of the lookup table is involved in the comparison with the target point. The row number M of the one closest to the target point in the X-direction can be determined through binary search procedure. Then, all the actual points at row M of the lookup table are utilized for the comparison with the target point. The column number N of the one closest to the target point in the Y-direction can be determined by binary search as well. The attention is finally focused on the actual point at row M and column N of the lookup table, denoted by T_{MN} . Other relevant points, including $T_{(M-1)(N-1)}$, $T_{(M-1)N}$, $T_{(M-1)(N+1)}$, $T_{M(N-1)}$, $T_{(M+1)(N-1)}$, $T_{(M+1)(N-1)}$, and $T_{(M+1)(N+1)}$, are taken in the neighborhood of the point T_{MN} . Among these actual points, the one closest to the target point is required

to obtain the corresponding tilting angles of two prisms, which are considered as one set of inverse solution to the target point.

It is evident that the complexity of calculation is greatly reduced by the binary lookup-table method. This method is outstanding with the solving efficiency superior to that of the lookup-table method. For example, only hundreds of calculating operations are demanded for the inverse solution to one target point, if the size of lookup table is set to 1001×1001 .

2. Application of Binary Lookup-Table Method

As shown in Figs. 3.38 and 3.39, the peanut-like and peach-like scan cases are presented to evaluate the solving accuracy and efficiency of the binary lookup-table method. The geometrical parameters of the tilting double-prism system are $\alpha=10^\circ$, n=1.517, $D_p=80$ mm, $d_0=5$ mm, $D_1=100$ mm and $D_2=400$ mm. Both prisms are limited within the tilting angle range of $0^\circ-10^\circ$. On these basis, a 1001×1001 lookup table with the step angle of 0.01° is established for search.

Case 1: a peanut-like target trajectory given by
$$\begin{cases} x = \left(0.3 + 0.64 \sin^2 t\right) \cos t - 46 \\ y = \left(0.3 + 0.64 \sin^2 t\right) \sin t - 38.5 \end{cases},$$
 $t \in [0, 2\pi].$ Case 2: a peach-like target trajectory given by
$$\begin{cases} x = 0.6(1 + \cos t) \cos t - 46.6 \\ y = 0.6(1 + \cos t) \sin t - 38.5 \end{cases},$$
 $t \in [0, 2\pi].$

As one common issue between traditional and binary lookup-table methods, establishing a lookup table takes much storage space and most calculation time, which approaches 72 s in the above cases. Worth noting is that 400 sample points are extracted from the target trajectory in every scan case. Based on the same lookup table, there are 0.0817 and 0.0805 s spent on finding the inverse solutions to peanut-like and peach-like target trajectories, respectively. In addition, the average solving

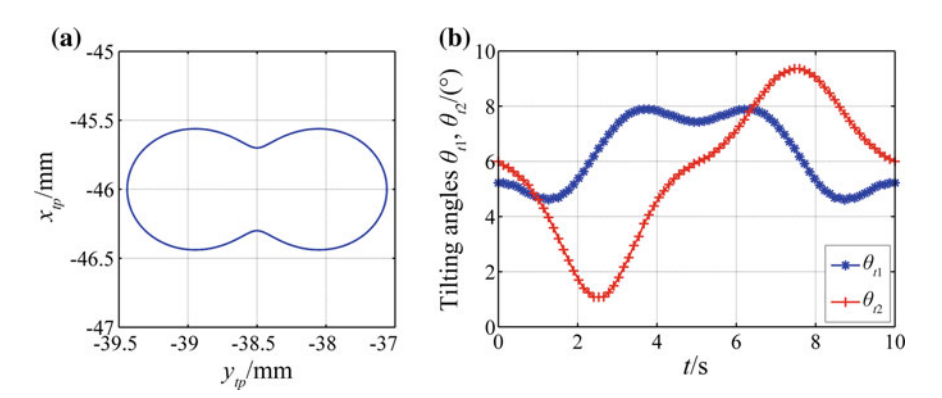


Fig. 3.38 A peanut-like scan case, where **a** shows the peanut-like target trajectory and **b** manifests the inverse solution obtained by binary lookup-table method

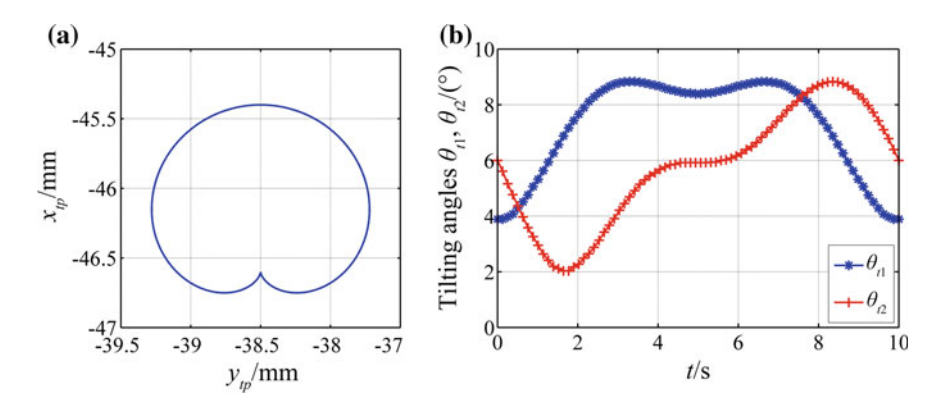


Fig. 3.39 A peach-like scan case, where a shows the peach-like target trajectory and b manifests the inverse solution obtained by binary lookup-table method

accuracy at all target points is determined to be 0.0046 mm in the former case and 0.0043 mm in the latter one. It is validated that the binary lookup-table method offers a more efficient approach to solve the inverse problem of tilting double prisms, without any loss of solving accuracy.

3.2.4 Region-Converging Iterative Method

1. Principle of Region-Converging Iterative Method

Owing to the nature of lookup-table methods, the accuracy and efficiency of inverse solving process are greatly concerned with the size of lookup table. Either traditional or binary lookup-table method should allocate most operation time to establish a lookup table. To overcome these inherent shortcomings, however, requires more attention on developing a novel method for inverse solution. We thus proposes a region-converging iterative method based on beam scan properties in the tilting double-prism system. This method can successively narrow down the possible range of each prism orientation until the consequent beam scan point comes close enough to the target point.

Figure 3.40 shows the iterative procedure where the tilting angle of each prism converges from its initial range to the final solution. For any target point given by $P_d = (x_d, y_d)$, the procedure can be further demonstrated as follows.

Initially, there is a two-dimensional search region specified by the tilting angle ranges of prism 1 and prism 2, denoted by $\theta_{t1\min}-\theta_{t1\max}$ and $\theta_{t2\min}-\theta_{t2\max}$, respectively. Then the search region is equally divided into 9 sub-regions by introducing 16 specific nodes. These nodes are labeled by T_{ij} , where i and j are both integers ranging from 1 to 4. Following the formulae in Sect. 2.5.2, the tilting angles of two prisms at the node T_{ij} are utilized to determine the consequent beam scan point

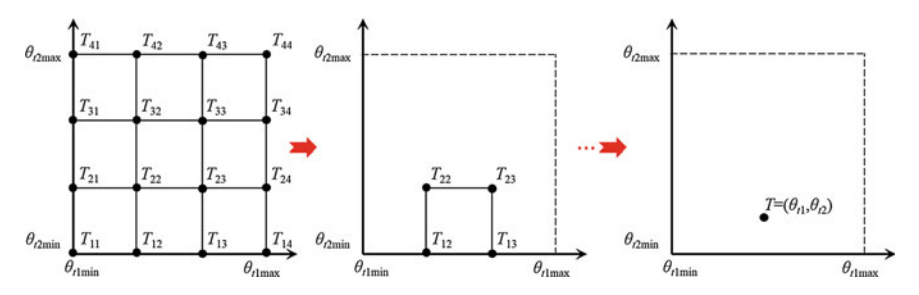


Fig. 3.40 Schematic diagram illustrating the principle of region-converging iterative method

 $P_{ij} = (x_{ij}, y_{ij})$. In order to distinguish the sub-region at which the inverse solution to the target point P_d locates, the coordinates of beam scan point P_{ij} at each division node are substituted into the judging conditions shown in (3.18). If these conditions are satisfied, the search region can be narrowed to the sub-region specified by four vertex nodes T_{ij} , $T_{(i+1)j}$, $T_{(i+1)(j+1)}$ and $T_{i(j+1)}$.

$$\begin{cases} (x_{ij} - x_d) [x_{(i+1)(j+1)} - x_d] < 0\\ (y_{ij} - y_d) [y_{(i+1)(j+1)} - y_d] < 0 \end{cases}, \quad i, j = 1, 2, 3$$
(3.18)

Sometimes it happens that none of the beam scan points at 16 division nodes satisfies the conditions of (3.18). Hence, there should be extra effort to narrow the search region, and more importantly, to keep the iterative procedure converging. Among 9 sub-region centers in the current search region, the one which corresponds to a beam scan point closest to the target point P_d is applied to locate the next search region. In addition, the next search region is required with a side length larger than one sub-region, which guarantees the availability of inverse solution.

After finite iterations in the above fashion, the search region becomes converging enough to achieve the desired accuracy of inverse solving process. Therefore, the inverse solution to the given target point can be obtained once the side length of search region is under a prescribed threshold δ , namely the solving accuracy.

2. Application of Region-Converging Iterative Method

The triangular and rose-like scan cases are, respectively, presented in Figs. 3.41 and 3.42 to validate the performance of our region-converging iterative method. In simulation, the geometrical parameters of the tilting double-prism system are still set to $\alpha=10^\circ$, n=1.517, $D_p=80$ mm, $d_0=5$ mm, $D_1=100$ mm and $D_2=400$ mm, and the tilting angle range of each prism is limited within $0^\circ-10^\circ$. The desired solving accuracy remains to be $\delta=0.001$ mm in both cases.

Case 1: a triangular target trajectory given by
$$\begin{cases} x = 0.35(2\cos t + \cos 2t) - 46.6 \\ y = 0.35(2\sin t - \sin 2t) - 38.5 \end{cases}$$
, $t \in [0, 2\pi]$.

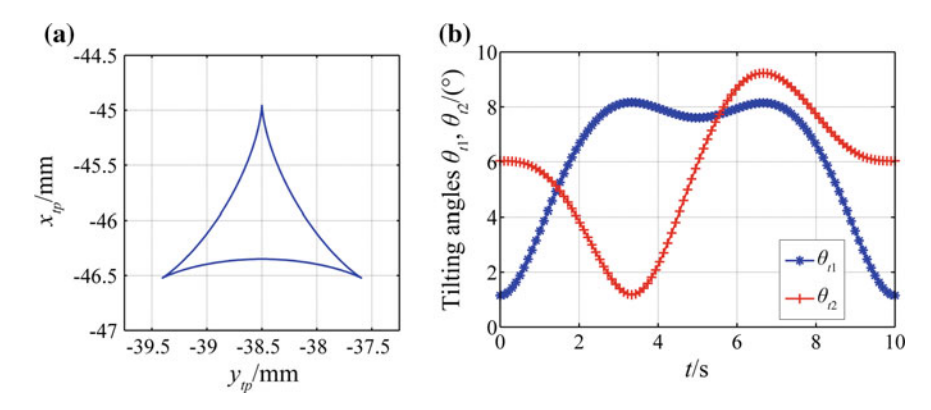


Fig. 3.41 A triangular scan case, where a shows the triangular target trajectory and b manifests the inverse solution obtained by region-converging iterative method

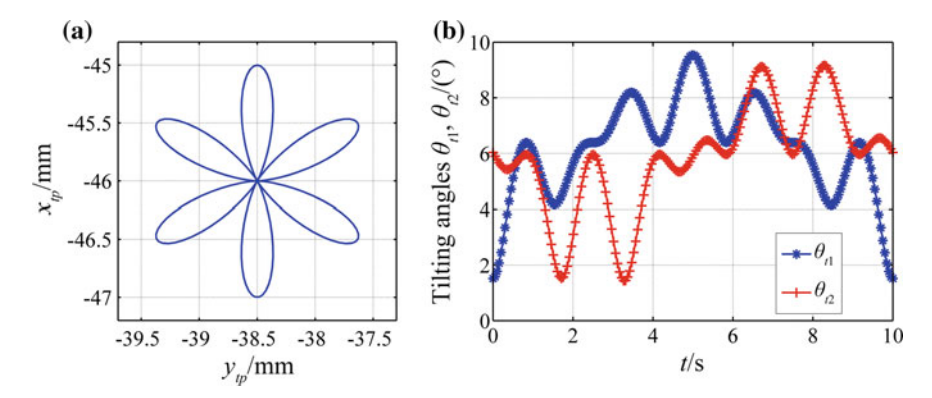


Fig. 3.42 A rose-like scan case, where a shows the rose-like target trajectory and b manifests the inverse solution obtained by region-converging iterative method

Case 2: a rose-like target trajectory given by
$$\begin{cases} x = 0.5 \cos t(\cos 6t + 1) - 46 \\ y = 0.5 \sin t(\cos 6t + 1) - 38.5 \end{cases}, t \in [0, 2\pi].$$

There are 400 sample points extracted from both triangular and rose-like target trajectories for simplification. Without establishing a lookup table, the region-converging iterative method requires 4.7951 and 5.0559 s to find inverse solutions in the above cases, respectively. It thus proves that such an iterative method is advantageous in its impressive solving accuracy and stability, as well as the greatly enhanced solving efficiency for either simple or complex target trajectory. Nevertheless, the region-converging iterative method will be less efficient than the binary lookup-table method, once the establishment of lookup table takes a relatively small part of the total computation time.

3.3 Summary 151

3.3 Summary

This chapter overviews several representative methods that can solve the inverse problem of rotating or tilting double prisms, exemplified by a variety of implementation cases. With regard to rotating double prisms, the two-step method [4, 10] is reviewed in a logical and detailed manner, which generates two sets of approximate prism orientations during one revolution. In order to obtain more precise inverse solutions, the lookup-table method is step-by-step demonstrated on the basis of the mapping relation from prism orientations to the beam scan position. Unfortunately, the lookup-table method has some shortcomings, such as limited solving accuracy and large time consumption. Aiming at dynamic target tracking applications, the iterative method that combines two-step method with non-paraxial ray tracing procedure is proposed to inversely solve the rotation angles of two prisms in real time. Since the iterative method requires much less computation to achieve superior solving accuracy and efficiency, it can serve as a potential approach to track dynamic targets. In addition, the damped least-squares iterative method is introduced for more generality to overcome the inverse problem of rotating double prisms, where the incident beam may be aligned or inclined with respect to the optical axis of the system. As for tilting double prisms, the analytical method is clearly elucidated by a mathematical derivation process from the horizontal and vertical field angles of the emergent beam to the consequent tilting angles of two prisms. Then the lookup-table method suited with tilting double prisms is also expounded to obtain inverse solution with higher precision. For target tracking applications, the binary lookup-table method is further developed, which can greatly improve the solving efficiency of the lookup-table method using binary search procedure. Moreover, the region-converging iterative method is presented so that the two-dimensional search region for inverse solution can be narrowed down at each iteration. Simulation results has proven this method as one of the most precise approaches to the inverse solution for tilting double prisms.

References

- Li AH, Ding Y, Bian YM et al (2014) Inverse solutions for tilting orthogonal double prisms. Appl Opt 53(17):3712–3722
- 2. Zhou Y, Lu YF, Hei M et al (2013) Motion control of the wedge prisms in Risley-prism-based beam steering system for precise target tracking. Appl Opt 52(12):2849–2857
- Tao XD, Cho H, Janabi-Sharifi F (2008) Active optical system for variable view imaging of micro objects with emphasis on kinematic analysis. Appl Opt 47(22):4121–4132
- Amirault CT, DiMarzio CA (1985) Precision pointing using a dual-wedge scanner. Appl Opt 24(9):1302–1308
- 5. Gao XJ (2015) Research on rotating double-prism dynamic tracking system. School of Mechanical Engineering, Tongji University, Shanghai
- Ding Y (2014) Mathematical modeling and simulation analysis of double-prism scanning system. Tongji University, Shanghai
- Li AH, Gao XJ, Ding Y (2014) Comparison of refractive rotating dual-prism scanner used in near and far field. Proc SPIE 9192:919216-919216-13

- 8. Li AH, Gao XJ, Sun WS et al (2015) Inverse solutions for a Risley prism scanner with iterative refinement by a forward solution. Appl Opt 54(33):9981–9989
- 9. Li AH, Liu XS, Sun WS (2017) Forward and inverse solutions for three-element Risley prism beam scanners. Opt Express 25(7):7677–7688
- Li YJ (2011) Closed form analytical inverse solutions for Risley-prism-based beam steering systems in different configurations. Appl Opt 50(22):4302

 –4309

Chapter 4 Performance Characterization of Double-Prism Multi-mode Scanning



Abstract Crucial issues that influence the beam scan performance are thoroughly investigated in both rotating and tilting double-prism systems. For quantitative analysis, the nonlinearity problem is described with the motion variables of two prisms during a dynamic beam scan process. The control singularity is well illustrated on the basis of mapping relation between beam steering rate and beam scan speed. Through mathematical derivation, the distortion of any beam emerging from rotating or tilting double prisms is determined to evaluate the stretching and squeezing effects on beam shape. The error modeling method is further introduced to help demonstrate the potential sources of beam pointing error in a double-prism system.

In this chapter, we will introduce the double-prism multi-mode beam scan performance, including four issues of nonlinear relation, singularity issue, beam distortion and beam scan error modeling. First, because of the nonlinear relation between the rotation or tilting angles of two prisms and the final beam deviation angle [1-3], the reasonable control strategies should be formulated to facilitate the nonlinear motion of two prisms. Second, it is the singularity issue. When the double-prism system is used to track any target near the edge of beam scan region, the rotating double prisms are required with infinite angular velocities, which poses significant challenges to control the overall system in real time [1]. Third, induced by the refraction of double prisms, the beam distortion may introduce undesired variation to the far-field beam energy distribution, and thus produce adverse effects on the application of double prisms for directional beam energy. The last, it is of great importance and necessity to establish the beam scan error model of double-prism multi-mode system with different motion types, considering the influence of both optical and mechanical errors on the beam propagation. Such an error model will offer much convenience to quantitatively demonstrate the high-precision beam scan mechanism using double prisms.

4.1 Nonlinearity Issue

According to the beam propagation model through rotating double prisms, the deviation angle of emergent beam is determined by the motion status and the structural parameters of the system. Consequently, the beam deviation law can be expressed as nonlinear relations in three aspects [1, 3]: (1) nonlinear relation between the rotation angles of prisms and the beam deviation angle; (2) that between the rotation angular velocities of prisms and the beam steering rate; and (3) that between the rotation angular accelerations of prisms and the angular acceleration of beam deviation.

In order to investigate the nonlinearity issue in a rotating double-prism system, we take the first set of inverse solution for example. As illustrated in Sect. 3.1.1, the rotation angle θ_{r1} of prism 1 is limited by $0^{\circ}-360^{\circ}$, and the relative rotation angle $\Delta\theta_r$ of two prisms varies within $-180-0^{\circ}$.

The pitch angle ρ of emergent beam is generally resolved into the *X*-component ρ_X and the *Y*-component ρ_Y , defined as [3]

$$\rho_X = \rho \, \cos \varphi, \, \rho_Y = \rho \, \sin \varphi \tag{4.1}$$

From (2.11), the functional relation of the components ρ_X and ρ_Y with respect to the rotation angles θ_{r1} and θ_{r2} of two prisms can be obtained as shown in Fig. 4.1 [3], where each prism has the wedge angle $\alpha=15^{\circ}$ and the refractive index n=1.517.

It is evident in Fig. 4.1 that prism orientations θ_{r1} and θ_{r2} are nonlinear with the components ρ_X and ρ_Y of pitch angle, which reduces the availability of inverse solutions by any analytical method. Therefore, those numerical techniques introduced in Sect. 3.1 are usually employed to solve the inverse problem of rotating double prisms.

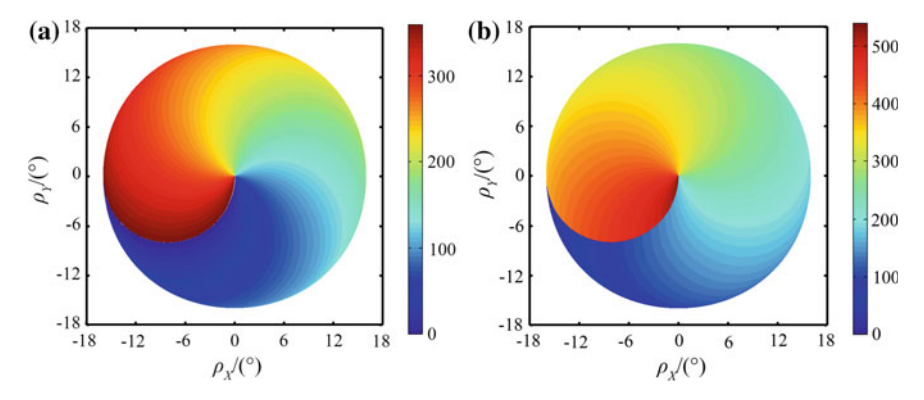


Fig. 4.1 Nonlinearity between the rotation angles of two prisms and the beam deviation angle, where **a** shows the variation of ρ_X and ρ_Y with θ_{r1} , and **b** shows the variation of ρ_X and ρ_Y with θ_{r2}

In order to reveal the nonlinearity between the rotation angular velocities of two prisms and the steering rate of the emergent beam, the beam steering rate is resolved into the tangential component ω_{ft} and the radial component ω_{fr} [1, 3]. The two components are, respectively, determined by the time derivatives of azimuth angle and pitch angle, as follows [1, 3]

$$\omega_{ft} = \frac{\mathrm{d}\varphi}{\mathrm{d}t}, \omega_{fr} = \frac{\mathrm{d}\rho}{\mathrm{d}t} \tag{4.2}$$

According to the two-step method in Sect. 3.1.1, once the pitch angle reaches its desired value at the first step, the desired azimuth angle can be achieved by synchronous rotation of two prisms at the second step. In other words, for the purely tangential motion of a scan beam, the rotation angular velocities ω_{r1} and ω_{r2} of two prisms are required to accord with the tangential beam steering rate ω_{ft} . Thus, we can just consider the relation of the angular velocities ω_{r1} and ω_{r2} with respect to the radial beam steering rate ω_{fr} , as shown in Fig. 4.2. Note that the wedge angle of each prism is set to $\alpha = 5^{\circ}$, 10° and 15° in turn. The pitch angle ρ of the emergent beam ranges from 0° to the maximum ρ_{max} , while the azimuth angle φ remains invariable.

Figure 4.2 shows that the rotation angular velocities ω_{r1} and ω_{r2} of two prisms vary severely with the pitch angle ρ increasing from 0° to ρ_{max} . As the pitch angle ρ approaches ρ_{max} , the ratios of the angular velocities relative to the radial beam steering rate, denoted by ω_{r1}/ω_{fr} and ω_{r2}/ω_{fr} , even tend to infinity. These requirements will bring some significant challenges to the motion control of driving motors. Moreover, for the cooperative motion of rotating double prisms and tracking target, the prisms are required with frequently regulated angular velocities to perform beam steering operation in real-time target tracking applications.

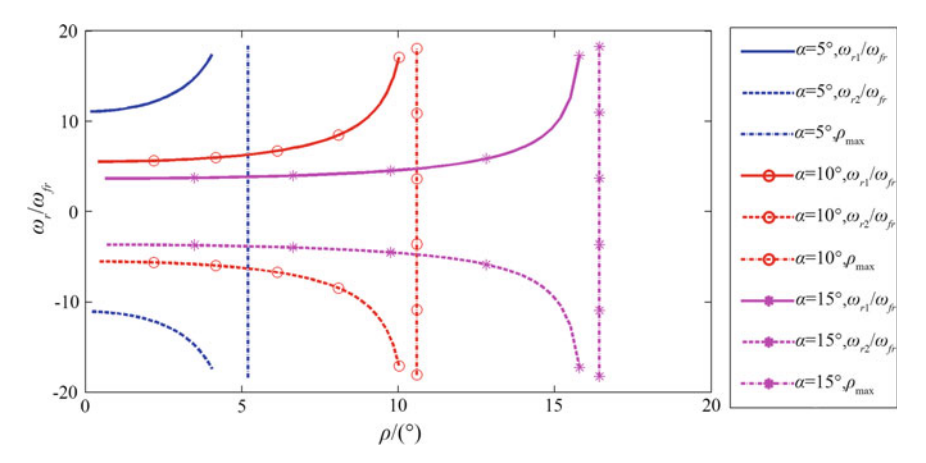


Fig. 4.2 Nonlinearity between the rotation angular velocities ω_{r1} , ω_{r2} of two prisms and the radial beam steering rate ω_{fr}

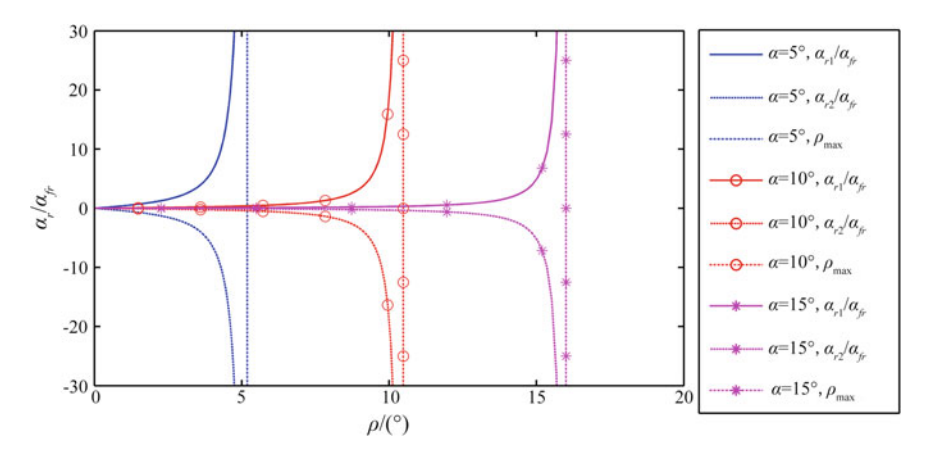


Fig. 4.3 Nonlinearity between the rotation angular accelerations α_{r1} , α_{r2} of two prisms and the radial angular acceleration α_{fr} of beam deviation

Similar to (4.2), the angular acceleration of final beam deviation can also be resolved into the tangential component α_{ft} and the radial component α_{fr} , expressed as

$$\alpha_{ft} = \frac{\mathrm{d}^2 \varphi}{\mathrm{d}t^2}, \alpha_{fr} = \frac{\mathrm{d}^2 \rho}{\mathrm{d}t^2} \tag{4.3}$$

The nonlinear relation between the angular accelerations α_{r1} , α_{r2} of two prisms and the radial angular acceleration α_{fr} of beam deviation is displayed in Fig. 4.3, where the nonlinearity appears to be more apparent. Compared to the angular velocities ω_{r1} and ω_{r2} , the angular accelerations α_{r1} and α_{r2} undergo more dramatic variation when the pitch angle ρ increases from 0° to ρ_{max} . The ratios between the angular accelerations of two prisms and the radial angular acceleration of final beam deviation, denoted by α_{r1}/α_{fr} and α_{r2}/α_{fr} , also tend to infinity as the pitch angle ρ approaches ρ_{max} . To actualize target tracking application in real time, the angular velocities and angular accelerations of two prisms should be restricted with reasonable upper tolerances, respectively, for the synchronous motion of double prisms and the target.

As for tilting double prisms, the mapping relation from the tilting angles of two prisms to the deviation angle of the emergent beam can be deduced from (2.16). Provided that only one prism is tilting while the other prism remains stationary, the vertical field angle ρ_V and the horizontal one ρ_H of the emergent beam are both dependent on the tilting angles θ_{t1} and θ_{t2} of two prisms, as shown in Fig. 4.4. Note that each prism has the wedge angle $\alpha = 10^\circ$ and the refractive index n = 1.517.

Figure 4.4 manifests the nonlinear relation from the tilting angle θ_{t1} of prism 1 to the vertical field angle ρ_V and that from the tilting angle θ_{t2} of prism 2 to the horizontal field angle ρ_H . Given the one-to-one mapping relation from the tilting

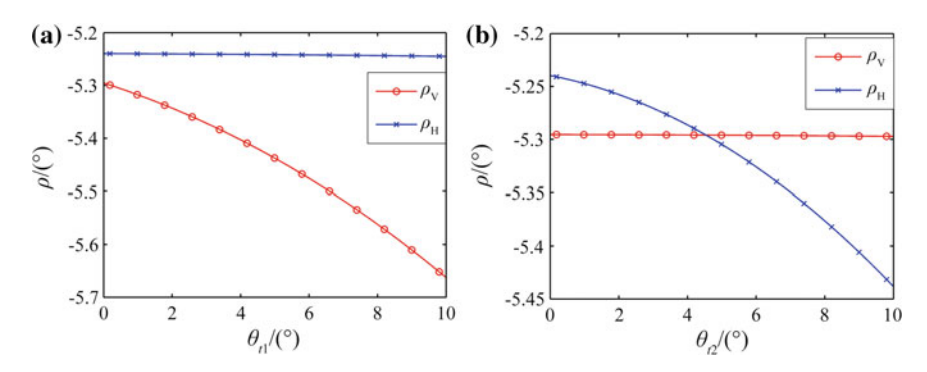


Fig. 4.4 Nonlinearity between the tilting angles of two prisms and the beam deviation angle, where **a** shows the variation of ρ_V and ρ_H with θ_{t1} , and **b** shows the variation of ρ_V and ρ_H with θ_{t2}

angles of two prisms to the deviation angle of the emergent beam, there is one unique set of inverse solution for tilting double prisms in correspondence to the desired vertical and horizontal field angles. In other words, tilting double prisms are confronted with less complicated nonlinear relation than rotating double prisms. However, it is always preferable to overcome the inverse problem of tilting double prisms using numerical techniques immune to the nonlinearity issue.

The steering rate of the emergent beam from tilting double prisms can be resolved into the vertical component ω_{fV} and the horizontal component ω_{fH} . The two components are, respectively, defined as the time derivatives of vertical and horizontal field angles, given by

$$\omega_{fV} = \frac{d\rho_V}{dt}, \omega_{fH} = \frac{d\rho_H}{dt}$$
 (4.4)

Accordingly, the nonlinear relation between the tilting angular velocities ω_{t1} , ω_{t2} of two prisms and the components ω_{fV} , ω_{fH} of beam steering rate can be plotted in Fig. 4.5. Obviously, the ratio ω_{t1}/ω_{fV} of the tilting angular velocity of prism 1 and the vertical beam steering rate is relatively large, as well as the ratio ω_{t2}/ω_{fH} of the tilting angular velocity of prism 2 and the horizontal beam steering rate. In other words, both prisms should tilt with considerable angular velocities in order to track any target of interest. As the target approaches the optical axis of the system, two prisms are required with even larger angular velocities. Thus, a suitable control strategy should be formulated to perform the nonlinear beam scan function. It is also visible that ω_{t1}/ω_{fV} undergoes large variation with the increment of ρ_V , whereas ω_{t2}/ω_{fV} is almost constant at zero. Similarly, the increment of ρ_H leads to great variation of ω_{t2}/ω_{fH} but has negligible influence on ω_{t1}/ω_{fH} . These analysis can further verify the conclusion that the vertical field angle is primarily affected by the tilting angle of prism 1, and the horizontal field angle mainly depends on the tilting angle of prism 2.

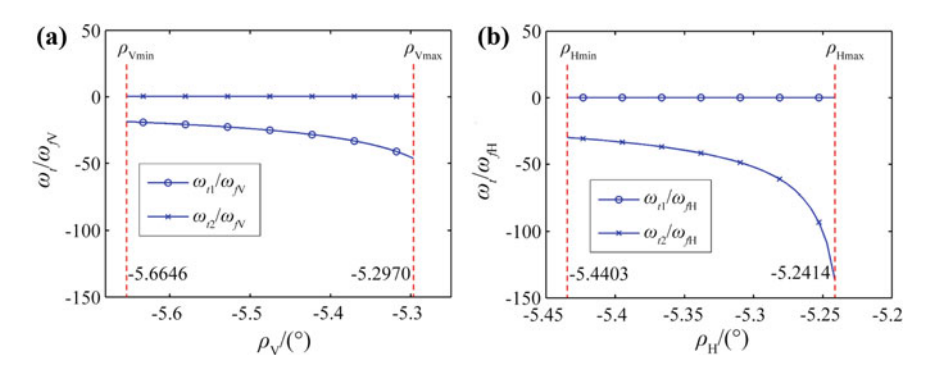


Fig. 4.5 Nonlinearity between the tilting angular velocities of two prisms and the beam steering rate, where **a** shows the variation of ω_{t1}/ω_{fV} and ω_{t2}/ω_{fV} with ρ_{V} , and **b** shows the variation of ω_{t1}/ω_{fH} and ω_{t2}/ω_{fH} with ρ_{H}

4.2 Singularity Issue

To actualize continuous beam steering function using rotating double prisms, the prisms are required with nearly infinite angular velocities whenever the beam scan trajectory approaches the center or edge of scan region, which claims for strong accelerations of two driving motors. In other words, the beam steering process along a continuous target trajectory can hardly be smooth enough at the center or edge of scan region. Such a phenomenon is usually called the singularity issue in rotating double-prism beam scan system [1].

Based on (4.2), the tangential steering rate ω_{ft} and radial steering rate ω_{fr} of the emergent beam can be further given by [4]

$$\omega_{ft} = \frac{d\varphi}{dt} = \frac{1}{x} \cdot \frac{1}{1 + (y/x)^2} \cdot \frac{\partial y}{\partial t} - \frac{y}{x^2} \cdot \frac{1}{1 + (y/x)^2} \cdot \frac{\partial x}{\partial t}$$
(4.5a)

$$\omega_{fr} = \frac{d\rho}{dt} = \frac{1}{D_2} \cdot \frac{1}{1 + (r/D_2)^2} \cdot \frac{x}{r} \cdot \frac{\partial x}{\partial t} + \frac{1}{D_2} \cdot \frac{1}{1 + (r/D_2)^2} \cdot \frac{y}{r} \cdot \frac{\partial y}{\partial t}$$
(4.5b)

where $r = \sqrt{x^2 + y^2}$ and $D_2 = 1$ mm. In addition, x and y represent the X- and Y-differences between the beam exiting point $N_r(x_m, y_m, z_m)$ from prism 2 and the beam scan point $P_r(x_{rp}, y_{rp}, z_{rp})$.

The relation of the beam steering rates ω_{ft} and ω_{fr} relative to the moving speeds of beam scan point, denoted by v_x in the *X*-direction and v_y in the *Y*-direction, is thus expressed as

$$\frac{\omega_{ft}}{v_x} = \frac{\partial \varphi}{\partial x} = -\frac{y}{x^2} \cdot \frac{1}{1 + (y/x)^2} \tag{4.6a}$$

$$\frac{\omega_{ft}}{v_y} = \frac{\partial \varphi}{\partial y} = \frac{1}{x} \cdot \frac{1}{1 + (y/x)^2} \tag{4.6b}$$

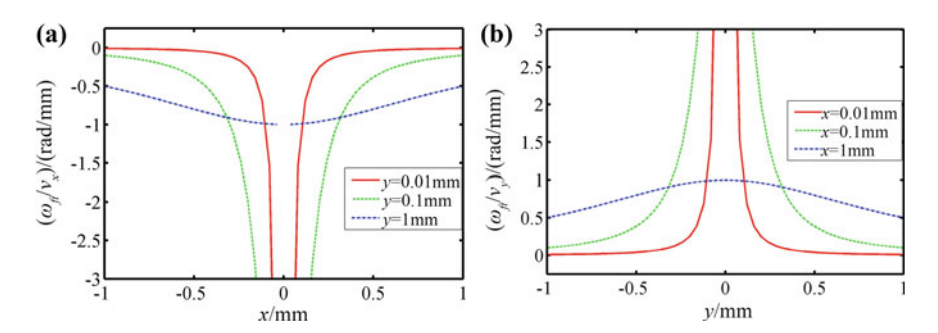


Fig. 4.6 Relation of the tangential beam steering rate ω_{ff} relative to the moving speeds v_x , v_y of beam scan point, where **a** and **b** show the variation of ω_{ff}/v_x and ω_{ff}/v_y , respectively

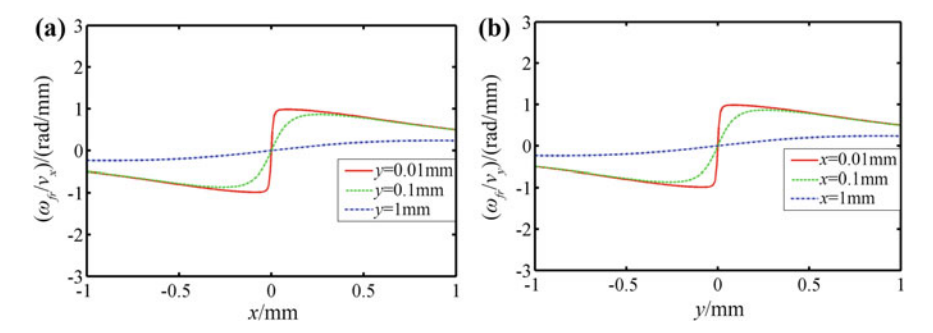


Fig. 4.7 Relation of the radial beam steering rate ω_{fr} relative to the moving speeds v_x , v_y of beam scan point, where **a** and **b** show the variation of ω_{fr}/v_x and ω_{fr}/v_y , respectively

$$\frac{\omega_{fr}}{v_x} = \frac{\partial \rho}{\partial x} = \frac{1}{D_2} \cdot \frac{1}{1 + (r/D_2)^2} \cdot \frac{x}{r}$$
(4.6c)

$$\frac{\omega_{fr}}{v_y} = \frac{\partial \rho}{\partial y} = \frac{1}{D_2} \cdot \frac{1}{1 + (r/D_2)^2} \cdot \frac{y}{r}$$

$$\tag{4.6d}$$

It is illustrated in Figs. 4.6 and 4.7 that ω_{fr} tends to infinity and ω_{fr} tends to zero as the beam scan trajectory travels at a uniform speed towards the inner edge of scan region, namely the edge of scan blind zone, where (x,y) approaches (0,0) and r approaches zero. That is, the rotation angular velocities of two prisms have primary influence on the tangential beam steering rate ω_{fr} rather than the radial one ω_{fr} . Theoretically, the rotating prisms are required with infinite angular velocities to steer the beam across the center of scan region, which thus results in a singularity issue.

As the beam scan trajectory travels towards the outer edge of scan region at a uniform speed, the ratios ω_{r1}/ω_{fr} and ω_{r2}/ω_{fr} from the rotation angular velocities of two prisms to the radial beam steering rate tend to infinity, while the ratios ω_{r1}/ω_{ft} and ω_{r2}/ω_{ft} from the angular velocities of two prisms to the tangential beam steering

rate are both constant at 1. In other words, the rotation angular velocities of prisms mainly contribute to the radial beam steering rate ω_{fr} other than the tangential one ω_{ft} . Consequently, the other singularity issue occurs near the outer edge of scan region, where the rotating prisms are also required with theoretically infinite angular velocities so as to actualize the continuous beam scan process.

Due to the limited acceleration capability of driving motors, the smooth and steady beam steering cannot be performed at the center or edge of scan region, which may lead to the loss of target in many optical tracking applications. Fortunately, [4] has suggested that the addition of a third prism is promising to eliminate the control singularities of rotating double prisms.

There is always a 180° sudden change in the azimuth angle φ obtained by two-step method once the beam scan trajectory travels across the center of scan region, namely from the 1st quadrant to the 3rd one or from the 2nd quadrant to the 4th one of Cartesian coordinate system. Consequently, two prisms suffer from periodic sudden changes of 180° in their rotation angles, as indicated by the cases in Sect. 3.1.1.

4.3 Beam Distortion

For double-prism multi-mode scan system, the distortion of scan beam will get more aggravated when either prism has larger wedge angle or refractive index. The beam distortion cannot be neglected under some specific conditions [5, 6]. Therefore, the inverse solution methods in Chap. 3 are combined with the ray tracing method to elucidate the beam distortion issues at rotating and tilting scan modes, respectively.

4.3.1 Rotating Scan Mode

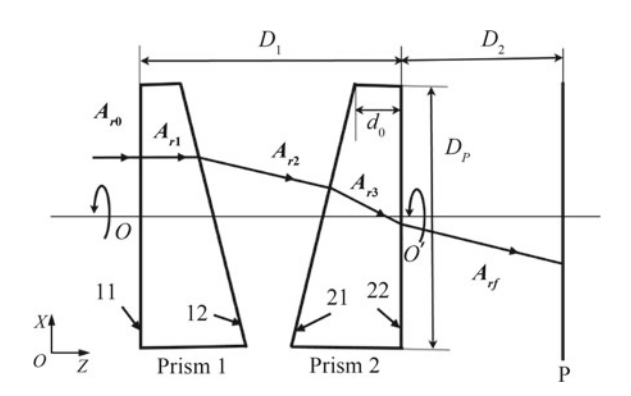
The distortion of scan beam steered by rotating double prisms has ever been studied in [7], which merely discusses the influence of prism orientations on the beam distortion. Considering the influence of other system parameters, the distortion of scan beam can be further investigated as follows.

1. Incident Beam Parallel to the Optical Axis of the System

Figure 4.8 illustrates a typical rotating double-prism scan system, where prism 1 and prism 2 are capable of coaxial rotation around the Z-axis. In this system, D_1 and D_2 represent the distance between two prisms and the one from prism 2 to the receiving screen P, respectively, and A_{r0} is the incident beam vector. Assume that the incident beam is circular with the radius r, and it propagates parallel to the optical axis of the system, namely in the positive Z-direction. With the incident beam centered at $(\Delta_x, \Delta_y, 0)$, the beam edge on the surface 11 can be determined from

4.3 Beam Distortion 161

Fig. 4.8 Rotating double-prism scan system with the incident beam parallel to the optical axis



$$\begin{cases} x = \Delta_x + r \cos \theta \\ y = \Delta_y + r \sin \theta \\ z = 0 \end{cases}$$
 (4.7)

where $\theta \in [0^{\circ}, 360^{\circ}]$.

To visualize beam distortion effects in simulation, the geometrical parameters of each prism are refractive index n=3, wedge angle $\alpha=10^{\circ}$, thinnest-end thickness $d_0=10$ mm and clear aperture $D_p=400$ mm, and the defined distances are set to $D_1=400$ mm and $D_2=400$ mm. Specially, the incident beam has a radius of r=20 mm, and the beam center at the surface 11 is specified by (0,0,0).

The intersection coordinates between the beam propagation path and the surfaces of rotating double prisms can be successively deduced from the formulae in Sect. 2.5.1.

A variable ε is defined in Fig. 4.9 to evaluate the degree of beam distortion. Given the circular incident beam with a diameter of D_0 , the emergent beam is usually distorted to be noncircular by rotating double prisms. The most stretched or squeezed diameter of the emergent beam is denoted by D_0' . Thus, the beam distortion degree can be expressed as $\varepsilon = |D_0 - D_0'| / D_0 \times 100\%$.

Figure 4.10 illustrates the beam distortion under four specific combinations of prism orientations θ_{r1} and θ_{r2} , including (a) $\theta_{r1} = 0^{\circ}$, $\theta_{r2} = 0^{\circ}$; (b) $\theta_{r1} = 0^{\circ}$, $\theta_{r2} = 45^{\circ}$; (c) $\theta_{r1} = 0^{\circ}$, $\theta_{r2} = 90^{\circ}$; and (d) $\theta_{r1} = 0^{\circ}$, $\theta_{r2} = 180^{\circ}$. Consequently, the beam distortion degree ε is determined to be 9.16, 9.25, 8.46% and 0 in turn.

Regarding the incident beam with unchanged shape and incidence angle, we can quantify the influence of wedge angle α , refractive index n and spatial distance D_1 on the beam distortion degree ε , as listed in Table 4.1. Note that the rotation angles of two prisms are held constant at $\theta_{r1}=0^\circ$ and $\theta_{r2}=0^\circ$, respectively.

It is evident in Table 4.1 that the beam distortion degree ε will increase once the refractive index n or the wedge angle α becomes larger. For example, the beam distortion degree ε increases greatly from 1.14 to 9.16% when the refractive index n varies from 1.517 to 3. Nevertheless, the distance D_1 has no influence on the beam distortion degree ε . It also turns out that the emergent beam is usually squeezed by rotating double prisms in some directions while stretched in the mutual perpendicular

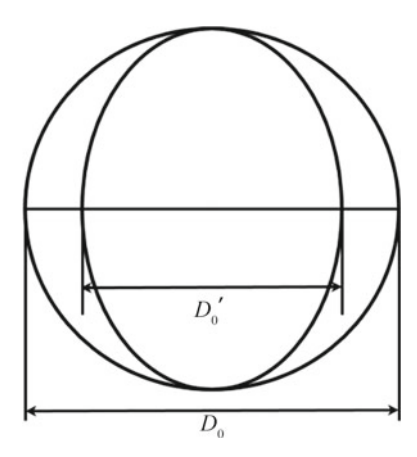


Fig. 4.9 Definition of the beam distortion degree ε

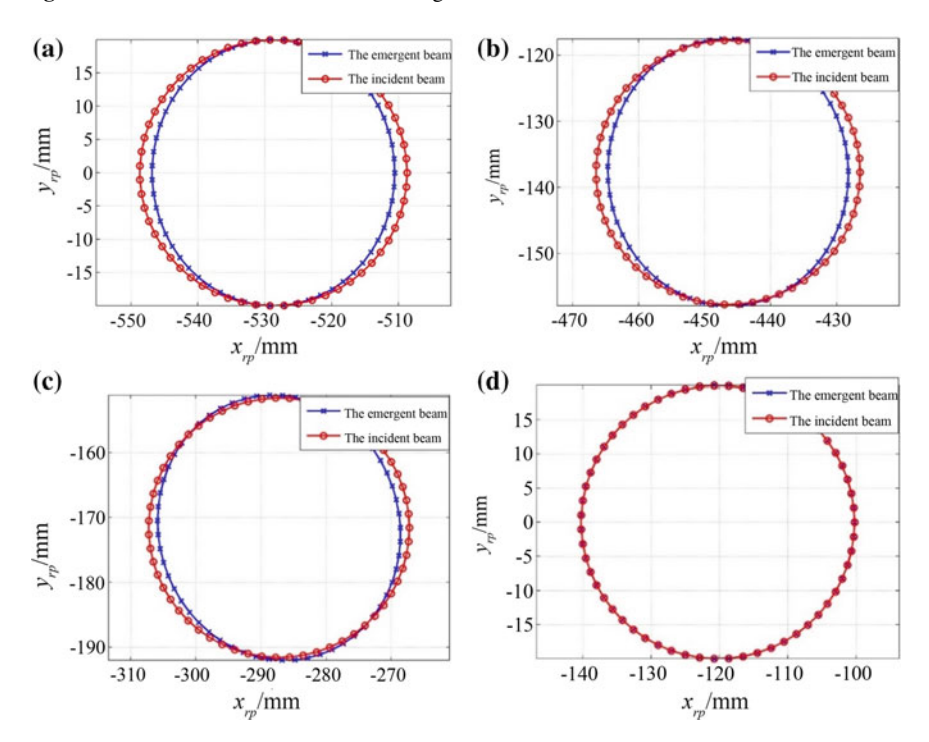


Fig. 4.10 Beam distortion under different combinations of rotation angles of double prisms, where $\mathbf{a} \ \theta_{r1} = 0^{\circ}, \theta_{r2} = 0^{\circ}; \mathbf{b} \ \theta_{r1} = 0^{\circ}, \theta_{r2} = 45^{\circ}; \mathbf{c} \ \theta_{r1} = 0^{\circ}, \theta_{r2} = 90^{\circ}; \text{ and } \mathbf{d} \ \theta_{r1} = 0^{\circ}, \theta_{r2} = 180^{\circ}$

directions. In particular, the emergent beam can only be squeezed when the relative rotation angle of two prisms $\Delta\theta_r=0^\circ$, and there is no more beam distortion when $\Delta\theta_r=180^\circ$.

4.3 Beam Distortion 163

Refractive index n	Wedge angle $\alpha/(^{\circ})$	Distance between two prisms D_1 /mm	Beam distortion degree ε (%)
1.517	10	400	1.14
2			3.26
3			9.16
	5		2.09
	13		1.714
	10	600	9.16
		800	9.16

Table 4.1 Beam distortion degree ε affected by several parameters of rotating double-prism scan system

2. Incident Beam with an Arbitrary Incidence Angle

Two variables δ_{ν} and δ_{h} are introduced to specify the relative angle between the incident beam and the *Z*-axis. As shown in Fig. 4.11, the pitch angle δ_{ν} is defined as the angle of the incident beam vector with respect to the positive *Z*-direction, and the azimuth angle δ_{h} is defined as the angle of the incident beam projection in the *XOY* plane with respect to the positive *Y*-direction.

Generally, we can assume that a circular beam with the radius of r is incident to rotating double prisms with an arbitrary incidence angle, and the central axis of incident beam intersects the surface 11 at the point $(\Delta_x, \Delta_y, 0)$. Since the projection of the circular incident beam is elliptical on the surface 11, the beam distortion issue can be discussed under the following two situations.

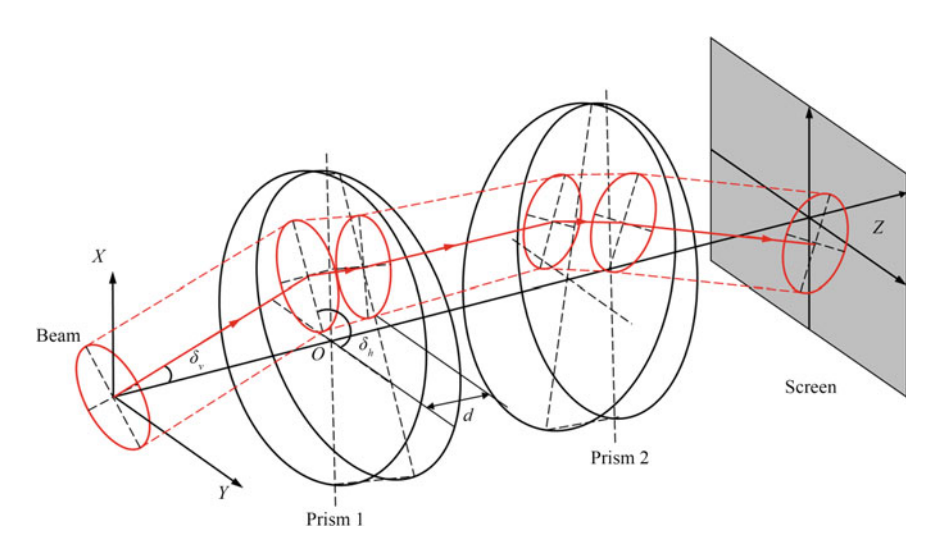


Fig. 4.11 Schematic diagram illustrating the beam propagation through rotating double prisms

(1) When the circular beam is incident with the azimuth angle $\delta_h = 0^\circ$ and the pitch angle $\delta_v \neq 0^\circ$, the elliptical beam projection has the major semi-axis of $r/\cos \delta_v$ and the minor semi-axis of r. Thus, the incident beam projected on the surface 11 can be specified by its edge equation:

$$\begin{cases} x = \Delta_x + r \cos \theta / \cos \delta_v \\ y = \Delta_y + r \sin \theta \\ z = 0 \end{cases}$$
 (4.8)

(2) When the the azimuth angle and the pitch angle of incident beam are, respectively, $\delta_h \neq 0^\circ$ and $\delta_v \neq 0^\circ$, there is an angle δ_h between the major axis of the elliptical beam projection and the *Y*-axis. As a result, the edge equation for the incident beam projected on the surface 11 can be transformed as follows:

$$\begin{cases} X \\ Y \\ Z \end{cases} = \begin{bmatrix} \cos \delta_h - \sin \delta_h & 0 \\ \sin \delta_h & \cos \delta_h & 0 \\ 0 & 0 & 1 \end{bmatrix} \begin{cases} x \\ y \\ z \end{cases}$$
 (4.9)

Substituting (4.8) into (4.9), the intersection coordinates of the incident beam and the surface 11 are finally expressed as

$$\begin{cases} X = \cos \delta_h(\Delta_x + r \cos \theta / \cos \delta_v) - \sin \delta_h(\Delta_y + r \sin \theta) \\ Y = \cos \delta_h(\Delta_y + r \sin \theta) + \sin \delta_h(\Delta_x + r \cos \theta / \cos \delta_v) \\ Z = 0 \end{cases}$$
(4.10)

Given the incident beam vector $A_{\mathbf{r0}} = (\sin \delta_{\nu} \cos \delta_{h}, \sin \delta_{\nu} \sin \delta_{h}, \cos \delta_{\nu})^{\mathrm{T}}$, the intersection of the beam propagation path and every prism surface can be successively determined according to the vector refraction theorem.

In simulation, the geometrical parameters of each prism include n=3, $\alpha=10^\circ$, $d_0=10$ mm and $D_p=400$ mm. The coordinate origin O(0,0,0) coincides with the center of the surface 11. The distance between two prisms and that from prism 2 to the screen P are, respectively, set to $D_1=400$ mm and $D_2=400$ mm. To confine the final emergent beam within the field of view, the incident beam of a radius r=20 mm is prescribed with pitch angle $\delta_v=4^\circ$ and azimuth angle $\delta_h=60^\circ$, and the central axis of incident beam intersects the surface 11 at the point (10,0,0).

On the above basis, Fig. 4.12 presents the beam distortion under four specific combinations of prism orientations θ_{r1} and θ_{r2} , including (a) $\theta_{r1} = 0^{\circ}$, $\theta_{r2} = 0^{\circ}$; (b) $\theta_{r1} = 0^{\circ}$, $\theta_{r2} = 45^{\circ}$; (c) $\theta_{r1} = 0^{\circ}$, $\theta_{r2} = 90^{\circ}$; and (d) $\theta_{r1} = 0^{\circ}$, $\theta_{r2} = 180^{\circ}$. Consequently, the beam distortion degree ε becomes 8.145, 7.971, 6.537 and 0.244% in turn

It is validated in Fig. 4.12 that rotating double prisms can squeeze the emergent beam in some directions but stretch the beam in the mutual perpendicular directions.

4.3 Beam Distortion 165

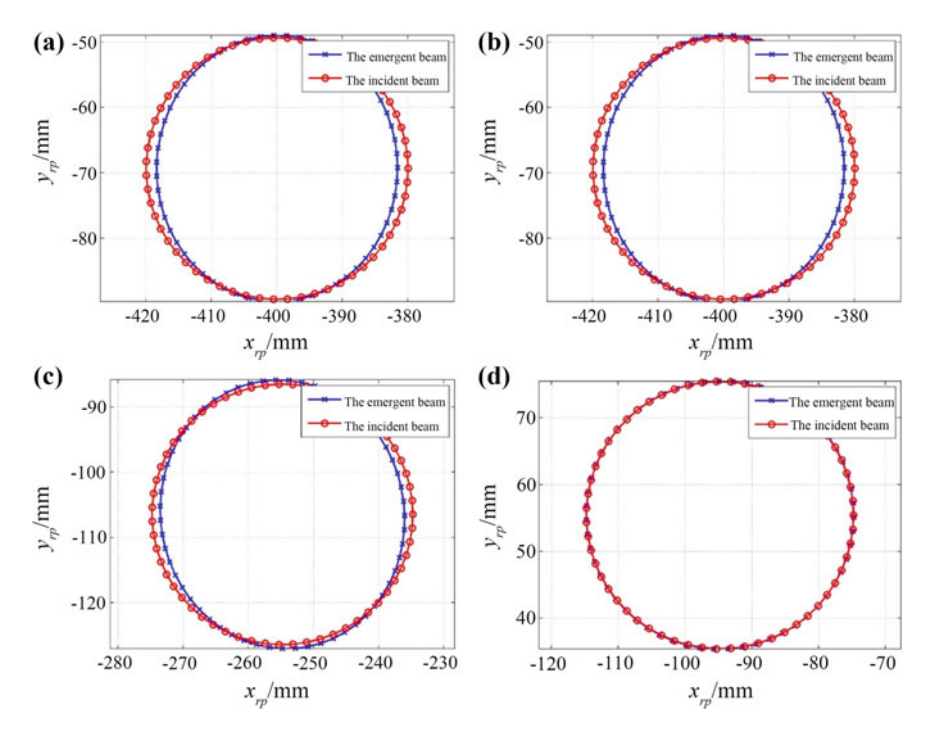


Fig. 4.12 Beam distortion under different combinations of prism orientations, where **a** $\theta_{r1} = 0^{\circ}$, $\theta_{r2} = 0^{\circ}$; **b** $\theta_{r1} = 0^{\circ}$, $\theta_{r2} = 45^{\circ}$; **c** $\theta_{r1} = 0^{\circ}$, $\theta_{r2} = 90^{\circ}$; and **d** $\theta_{r1} = 0^{\circ}$, $\theta_{r2} = 180^{\circ}$

In particular, the emergent beam is purely squeezed when the rotation angles of two prisms are $\theta_{r1} = 0^{\circ}$ and $\theta_{r2} = 0^{\circ}$, and the beam distortion almost disappears when $\theta_{r1} = 0^{\circ}$ and $\theta_{r2} = 180^{\circ}$.

Providing the relative rotation angle of two prisms $\Delta\theta_r$ with some fixed value, Fig. 4.13 shows the relation between the beam distortion degree ε and the rotation angle θ_{r1} of prism 1. As shown in Fig. 4.13a, the beam distortion degree ε is independent of the rotation angle θ_{r1} when the incident beam propagates parallel to the Z-axis. However, ε gets associated with θ_{r1} once the incident beam is inclined with respect to the Z-axis, as shown in Fig. 4.13b. In particular, the beam distortion can usually be neglected when $\Delta\theta_r = 180^\circ$.

To help investigate the beam distortion issue when the incident beam is inclined to the Z-axis, the relation of the beam distortion degree ε with respect to the prism orientation θ_{r1} or θ_{r2} can be established by fixing one prism and adjusting the other prism. Hereby, Fig. 4.14a shows the variation of ε with θ_{r2} when θ_{r1} remains unchanged, and Fig. 4.14b manifests the variation of ε with θ_{r1} when θ_{r2} is held constant. It is common in Fig. 4.14 that the beam distortion will be minimized as long as the relative rotation angle $\Delta\theta_r = 180^\circ$.

Even though both prisms are kept stationary, the beam distortion may still be significant when the incident beam propagates with different combinations of pitch

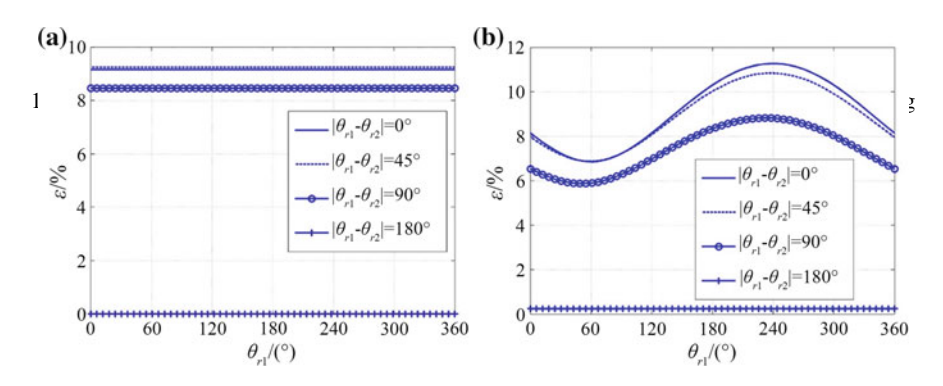


Fig. 4.13 Relation between the beam distortion degree ε and the rotation angle θ_{r1} of prism 1, when **a** the incident beam propagates parallel to the *Z*-axis or **b** the incident beam travels with an arbitrary incidence angle

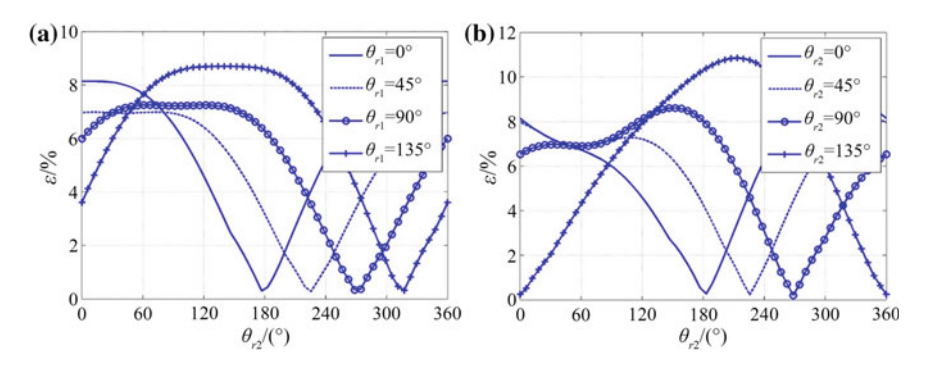


Fig. 4.14 Relation between the beam distortion degree ε and the rotation angle of each prism, where $\mathbf{a} \theta_{r1}$ and $\mathbf{b} \theta_{r2}$ are held constant, respectively

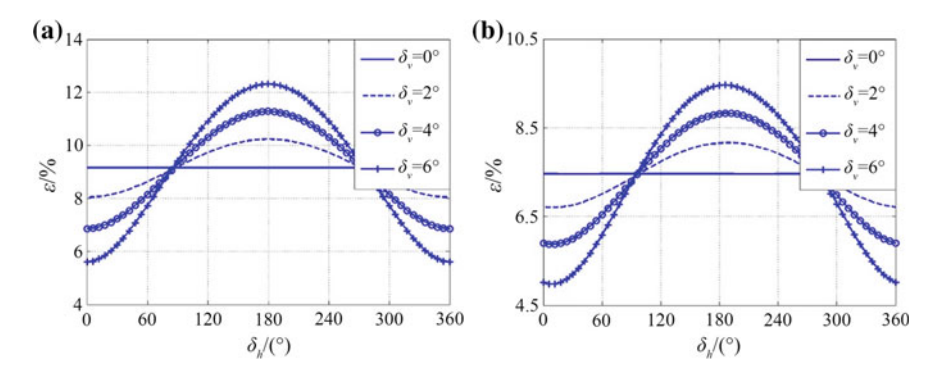


Fig. 4.15 Relation of the beam distortion degree ε with respect to the pitch angle δ_v and the azimuth angle δ_h of incident beam, where the prism orientations are \mathbf{a} $\theta_{r1}=0^{\circ}$, $\theta_{r2}=0^{\circ}$ and \mathbf{b} $\theta_{r1}=0^{\circ}$, $\theta_{r2}=90^{\circ}$

angle δ_v and azimuth angle δ_h . In contrast, Fig. 4.15a indicates the relation of the beam distortion degree ε with respect to δ_v and δ_h when the rotation angles of two prisms are respectively constant at $\theta_{r1}=0^\circ$ and $\theta_{r2}=0^\circ$, while Fig. 4.15b indicates the one when $\theta_{r1}=0^\circ$ and $\theta_{r2}=90^\circ$.

4.3 Beam Distortion 167

It is shown in Fig. 4.15a that the variation of beam distortion degree ε is always symmetric about the line $\delta_h=180^\circ$ as long as $\theta_{r1}=0^\circ$ and $\theta_{r2}=0^\circ$. Clearly, ε increases monotonously as δ_h ranges from 0° to 180° . Given δ_h within $0^\circ-90^\circ$, ε is limited by 8.04–9.07% when $\delta_v=2^\circ$ and 5.61–9.07% when $\delta_v=6^\circ$, which implies that ε decreases with the increment of δ_v . Given δ_h within $90^\circ-180^\circ$, ε ranges within 9.07-10.23% when $\delta_v=2^\circ$ and 9.07-12.31% when $\delta_v=6^\circ$, i.e., the increment of δ_v will result in a larger ε . In addition, similar conclusions can be drawn from Fig. 4.15b.

Besides the aforementioned factors, there are other system parameters that may make influence on beam distortion, such as the wedge angle α , the refractive index n, the central-axis thickness d of each prism and the distance D_1 between two prisms. Therefore, Fig. 4.16 shows the beam distortion degree ε varying with any one of these parameters, where the incident beam is inclined to the Z-axis with a certain angle.

In accordance with the analysis on Fig. 4.13b and 4.16 proves that these system parameters can hardly affect the beam distortion once the relative rotation angle of two prisms $\Delta\theta_r=180^\circ$. However, the beam distortion issue should be considered if $\Delta\theta_r\neq180^\circ$. For example, when the rotation angles of two prisms are set to $\theta_{r1}=0^\circ$ and $\theta_{r2}=0^\circ$, the beam distortion degree ε increases from 2.676 to 8.145% as the refractive index n changes from 2 to 3, and ε varies from 1.714 to 8.145% as the wedge angle α changes from 5° to 10°. Similar analysis can be presented when

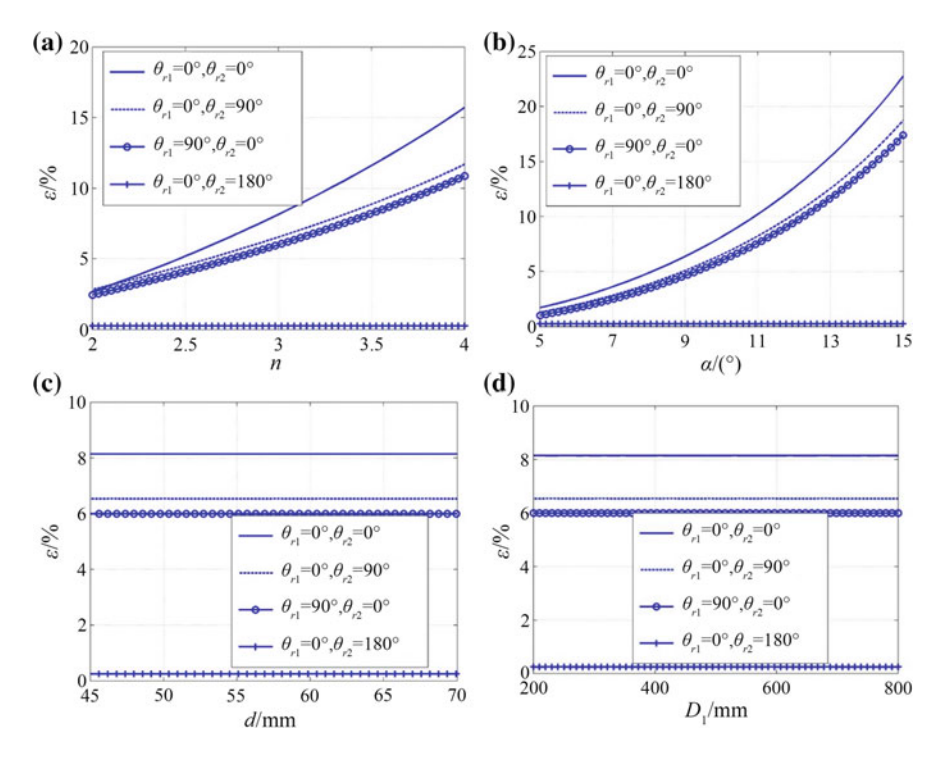


Fig. 4.16 Influence of system parameters on the beam distortion degree ε , where \mathbf{a} - \mathbf{d} illustrate the relation of ε relative to the refractive index n, the wedge angle α , the central-axis thickness d and the distance D_1 , respectively

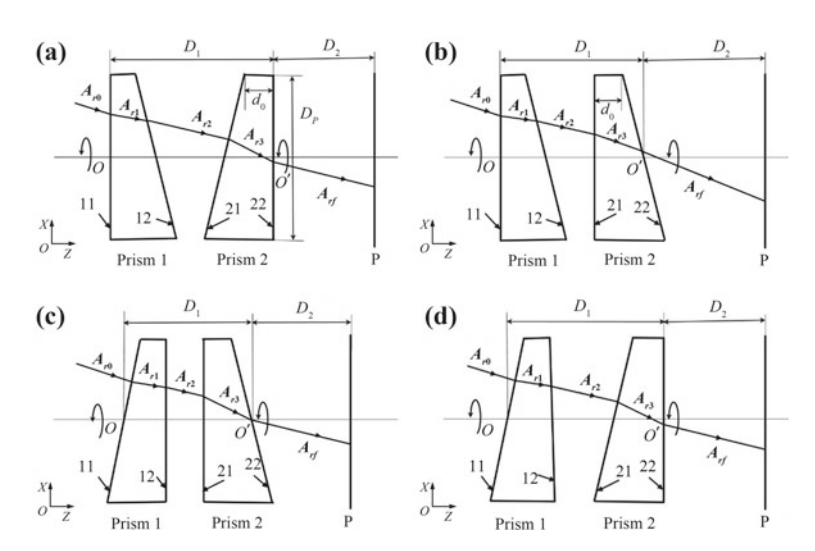


Fig. 4.17 Four different configurations in a rotating double-prism system, where **a**–**d** represent configurations 1, 2, 3 and 4, respectively

 $\theta_{r1} = 0^{\circ}$ and $\theta_{r2} = 90^{\circ}$ or when $\theta_{r1} = 90^{\circ}$ and $\theta_{r2} = 0^{\circ}$. It is also worth mentioning that either the central-axis thickness d or the distance D_1 is not concerned with the beam distortion degree ε .

3. Influence of Prism Configurations on Beam Distortion

Since one prism can be situated with its plane facet inward or outward, there are totally four different configurations for rotating double prisms [8], as exemplified in Fig. 4.17. Obviously, the one in Fig. 4.17a has been chosen as the double-prism configuration in Fig. 4.8.

In the following simulation, the coordinate origin O(0,0,0) is fixed to the center of the surface 11, the involved prism parameters are n=3, $\alpha=10^\circ$, $d_0=10$ mm and $D_p=400$ mm, the defined distances are $D_1=400$ mm and $D_2=400$ mm. In addition, the incident beam is inclined to the Z-axis with the pitch angle $\delta_v=4^\circ$ and the azimuth angle $\delta_h=60^\circ$.

Under any configuration in Fig. 4.17, the beam distortion degree ε induced by specific prism orientations, the maximum beam distortion degree ε_{max} and its corresponding prism orientations (θ_{r1} , θ_{r2}) are determined as listed in Table 4.2. Meanwhile, Fig. 4.18 compares the most significant beam distortion under four different configurations.

Table 4.2 reveals that the beam distortion degree is comparatively large under configuration 1, which can be minimized under configuration 4. Nevertheless, there are other influencing factors that should be taken into account for the system design, such as beam deviation coverage and scan blind zone.

4.3 Beam Distortion 169

Configurations	ε				ε _{max} (%)	$ \begin{array}{c} (\theta_{r1}, \theta_{r2}) \\ \text{corresponding to } \varepsilon_{\text{max}} \end{array} $
	(0°,0°) (%)	(0°,90°) (%)	(90°,0°) (%)	(0°,180°) (%)		
1	8.145	7.971	6.537	0.244	11.276	(240°,240°)
2	22.743	16.668	8.034	8.407	36.372	(240°,240°)
3	22.743	10.423	6.490	0.244	25.310	(240°,240°)
4	1.689	1.043	3.516	6.917	7.692	(240°,60°)
600 580 580	330 344 x _η			730 410	420 43 <i>x_m</i>	The incident beam 0 440 450 /mm
(c)		-0-0-0	(d)		H H
610 mm/ _g , 590		The state of the s	ergent beam ident beam mm/ds/	630 620	A PARTICION OF THE PART	The emergent beam The incident beam
580	So The second		7	600	A Barre	

Table 4.2 Beam distortion degree under four different double-prism configurations

Fig. 4.18 Comparison of the most distorted beams under **a** configuration 1, **b** configuration 2, **c** configuration 3 and **d** configuration 4

 x_{rp}/mm

4.3.2 Tilting Scan Mode

 x_{rp}/mm

The beam propagation path through tilting double prisms has been illustrated in Fig. 2.7, where prism 1 and prism 2 tilt around the X- and Y-axes, respectively, and the incident beam vector is given by A_{t0} . To quantatively describe the beam distortion induced by tilting prisms, we assume that the incident beam is circular with a radius of r=20 mm, and each prism has refractive index n=3, wedge angle $\alpha=10^{\circ}$, thinnest-end thickness $d_0=10$ mm and clear aperture $D_p=400$ mm. In addition, the distance between two prisms is $D_1=400$ mm and that from prism 2

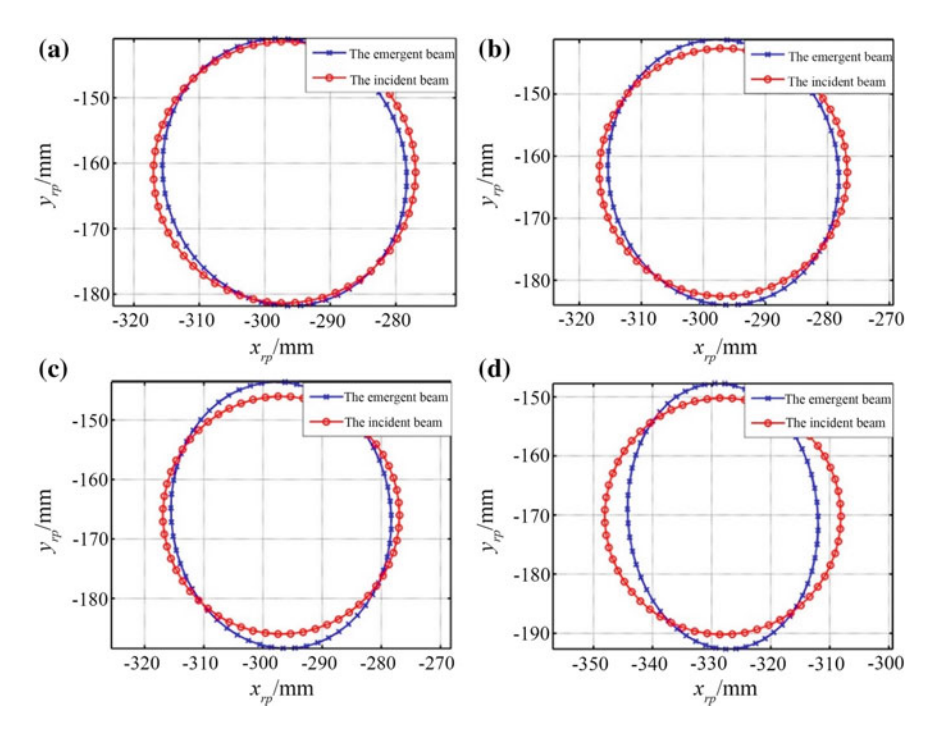


Fig. 4.19 Beam distortion under different combinations of tilting angles of double prisms, where $\mathbf{a} \ \theta_{t1} = 0^{\circ}, \ \theta_{t2} = 0^{\circ}; \ \mathbf{b} \ \theta_{t1} = 0^{\circ}, \ \theta_{t2} = 5^{\circ}; \ \mathbf{c} \ \theta_{t1} = 0^{\circ}, \ \theta_{t2} = 10^{\circ}; \ \mathbf{and} \ \mathbf{d} \ \theta_{t1} = 10^{\circ}, \ \theta_{t2} = 10^{\circ}$

to the screen P is $D_2 = 400$ mm. With the incident beam centered at (0,10,0), the beam edge on the surface 11 is determined from

$$\begin{cases} x = 20\cos\theta \\ y = 10+20\sin\theta \\ z = 0 \end{cases}$$
 (4.11)

where $\theta \in [0^{\circ}, 360^{\circ}]$.

Using the formulae in Sect. 2.5.2, the intersection coordinates between the beam propagation path and the surfaces of tilting double prisms can be obtained in turn.

In simulation, Fig. 4.19 shows the beam distortion under four specific combinations of tilting angles $(\theta_{t1}, \theta_{t2})$ of double prisms, including (a) $\theta_{t1} = 0^{\circ}$, $\theta_{t2} = 0^{\circ}$; (b) $\theta_{t1} = 0^{\circ}$, $\theta_{t2} = 5^{\circ}$; (c) $\theta_{t1} = 0^{\circ}$, $\theta_{t2} = 10^{\circ}$; and (d) $\theta_{t1} = 10^{\circ}$, $\theta_{t2} = 10^{\circ}$. Specifically, the beam distortion degree ε is determined to be 8.46, 9.52, 13.01 and 20.30% in turn.

The beam distortion dependent on the geometrical parameters of tilting double prisms can be separately investigated as long as the incident beam is unchanged in its shape and incidence angle. Specifically, the beam distortion degree ε induced by the

4.3 Beam Distortion 171

Refractive index n	Wedge angle $\alpha/(^{\circ})$	Distance between two prisms D_1 /mm	Beam distortion degree ε (%)
1.517	10	400	2.56
2			4.61
3			9.52
	5		2.91
	13		16.97
	10	350	9.52
		300	9.52

Table 4.3 Beam distortion degree ε induced by several parameters of tilting double-prism scan system

wedge angle α , the refractive index n as well as the distance D_1 is listed in Table 4.3, where the tilting angles of two prisms remain at $\theta_{t1} = 0^{\circ}$ and $\theta_{t2} = 5^{\circ}$, respectively.

By contrast between Figs. 4.12 and 4.19, it can be found that the emergent beam is also squeezed by tilting double prisms in some directions while stretched in the mutual perpendicular directions. Nevertheless, there is an inherent distinction that tilting double prisms may cause more significant beam distortion than rotating double prisms, as exemplified by Tables 4.1 and 4.3. The beam distortion degree ε will get larger owing to the increment of wedge angle α or refractive index n. For example, ε increases from 2.56 to 9.52% as n varies from 1.517 to 3. Besides, it is noteworthy that the distance D_1 has completely no influence on beam distortion.

4.4 Error Modeling for Double-Prism Multi-mode Scanning

If we do not consider the effects of systematic errors, the beam pointing error of double-prism scan system is mainly determined by the coupling motion accuracy of two prisms, mainly affected by prism assembly errors, bearing assembly errors and mechanical transmission errors. The above errors can be attributed to the position errors of double prisms by means of equivalent analysis.

To formulate the exact expression of beam pointing error, a position error model that integrates the rotating and tilting motion modes of double prisms should be established. Such an error model is also useful to elucidate the influence of prism and bearing assembly errors on the beam pointing accuracy. For convenience, the transmission errors in mechanical devices developed in Chap. 5 are equavilent to prism orientation errors, namely the rotation or tilting angle errors of two prisms. Given the desired beam pointing accuracy, it is thus possible to estimate the error tolerances for the development of double-prism scan system in practice. Moreover, the error analysis method proposed in this section is available for reference in assembly analysis of dynamic optical systems.

As two significant error items, the assembly errors of prism and bearing confine the beam pointing accuracy, which mainly result from the initial installation angle errors due to prism tilt and bearing tilt, respectively [9]. To perform quantitative analysis, an imaginary error item can be introduced to the prism or bearing position. In other words, the prism or bearing should deviate from its theoretical position around a spin axis. Now that the deviation error and the spin axis are both planned, the actual emergent beam vector $\boldsymbol{A_{f1}}$ can be obtained in contrast to the theoretical one $\boldsymbol{A_{f0}}$.

Any vector that rotates around a spin axis will produce a new vector available from Rodrigues transformation [10]. Therefore, given the unit vector $(u_x, u_y, u_z)^T$ for the spin axis, the incident or emergent beam vector of one rotating prism can be specified by a rotation matrix M_P :

$$M_P = A_p + \cos \delta \cdot (\mathbf{I} - A_p) + \sin \delta \cdot B_p \tag{4.12}$$

Here I is a three-order unit matrix; δ represents the rotation angle of the vector; and A_p and B_p are, respectively, given by

$$\mathbf{A}_{p} = \begin{bmatrix} u_{x}^{2} & u_{x}u_{y} & u_{x}y_{z} \\ u_{y}u_{x} & u_{y}^{2} & u_{y}u_{z} \\ u_{z}u_{x} & u_{z}u_{y} & u_{z}^{2} \end{bmatrix}$$
(4.13a)

$$\boldsymbol{B_p} = \begin{bmatrix} 0 & -u_z & u_y \\ u_z & 0 & -u_x \\ -u_y & u_x & 0 \end{bmatrix}$$
 (4.13b)

In either a rotating double-prism system or a tilting one, the prism elements may be tilted around the X- or Y-axis and rotated around the Z-axis due to imperfect assembly. For further explanation, Fig. 4.20a and b exemplify one rotating prism that has been tilted around the Y-axis and one tilting prism that has been rotated around the Z-axis, respectively. This section is to reveal what influence the assembly errors of tilting double prisms have on the beam pointing accuracy. The same analysis means is also available for the assembly error survey in rotating double prisms.

4.4.1 Pointing Error Caused by Prism Assembly

Since tilting double prisms are asymmetric, both the amplitude and the direction of prism tilt should be considered for the analysis on beam pointing errors [11]. Accordingly, the beam pointing errors induced by the misassembly of prism 1 and prism 2 are separately investigated as follows.

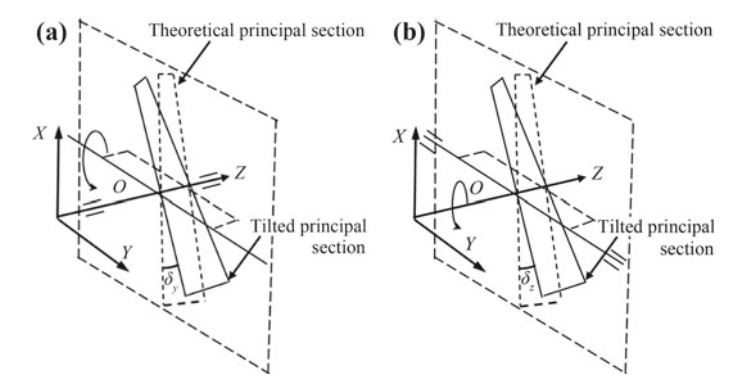


Fig. 4.20 Modeling of prism assembly errors, where **a** shows one rotating prism that has been tilted around the Y-axis, and **b** shows one tilting prism that has been rotated around the Z-axis

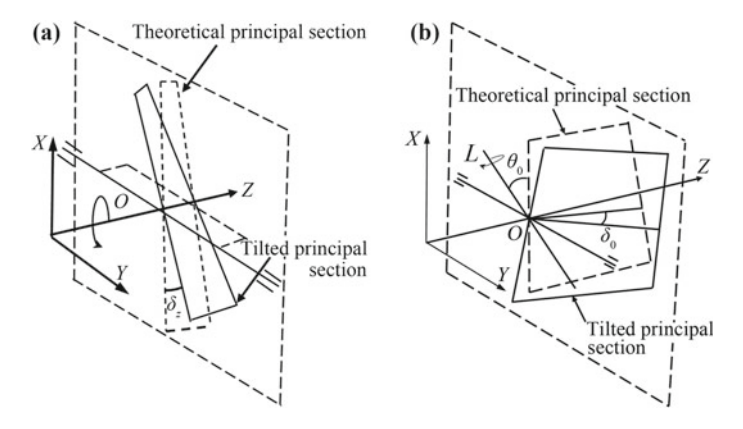


Fig. 4.21 Modeling of assembly errors of prism 1, where **a** and **b** indicate the prism assembly error δ_z around the *Z*-axis and the one δ_0 around the axis *OL*, respectively

Usually, prism 1 tilts around the *Y*-axis while prism 2 tilts around the *X*-axis in a tilting double-prism system. Taking prism 1 for example, the incident surface 11 is parallel to the *XOY* plane on the initial state. As shown in Fig. 4.21, the assembly errors of prism 1 at an arbitrary tilting angle can be divided into two types. One type has been illustrated in Fig. 4.21(a), where prism 1 is rotated around the *Z*-axis with an angle δ_z . Thus, the normal vectors to the incident and emergent surfaces of prism 1 are both specified by a rotation matrix M_{P1} :

$$M_{P1} = Rot(Z, \delta_z) \tag{4.14}$$

As shown in Fig. 4.21b, the spin axis OL is introduced to help describe the prism tilt around the X- or Y-axis. The axis OL can be defined by rotating the X-axis counterclockwise around the Z-axis with an angle θ_0 . In other words, OL passes the

coordinate origin and locates in the *XOY* plane, which is further determined by the unit vector $(u_x, u_y, u_z)^T = (\cos\theta_0, \sin\theta_0, 0)^T$. Hence, the prism tilt around *OL* can be equivalent to that around the *X*-axis when *OL* coincides with the *X*-axis and that around the *Y*-axis when *OL* coincides with the *Y*-axis.

Figure 4.21b indicates the other type of prism assembly errors, where prism 1 is tilted around the axis OL with an angle δ_0 . Specially, the angle δ_0 of prism tilt represents the assembly error around the X-axis when $\theta_0 = 0$ and the one around the Y-axis when $\theta_0 = 90^\circ$. According to Rodrigues formulae, the rotation matrix M_{P2} that specifies the incident or emergent surface normal of prism 1 can be expressed as

$$M_{P2} = A_p + \cos \delta_0 \cdot (\mathbf{I} - A_p) + \sin \delta_0 \cdot B_p \tag{4.15}$$

1. Assembly Errors of Prism 1

In this situation, prism 1 suffers from an assembly error of δ_z or δ_0 , while prism 2 is perfectly mounted. When the tilting angle of prism 1 is 0°, the normal vector N'_{110} to the prism surface 11 and the one N'_{120} to the prism surface 12 are, respectively, written as

$$N'_{110} = M_{P2} \cdot M_{P1} \cdot (0, 0, 1)^{\mathrm{T}}$$
 (4.16a)

$$N'_{120} = M_{P2} \cdot M_{P1} \cdot (\sin \alpha, 0, \cos \alpha)^{\mathrm{T}}$$

$$(4.16b)$$

When the tilting angle of prism 1 becomes θ_{t1} , the normal vector N'_{11} to the surface 11 and the one N'_{12} to the surface 12 are, respectively, deduced from

$$N'_{11} = Rot(Y, \theta_{t1}).N'_{110}$$
 (4.17a)

$$N'_{12} = Rot(Y, \theta_{t1}).N'_{120}$$
(4.17b)

Given the tilting angle θ_{12} of prism 2, the normal vector N'_{21} to the prism surface 21 and the one N'_{22} to the prism surface 22 can be, respectively, expressed as

$$N'_{21} = (0, \sin(\alpha + \theta_{t2}), \cos(\alpha + \theta_{t2}))^{\mathrm{T}}$$
 (4.17c)

$$N'_{22} = (0, -\sin\theta_{t2}, \cos\theta_{t2})^{\mathrm{T}}$$
 (4.17d)

Using the vector refraction theorem, the vector expressions for the beam propagation path through tilting double prisms are sequentially given by

$$A'_{t1} = A_{t0} = (0, 0, 1)^{\mathrm{T}}$$
 (4.18a)

$$A'_{t2} = nA'_{t1} + \left\{ \sqrt{1 - n^2 \cdot [1 - (A'_{t1} \cdot N'_{12})^2]} - nA'_{t1} \cdot N'_{12} \right\} \cdot N'_{12} = (x'_{t2}, y'_{t2}, z'_{t2})^{\mathrm{T}}$$
(4.18b)

$$A'_{3} = \frac{1}{n}A'_{2} + \left\{ \sqrt{1 - \left(\frac{1}{n}\right)^{2} \cdot [1 - (A'_{2}.N'_{21})^{2}]} - \frac{1}{n}A'_{2} \cdot N'_{21} \right\} \cdot N'_{21}$$

$$= (x'_{t3}, y'_{t3}, z'_{t3})^{T}$$

$$(4.18c)$$

$$A'_{tf} = nA'_{t3} + \left\{ \sqrt{1 - n^{2} \cdot [1 - (A'_{t3}.N'_{22})^{2}]} - nA'_{t3}.N'_{22} \right\} \cdot N'_{22} = \left(x'_{tf}, y'_{tf}, z'_{tf}\right)^{T}$$

$$(4.18d)$$

where A_{t0} , A'_{t1} and A'_{t2} represent the incident, refracted and emergent beam vectors of prism 1 in turn; A'_{t3} and A'_{tf} are, respectively, the refracted and emergent beam vectors of prism 2.

Therefore, the vertical field angle ρ_V' and the horizontal field angle ρ_H' of the final emergent beam can be determined by

$$\rho_{V}' = \arctan\left(\frac{x_{ff}'}{z_{ff}'}\right) \tag{4.19a}$$

$$\rho_{\rm H}' = \arctan\left(\frac{y_{tf}'}{z_{tf}'}\right) \tag{4.19b}$$

Comparing the theoretical field angles ρ_V and ρ_H to the actual field angles ρ_V' and ρ_H' dependent on prism assembly errors, the resultant errors in vertical field angle and horizontal field angle are, respectively, given by

$$\Delta \rho_{\rm V} = \left| \rho_{\rm V}' - \rho_{\rm V} \right| \tag{4.20a}$$

$$\Delta \rho_{\rm H} = \left| \rho_{\rm H}' - \rho_{\rm H} \right| \tag{4.20b}$$

Since prism 1 is only capable of tilting motion around the Y-axis, the prism tilt around the X-axis cannot be modified by the linear driving motor.

For the following analysis, each identical prism has the wedge angle $\alpha=5^\circ$ and the refractive index n within 1.517–4, and the tilting angle θ_{t1} or θ_{t2} within $0^\circ-10^\circ$. Meanwhile, the prism tilt amplitude around the X-axis is held constant at $\delta_0=0.2''$ in order to simulate the assembly conditions in practice. Figure 4.22 describes the influence of the prism tilt direction θ_0 on the maximum error $\Delta \rho_{\rm Hmax}$ of horizontal field angle and the maximum error $\Delta \rho_{\rm Vmax}$ of vertical field angle. In the case of n=1.517, $\Delta \rho_{\rm Hmax}$ reaches its maximum value of 0.51 μ rad when $\theta_0=0^\circ$ or 180°, whereas $\Delta \rho_{\rm Vmax}$ reaches its maximum value of 0.52 μ rad when $\theta_0=90^\circ$. Likewise, providing the prism tilt amplitude around the Y-axis as the stepping angle of linear motor, namely $\delta_0=0.08''$, the error of vertical field angle $\rho_{\rm V}$ can be up to 0.21 μ rad.

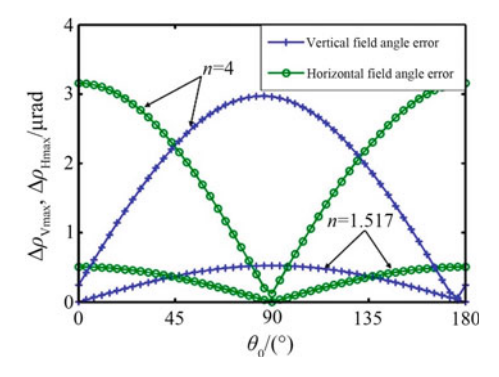


Fig. 4.22 Influence of the prism tilt direction θ_0 on $\Delta \rho_{Hmax}$ and $\Delta \rho_{Vmax}$ when the tilt amplitude of prism 1 is $\delta_0 = 0.2''$

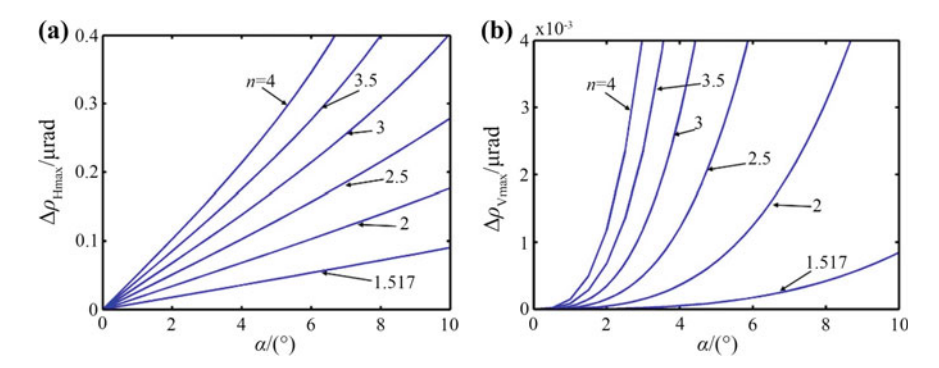


Fig. 4.23 Influence of the wedge angle α on $\Delta \rho_{\rm Hmax}$ and $\Delta \rho_{\rm Vmax}$ when the assembly error of prism 1 is $\delta_z = 0.2''$, where **a** plots $\Delta \rho_{\rm Hmax}$ as a function of α and **b** plots $\Delta \rho_{\rm Vmax}$ as a function of α

Supposing that the assembly error of prism 1 exists only around the Z-axis, namely $\delta_z=0.2''$, the variation of $\Delta\rho_{\rm Hmax}$ and $\Delta\rho_{\rm Vmax}$ with the wedge angle α ranging from 0° to 10° can be illustrated in Fig. 4.23. Furthermore, the impact of the refractive index n on $\Delta\rho_{\rm Hmax}$ and $\Delta\rho_{\rm Vmax}$ is revealed. For example, $\Delta\rho_{\rm Hmax}$ reaches about 0.044 μ rad while $\Delta\rho_{\rm Vmax}$ is negligible when $\alpha=5^\circ$ and n=1.517.

2. Assembly Errors of Prism 2

Regarding the situation that prism 2 suffers from an assembly error of δ_z or δ_0 while prism 1 is perfectly mounted, the resultant beam pointing errors are still available by the above means.

Since prism 2 can only perform tilting motion around the *X*-axis, it is impossible to modify the prism tilt around the *Y*-axis by the linear driving motor. Therefore, the prism tilt amplitude around the *Y*-axis is set to $\delta_0 = 0.2''$ in simulation.

Given $\delta_0 = 0.2''$, the maximum error $\Delta \rho_{Hmax}$ of horizontal field angle and the maximum error $\Delta \rho_{Vmax}$ of vertical field angle are both nonlinear functions dependent

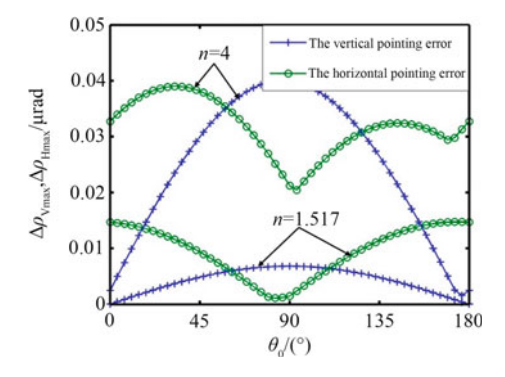


Fig. 4.24 Influence of the prism tilt direction θ_0 on $\Delta \rho_{Hmax}$ and $\Delta \rho_{Vmax}$ when the tilt amplitude of prism 2 is $\delta_0 = 0.2''$

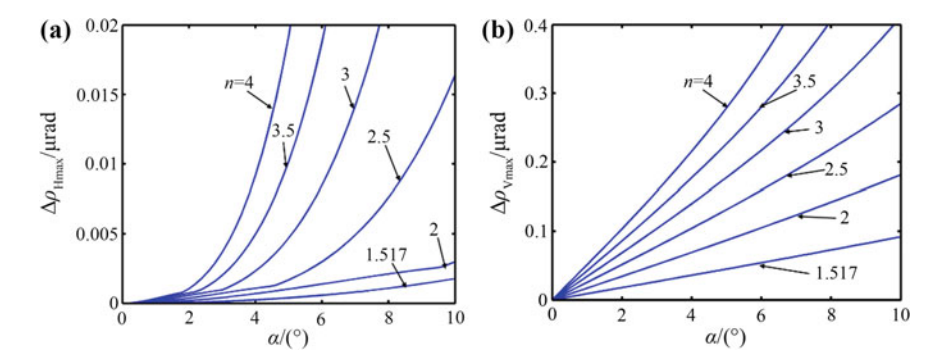


Fig. 4.25 Influence of the wedge angle α on $\Delta \rho_{\rm Hmax}$ and $\Delta \rho_{\rm Vmax}$ when the assembly error of prism 2 is $\delta_z = 0.2''$, where **a** plots $\Delta \rho_{\rm Hmax}$ as a function of α and **b** plots $\Delta \rho_{\rm Vmax}$ as a function of α

on the prism tilt direction θ_0 , as shown in Fig. 4.24. In the case of n=1.517, $\Delta \rho_{\rm Hmax}$ reaches 0.015 μ rad at maximum when $\theta_0=172^{\circ}$, whereas $\Delta \rho_{\rm Vmax}$ reaches 0.0068 μ rad at maximum when $\theta_0=90^{\circ}$. Moreover, the error of vertical field angle $\rho_{\rm V}$ is about 0.006 μ rad, providing the prism tilt amplitude around the *X*-axis as the stepping angle of linear motor, namely $\delta_0=0.08''$.

Supposing that the assembly error of prism 2 exists only around the Z-axis, namely $\delta_z = 0.2''$, Fig. 4.25 indicates the variation of $\Delta \rho_{\rm Hmax}$ and $\Delta \rho_{\rm Vmax}$ with the wedge angle α ranging from 0° to 10°, as well as the impact of the refractive index n on $\Delta \rho_{\rm Hmax}$ and $\Delta \rho_{\rm Vmax}$. For example, when $\alpha = 5^\circ$ and n = 1.517, $\Delta \rho_{\rm Vmax}$ reaches about 0.045 μ rad while $\Delta \rho_{\rm Hmax}$ is comparatively small.

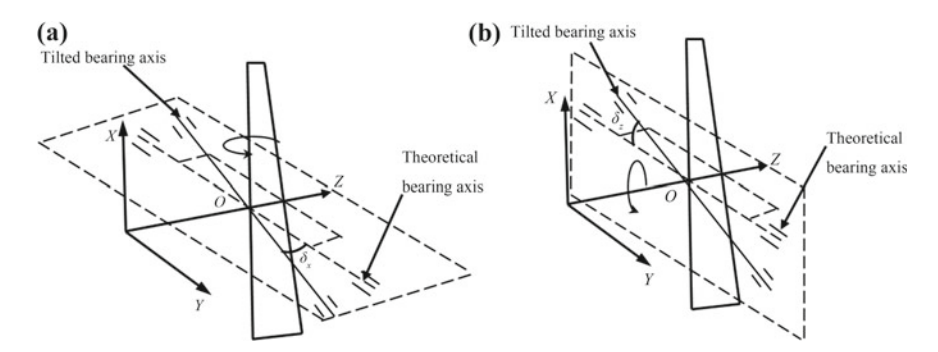


Fig. 4.26 Modeling of bearing assembly errors of prism 1, where **a** and **b** indicate the bearing assembly error δ_x around the *X*-axis and the one δ_z around the *Z*-axis, respectively

4.4.2 Pointing Error Caused by Bearing Assembly

Typical bearing assembly errors are illustrated in Fig. 4.26, where the bearing configuration is simply described by a tilted bearing axis. Taking prism 1 for example, its bearing axis may be tilted around the *X*-axis with an amplitude δ_x or rotated around the *Z*-axis with an amplitude δ_z , as shown in Fig. 4.26a and b. Therefore, any bearing assembly error of prism 1 can be specified by the combination of δ_x and δ_z .

To distinguish what influence the bearing assembly errors of prism 1 and prism 2 have on the beam pointing accuracy, we usually assume that one bearing axis is misaligned with the optical axis of the system while the other bearing is perfectly mounted in the mechanical structure [11].

1. Bearing Assembly Errors of Prism 1

In this situation, there are bearing assembly errors of prism 1 rather than prism 2. Theoretically, the bearing axis of prism 1 is specified by

$$(u_x, u_y, u_z)^{\mathrm{T}} = (0, 1, 0)^{\mathrm{T}}$$
 (4.21)

The tilted bearing axis of prism 1 can be further specified by

$$(u'_{x}, u'_{y}, u'_{z})^{\mathrm{T}} = \mathbf{Rot}(Z, \delta_{z}) \cdot \mathbf{Rot}(X, \delta_{x}) \cdot (u_{x}, u_{y}, u_{z})^{\mathrm{T}}$$
$$= (-\sin \delta_{z} \cos \delta_{x}, \cos \delta_{z} \cos \delta_{x}, \sin \delta_{x})^{\mathrm{T}}$$
(4.22)

Providing prism 1 with the initial tilting angle of 0° , the normal vector N'_{110} to the prism surface 11 and the one N'_{120} to the prism surface 12 are, respectively, expressed as

$$N'_{110} = (0, 0, 1)^{\mathrm{T}} \tag{4.23a}$$

$$N'_{120} = (\sin \alpha, 0, \cos \alpha)^{\mathrm{T}} \tag{4.23b}$$

When the tilting angle of prism 1 becomes θ_{t1} , the rotation matrix M_b for normal vectors to the incident and emergent surfaces of prism 1 are obtained in terms of Rodrigues formulae, as follows

$$\boldsymbol{M_b} = \boldsymbol{A_b} + \cos \theta_{t1}.(\mathbf{I} - \boldsymbol{A_b}) + \sin \theta_{t1}.\boldsymbol{B_b}$$
 (4.24a)

where

$$\mathbf{A_b} = \begin{bmatrix} u_x'^2 & u_x' u_y' & u_x' u_z' \\ u_y' u_x' & u_y'^2 & u_y' u_z' \\ u_z' u_x' & u_z' u_y' & u_z'^2 \end{bmatrix}$$
(4.24b)

$$\boldsymbol{B_{b}} = \begin{bmatrix} 0 & -u'_{z} & u'_{y} \\ u'_{z} & 0 & -u'_{x} \\ -u'_{y} & u'_{x} & 0 \end{bmatrix}$$
(4.24c)

Based on the knowledge of M_b , the resultant normal vector N'_{11} to the surface 11 and the one N'_{12} to the surface 12 are given by

$$N'_{11} = M_b.N'_{110} \tag{4.25a}$$

$$N'_{12} = M_b.N'_{120} \tag{4.25b}$$

Given the tilting angle θ_{12} of prism 2, the normal vector N'_{21} to the prism surface 21 and the one N'_{22} to the prism surface 22 are expressed as

$$N'_{21} = (0, \sin(\alpha + \theta_{t2}), \cos(\alpha + \theta_{t2}))^{\mathrm{T}}$$
 (4.25c)

$$N'_{22} = (0, -\sin\theta_{t2}, \cos\theta_{t2})^{\mathrm{T}}$$
 (4.25d)

Using the vector refraction theorem, these normal vectors N'_{11} , N'_{12} , N'_{21} and N'_{22} can be utilized to deduce the actual horizontal field angle $\rho'_{\rm H}$ and vertical field angle $\rho'_{\rm V}$ of the final emergent beam. Therefore, it is allowed to calculate the errors of vertical and horizontal field angles from (4.20a) and (4.20b), respectively.

If the bearing tilt of prism 1 occurs around the *X*-axis with an amplitude $\delta_x = 0.2''$, the maximum field angle errors $\Delta \rho_{\rm Hmax}$ and $\Delta \rho_{\rm Vmax}$ are both functions dependent on the wedge angle α and the refractive index n, as shown in Fig. 4.27. Clearly, the bearing assembly error around the *X*-axis has more significant influence on the horizontal field angle error $\Delta \rho_{\rm Hmax}$ than the vertical one $\Delta \rho_{\rm Vmax}$. For example, $\Delta \rho_{\rm Hmax}$ can be up to 0.015 μ rad when $\alpha = 5^{\circ}$ and n = 1.517.

If the bearing assembly error of prism 1 exists around the Z-axis, namely $\delta_z = 0.2''$, the variation of $\Delta \rho_{\text{Hmax}}$ and $\Delta \rho_{\text{Vmax}}$ with respect to α can be illustrated in

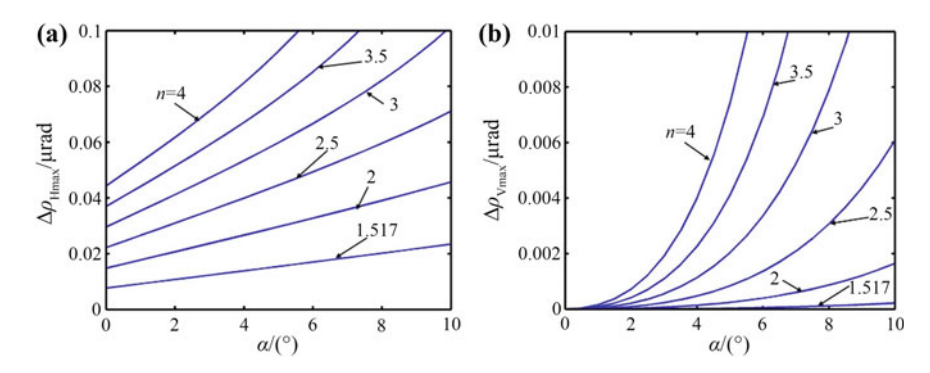


Fig. 4.27 Influence of the wedge angle α on $\Delta \rho_{\rm Hmax}$ and $\Delta \rho_{\rm Vmax}$ when the bearing assembly error of prism 1 is $\delta_x = 0.2''$, where **a** plots $\Delta \rho_{\rm Hmax}$ as a function of α and **b** plots $\Delta \rho_{\rm Vmax}$ as a function of α

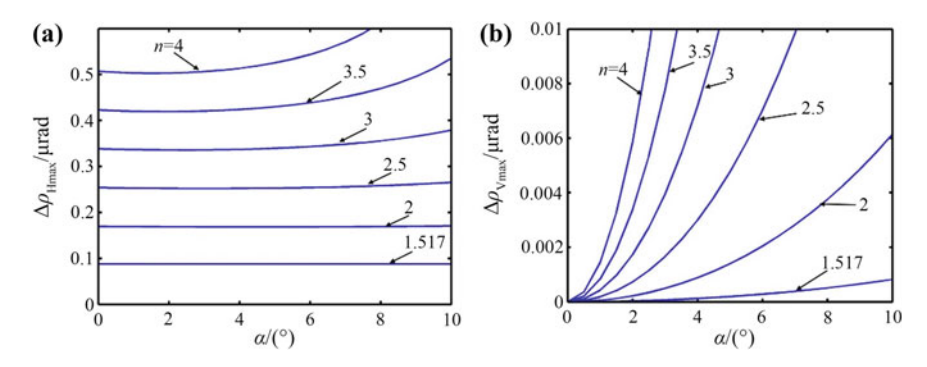


Fig. 4.28 Influence of the wedge angle α on $\Delta \rho_{\rm Hmax}$ and $\Delta \rho_{\rm Vmax}$ when the bearing assembly error of prism 1 is $\delta_z = 0.2''$, where **a** plots $\Delta \rho_{\rm Hmax}$ as a function of α and **b** plots $\Delta \rho_{\rm Vmax}$ as a function of α

Fig. 4.28. The impact of n on $\Delta \rho_{\rm Hmax}$ and $\Delta \rho_{\rm Vmax}$ can also be revealed. It is evident that the bearing assembly error around the Z-axis will result in $\Delta \rho_{\rm Hmax}$ larger than $\Delta \rho_{\rm Vmax}$. Specifically, $\Delta \rho_{\rm Hmax}$ reaches 0.088 μ rad when $\alpha = 5^{\circ}$ and n = 1.517.

2. Bearing Assembly Errors of Prism 2

As for the situation that prism 2 suffers from bearing assembly errors whereas the bearing of prism 1 is perfectly mounted, the resultant beam pointing errors can also be determined in the above way.

If the bearing tilt of prism 2 occurs around the *Y*-axis with an amplitude $\delta_y = 0.2''$, the maximum field angle errors $\Delta \rho_{\rm Hmax}$ and $\Delta \rho_{\rm Vmax}$ are both associated with the wedge angle α and the refractive index n, as shown in Fig. 4.29. Compared to the horizontal field angle error $\Delta \rho_{\rm Hmax}$, the vertical one $\Delta \rho_{\rm Vmax}$ is obviously more affected by the bearing assembly error around the *Y*-axis. For example, $\Delta \rho_{\rm Vmax}$ turns out to be 0.0079 μ rad when $\alpha = 5^{\circ}$ and n = 1.517.

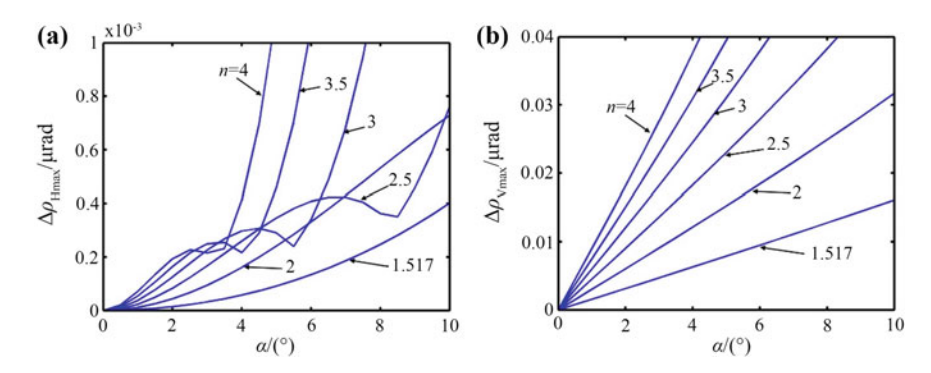


Fig. 4.29 Influence of the wedge angle α on $\Delta \rho_{Hmax}$ and $\Delta \rho_{Vmax}$ when the bearing assembly error of prism 2 is $\delta_y = 0.2''$, where **a** plots $\Delta \rho_{Hmax}$ as a function of α and **b** plots $\Delta \rho_{Vmax}$ as a function of α

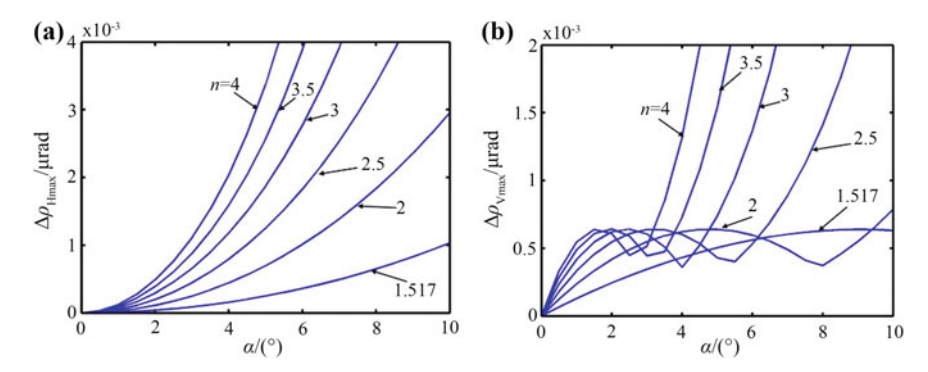


Fig. 4.30 Influence of the wedge angle α on $\Delta \rho_{\rm Hmax}$ and $\Delta \rho_{\rm Vmax}$ when the bearing assembly error of prism 2 is $\delta_z = 0.2''$, where **a** plots $\Delta \rho_{\rm Hmax}$ as a function of α and **b** plots $\Delta \rho_{\rm Vmax}$ as a function of α

If the bearing assembly error of prism 2 exists around the Z-axis, namely $\delta_z = 0.2''$, the variation of $\Delta \rho_{\rm Hmax}$ and $\Delta \rho_{\rm Vmax}$ with α can be described in Fig. 4.30, as well as the impact of n on $\Delta \rho_{\rm Hmax}$ and $\Delta \rho_{\rm Vmax}$. Nevertheless, it is interesting to find that the bearing assembly error around the Z-axis has little influence on either $\Delta \rho_{\rm Hmax}$ or $\Delta \rho_{\rm Vmax}$.

4.5 Summary

In this chapter, some crucial issues that influence the beam scan performance are thoroughly investigated in both rotating and tilting double-prism systems. First, the nonlinearity issue is described by the motion variables of two prisms to view the dynamic scan process, including the change laws of prism orientations, angular velocities and angular accelerations. Then, the control singularity is illustrated. The

relation of the tangential beam steering rate ω_{fr} as well as the radial one ω_{fr} relative to the moving speeds v_x and v_y of beam scan point is established to demonstrate the formation and distribution of singularity phenomenon. Moreover, the distortion degree of the beam emerging from rotating or tilting double prisms is assessed by a quantitative derivation. Simulation results indicate that the change of the wedge angle and the refractive index may have both stretching and squeezing effects on the emergent beam. Such conclusions can provide significant guidance on compensating and correcting the beam distortion. Finally, an error modeling method is introduced to elaborate the potential sources of beam pointing error in double-prism scan system, exemplified by comprehensive analysis on prism and bearing assembly errors.

References

- Li AH, Sun WS, Yi WL et al (2016) Investigation of beam steering performances in rotation Risley-prism scanner. Opt Express 55(19):12840–12850
- Tao XD, Cho H, Janabi-Sharifi F (2008) Active optical system for variable view imaging of micro objects with emphasis on kinematic analysis. Appl Opt 47(22):4121–4132
- 3. Zhou Y, Lu YF, Hei M et al (2013) Motion control of the wedge prisms in Risley-prism-based beam steering system for precise target tracking. Appl Opt 52(12):2849–2857
- Sánchez M, Gutow D (2006) Control laws for a 3-element Risley prism optical beam pointer. Proc SPIE 6304:630403–630403-7
- Mao WW, Xu YZ (1999) Distortion of optical wedges with a large angle of incidence in a collimated beam. Opt Eng 38(4):580–585
- Li AH, Zuo QY, Sun WS et al (2016) Beam distortion of rotation double prisms with an arbitrary incident angle. Appl Opt 55(19):5164–5171
- 7. Sun JF, Liu LR, Yun MJ et al (2006) Distortion of beam shape by a rotating double-prism wide-angle laser beam scanner. Opt Eng 45(4):043004–043004-4
- 8. Li YJ (2011) Closed form analytical inverse solutions for Risley-prism-based beam steering systems in different configurations. Appl Opt 50(22):4302–4309
- 9. Li AH, Zuo QY, Bian YM et al (2016) Assembly error analysis of laser tracking steering prisms with sub-microradian order accuracy. J Mech Eng 52(10):9–16
- Mebius JE. Derivation of the Euler–Rodrigues formula for three-dimensional rotations from the general formula for fourdimensional rotations [EB/OL] [2016-10-13]. http://arxiv.org/pdf/math/0701759v1.pdf
- Zhou Y, Lu YF, Hei M et al (2014) Pointing error analysis of Risley-prism-based beam steering system. Appl Opt 53(25):5775–5783

Chapter 5 Design of Double-Prism Multi-mode Scan System



Abstract Opto-mechanical design principle and techniques are investigated for the development of double-prism scan devices at rotating, tilting or composite motion mode. Design schemes based on the most suitable double-prism configuration are proposed for any scan device, where different drive mechanisms are applied. Particularly, the rotating double-prism scan device driven by worm and gear mechanism is implemented to verify beam scan performance. The tilting double-prism scan device driven by cam-based mechanism is presented to transfer the nonlinear problem to cam profile design. As for composite motion double-prism scan device, the four-axis joint control strategy is used to enhance the adaptability to wide-range, high-precision and multi-scale beam scanning.

In order to improve the performance of double-prism multi-mode scan system, such as scan mode, scan coverage, scan precision, scan efficiency and trajectory characteristics, this chapter places special emphasis on several critical techniques for the system design, including double-prism configuration form, drive mechanism and implementation methods, as well as structure design and performance simulation. A series of optical scan devices are well developed on the basis of rotating or tilting double prisms. Essentially, the proposed devices in this chapter can be generalized with different setup of motion modes of two prisms, such as rotating, tilting and composite motion.

5.1 Configuration

A circular wedge prism has two sides including a flat side and a wedge one, the former is called plane facet, which is perpendicular to the optical axis, and the latter is called wedge facet. For simplicity, the plane facet is denoted by a symbol A while the wedge facet is labeled with a symbol B. Considering that one prism may be situated with the plane facet or the wedge facet outward, there are totally four configuration forms for

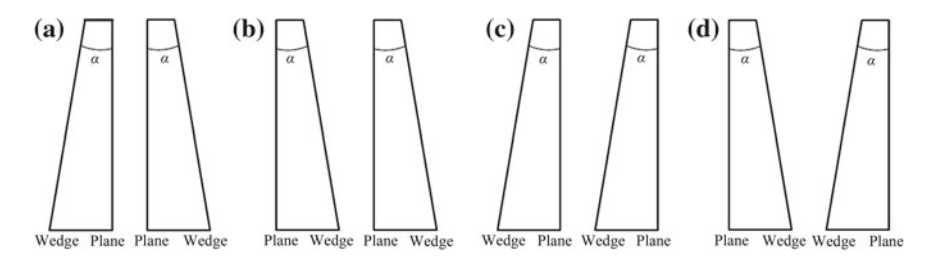


Fig. 5.1 Four different configurations for a double-prism system, where **a-d** illustrate the forms of BA-AB, AB-AB, BA-BA and AB-BA, respectively

a double-prism system as shown in Fig. 5.1, described by BA-AB, AB-AB, BA-BA and AB-BA, respectively [1].

Depending on the arrangement of prisms 2, the above four configurations can be divided into two groups. The BA-AB and AB-AB configurations are included by group 1, while the BA-BA and AB-BA configurations are two members in group 2 [1]. Under the coordinate system shown in Fig. 2.5, the incident beam propagates parallel to the *Z*-axis. Providing prism 1 and prism 2 with their individual rotation angles θ_{r1} and θ_{r2} , the emergent beam vector $A_{rf1} = (x_{rf1}, y_{rf1}, z_{rf1})^T$ that exits from rotating double prisms under either configuration in group 1 can be further obtained from the vector refraction theorem, expressed as [1].

$$x_{rf1} = a_1 \cos \theta_{r1} + a_3 \sin \alpha \cos \theta_{r2} \tag{5.1a}$$

$$y_{rf1} = a_1 \sin \theta_{r1} + a_3 \sin \alpha \sin \theta_{r2} \tag{5.1b}$$

$$z_{rf1} = a_2 - a_3 \cos \alpha \tag{5.1c}$$

Similarly, the emergent beam vector $A_{rf2} = (x_{rf2}, y_{rf2}, z_{rf2})^{T}$ from rotating double prisms under either configuration in group 2 can be expressed as [1]

$$x_{rf2} = b_1 \cos \theta_{r1} - b_3 \sin \alpha \cos \theta_{r2} \tag{5.2a}$$

$$y_{rf2} = b_1 \sin \theta_{r1} - b_3 \sin \alpha \sin \theta_{r2} \tag{5.2b}$$

$$z_{rf2} = -\sqrt{1 - n^2 + (b_2 + b_3 \cos a)^2}$$
 (5.2c)

The coefficients a_1 , a_2 and a_3 of (5.1a) are determined from the expressions in Table 5.1, while the coefficients b_1 , b_2 and b_3 of (5.2a) are given by the expressions in Table 5.2.

Using (5.1a) and (5.2a), the beam deviation induced by rotating double prisms can be quantitatively compared under different configurations. Given that each prism has the wedge angle $\alpha = 10^{\circ}$ and the refractive index n = 1.517, the pitch angle ρ of the emergent beam ranges from 0° to 10.6255° under the BA-AB configuration, from 0.0709° to 10.6986° under the AB-AB configuration, from 0.0690° to 10.4086° under the BA-BA configuration, and from 0° to 10.4796° under the AB-BA configuration.

5.1 Configuration 185

group 1		
Coefficients	BA-AB configuration	AB-AB configuration
a_1	$\frac{\sin\alpha(\cos\alpha - \sqrt{n^2 - \sin^2\alpha})}{\sqrt{n^2 - \sin^2\alpha}}$	$\sin\alpha(-n\cos\alpha+\sqrt{1-n^2\sin^2\alpha})$
a_2	$-\sin^2\alpha + \cos\alpha\sqrt{n^2 - \sin^2\alpha}$	$-\sqrt{n^2 - 1 + \left[n\sin^2\alpha + \cos\alpha\sqrt{1 - n^2\sin^2\alpha}\right]^2}$
<i>a</i> ₃	$-(a_1 \sin \alpha \cos \Delta \theta_r - a_2 \cos \alpha) + \sqrt{1 - n^2 + (a_1 \sin \alpha \cos \alpha)}$ $\theta_{r2} - \theta_{r1}$	$\cos \Delta \theta_r - a_2 \cos \alpha)^2 \Delta \theta_r =$

Table 5.1 Coefficients used to express the emergent beam vectors under two configurations in group 1

Table 5.2 Coefficients used to express the emergent beam vectors under two configurations in group 2

Coefficients	BA-BA configuration	AB-BA configuration
b_1	$\sin\alpha(\cos\alpha - \sqrt{n^2 - \sin^2\alpha})$	$\sin\alpha(-n\cos\alpha+\sqrt{1-n^2\sin^2\alpha})$
b_2	$\sqrt{1 - n^2 + (\sin^2 \alpha + \cos \alpha \sqrt{n^2 - \sin^2 \alpha})^2}$	$n\sin^2\alpha + \cos\alpha\sqrt{1 - n^2\sin^2\alpha}$
<i>b</i> ₃	$b_1 \sin \alpha \cos \Delta \theta_r - b_2 \cos \alpha + \sqrt{n^2 - 1 + (b_1 \sin \alpha \cos \Delta \theta_r - b_2 \cos \alpha)^2} \Delta \theta_{r2} - \theta_{r1}$	$\Delta heta_r =$

Although the minimum pitch angle seems relatively small under the AB-AB or BA-BA configuration, it may result in large beam deviation and even generate blind zone issues in far-field scan applications. Differently, the minimum pitch angle is 0° under the BA-AB or AB-BA configuration, which implies no blind zone once the emergent surface center of prism 2 can be regarded as the exiting position of the emergent beam. To guarantee the adaptability of beam scanning in a variable distance, rotating double prisms should not be arranged in the AB-AB or BA-BA configuration. As for rotating double prisms in the BA-AB configuration, there are multiple beam reflections between the plane facets of two prisms, and the resultant beam refractions may interfere with the beam scan point. Therefore, the AB-BA configuration is applied to most rotating double-prism scan devices presented in this chapter.

Likewise, tilting double prisms can be arranged in the above four configurations, namely BA-AB, AB-AB, BA-BA and AB-BA. These configurations are different in the thinnest-end pointing direction of each prism, and as a result, the consequent beam scan point is steered towards different coordinate quadrants. However, the horizontal and vertical field angles of the emergent beam from tilting double prisms are both non-monotonic functions that depend on the tilting angles θ_{t1} and θ_{t2} varying within -45° to 45° , as shown in Fig. 2.16. To facilitate the motion control of the

system, it is preferable to restrict the horizontal and vertical field angles within their monotonic intervals. Such a requirement can be satisfied by placing double prisms in the AB-BA configuration, once the tilting angle of each prism increases from 0°. Consequently, the AB-BA configuration is also applied to the tilting double-prism scan devices presented in this chapter, where prism 1 and prism 2 are situated with the thinnest ends pointing upwards and outwards, respectively.

5.2 Motion Mechanism

5.2.1 Rotating Double Prisms

The motion mechanism of the double-prism scan device directly determines the key technical indexes such as the scan mode, scan speed and scan precision of the beam. Different motion forms have great differences in the space layout, mechanism design and control requirements.

1. Driven by Torque Motor Directly

Figure 5.2 shows a motor direct-drive rotating double-prism device developed by Optra Company [2], which uses a torque motor coupling the prism to achieve full-circle rotation. In this form, the device has advantages of high scan precision, multiple scan mode, and stable scan trajectory by controlling the rotation angles and angular velocities of two prisms separately. However, for the full-circle rotating prism, there are problems such as torque ripple and slot effect, which will affect the control precision of the prisms. Moreover, direct-drive motors for large-aperture prism systems generally require special customization that the cost of process are relatively high. The author [3] proposed a device where two torque motors coupled to prism frames are respectively used to drive two prisms to achieve a wide range scanning of the beam.

2. Synchronous Belt Drive

The motion mechanism of the prism driven by servo motor through tension belt has the advantages of simple structure and flexible arrangement. Meanwhile, it facilitates adjusting the speed and position of the prism to meet the different scan requirements in various occasions. In 2007, García-Torales et al. [4] proposed a high precision prism scanning system driven by the synchronous belt. Three-phase brushless motor is employed with the size less than 40 mm² and a peak torque of 7.2 N m, which has a fast response speed. Moreover, the sine-wave driving is easy to achieve smooth operation and high resolution control.

Li and Gao [5] proposed a synchronous belt drive device for the large-aperture rotating prisms, as shown in Fig. 5.3. Combined with a rotary encoder to achieve the feedback adjustment, the precise control of the prism rotation can be accomplished. The synchronous belt drive system has the advantages of smooth transmission, vibration absorption, small noise, flexible arrangement, compact structure and accurate transmission ratio.

5.2 Motion Mechanism 187

Fig. 5.2 Rotating double-prism system driven by torque motor directly, where 1 is encoder, 2 is stator, 3 is rotor, 4 is bearing and 5 is frame

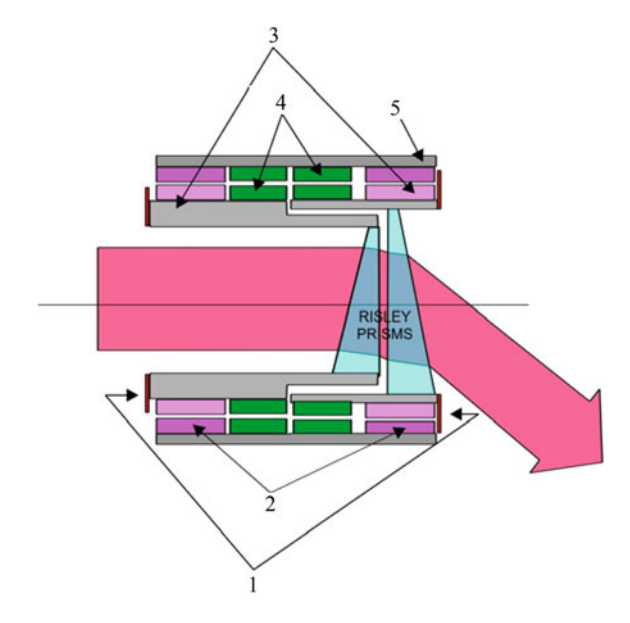
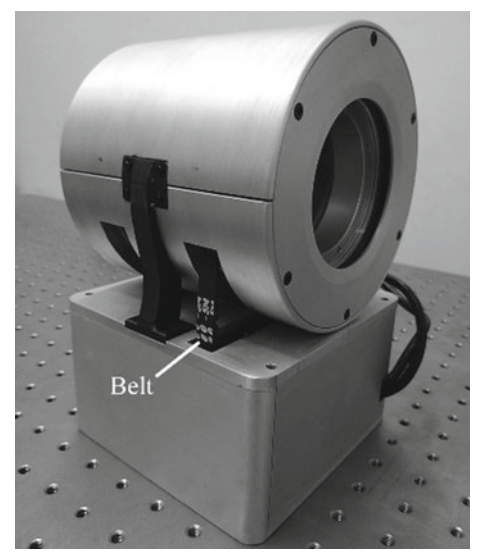


Fig. 5.3 Rotating double-prism scan device driven by synchronous belt



3. Gear Drive

Yuan et al. [6] proposed a gear-driven rotating double-prism device. Two sets of gear pairs are used to drive the two prisms, independently. With the drive of DC torque motor, the transmission of spur gear meshing, the supporting of optical wedge precision shaft, as well as the reliable clamping and positioning of optical wedges, the high-precision scanning can be ensured for large-aperture incident beam. But

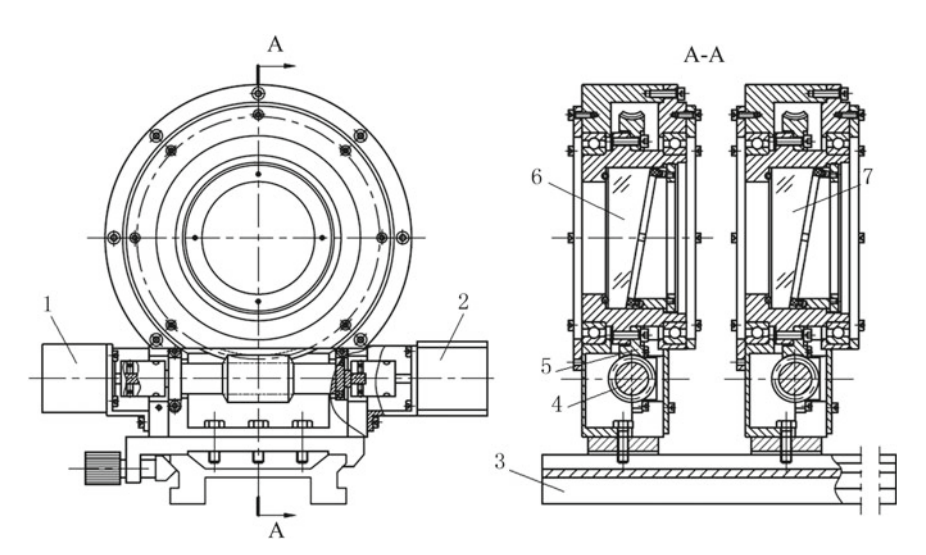


Fig. 5.4 Rotating double-prism device driven by worm and worm gear, where 1 is encoder, 2 is stepping motor, 3 is base rail, 4 is worm, 5 is worm gear, 6 is prism 1 and 7 is prism 2

with its large size in diametrical dimension, the structure is complicated and not compact.

Yun et al. [7] mentioned a control method of the rotating prism driven by gears, but did not give a detailed structural design. Zu et al. [8] proposed a method of using electromotor unit with the transmission of gears to implement different combinations of rotating double prisms, which can be used to simulate the relative motion of the satellite. However, the motor-unit driving scheme and control system are complex, as well as the space layout of the whole system.

4. Worm Gear Drive

The author [9] proposes a coarse-fine scanning double-prism device. The coarse scanning is achieved through the worm gear mechanism to drive the prism around the optical axis. But the fine scanning can be performed by the main section of the prism tilted around the horizontal rotating axis (or vertical rotating axis). The author team also proposed a double-prism scan device driven by two sets of worm gear mechanisms [10], as shown in Fig. 5.4.

The characteristics of motion mechanisms above mentioned are compared in Table 5.3.

5.2 Motion Mechanism 189

Table 5.3 Comparison of several rotating double-prism motion mechanisms

Motion mechanism	Basic transmission principle	Advantages	Limitations	Applications
Torque motor	Torque motor directly drives the prism	The speed and orientation are controlled separately; rich scan mode and stable track trojectory	Torque ripple and slot effect affect the precision, large motors need to be customized	Small aperture, motion continuity and precision are not high
Synchronous belt	Servo motor drives prism rotation through synchronous belt	Simple structure, convenient for angle and angular velocity adjustment of the prism; smooth, shock-absorbing, low noise; accurate transmission ratio, no slip	Cracking, deformation, lengthening and breaking occur to the belt when it ages	Prism and drive split; not suitable for harsh environments
Gear	Transmit torque by two sets of gear pairs, which drive the two prisms respectively	The speed and orientation are controlled separately; high-precision, stable scanning for large-aperture beams	Large in size along the optical axis and the structure is complex and not compact	Large-aperture system, high-precision scanning, and low limitation to the size of the device
Worm and gear	Rotary motor drives the worm, then the worm gear drives prism	Large transmission ratio, simple and compact structure	There is a meshing gap and the backlash is difficult to eliminate	Large aperture; no need of changing orientation, and low speed scanning

5.2.2 Tilting Double Prisms

The characteristic of the tilting double-prism motion mechanism is reciprocating motion and short stroke without backhaul clearance.

1. Stepper Motor Direct Drive

Sun et al. [11] proposed that the tilting motion of the optical element can be achieved by a stepper motor coupled with the rotating shaft. It has the compact structure and no mechanical transmission error. However, the resolution of the prism angle is directly constrained by the step angle of stepper motor. Meanwhile, the feedback of the tilting

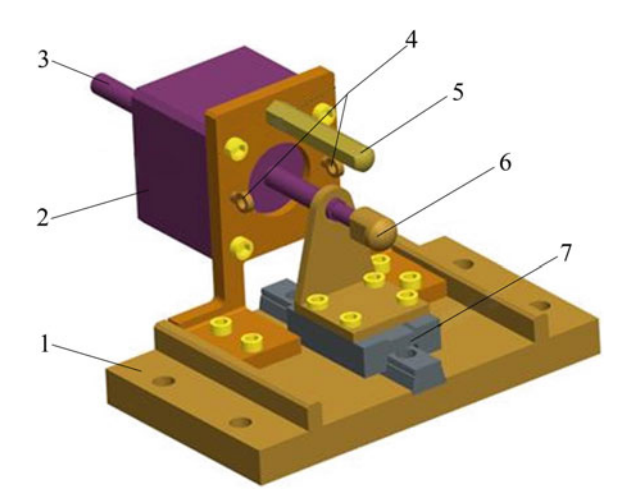


Fig. 5.5 Linear motor screw propulsion prism-swinging mechanism, where 1 is base, 2 is linear stepper motor, 3 is motor screw, 4 is preloaded spring loop, 5 is stop screw, 6 is nut (top in V-groove) and 7 is slider

angles of the prisms is not given, which make it difficult to correct the tilting angle error of the double prisms in real time.

2. Linear Motor Screw Drive

The author [12] proposed a screw propulsion mechanism driven by a linear motor to tilt the prism. Figure 5.5 shows the model of the linear motor screw propulsion mechanism, which is mainly composed of a linear stepper motor, a motor screw, a nut, a stop screw, a slider, a base, and a tilting plate. As we can see, the nut is installed at the front end of the motor screw. There are two preloaded springs at the left and right sides to make sure that the V-groove of the tilting plate keeps always in contact with the nut. Before tilting, the stop screw ensures that the prism frame does not deviate from its original position. To stay stationary in motion, the motor screw is connected with the guide rail slider through the guide frame. This mechanism converts the linear motion of the motor into a small-angle tilting of the prism, which improves the control precision in principle. The main disadvantage is that the motion relationship between motor and the prism is relatively complicated as the speed and acceleration of them are nonlinearly related. In addition, friction and abnormal noise are easily generated between the nut and the V-groove.

5.2 Motion Mechanism 191

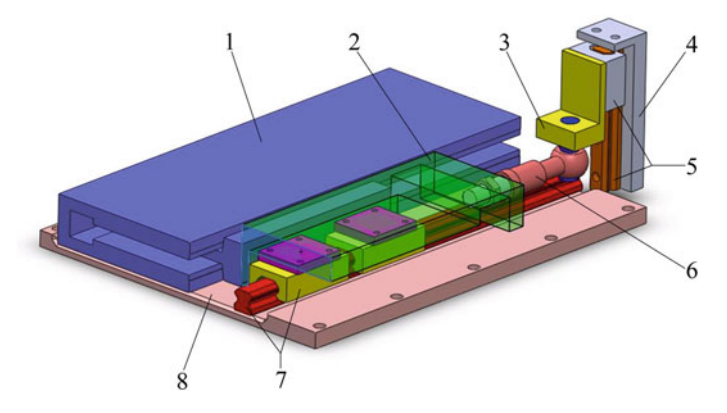


Fig. 5.6 Double-slider implicated tilting prism mechanism composed of 1-linear motor, 2-cover plate, 3-L-shaped plate, 4-tilting plate, 5-vertical guide rail and slider, 6-joint bearing, 7-horizontal guide rail and slider and 8-base

3. Double-Slider Implicating Drive

In order to overcome the friction and abnormal noise generated between the nut and the V-groove in the linear motor screw propulsion mechanism, the author [13] designed a tilting double-prism scan device based on a double-slider-implicated mechanism, as shown in Fig. 5.6.

It is mainly composed of a linear motor, a cover plate, a horizontal guide rail, a horizontal slider, a joint bearing, a vertical guide rail, a vertical slider, a base, an L-shaped plate, and a tilting plate. Connected rigidly with the cover plate and the horizontal slider, the motor mover drives the horizontal slider reciprocates on the horizontal guide rail. Similarly, connected with the L-shaped plate, the vertical slider is driven to reciprocate on the vertical guide rail by the joint bearing. In this way, the linear motion of the motor mover is converted into the tilting motion of the prism frame through the joint bearing. Compared with the point contact between the nut and the V-groove in the linear motor screw propulsion mechanism, the surface contact between the vertical slider and the guide rail has the advantages of smaller friction.

4. Cam Drive

Figure 5.7 illustrates a cam-based drive tilting prism mechanism [14]. For a specific scan trajectory, the cam-drive mechanism can transform the complex nonlinear control into the profile design of the cam and improve the robustness of the control system. The mechanism is mainly composed of a cam, a motor, two spiral spring, a synchronous belt, a belt wheel and a tilting plate. The tilting axis is subjected to the pre-tightening force of the spiral springs to keep the tilting plate in contact with the cam. In the cam-based drive mechanism, only a proper cam profile is needed to be designed to precisely realize the predetermined motion law of the prism. However, due to the relative sliding at the contact line between the cam and the tilting plate,

Fig. 5.7 Cam drive tilting prism mechanism, where 1 is motor, 2 is cam, 3 is tilting plate, 4 is spiral spring, 5 is belt wheel and 6 is synchronous belt

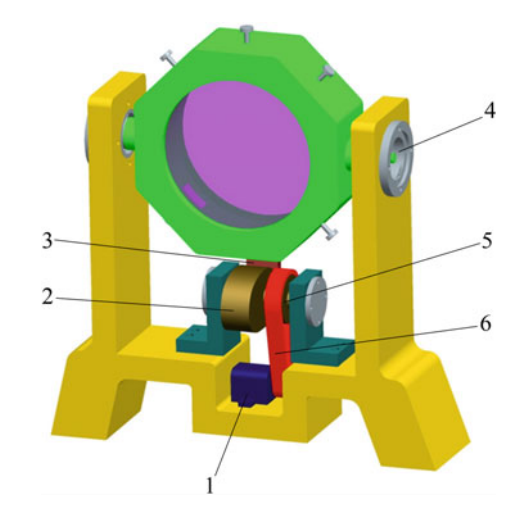
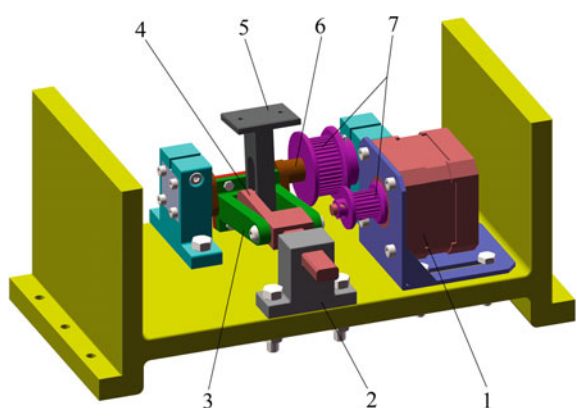


Fig. 5.8 Slider-crank tilting prism mechanism, where 1–7 denote motor, horizontal guide rail, connecting rod, horizontal slider, L-shaped prism frame connecting block, crankshaft and belt wheel, respectively



the system precision will be affected by the abrasion. The measure of adding rollers at the contact line can be considered to solve the problem.

5. Slider-Crank Drive

Figure 5.8 shows a slider-crank tilting prism mechanism [15]. This mechanism is mainly composed of a motor, a crankshaft, a connecting rod, a horizontal slider, a horizontal guide rail, a synchronous belt, two belt wheels, and an L-shaped prism frame connecting block. Through the slider-crank mechanism, a continuous rotating motion of the crankshaft can be converted into the reciprocating tilting motion of the prism. The motion accuracy of double-prism scanner can be ensured.

The comparisons of the above-mentioned tilting double-prism motion mechanisms are shown in Table 5.4.

Table 5.4 Comparisons of several tilting double-prism motion mechanisms

Motion mechanism	Basic transmission principle	Advantages	Limitations	Applications
Stepping motor	Stepper motor directly coupled to the tilting axis	Small mechanical transmission error; easy to control the tilting angle; compact structure	High precision for stepper motors; prone to vibration	High-speed scanning; low requirements for motion continuity and precision
Linear motor screw	The linear motor screw pushes the tilting plate fixed on the prism frame to tilt	Simple structure; high control precision	Non-linear relationship between motor and prism tilting angle; friction and abnormal sound	Small-aperture lightweight system; high-precision scanning
Joint bearing, double-slider guide rail	The linear motor drives the horizontal slide rail, which drives the vertical slide guide through the joint bearing and drives the prism to tilt	Small friction, no abnormal noise	The non-linear relationship between the motor and prism tilting angle; multiple links and large devices; large accumulated mechanical errors	Large-aperture heavy system; low requirement for scan precision
Cam, synchronous belt	The cam rotates at a constant speed and the prism frame is continuously driven to tilt by the connecting rod	Simplify nonlinear control; compact structure, easy to design	The mechanical processing is difficult; the line contact is easy to wear	Constant trajectory scanning; small-aperture lightweight system
Slider and crank, synchronous belt	The motor drives prism to tilt through synchronous belt and slider-crank mechanism	High control precision	The friction at the slider contact area affects the precision	Small-aperture lightweight system

5.3 Design of Rotating Double-Prism Scan Device

5.3.1 Design Requirements

According to the requirements of beam scan performance, two sets of rotating double-prism multi-mode scan system are designed. One is driven directly by a torque motor

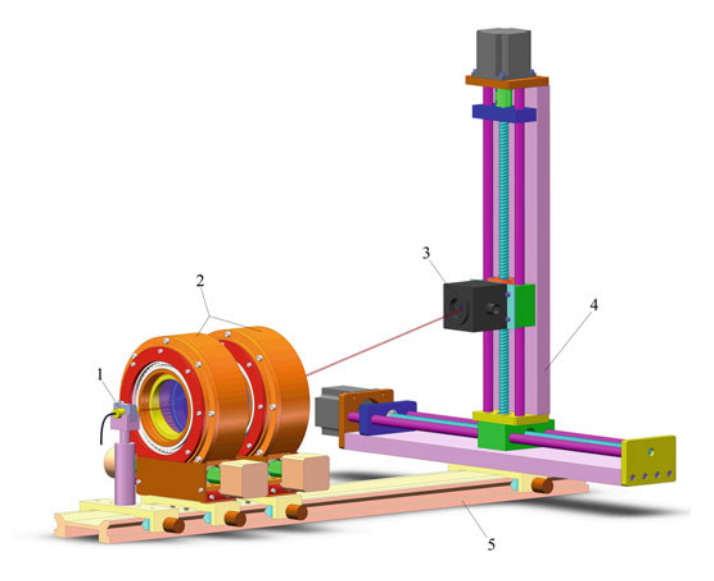


Fig. 5.9 Diagram of the worm and gear rotating double prism scan system, where 1 is laser source, 2 is rotating double prisms, 3 is four-Quadrant detector, 4 is two-dimensional electric slider and 5 is guide rail

[3] and the other is by a worm gear mechanism. Taking the worm gear drive scan system as an example, as shown in Fig. 5.9. The design requirements are as follows:

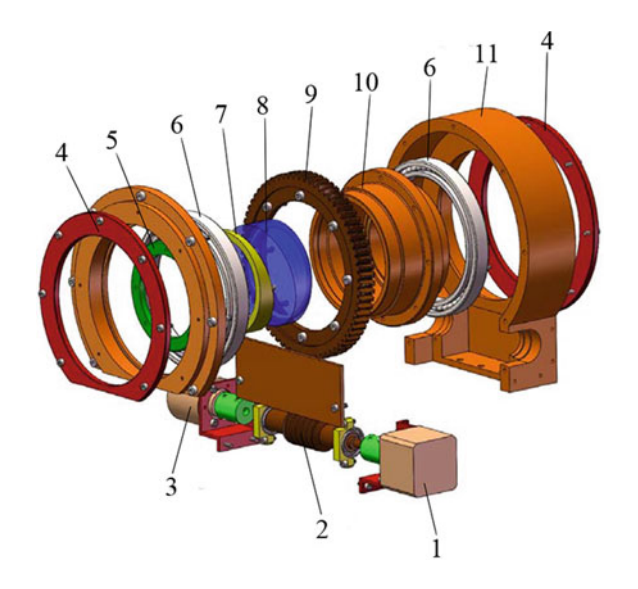
- (1) The beam scan coverage should allow the pitch angle within $\pm 10^{\circ}$ and the azimuth angle across 0° –360°.
- (2) The beam scan precision should be better than 50 μ rad.
- (3) The clear aperture of the system is $D_p = 60$ mm.
- (4) The refractive index of each prism is n = 1.517.
- (5) The rotating double prisms are driven by worm and gear mechanism.
- (6) The applicable wavelength ranges from 500 to 1550 nm (λ =650 nm in the experiment).

5.3.2 Mechanical Structure Design

The rotating double-prism scan system is shown in Fig. 5.9 [10]. Figure 5.10 shows the exploded view of the single rotating prism assembly, including the base, bearing ring, prism frame, prism, wedge ring, threaded ring, worm gear, worm, bearing, stepping motor, and feedback encoder.

The structure parameters of the prism are as follows: the prism wedge angle $\alpha = 10^{\circ}$, the refractive index n = 1.517, the diameter D = 80 mm, the effective clear aperture $D_p = 60$ mm and the thinnest-end thickness $d_0 = 5$ mm.

Fig. 5.10 Exploded view of single rotating prism assembly, where 1 is stepping motor, 2 is worm, 3 is feedback encoder, 4 is bearing ring, 5 is thread ring, 6 is bearing, 7 is wedge ring, 8 is prism, 9 is worm gear, 10 is prism frame and 11 is base



The rotation angle and angular velocity of the prism can be precisely controlled by the number and the frequency of pulses of the stepping motor. When the rotating double-prism scan device is applied to tracking and scanning, the stepping motor is expected to start and stop continuously and can be accurately positioned as the target moves. Thus, the detailed parameters of the stepping motor selected for this device are shown in Table 5.5.

The device is driven by the worm gear mechanism with small impact load, stable transmission, and low noise, which can effectively reduce the size of the entire device and can be self-locked to ensure the stability and reliability of the prism position. The worm is fixed on the prism frame with screws to drive the prism to rotate. The parameters of the worm and gear are shown in Table 5.6, while the main geometric parameters are shown in Table 5.7.

A physical photograph of the entire device is shown in Fig. 5.11.

5.3.3 Control System Design

In the rotating double-prism scan system, when two prisms are driven by two stepping motors, respectively, two rotary encoders collect the rotation angle values of two prisms and automatically adjust the rotation angles and angular velocities of two stepping motors, and a LCD is used to display the status of the angular velocities and angles of two prisms. Furthermore, a series of buttons are designed for parameters input and interface set. The control functions are shown in Table 5.8.

A LPC1114 processor is used in the control system based on the ARM Cortex-M0 core. With an integrated 32 KB Flash memory, a LPC1114 processor has a

 Table 5.5
 Parameters of the stepping motor

Model	Step angle/(°)	Current/A	Resistance/Ω	Inductance/mH	Static moment/(N cm)	Positioning moment/(N cm)	Moment of inertia/(g cm ²)	Body length/mm
42HS	1.8	1.3	2.5	5	40	2.2	54	40

Table 5.6	Main	parameters of the	he worm	and gear

Main parameters	Worm gear	Worm
Center distance a/mm	80	
Transmission ratio i	69	
Modulus m/mm	2	
Tooth number/head number Z	69	1
Modification coefficient x_2	-0.100	
Tooth angle α	20°	
Addendum coefficient h* a	1	
Clearance coefficient c^*	0.25	
Worm type	_	Involute

Table 5.7 Main geometric parameters of the worm and gear

Geometric parameters	Worm gear	Worm
Reference circle diameter d/mm	138	22.4
Root circle diameter d_f /mm	132.6	17.4
Addendum circle diameter $d_e(\text{or } d_a)/\text{mm}$	144	26.4
Gorge diameter d _a /mm	141.6	_
Lead angle	5°06′08″	
Tooth depth h/mm	4.5	
Tooth width b/mm	14	_
Axial tooth thickness S_x /mm	3.14	

Universal Asynchronous Serial Transceiver (UART), two SSP controllers, one I2C bus interface, eight 10-bit AD converters, two 32-bit timers, four 16-bit timers and up to 42 GPIO interfaces. Figure 5.12 shows the overall design planning of a LPC1114-based motion controller.

The motion controller mainly includes the following parts:

- (1) LPC1114 minimum system: including crystal oscillator, power-on reset circuit and manual reset circuit:
- (2) Power circuit: convert 24–5 V and convert 5–3.3 V;
- (3) 24 V digital input circuit;
- (4) 5 V digital and PWM output circuit;
- (5) RS485 communication circuit;
- (6) RS232 program download interface;
- (7) LCD12864 control interface;
- (8) 4×4 matrix keyboard control interface;
- (9) I2C communication interface;
- (10) SPI communication interface.

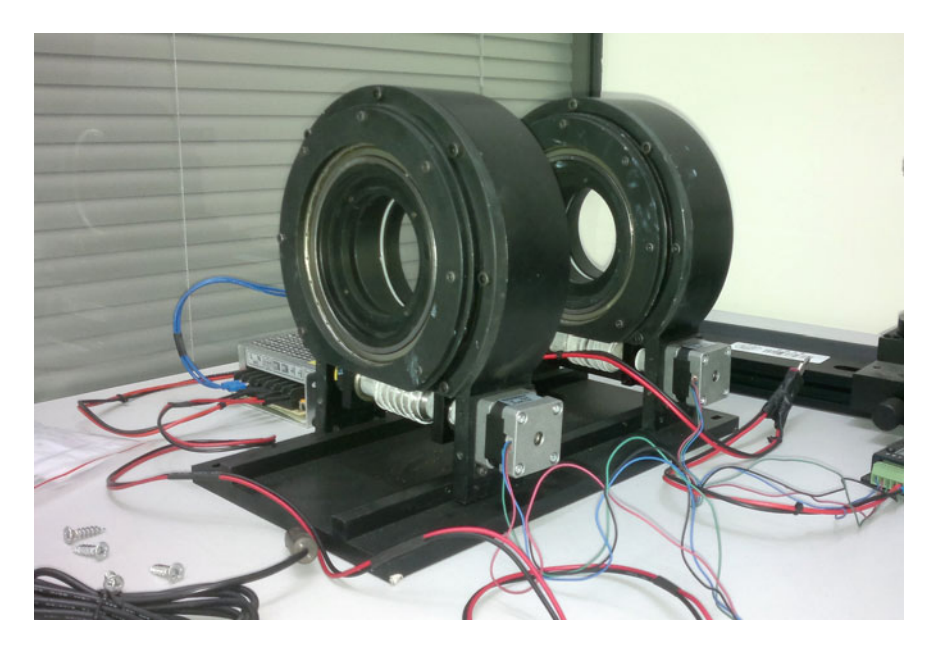


Fig. 5.11 Physical photo of the rotating double prisms

Figure 5.13 shows the printed circuit board (PCB) of the controller. The whole appearance of the controller with a shell is shown in Fig. 5.14.

The control box contains a 24 V switchable power supply, 2 stepping motor drivers and a motion controller, as shown in Fig. 5.15.

A two-phase hybrid stepping motor driver typed by M542 is used in the control system, as shown in Fig. 5.16. It uses DC 18–50 V power supply, which is suitable for the two-phase hybrid stepping motor with driving voltage 24–50 V, current less than 4.2 A and external diameter 42–86 mm. The driver is subdivided by the current loop of the AC servo driver. The motor has the characteristics of small torque fluctuation, smooth running at low speed, and few vibration or noise. Compared with other two-phase drivers, the torque is much higher at high speed and the positioning precision is high enough to meet the requirements.

5.3.4 Assembly Error Analysis

In a double-prism scan system, the main error sources that impact on the assembly accuracy of double prisms can be summarized as tilt errors of the prism and bearing [16, 17]. The specific analysis is as follows.

Serial number	Function	Quantity required	Quantity designed	Remarks
1	24 V Digital input (encoder)	4	8	4 spare
2	5 V PWM output	2	4	2 spare
3	RS232 communication (program download)	1	1	-
4	RS485 communication (online communication)	1	1	_
5	I2C	1	1	_
6	SPI	1	1	_
7	LCD display screen (data display)	1	1	-
8	LED Indicator (debugging)	1	1	-
9	Buzzer (alarm)	1	1	_

Table 5.8 Requirements for the control functions of the rotating double-prism scan system

1. Pointing Error Affected by Prism Assembly

In the rotating double-prism scan system, t rotate around the Z-axis. However, the rotation angle error around the Z-axis may occur during the prism installation process, that is, the initial position of the prism is not at the 0° position. By rotating the prism around the axis, the initial position of the prism can be returned to the 0° position, so in this section we do not discuss about the rotation angle error of the prism around the Z-axis.

The spin axis OL is introduced to help describe the prism tilt around the X- or Y-axis, and the axis OL can be defined by rotating the X-axis counterclockwise around the Z-axis with an angle θ_0 . In other words, OL passes the coordinate origin and locates in the XOY plane, which is further determined by the unit vector $(u_x, u_y, u_z)^T = (\cos \theta_0, \sin \theta_0, 0)^T$. Hence, the prism tilt around OL can be equivalent to that around the X-axis when OL coincides with the X-axis and that around the X-axis when OL coincides with the X-axis.

Assumed that prism 1 is tilted around the axis OL with an angle δ_0 . Specially, the angle δ_0 of prism tilt represents the assembly error around the X-axis when $\theta_0 = 0$ and the one around the Y-axis when $\theta_0 = 90^\circ$. According to Rodrigues formulae, the rotation matrix M_p that specifies the incident or emergent surface normal of prism 1 can be expressed as

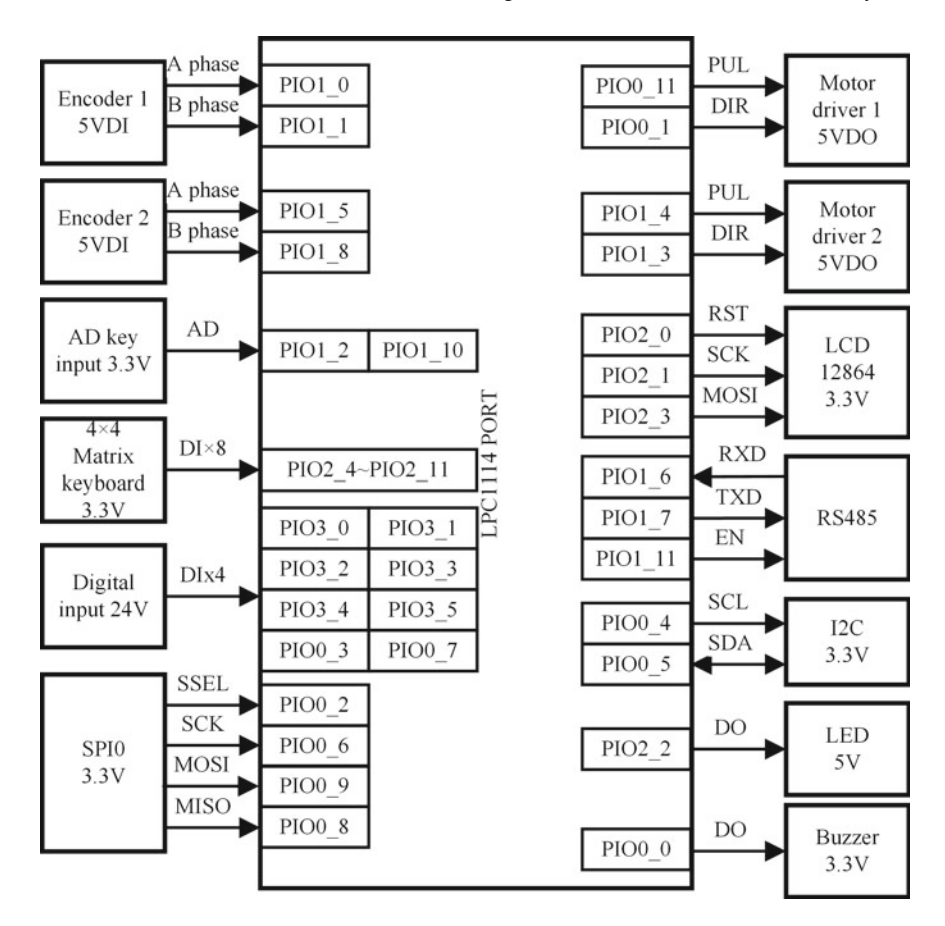


Fig. 5.12 LPC1114 Overall design planning

$$\boldsymbol{M}_{p} = \boldsymbol{A}_{p} + \cos \delta_{0} \cdot (\boldsymbol{I} - \boldsymbol{A}_{p}) + \sin \delta_{0} \cdot \boldsymbol{B}_{p}$$
 (5.3)

where I is a three-order unit matrix, and A_p and B_p are, respectively, given by (4.13a) and (4.13b).

(1) Assembly Errors of Prism 1

In this situation, prism 1 suffers from an assembly error of δ_0 , while prism 2 is perfectly mounted. According to the rotation matrix M_P , the normal vectors N'_{11} , N'_{12} , N'_{21} and N'_{22} to the prism surfaces 11, 12, 21 and 22 can be obtained, respectively. Using the vector refraction theorem, the incident, refracted and emergent beam vectors A_{r0} , A'_{r1} and A'_{r2} of prism 1 and those of prism 2, A'_{r2} , A'_{r3} and A'_{rf} , can be sequentially given.

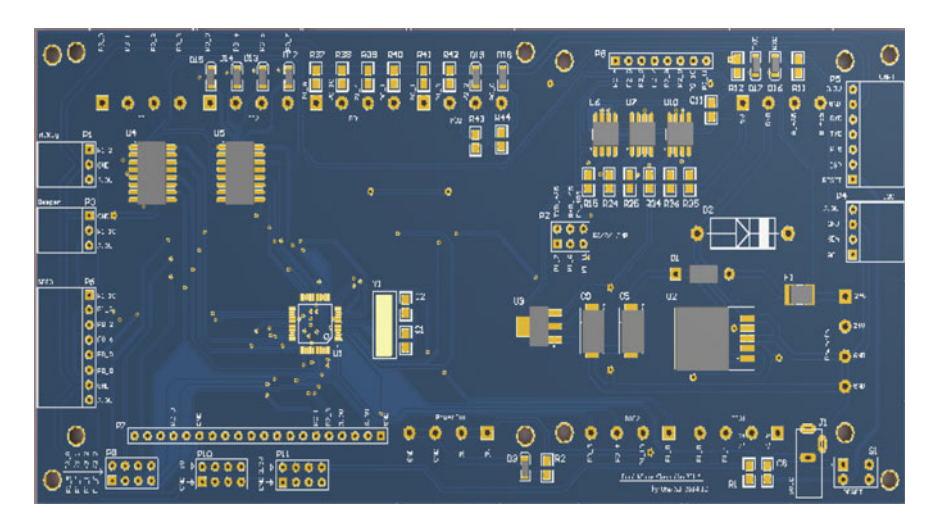


Fig. 5.13 PCB of the controller

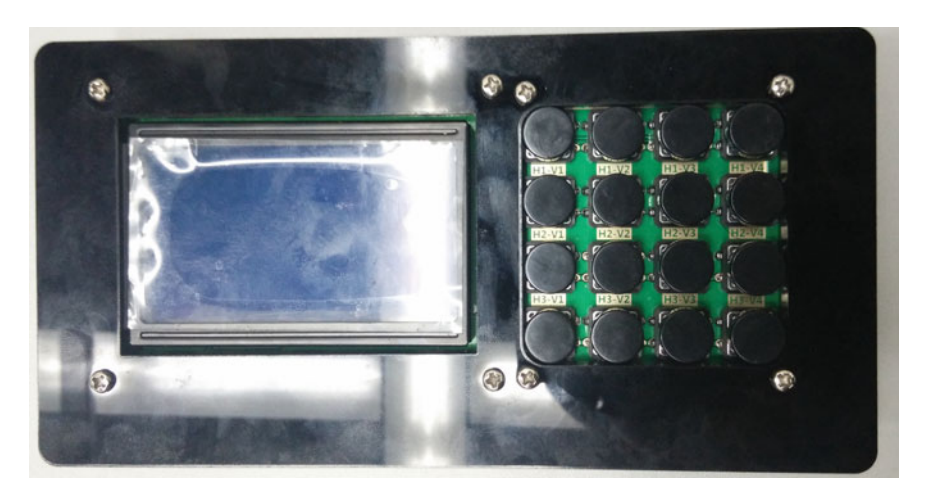


Fig. 5.14 Appearance of the controller

According to (2.6a–2.6d) and (2.7a–2.7e), the theoretical emergent beam vector A_{rf} of prism 2 can be worked out, and then the pointing error of the rotating double-prism system, which is the angle Δ between A_{rf} and A'_{rf} , can be expressed as

$$\Delta = \arccos\left(\frac{A_{rf} \cdot A_{rf}'}{|A_{rf}| \cdot |A_{rf}'|}\right) \tag{5.4}$$

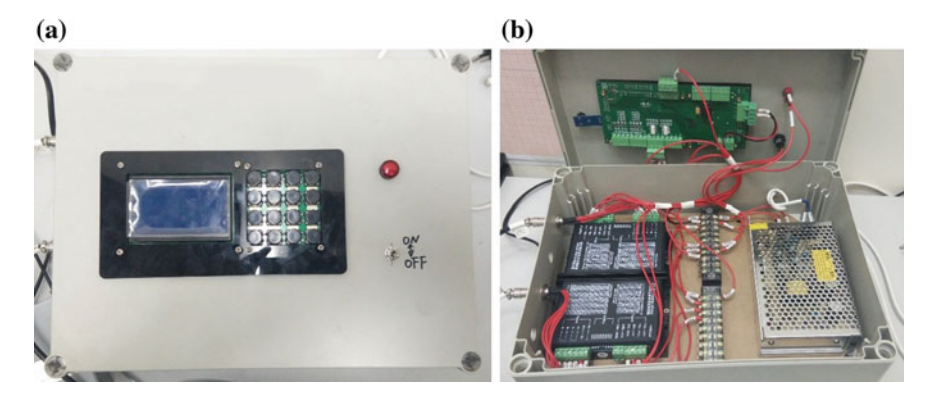


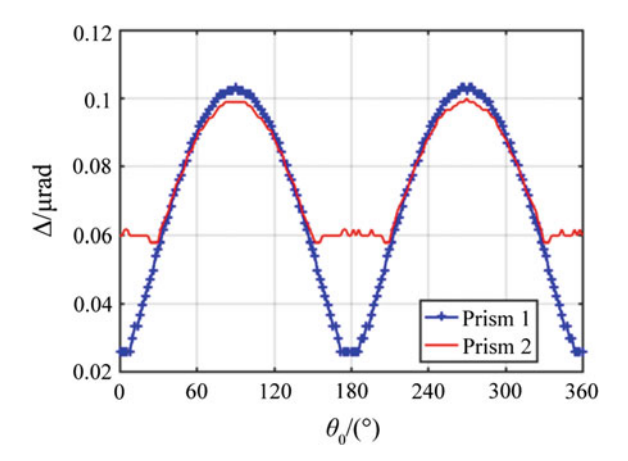
Fig. 5.15 Drive control box. a Front appearance. b Internal structure

Fig. 5.16 Two-phase hybrid stepping motor driver (M542)



According to the assembly conditions in practice, the tilt amplitude of prism 1 around the axis OL is held constant at $\delta_0 = 1''$ in order to investigate the pointing error Δ_1 caused by the tilt error of prism 1.

Fig. 5.17 Influence of the prism tilt direction θ_0 on the pointing error Δ when the prism tilt amplitude is $\delta_0 = 1''$



(2) Assembly Errors of Prism 2

Regarding the situation that prism 2 suffers from an assembly error of δ_0 while prism 1 is perfectly mounted, the resultant beam pointing errors are still available by the above means. According to practical applications, the tilt amplitude of prism 2 around the axis OL is set to $\delta_0 = 1''$ in simulation, to investigate the pointing error Δ_2 caused by the tilt error of prism 2.

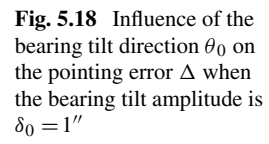
Figure 5.17 describes the influence of the prism tilt direction θ_0 on the pointing error Δ when prism 1 and prism 2, respectively, suffer from an assembly error of δ_0 . From Fig. 5.17, when $\theta_0 = 90^\circ$ or 270° , the pointing errors Δ_1 and Δ_2 all reach their maximum values, which are 0.1032 and 0.0988 μ rad, respectively.

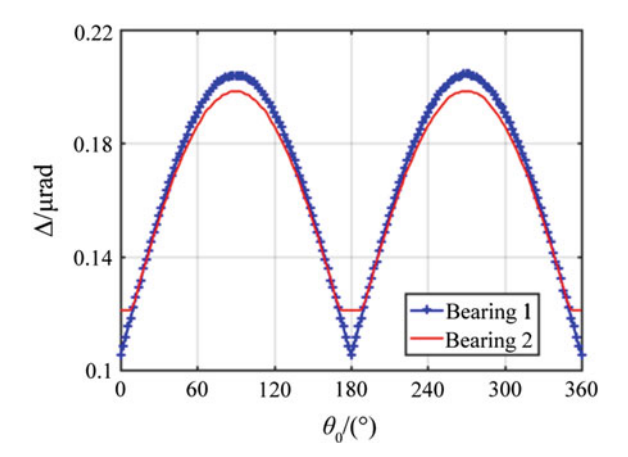
2. Pointing Error Affected by Bearing Assembly

The bearing of the rotating prism may deviate from the ideal position during installation, and the bearing assembly error can be described by a tilted bearing axis. Similar to the bearing assembly error of the tilting double-prism in Sect. 4.4, prism 1 and prism 2 rotate around the Z-axis, and the bearing assembly error can be expressed by the rotation angle of the bearing axis around the axis OL. The unit direction vector of OL is: $(u_x, u_y, u_z)^T = (\cos \theta_0, \sin \theta_0, 0)^T$. Supposed that the bearing axis of the prism is rotated counterclockwise around the axis OL with an angle δ_0 , and the rotation matrix is M_p from the previous section. Therefore, the unit direction vector of the bearing axis is expressed by: $(u_x', u_y', u_z')^T = M_p \cdot (\cos \theta_0, \sin \theta_0, 0)^T$. According to Rodrigues formulae, the rotation matrix M_b that specifies the incident or emergent surface normal of the prism can be expressed as

$$\mathbf{M}_b = \mathbf{A}_b + \cos \theta_r \cdot (\mathbf{I} - \mathbf{A}_b) + \sin \theta_r \cdot \mathbf{B}_b \tag{5.5}$$

where θ_r is the rotation angle of the prism, and A_b and B_b are, respectively, given by (4.13a) and (4.13b).





To distinguish what influence the bearing assembly errors of prism 1 and prism 2 have on the beam pointing accuracy, we usually assume that one bearing axis is misaligned with the optical axis of the system while the other bearing is perfectly mounted in the mechanical structure.

(1) Bearing Assembly Errors of Prism 1

In this situation, there are bearing assembly errors of prism 1 rather than prism 2. Similar to the analysis method in Sect. 4.4, the resultant normal vectors, N'_{11} , N'_{12} , N'_{21} and N'_{22} , and beam vectors, A_{r0} , A'_{r1} , A'_{r2} , A'_{r3} and A'_{rf} , are still available by using the vector refraction theorem.

Likewise, it is allowed to calculate the pointing error Δ of the rotating double-prism system from (5.4).

According to the assembly conditions in practice, the bearing tilt of prism 1 around the axis OL is held constant at an amplitude $\delta_0 = 0.2''$, in order to investigate the pointing error Δ_1 caused by the bearing tilt of prism 1.

(2) Bearing Assembly Errors of Prism 2

As for the situation that prism 2 suffers from bearing assembly errors whereas the bearing of prism 1 is perfectly mounted, the resultant beam pointing errors can also be determined in the above way.

According to the assembly conditions in practice, the bearing tilt of prism 2 around the axis OL is held constant at an amplitude $\delta_0 = 1''$, in order to investigate the pointing error Δ_2 caused by the bearing tilt of prism 2.

Figure 5.18 describes the influence of the bearing tilt direction θ_0 on the pointing error Δ when prism 1 and prism 2, respectively, suffer from a bearing assembly error of δ_0 . From Fig. 5.18, when $\theta_0 = 90^\circ$ or 270° , the pointing errors Δ_1 and Δ_2 all reach their maximum values, which are 0.2043 and 0.1977 μ rad, respectively.

In a word, when the tilt amplitude δ_0 is less than 1", the pointing error caused by the assembly errors of the prism and bearing are controlled within the range of 0.22 μ rad, which can satisfy the design requirements for the scan device.

5.3.5 Beam Scan Property and Test

For the rotating double-prism scan system, the spatial distance D_1 between two prisms must be kept within a certain range. Referring to Sect. 2.6.1, the range of D_1 , 38–439 mm, can be obtained by the one-dimensional search method. According to the analysis in Sect. 2.7.1, there is a scan blind zone at the center of the whole scan region. In the near-field case, a unique minimum value of $|P_r O_P|$, which is the distance between the beam scan point P_r and the center point O_P on the screen, can be determined when D_1 varies from 38 to 315 mm, accompanied by $|\Delta\theta_r|$ = 180°. For example, when $D_1 = 100$ mm and $|\Delta\theta_r| = 180^\circ$, the minimal $|P_r O_P|$ of 7.1207 mm occurs and remains unchanged as D_2 varies. Nevertheless, when D_1 varies within [316, 439] mm, the minimal $|P_rO_P|$ is related to the factor D_2 . In the case of $D_1 = 400$ mm and D_2 increasing within the range of [1, 2.37] mm, the minimal $|P_r O_P|$ increases from 35.258 to 35.268 mm. In contrast, when $D_2 \ge 2.37$ mm, the minimal $|P_r O_P|$ equals to 35.268 mm where $|\Delta \theta_r| = 180^\circ$, and there is no change in the radius of blind zone. When two prisms are rotating at different combinations of angular velocities, the corresponding different scan trajectories can be generated (as shown in Fig. 2.26). Generally, the scan trajectories do not pass the origin any longer when two prisms are rotating at different uniform speeds matched in near-field cases. Moreover, the position of intersection points at the emergent surface of prism 2 has significant influence on the final scan trajectory, which should not be ignored.

In this section, two methods are, respectively, employed to measure the variation range and random error of the beam scan angle.

The beam scan random errors of the rotating double-prism scanner are measured by the collimator light source and long focal-length observation collimator [16]. The reticle pattern of the illumination collimator is imaged on the focal plane of the observation collimator, and the rotation motion of two prisms will generate a corresponding image movement. Holding the scan trajectory constant, sectional beam scan trajectory can be observed on the CCD of the observation collimator and the measurement of trajectory fluctuation amount can be realized. In this test, the observation collimator is required for a sufficiently high resolution and suitable field of view (FOV).

The beam scan angle of the rotating double-prism is measured by using collimator light source and imaging system [16]. Regarding the CCD optical system as the receiving system of scan beams, the receiving FOV of the CCD optical system is determined according to the scan region of the rotating double-prism, which is rotated to obtain the beam scan angle.

5.4 Design of Tilting Double-Prism Scan Device

5.4.1 Design Requirements

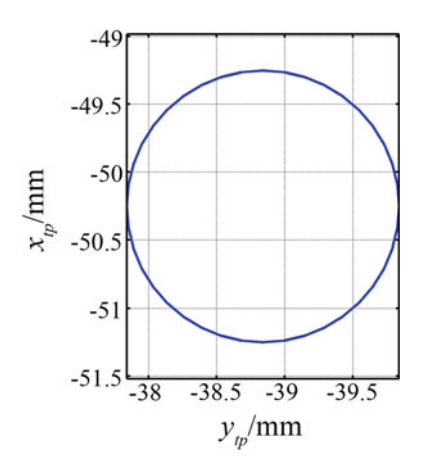
With regard to the tilting double-prism scan device driven by cam-based mechanism, the specific design requirements are listed as follows.

- (1) The beam scan coverage should allow the vertical field angle no less than $6000 \, \mu \text{rad}$ and the horizontal field angle no less than $3500 \, \mu \text{rad}$.
- (2) The beam scan precision should be superior to 1 μrad.
- (3) The clear aperture of the system is $D_p = 60$ mm.
- (4) The refractive index of each prism is n = 1.517.
- (5) The tilting double prisms are driven by cam-based mechanism.
- (6) The applicable wavelength ranges from 500 to 1550 nm.

5.4.2 Motion Law of Two Prisms

In order to meet the above design requirements, each prism element in the tilting double-prism scan system has the clear aperture D_p =60 mm, wedge angle α =10°, refractive index n=1.517 and thinnest-end thickness d_0 =10 mm. The distance between prism 1 and prism 2 is D_1 =150 mm, and the one from prism 2 to the receiving screen is D_2 =400 mm. As shown in Fig. 5.19, the target trajectory is given by $(x+50.251)^2 + (y+38.840)^2 = 1$. If the elapsed time for scanning the circular trajectory is set to t=10 s, the driving cams for double prisms should rotate at the uniform speed of ω_c =0.2 π rad/s, and the total rotation angle of each cam is deduced from δ = ω_c × t [18].

Fig. 5.19 A given target trakectory



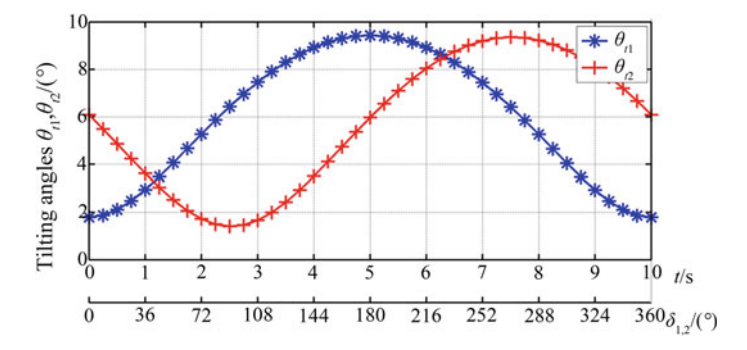


Fig. 5.20 Tilting angle curves of two prisms

Using the lookup-table method [19], the tilting angle curves of two prisms can be obtained in correspondence to the target trajectory, as shown in Fig. 5.20.

Clearly, the tilting angle curves are displayed with identical tendencies, similar amplitudes but different phases. Since the X- and Y-coordinates are different at the initial beam scan point, the initial phases of two curves cannot be consistent with each other. Meanwhile, the beam exiting position deviates from the emergent surface center of prism 2 due to the refraction effects, which results in the slight difference in the amplitudes of two curves.

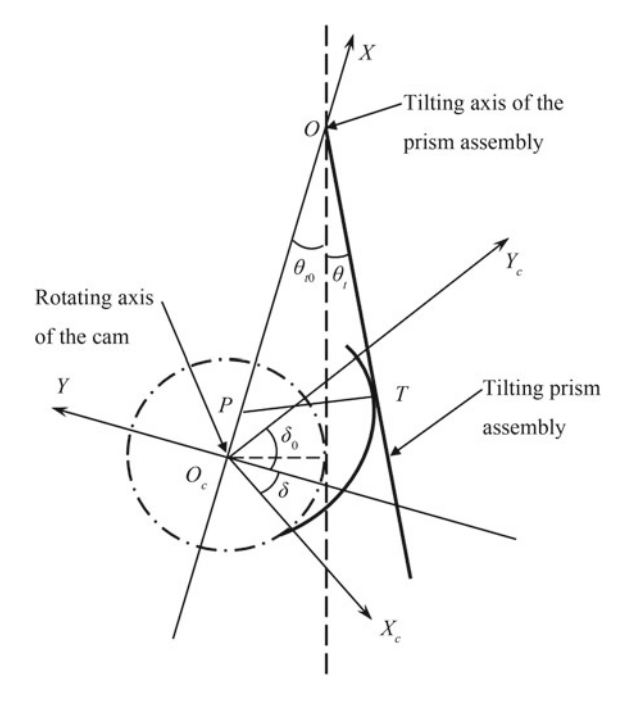
5.4.3 Cam-Based Oscillating Mechanism

The tilting angle curves of two prisms are generally nonlinear to perform beam scanning along any specific target trajectory, which requires complicated control strategies for the driving motors. However, if tilting double prisms are driven by cam-based mechanisms, the motion control process will be greatly simplified by transferring the nonlinear relation to the corresponding profiles of two cams. In other words, the nonlinear motion laws of two prisms can be actualized through uniform rotation of the driving cams.

1. Analytical Method for Cam Profile

The derivation of cam profile is essential to design the cam-based mechanism. In principle, the cam profile is determined by the motion law of the follower, namely the variation law of the angular displacement, angular velocity, and angular acceleration of the follower with respect to the rotation angle of the cam. The basic motion laws of a follower include uniform motion, constant acceleration motion, simple harmonic motion, and so on. Now that the tilting prism acts as the follower of cam-based mechanism in this section, the cam profile can be obtained from the prism motion law. Hence, an analytical method is used to solve the mathematical expression for cam profile [20].

Fig. 5.21 Sketch of the relation between the rotation angle of cam and the tilting angle of prism



As illustrated in Fig. 5.21, the point O_c represents the rotating axis of cam, the point O stands for the tilting axis of prism assembly. For simplicity, the distance from O_c to O is denoted by D_c , and the base circle of each cam is specified with a radius r_0 . Under the fixed coordinate system XO_cY , the positive direction of the O_cX axis is defined by the direction from O_c to O, and the positive direction of the O_cY axis is determined by counterclockwise rotating the positive O_cX axis with 90° . Meanwhile, there is also a dynamic coordinate system $X_cO_cY_c$ attached to the cam. The tilting prism assembly is tangent to the cam at the point T. Thus, the instantaneous center of velocity between the cam and the prism assembly locates at the point P, namely the intersection of the line OO_c and the common normal passing the point T. Note that δ is rotation angle of the cam and θ_t is tilting angle of the prism. At the start point of actuating travel of the cam, the angle of the follower relative to the line OO_c can be expressed as $\angle O_cOT = \theta_{t0} = \arcsin(r_0/D_c)$, and thus, its complementary angle is given by $\angle TO_cO = \delta_0 = \pi/2 - \theta_{t0}$.

The distance between the rotation center O_c of cam and the instantaneous center P of velocity is determined from

$$l_{O_{c}P} = \frac{D_{c}|d\theta_{t}/d\delta|}{1 + d\theta_{t}/d\delta}$$
(5.5)

In addition, the coordinates of the tangent point T are given by

$$\begin{cases} x_T = x_P + l_{PT} \sin(\theta_t + \delta_0) \\ y_T = -l_{PT} \cos(\theta_t + \delta_0) \end{cases}$$
 (5.6)

where $l_{PT}=(D_{\rm c}-x_P)\sin(\theta_t+\theta_{t0})$, and x_P is the *X*-coordinate of point *P* in the fixed coordinate system. It can be found that ${\rm d}\theta_t/{\rm d}\delta \ge 0$ and $x_P=l_{OcP}$ during the actuating travel of the cam. Contrarily, ${\rm d}\theta_t/{\rm d}\delta \le 0$ and $x_P=-l_{OcP}$ during the return travel of the cam.

Through the transformation relation from the fixed coordinate system XO_cY to the dynamic coordinate system $X_cO_cY_c$, the analytical expression for cam profile is obtained as follows:

$$\begin{cases} x_{c} = x_{T} \cos(\delta + \delta_{0}) - y_{T} \sin(\delta + \delta_{0}) \\ y_{c} = x_{T} \sin(\delta + \delta_{0}) + y_{T} \cos(\delta + \delta_{0}) \end{cases}$$

$$(5.7)$$

2. Design Procedure of Cam Profile

Referring to the equation $\delta = \omega_c \times t$, each cam for tilting prism rotates at a uniform speed. Thus, the relation between the tilting angle of each prism and the rotation angle of the corresponding cam can also be indicated in Fig. 5.20, where $\delta_{1,2}$ is considered as the *X*-coordinate. Specifically, δ_1 and δ_2 represent the rotation angles of two cams for driving prism 1 and prism 2, respectively.

To establish the quantitative motion law of prism tilting angles relative to cam rotation angles, the variation curves shown in Fig. 5.20 need to be fitted by the least-squares method. The general formula of each fitting curve can be expressed as an *n*-order polynomial:

$$\theta_t = C_0 + C_1 \delta + C_2 \delta^2 + \dots + C_n \delta^n$$
 (5.8a)

In comparison, the relation curve of the tilting angle of prism 1 with respect to the cam rotation angle is successively fitted with 5-order, 6-order and 7-order polynomials. Every sum of squared errors between the fitted and actual values of all sample tilting angles has been listed in Table 5.9. Obviously, the sum of squared errors of a 6-order polynomial is much less than the one of a 5-order polynomial and close to the one of a 7-order polynomial. Considering that the curve fitted with a 7-order polynomial is definitely more complex, the 6-order polynomial can be employed as the fitting function for prism 1. In a similar way, the fitting function for prism 2 is determined to be a 9-order polynomial with better fitting results.

Accordingly, the function for fitting the tilting angle curve of prism 1 is expressed as

$$\theta_{t1} = C_{10} + C_{11}\delta_1 + C_{12}\delta_1^2 + \dots + C_{16}\delta_1^6$$
 (5.8b)

The function for fitting the tilting angle curve of prism 2 is given by

$$\theta_{t2} = C_{20} + C_{21}\delta_2 + C_{22}\delta_2^2 + \dots + C_{29}\delta_2^9$$
 (5.8c)

	Different fitting functions	Sums of squared errors/rad ²
Prism 1	5-order polynomial	4.447×10^{-5}
	6-order polynomial	1.130×10^{-7}
	7-order polynomial	1.129×10^{-7}
Prism 2	8-order polynomial	5.426×10^{-6}
	9-order polynomial	7.338×10^{-7}
	10-order polynomial	7.313×10^{-7}

Table 5.9 Comparison of fitting results produced by different fitting functions

Table 5.10 Coefficients of the fitting functions for two prisms

Coefficients	Prism 1 (<i>i</i> =1)	Prism 2 (<i>i</i> =2)
C_{i0}	0.0313	0.1064
C_{i1}	-0.00289	-0.0741
C_{i2}	0.0758	0.0375
C_{i3}	-0.0364	-0.0909
C_{i4}	0.00782	0.0975
C_{i5}	-0.000940	-0.0459
C_{i6}	0.0000499	0.01160
$\frac{C_{i7}}{C_{i8}}$		-0.00166
C_{i8}		0.000128
C_{i9}		-0.00000410

Furthermore, the coefficients of the fitting functions for prism 1 and prism 2 can be obtained as shown in Table 5.10.

The height difference between the rotating axis of cam and the tilting axis of prism assembly is set to 120 mm, namely the vertical distance of two points O and O_c . In general, the radius of base circle of each cam is determined according to the mechanical principle that the actual pressure angle should not be greater than the allowable pressure angle. However, since the pressure angle of cam-based mechanism is constant at 90°, the radius of base circle can be selected with reference to the cam eccentricity and the principle that avoids the interference among mechanical components. On these basis, each cam is designed with the radius of base circle $r_0 = 10$ mm. Furthermore, the profile curves of two cam components can be deduced from (5.7), as shown in Fig. 5.22. Note that the outer curve and the inner curve, respectively, specify the theoretical profile and the base circle of each cam, and the point marked "*" denotes the initial contact position between each prism assembly and its driving cam during installation.

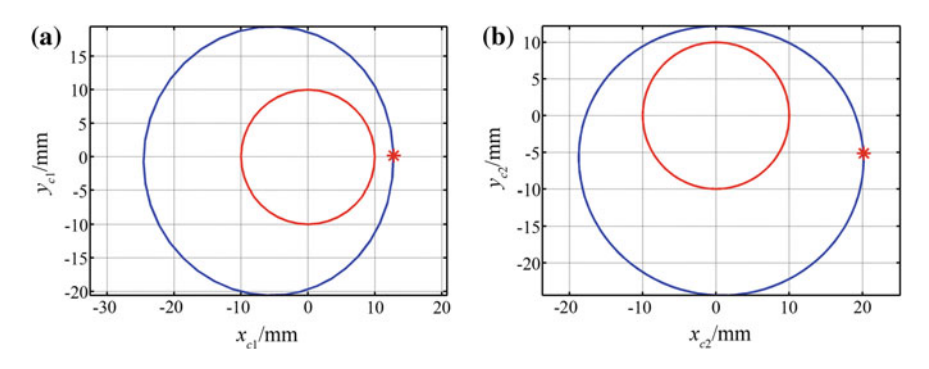


Fig. 5.22 Profile curves of a the cam driving prism 1 and b the cam driving prism 2

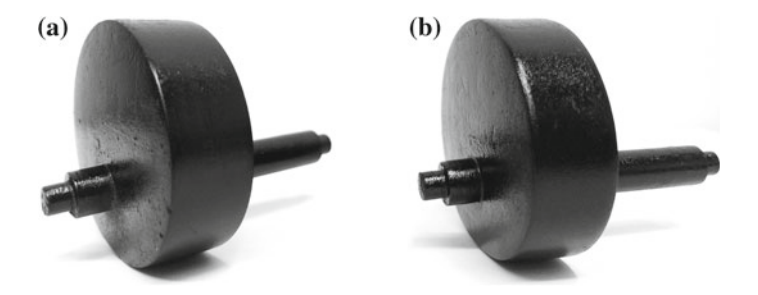


Fig. 5.23 Photos of a the first cam component and b the second cam component

5.4.4 Mechanical Structure Design

Through the above theoretical analysis, the cam components used to drive tilting double prisms are well designed and fabricated as shown in Fig. 5.23.

In practice, the cam drive mechanism suffers from friction, heat and abrasion generated from the relative movement between cam and follower. Regarding the overhead cam mechanism shown in Fig. 5.24a, the contact point P between the cam and the follower always locates at the bottom of push rod. In case of large transmission force, the addition of a roller is effective to reduce friction, heat and abrasion. However, the cam mechanism with oscillating follower is a preferable approach to drive each tilting prism, as shown in Fig. 5.24b. Considering that the prism assembly has light weight (about 1.224 kg here) and its tilting angle θ is 10° at maximum, the transmission force given by $F = G \cdot \sin\theta$ can be comparatively low, where G represents the gravity of the follower and F stands for the normal pressure on the cam. Consequently, there is less friction, heat and abrasion generated in the cam mechanism with oscillating follower. On the other hand, the contact point P between the cam and the follower is always changing back and forth, which accounts for the instantaneous heat much lower than that in the overhead cam mechanism.

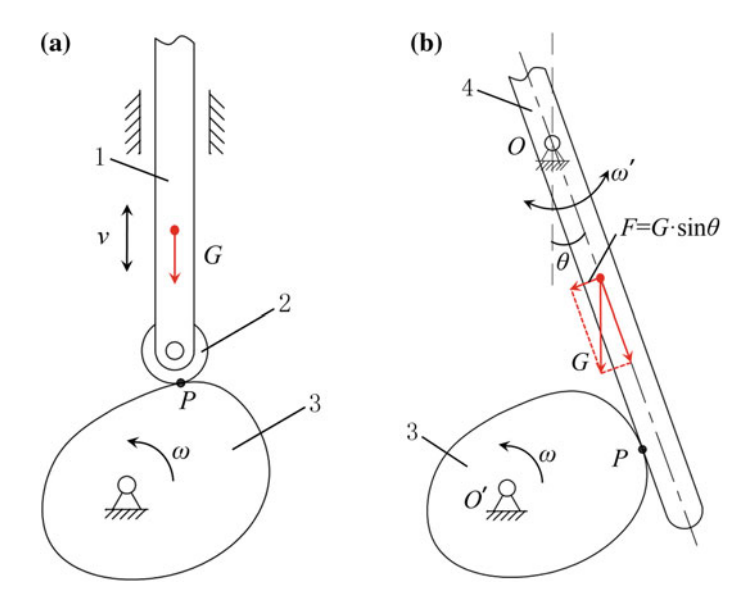


Fig. 5.24 Schematic diagram illustrating the principle of **a** overhead cam drive mechanism and **b** cam drive mechanism with oscillating follower, where 1–4 denote push rod, roller, cam and oscillating rod in turn

Figure 5.25 presents a three-dimensional model of the tilting double-prism scan device driven by cam-based mechanism. The device consists of two identical subsystems mounted on the guide rail of the base, each of which comprises a frame, a cam-based mechanism for tilting prism, a prism cell assembly, a rotary encoder and so on. The guide rail offers the possibility to adjust the distance between two prisms and the distance from prism 2 to the receiving screen. The prism cell assembly is used to fix the prism element and is connected with one end of the oscillating rod. Significantly, there is a screw inserted into the prism cell, which can be manually adjusted to keep the principal section of prism vertical or horizontal. The rotary encoder is used for real-time acquisition of prism orientation. In addition, the cam-based drive mechanism is mainly composed of a stepping motor, a synchronous belt, two belt wheels, a plate cam, an oscillating rod and its return facility. The plate cam is driven by the stepping motor through the synchronous belt. As the follower, the oscillating rod together with the prism assembly can perform tilting motion within the range of 0° – 10° .

5.4.5 Kinematics Simulation and Analysis

The three-dimensional models of two tilting prism assemblies are, respectively, imported into the Adams software, where the constraints and kinematic pairs between

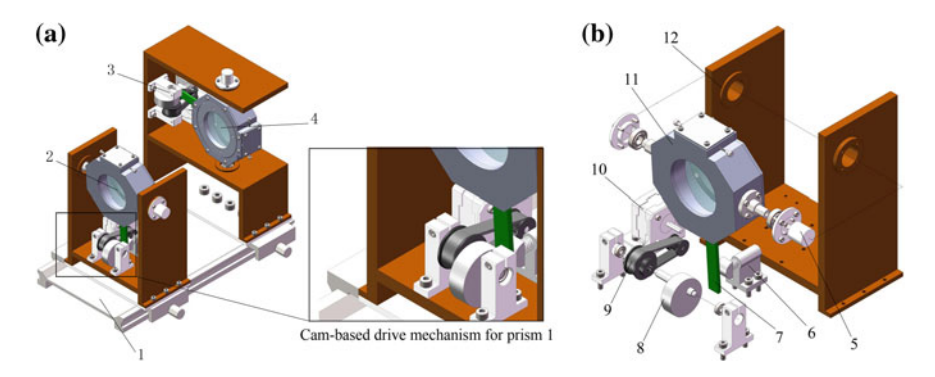


Fig. 5.25 Tilting double-prism scan device presented in **a** the three-dimensional model and **b** the explosion view, where 1 is guide rail of the base, 2 is prism 1, 3 is cam-based drive mechanism for prism 2, 4 is prism 2, 5 is rotary encoder, 6 is return facility for oscillating rod, 7 is oscillating rod, 8 is plate cam, 9 is one synchronous belt with two belt wheels, 10 is stepping motor, 11 is prism cell assembly and 12 is frame

any two components are placed for further simulation. Since each tilting prism assembly has single degree-of-freedom, only one rotary drive at a uniform speed of $36(^{\circ})$ /s is required on the rotary shaft of stepping motor. For convenience, the transmission ratio of the synchronous belt drive mechanism is set to 1. Then the rotary drive at $36(^{\circ})$ /s can be directly added on the rotary shaft of plate cam. After careful inspection on the kinematics simulation animations, it is ensured that no physical interference exists between any two components within the preset stroke.

By dividing the 20 s simulation into 200 steps, the tilting angles, angular velocities as well as angular accelerations of prism 1 and prism 2 are obtained as shown in Fig. 5.26.

The following analysis can be performed on the basis of Fig. 5.26.

- (1) The tilting angle of prism 1 is 9.4346° at maximum and 1.7890° at minimum, and the one of prism 2 is 9.3553° at maximum and 1.4141° at minimum. These results in simulation are mostly consistent with the calculation results in Sect. 5.4.2.
- (2) The absolute value of the tilting angular velocity of prism 1 is 2.4276(°)/s at maximum, and that of prism 2 is 2.5065(°)/s at maximum. Referring to the 36(°)/s rotation speed of cam, it is found that the cam-based transmission mechanism can provide a large reduction ratio.
- (3) There is no sudden change in either angular velocities or angular accelerations of prism 1 and prism 2, which validates the motion smoothness of the cam-based transmission mechanism.

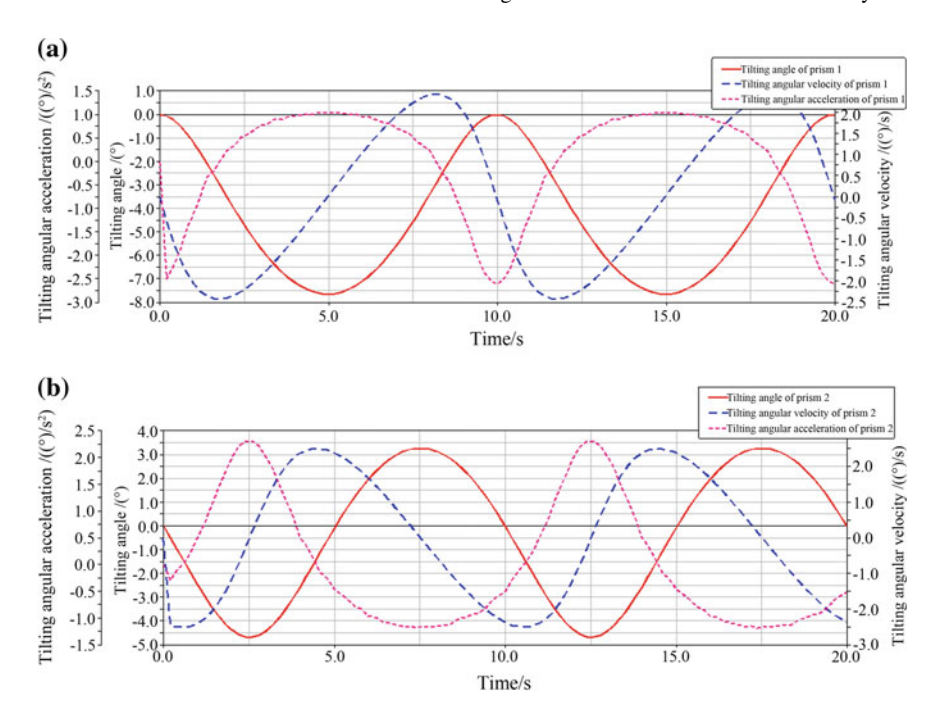


Fig. 5.26 Tilting angles, angular velocities as well as angular accelerations of $\bf a$ prism 1 and $\bf b$ prism 2. Note that the initial tilting angle of prism 1 is 1.789° and the one of prism 2 is 6.088° , but they are both equivalent to 0° in simulation. Therefore, the actual tilting angles of prism 1 and prism 2 can be determined by adding 1.789° and 6.088° to the equivalent tilting angles, respectively

5.4.6 Scan Error Analysis

Considering the initial prism orientations, the tilting angle curves of two prisms are displayed in Fig. 5.27. These curves are involved to obtain the beam scan trajectory in comparison to the target trajectory, as shown in Fig. 5.28. Obviously, the scan trajectory is almost coincident with the target trajectory. The left part in Fig. 5.28 highlights an enlarged view of the area surrounding the point marked "+", which represents the position with a maximum error between two trajectories. Given that the maximum scan error is 0.0075 mm and the diameter of circular target trajectory is 2 mm, the maximum scan error accounts for only 0.375% of the diameter of target trajectory. Therefore, the proposed tilting double-prism scan device is proven with relatively high scan precision.

The primary sources of beam scan error are demonstrated as follows.

(1) To establish a 2501×2501 lookup table, the step angle is constant at $\theta_{\text{tre}} = 0.004^{\circ}$. The tilting angles of two prisms are obtained by searching the lookup table for the point closest to each sample point on the target trajectory. In other words, the obtained tilting angles correspond to some points in the lookup table

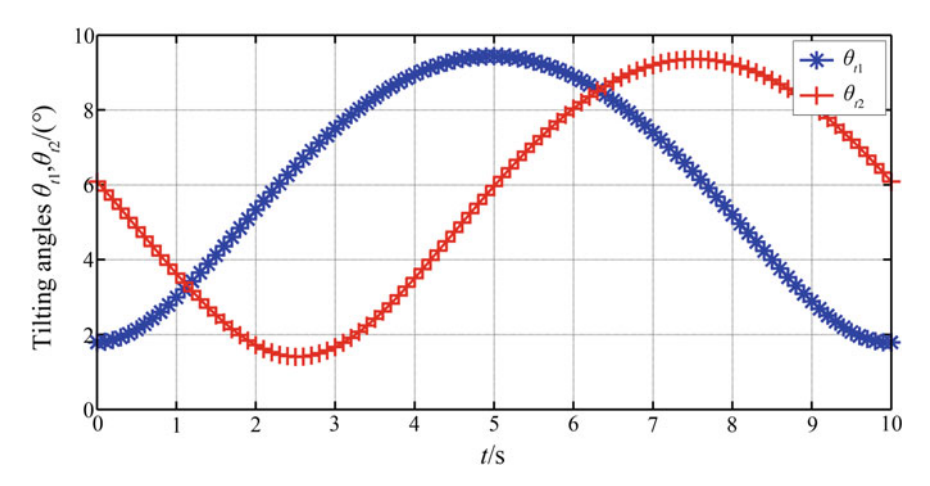


Fig. 5.27 Tilting angles of two prisms under the consideration of initial prism orientations

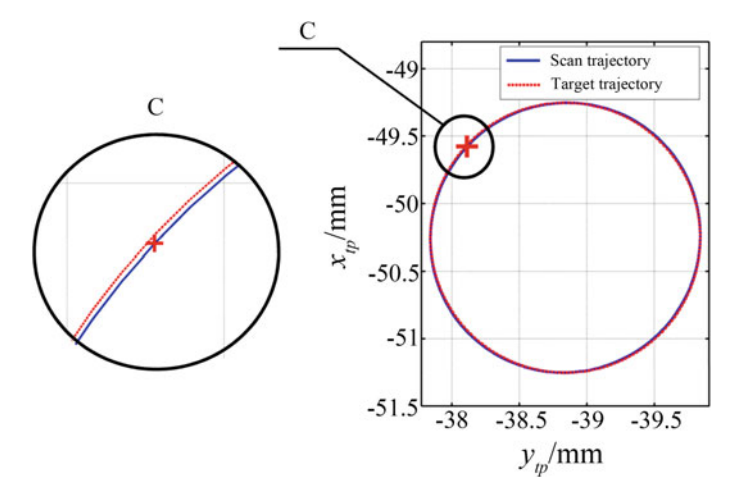


Fig. 5.28 Comparison of beam scan trajectory and target trajectory, along with an enlarged view of maximum scan error

but not exactly the sample points on the target trajectory. Such errors in tilting angles of two prisms will definitely contribute to the beam scan error.

- (2) The polynomial fitting method is employed to derive the functional relation of prism tilting angles with respect to cam rotation angle. Consequently, there are fitting errors that may generate the beam scan error.
- (3) The cam profiles are actually not closed due to the limitations of polynomial fitting method. For the closed cam profiles, the last fitted point in each cam profile should be replaced by the first one. The design errors in cam profiles can result in the beam scan error as well.

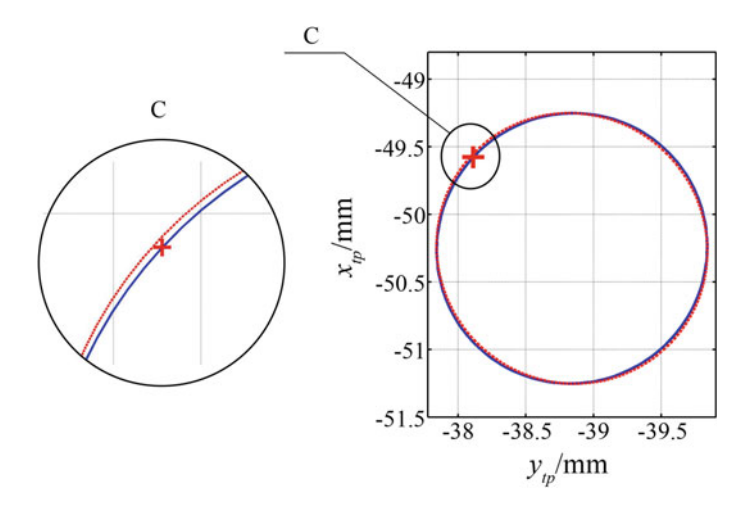


Fig. 5.29 Beam scan trajectories when $\omega_{c2} = \omega_{c1}$ and $\omega_{c2} = -\omega_{c1}$, respectively

5.4.7 Influence of Scan Speed on Scan Trajectory

To help reveal what influence the rotation speeds of two cam components have on the beam scan trajectory, the rotation speed ω_{c1} of the first cam is held constant, while the rotation speed ω_{c2} of the second cam is set to $\omega_{c2} = \omega_{c1}$, $\omega_{c2} = 2\omega_{c1}$, $\omega_{c2} = 3\omega_{c1}$, $\omega_{c2} = -\omega_{c1}$, $\omega_{c2} = -2\omega_{c1}$ and $\omega_{c2} = -3\omega_{c1}$ in turn. Consequently, six different scan trajectories are obtained and then divided into three groups for comparison, as shown in Figs. 5.29, 5.30 and 5.31. The dashed lines stand for scan trajectories produced under the cam rotation speeds in the same direction, and the solid lines represent scan trajectories produced when two cam components rotate in opposite directions. Upon comparing three groups of beam scan trajectories, the following conclusions can be drawn.

- (1) The maximum deviation between the dashed line and the solid line is 0.0244 mm in Fig. 5.29, 0.0344 mm in Fig. 5.30 and 0.0300 mm in Fig. 5.31. It can be seen that the dashed lines and the solid lines substantially coincide with each other. In other words, the rotation direction of the second cam is hardly associated with the shape of beam scan trajectory. Despite the difference in the rotation speeds of two cam components, the resultant beam scan trajectories are centrally symmetric due to the structural symmetry of each cam.
- (2) If the second cam rotates more rapidly than the first one, the beam scan trajectory will travel throughout its *Y*-range at higher frequency than its *X*-range. The multiple of travelling frequency is always equal to the rotation speed of the second cam divided by that of the first cam. Similar analysis can be performed if the first cam rotates more rapidly than the second one.

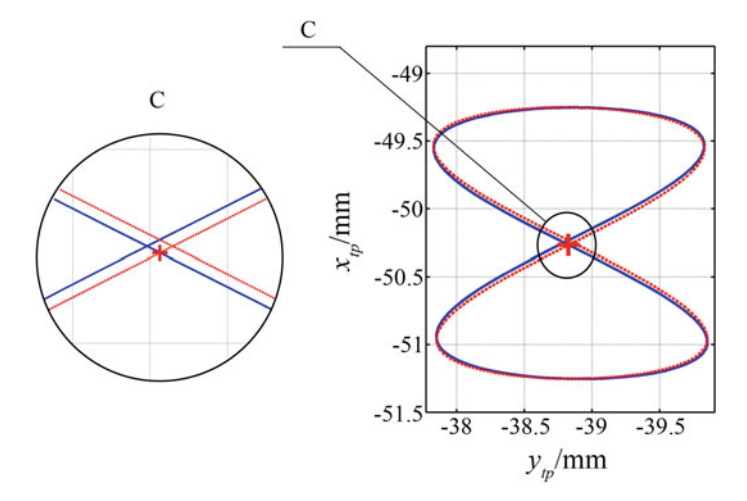


Fig. 5.30 Beam scan trajectories when $\omega_{c2} = 2\omega_{c1}$ and $\omega_{c2} = -2\omega_{c1}$, respectively

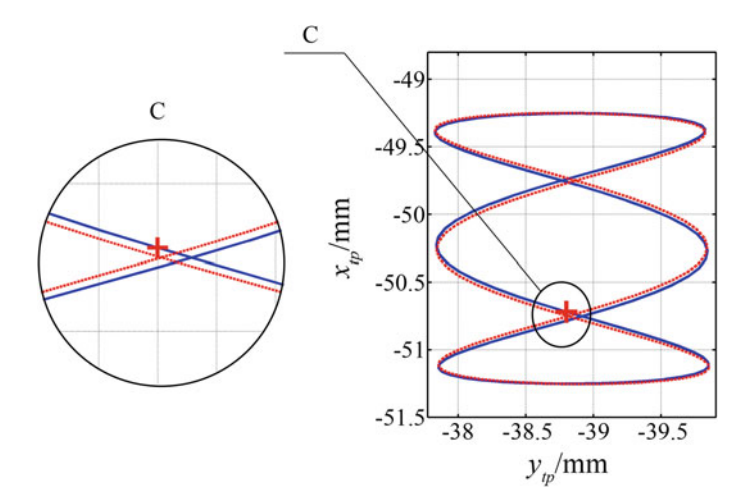


Fig. 5.31 Beam scan trajectories when $\omega_{c2} = 3\omega_{c1}$ and $\omega_{c2} = -3\omega_{c1}$, respectively

(3) Regardless of how the rotation speed of the second cam varies with respect to that of the first cam, the *X*-range and *Y*-range of beam scan trajectory are both unchanged.

5.5 Design of Composite Motion Double-Prism Scan Device

5.5.1 Design Requirements

In the composite motion double-prism scan device, each prism is capable of both rotating motion within 0° –360° to perform coarse scanning and tilting motion within 0° –5° to perform fine scanning. Accordingly, the specific design requirements are listed as follows.

- (1) The coarse scan coverage should allow the vertical field angle and the horizontal field angle ranging from -10° to 10° . The fine scan coverage should allow the vertical field angle no less than 2500 μ rad and the horizontal field angle no less than 1200 μ rad.
- (2) The beam steering precision should be superior to 50 μ rad during coarse scanning and 1 μ rad during fine scanning.
- (3) The clear aperture of the system is $D_p = 60$ mm.
- (4) The refractive index of each prism is n = 1.517.
- (5) The rotation motion is directly driven by torque motors, while the tilting motion is realized through the coordination of linear motors and linkages.
- (6) The applicable wavelength ranges from 500 to 1550 nm.

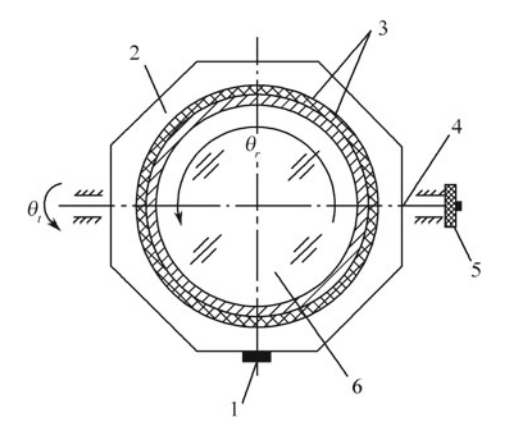
5.5.2 Layout Scheme of the System

In addition to the performance requirements of composite motion, the characteristics of nested mechanisms should also be considered in the system design. The proposed scan device mainly consists of double wedge prisms, driving unit (including two torque motors and two linear motors), position feedback unit (including two tilting angle encoders and two rotation angle encoders), four-axis joint control unit, and other electronic and mechanical support components. Figure 5.32 shows a schematic diagram illustrating the structure design of one prism assembly. The layout of the other prism assembly is almost identical with the one shown in Fig. 5.32.

Each prism is made of K9 glass material. For sufficient clear aperture of the system, the plane and wedge facets of each prism are, respectively, fixed by one circular pressure ring and one wedge-shaped retaining ring that has the same wedge angle as the prism. The pressure ring and the retaining ring are separated from the prism by special plastic screws made of nylon material, in order to avoid prism damage induced by uneven forces.

A pair of cross roller bearings are arranged on the internal prism cell to withstand loads in all directions, including radial load, axial load and impact load. The external prism cell is only required to perform tilting motion, which results in relatively less impact. Therefore, a pair of high-precision angular contact ball bearings are mounted around the horizontal tilting axis, one of which is fixed while the other is flexible. A

Fig. 5.32 Structure diagram of one prism assembly, where 1 is linear motor, 2 is external prism cell, 3 is torque motor, 4 is tilting axis of prism, 5 is angle encoder and 6 is prism mounted into the internal prism cell



pair of cross roller bearings are also mounted around the vertical tilting axis to carry a certain axial load.

The high-precision angle encoders are employed to obtain real-time feedback from the rotating and tilting motion of each prism. Accordingly, the rotation angle encoder is placed on the internal prism cell, and the tilting angle encoder is placed around the tilting axis of the external prism cell. These encoders come with reading heads and zero marks, and are equipped with PC counting cards and driver software.

A four-axis joint control scheme is applied to the control unit of the scan device, as shown in Fig. 5.33. The industrial PC communicates with the logic/motion controller through USB, and the controller is equipped with I/O expansion ports. The driver interface of rotating axes 1 and 2 (driven by torque motors) and that of tilting axes 1 and 2 (driven by linear motors) are, respectively, connected to the corresponding motor interface. Meanwhile, the rotating axes 1 and 2 are connected with the independent servo-axis channel so that any time-based beam scan trajectory can be planned using the control unit.

5.5.3 Analysis on the Center of Gravity

The analysis on the center of gravity can be performed in two parts, namely adjusting the center of gravity and calculating the moment of inertia. It is necessary to adjust the center of gravity, mostly because the center of gravity of rotating components deviates from the optical axis owing to uneven quality of the prism element. The moment of inertia can be involved to determine the driving torques required for rotating and tilting motion of each prism assembly, as a reference for motor selection.

Generally, the center-of-gravity adjustment should be performed with emphasis on the rotating components of each prism assembly, mainly including internal prism cell, prism and wedge-shaped retaining ring. Given the prism assembly modelled in Solidworks software, the center of plane facet of the prism is defined as the coordinate

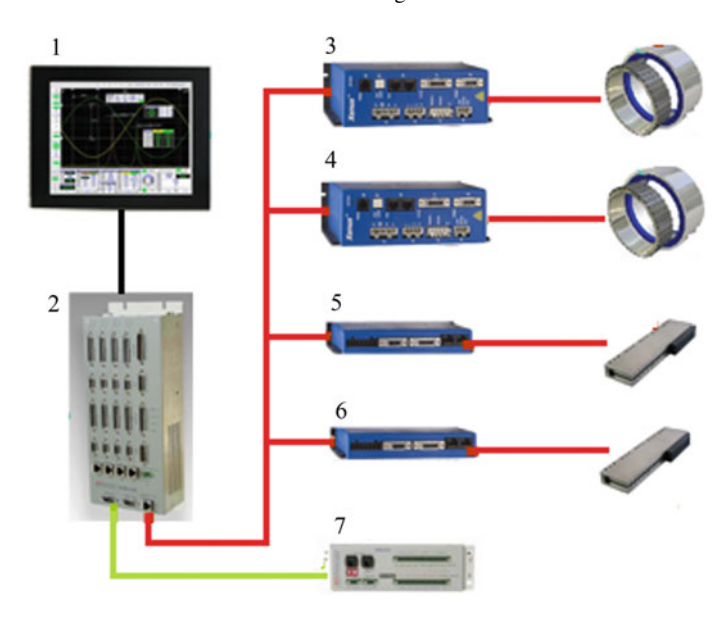


Fig. 5.33 Control unit composed of 1-industrial PC, 2-logic/motion controller, 3-rotating axis 1, 4-rotating axis 2, 5-tilting axis 1, 6-tilting axis 2 and 7-I/O expansion ports

 Table 5.11 Mass properties analysis on overall rotating components

Total mass/kg	200.79		
Volume/mm ³	3.85×10^{7}		
Surface area/mm ²	2.27×10^{6}		
Center-of-gravity coordinates/mm	X	Y	Z
	0	0.913	34.88

origin, and the direction of the optical axis specifies the *Z*-direction. Once the material parameters are selected for each rotating component, the geometrical parameters of overall rotating components, such as mass, volume, surface area and center-of-gravity coordinates, can be obtained through the analysis on mass properties. For convenience, the analysis results are listed in Table 5.11.

Influenced by the wedge-shaped retaining ring, the center of gravity of rotating components only deviates from the Y-direction with 0.913 mm. To reduce such deviation as much as possible, a 45° arc groove having a width of 20 mm in the Z-direction and a depth of 16 mm in the Y-direction is cut out on the top of the internal prism cell (in the positive Y-direction). In addition, the arc groove is symmetric about the principal section of the prism element. The optimized internal prism cell and other rotating components are presented in Fig. 5.34, where the Y-coordinate of the center of gravity is 6.45×10^{-3} mm and the total mass becomes 199.21 kg.

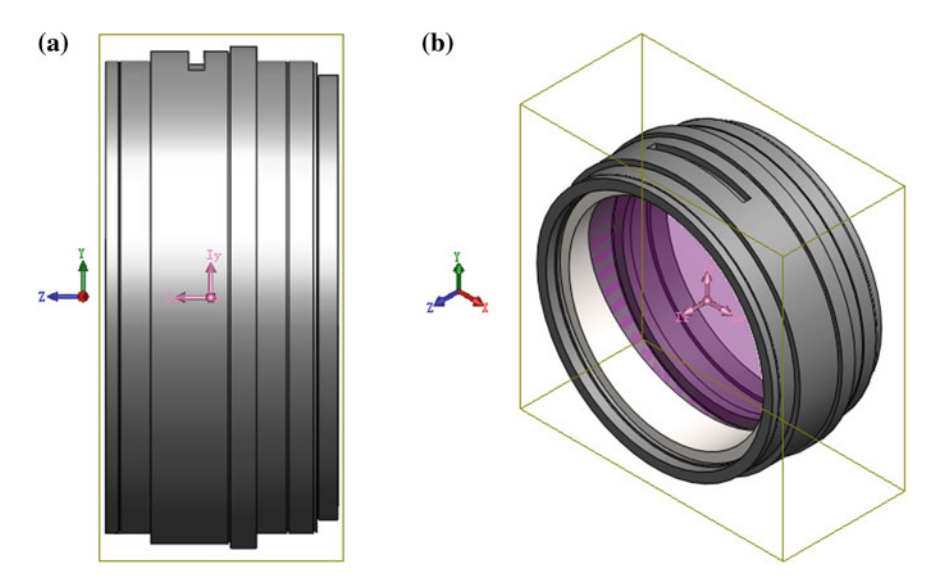


Fig. 5.34 Optimized internal prism cell and other rotating components **a** in the lateral view and **b** in the isometric view

Table 5.12 Rey param	Table 5.12 They parameters of foliating components					
	Internal prism cell	Prism	Wedge-shaped retaining ring			
Volume/mm ³	1.71×10^{7}	1.91×10^{7}	2.14×10^9			
Density/(kg mm ⁻³)	7.85×10^{-6}	2.53×10^{-6}	7.85×10^{-6}			
Surface area/mm ²	1.40×10^{6}	6.18×10^5	2.63×10^5			
Mass/kg	135.11	48.32	16.78			

Table 5.12 Key parameters of rotating components

The moments of inertia to be calculated include the one J_r of rotating components and the other one J_t of tilting components. For further calculation, the key parameters of each rotating component are listed in Table 5.12.

The inertia tensor of overall rotating components relative to the global coordinate system can be expressed as (unit: kg m²)

$$I_{r} = \begin{bmatrix} I_{XX} & I_{XY} & I_{XZ} \\ I_{YX} & I_{YY} & I_{YZ} \\ I_{ZX} & I_{ZY} & I_{ZZ} \end{bmatrix} = \begin{bmatrix} 8.24 & 0 & 0 \\ 0 & 8.29 & 0.01 \\ 0 & 0.01 & 14.28 \end{bmatrix}$$
 (5.9)

Since the rotating components rotate around the Z-axis, the corresponding moment of inertia is given by $J_r = I_{ZZ} = 14.28$ kg m². As required in most applications, any rotating scanner should offer rapid initial response as well as stable and continuous output. Thus, the rotation angular acceleration of each prism can reach

Total mass/kg	863		
Volume/mm ³	1.87×10^{8}		
Surface area/mm ²	1.23×10^{7}		
Center-of-gravity coordinates/mm	X	Y	Z
	-0.72	-0.005	35.21

Table 5.13 Mass properties analysis on overall tilting components

 β_r =9.42 rad/s², and the available torque from each torque motor selected for rotating components must be greater than 134.52 N m.

The tilting components refer to the external prism cell and all components mounted inside the cell. Considering that some components are properly simplified during modelling, the moment of inertia of overall tilting components can only be determined in approximation. Based on the mass properties analysis shown in Table 5.13, the inertia tensor of overall tilting components relative to the global coordinate system can be expressed as (unit: kg m²)

$$I_{t} = \begin{bmatrix} I'_{XX} & I'_{XY} & I'_{XZ} \\ I'_{YX} & I'_{YY} & I'_{YZ} \\ I'_{ZX} & I'_{ZY} & I'_{ZZ} \end{bmatrix} = \begin{bmatrix} 73.11 & -0.47 & -0.02 \\ -0.47 & 78.20 & -0.01 \\ -0.02 & -0.01 & 137.85 \end{bmatrix}$$
(5.10)

For tilting components that tilt around the *X*-axis, the corresponding moment of inertia is given by $J_t = I'_{XX} = 73.11 \,\mathrm{kg}$ m². Under different application requirements, the tilting angular acceleration of each prism can reach β_t =0.0872 rad/s² instantaneously. Providing the arm of each linear motor as 0.525 m in this device, it can be found that the available thrust force from the linear motor selected for tilting components must be larger than 12.143 N.

5.5.4 Design of Drive Mechanism

The drive mechanism should be responsive, stable and reliable enough, since each prism has the maximum angular acceleration up to 9.42 rad/s² when it is activated and the maximum rotation angular velocity up to 9.42 rad/s once it is stabilized. Therefore, the rotating motion of each prism assembly can be achieved through a torque motor controlled with real-time feedback. Characterized by low speed, large torque, small torque ripple, superior overload capacity, rapid response and good linearity, the torque motor is used to eliminate the necessity of transmission gears and directly drive the load, which can greatly improve the system operation accuracy. A drive scheme for the rotating components in each prism assembly is formulated as shown in Fig. 5.35, where the rotor and stator of the torque motor are, respectively,

Fig. 5.35 Drive scheme for rotating motion, where 1 is wedge-shaped retaining ring, 2 is prism element, 3 is torque motor and 4 is internal prism cell

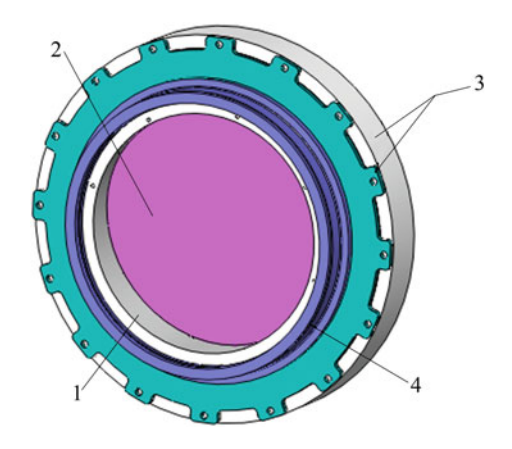


Table 5.14 Main parameters of torque motor

Supply voltage/V	340	Continuous locked-rotor current/A	6
Continuous locked-rotor torque/N m	180	Peak locked-rotor current/A	36
Armature resistance/Ω	8.5	Inductance/mH	29
Maximum no-load speed/r min ⁻¹	95	Moment of inertia/kg m ²	2.4

mounted on the internal prism cell and the external one. The main parameters of the torque motor are listed in Table 5.14.

The tilting motion of each prism assembly is achieved through the slide and linkage mechanism, as shown in Fig. 5.36. Using a joint bearing, the horizontal displacement of the linear motor can be converted into the angular deviation of the junction plate connected to the external prism cell. Both the horizontal slide and the vertical slide can realize effective stroke of 100 mm. Since the joint bearing offers the benefits of self-aligning, self-lubrication, simple structure as well as convenient installation and uninstallation, it is especially suitable for low-speed, heavy-load and lubrication-free mechanism. The inner ring of the joint bearing has the maximum deviation range of $\pm 10^{\circ}$. A grating scale is arranged parallel to the horizontal guide on the base, which can accurately locate the rotor of linear motor. Furthermore, the linear motor is equipped with two stop blocks placed at the extreme positions of its rotor motion.

As shown in Fig. 5.37, the ironless linear motor is selected to drive the tilting motion of prism assembly, which employs more lightweight actuator than the iron-core linear motor. The ironless linear motor is also advantageous in strong acceleration capacity, good dynamic performance, long service life, low full-load rate and compact structure, so it can be preferable to drive high-precision and small-stroke motion. Table 5.15 lists the main parameters of the selected motor. The effective stroke of the linear motor is 75 mm. In order to achieve the prism tilting motion within the angular range of $-1^{\circ}-5^{\circ}$, it is necessary to mark the extreme positions of 0° and 5° on the guide and place corresponding stop blocks on the base.

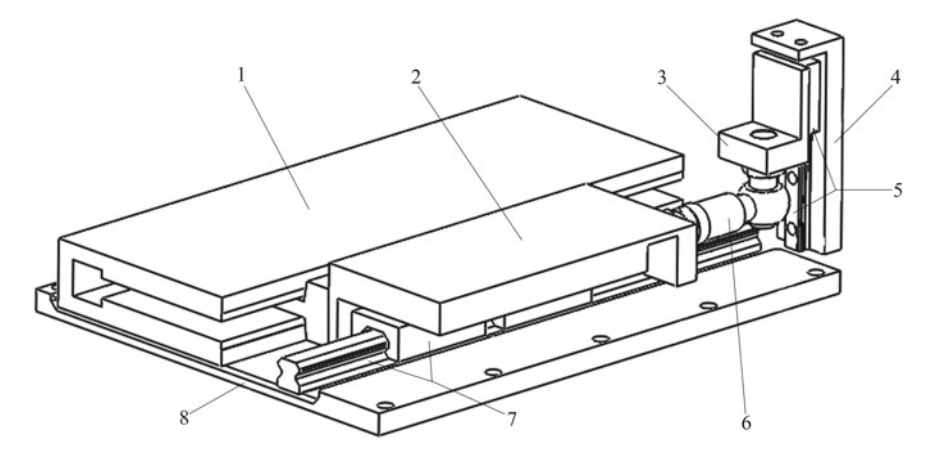


Fig. 5.36 Drive mechanism for tilting motion, where 1 is linear motor, 2 is cover plate, 3 is L-shaped plate, 4 is junction plate connected to prism cell, 5 is vertical slide on the guide, 6 is joint bearing, 7 is horizontal slide on the guide, and 8 is base

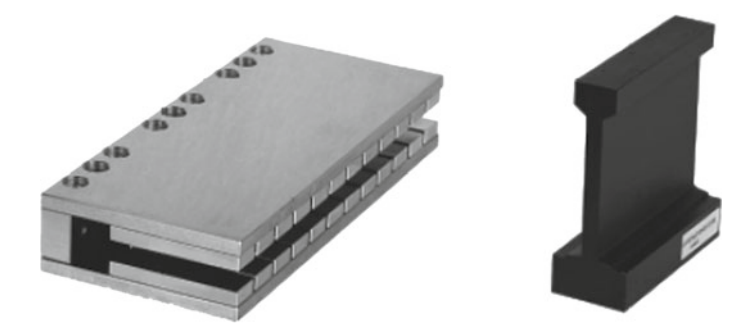


Fig. 5.37 Stator and rotor of ironless linear motor

Table 5.15 Main parameters of linear motor

I		***	
Peak thrust force/N	60	Thrust force constant/V A ⁻¹	15.28
Continuous thrust force/N	20	Counter electromotive force/V m ⁻¹ s ⁻¹	8.82
Peak power/W	180	Motor constant/N W ⁻¹	5.65
Rated power/W	20	Interphase inductance/mH	1.51
Peak current/A	4.8	Interphase resistance/Ω	4.8
Continuous current/A	1.6		

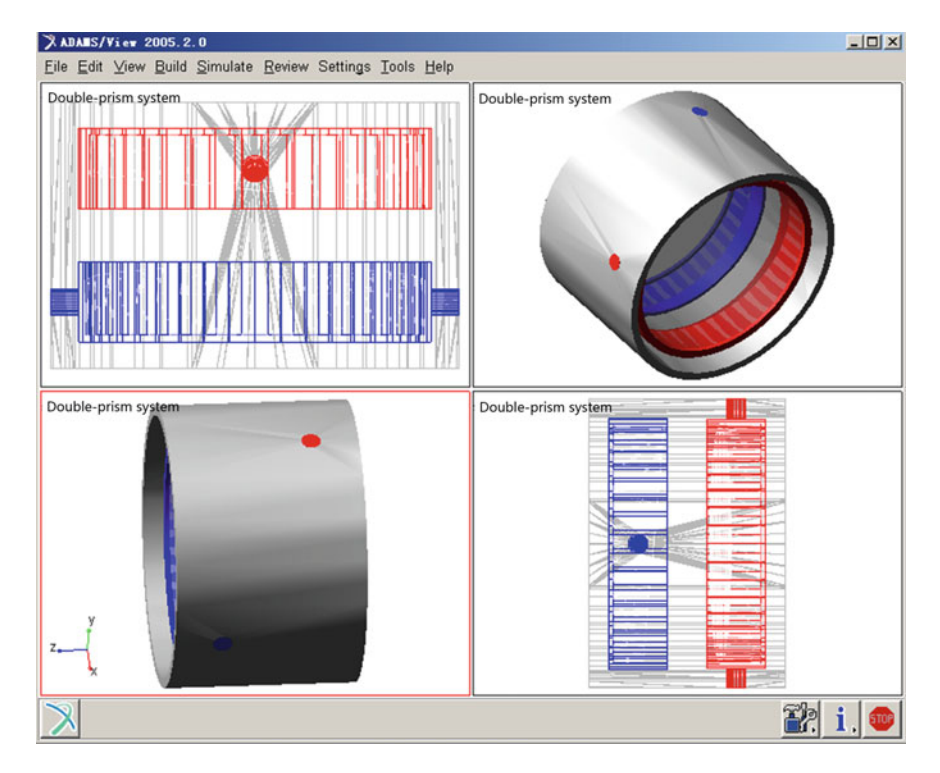


Fig. 5.38 Sketch of overall model in Adams

5.5.5 Kinematics Simulation and Analysis

Considering the existence of wedge facets of two prisms and the special integration of rotating motion and tilting motion during beam scan process, the multi-body dynamics software Adams is used to perform kinematics analysis on the displacement, velocity and acceleration at any arbitrary point on each prism. The modeling of prism element, internal prism cell and external prism cell can be properly simplified, because the kinematics analysis is only involved with some arbitrary points on each prism. Further investigation on the simplified model are demonstrated as follows.

Through the three-dimensional modeling software Solidworks, the above model is established according to the given physical dimensions. After perfect assembly, the overall model is imported into Adams, where the material and shape of each part are defined as shown in Fig. 5.38.

The next step is to place constraints on the model, including the definition of kinematic pairs and the addition of driving forces. The kinematic pairs mainly refer to four revolute joints, namely join1 between prism 1 and the first internal prism cell, join2 between prism 2 and the second internal prism cell, join3 between the first internal prism cell and the external prism cell, and join4 between the second

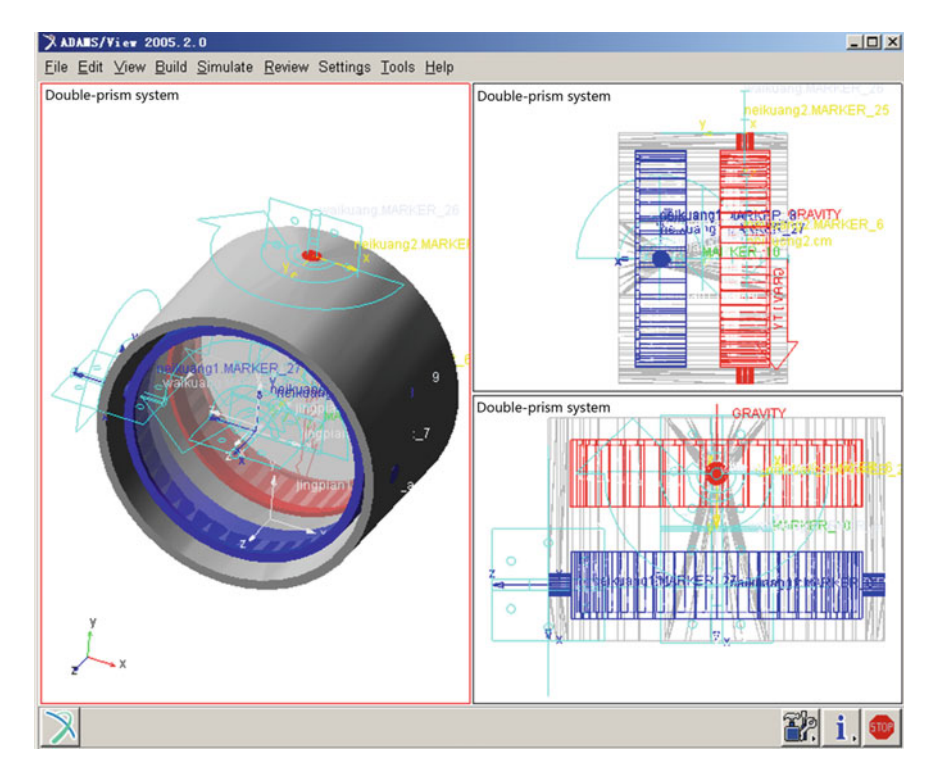


Fig. 5.39 Sketch of overall model after adding constraints

internal prism cell and the external prism cell. The marker points of join1 and join2 are, respectively, specified at the CM (center of mass) points of two internal prism cells. Join1 and join2 can directly free the rotating motion of two prisms, while join3 and join4 can free the rotating motion of two internal prism cells to achieve the tilting motion of two prisms. Moreover, one fixed pair is defined between the external prism cell and the ground so as to fix the overall model.

During coarse beam scanning, join 1 and join 2 are actuated by two rotary drives at the uniform speed of $36(^\circ)$ /s. The simulation period is set to 5 s in order to accomplish the rotating motion of two prisms within $0^\circ-180^\circ$. As for fine beam scanning, join 3 and join 4 are actuated by two oscillatory drives at the uniform speed of $1(^\circ)$ /s. The simulation period is also set to 5 s in order to realize the tilting motion of two prisms within $0^\circ-5^\circ$. On these basis, the model can be well prepared for the following simulation and analysis, as shown in Fig. 5.39.

For example, the kinematics simulation is performed on the point a on the thinnest end of prism 1. Provided that prism 1 works at rotating, tilting or composite motion mode, the simulation results on the displacement, velocity and acceleration of the point a are plotted in Figs. 5.40, 5.41, 5.42, 5.43, 5.44, 5.45, 5.46, 5.47 and 5.48.

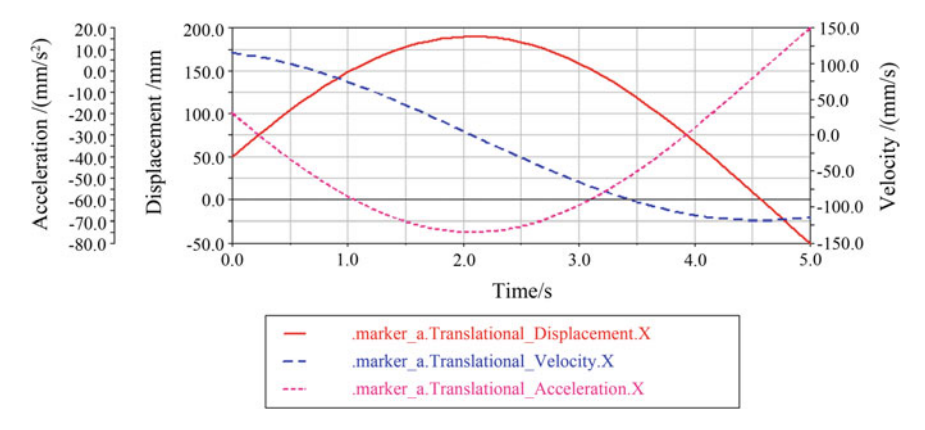


Fig. 5.40 Displacement, velocity and acceleration of the point *a* in the *X*-direction, when prism 1 works at rotating motion mode

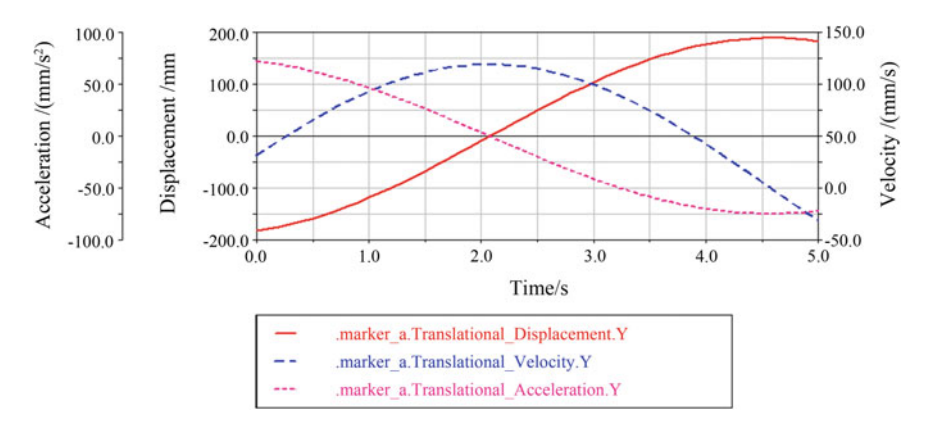


Fig. 5.41 Displacement, velocity and acceleration of the point a in the Y-direction, when prism 1 works at rotating motion mode

As shown in Figs. 5.40, 5.41 and 5.42, there is no change in the Z-displacement of the point a once prism 1 can only achieve rotating motion, and the corresponding velocity and acceleration are both constant at 0. However, the displacement, velocity and acceleration of the point a are variable in the X- and Y-directions owing to the wedge angle of prism 1. The maximum X- and Y-velocities can be found when the X- and Y-coordinates of the point a are 0, respectively, while the minimum X- and Y-velocities can be found when the X- and Y-coordinates of the point a are maximum, respectively. In other words, the point a has maximum Y-velocity (or X-velocity) when the thinnest end of prism 1 is aligned with the negative X-axis (or Y-axis), while the point a has minimum Y-velocity (or X-velocity) when the thinnest end of prism 1 is aligned with the positive X-axis (or Y-axis). Similarly, the X-acceleration (or Y-acceleration) reaches its maximum value when the X-velocity (or Y-velocity)

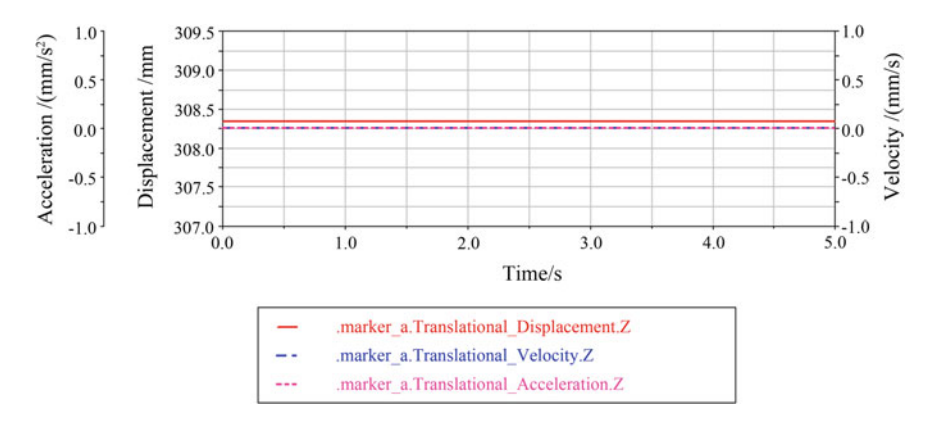


Fig. 5.42 Displacement, velocity and acceleration of the point a in the Z-direction, when prism 1 works at rotating motion mode

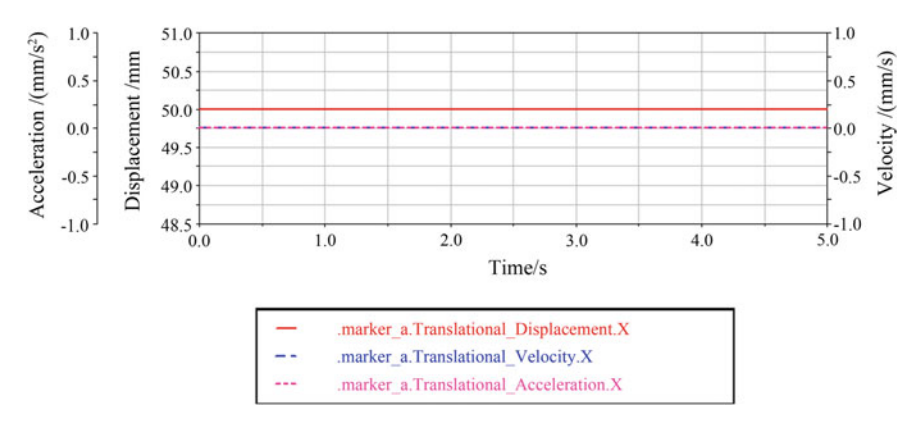


Fig. 5.43 Displacement, velocity and acceleration of the point a in the X-direction, when prism 1 works at tilting motion mode

is minimum, while the *X*-acceleration (or *Y*-acceleration) reaches its minimum value when the *X*-velocity (or *Y*-velocity) is maximum.

Given prism 1 at tilting motion mode, the kinematics simulation results are presented in Figs. 5.43, 5.44 and 5.45. Concerning that the principal section of the tilting prism 1 locates in the YOZ plane, the X-displacement of the point a is constant, and the velocity and acceleration are both 0 in the X-direction. Due to the large diameter and small tilting angle of prism 1, there is approximately linear change in the Z-displacement of the point a, and the velocity and acceleration are almost unchanged in the Z-direction. With the increment of the tilting angle of prism 1, the velocity increases but the acceleration decreases in the Y-direction.

As for prism 1 at composite motion mode, the simulation results are shown in Figs. 5.46, 5.47 and 5.48. The maximum *X*-velocity (or *Y*-velocity) occurs when the *X*-coordinate (or *Y*-coordinate) of the point *a* is 0, while the minimum *X*-velocity

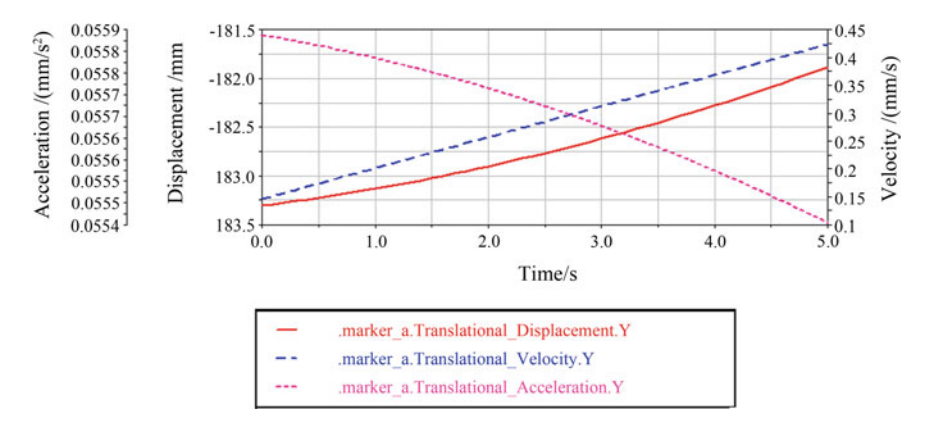


Fig. 5.44 Displacement, velocity and acceleration of the point a in the Y-direction, when prism 1 works at tilting motion mode

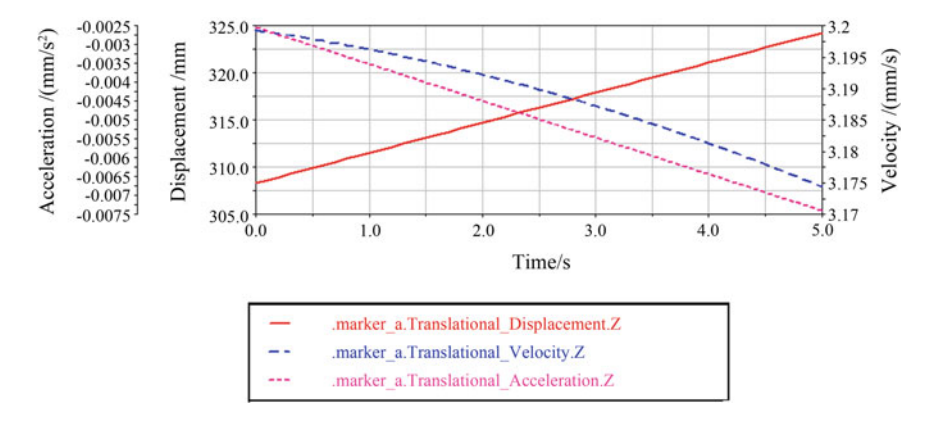


Fig. 5.45 Displacement, velocity and acceleration of the point a in the Z-direction, when prism 1 works at tilting motion mode

(or Y-velocity) occurs when the point a arrives at maximum X-coordinate (or Y-coordinate). In other words, the point a has maximum Y-velocity (or X-velocity) when the thinnest end of prism 1 is aligned with the negative X-axis (or Y-axis), while the point a has minimum Y-velocity (or X-velocity) when the thinnest end of prism 1 is aligned with the positive X-axis (or Y-axis). Likewise, the X-acceleration (or Y-acceleration) reaches its maximum value when the X-velocity (or Y-velocity) is minimum, while the X-acceleration (or Y-acceleration) reaches its minimum value when the X-velocity (or Y-velocity) is maximum. As the X-displacement of the point X-acceleration occurs when the tilting angle of prism 1 is 3°, while the minimum X-acceleration occurs when the tilting angle of prism 1 is 0°.

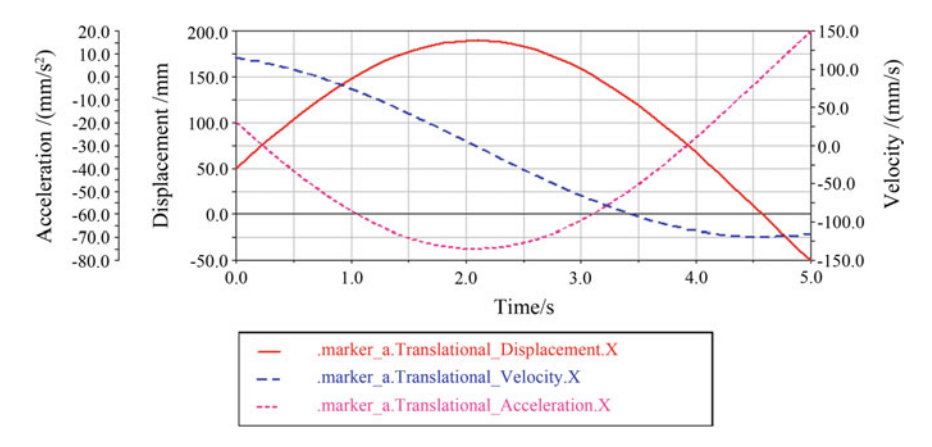


Fig. 5.46 Displacement, velocity and acceleration of the point a in the X-direction, when prism 1 works at composite motion mode

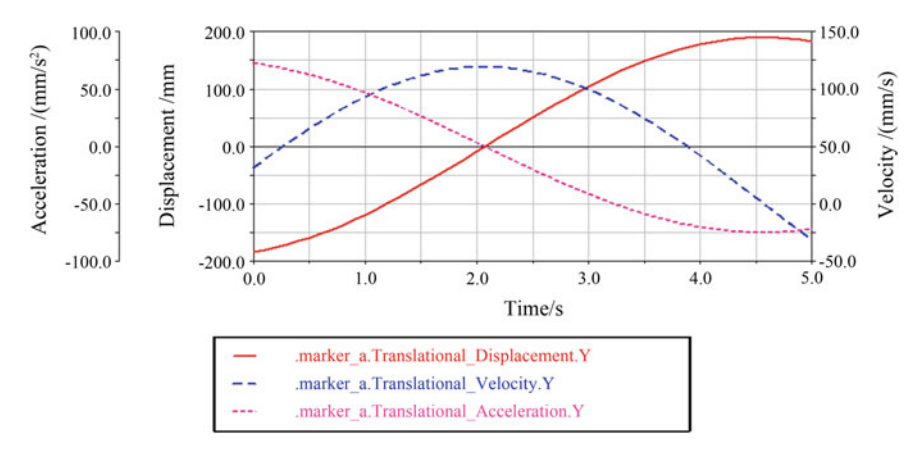


Fig. 5.47 Displacement, velocity and acceleration of the point a in the Y-direction, when prism 1 works at composite motion mode

5.5.6 Scan Error Analysis

Generally, the primary sources of beam scan error fall under two categories, namely systematic errors and random errors. Systematic errors mainly include the processing errors in the wedge angle and refractive index of each prism and the perpendicularity error between the principal sections of two prisms. Random errors mainly refer to the orientation errors in the rotation or tilting angles of two prisms.

1. Rotating Motion Mode

At rotating motion mode, two prisms in the proposed device are supposed to rotate at the same speed around the Z-axis, expressed as $\Delta\theta_r = \theta_{r2} - \theta_{r1} = 0$. Thus, the

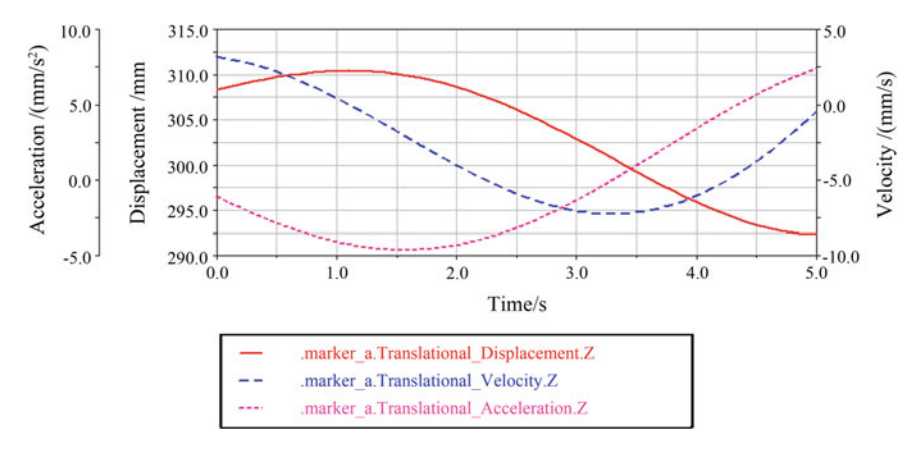


Fig. 5.48 Displacement, velocity and acceleration of the point *a* in the *Z*-direction, when prism 1 works at composite motion mode

pitch angle of emergent beam can be determined from the formulae in Sect. 2.3.1, as follows

$$\rho = \arccos(\cos \delta_2 \cos \delta_1 - \sin \delta_2 \sin \delta_1) = \delta_1 + \delta_2 \tag{5.11}$$

where ρ is the pitch angle of emergent beam, δ_1 and δ_2 represent the beam deviation angles induced by prism 1 and prism 2, respectively.

According to our previous research, δ_1 is associated with the wedge angle α and the refractive index n, and δ_2 is dependent on α , n and the relative rotation angle $\Delta\theta_r$ of two prisms. Now that two prisms rotate synchronously with $\Delta\theta_r$ =0, the pitch angle reaches its maximum value that equals to the sum of beam deviation angles induced by two prisms, namely ρ =10°30′. In addition, there is a reduction ratio close to 18:1 between the prism rotation angle and the beam deviation angle. Such a reduction ratio allows lower accuracy requirement for each rotating prism assembly, which can be significant to achieve high-precision scanning and tracking.

To help reveal the influence of prism orientation errors, an imaginary error $d\Delta\theta_r$ is introduced to the relative rotation angle $\Delta\theta_r$. Since $d\Delta\theta_r$ is relatively small, the pitch angle ρ can still be obtained from (5.11) in approximation, and δ_1 is always independent of the rotation angles of two prisms. Therefore, the total differential of the pitch angle ρ is derived through the following differentiation calculus:

$$d\rho = \frac{\partial \delta_1 + \partial \delta_2}{\partial \alpha} d\alpha + \frac{\partial \delta_1 + \partial \delta_2}{\partial n} dn + \frac{\partial \delta_2}{\partial \theta_r} d\Delta \theta_r$$
 (5.12)

where $d\alpha$ and dn denote the wedge angle error and refractive index error of each prism, respectively.

		•
Systematic errors	$dn = 1 \times 10^{-6}$	$d\alpha = 1''$
Pitch angle error $d\rho/\mu$ rad	0.4311	2.259

Table 5.16 Analysis on the systematic errors in rotating double prisms

The error analysis results with regard to rotating double prisms are listed in Table 5.16. It turns out that the wedge angle error has comparatively large impact on the pitch angle error.

It has been mentioned in Sect. 5.5.1 that rotating double prisms are required to achieve beam scan precision better than 50 μ rad. Given the ratio between prism rotation angle and beam deviation angle as 18:1, the overall mechanical error of each rotating prism cannot exceed the upper tolerance of 900 μ rad. Accordingly, the comprehensive accuracy of the mechanical structure and control unit used for prism rotation should be superior to 185.73".

2. Tilting Motion Mode

Once both prisms work at tilting motion mode, the proposed device is regarded as the tilting double-prism system shown in Fig. 2.7, where prism 1 tilts around the *Y*-axis and prism 2 tilts around the *X*-axis. Given the incident beam vector $\mathbf{A_0} = (x_0, y_0, z_0)^{\mathrm{T}} = (0, 0, 1)^{\mathrm{T}}$ and the emergent beam vector $\mathbf{A}_f = (x_f, y_f, z_f)^{\mathrm{T}}$, the pitch angle of emergent beam can be deduced from (2.15) as follows

$$\rho = \arccos(x_0 x_f + y_0 y_f + z_0 z_f) = \arccos(z_f) = \arccos\left[\sin \beta_{t2} \cos(\gamma_{t2} - \delta_2)\right]$$
(5.13)

where $\beta_{t2} = \arccos[\cot(-\delta_1)]$ is the angle of the emergent beam vector A_2 from prism 1 relative to the positive *X*-direction, $\gamma_{t2} = 0$ is the relative angle between the projection of A_2 in the *YOZ* plane and the positive *Z*-direction, δ_1 and δ_2 represent the beam deviation angles induced by prism 1 and prism 2, respectively.

Seen from Fig. 2.16, the vertical field angle error of the emergent beam is mostly affected by the tilting angle θ_{t1} of prism 1, whereas the horizontal field angle error mainly depends on the tilting angle θ_{t2} of prism 2. Therefore, the total differential of the pitch angle is expressed in terms of tilting angle errors $d\theta_{t1}$ and $d\theta_{t2}$, wedge angle error $d\alpha$ and refractive index error dn, as follows

$$d\rho = \frac{\partial \rho}{\partial \delta_1} \left(\frac{\partial \delta_1}{\partial \theta_{t1}} d\theta_{t1} + \frac{\partial \delta_1}{\partial \alpha} d\alpha + \frac{\partial \delta_1}{\partial n} dn \right) + \frac{\partial \rho}{\partial \delta_2} \left(\frac{\partial \delta_2}{\partial \theta_{t2}} d\theta_{t2} + \frac{\partial \delta_2}{\partial \alpha} d\alpha + \frac{\partial \delta_2}{\partial n} dn \right)$$
(5.14)

where
$$\frac{\partial \rho}{\partial \delta_1} = -\frac{\partial \beta_{r2}}{\partial \delta_1} = \frac{1}{\sqrt{1-\cot(\delta_1)^2}}$$
 and $\frac{\partial \rho}{\partial \delta_2} = 1$.

Using (5.14), we can separately quantify the influence of the systematic errors and random errors in tilting double prisms. Particularly, there is a perpendicularity error $d\tau$ between the principal sections of two prisms, which can be equivalent

Systematic errors

 $d\tau = 1''$

Pitch angle error $d\rho/\mu$ rad	0.258	3.844	0.332
(a) 0.2592		(b) 3.87	
Q 0.2588-		3.86- (o)/pl 3.85	
0.2584		3.85.	

 $d\alpha = 1''$

Table 5.17 Analysis on the systematic errors in tilting double prisms

 $dn = 1 \times 10^{-6}$

0.2584 0.2584 0.2576 1.5 1.52 1.54 1.56 1.58 1.6 3.82 0.2576 0.2576

Fig. 5.49 Relation of the change rate of pitch angle with respect to **a** the refractive index n and **b** the wedge angle α of each prism

to an undesired deviation of the incident beam in calculation. On the above basis, Table 5.17 indicates the analysis results on the systematic errors of tilting double prisms.

Figure 5.49 illustrates the relation between the change rate of pitch angle and the refractive index as well as the wedge angle of each prism. Providing the refractive index n within 1.5–1.6, the change rate of pitch angle $d\rho/dn$ reaches the maximum value 0.2593 rad and the minimum value 0.2578 rad. The pitch angle error increases with the increment of refractive index or wedge angle. Specifically, the pitch angle error can be 0.258 μ rad once an error of 1×10^{-6} is introduced to the nominal refractive index n=1.517, and the pitch angle error becomes 3.844 μ rad if there is an error of 1″ in the nominal wedge angle α =10°.

Figure 5.50 reveals the relation of the change rate of pitch angle relative to the tilting angles of two prisms. As the tilting angle θ_{t1} of prism 1 ranges within $0^{\circ}-5^{\circ}$, the change rate of pitch angle $d\rho/d\theta_{t1}$ takes the maximum value of 0.0262 or 0.1276 μ rad/(") (when $\theta_{t1}=5^{\circ}$), the minimum value of 0.0150 or 0.0726 μ rad/(") (when $\theta_{t1}=0^{\circ}$) and the average value of 0.1001 μ rad/("). Likewise, as the tilting angle θ_{t2} of prism 2 varies within $0^{\circ}-5^{\circ}$, the change rate of pitch angle $d\rho/d\theta_{t2}$ takes 0.0138 or 0.0678 μ rad/(") at maximum (when $\theta_{t2}=5^{\circ}$), 0.0045 or 0.0216 μ rad/(") at minimum (when $\theta_{t2}=0^{\circ}$) and 0.0447 μ rad/(") on average. Consequently, the average scale factor between the tilting angle of prism 1 and the beam deviation angle is 48:1, while the one between the tilting angle of prism 2 and the beam deviation angle is 108:1.

As mentioned in Sect. 5.5.1, the beam steering precision of this device should be superior to 1 μ rad during fine scanning. Since the maximum change rate of pitch angle takes 0.1276 μ rad/(") for prism 1 and 0.0678 μ rad/(") for prism 2, the tilting

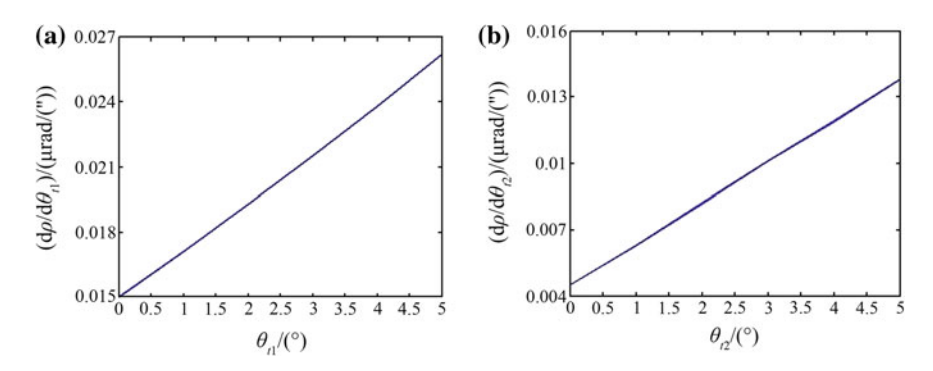


Fig. 5.50 Relation of the change rate of pitch angle with respect to **a** the tilting angle θ_{t1} of prism 1 and **b** the tilting angle θ_{t2} of prism 2

motion accuracy of prism 1 should be better than 7.840", and that of prism 2 should be better than 14.749". In other words, the mechanical structure and control unit used for the tilting motion of prism 1 and prism 2 are, respectively, required with the comprehensive accuracy better than 7.840" and 14.749".

5.6 Summary

This chapter concentrates on the design principle and techniques of the rotating double-prism scan device, the tilting double-prism scan device as well as the composite motion double-prism scan device. Through the comparison of four different double-prism configurations, we select the most suitable configuration form for rotating or tilting double prisms. Many design schemes of rotating double-prism scan device and tilting double-prism scan device are further presented on the basis of various drive mechanisms. For the verification of beam scan performance, the rotating double-prism device driven by the worm and gear mechanism is well developed with both mechanical structure and control system. In order to simplify the motion control process and improve the control accuracy of tilting double prisms, the cam-based drive mechanism is adopted in the proposed tilting double-prism device, which can transfer the nonlinear control problem to the cam profile design. As for the composite motion double-prism device, the four-axis joint control strategy is employed to achieve independent rotating motion and tilting motion of each prism. It turns out that the composite motion double-prism device has the enhanced adaptability to perform wide-range, high-precision and multi-scale beam scanning.

References 235

References

 Li YJ (2011) Closed form analytical inverse solutions for Risley-prism-based beam steering systems in different configurations. Appl Opt 50(22):4302–4309

- 2. Schwarze CR (2006) A new look at Risley prisms [EB/OL]. Tospfield, MA: Optra Inc, (2006-6), 13 Oct 2016. http://www.optra.com/images/TP-A_New_Look_at_Risley_Prisms.pdf
- 3. Li AH, Jiang XC, Sun JF et al (2012) Laser coarse–fine coupling scanning method by steering double prisms. Appl Opt 51(3):356–364
- García-Torales G, Flores JL, Muñoz RX (2007) High precision prism scanning system. Proc SPIE 6422:64220X-64220X-8
- Li AH, Gao XJ (2013) Rotating prism device driven by synchronous belt: CN, 201310072421.0
 [P], 12 June 2013
- 6. Yuan Y, Zhao YY, Su LJ (2013) A beam scanning mechanism based on rotating double-wedge prisms: CN, 201210432016.0 [P], 13 Feb 2013
- 7. Yun MJ, Zu JF, Sun JF et al (2004) Precision rotating double-prism beam scanner and its control method: CN, 200310108487.7 [P], 3 Sept 2004
- 8. Zu JF, Liu LR, Yun MJ et al (2003) Satellite trajectory optical simulation device: CN, 03129234.8 [P], 24 Dec 2003
- Li AH (2013) Rotating prism device for realizing coarse-fine scanning: CN, 201210439061.9
 [P], 6 Mar 2013
- Gao XJ (2015) Research on rotating double-prism dynamic tracking system. Tongji University, Shanghai
- 11. Sun JF, Liu LR, Yun MJ et al (2005) High precision dynamic and static measuring device for intersatellite laser communication terminal: CN, 200410024986.2 [P], 23 Feb 2005
- Li AH, Liu LR, Sun JF, et al (2011) Dual-wedge beam deflection mechanism: CN, 200510026553.5 [P], 28 Dec 2005
- Li A H, Li ZZ, Jiang XC (2011) A tilting optical wedge scanning device: CN, 201010588924.X
 [P], 18 May 2011
- Li AH, Wang W, Ding Y et al (2013) Cam-driven tilting prism mechanism: CN, 201210375722.6 [P], 16 Jan 2013
- Li AH, Sun WS (2015) A tilt mirror mechanism driven by a crank slider: CN, 201510560372.4
 [P], 25 Sept 2015
- 16. Sun JF (2005) Research on the satellite trajectory optical simulator. Shanghai Institute of Optics and Fine Mechanics. The Chinese Academy of Sciences, Shanghai
- 17. Zhou Y, Lu YF, Hei M et al (2014) Pointing error analysis of Risley-prism-based beam steering system. Appl Opt 53(24):5775–5783
- Li AH, Yi WL, Sun WS et al (2015) Tilting double-prism scanner driven by cam-based mechanism. Appl Opt 54(18):5788–5796
- Li AH, Ding Y, Bian YM et al (2014) Inverse solutions for tilting orthogonal double prisms. Appl Opt 53(17):3712–3722
- Zhang JY (2007) Solutions of motion analysis and synthesis in mechanisms. China Communications Press, Beijing

Chapter 6 Performance Test on Double-Prism Multi-mode Scan System



Abstract Performance tests are conducted for the scan devices based on rotating double prisms, tilting double prisms and cascaded Risley prism pairs. Given a rotating double-prism scan device, the multi-mode beam scan test and directional beam tracking test are accomplished to validate the multi-mode beam scan theory using rotating double prisms, and another test is about the accuracy of inverse solutions obtained from lookup-table method. A tilting double-prism scan device is tested to evaluate prism motion accuracy, reduction ratio from prism orientation to beam deviation, beam deflection range and accuracy. Additionally, the coarse-fine coupling tracking test is performed on a scan device composed of two Risley prism pairs.

6.1 Introduction

To verify the design principle of the scan system and the functionality of the designed devices, this chapter mainly focuses on the static and dynamic performance tests of the double-prism multi-mode scan system [1].

For rotating double prisms, the verification tests incorporate: (1) multi-mode scan performance; (2) directional tracking performance, which can be expressed as the deviation between the actual scan point and the theoretical one; (3) lookup-table method, which can be validated by measuring the beam tracking precision at the prism orientations reversely solved with lookup-table method [2].

The verification tests on tilting double prisms mainly include: (1) tilting accuracy of the prism, which is shown as the relation between the tilting angle of the prism measured by high-precision collimator and that read from the encoder; (2) the function between the tilting angle of the prism and the corresponding beam deflection; (3) the scan range of the emergent beam in the vertical and horizontal directions; (4) beam pointing precision, namely the error between the actual beam deflection caused by an unit tilting angle of the prism and the corresponding theoretical beam deflection; test (1)–(3) are measured using autocollimator [3–6], and test (4) is gauged by an interferometer.

In addition, a coarse-fine tracking method based on two pairs of rotating Risley prisms with different wedge angles is proposed, and the verification test mainly focuses on measuring the tracking errors of the coarse tracking subsystem and the fine tracking subsystem.

The above performance tests should be accomplished softly without vibration and shocks. Specially, the experimental equipment used in the tilting double-prism system should be positioned on an air bearing worktable in a super-clean temperature-controlled laboratory.

6.2 Performance Test on Rotating Double Prisms

6.2.1 Hardware of the Test Platform

A two-dimensional slipway system, composed of two orthogonal guide rails and a slider mounted on the vertical slipway, is adopted to simulate the motion of any moving target. A four-quadrant detector, of which the center is regarded as the target point, is fixed on the slider. Thus, arbitrary planar target trajectories in the *XOY* plane can be simulated by controlling the movement of the slider.

The scan range of the designed rotating double-prism system is a circular ring with the radius of the outer circle R=82 mm, and therefore the effective stroke of two guide rails must be greater than 164 mm. Considering the limit switch at each rail end and the influence of structure parameters, the effective strokes of the *X*-axis and *Y*-axis guide rails are set to 300 mm and 400 mm, respectively.

The guide rails, driven by step motors with step angle of 1.8° , move the slider through ball screw pairs, of which the type specification is 1204, the diameter is 12 mm, the lead is 4 mm and the round trip accuracy is 0.02 mm. Figure 6.1 is the picture of the selected two-dimensional slipway, and the functional requirements of the control system are listed in Table 6.1.

Comparing Table 5.8 and Table 6.1, the functional requirements of the slipway control system are consistent with those of the prism control system. Hence we employ the same controller as shown in Sect. 5.3.3 for the motion control of the two-dimensional slipway.

Four-quadrant detectors, characterized by high homogeneity, symmetry, reliability, high sensitivity, wide spectral response range and small blind zone, are widely used in many high-precision measurement occasions such as laser aiming and displacement monitoring. Therefore, in this test, a four-quadrant detector is selected to detect the position of the laser spot, and further evaluate the accuracy of the rotating double-prism system.

A four-quadrant detector is a reverse bias array of four semiconductor diodes, which are totally identical in theory. Given the constant radiation flux irradiating from the laser to each quadrant, the photocurrent generated on each quadrant are equal. Furthermore, the radiation fluxes on each quadrant will redistribute if the laser

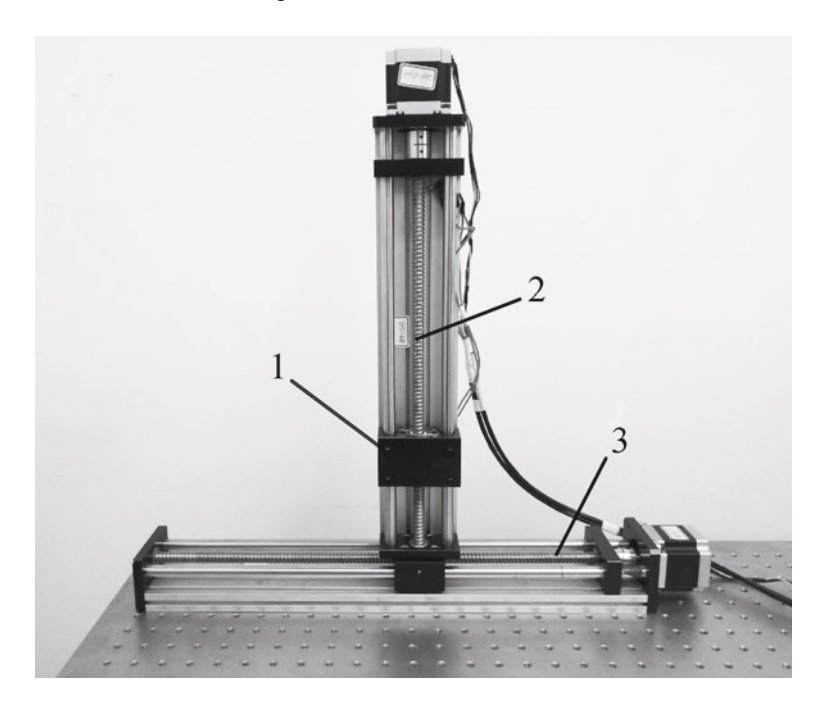


Fig. 6.1 Two-dimensional slipway, where 1 is the slider, 2 and 3 are the ball screws of the X and Y axis, respectively

Table 6.1 Functional requirements of the two-dimensional slipway control system

No.	Function	Demand quantity	Design quantity	Remark
1	24 V digital input (for limit switch)	4	8	4 spare sets
2	5 V PWM output	2	4	2 spare sets
3	RS232 communication (for program loading)	1	1	_
4	RS485 communication (for online communication)	1	1	_
5	I2C	1	1	_
6	SPI	1	1	_
7	LCD display (for data display)	1	1	-
8	LED (for debugging)	1	1	-
9	Buzzer (for alarm)	1	1	-

spot moves, and thus the position of the laser spot on the detector can be calculated according to the proportion of the photocurrent on each quadrant.

A set of four-quadrant detector instrument mainly consists of an amplifier, a four-quadrant probe, a power adapter and some other components. The four-quadrant

amplifier and four-quadrant probe are shown in Fig. 6.2a and b, with the individual technical parameters shown in Tables 6.2 and 6.3.

As shown in Table 6.2, the laser spot positioning accuracy of the selected four-quadrant detector is superior to 0.01 mm, which satisfies the requirement of the performance test on rotating double-prism system. An USB cable is used to transfer data from the amplifier to the computer. And the user interface of the four-quadrant detector software, as shown in Fig. 6.3, is intuitive and easy to use.

6.2.2 Software of the Test Platform

As shown in Fig. 6.4, the test platform mainly consists of the laser, the rotating double-prism scanner and its controller, the two-dimensional slipway and its controller, as well as the four-quadrant detector. For the collaborative operation of the test system, a piece of dynamic tracking software is developed for data exchange and motion control.

In general, the dynamic tracking software can be divided into two parts, namely the host computer software and the slave computer software. The former one, embed-

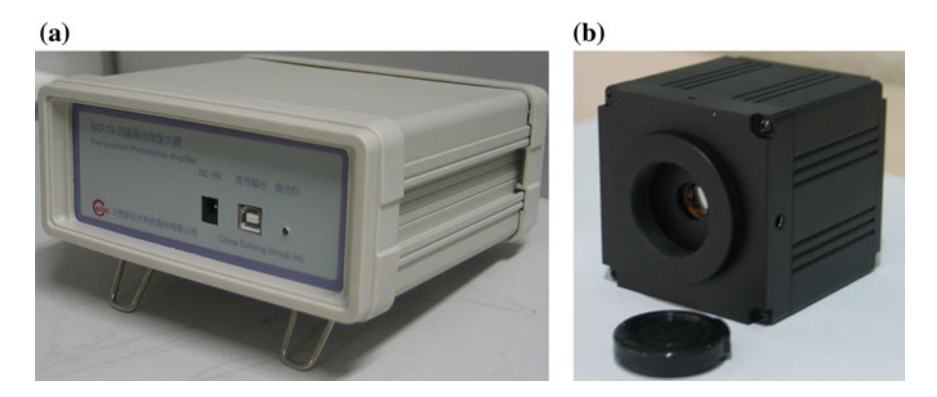


Fig. 6.2 Components of the four-quadrant detector where \mathbf{a} is the four-quadrant amplifier and \mathbf{b} is the four-quadrant probe

Table 6.2 Parameters of the four-quadrant amplifier

Accuracy	Power supply	A/D conversion cycle	Dimension $(W \times H \times L)$	Weight
0.01 mm	DC33 V/± 15 V	3 μs	160 mm × 80 mm × 155 mm	960 g

Table 6.3 Parameters of the four-quadrant probe

Diameter of the photosensitive area	Screw	Dimension $(W \times H \times L)$	Weight
φ6 mm	M4	54.5 mm × 54.5 mm × 74 mm	150 g

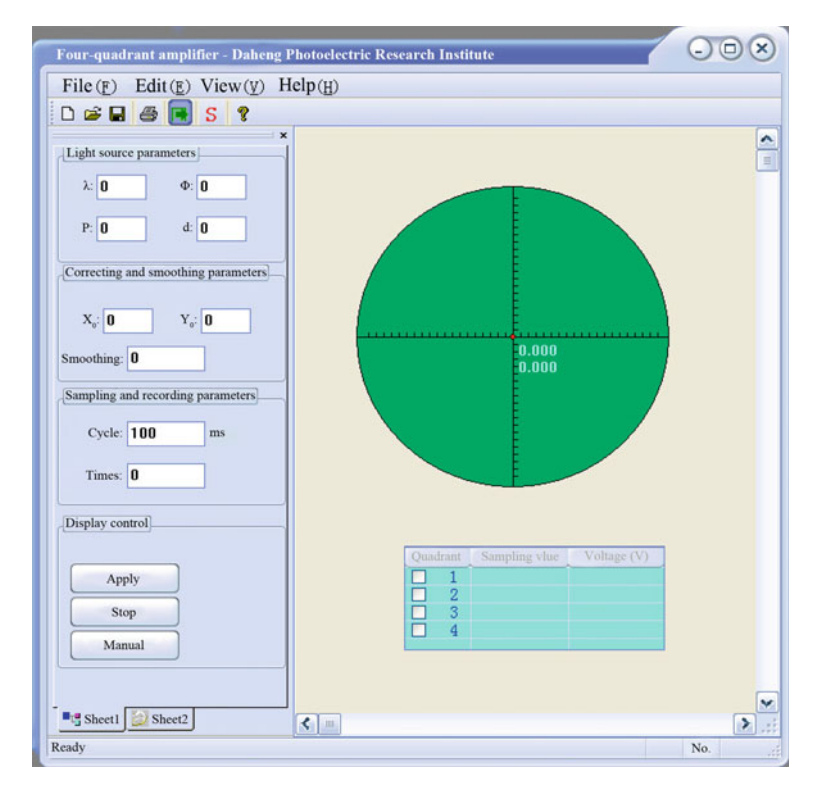


Fig. 6.3 User interface of the four-quadrant detector software

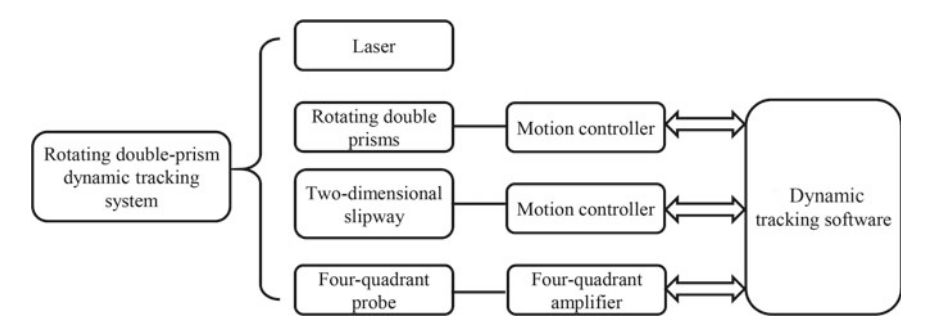


Fig. 6.4 Block diagram of the test platform for the rotating double-prism multi-mode scan system

ded with the inverse algorithm of rotating double-prism system and programmed in Matlab, is used for target point data processing, inverse solution computing, and data exchange with the slave computer. The latter one, designed on the basis of LPC1114 MCU in Keil for ARM, can not only receive the order from the host computer to control the step motors, but also monitor the running status of the tracking system and transfer the feedback data. The RS485 serial bus is used for communication

between the host computer and the slave computer. Detailed descriptions of the host and the slave computer software are as follows.

The functions of the host computer software, whose user interface is built based on Matlab GUIDE, mainly include: (1) obtaining the target coordinate from the two-dimensional slipway controller through RS485 serial bus; (2) figuring out the corresponding prism angles using the integrated inverse algorithm; (3) sending the rotation angles and velocities to the rotating double-prism controller through RS485 serial bus. The block diagram and the user interface of the host computer software are shown in Figs. 6.5 and 6.6, respectively.

Two controllers, namely the rotating double-prism controller and the twodimensional slipway controller, make up the slave computer. Hence the main function of the slave computer software is to control the rotation angles and velocities of the step motors. As the block diagram shown in Fig. 6.7, the slave computer can work in four different control modes. Taking the rotating double-prism controller for example, the four different modes are as follows:

- (1) Manual mode. The rotation angles, velocities and directions of two prisms are regulated manually through a 4 × 4 matrix keyboard. Moreover, two keys in the matrix are specially designed for origin setting and zeroing.
- (2) Automatic uniform scan mode. The rotation velocities, directions and the RUN/STOP switch status are all preset for continuous and uniform rotation of two prisms. This mode is specialized for the uniform scan test on double prisms.
- (3) Single-step mode. In this mode, a series of rotation angles are pre-stored in the controller, and the prisms rotate towards the preset angles in single steps according to key pressing.
- (4) Linkage tracking mode. The host computer takes complete control of the prism motion by sending the motion order to the rotating double-prism controller through RS485 serial bus.

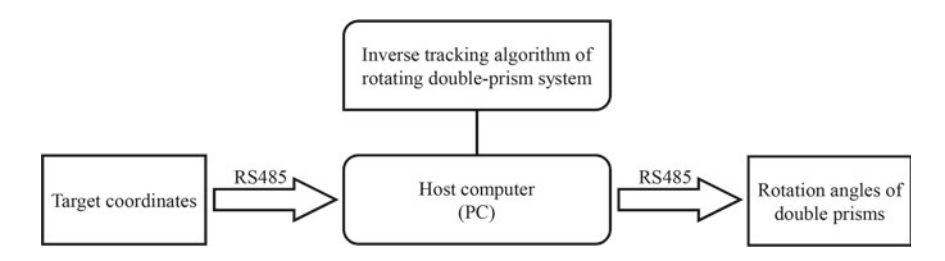


Fig. 6.5 Block diagram of the host computer software

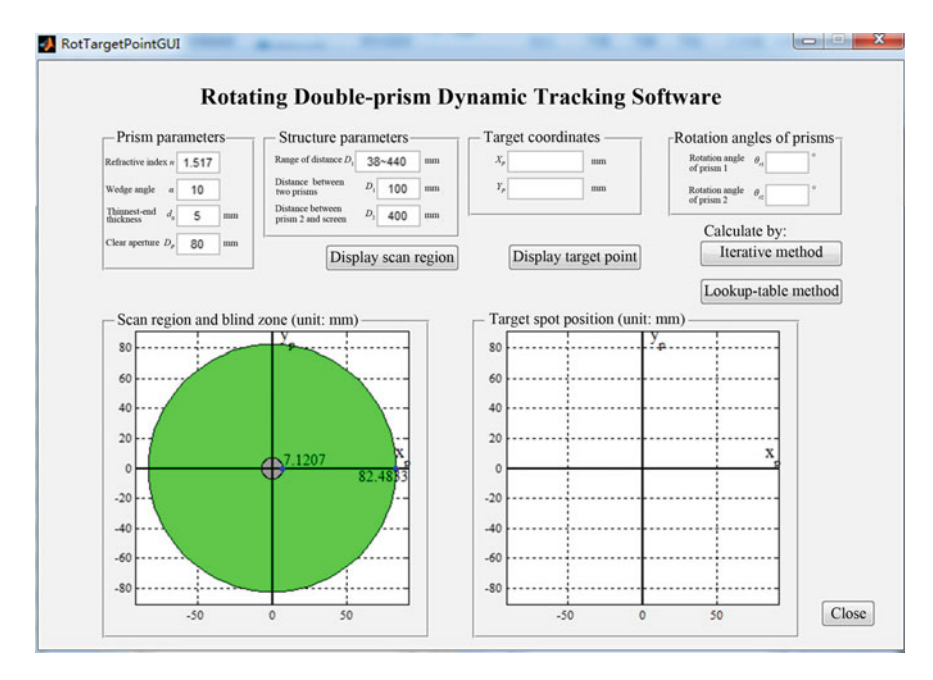


Fig. 6.6 User interface of the host computer software

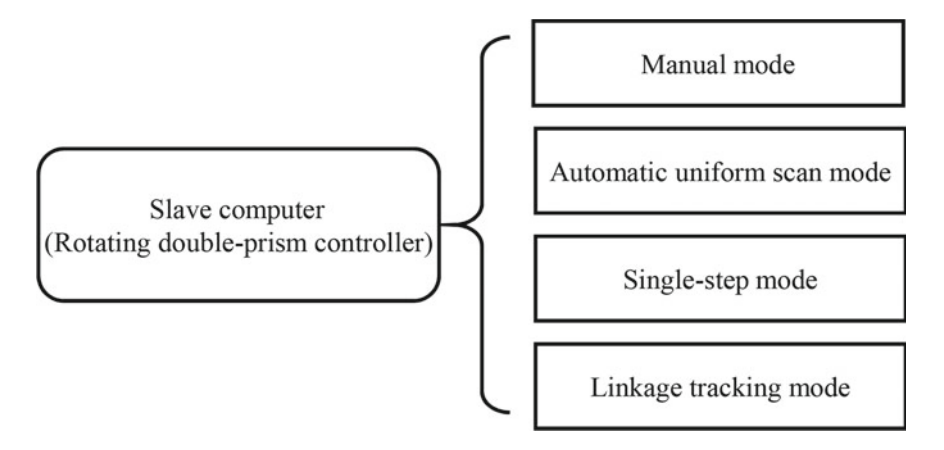


Fig. 6.7 Block diagram of the slave computer software

6.2.3 Multi-mode Scan Performance Test

In order to test the beam scan modes of the designed rotating double-prism system and evaluate the directional tracking performance, a test platform is established as

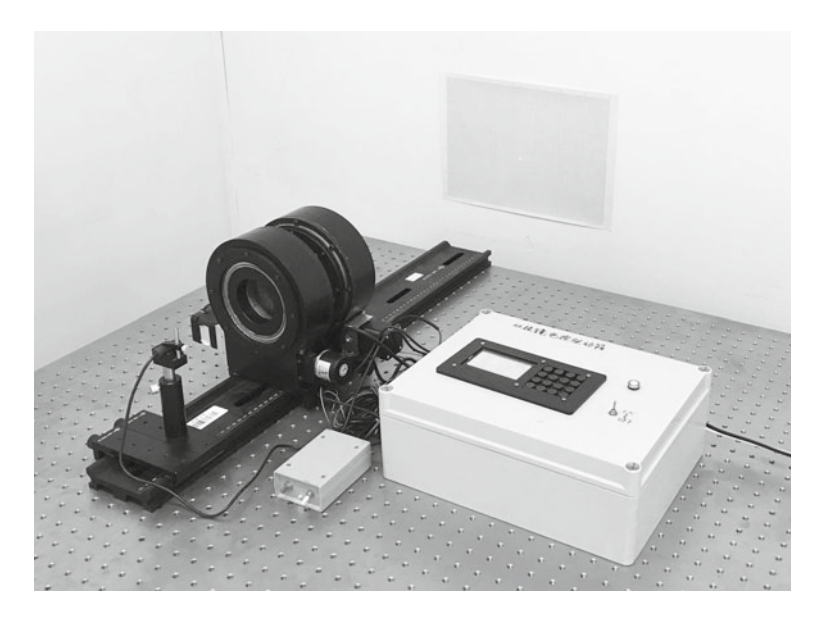


Fig. 6.8 Eexperimental platform for testing the rotating double-prism multi-mode scan performance

shown in Fig. 6.8. The test platform mainly includes rotating double-prism device and its motion controller, laser, coordinate screen, guide rail and slider. More detailed descriptions of the used components are listed in Table 6.4.

Table 6.4 Parameters and functions of the components used in the multi-mode scan performance test platform

Device	Parameter	Function
Rotating double prisms	Wedge angle: $\alpha = 10^{\circ}$ Refractive index: $n = 1.517$ Diameter: $D = 80$ mm	Deflect laser beam
	Thinnest-end thickness: $d_0 = 5 \text{ mm}$ Distance between two prisms: $D_1 = 100 \text{ mm}$	
Motion controller	MCU: LPC1114	Motion control of double prisms
Laser	Wavelength: 650 nm Power: $P \ge 2.5$ mW Focus: variable focus	Emit collimated laser beam
Coordinate screen	Resolution ratio: 1 mm Distance away from the emergent surface of prism 2: $D_2 = 400 \text{ mm}$	Receive the laser and measure the coordinates of the laser spot
Guide rail and slider	Stroke of the guide rail: 1000 mm	Support components

Main steps of the multi-mode scan performance test are as follows:

- (1) Device installation. Firstly mount the laser on the guide rail while keep the laser beam parallel to the guide rail and pointing at the origin of the coordinate screen. Then install the rotating double prisms on the guide rail, and adjust the prism devices in the radial direction until the optical axis of two prisms are coaxial with the laser beam. Finally, move two prisms in the axial direction to the position where the distance between the emergent surface of prism 2 and the coordinate screen is $D_2 = 400$ mm, and the separation between two plane facets of the prisms is $D_1 = 100$ mm.
- (2) Set the control mode to manual mode. Rotate the prisms at low speeds and set each prism origin at the position where the thinnest end is strictly upward.
- (3) Set the control mode to single-step mode. Rotate two prisms to the pre-stored orientation combination obtained from the inverse solution to those sampling points on the given scan trajectory, and take notes of the laser spot coordinates on the coordinate screen. Then press the single-step key to measure the next sampling point and repeat until all the sampling points on the trajectory are measured. Note that the grid density of the coordinate screen is 1 mm and the accuracy of the reading coordinate is 0.1 mm, since the last place of the reading is estimated.
- (4) Set the control mode to manual mode and return to zero.
- (5) Repeat from step (3) to step (4), and finish the measurement of all four trajectories.
- (6) Based on the prism orientations obtained from inverse solutions, calculate the theoretical laser spot coordinates on the screen using the forward formulae in Sect. 2.1. Then compare the measured coordinates with the theoretical ones, and evaluate the multi-mode scan performance of the designed system.

In the test, we set 32 sampling points for each trajectory. And the distance between the measured actual scan point (x_{rp}, y_{rp}) and the calculated theoretical scan point (X_{rp}, Y_{rp}) is defined as scan error Δ , namely, $\Delta = \sqrt{(X_{rp} - x_{rp})^2 + (Y_{rp} - y_{rp})^2}$ (unit: mm). Tables 6.5, 6.6, 6.7 and 6.8 show the measurement results of four trajectories, respectively.

Trajectory 1 is a circle which can be obtained by rotating two prisms at the same speed and in the same direction, namely $\theta_{r1}:\theta_{r2}=1:1$. Figure 6.9 shows the actual scan points and theoretical scan points of trajectory 1. Seen from the figure, the actual scan point with symbol "x" and the corresponding theoretical scan point with symbol "o" are almost coincident. Actually, calculation results indicate that the average scan error is 1.06 mm.

Trajectory 2 is an ellipse which can be obtained by rotating two prisms at the same speed but in the opposite direction, namely θ_{r1} : $\theta_{r2} = 1$:-1. Seen from Fig. 6.10, both the actual trajectory and the theoretical trajectory are elliptical, and the actual scan point with symbol "x" and the corresponding theoretical scan point with symbol "o" are almost coincident. Likewise, the average scan error of trajectory 2 is 0.97 mm.

For trajectory 3 and trajectory 4, the rotation angles of two prisms are set to θ_{r1} : $\theta_{r2}=1:2$ and θ_{r1} : $\theta_{r2}=1:-2$, respectively. Test results shown in Figs. 6.11

ectory 1	
of trai	
t data	
z Tesi	
able 6.	
Ξ	

of prisms/(°) scan point/mm point/mm error/mm of prisms/(°) scan point/mm	No	Rotation angle	n angle	Theoretical	ical	Actual scan	can	Scan	No.	Rotation angle	angle	Theoretical	cal	Actual scan	can	Scan error/mm
$ \begin{array}{c ccccccccccccccccccccccccccccccccccc$			(°)/sr	scan poi	int/mm	point/mı	E	error/mm		of prism	(°)/sr	scan poi	nt/mm	point/mr	п	
0 0 -82.5 0.0 -82.5 0.0 17 160 160 77.5 -28.2 75.5 - 10 10 -81.2 -14.3 -81.0 -14.0 0.36 18 170 170 81.2 -14.3 80.0 - 20 20 -77.5 -28.2 -77.5 -27.5 0.70 190 180 81.2 14.3 80.0 - 30 20 -77.5 -28.2 -77.5 0.71 20 190 180 81.2 14.3 80.0 - 40 40 -63.2 -53.6 62.5 0.78 21 20 190 14.3 14.3 79.5 50 50 -53.0 -63.5 -62.5 0.86 22 200 77.5 28.0 14.4 11.2 11.0 11.0 11.0 11.0 11.0 11.0 11.0 11.0 11.0 11.0 11.0 11.0 11.0		θ_{r1}	θ_{r2}		Y_{rp}	x_{rp}	Угр	◁		θ_{r1}	θ_{r2}	X_{rp}	Y_{rp}	χ_{rp}	yrp	\\\\\\\\\\\\\\\\\\\\\\\\\\\\\\\\\\\\\\
10 10 -81.2 -14.3 -81.0 -14.0 0.36 18 170 170 81.2 -14.3 80.0 -2 20 20 -77.5 -28.2 -77.5 -27.5 0.70 19 180 81.2 14.3 80.0 - 30 -71.4 -41.2 -71.5 -40.5 0.71 20 190 180 81.2 14.3 79.5 40 40 -63.2 -53.0 -63.5 -52.5 0.58 21 200 200 77.5 28.2 76.5 50 -63.0 -63.2 -52.5 0.58 21 200 200 77.5 28.2 76.5 60 60 -41.2 -71.4 -41.5 -70.5 1.04 24 230 230 53.0 63.0 50.0 70 -28.2 -77.5 -28.5 -76.5 1.04 24 230 230 230 230 230 23	_	0	0	-82.5	0.0	-82.5	0.0	0.00	17	160	160	77.5	-28.2	75.5	-29.0	2.15
20 20 -77.5 -28.2 -77.5 -27.5 -27.5 0.70 19 180 82.5 0.0 81.0 30 30 -71.4 -41.2 -71.5 -40.5 0.71 20 190 180 81.2 14.3 79.5 40 40 -63.2 -53.0 -63.5 -52.5 0.58 21 200 200 77.5 28.2 76.5 50 50 -53.0 -63.2 -52.5 0.58 22 210 210 71.4 41.2 70.0 60 60 -41.2 -71.4 -41.5 -76.5 1.04 24 220 220 63.2 53.0 62.0 80 60 -41.2 -71.4 -41.5 -76.5 1.04 24 230 230 63.2 52.0 80 80 -14.3 -81.2 -15.0 -80.0 1.34 27 240 240 41.2 71.4 4	2	10	10	-81.2	-14.3	-81.0	-14.0	0.36	18	170	170	81.2	-14.3	80.0	-14.5	1.22
30 30 -714 -41.2 -71.5 -40.5 0.71 20 190 81.2 14.3 79.5 40 40 -63.2 -53.0 -63.5 -52.5 0.58 21 200 200 77.5 28.2 76.5 50 50 -53.0 -63.2 -53.5 -62.5 0.86 22 210 210 71.4 41.2 70.0 60 60 -41.2 -71.4 -41.5 -70.5 0.95 23 220 220 63.2 53.0 62.0 70 70 -28.2 -77.5 -88.5 1.04 24 230 230 63.2 52.0 80 80 -14.3 -81.2 1.50 -81.5 1.12 26 250 240 240 240 240 240 230 63.2 25.0 80 80 -14.3 -81.2 1.12 -1.65 1.14 27 240 240	8	20	20	-77.5	-28.2	-77.5	-27.5	0.70	19	180	180	82.5	0.0	81.0	0.0	1.50
40 40 -63.2 -53.0 -63.5 -52.5 0.58 21 200 200 77.5 28.2 76.5 50 50 -53.0 -63.2 -52.5 0.86 22 210 210 71.4 41.2 70.0 60 60 -41.2 -71.4 -41.5 -70.5 0.98 23 220 63.2 53.0 62.0 70 70 -28.2 -77.5 -28.5 -76.5 1.04 24 230 63.2 53.0 62.0 80 80 -14.3 -81.2 -1.60 1.39 25 240 240 41.2 71.4 40.5 90 90 0.0 -82.5 -0.5 -81.5 1.12 26 250 250 28.2 77.5 27.5 110 110 18.3 -80.0 1.44 27 260 260 14.3 81.2 14.5 120 120 280	4	30	30	-71.4	-41.2	-71.5	-40.5	0.71	20	190	190	81.2	14.3	79.5	14.0	1.73
50 50 -53.0 -63.2 -53.5 -62.5 0.86 22 210 71.4 41.2 700 60 60 -41.2 -71.4 -41.5 -70.5 0.95 23 220 220 63.2 53.0 62.0 70 70 -28.2 -77.5 -28.5 -76.5 1.04 24 230 53.0 63.2 52.0 80 80 -14.3 -81.2 -15.0 -80.0 1.39 25 240 240 41.2 71.4 40.5 90 90 0.0 -82.5 -0.5 -81.5 1.12 26 250 250 28.2 77.5 27.5 100 100 14.3 -81.2 1.35 -80.0 1.44 27 260 260 14.3 81.2 1.35 110 110 28.2 -77.5 26.5 1.66 290 290 290 290 290 290 290 <th>S</th> <th>40</th> <th>40</th> <th>-63.2</th> <th>-53.0</th> <th>-63.5</th> <th>-52.5</th> <th>0.58</th> <th>21</th> <th>200</th> <th>200</th> <th>77.5</th> <th>28.2</th> <th>76.5</th> <th>27.5</th> <th>1.22</th>	S	40	40	-63.2	-53.0	-63.5	-52.5	0.58	21	200	200	77.5	28.2	76.5	27.5	1.22
60 60 41.2 -71.4 -41.5 -70.5 0.95 23 220 220 63.2 53.0 62.0 70 70 -28.2 -77.5 -28.5 -76.5 1.04 24 230 230 53.0 63.2 52.0 80 80 -14.3 -81.2 -15.0 -80.0 1.39 25 240 240 41.2 71.4 40.5 90 90 0.0 -82.5 -0.5 -81.5 1.12 26 250 250 28.2 77.5 27.5 110 110 28.2 -77.5 26.5 1.97 28 270 20 82.5 -0.5 120 120 41.2 -71.4 40.0 -70.5 1.50 28 270 20 82.5 -0.5 130 130 53.0 -63.2 1.65 1.66 30 290 290 28.2 77.5 28.5 140	9	50	50	-53.0	-63.2	-53.5	-62.5	98.0	22	210	210	71.4	41.2	70.0	40.5	1.57
70 70 -28.2 -77.5 -28.5 -76.5 1.04 24 230 230 53.0 63.2 52.0 80 80 -14.3 -81.2 -15.0 -80.0 1.39 25 240 240 41.2 71.4 40.5 90 90 -0.0 -82.5 -0.5 -81.5 1.12 26 250 28.0 77.5 77.5 27.5 110 110 28.2 -77.5 26.5 -76.5 1.97 28 270 20.0 82.5 -0.5 120 120 41.2 -71.4 40.0 -70.5 1.50 28 270 20 82.5 -0.5 130 130 53.0 -63.2 51.5 -62.5 1.66 30 290 280 -14.5 -14.5 140 140 -73.5 1.66 30 290 290 -28.2 77.5 -28.5 140 140 -75.	7	09	09	-41.2	-71.4	-41.5	-70.5	0.95	23	220	220	63.2	53.0	62.0	52.0	1.56
80 80 -14.3 -81.2 -15.0 -80.0 1.39 25 240 240 41.2 71.4 40.5 90 90 0.0 -82.5 -0.5 -81.5 1.12 26 250 250 28.2 77.5 27.5 100 100 14.3 -81.2 13.5 -80.0 1.44 27 260 260 14.3 81.2 13.5 110 110 28.2 -77.5 26.5 1.66 29 280 280 -14.3 81.2 14.5 120 130 53.0 -63.2 51.5 -62.5 1.66 30 290 290 -28.2 77.5 -28.5 140 140 -63.2 1.66 30 290 290 -28.2 77.5 -28.5 140 140 -62.5 1.66 30 290 290 -41.5 71.4 -41.5 150 150 71.4 -41.5	∞	70	70	-28.2	-77.5	-28.5	-76.5	1.04	24	230	230	53.0	63.2	52.0	62.0	1.56
90 90 0.0 -82.5 -0.5 -81.5 1.12 56 250 250 250 27.5 77.5 27.5 100 100 14.3 -81.2 1.35 -80.0 1.44 27 260 260 14.3 81.2 13.5 110 110 28.2 -77.5 26.5 -76.5 1.97 28 270 0.0 82.5 -0.5 120 120 41.2 -71.4 40.0 -70.5 1.50 29 280 280 -14.3 81.2 -14.5 130 130 53.0 -63.2 51.5 -62.5 1.66 30 290 290 -28.2 77.5 -28.5 140 140 63.2 -52.5 1.77 31 300 -41.2 71.4 -41.5 150 150 71.4 -41.5 70.0 -41.0 1.41 32 310 310 -53.0 63.2 -53.0	6	80	80	-14.3	-81.2	-15.0	-80.0	1.39	25	240	240	41.2	71.4	40.5	70.5	1.14
100 100 14.3 -81.2 13.5 -80.0 1.44 27 260 260 14.3 81.2 13.5 110 110 28.2 -77.5 26.5 -76.5 1.97 28 270 270 0.0 82.5 -0.5 120 120 41.2 -71.4 40.0 -70.5 1.50 29 280 280 -14.3 81.2 -14.5 130 53.0 -63.2 51.5 -62.5 1.66 30 290 290 -28.2 77.5 -28.5 140 140 63.2 -52.5 1.77 31 300 300 -41.2 71.4 -41.5 150 150 71.4 -41.2 70.0 -41.0 1.41 32 310 310 -53.0 63.2 -53.0	10	06	06	0.0	-82.5	-0.5	-81.5	1.12	26	250	250	28.2	77.5	27.5	76.5	1.22
110 110 28.2 -77.5 26.5 -76.5 1.97 28 270 270 270 60.0 82.5 -0.5 120 120 41.2 -71.4 40.0 -70.5 1.50 29 280 280 -14.3 81.2 -14.5 130 130 53.0 -63.2 51.5 -62.5 1.66 30 290 290 -28.2 77.5 -28.5 140 140 63.2 -53.0 61.5 -52.5 1.77 31 300 -41.2 71.4 -41.5 150 150 71.4 -41.2 70.0 -41.0 1.41 32 310 310 -53.0 63.2 -53.0	11	100	100	14.3	-81.2	13.5	-80.0	1.44	27	260	260	14.3	81.2	13.5	80.5	1.06
120 120 41.2 -71.4 40.0 -70.5 1.50 29 280 280 280 -14.3 81.2 -14.5 130 130 53.0 -63.2 51.5 -62.5 1.66 30 290 290 -28.2 77.5 -28.5 140 140 63.2 -53.0 61.5 -52.5 1.77 31 300 -41.2 71.4 -41.5 150 150 71.4 -41.2 70.0 -41.0 1.41 32 310 310 -53.0 63.2 -53.0	12	110	110	28.2	-77.5	26.5	-76.5	1.97	28	270	270	0.0	82.5	-0.5	82.0	0.71
130 53.0 -63.2 51.5 -62.5 1.66 30 290 290 -28.2 77.5 -28.5 140 140 63.2 -53.0 61.5 -52.5 1.77 31 300 300 -41.2 71.4 -41.5 150 150 71.4 -41.2 70.0 -41.0 1.41 32 310 310 -53.0 63.2 -53.0	13	120	120	41.2	-71.4	40.0	-70.5	1.50	29	280	280	-14.3	81.2	-14.5	80.5	0.73
140 140 63.2 -53.0 61.5 -52.5 1.77 31 300 300 -41.2 71.4 -41.5 150 150 71.4 -41.2 70.0 -41.0 1.41 32 310 310 -53.0 63.2 -53.0	14	130	130	53.0	-63.2	51.5	-62.5	1.66	30	290	290	-28.2	77.5	-28.5	77.0	0.58
150 150 71.4 -41.2 70.0 -41.0 1.41 32 310 310 -53.0 63.2 -53.0	15	140	140	63.2	-53.0	61.5	-52.5	1.77	31	300	300	-41.2	71.4	-41.5	71.0	0.50
	16	150	150	71.4	-	70.0	-41.0	1.41	32	310	310	-53.0	63.2	-53.0	63.0	0.20

Table 6.6 Test data of trajectory 2

			,												
OZ		n angle	Theoretical	ical	Actual scan	can	Scan	No.	Rotation angle	angle	Theoretical	cal	Actual scan	can	Scan error/mm
	of prisms/(°))/st	scan point/mm	int/mm	point/mm	m	error/mm		of prisms/(°)	(°)/s	scan point/mm	nt/mm	point/mm	n	
	θ_{r1}	θ_{r2}	X_{rp}	Y_{rp}	Xrp	yrp	Δ		θ_{r1}	θ_{r2}	X_{rp}	Y_{rp}	x_{rp}	y_{rp}	Δ
-	0	0	-82.5	0.0	-82.5	0.0	0.00	17	160	-160	77.5	-28.2	75.5	-29.0	2.15
2	10	-10	-81.2	-14.3	-81.0	-14.0	0.36	18	170	-170	81.2	-14.3	80.0	-14.5	1.22
8	20	-20	-77.5	-28.2	-77.5	-27.5	0.70	19	180	-180	82.5	0.0	81.0	0.0	1.50
4	30	-30	-71.4	-41.2	-71.5	-40.5	0.71	20	190	-190	81.2	14.3	79.5	14.0	1.73
S	40	-40	-63.2	-53.0	-63.5	-52.5	0.58	21	200	-200	77.5	28.2	76.5	27.5	1.22
9	50	-50	-53.0	-63.2	-53.5	-62.5	0.86	22	210	-210	71.4	41.2	70.0	40.5	1.57
7	09	09-	-41.2	-71.4	-41.5	-70.5	0.95	23	220	-220	63.2	53.0	62.0	52.0	1.56
∞	70	-70	-28.2	-77.5	-28.5	-76.5	1.04	24	230	-230	53.0	63.2	52.0	62.0	1.56
6	80	-80	-14.3	-81.2	-15.0	-80.0	1.39	25	240	-240	41.2	71.4	40.5	70.5	1.14
10	06	06-	0.0	-82.5	-0.5	-81.5	1.12	26	250	-250	28.2	77.5	27.5	76.5	1.22
1	100	-100	14.3	-81.2	13.5	-80.0	1.44	27	260	-260	14.3	81.2	13.5	80.5	1.06
12	110	-110	28.2	-77.5	26.5	-76.5	1.97	28	270	-270	0.0	82.5	-0.5	82.0	0.71
13	120	-120	41.2	-71.4	40.0	-70.5	1.50	29	280	-280	-14.3	81.2	-14.5	80.5	0.73
14	130	-130	53.0	-63.2	51.5	-62.5	1.66	30	290	-290	-28.2	77.5	-28.5	77.0	0.58
15	140	-140	63.2	-53.0	61.5	-52.5	1.77	31	300	-300	-41.2	71.4	-41.5	71.0	0.50
16	150	-150	71.4	-41.2	70.0	-41.0	1.41	32	310	-310	-53.0	63.2	-53.0	63.0	0.20

3
α
\geq
\Box
0
÷
ွှ
<u>.e</u> .
<u>.e</u> .
Ħ
+
ų.
0
~
ţ
Б
d
ū
\mathbf{z}
a)
H
_
r-
ė
$\overline{}$
e
≂
은
_00

Z	Rotation angle	anole	Theoretical	ical	Actual scan	can	Scan	N	Rotation angle	anole	Theoretical	cal	Actual scan	can	Scan error/mm
	of prisms/(°)	(°)/sr	scan point/mm	int/mm	point/mm	ц	error/mm		of prisms/(°)	(°)/sı	scan point/mm	nt/mm	point/mm	g	
	θ_{r1}	θ_{r2}	X_{rp}	Y_{rp}	χ_{rp}	Уrр	4		θ_{r1}	θ_{r2}	X_{rp}	Y_{rp}	Xrp	Угр	\\\\\\\\\\\\\\\\\\\\\\\\\\\\\\\\\\\\\\
_	0	0	-82.5	0.0	-82.5	0.0	0.00	17	160	320	13.2	8.8	12.0	8.5	1.24
2	10	20	-79.5	-20.6	-79.5	-20.0	09.0	18	170	340	8.7	5.1	7.5	4.5	1.34
ω	20	40	-71.0	-39.5	-71.0	-38.5	1.00	19	180	360	7.1	0.0	0.9	-0.5	1.21
4	30	09	-57.7	-54.9	-58.5	-54.0	1.20	20	190	380	8.7	-5.1	7.5	-5.5	1.26
S	40	80	-41.0	-65.8	-41.5	-65.0	0.94	21	200	400	13.2	-8.8	12.0	-9.5	1.39
9	50	100	-22.4	-71.3	-23.5	-70.5	1.36	22	210	420	19.9	-10.1	19.0	-10.5	0.98
7	09	120	-3.8	-71.3	-5.0	-70.5	1.44	23	220	440	7.72	-8.2	26.5	-8.5	1.24
∞	70	140	13.3	-66.2	11.5	-65.5	1.93	24	230	460	35.2	-2.7	34.0	-3.0	1.24
6	80	160	27.4	-57.0	25.5	-56.5	1.96	25	240	480	41.0	6.3	40.0	0.9	1.04
10	06	180	37.4	-44.8	35.5	-44.5	1.92	26	250	500	44.0	18.0	43.0	17.5	1.12
11	100	200	42.9	-31.3	41.0	-31.5	1.91	27	260	520	42.9	31.3	42.0	30.5	1.20
12	110	220	0.44	-18.0	42.0	-18.5	2.06	28	270	540	37.4	44.8	36.5	44.0	1.20
13	120	240	41.0	-6.3	39.5	-6.5	1.51	29	280	995	27.4	57.0	26.5	56.5	1.03
14	130	260	35.2	2.7	34.0	2.5	1.22	30	290	580	13.3	66.2	13.0	65.5	0.76
15	140	280	27.7	8.2	26.0	7.5	1.84	31	300	009	-3.8	71.3	-4.0	71.5	0.28
16	150	300	19.9	10.1	19.0	9.5	1.08	32	310	620	-22.4	71.3	-22.5	71.0	0.32

Table 6.8 Test data of trajectory 4

No.	No. Rotation angle of prisms/(°)	n angle is/(°)	Theoretical scan point/mm	ical nt/mm	Actual scan point/mm	can	Scan error/mm	No.	Rotation angle of prisms/(°)	n angle Is/(°)	Theoretical scan point/mm	cal nt/mm	Actual scan point/mm	can	Scan error/mm
	θ_{r1}	θ_{r2}	X_{rp}	Y_{rp}	χ_{rp}	Уrр	4		θ_{r1}	θ_{r2}	X_{rp}	Y_{rp}	χ_{rp}	Уrр	\\ \dag{\dagger}
-	0	0	-82.5	0.0	-82.5	0.0	0.00	17	160	-320	13.3	-39.3	12.0	-39.5	1.32
2	10	-20	-79.5	5.0	-80.0	5.5	0.71	18	170	-340	8.7	-20.5	8.0	-21.0	0.86
8	20	-40	-70.9	8.7	-71.0	0.6	0.32	19	180	-360	7.1	0.0	0.9	-0.5	1.21
4	30	09-	-57.5	10.0	-57.5	10.0	0.00	20	190	-380	8.7	20.5	7.5	20.0	1.30
S	40	-80	-40.7	8.1	-41.5	8.5	0.89	21	200	-400	13.3	39.3	12.0	38.5	1.53
9	50	-100	-22.2	2.7	-23.0	3.0	0.85	22	210	-420	20.1	54.8	19.0	54.0	1.36
7	09	-120	-3.6	-6.2	-5.0	-5.5	1.57	23	220	-440	27.9	65.7	26.5	65.0	1.57
∞	70	-140	13.4	-17.8	12.0	-17.5	1.43	24	230	-460	35.5	71.3	34.0	71.0	1.53
6	80	-160	27.4	-31.2	25.5	-30.5	2.02	25	240	-480	41.2	71.4	40.0	71.0	1.26
10	06	-180	37.4	-44.8	35.5	-44.0	2.06	26	250	-500	44.1	66.4	43.0	0.99	1.17
11	100	-200	43.0	-57.1	41.0	-56.5	2.09	27	260	-520	43.0	57.1	42.0	57.0	1.00
12	110	-220	44.1	-66.4	43.0	-65.5	1.42	28	270	-540	37.4	44.8	36.0	44.5	1.43
13	120	-240	41.2	-71.4	40.0	-71.0	1.26	29	280	-560	27.4	31.2	26.5	31.5	0.95
14	130	-260	35.5	-71.3	34.5	-71.0	1.04	30	290	-580	13.4	17.8	13.0	18.0	0.45
15	140	-280	27.9	-65.7	27.0	-65.5	0.92	31	300	009-	-3.6	6.2	-4.0	0.9	0.45
16	150	-300	20.1	-54.8	19.0	-55.0	1.12	32	310	-620	-22.2	-2.7	-22.0	-3.0	0.36

and 6.12 and Tables 6.7 and 6.8, indicate that the actual and the theoretical scan trajectory are well matched and the average scan errors are 1.13 mm and 1.02 mm, respectively.

The above four scan trajectory tests indicate that the actual and the theoretical scan trajectories are almost coincident, which verifies the theoretical model of rotating double-prism system and the feasibility of multi-mode scanning. Because of insufficient test conditions such as the measurement accuracy of the laser spot and the errors introduced by part manufacturing and device assembly, the measured scan error is too large to fully exemplify the high-precision scan characteristic of rotating double prisms. Thus the experiment needs further improvement.

6.2.4 Lookup-Table Method Validation

In this section, the lookup-table method is validated by measuring the tracking precision of the laser beam directed by the prism orientations reversely solved with lookup-table method. As shown in Fig. 6.13, the test platform mainly includes rotating double-prism device and its motion controller, two-dimensional slipway and its motion controller, laser, guide rail and slider. Detailed descriptions of the used components are listed in Table 6.9.

Main steps of the lookup-table method validation test are as follows:

(1) Device installation. Firstly mount the laser on the guide rail while keep the laser beam parallel to the guide rail. The two-dimensional slipway, with a four-quadrant probe fixed on the *X*-axis slider, is then placed at the end of the rail and adjusted to enable its *XOY* plane perpendicular to the optical axis of the double prisms. Finally, move two prisms in the axial direction to the position where the

Fig. 6.9 Actual and theoretical points on scan trajectory 1

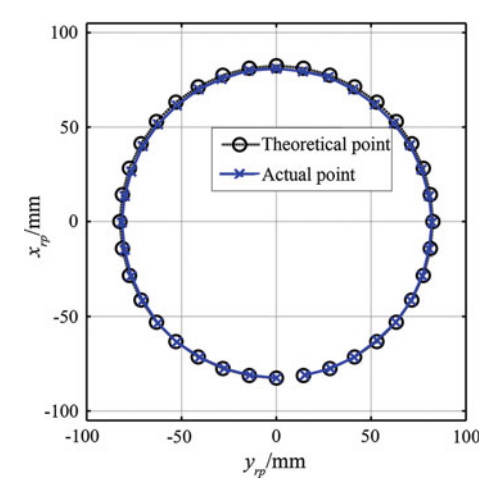


Fig. 6.10 Actual and theoretical points on scan trajectory 2

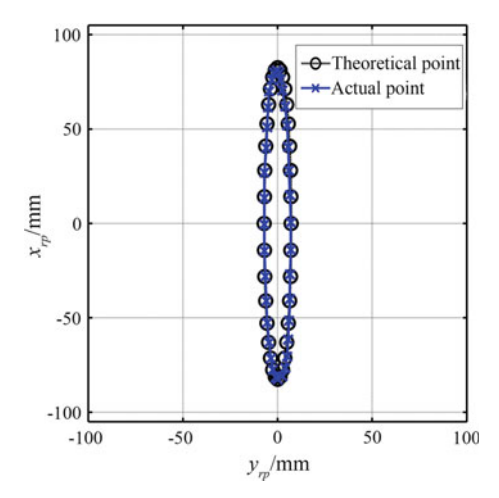
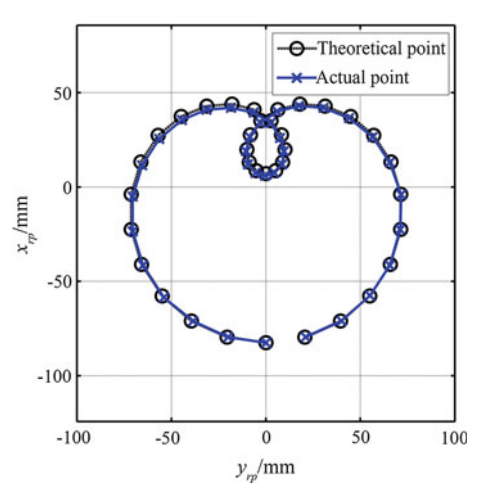


Fig. 6.11 Actual and theoretical points on scan trajectory 3



distance between the emergent surface of prism 2 and the four-quadrant probe is $D_2 = 400$ mm, and the separation between two plane facets of the prisms is $D_1 = 100$ mm.

- (2) Set the two-dimensional slipway system to manual mode. Adjust the four-quadrant detector in the radial direction until the optical axis is aligned with the detector center, namely the coordinate origin of the target trajectory plane.
- (3) Set the rotating double-prism system to manual mode. Rotate the prisms at low speeds and set the prism origin at the position where the thinnest end is strictly upward.
- (4) A lookup table with the step of 0.1° is established to reversely calculate the rotation angles of the double prisms according to the coordinates of the sampling points on the target trajectory. Then the coordinates and the rotation angles are

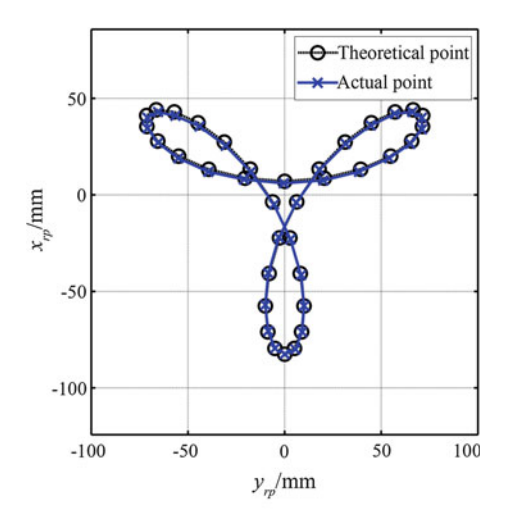


Fig. 6.12 Actual and theoretical points on scan trajectory 4

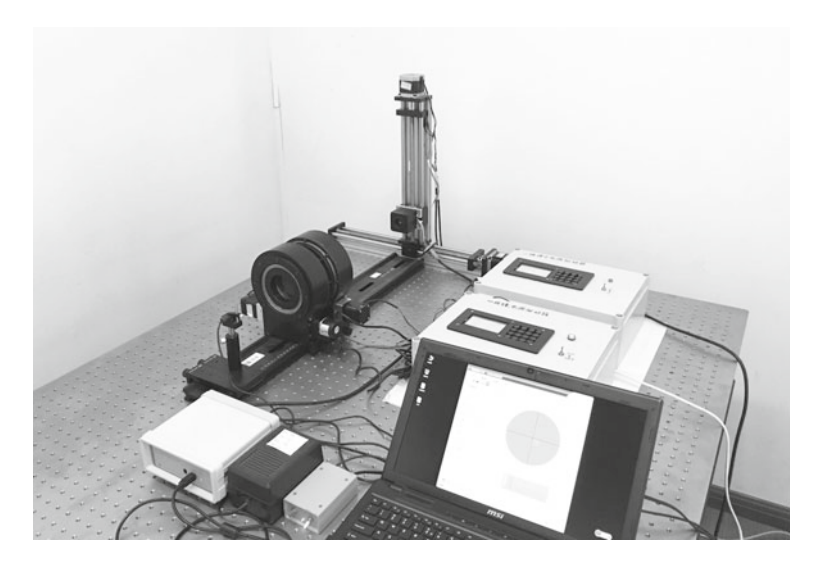


Fig. 6.13 Experimental platform for validating the lookup-table method

- written into the two-dimensional slipway control system and the double-prism control system separately.
- (5) Set two control systems to single-step mode. According to the pre-written coordinates and rotation angles, move the four-quadrant detector to the given sampling point and rotate the double prisms to the corresponding orientations. Then the deviation from the laser spot to the detector origin can be measured by the

test platform		
Device	Parameter	Function
Rotating double prisms	Wedge angle: $\alpha = 10^{\circ}$ Refractive index: $n = 1.517$ Diameter: $D = 80$ mm Thinnest-end thickness: $d_0 = 5$ mm Distance between two prisms: $D_1 = 100$ mm	Deflect laser beam
Two-dimensional slipway	Effective stroke of X axis: 300 mm Effective stroke of Y axis: 400 mm Lead of the ball screw: 4 mm Round trip accuracy of the ball screw: 0.02 mm	Install the four-quadrant detector Simulate the target motion trajectory
Motion controller	MCU: LPC1114	Motion control of double prisms Motion control of two-dimensional slipway
Laser	Wavelength: 650 nm Power: $P \ge 2.5$ mW Focus: variable focus	Emit collimated laser beam
Four-quadrant detector	Laser spot positioning accuracy: superior to 0.01 mm Measuring range: ϕ 3 mm Distance from the emergent surface of prism 2: $D_2 = 400$ mm	Detect the laser spot and measure its deviation from the slider origin
Guide rail and slider	Stroke of the guide rail: 1000 mm	Support components

Table 6.9 Parameters and functions of the components used in the lookup-table method validation test platform

detector itself. Record the deviation and repeat the measurement process until all the sampling points are measured.

To validate the lookup-table method and evaluate its precision, the control systems of both the two-dimensional slipway and the double prisms are considered ideal, without the errors introduced by mechanical system or control algorithm. Under the above hypothetical conditions, the precision of the lookup-table method can be evaluated by the deviations from the detector origin to the actual scan spots of laser beam at the prism orientations reversely solved with lookup-table method. In this particular test, an ellipse expressed by $x^2/40^2 + y^2/60^2 = 1$ is chosen as the target trajectory, and the reading of the detector is accurate to 0.001 mm with the last place estimated.

The coordinates of 64 sampling points on the ellipse target trajectory shown in Fig. 6.14 are put into the lookup-table method to reversely calculate the corresponding rotation angles. Then the coordinates of sampling points and two sets of prism rotation angles, as shown in Fig. 6.15a and b respectively, are utilized for motion control of the two-dimensional slipway and double prisms. The measured deviations corresponding to two sets of rotation angles are listed in Tables 6.10 and 6.11, respectively. It is

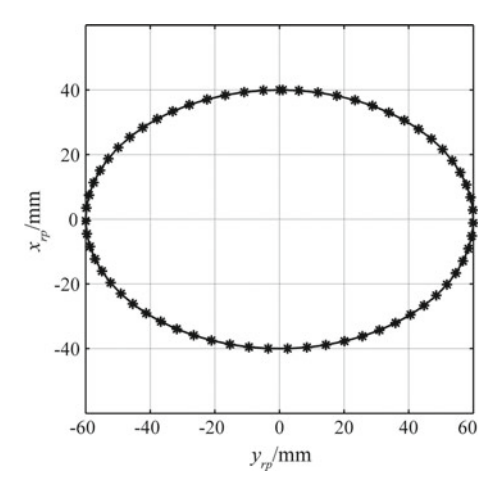


Fig. 6.14 Ellipse target trajectory and sampling points

easy to figure out that the average deviation of the first set is 0.342 mm, and that of the second set is 0.233 mm.

The test results show that, the actual beam scan trajectory directed by the prism orientations reversely solved with lookup-table method is almost coincident with the given target trajectory, which well verifies the lookup-table method. Specifically, the maximal deviation between the actual scan point and the target point is as low as 0.046 mm when the step angle of lookup table is 0.1°. In the actual test, the deviation is generally larger than the theoretical calculation. It should be noted that this phenomenon do not result from the solving precision of the lookup-table method itself, but the comprehensive influence of various system errors, such as parameter error of the prisms (wedge angle, refractive index, etc.), machining error of the mechanical parts, assembly error and so on.

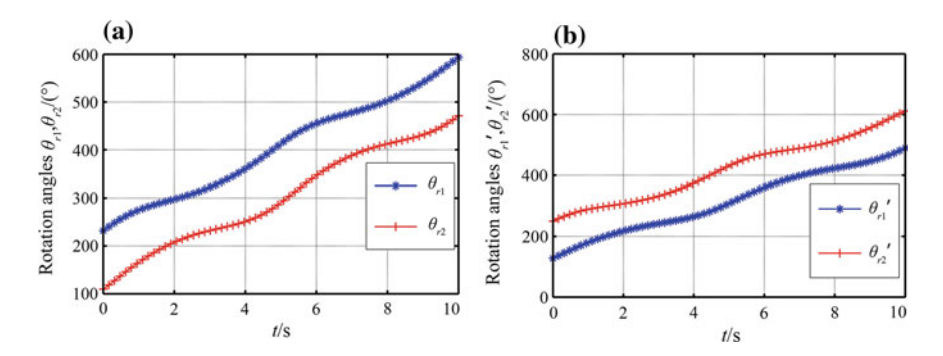


Fig. 6.15 Rotation angles of double prisms corresponding to the ellipse target trajectory where **a** is the first set and **b** is the second set

Table 6.10 Tracking data of the ellipse target trajectory solved by lookup table (first set)

Z	Taroet noint/r	nt/mm	Rotation anole of	ation anole of	Deviation/mm	N	Taroet noint/mm	t/mm	Rotation angle of	ole of	Deviation/mm
			prisms/(°)	10 21 3 11			magna l		prisms/(°)	5 2.4	
	X_{rp}	$ Y_{rp} $	θ_{r1}	θ_{r2}	Δ		X_{rp}	Y_{rp}	θ_{r1}	θ_{r2}	Δ
	40.0	0.0	233.1	111.0	0.322	33	-39.9	-3.5	418.0	296.1	0.375
2	39.8	0.9	241.5	119.9	0.316	34	-39.5	-9.5	426.2	305.2	0.368
æ	39.2	11.9	249.4	129.0	0.333	35	-38.7	-15.3	433.8	314.4	0.384
4	38.2	17.7	256.7	138.2	0.336	36	-37.5	-21.0	440.7	323.5	0.390
S	36.8	23.4	263.3	147.2	0.323	37	-35.9	-26.6	446.8	332.4	0.391
9	35.1	28.8	269.2	156.1	0.328	38	-33.9	-31.8	452.3	341.0	0.395
7	33.0	33.9	274.3	164.5	0.354	39	-31.6	-36.7	457.0	349.2	0.388
∞	30.6	38.7	278.9	172.5	0.350	40	-29.0	-41.3	461.3	357.0	0.386
6	27.9	43.0	282.9	180.0	0.318	41	-26.1	-45.4	465.0	364.2	0.385
10	24.9	47.0	286.5	187.1	0.305	42	-23.0	-49.1	468.5	371.0	0.389
11	21.6	50.5	289.9	193.7	0.366	43	-19.6	-52.3	471.8	377.4	0.391
12	18.1	53.5	293.1	199.9	0.317	4	-16.0	-55.0	474.9	383.3	0.387
13	14.5	55.9	296.2	205.6	0.320	45	-12.3	-57.1	478.1	388.7	0.391
14	10.7	57.8	299.4	210.8	0.313	46	-8.4	-58.7	481.3	393.6	0.381
15	8.9	59.1	302.7	215.6	0.308	47	-4.5	-59.6	484.7	398.1	0.376
16	2.8	59.8	306.2	219.9	0.310	48	-0.5	0.09-	488.4	402.2	0.378
17	-1.2	0.09	310.0	223.8	0.309	49	3.5	-59.8	492.3	405.9	0.373

(bossessing)

$\overline{}$
T
\bar{g}
⋾
=
.=
Ξ.
Ξ
8
ပ
$\overline{}$
_
_
_ _
91:
6.10
6.10
e 6.10
le 6.1
le 6.1
le 6.1
Table 6.10

s/(°) (°)							
X_{rp} Y_{rp} θ_{r1} -5.2 59.5 314.0 -9.1 58.4 318.4 -12.9 56.8 323.2 -16.6 54.6 328.3 -20.2 51.8 33.8 -20.2 51.8 33.8 -23.5 48.5 339.7 -26.7 44.7 346.0 -20.7 44.7 346.0 -32.0 35.9 359.8 -34.3 30.9 367.3 -34.3 30.9 367.3 -36.2 25.6 375.0 -38.8 14.4 392.0 -39.6 8.5 400.7	Rotation angle of prisms/(°)	Deviation/mm No.	Target point/mm	/mm	Rotation angle of prisms/(°)	ngle of	Deviation/mm
-5.2 59.5 314.0 -9.1 58.4 318.4 -12.9 56.8 323.2 -16.6 54.6 328.3 -20.2 51.8 333.8 -23.5 48.5 339.7 -26.7 44.7 346.0 -26.7 44.7 346.0 -32.0 35.9 359.8 -34.3 30.9 367.3 -36.2 25.6 375.2 -36.2 25.6 375.2 -38.8 14.4 392.0 -39.6 85 400.7	θ_{r1}		X_{rp}	Y_{rp}	θ_{r1}	θ_{r2}	∇
-9.1 58.4 318.4 -12.9 56.8 323.2 -16.6 54.6 328.3 -20.2 51.8 333.8 -23.5 48.5 339.7 -26.7 44.7 346.0 -29.5 40.5 352.7 -32.0 35.9 359.8 -34.3 30.9 367.3 -36.2 25.6 375.2 -37.7 20.1 383.4 -38.8 14.4 392.0 -39.6 85 400.7	314.0	8 50	7.5	-58.9	496.6	409.2	0.366
-12.9 56.8 323.2 -16.6 54.6 328.3 -20.2 51.8 33.8 -23.5 48.5 339.7 -26.7 44.7 346.0 -29.5 40.5 352.7 -32.0 35.9 359.8 -34.3 30.9 367.3 -36.2 25.6 375.2 -36.2 25.6 375.2 -38.8 14.4 392.0 -39.6 8.5 400.7	318.4	7 51	11.3	-57.5	501.2	412.3	0.389
-16.6 54.6 328.3 -20.2 51.8 333.8 -23.5 48.5 339.7 -26.7 44.7 346.0 -29.5 40.5 352.7 -32.0 35.9 359.8 -34.3 30.9 367.3 -36.2 25.6 375.2 -36.2 25.6 375.2 -37.7 20.1 383.4 -38.8 14.4 392.0 -39.6 8.5 400.7	323.2	8 52	15.1	-55.5	506.1	415.1	0.369
-20.2 51.8 333.8 -23.5 48.5 339.7 -26.7 44.7 346.0 -29.5 40.5 352.7 -32.0 35.9 359.8 -34.3 30.9 367.3 -34.3 30.9 367.3 -36.2 25.6 375.2 -37.7 20.1 383.4 -38.8 14.4 392.0 -39.6 8.5 400.7	328.3	6 53	18.7	-53.0	511.5	417.8	0.375
-23.5 48.5 339.7 -26.7 44.7 346.0 -29.5 40.5 352.7 -32.0 35.9 359.8 -34.3 30.9 367.3 -36.2 25.6 375.2 -37.7 20.1 383.4 -38.8 14.4 392.0 -39.6 85 400.7	333.8	2 54	22.2	-49.9	517.2	420.5	0.391
-26.7 44.7 346.0 -29.5 40.5 352.7 -32.0 35.9 359.8 -34.3 30.9 367.3 -36.2 25.6 375.2 -37.7 20.1 383.4 -38.8 14.4 392.0 -39.6 85 400.7	339.7	5 55	25.4	-46.4	523.3	423.4	0.472
-29.5 40.5 352.7 -32.0 35.9 359.8 -34.3 30.9 367.3 -36.2 25.6 375.2 -37.7 20.1 383.4 -38.8 14.4 392.0 -39.6 8.5 400.7	346.0	0 56	28.3	-42.3	529.9	426.4	0.498
-32.0 35.9 359.8 -34.3 30.9 367.3 -36.2 25.6 375.2 -37.7 20.1 383.4 -38.8 14.4 392.0 -39.6 8.5 400.7	352.7	4 57	31.0	-37.9	536.8	429.8	0.493
-34.3 30.9 367.3 -36.2 25.6 375.2 -37.7 20.1 383.4 -38.8 14.4 392.0 -39.6 8.5 400.7	359.8	1 58	33.4	-33.0	544.1	433.7	0.535
-36.2 25.6 375.2 -37.7 20.1 383.4 -38.8 14.4 392.0 -39.6 85 400.7	367.3	7 59	35.4	-27.9	551.8	438.2	0.542
-37.7 20.1 383.4 -38.8 14.4 392.0 -39.6 8.5 400.7	375.2	09 9	37.1	-22.4	559.9	443.4	0.545
-38.8 14.4 392.0 -39.6 8.5 400.7	1 383.4	1 61	38.4	-16.8	568.4	449.5	0.554
8.5 400.7	392.0	4 62	39.3	-10.9	577.1	456.4	0.539
	5 400.7 279.5 0.147	7 63	39.9	-5.0	585.9	464.1	0.550
32 -40.0 2.5 409.5 287.5	409.5	8 64	40.0	1.0	594.5	472.5	0.540

Table 6.11 Tracking data of the ellipse target trajectory solved by lookup table (second set)

140000	manus anna	מנת כז מוכ כ	mpse meer	rance of the	the course of th	os puosse) e	•				
No.	Target point/mm	nt/mm	Rotation angle of prisms/(°)	ngle of	Deviation/mm	No.	Target point/mm	ıt/mm	Rotation angle of prisms/(°)	igle of	Deviation/mm
	X_{rp}	Y_{rp}	θ'_{r1}	θ_{r2}'	Δ'		X_{rp}	Y_{rp}	θ' _{r1}	9,2	Δ'
-	40.0	0.0	127.9	250.4	0.308	33	-39.9	-3.5	313.0	435.3	0.040
2	39.8	0.9	136.6	258.7	0.305	34	-39.5	-9.5	321.7	443.2	0.039
3	39.2	11.9	145.3	266.2	0.300	35	-38.7	-15.3	330.4	450.3	0.036
4	38.2	17.7	153.9	272.9	0.312	36	-37.5	-21.0	338.9	456.5	0.041
S	36.8	23.4	162.3	278.8	0.293	37	-35.9	-26.6	347.0	461.8	0.046
9	35.1	28.8	170.3	283.9	0.302	38	-33.9	-31.8	354.8	466.5	0.324
7	33.0	33.9	177.9	288.2	0.311	39	-31.6	-36.7	362.1	470.4	0.045
~	30.6	38.7	185.1	291.9	0.300	40	-29.0	-41.3	369.1	473.9	0.040
6	27.9	43.0	191.9	295.2	0.306	41	-26.1	-45.4	375.6	476.9	0.043
10	24.9	47.0	198.2	298.1	0.302	42	-23.0	-49.1	381.8	479.8	0.033
11	21.6	50.5	204.3	300.9	0.309	43	-19.6	-52.3	387.6	482.5	0.030
12	18.1	53.5	209.9	303.6	0.312	4	-16.0	-55.0	393.0	485.2	0.308
13	14.5	55.9	215.1	306.3	0.307	45	-12.3	-57.1	398.0	488.0	0.039
14	10.7	57.8	220.0	309.2	0.309	46	-8.4	-58.7	402.7	490.9	0.305
15	8.9	59.1	224.5	312.3	0.308	47	-4.5	-59.6	407.0	494.2	0.256
16	2.8	59.8	228.7	315.6	0.309	48	-0.5	-60.0	411.0	8.764	0.244
17	-1.2	0.09	232.6	319.4	0.300	49	3.5	-59.8	414.8	501.7	0.242
											(F)

(continued)

_	
\sim	
• ┌─ ₹	
=	
0	
8	
_	
_	
Ξ	
Ξ	
<u>.</u>	
.11.	
6.11	
6.11	
6.11	
e 6.11	
e 6.11	
le 6.11	
ē	
ble 6.11	
ē	
ē	
able	
ē	

Target point/mm Rotation angle of prisms/(°) X_{rp} Y_{rp} θ'_{r1} θ'_{r2} -5.2 59.5 236.2 323.5 -9.1 58.4 239.6 328.1 -12.9 56.8 242.9 338.1 -12.9 56.8 242.9 338.1 -12.9 56.8 242.9 338.1 -20.2 51.8 249.2 344.6 -20.2 51.8 249.2 344.6 -20.2 51.8 249.2 344.6 -20.7 44.7 256.1 358.0 -20.7 44.7 256.1 358.0 -20.7 44.7 256.1 358.0 -20.7 44.7 256.1 358.0 -30.0 35.9 269.3 381.6 -34.3 30.9 269.3 381.6 -36.2 25.6 275.0 390.3 -36.2 25.6 275.0 390.3 -39.6 8.5	Table 6.11	Table 6.11 (continued)	1)									
X_{rp} Y_{rp} θ'_{r1} θ'_{r2} -5.2 59.5 236.2 323.5 -9.1 58.4 239.6 323.5 -12.9 56.8 242.9 333.1 -16.6 54.6 246.0 338.6 -20.2 51.8 249.2 344.6 -20.2 51.8 249.2 344.6 -23.5 48.5 252.6 351.1 -26.7 44.7 256.1 358.0 -20.7 44.7 256.1 358.0 -20.7 40.5 260.0 365.4 -32.0 35.9 264.4 373.3 -34.3 30.9 269.3 381.6 -34.3 30.9 269.3 381.6 -34.7 20.1 281.3 399.3 -39.6 8.5 296.1 417.8 -40.0 25 304.4 426.8	No.	Target poi	int/mm	Rotation a prisms/(°)	ngle of	Deviation/mm	No.	Target point/mm	nt/mm	Rotation angle of prisms/(°)	ngle of	Deviation/mm
-5.2 59.5 236.2 323.5 -9.1 58.4 239.6 328.1 -12.9 56.8 242.9 333.1 -16.6 54.6 246.0 338.6 -20.2 51.8 249.2 344.6 -23.5 48.5 252.6 351.1 -23.5 48.5 252.6 351.1 -26.7 44.7 256.1 358.0 -29.5 40.5 260.0 365.4 -32.0 35.9 264.4 373.3 -34.3 30.9 269.3 381.6 -34.3 30.9 269.3 381.6 -36.2 25.6 275.0 390.3 -37.7 20.1 281.3 399.3 -39.6 8.5 296.1 417.8 -40.0 25 304.4 426.8		X_{rp}	Y_{rp}	θ'_{r1}	θ'_{r2}	Δ'		X_{rp}	Y_{rp}	θ'_{r1}	θ'_{r2}	Δ'
-9.1 58.4 239.6 328.1 -12.9 56.8 242.9 333.1 -16.6 54.6 246.0 338.6 -20.2 51.8 249.2 344.6 -23.5 48.5 252.6 351.1 -26.7 44.7 256.1 358.0 -26.7 44.7 256.1 358.0 -29.5 40.5 260.0 365.4 -32.0 35.9 264.4 373.3 -34.3 30.9 269.3 381.6 -36.2 25.6 275.0 390.3 -37.7 20.1 281.3 399.3 -38.8 14.4 288.4 408.6 -39.6 8.5 296.1 417.8 -40.0 25 304.4 426.8	18	-5.2	59.5	236.2	323.5	0.306	50	7.5	-58.9	418.2	506.1	0.276
-12.9 56.8 242.9 333.1 -16.6 54.6 246.0 338.6 -20.2 51.8 249.2 344.6 -23.5 48.5 252.6 351.1 -26.7 44.7 256.1 358.0 -26.7 44.7 256.1 358.0 -29.5 40.5 260.0 365.4 -32.0 35.9 264.4 373.3 -34.3 30.9 269.3 381.6 -36.2 25.6 275.0 390.3 -36.2 25.6 275.0 390.3 -38.8 14.4 288.4 408.6 -39.6 8.5 296.1 417.8	19	-9.1	58.4	239.6	328.1	0.309	51	11.3	-57.5	421.5	511.0	0.284
-16.6 54.6 246.0 338.6 -20.2 51.8 249.2 344.6 -23.5 48.5 252.6 351.1 -26.7 44.7 256.1 358.0 -29.5 40.5 260.0 365.4 -32.0 35.9 264.4 373.3 -34.3 30.9 269.3 381.6 -34.3 30.9 269.3 381.6 -36.2 25.6 275.0 390.3 -37.7 20.1 281.3 399.3 -38.8 14.4 288.4 408.6 -40.0 25 304.4 476.8	20	-12.9	56.8	242.9	333.1	0.312	52	15.1	-55.5	424.7	516.3	0.289
-20.2 51.8 249.2 344.6 -23.5 48.5 252.6 351.1 -26.7 44.7 256.1 358.0 -29.5 40.5 260.0 365.4 -32.0 35.9 264.4 373.3 -34.3 30.9 269.3 381.6 -34.3 30.9 269.3 381.6 -36.2 25.6 275.0 390.3 -37.7 20.1 281.3 399.3 -38.8 14.4 288.4 408.6 -39.6 8.5 296.1 417.8 -40.0 2 304.4 426.8	21	-16.6	54.6	246.0	338.6	0.310	53	18.7	-53.0	427.9	522.1	0.287
-23.5 48.5 252.6 351.1 -26.7 44.7 256.1 358.0 -29.5 40.5 260.0 365.4 -32.0 35.9 264.4 373.3 -34.3 30.9 269.3 381.6 -36.2 25.6 275.0 390.3 -37.7 20.1 281.3 399.3 -38.8 14.4 288.4 408.6 -39.6 8.5 296.1 417.8 -40.0 25 304.4 426.8	22	-20.2	51.8	249.2	344.6	0.326	54	22.2	-49.9	431.2	528.3	0.296
-26.7 44.7 256.1 358.0 -29.5 40.5 260.0 365.4 -32.0 35.9 264.4 373.3 -34.3 30.9 269.3 381.6 -36.2 25.6 275.0 390.3 -37.7 20.1 281.3 399.3 -38.8 14.4 288.4 408.6 -39.6 8.5 296.1 417.8 -40.0 25 304.4 426.8	23	-23.5	48.5	252.6	351.1	0.352	55	25.4	-46.4	434.6	535.1	0.304
-29.5 40.5 260.0 365.4 -32.0 35.9 264.4 373.3 -34.3 30.9 269.3 381.6 -36.2 25.6 275.0 390.3 -37.7 20.1 281.3 399.3 -38.8 14.4 288.4 408.6 -39.6 8.5 296.1 417.8 -40.0 25 304.4 426.8	24	-26.7	44.7	256.1	358.0	0.351	99	28.3	-42.3	438.4	542.3	0.305
-32.0 35.9 264.4 373.3 -34.3 30.9 269.3 381.6 -36.2 25.6 275.0 390.3 -37.7 20.1 281.3 399.3 -38.8 14.4 288.4 408.6 -39.6 8.5 296.1 417.8 -40.0 25 304.4 426.8	25	-29.5	40.5	260.0	365.4	0.343	57	31.0	-37.9	442.5	550.0	0.298
-34.3 30.9 269.3 381.6 -36.2 25.6 275.0 390.3 -37.7 20.1 281.3 399.3 -38.8 14.4 288.4 408.6 -39.6 8.5 296.1 417.8 -40.0 2 304.4 426.8	26	-32.0	35.9	264.4	373.3	0.048	58	33.4	-33.0	447.2	558.1	0.286
-36.2 25.6 275.0 390.3 -37.7 20.1 281.3 399.3 -38.8 14.4 288.4 408.6 -39.6 8.5 296.1 417.8 -40.0 25 304.4 426.8	27	-34.3	30.9	269.3	381.6	0.045	59	35.4	-27.9	452.5	9.995	0.298
-37.7 20.1 281.3 399.3 -38.8 14.4 288.4 408.6 -39.6 8.5 296.1 417.8 -40.0 25 304.4 426.8	28	-36.2	25.6	275.0	390.3	0.047	09	37.1	-22.4	458.6	575.6	0.303
-38.8 14.4 288.4 408.6 -39.6 8.5 296.1 417.8 -40.0 25 304.4 426.8	29	-37.7	20.1	281.3	399.3	0.043	61	38.4	-16.8	465.3	584.7	0.288
-39.6 8.5 296.1 417.8 -40.0 25 304.4 426.8	30	-38.8	14.4	288.4	408.6	0.325	62	39.3	-10.9	472.8	593.9	0.301
25 304 4 4268	31	-39.6	8.5	296.1	417.8	0.043	63	39.9	-5.0	480.9	603.1	0.286
	32	-40.0	2.5	304.4	426.8	0.045	64	40.0	1.0	489.3	611.8	0.306

6.3 Performance Test on Tilting Double Prisms

To test the performance of tilting double prisms, namely tilting accuracy, reduction ratio, beam deflection range and beam deflection accuracy, static testing methods based on autocollimator and interferometer are employed in a temperature-controlled laboratory.

6.3.1 Test on Tilting Accuracy, Reduction Ratio and Beam Deflection Range

In the section, three technical indicators of tilting double prisms are tested with autocollimation method, including (1) prism tilting accuracy, which is shown as the relation between the tilting angle of the prism measured by high-precision collimator and that read from the encoder; (2) reduction ratio, namely the ratio of the prism tilting angle with respect to the consequent beam deflection angle; and (3) beam deflection range, which is specified by the vertical scan range and the horizontal scan range of the emergent beam.

The test equipment consists of two identical high-precision autocollimator, high-precision collimator, tilting double-prism system, multi-dimensional adjusting mount, level platform, air bearing worktable, bracket and so on. The parameters of the autocollimator are as follows: the focal length is 1000 mm, the effective aperture is φ 100 mm, the scale value is 10" (48.48 μ rad), the field of view is 58' (the resolution is 1.3" and the full field of view is 1°38') and the outline dimensions $l \times d$ are 1160 mm $\times \varphi$ 150 mm. The parameters of two identical prisms are as follows: the wedge angle is 5°, the refractive index is 1.517 and the tilting angle range is 0°–5°.

As shown in Fig. 6.16, two autocollimators and the collimator are fixed on the level platform without vibration and shocks, respectively for emitting and receiving laser beam. Two stepping motors are controlled to dynamically adjust the tilting angles of the horizontal prism and the vertical prism (hereinafter referred to as prism 1 and prism 2). Alongside the prisms, the horizontal axis encoder and the vertical axis encoder (hereinafter referred to as encoder 1 and encoder 2) acquire the tilting angles of two prisms in real time. Synchronously, the collimator measures the angle of the beam reflected by the plane facet of each prism, and the autocollimilator measures the deflection angle of the beam emergent from the plane facet of each prism. By comparing the encoder readings and the beam reflection or deflection angles, the above three indicators can be obtained. According to the above experimental platform, the test methods are summarized as follows.

(1) Tilting accuracy can be obtained by comparing the tilting angle of the rotation axis and the beam reflection angle on the plane facet of each prism, which can be measured by the encoder and the collimator, respectively. Taking the tilting accuracy of prism 1 for example, the laser beam emitted from autocollimator 1 is reflected by prism 1 and finally received by the collimator. The collimator

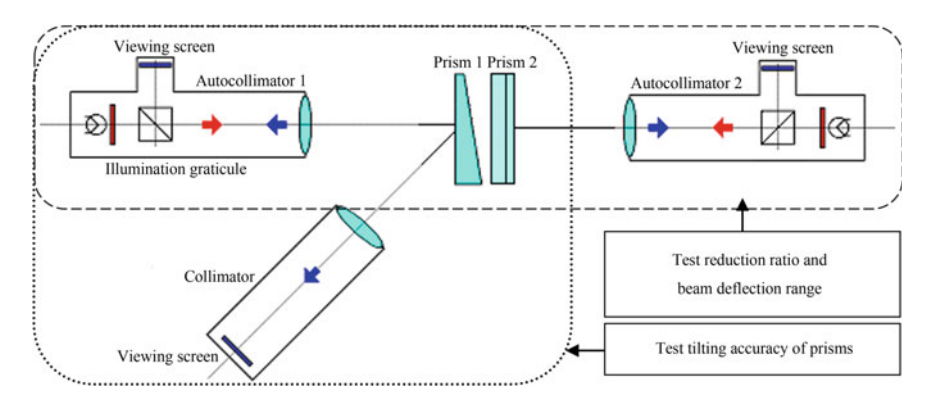


Fig. 6.16 Schematic diagram illustrating the experimental platform for tilting accuracy, reduction ratio and beam deflection range test

reading, namely the position difference value between the cross hair image from autocollimator 1 and the cross hair of the collimator itself, are equivalent to the angle of the beam reflected by prism 1.

- (2) The reduction ratio test is performed in a similar fashion, where the encoders are used to measure the tilting angles of two prisms, and the autocollimators are used to measure the deflection angle of the beam propagating through the double-prism system.
- (3) The beam deflection range, expressed by the vertical and the horizontal scan ranges of the emergent beam, can reach its maximum value through independent adjustment of prism 1 and prism 2 to their individual limit positions, which can be read from autocollimator 2.

Based on the above test methods, specific experimental procedures are designed as below.

- (1) Turn on the power of two autocollimators to illuminate the reticle. Then adjust two autocollimators on the level platform fixed on the air bearing worktable until the optical axis of two autocollimators are strictly aligned. As a result, two autocollimators can receive the cross hair image from each other, which is coincident with their own.
- (2) Put the horizontal and the vertical tilting prism devices between autocollimator 1 and 2 sequentially. Connect between the prism devices, the step motor control system and the encoders, and then power on the system. Then tilt prism 1 and 2 respectively until they are basically perpendicular to the optical axis.
- (3) Precisely adjust the position of the tilting double prisms and gently tilt prism 1 until the cross hair image returned from the plane facet of prism 1 coincides with the cross hair of autocollimator 1 itself. Then take notes of the readings of encoder 1 as the tilting origin of prism 1. Gradually rotate step motor 1 with equal step length and synchronously take notes of the readings of encoder 1 and the corresponding cross hair image position in autocollimator 1. After finishing

Autocolli	Autocollimator/(")		The difference/(")		Encoder reading/(°)		Encoder reading/(°) Th		rence/(°)	Error	ε/(")
1	2	1	2	1	2	1	2	1	2		
-23	-258	240	110	-0.0112	0.0527	0.0722	0.0227	15.00	2.22		
225	-139	248	119	-0.0845	0.0190	0.0733	0.0337	-15.88	-2.32		
102	-18	123 112	121 116	-0.0508	-0.0131	0.0377 0.0352	0.0321 0.0353	-12.72 -14.72	-5.54 -11.08		
-10	98	122	122	-0.0156	-0.0484	0.0332	0.0333	-14.72 -3.56	-0.32		
-132	220	122	122	0.0173	-0.0822	0.0329	0.0366	-3.30	-0.32		

Table 6.12 Tilting accuracy of prism 1 and prism 2

the test of all the preset tilting angles and the corresponding beam reflection angles, readjust prism 1 to its origin.

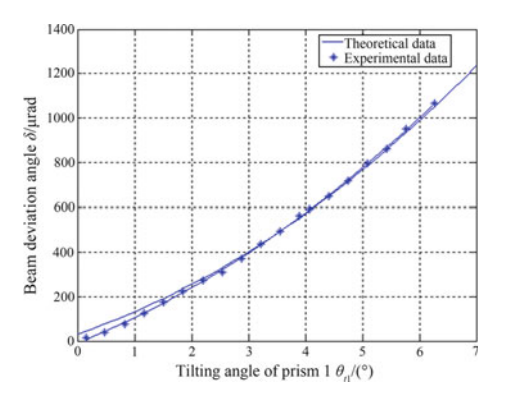
- (4) Similarly, do the tilting accuracy test for prism 2.
- (5) Remove prism 2, precisely readjust the position and the tilting angle of prism 1 and recalibrate its origin.
- (6) Gradually rotate step motor 1 with equal step length and encoder 1 gives the corresponding tilting angles of prism 1. Meanwhile, take notes of the cross hair image position in autocollimator 2 step by step. By this means, a series of tilting angles of prism 1 and the corresponding beam deflection angles are recorded as well as the reduction ratio after simple calculations. Particularly, when prism 1 is tilted to its limit position, the maximal beam deflection range in the vertical direction can be obtained by the reading in autocollimator 2.
- (7) Similarly, finish the reduction ratio test and the horizontal beam deflection range test for prism 2.

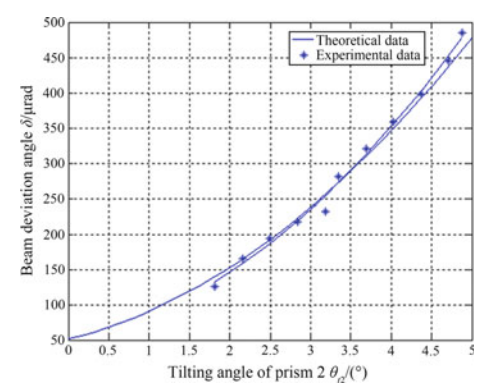
The relationship between the tilting angle of each prism recorded by the encoder and the beam reflection angle detected by the autocollimator reflects comprehensive accuracy of the mechanical system and the control system, which should be better than 13.873" according to the design requirements. Table 6.12 shows the test results of tilting accuracy for prism 1 and prism 2. Through calculations, the average error between the beam reflection caused by prism 1 and the reading of encoder 1 is 11.72", and that of prism 2 is 4.815", which demonstrates that the tilting accuracy of the designed mechanical system and control system satisfies the accuracy indicator.

The reduction ratio and the beam deflection range are further analyzed as follows. Firstly, measure the accurate wedge angles of the prisms, which are $\alpha_1=5^\circ 10''$ and $\alpha_2=5^\circ 55''$ in the test. Then draw the curve of the theoretical beam deflection angle according to the forward calculation based on accurate wedge angles. Finally, compare the theoretical curve with the measured one. Figure 6.17 not only shows the vertical beam deflection range, but also illustrates how the beam deflection angle change along with the tilting angle of prism 1. As the reading of encoder 1 changes from 0.1449° to 6.2714° , the vertical beam deflection range is $1053.9052\,\mu$ rad. So the reduction ratio of the prism tilting angle to the beam deflection angle reaches 102:1 while the corresponding theoretical value is 105:1. Similarly, Fig. 6.18 illustrates the above two indicators of prism 2. As the reading of encoder 2 changes from 1.8159° to 4.8744° , the horizontal beam deflection range is $358.752\,\mu$ rad. So the reduction ratio reaches 149:1 while the corresponding theoretical value is 165:1.

Fig. 6.17 Relationship between the tilting angle and the beam deflection angle of prism 1. The curve with "*" symbol is the fitting one based on the measured data while the other is the theoretical calculation curve

Fig. 6.18 Relationship between the tilting angle and the beam deflection angle of prism 2. The curve with "*" symbol is the fitting one based on the measured data while the other is the theoretical calculation curve





6.3.2 Test on Beam Deflection Accuracy

Beam deflection accuracy of the tilting double-prism system is tested through interferometry. The interferometer parameters are given as follows. The accuracy is better than $\lambda/100$, the diameter of the test beam is $\varphi150$ mm, the system quality (plane) is $\lambda/100$, the resolution is better than $\lambda/1000$ (double pass). Two identical prisms have the following parameters, namely the wedge angle equal to 5° , the refractive index constant at 1.517 and the tilting angle range within $0^{\circ}-5^{\circ}$.

Figure 6.19 illustrates the test method of beam deflection accuracy with an interferometer. As shown in the figure, the tilting double-prism device is placed between the interferometer and the reference mirror, and the test beam propagates through the optical system twice (the path is A_{t1} – A_{t5} – A_{t51} – A_{t11}). In the test, the interferometer gives the P-V value of the angle between the emergent beam A_{t1} and the return beam A_{t11} , which can be converted to beam deflection angle. Meanwhile the encoders record the corresponding tilting angle of the prisms. Therefore the error between the measured beam deflection angle and the theoretical one can be solved to precisely calibrate the beam deflection accuracy of the tilting double-prism device.

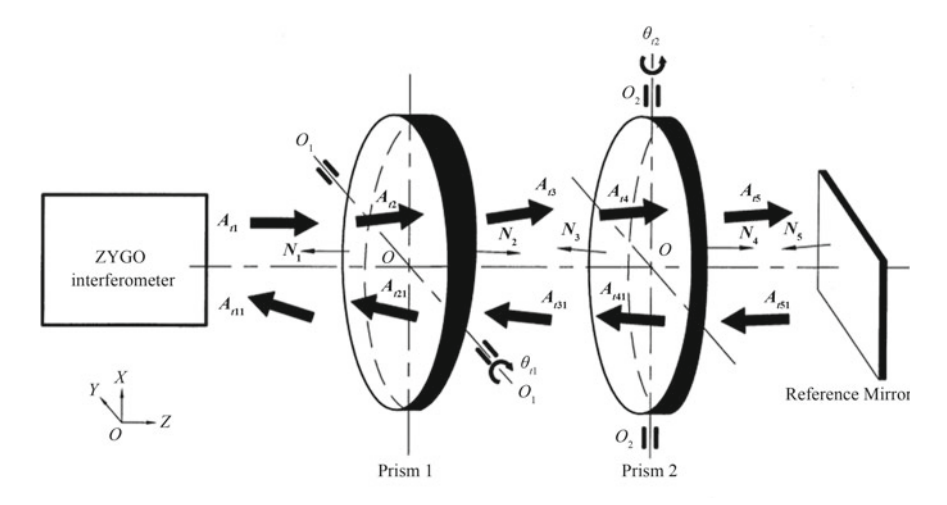


Fig. 6.19 Schematic diagram of the beam deflection accuracy test with an interferometer

Based on the above test system, the exact expression of the beam deflection is deduced as follows. Firstly, prism 1 and prism 2 are adjusted to the position where their plane facets are perpendicular to the initial incident beam. According to the vector refraction theorem, the unit vector of the refracted beam can be described as:

$$A_{2} = \frac{n_{1}}{n_{2}}A_{1} + \left(\sqrt{1 - \left(\frac{n_{1}}{n_{2}}\right)^{2} \left(1 - (A_{1} \cdot N)^{2}\right)} - \frac{n_{1}}{n_{2}}(A_{1} \cdot N)\right)N$$
 (6.1)

where A_1 and A_2 are the unit vectors of the incident beam and the refracted beam respectively, N denotes the unit normal vector of the refracting surface, pointing from medium 1 to medium 2, n_1 and n_2 are the refractive indexes of the two media respectively.

As shown in Fig. 6.19, A_{t1} – A_{t5} are the unit vectors of the beam on every optical path, and $A_{t1} = (0,0,1)^{\text{T}}$. N_1 – N_5 are the initial unit normal vector of the five surfaces on the optical path. And the posture of the reference mirror is set to satisfy $N_5 = A_{t5}$.

Assume that prism 1 and prism 2 tilt about the Y axis and the X axis by θ_{t1} and θ_{t2} , respectively. Then the unit vector expression for A_{t1} – A_{t5} can be derived again. Similarly, the unit vectors of the return beam, namely A_{t11} – A_{t51} , can also be obtained.

The total beam deflection angle after a complete round trip is:

$$\delta_3 = \operatorname{arc} \cos(-A_{t11}) \tag{6.2}$$

The reflection angle on the reference mirror caused by the tilt of the prisms is:

$$\delta_4 = \operatorname{arc} \cos(-A_{t51}) - \operatorname{arc} \cos(A_{t5}) \tag{6.3}$$

Therefore, the error accumulation coefficient caused by reflection is: $R = \delta_3/\delta_4$. Assume that δ_{3i} is the theoretical beam deflection angle caused by the prism tilting angle $\theta_{t(i)}$, while δ_{ti} is the actual one measured by the interferometer. Then the beam

deflection error can be expressed as:

$$s_i = \frac{(\delta_{3i} - \delta_{ti})}{R} \tag{6.4}$$

The root mean square value of the beam deflection error is:

$$\sigma = \left(\frac{1}{n-1} \sum_{i=1}^{n} (s_i - \bar{s})^2\right)^{\frac{1}{2}}$$
 (6.5)

where $\bar{s} = \frac{1}{n} \sum_{i=1}^{n} s_i$, and *n* is the amount of the measured data.

Three sets of data are measured. The theoretical beam deflection angles and the actual measured ones are compared in Figs. 6.20, 6.21 and 6.22. The calculation results show that the root mean square values of the beam deflection error are $\sigma_1 = 0.437 \,\mu$ rad, $\sigma_2 = 0.418 \,\mu$ rad and $\sigma_3 = 0.402 \,\mu$ rad, respectively.

The error sources that influence the beam deflection accuracy mainly include reading error, prism position error, dimension error and surface shape error of each prism, flatness error of the worktable and operation error. These error sources are analyzed as follows.

The position error and the dimension error of the prisms are categorized as system error, which can be determined through strict optical system alignment. As for the surface shape of the prisms, the P-V value is the key influence factor to the measurement accuracy. Hence it is necessary to take a few more measurements and get the average. Moreover, when observing the autocollimator, we need to adjust the position repeatedly until the cross hair image is clear. However, due to the dimension error and the dispersion induced by two prisms, it is possible that the clear image cannot be reached no matter how the autocollimator is shifted. Then a position where

Fig. 6.20 Fitting result of the first set of data

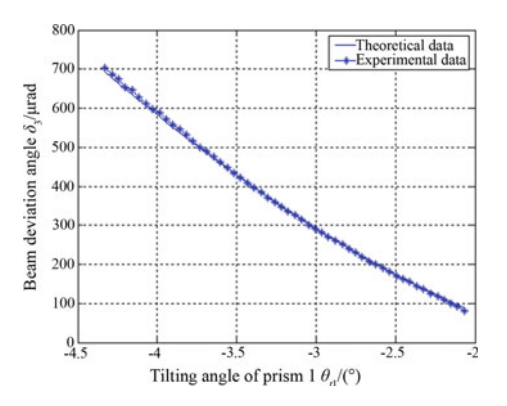


Fig. 6.21 Fitting result of the second set of data

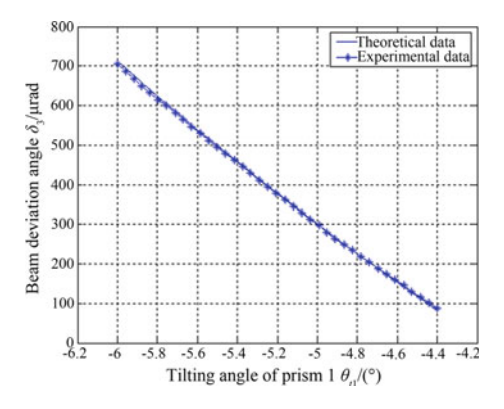
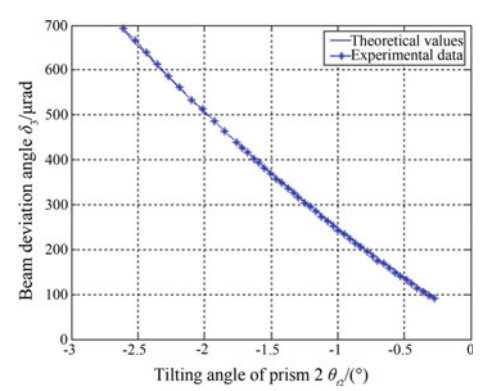


Fig. 6.22 Fitting result of the third set of data



the cross hair image is relatively clear should be calibrated as the standard position for measurement [7].

The random error sources mainly include operation error, reading error, vibration and so on. Because the requirement of the measurement accuracy is relatively high, while the accuracy of the autocollimator is generally limited, the random errors may result in large deviation between the measured values and the theoretical values and further influence the test results. Therefore, multiple measurements and averaging is required to minimize the influence of all kinds of random errors.

6.4 Laser Coarse-Fine Coupling Tracking Test on Double Rotating Risley-Prism Pairs

A novel laser coarse-fine tracking method based on two pairs of rotating Risley prisms is proposed to perform the forward and inverse tracking function. The second pair of rotating Risley prisms with narrower wedge angle can achieve higher precision tracking with narrower field of view (FOV) than the first pair, which largely enriches

the coarse-fine coupling tracking patterns. In this section, a test platform is established to validate the effectiveness of the double rotating Risley-prism pairs (DRRP) to perform laser coarse-fine coupling tracking.

6.4.1 Hardware of the Test Platform

As shown in Fig. 6.23, the experimental setup of the coarse-fine coupling tracking DRRP consists of a coarse tracking subsystem (CTS), a fine tracking subsystem (FTS), two controllers, a laser, a coordinate screen, a slider and so on. The CTS refers to the rotating Risley-prism pair with large wedge angle, which consists of prism 1 and prism 2. And the FTS is composed of prism 3 and prism 4 with narrow wedge angle. The distances between the adjacent prisms are $D_1 = 100$ mm, $D_2 = 80$ mm and $D_3 = 68$ mm, respectively. The laser with 650 nm wavelength is adjusted to be coincident with the optical axis. The laser beam propagates through four prisms sequentially and finally hits the coordinate screen with a distance of $D_4 = 1000$ mm from prism 4. The coordinates of each tracking points can be measured according to the laser spot on the coordinate screen. Table 6.13 shows the detail parameters of the experimental setup.

In order to realize coarse-fine coupling tracking, the inverse control strategy of four prisms is summarized as four steps.

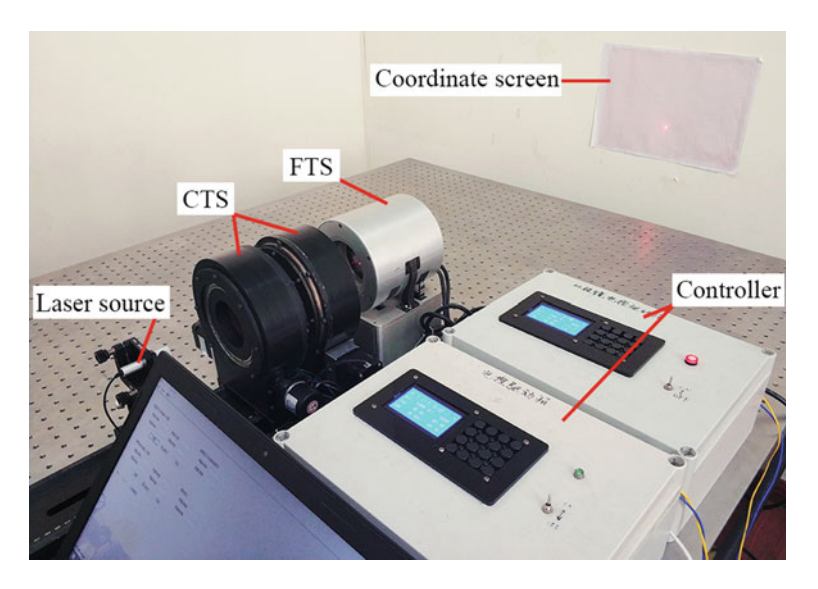


Fig. 6.23 Experimental setup

Device	Parameter	Function
CTS	Wedge angle: $\alpha_1 = 10^\circ$ Refractive index: $n_1 = 1.517$ Diameter: $D = 80$ mm Thinnest-end thickness: $d_0 = 5$ mm	Coarsely deflect laser beam for coarse tracking
FTS	Wedge angle: $\alpha_2 = 5^{\circ}$ Refractive index: $n_2 = 1.517$ Diameter: $D = 80 \text{ mm}$ Thinnest-end thickness: $d_0 = 5 \text{ mm}$	Finely deflect laser beam for fine tracking
Motion controller	MCU: LPC1114	Motion control of the rotating Risley-prism pairs
Laser	Wavelength: 650 nm Power: $P \ge 2.5$ mW Focus: variable focus	Emit collimated laser beam
Coordinate screen	Resolution ratio: 1 mm Distance away from the emergent surface of prism 4: $D_4 = 1000 \text{ mm}$	Receive the laser and measure the coordinates of the laser spot
Guide rail and	Stroke of the guide rail: 1000 mm	Support component

Table 6.13 System parameters of the platform

- (1) Keep the separated angle between prism 1 and prism 2 constant at $\Delta\theta=180^\circ$ to locate the FOV of the CTS at the center of the overall FOV of the proposed system.
- (2) Calculate the rotation angles θ_1 and θ_2 based on the two-step method to track a global trajectory rapidly [8], where θ_1 and θ_2 denote the rotation angles of prism 1 and prism 2, respectively.
- (3) Given the local feature, rotate prism 1 and prism 2 to steer the beam towards the specified region of interest.
- (4) Solve the rotation angles θ_3 and θ_4 based on the Newton's iterative method to track the local feature accurately [9], where θ_3 and θ_4 denote the rotation angles of prism 3 and prism 4, respectively.

6.4.2 Performance Test on Coarse-Fine Coupling Tracking

Given the global and local features of the tracking trajectories in Fig. 6.24a and b, the corresponding rotation angle curves of four prisms are solved according to the inverse algorithm, as shown in Fig. 6.24c and d. In the experiment, four prisms are controlled to rotate to the preset rotation angles according to the calculated curves. And then the real coordinates of the tracking points on the coordinate screen can be measured, as shown in Fig. 6.24a and c. Tables 6.14 and 6.15 show the detail experimental data.

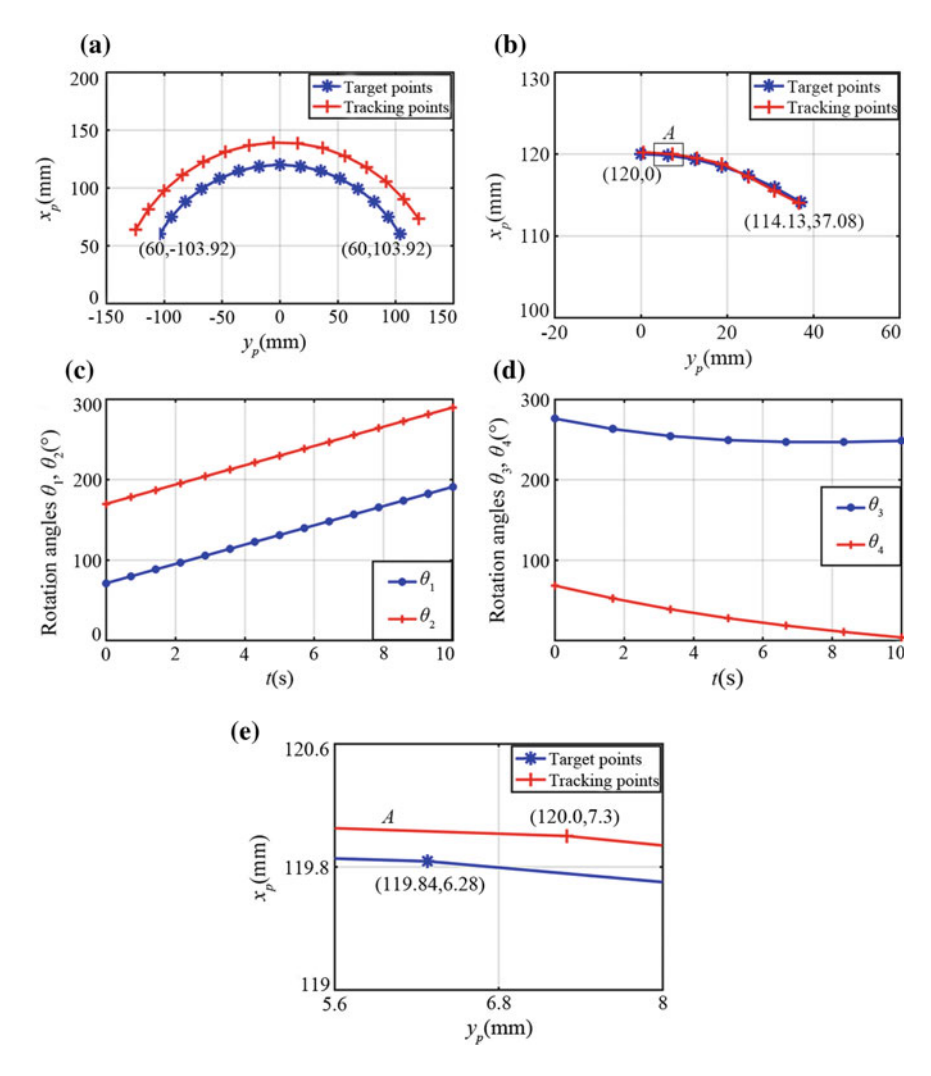


Fig. 6.24 Experimental results for coarse-fine tracking. a The difference between the target points and the tracking points of the global trajectory; b The difference between the target points and the tracking points of the local trajectory; c The rotation angles of CTS for tracking the global trajectory; d The rotation angles of FTS for tracking the local trajectory; e The enlargement of the zone surrounded the point with the maximal error of 1.033~mm

According to the two-step method, prism 1 and prism 2 are controlled to steer the laser beam to approach the target point during the coarse tracking process, and then prism 3 and prism 4 are controlled to perform precise tracking during the fine tracking process based on the Newton's iterative method. As shown in Table 6.14, because the emergent point from the DRRP is regarded as the center of the plane facet of prism 4 during the coarse process, the tracking points differ greatly from the target

 Table 6.14 Experimental data of CTS

No.	Rotation an	gle/(°)	Target point	Target point/mm Tracking p		int/mm	Error/mm
	θ_1	θ_2	X_p	Y_p	x_p	y_p	Δ
1	70.9261	529.0739	60	-103.923	63.7	-124.6	21.00539
2	79.49753	537.6453	74.81878	-93.8198	81.4	-113.6	20.84634
3	88.06896	546.2168	87.96622	-81.6207	97.5	-100.0	20.70484
4	96.64039	554.7882	99.14865	-67.5984	111.2	-84.1	20.43374
5	105.2118	563.3596	108.1163	-52.066	122.6	-66.0	20.09810
6	113.7832	571.931	114.6687	-35.3706	131.1	-47.0	20.13030
7	122.3547	580.5025	118.6597	-17.8851	136.7	-26.5	19.99173
8	130.9261	229.0739	120	0	139.1	-5.3	19.82171
9	139.4975	237.6453	118.6597	17.88507	138.5	15.5	19.98315
10	148.069	246.2168	114.6687	35.37062	134.6	37.0	19.99775
11	156.6404	254.7882	108.1163	52.06605	127.5	56.4	19.86233
12	165.2118	263.3596	99.14865	67.59841	117.7	75.0	19.97338
13	173.7832	271.931	87.96622	81.62073	105.5	92.0	20.37554
14	182.3547	280.5025	74.81878	93.81978	90.2	107.1	20.32108
15	190.9261	289.0739	60	103.923	73.3	120.0	20.86524

Table 6.15 Experimental data of FTS

No.	Rotation angles/(°)		Target point	Target points/mm		Tracking points/mm	
	θ_3	θ_4	X_p	Y_p	x_p	y_p	Δ
1	276.1177	68.07858	120	0	120.2	0.6	0.632456
2	263.204	52.25839	119.8355	6.280315	120.0	7.3	1.032862
3	254.3603	38.63871	119.3426	12.54342	119.5	13.0	0.482945
4	249.2697	27.46227	118.5226	18.77214	118.8	18.8	0.278795
5	247.0608	18.23676	117.3777	24.9494	117.2	25.0	0.184775
6	246.9525	10.38621	115.9111	31.05829	115.5	31.0	0.415210
7	248.395	3.44211	114.1268	37.08204	114.0	36.7	0.402527
Aver	age error/mn	1					0.489938

points. That is to say, the emergent point has relatively high effect on the pointing position in the near-field applications, where the Newton's iterative method can be applied to improve the tracking precision. As shown in Table 6.15, the maximal error between the tracking points and the target points during the fine tracking process is 1.033 mm with the average value of 0.49 mm. Therefore, the Newton's iterative method is available in the FTS during the fine tracking process. In conclusion, the experiment of coarse-fine coupling tracking demonstrates that the DRRP can be a promising solution to achieving coarse-fine coupling tracking, which shows great potentials in spatial orientation tracking applications.

6.5 Summary

The performance tests in this chapter are classified into three groups according to three kinds of double-prism devices, namely the rotating double prisms, the tilting double prisms and the coarse-fine coupling double-prism pairs. Firstly, a series of performance tests on rotating double-prism multi-mode scan system are carried out, including the multi-mode scan performance, the directional tracking performance and the inverse solution based on lookup-table method. The first two experiments verify the model of the rotating double-prism multi-mode scan theory and could provide references for the applications of the rotating double-prism scan system, while the third experiment validates the correctness of the lookup-table method for inverse solution. Secondly, the tilting accuracy, reduction ratio and the beam deflection range and accuracy of the tilting double-prism multi-mode scan system are tested, respectively. Test results indicate that the hundredfold reduction ratio from the tilting angle of each prism to the beam deflection angle can be achieved with the prism wedge angle of 5°, which validates the characteristic of high-precision scanning. Finally, a novel coarse-fine tracking method based on two pairs of rotating Risley prisms is proposed and the performance test results show great potential in spatial orientation tracking applications.

References

- 1. Li AH (2007) Research on large-aperture high-accuracy optical scanner. Shanghai Institute of Optics and Fine Mechanics, Chinese Academy of Sciences, Shanghai
- Gao XJ (2014) Research on rotating double-prism dynamic tracking system. Tongji University, Shanghai
- Li AH, Liu LR, Sun JF (2009) Large-aperture high-accuracy optical scanner. J Mech Eng 45(1):200–204
- Li AH, Liu LR, Luan Z (2005) Multi-dimensional adjustable optical phase shifter: CN, 200510029378.5 (2005-2-22)
- Li AH, Bian YM, Zhang Q (2009) Precise one-dimensional rotation and two-dimensional tilt worktable: CN, 200710170500.X (2009-5-20)
- Li AH, Bian YM (2009) Variable angle micro-displacement adjusting device with combined transmission: CN, 200910196308.7 (2009-3-17)
- Li AH, Liu LR, Sun JF et al (2006) Research on a scanner for tilting orthogonal double prisms. Appl Opt 45(31):8063–8069
- Li Y (2011) Closed form analytical inverse solutions for Risley-prism-based beam steering systems in different configurations. Appl Opt 50(22):4302–4309
- Tao XD, Cho HS, Janabi-Sharifi F (2008) Active optical system for variable view imaging of micro objects with emphasis on kinematic analysis. Appl Opt 47(22):4121–4132

Chapter 7 Support Design Technology of Large-Aperture Prism



Abstract A radial multi-segmental adjustable support, characterized by easy installation and radial fine adjustment, is designed to meet the rotational motion requirements of the large-aperture scan prism. A dynamic analysis method is established to study the dynamic response of variable loads on a rotating prism, which is suitable for the dynamic performance analysis on the optical system, and can provide references for the performance analysis on similar optical systems. The surface deformation of the prism is fitted by the Zernike polynomial. The fitting errors of PV and RMS values are all within the allowable range, which can meet precision requirements for the surface figure.

7.1 Design and Analysis of Multi-segmental Support

For a large-aperture rotating prism (e.g. 300 mm and above), the radial support is crucial to ensure the opto-mechanical system performance. A Risley prism discussed in this chapter is provided with the geometrical properties of large size and nonuniform mass distribution. When variable directions of external loads act at different moving positions of the rotating prism, the different surface deformations as well as stress distributions maybe occur. The key to solving the problem is appropriately mounting the optics to minimize some unexpected external load effects. Many scholars have carried out research on the support technology of large-size movement mirror, including active support technology, adaptive support technology and anti-rotation technology. For example, Cui Xiangqun et al. [1] proposed an active support technology of thin mirror, aiming at the tentative fabrication test for largeaperture thin astronomical mirror. Zhu Bo et al. [2] designed the tertiary mirror M3 of the large-aperture ground-based electro-optical telescope (LGEOT) with rear threepoint support way, to ensure the imaging quality of telescope optical system. Salas et al. [3] used 18 air bags as the suspension supports of the primary mirror in the 2.1 m telescope and analyzed the control problems. Vukobratovich and Richard [4] applied roller chain supports to the design of support structures for a large-aperture mirror and demonstrated its superiority. However, most previous researches focused

on the modes of static or quasi-static (slow motion) supports, and less on motion performance analysis of optical systems, especially for large size mirrors.

For the rotating Risley prisms discussed in this book, the radial support is the key component to ensure the motion accuracy of the whole system. In general, the radial support ways include multi-point support, mercury belt support, steel support and roller chain support. Traditional mercury belt support, roller chain support, steel support and other support ways are hard to meet the movement requirements, while the flexible support will induce the optical element sensitive to the changes of external loads, vibration, and other external factors. Theoretically, the multi-point support way can meet the requirements for dynamic optical systems, but for a large-aperture rotating prism, especially when the width-radius ratio is small, the multi-point support way maybe result in large stress concentration and surface deformation. Therefore, the above support ways are not optimal choices for a large-aperture rotating prism.

In this chapter, a novel radial support method is firstly proposed for the large-aperture rotating prisms. Then a dynamic analysis method is established to study the dynamic response of variable loads on a rotating prism. Finally, the prism's surface deformation with the rotation angle change are concluded.

7.1.1 Radial Multi-segmental Support

Radial support ways mainly incorporate point support (as shown in Fig. 7.1) and surface support (as shown in Fig. 7.2). For a static structure, the point support is convenient to be adjusted with high accuracy, and is widely applied to the situation in which the displacement or angle needs to be regulated, but the local stress concentration is usually inevitable. Comparatively, the surface support way can attenuate the stress concentration especially for large optical components, but its adjustability is relatively poor [5].

The analysis results of point support for a Risley prism is given in Table 7.1. The prism is characterized by diameter of 600 mm, wedge angle of 10° and thinnest-end thickness of 30 mm. We choose three-point support, six-point support, nine-point support and twelve-point support as four typical examples. As shown in Fig. 7.1,

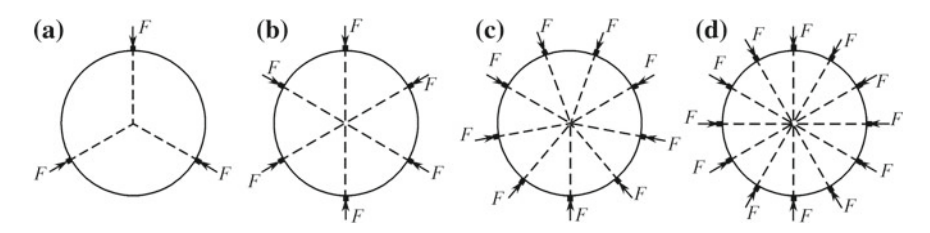


Fig. 7.1 Multi-point support. a Three-point support; b Six-point support; c Nine-point support; d Twelve-point support

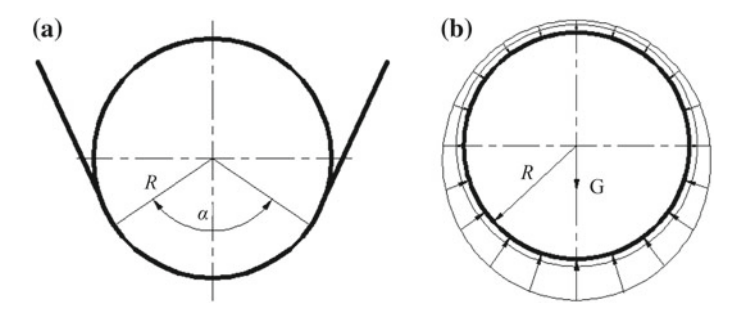


Fig. 7.2 Surface support. a Steel-belt support; b Mercury-belt support

Table 7.1 Results comparisons of surface deformation and maximum von Mises stress for multipoint supporting prisms

Support way	Deformation	von Mises stress/Pa		
	PV/nm RMS/nm			
Three-point	150.33	57.48	1.0×10^{6}	
Six-point	67.13	22.61	533,830	
Nine-point	99.01	47.37	309,040	
Twelve-point	87.37	44.07	214,718	

the support points are uniformly distributed along the radial direction, and all are arranged in the same plane 20 mm away from the plane side of the prism. A certain pre-tightening force is applied to each support point to ensure the support fastened, and axial displacement constraints are added on both sides of the prism [5, 6].

In order to lessen the stress concentration caused by the impact loads, the surface support way for a large-aperture mirror are relatively preferred to keep the stability of motion structure, while the point support and line support ways are rarely used. A structure of flexible surface support style is proposed in [7] to solve the problem of support in the mirror movement, as shown in Fig. 7.3. In addition, there are other surface support ways such as the steel belt support and mercury belt support proposed in [8].

The above-mentioned flexible support ways are effective for symmetrical optical mirrors (such as plane mirrors) [9], but they are hardly considered as optimal schemes for asymmetrical optical components (like wedge-shaped prisms). When the symmetrical optical element is in motion, the impact loads brought about by the mass eccentricity can result in the deformation of flexible support, further induce the shift of prism center, and finally lead the direction error of the output beam.

In order to solve the problem of supporting the dynamic non-uniform prism system, we propose a multi-segmental adjustable support method that can solve the problem of non-uniform mass prism deformation caused by the shift of gravity center. As shown in Fig. 7.4, three segments of arc-shaped support blocks are placed on the circumference of the large-aperture circular prism (the number of segments of

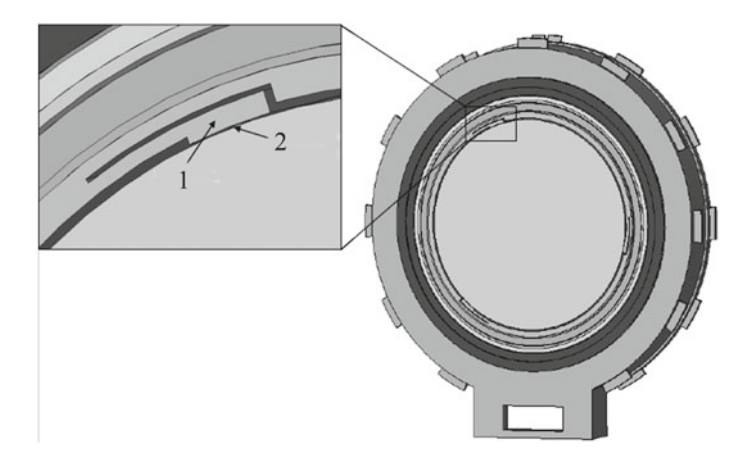


Fig. 7.3 Flexible surface support structure where 1 is tangential groove and 2 is key (material is epoxy)

the arc-shaped surface can be selected according to the actual conditions), and the arc-shaped support blocks are placed in the grooves of the frame. The screw passes through the frame wall and the screw head is wrung into the screw hole of the support block. When the screws are tightened, the arc blocks will support the prism together, but when the screws are reversed, the blocks will separate from the prism easily, which not only facilitates to disassemble the prism mechanism, but also allows the fine adjustment of the position of the prism in use. In the design, the clearance fit is properly ensured between the inner circumference of the frame and the outer one of the prism. When the supporting block is pulled to the bottom of the groove of the frame, the circumference of the inner surface constituted by three supporting blocks is smaller than the inner diameter of the frame, which is advantageous for installation and adjustment of the prism [9, 10].

7.1.2 Three-Segmental Support Analysis

In order to improve the radial support effect for large-aperture rotating prisms, the point-surface support, multi-segmental surface support and full surface support have been compared in the previous research [6, 11, 12]. This section will focus on the design and analysis of the three- segmental support under two cases of the prism's thin end upward and downward, respectively.

1. Analysis Model

The analysis object is a wedge-shaped prism rotating around the optical axis, characterized with diameter D = 500 mm, wedge angle $\alpha = 10^{\circ}$, and thin end thickness $d_0 = 30$ mm. As shown in Fig. 7.5, it is supported by the radial multi-segmental

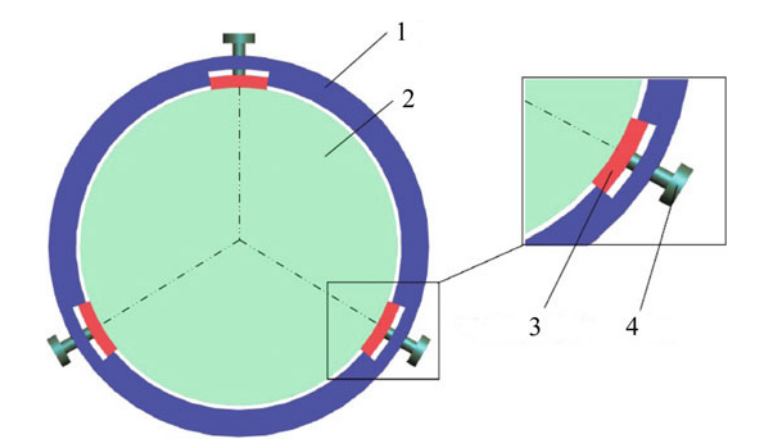


Fig. 7.4 Adjustable radial multi-segmental support configuration where 1 is cell, 2 is prism, 3 is support block and 4 is screw

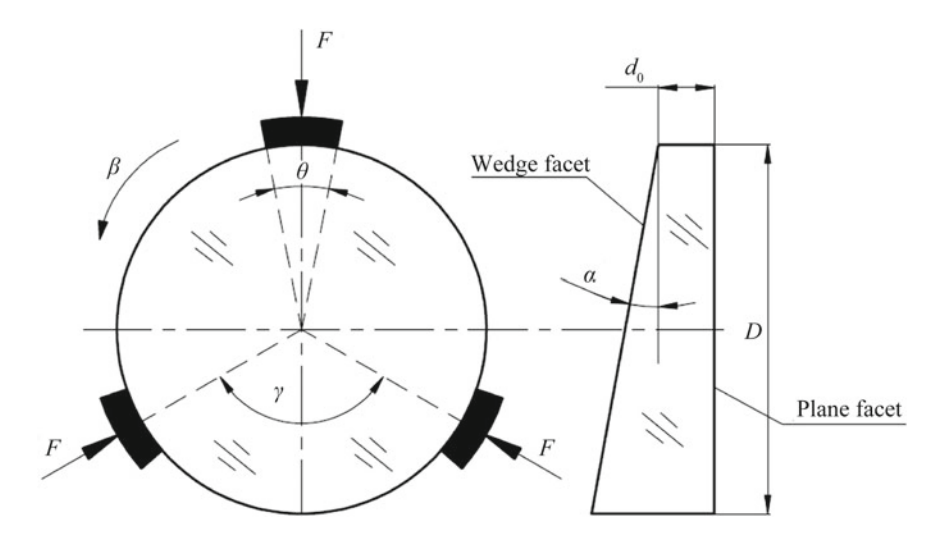


Fig. 7.5 Schematic diagram of geometric model of the prism

support, where θ indicates the center angle of support blocks covered around the circumference of mirrors ($\theta=20^{\circ}$), γ represents the support angle between two subjacent support blocks, β is the rotation angle of the prism, and F means the preload force ($F=10~\mathrm{N}$).

Using the finite element analysis software tool Ansys, the different layouts of the three-segmental support are analyzed, and the characteristics of various support modes are investigated during the rotation process of the prism. The evaluation indexes include the PV (Peak Value) and the RMS (Root Mean Square) values of the

prism surface deformation (including the plane facet and the wedge facet). The key parameters of material used are listed in Table 7.2.

2. Static Support Analysis

There are two kinds of static support situations for wedge-shaped prisms, the thin end upward and downward, and their support effects are analyzed respectively.

(1) Thin End Upward

When the thin end of the prism faces upwards, a three-segmental uniform support is firstly provided. One of the support blocks is arranged at the center of the thin end and forms an angle of $\gamma = 120^{\circ}$ with the other two support blocks. The finite element model of three-segmental uniform support is shown in Fig. 7.6. Both the prism and support block are meshed with 20-node SOLID95 elements, and axial displacement constraints are added on the prism side and the outermost circumferential node of the wedge surface side. A tangential displacement constraint and a radial preload force of F = 10 N were added to the outside nodes of the support block, and the acceleration of gravity was 9.8 N/kg. Surface-flexible contact with MPC (Multi-point Constraint) algorithm is added between support block and prism.

The static analysis results show that the total PV value of the prism (sum of the PV values of the plane facet and wedge facet), defined as T_PV, is 44.559 nm (the total PV and total RMS values are used in this section for convenience, the same below). The total RMS (sum of the RMS values of the plane facet and wedge facet), defined as T_RMS, is 22.948 nm, and the maximum value of von Mises equivalent stress is 0.0659 MPa. Figure 7.7 shows the contour chart of the prism axial deformation and the von Mises equivalent stress.

Under the static support, in order to seek a better support effect and improve the surface precision of the prism, the support angle γ of the curved support block is optimized. The two-step optimization method proposed by [6] is applied: in the first step, use DV SWEEPS algorithm to obtain the corresponding relationship between the deformed PV value and the support angle γ ; the second step is based on the first step optimization result, and use the First-Order optimization algorithm to obtain the global optimum.

Table 7.2 M	Iaterial paran	neters				
Part name	Material	Density $\rho/(\text{kg m}^{-3})$	Elastic modulus E/GPa	Poisson ratio μ	Linear expansion coefficient α /°C ⁻¹	Coefficient of thermal conductivity $\lambda/(W m^{-1} K^{-1})$
Prism	K9 glass	2530	81.32	0.209	7.5×10^{-6}	1.207
Support block	Nylon 66	1050	28.3	0.4	8.0×10^{-6}	0.27
Cell and others	45 steel	7800	196	0.24	11×10^{-6}	48

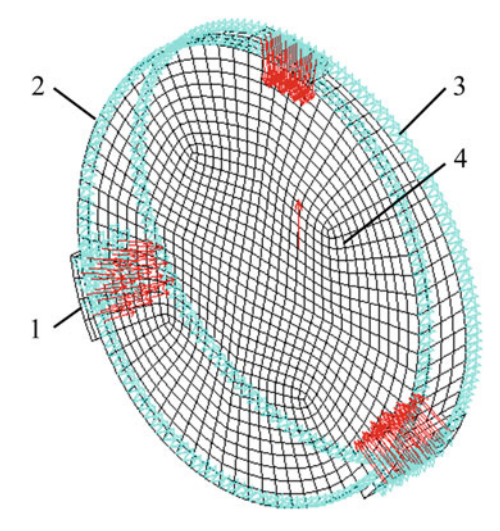


Fig. 7.6 Finite element model of the prism (thin end upward) where 1 is support block, 2 is wedge facet, 3 is plane facet and 4 is tracking mirror

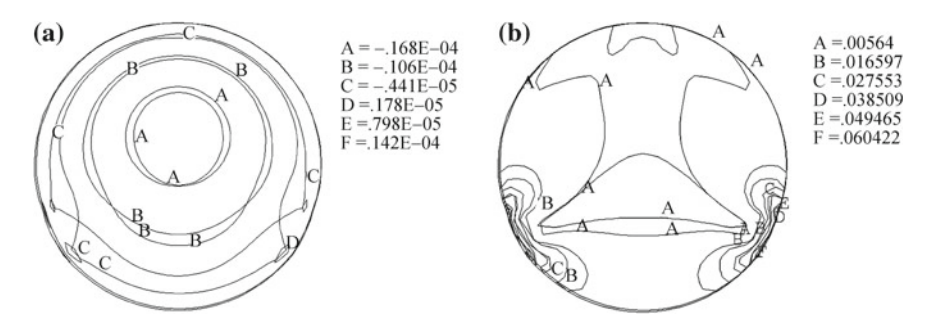


Fig. 7.7 Contour chart of the prism. a Axial deformation; b Von Mises stress

In the first step, the DV SWEEPS algorithm is an equal step length searching method, and the scan analysis is performed in the design space to obtain the trend of prism deformation T_PV value with support angle γ . Considering the support curvature of the support block and the support arrangement of the prism, the search range is set to [30°, 180°] with the step length 3° to obtain the change curve of the T_PV value of the prism deformation as a function of the support angle γ as shown in Fig. 7.8.

The second step First-Order optimization algorithm is based on the sensitivity of the objective function to the design variables. In each iteration, the gradient is calculated to determine the search direction. Therefore, the calculation accuracy is high and the occupancy time is relatively long. In the first step, the DV SWEEPS algorithm provides the initial optimization sequence for the second-step First-Order optimization algorithm and shortens the search scope of its design variables. We set

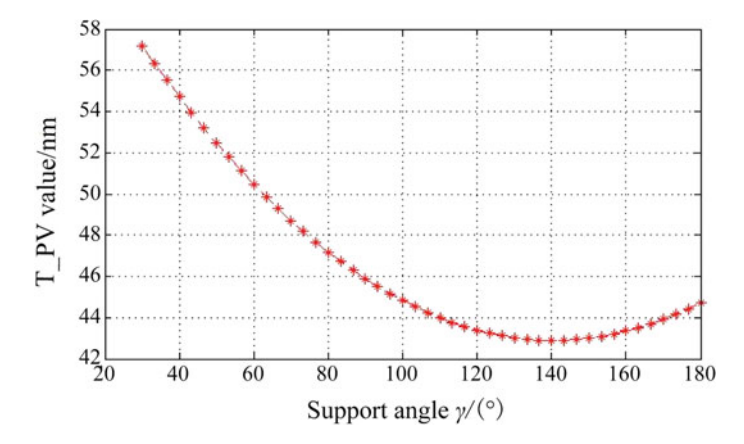


Fig. 7.8 Curve of deformation T_PV values and support angle γ

Table 7.3 Optimization results of support angle γ (thin end upward)

	SET 1	SET 2	*SET 3	SET 4
Maximum von Mises equivalent stress/MPa	0.06704	0.06508	0.07585	0.06671
Support angle γ/(°)	150	153.89	138.29	124.43
T_PV value/nm	43.65	43.72	43.23	44.91

the support angle γ as the design variable, the allowable stress [δ] of K9 glass as the state variable, the T_PV values of the surface deformation of tracking mirrors as the objective function, and 120° – 160° as the search region of the design variable. The designed optimization sequence obtained is shown in Table 7.3, where "*" is the optimal solution.

According to the optimization results, it can be seen that when the support angle $\gamma = 138.29^{\circ}$, the minimum T PV value of the prism is 43.23 nm.

The prism support model with the support angle $\gamma=138^\circ$ is established, and the static structure analysis is carried out. The analysis result shows that the T_PV value of the surface deformation is 43.25 nm, the T_RMS value is 22.49 nm and the maximum value of von Mises equivalent stress is 0.0799 MPa. Figure 7.9 shows the contour chart of the prism axial deformation and von Mises equivalent stress after optimization.

According to the analysis result, it can be seen that with the thin end of the prism upward, the PV value of the surface deformation, under the support optimization way, has reduced by 2.94%, and the RMS value has decreased by 2.0%, compared with the three-segmental support way before optimization. To a certain extent, the surface figure of the prism is improved by the two-step method.

(2) Thin End Downwards

For the case where the prism thin end faces downwards, the three-segment support and optimization support methods are also analyzed, and the same displacement

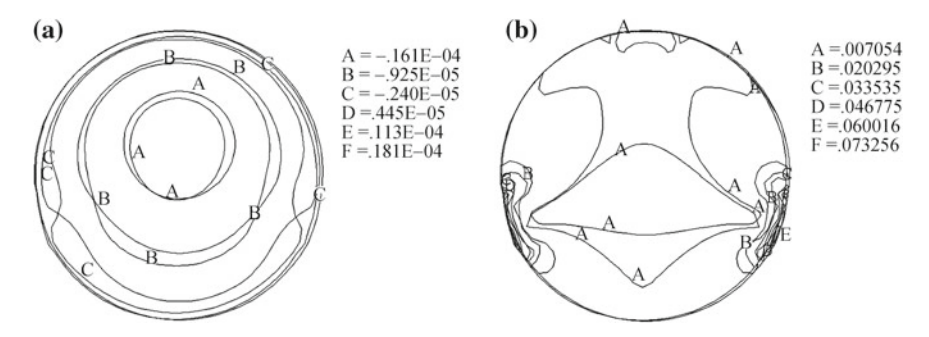


Fig. 7.9 Contour chart of the prism after optimization. a Axial deformation; b Von Mises stress

constraints, force constraints, gravitational accelerations, and contact settings are added, which are all same as the conditions of thin end upwards. The analysis results show that the T PV value of prism deformation under the three-segment uniform support mode is 45.33 nm, T RMS value is 22.45 nm, and the maximum equivalent stress value is 0.1190 MPa.

Similarly, the support angle γ is optimized by the aforementioned optimization method to obtain the design optimization sequence as shown in Table 7.4. It can be seen that when the support angle $\gamma = 133.72^{\circ}$, the T PV value of the prism deformation reaches the minimum value 42.97 nm.

A prism support model with an optimal support angle $\gamma = 133^{\circ}$ is established. The result shows that the T PV value of the surface deformation after optimization, is 43.03 nm, which has decreased by 5.07%, the T RMS value is 22.22 nm with the reduction of 1.02%, and the maximum value of von Mises equivalent stress is 0.1060 MPa. The surface quality of the prism is improved to some extent. Figures 7.10 and 7.11, respectively, are the contour chart of the axial deformation and the von Mises equivalent stress of the prism before and after optimization.

3. Analysis of Rotation Process

Regardless of whether the thin end of the prism is upward or downward, the optimized support method can improve the surface precision of the prism to some extent. When the prism rotates to different positions (the analysis of dynamic rotation processes will be discussed in detail in Sect. 7.2), is the support optimization way still advantageous? The following analysis will be carried out.

Table 7.4 Optimization results of the support angle γ (thin end downward)					
	SET 1	SET 2	*SET 3*	SET 4	
Maximum von Mises equivalent stress/MPa	0.09086	0.08502	0.10655	0.10608	
Support angle γ/(°)	150	145.42	133.72	137.49	
T_PV value/nm	44.00	43.17	42.97	44.29	

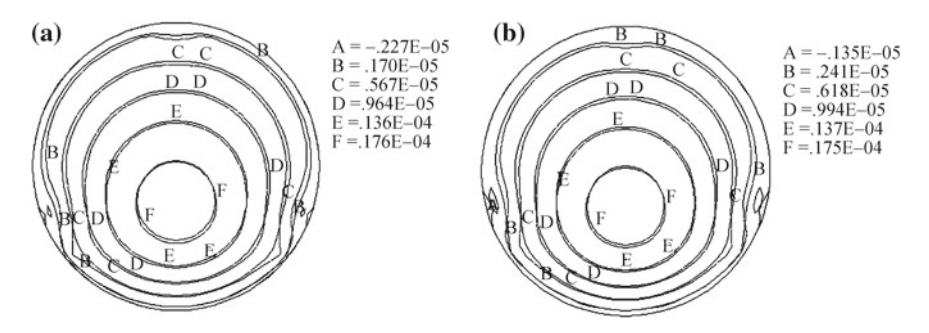


Fig. 7.10 Contour chart of axial deformation. a Before optimization; b After optimization

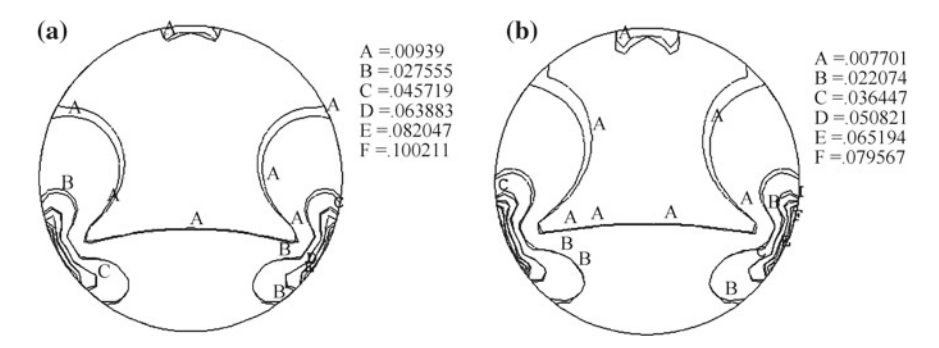


Fig. 7.11 Contour chart of von Mises stress. a Before optimization; b After optimization

Using the Ansys APDL language, the parametric model of the prism and its support structure are established. Similar to the above analysis process, the constraints, gravity acceleration and contact settings are added to the prism model. Here, we select 5° as the rotation step, and the prism model is analyzed within a rotation region of 0° –360°. Figures 7.12a and b, respectively, show the motion model (initial position) and the finite element model (with a rotation angle of 90°) of the prism.

Using Matlab software tool, the T_PV value of the prism deformation after rotation analysis is fitted, and the relationship between the T_PV value and the rotation angle β is obtained. Figures 7.13 and 7.14 are the comparison curves of the three-segment uniform support way and the optimized support way under the conditions of the thin end of the prism upward and downward.

From Figs. 7.13 and 7.14, it can be seen that when the prism with the thin end upward rotates in the ranges of $[0^{\circ}, 45^{\circ}]$, $[155^{\circ}, 210^{\circ}]$ and $[315^{\circ}, 360^{\circ}]$, the deformation T_PV value under the three-segmental surface support is greater than the T_PV value in the optimized support; while when the prism rotates within the ranges of in the ranges of $[45^{\circ}, 155^{\circ}]$ and $[210^{\circ}, 315^{\circ}]$, the deformation T_PV value under the optimizing the support is greater than that under the uniform support. For the case of the thin end down, when the prism rotates in the rotation ranges of $[0^{\circ}, 70^{\circ}]$, $[140^{\circ}, 220^{\circ}]$ and $[290^{\circ}, 360^{\circ}]$, the deformation T_PV value under the three-segment

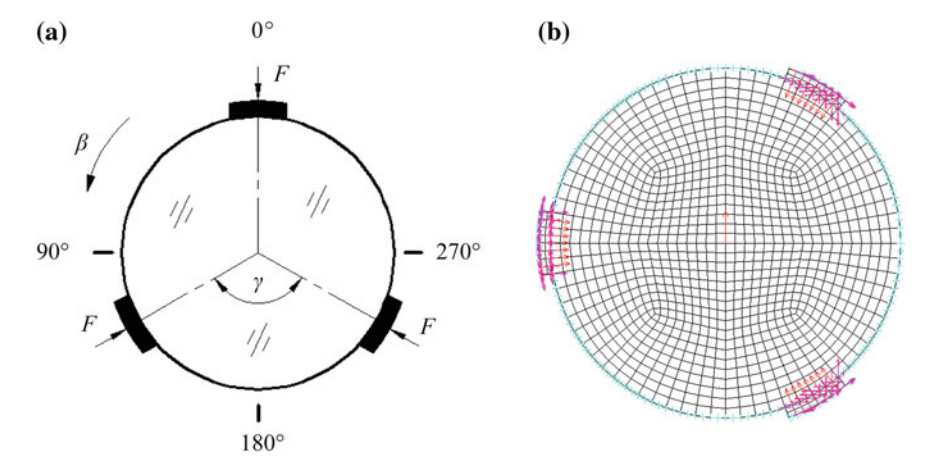


Fig. 7.12 Analysis model of prism rotation. a Motion model (initial position); b Finite element model (rotate to 90° position)

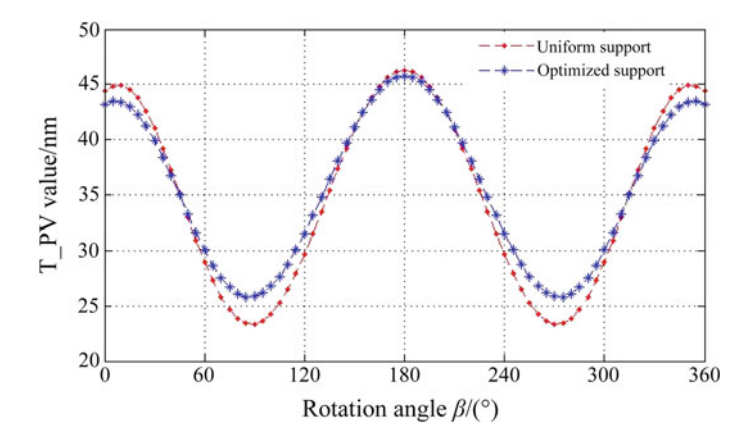


Fig. 7.13 Comparison curves of uniform support and optimized support (thin end upward)

uniform support is greater than that under the optimization support; while when the prism rotates in the ranges of $[70^{\circ}, 140^{\circ}]$ and $[220^{\circ}, 290^{\circ}]$, the deformation T_PV value under optimizing the support mode is greater than that under the uniform support way.

The above results indicate that whether the thin end of the prism is upward or downward, the optimized support way has certain advantages within several ranges of the rotation angle, and its support effect is not as good as the three-segmental support way in the rest ranges when the prism rotates from 0° to 360°. Therefore, for the static prism, the support way after optimization can improve the surface quality to a certain extent, but it is not necessarily ideal for the rotating prism.

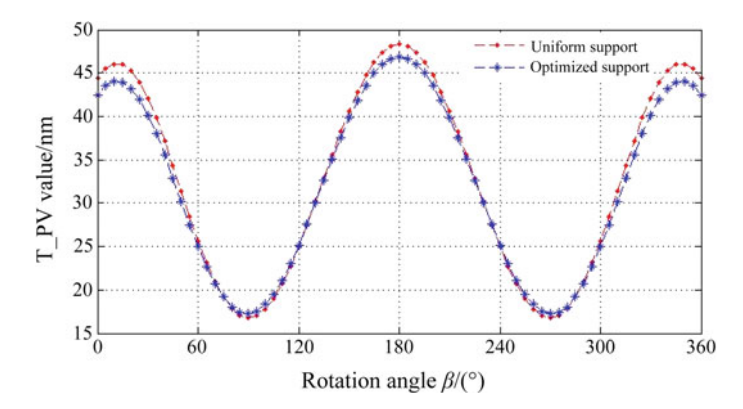


Fig. 7.14 Comparison curves of uniform support and optimized support (thin end downward)

7.1.3 Multi-segmental Support Analysis

In view of the rotating prism, it is generally considered that the method of increasing the number of segmental support surfaces is used to increase the support contact area and the surface quality can be improved.

In this section, the sensitivity of the prism to the positions of the uniform support with three, four and six support blocks is firstly analyzed. Then support effects under three, four and six blocks group for the same prism are compared to each other during the rotation process of the prism.

1. Study on Position Sensitivity of Support Blocks

Due to the multiple arrangement of multiple segments along the circumference of the prism, different uniform distribution methods will affect the prism deformation and stress in different levels, that is, the sensitivity of the prism to the uniform support block group position is different [10].

Figure 7.15 shows an analysis model for the sensitivity of the prism to the positions of support blocks. The prism is fixed with the thin end upwards, and the support blocks rotate from 0° to 360° with the step length of 5° . With the help of parametric modeling analysis by Ansys APDL language, and the powerful data processing ability of Matlab software tool, the relation curves of the T_PV value of the surface deformation and the rotation angle δ of support blocks are obtained, as shown in Fig. 7.16.

As shown in Fig. 7.16, the sensitivity of the prism to the positions of support blocks changes periodically, and the change periods of three, four and six support blocks are 120° , 90° and 60° , respectively, which are consistent with the actual situation.

Take the results of the first period for a brief analysis (other periods are the same, omitted here): The minimum T_PV value under the support of three blocks, which is 44.56 nm, occurs when support blocks rotate to the position of 0° or 120° , as the position shown in Fig. 7.15a, and it is the best support position for three segments where the prism is least sensitive to the three-segmental support way. The minimum

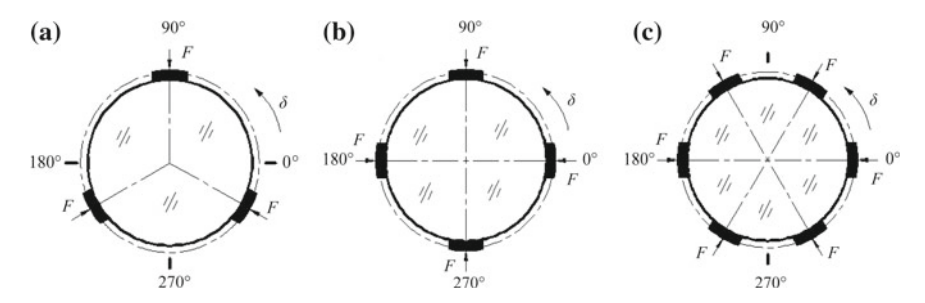


Fig. 7.15 Sensitivity analysis model of support blocks. **a** Initial position of three-segmental support; **b** Initial position of four-segmental support; **c** Initial position of six-segmental support

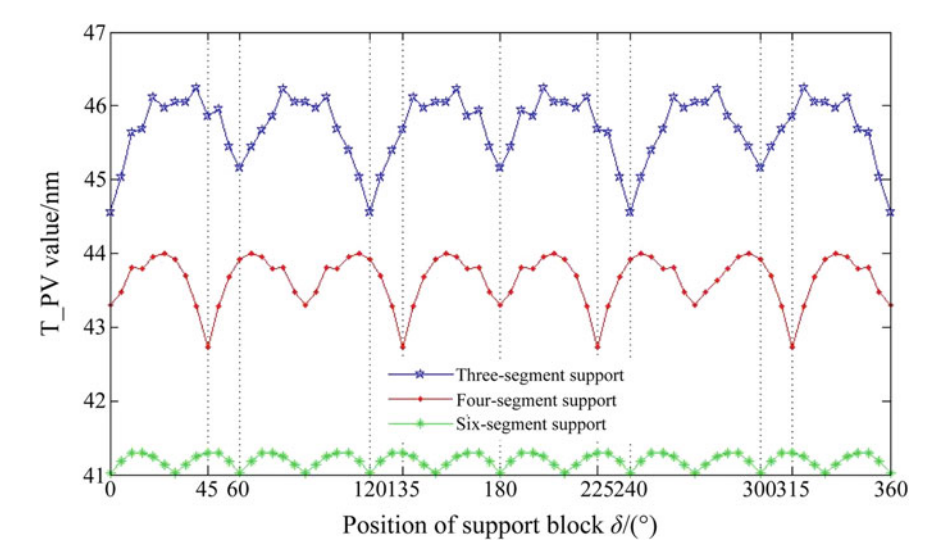


Fig. 7.16 Support effects of support blocks at different locations

T_PV value under the support of four blocks, which is 42.73 nm, occurs when support blocks rotate to the position of 45°, that is, the position where support blocks in Fig. 7.15b further rotate 45°. In this position, the surface deformation is the least sensitive to the four-segmental support way, which is the best support position for four segments. Similarly, the minimum T_PV value under the support of six blocks, which is 41.02 nm, occurs when support blocks rotate to the position of 0° or 60°, as the position shown in Fig. 7.15c, and it is the best support position for six segments where the prism is least sensitive to the six-segmental support way.

From Fig. 7.16, it can be found that the four-segmental support curve is under the four-segmental support curve and above the six-segmental support curve, which indicates that the support effect for a static prism can be improved with the number of support segments increasing.

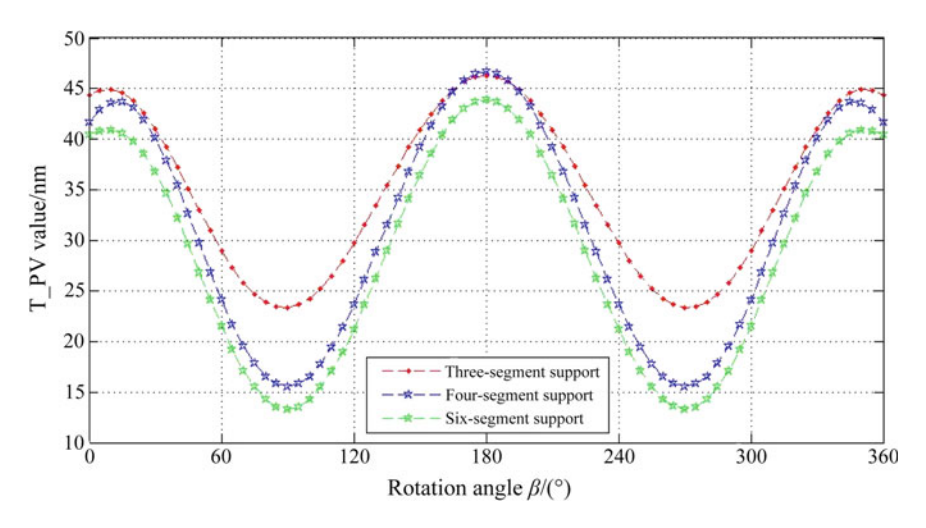


Fig. 7.17 Surface deformation under different support ways

2. Analysis of Rotation Process

After the above analysis, the optimal support positions of three, four and six support blocks are obtained. Then the surface deformation of prisms is evaluated during the prism rotation process in the rotation range of 0° – 360° and with the rotation step of 5° .

The relationship between the T_PV value of the surface deformation and the rotation angle β is shown in Fig. 7.17. As shown in Fig. 7.17, no matter whether the number of support segments is three, four or six, the maximum T_PV value of the surface deformation occurs on the rotation position of 180°, which is 46.65, 47.53 and 44.39 nm, respectively. It can be found by calculation that the T_PV range between the maximum value and the minimum value of three-segmental blocks is 22.55 nm, and that of four and six blocks is 32.05 and 30.63 nm, respectively, which indicates that the volatility of the surface deformation with three arc-shaped support blocks is relatively small during the rotation process, that is, the three-segmental support way can make a better support effect.

The following content of this chapter is mainly about the analysis of various performances of the prism with three arc-shaped support blocks.

7.1.4 Extension of Multi-segmental Support

In this section, we will investigate the support effect of multi-segmental support methods for different diameter and different wedge-angle prisms and try to find a local optimum wedge angle under the different multi-segmental support way within a certain wedge angle range.

1. Impact on Prism with Different Diameters

A large-aperture prism that has the thinnest-end thickness of 30 mm, the wedge angle of 10° and the diameter within 400–1200 mm is used for analysis. The impacts of different support methods, including three, four and six segments, on the prism are investigated. Figure 7.18 shows the relationship between the prism deformation T_PV values and different diameter under different multi- segmental supports.

As shown in Fig. 7.18, with the increase of the diameter, the T_PV value of the surface deformation is also increasing, that is, the effect of multi-segmental support ways becomes worse and worse. For example, when the clear aperture of the prism is equal to or larger than a diameter of 1000 mm, the existing multi-segmental support ways cannot meet the design requirement of the surface deformation PV values less than $1/4\lambda$ (wavelength $\lambda = 632.8$ nm).

2. Impact on Prism with Different Wedge Angles

For wedge-shaped optical prisms, increasing the wedge angle can expand the imaging field of view (FOV) and scan range and improve the operating performance of the optical system. To investigate the impact of the support way of three, four and six segments on the surface shape, a wedge-shaped prism, with thinnest-end thickness of 30 mm, diameter of 500 mm and wedge angle of 5°–30°, is selected as the analysis object. The relationship between the T_PV value of the surface deformation and the wedge angle, under different multi-segmental support ways, is shown in Fig. 7.19.

From Fig. 7.19, the surface deformation under the multi-segmental support way can meet the requirement of less than $1/4\lambda$ within the wedge angle range of 5° – 30° . The T_PV value of the surface deformation does not increase during the wedge angle increasing, instead, a minimum value occurs at a certain wedge angle. Theoretically, the surface deformation should be increasing with the increase of the prism wedge

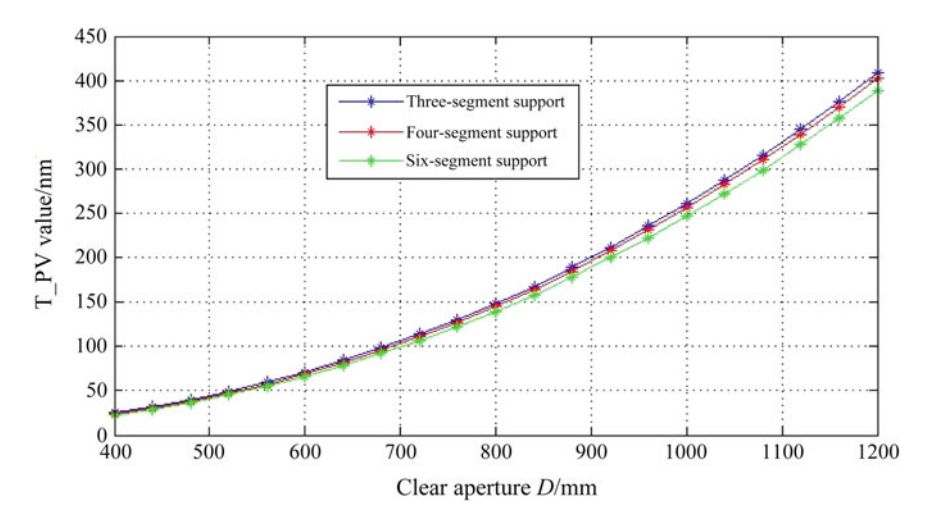


Fig. 7.18 Impact of multi-segmental support ways on the prism with different diameters

	Search region/(°)	Initial value/(°)	Optimal value/(°)	T_PV/nm
Three-segmental support	22–26	24	24.76	40.17
Four-segmental support	22–26	24	24.08	35.42
Six-segmental support	22–26	24	24.24	33.76

Table 7.5 Optimal wedge angle under different support ways

angle. However, as the wedge angle increases, the contact area between the prism facet and the support block also increases continuously, which compensates the deformation. The optimal wedge angle corresponding to the minimum T_PV value can be obtained by the following optimization method. Here, we select the wedge angle α as the design variable, the allowable stress [δ] of K9 glass as the state variable, the T_PV value of surface deformation as the objective function, and 22°–26° as the search region of the wedge angle. The optimization analysis results are shown in Table 7.5.

The above results show that three, four, and six segment support methods are suitable for the prisms with wedge angles of 24.76, 24.08, and 24.24 $^{\circ}$, respectively, within the prism wedge angle [5 $^{\circ}$, 30 $^{\circ}$].

In summary, the better surface quality of the prism in the static support can be ensured under the multi-segmental support way.

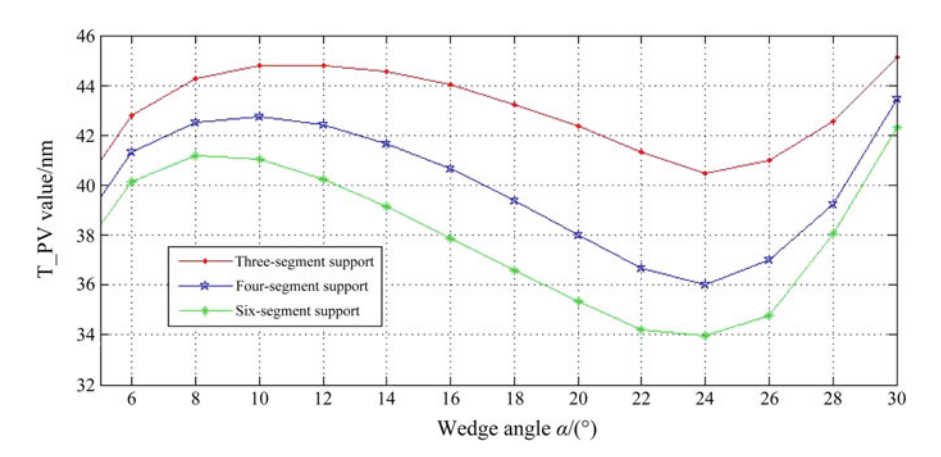


Fig. 7.19 Impact of multi-segmental support ways on the prism with different wedge angles

7.2 Dynamic Performance Analysis

In the course of dynamic motions such as tracking and scanning of a large-scale optomechanical system, the dynamic characteristics of optical elements are affected by self-weight, as well as the collision, impact and friction of the auxiliary mechanism (such as the support system), which may cause that the overall performance of the optical system cannot meet the expected design requirements. At present, the research on the structural optimization and performance analysis of optomechanical systems has been mature gradually by using the finite element method. However, most previous research focused on the statics characteristics and less on the dynamic analysis [9].

For the support structure of mirrors, Zhang et al. [13] investigated the dynamic conditions of mirrors to evaluate the surface deformation and surface quality. Xiao et al. [14] analyzed the static and dynamic characteristics of the moving reflector's mechanism with small coupling displacement according to the theories of mechanics and dynamics, which can meet the dynamic performance requirements of the mirror. Burns [15] analyzed the dynamic performance of the deformable mirror for the active support mechanism of the Gemini telescope. Although many scholars try to study the dynamic performance of the optomechanical system, an effective dynamic analysis method has not been established yet.

In this section, considering the influence of dynamic factors, ADAMS software and ANSYS software platforms are used for the dynamic simulation of the scan prism system, and the simulation results can be referred for the subsequent support performance research.

7.2.1 Dynamic Analysis Method

The dynamic analysis method employed in this section is shown in Fig. 7.20 [10].

The dynamic analysis method includes two aspects: First, the dynamic simulation of dynamic optical systems based on Adams software platform; Second, the performance analysis on the support structure of optical elements based on Ansys software platform.

The specific steps are as follows:

- (1) A simplified model of the dynamic optical system is built, and constraints, loading, and driving source are added by Adams software tool, which are used for the system dynamics analysis. After the structural dynamics solution, the load spectrum is obtained based on both the time domain and the spatial domain.
- (2) The obtained load spectrum, equivalent to external loads, is added to the optical element, and the prism surface deformation values and node dynamic response curves can be obtained.
- (3) The prism's surface shape is analyzed and evaluated. If the analysis results cannot satisfy the working requirement, the design parameters of the support

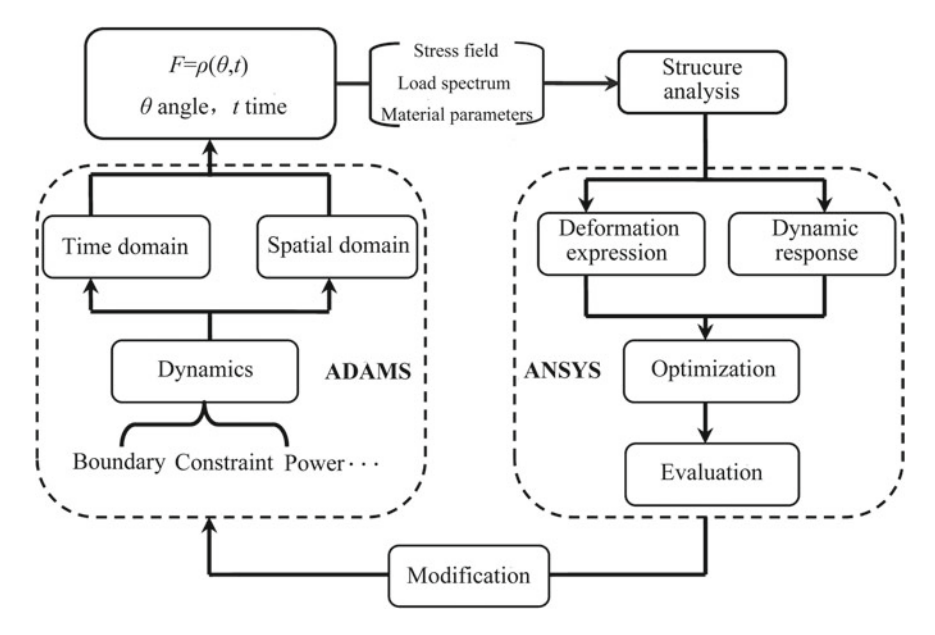


Fig. 7.20 Dynamic performance analysis method for the support structure of dynamic optical elements

should be modified to improve the system performance until it reaches the predictive accuracy requirement.

This method makes full use of the technical advantages of Adams and Ansys software tools, and fully considers external dynamic loads to make simulation conditions for the system close to an actual case, which offers a reliable reference for the subsequent test and analysis.

7.2.2 Dynamic Simulation and Analysis of Rotating Prism

In this section, the dynamic performance analysis method is used to perform the dynamic simulation analysis on the prism model under the three-segmental support way [10].

A simplified moving model of the prism system is built by Adams software tool, including a wedge-shaped prism, three support blocks, a wedge ring, and a prism cell. The prism material is K9 glass, characterized by diameter of 500 mm, wedge angle of 10° , and thinnest-end thickness of 30 mm; Support blocks adopt Nylon 66, with thickness of 15 mm and center angle of 20° ; The wedge ring and prism cell are made of 45 steel, and its size is set with the wedge-shaped prism and support blocks, omitted here.

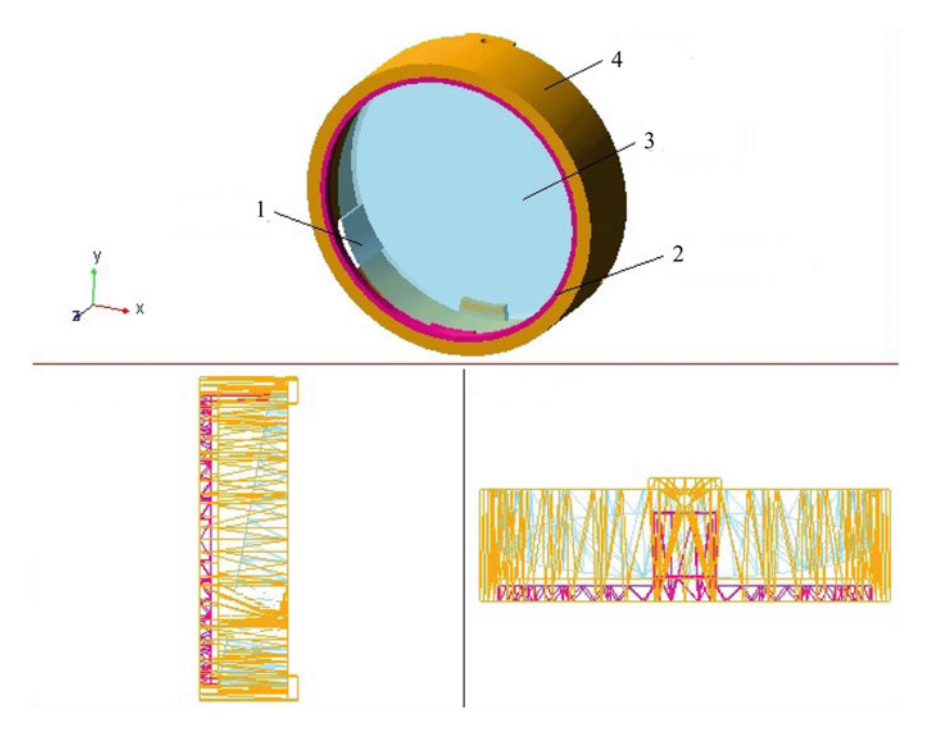


Fig. 7.21 Simplified mechanism model of the prism system where 1 is support block, 2 is prism cell, 3 is tracking mirror and 4 is wedge ring

The simplified model of the prism is established and assembled through the 3D modeling software tool Pro/Engineer, and imported into Adams to define the appearance and material of each component. The overall effect is shown in Fig. 7.21. Constraints and loads on the prism model include fixed pairs, rotating pairs, contact forces, preloads, and driving forces. Fixed pairs include JOINT_1, JOINT_2, and JOINT_3 between the support block *A*, *B*, and *C* and the cell, as well as JOINT_4 between the wedge ring and the cell. The rotating pair is added on the cell. Contact forces include CONTACT_4 and CONTACT_5 among wedge ring, cell, and prism; and the contact force between support blocks and the prism will be described in detail below. The preload FORCE_1, FORCE_2, and FORCE_3 are added on the mass center of support blocks *A*, *B*, and *C*, respectively, by 10 N along the radial direction. The gravity acceleration –9800 mm/s² is added on the whole model. Meanwhile, rotary driving is added on JOINT_ROTATE with a rotation speed of 30 (°)/s. The simulation time is set to 12 s, and the prism rotates from 0° to 360°.

During the dynamic simulation, contact forces cannot be measured in real time under normal conditions. To this end, the following steps are added in the process of adding constraints:

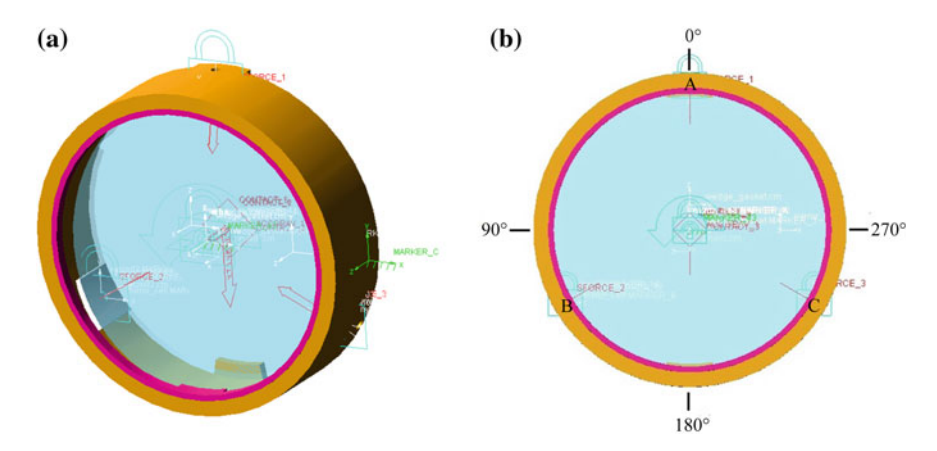


Fig. 7.22 Loading model of the prism system. a Constrain model; b Schematic diagram of the prism model

First, support blocks A, B and C are duplicated to obtain support blocks A_1 , B_1 and C_1 , and the fixed pairs, JOINT_A, JOINT_B and JOINT_C, are respectively added between the two corresponding support blocks. Supposed that support blocks A_1 , B_1 and C_1 have no mass, and then contact forces, CONTACT_A, CONTACT_B and CONTACT_C, are added between A_1 , B_1 and C_1 and the prism. Since support blocks A_1 , B_1 and C_1 have no mass, contact forces between A_1 , B_1 , C_1 and the prism are completely transmitted to support blocks A, B and C by fixed pairs JOINT_A, JOINT_B and JOINT_C, and support blocks A_1 , B_1 and C_1 have no effects on the dynamic characteristics of the prism system. By measuring the force size of the fixed pairs JOINT_A, JOINT_B and JOINT_C, the size of contact forces can be obtained in real time. Figure 7.22 shows the prism system with all constraints and loads added.

Through the dynamic simulation of the prism system, forces of the fixed pairs JOINT_A, JOINT_B and JOINT_C are extracted to obtain the simulation results as shown in Figs. 7.23, 7.24 and 7.25, which respectively shows the force F_A , F_B and F_C at support block A, B and C on the prism when the system rotates from 0° to 360° .

From Fig. 7.23, the contact force at support block A is 10.08 N when the prism rotates within the ranges of $[0^{\circ}, 73.44^{\circ}]$ and $[290.16^{\circ}, 360^{\circ}]$, i.e., only the preload applies on the prism. But when the prism rotates within the range of $[73.44^{\circ}, 290.16^{\circ}]$, the contact force at support block A gradually increases and then reduces to the preload, and a smaller value appears near the 180° position. This is because the gravity center is not at the geometric center of the prism, and the rotation prism is always subjected to an eccentric force during its rotation process; therefore, the maximum contact force at support block A occurs in the positions of 159.84° and 203.76° , that is 393.52 and 391.61 N, respectively.

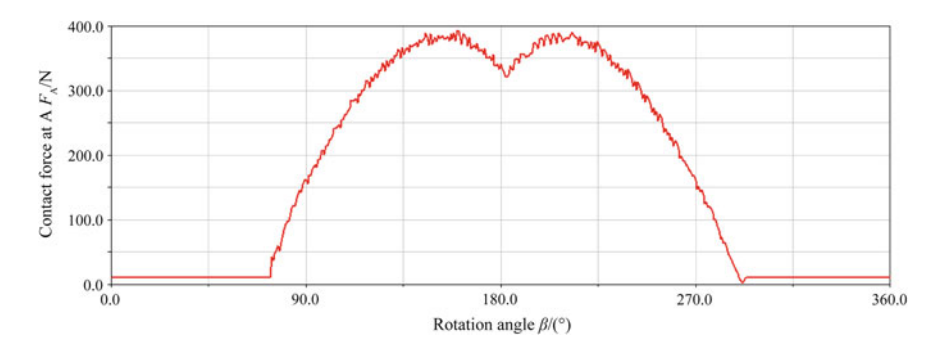


Fig. 7.23 Contact force curve at support block A

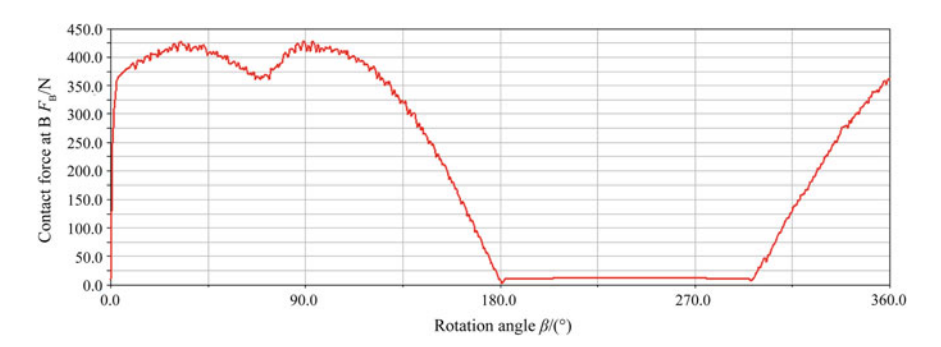


Fig. 7.24 Contact force curve at support block B

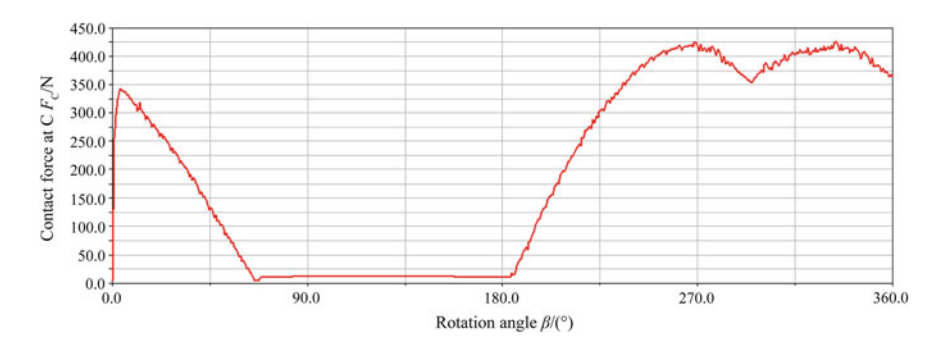


Fig. 7.25 Contact force curve at support block C

Figures 7.24 and 7.25 show the contact force at support blocks B and C. Due to the symmetric layout of two support blocks on both sides of the thick end of the prism, two contact force curves are basically symmetrical to each other. This indicates that the contact forces on support blocks B and C have identical effects, which accords with the actual situation. Maximum values at support block B occur

when the prism rotates to the 92.88° and 32.4° position—427.11 and 427.84 N, respectively. Maximum values at support block *C* occur when the prism rotates to the position of 334.08° and 269.28° —425.88 and 425.06 N, respectively.

According to the above analysis, the support forces in the case of three support blocks for the prism can be obtained when the prism rotates from 0° to 360° , and the force value under the worst condition is extracted. The PV values of the surface deformation under several worst conditions are calculated and analyzed as follows.

Due to the wedge-shaped structure of the prism, the direction of forces at support blocks for the prism does not point to the geometric center. Therefore, when performing the surface deformation analysis in Ansys software tool, the support force values need to be extracted along the X and Y directions (force along the Z direction is substantially unstressed, so not considered), with the aim of adding constraints and loads. Table 7.6 lists the support force components along the X and Y directions at support blocks A, B and C, for the prism under the six worst conditions during dynamic rotation.

As an example of the finite element analysis process, only one worst condition of the prism rotating to 32.4° is presented as follows. First, we set the material parameters of K9, establish a parametric model of the rotating prism (thin end upward), and counterclockwise turn the model by 32.4° . We use a SOLID95 unit with 20 s in Ansys software tool to mesh the finite element model, and divide the prism into 72 and 4 equal parts along the circumference and the axial direction, respectively. We apply support force of 5.19 N and -8.45 N along the *X* and *Y* directions at the nodes of support block *A*, apply force of 215.38 and 368.82 N along the *X* and *Y* directions at nodes of support block *B*, and apply support force of -209.93 N and -3.21 N along the *X* direction and the *Y* direction at the nodes of support block *C*. Meanwhile, the axial constraint and tangential constraints are added on the edges of the two sides of the prism, but excluding the corresponding location area of three support blocks. Gravity acceleration of 9.8 m/s 2 is applied on the model. The full model is shown in Fig. 7.26.

Table 7.0 Support to	ices along in	e A and I di	rections at st	ipport blocks	A, b and C	for the prism
Rotation angle $\beta/(^{\circ})$	32.40		92.88		159.84	
Force direction	X	Y	X	Y	X	Y
Force at A F _A /N	5.19	-8.45	177.20	-2.61	149.64	363.88
Force at B F _B /N	215.38	368.82	-216.72	368.89	-164.95	-28.40
Force at C F _C /N	-209.93	-3.21	4.56	9.64	-6.32	8.53
Rotation angle $\beta/(^{\circ})$	213.84		269.28		334.08	
Force direction	X	Y	X	Y	X	Y
Force at A F _A /N	-226.24	311.06	-167.12	-12.81	4.24	8.98
Force at B F _B /N	4.34	9.81	-4.89	9.52	247.34	25.04
Force at C F _C /N	232.96	23.09	201.15	374.49	-250.47	343.42

Table 7.6 Support forces along the X and Y directions at support blocks A, B and C for the prism

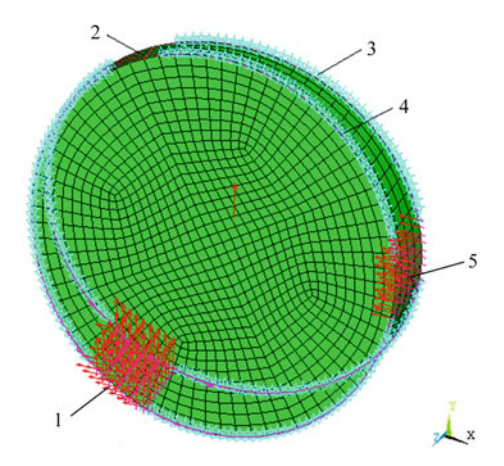


Fig. 7.26 Finite element model of prism (32.4° position) where 1 is block B position, 2 is block A position, 3 is plane facet, 4 is wedge facet and 5 is block C position

Table 7.7 PV Values	Table 7.7 PV Values of Surface Deformation (nm) and Von Mises Values (MPa)						
Rotation angle $\beta/(^{\circ})$	32.40	92.88	159.84	213.84	269.28	334.08	
The PV value on the plane facet/nm	26.42	42.13	103.16	98.64	39.02	26.31	
The PV value on the wedge facet/nm	52.27	62.58	61.14	74.38	61.31	56.49	
The von Mises stress/MPa	0.216	0.218	0.434	0.424	0.208	0.206	

For prisms in the other five cases, we perform the same finite element analysis. The PV values of the surface deformation and the von Mises equivalent stress values can also be obtained, as shown in Table 7.7. As we can see from the table, when the prism rotates to 159.84°, the PV value on the plane facet reaches a maximum value of 103.16 nm, and when it rotates to 213.84°, the PV value on the wedge facet has a maximum value of 74.38 nm. At the wavelength $\lambda = 632.8$ nm, the three-segmental support can meet the requirement of dynamic surface deformation of less than $\lambda/4$ (our design requirement).

Figures from 7.27, 7.28, 7.29, 7.30, 7.31, and 7.32 are the contour charts of the prism deformation on the plane facet and the wedge facet under dynamic working conditions of 32.40°, 92.88°, 159.84°, 213.84°, 269.28° and 334.08°, respectively.

Comparing Fig. 7.17 to Table 7.7, it can be found that the PV value of the surface deformation under the six worst conditions, obtained by the dynamic analysis method, is much greater than that obtained by the static analysis (In the static analysis ysis: the PV value on the plane facet is 23.06 nm, and the PV value on the wedge facet is 22.02 nm). Since the friction, impact, inertia and other dynamic factors are considered in dynamic analysis, it can nearly reflect the deformation changes over the full rotation under actual rotation conditions.

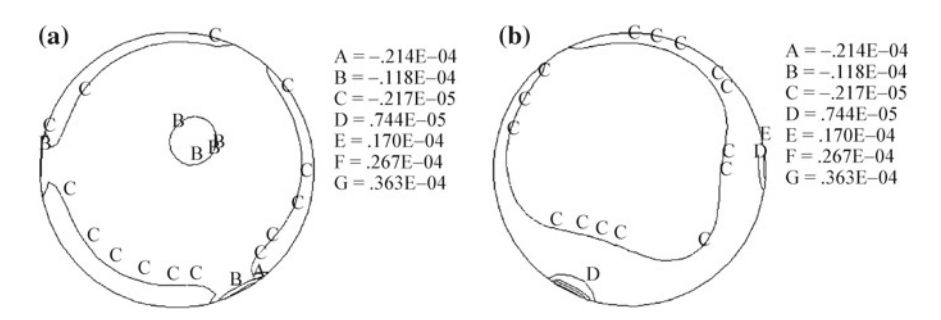


Fig. 7.27 Contour chart of prism deformation (32.40° dynamic working condition). **a** On the plane facet; **b** On the wedge facet

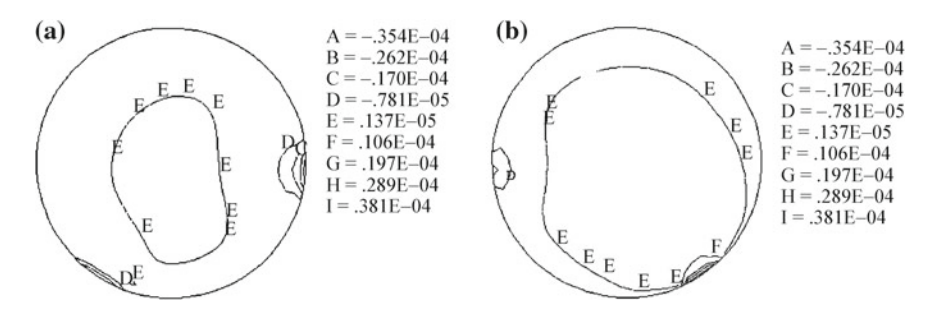


Fig. 7.28 Contour chart of prism deformation (92.88° dynamic working condition). **a** On the plane facet; **b** On the wedge facet

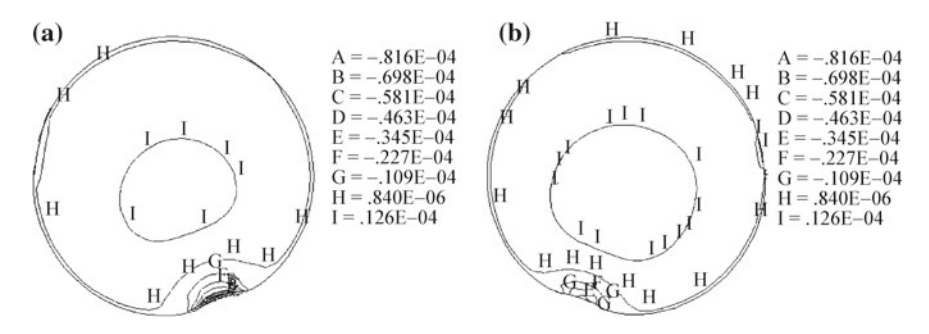


Fig. 7.29 Contour chart of prism deformation (159.84° dynamic working condition). a On the plane facet; b On the wedge facet

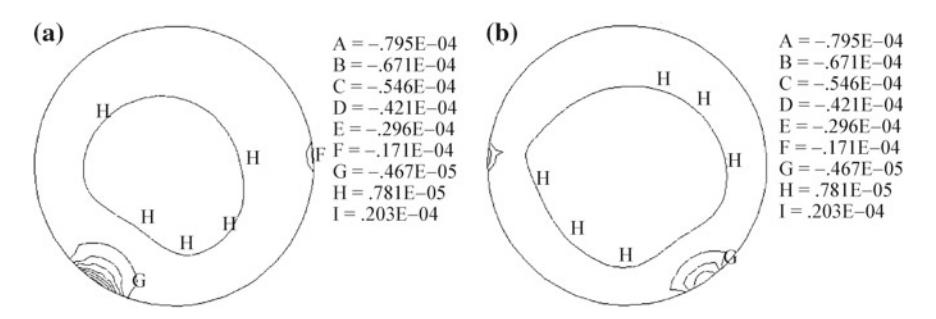


Fig. 7.30 Contour chart of prism deformation (213.84° dynamic working condition). **a** On the plane facet; **b** On the wedge facet

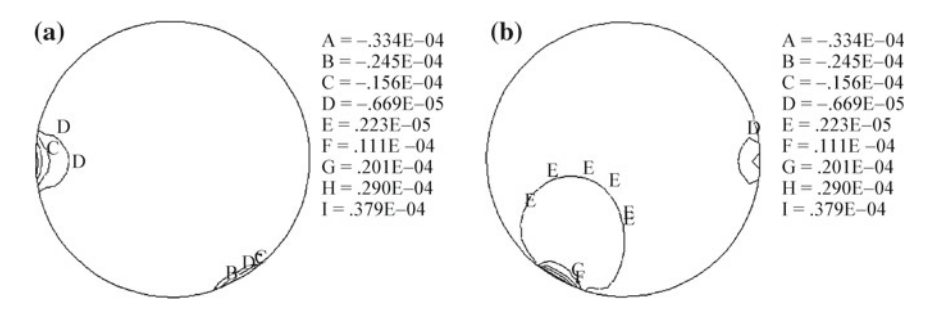


Fig. 7.31 Contour chart of prism deformation (269.28° dynamic working condition). a On the plane facet; b On the wedge facet

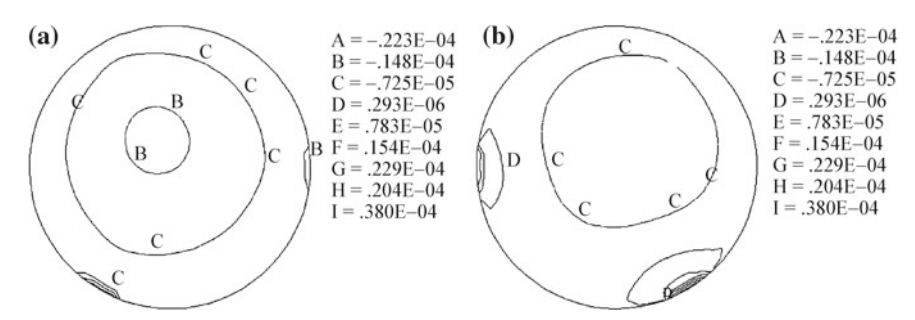


Fig. 7.32 Contour chart of prism deformation (334.08° dynamic working condition). **a** On the plane facet; **b** On the wedge facet

7.3 Deformation Value Fitting of Prism Surface

The optical elements of the optomechanical system are prone to produce surface deformations under the action of self-weight and external loads, which can lead to concentricity changes and wavefront distortions of the optical system and then affects the optical properties of the entire system. In order to investigate the wavefront

aberration, it is necessary to perform the deformation value fitting on the surface shape. The wavefront of the prism surface always tends to be smooth and continuous, so changes of the surface deformation can be represented by a linear combination of complete base functions or a combination of linearly independent base functions. The method of fitting surface deformation values with Zernike polynomials has been widely used in optical design software, interference detections and engineering projects. Zernike polynomials are linearly independent and orthogonal to each other, which can describe the wavefront boundary of the circular aperture, uniquely and normatively. In addition, Zernike polynomials have some correspondence with the primary aberration and are easy to establish contact with the Seidel aberration in the optical design. In practical optical experiments, the wavefront data is usually made up of a mixture of multiple aberrations. By the Zernike polynomial fitting method, it is easy to obtain the specific data information of various wavefront aberrations, which provides an effective method to solve the aberration coefficients and optimize the system performance.

In this section, prism surface is the main research object. In addition to the analysis of the Zernike polynomial and its fitting algorithm, the surface deformation is calculated under different static and dynamic conditions by the first 15 items of the Zernike polynomial, and is compared with the surface deformation of the actual simulation. In the meantime, errors of the PV and RMS values of the surface deformation are calculated, which can be used to evaluate the fitting precision.

7.3.1 Zernike Polynomial Fitting Theory

1. Aberration Introduction

Generally, the actual optical system is different from the ideal one. The light emitted from a point of space passes through the actual optical system and does not converge at a point of the image space but forms a diffuse spot, of which the size is related to the aberration system.

In the theory of wave optics, the spherical wave emitted by an object point within the paraxial region still remains a spherical wave after propagating through the optical system. Due to the presence of diffraction phenomena, the ideal of an object is like a complex Airy disk. For an actual optical system, due to the presence of aberrations, the wavefront formed by the optical system is not a spherical surface. The deviation value between the actual wave surface and the ideal wave surface is defined as the wave aberration, and its size can be directly used to evaluate the imaging quality of the optical system.

Generally speaking, it is a conventional method to describe the aberration of an optical system in the form of power series expansions. Since the form of Zernike polynomials is consistent with that of aberration polynomials obtained from the optical detection, it is often applied to describe wavefront characteristics.

2. Zernike Polynomial Expression

The polar coordinate expression of the Zernike polynomial is [16]:

$$W_n^k(\rho,\theta) = R_n^k(\rho) \cdot \Theta_n^k(\theta) \tag{7.1}$$

where $R_n^k(\rho)$ is an item only related to the radial direction; $\Theta_n^k(\theta)$ is an item only related to the amplitude angle; n is the order of the polynomial; k is a sequence number related to n, and its value is constant with the parity of n but its absolute value is less than or equal to n. If we define k = n - 2m, the expression of $R_n^k(\rho)$ is:

$$R_n^{n-2m}(\rho) = \begin{cases} \sum_{s=0}^m (-1)^s \frac{(n-s)!}{s!(m-s)!(n-m-s)!} \rho^{n-2s}, & (n-2m \ge 0) \\ R_n^{|n-2m|}, & (n-2m < 0) \end{cases}$$
(7.2)

The expression of $\Theta_n^k(\theta)$ is:

$$\Theta_n^{n-2m}(\theta) = \begin{cases} \cos[(n-2m)\theta], & (n-2m \ge 0) \\ -\sin[(n-2m)\theta], & (n-2m < 0) \end{cases}$$
 (7.3)

According to $R_n^k(\rho)$ and $\Theta_n^k(\theta)$, the specific expression of each Zernike polynomial item can be written out.

In Cartesian coordinates, the Zernike polynomial with n items can be expressed as follows:

$$V(x, y) = \sum_{k=0}^{n} a_k Z_k(x, y) = a_1 Z_1(x, y) + a_2 Z_2(x, y) + \dots + a_n Z_n(x, y)$$
 (7.4)

where n is the item number of the Zernike polynomial; a_k is the coefficient of kth item in the Zernike polynomial; Z_k (x,y) is the kth item of the Zernike polynomial; x and y are the coordinate of data points.

The item number of the Zernike polynomial in (7.4) is based on the actual situation, and it is not a correct fact that the more the item number, the higher the fitting precision is. In this section, the first 15 items of the Zernike polynomial are finally selected to fit the surface deformation of the tracking mirror, after the preliminary fitting program debugging. The expressions of the first 15 items of the Zernike polynomial in Cartesian coordinates are shown in Table 7.8.

There are many ways to fit the surface, such as triangular patches, cubic B-spline surfaces and so on. The Zernike polynomial is usually selected as the base function to fit the measured wavefront. That is because the Zernike polynomial also possesses several important features except for the highest precision of the fitting wavefront [16]:

Item number	Expression of Zernike kth	Item number	Expression of Zernike kth
k	item	k	item
1	1	9	$\sqrt{8}(3x^2 - y^2)y$
2	2x	10	$\sqrt{8}(3x^2 - y^2)x$
3	2y	11	$\sqrt{5}[6(x^2+y^2)^2-6(x^2+y^2)+1]$
4	$\sqrt{3}(2x^2 + 2y^2 - 1)$	12	$\sqrt{10}(4x^2 + 4y^2 - 3)(x^2 - y^2)$
5	$2\sqrt{6}xy$	13	$2\sqrt{10}(4x^2 + 4y^2 - 3)xy$
6	$\sqrt{6}(x^2 - y^2)$	14	$\sqrt{10}(x^4 - 6x^2y^2 + y^4)$
7	$\sqrt{8}(3x^2 + 3y^2 - 2)y$	15	$4\sqrt{10}(x^2 - y^2)xy$
8	$\sqrt{8}(3x^2 + 3y^2 - 2)x$		

Table 7.8 The expressions of the first 15 items of Zernike polynomial in Cartesian coordinates

- (1) Each item of the Zernike polynomial has a specific physical meaning, corresponding to the primary aberration, and is easy to establish contact with the Seidel aberrations habitually used in the optical design.
- (2) Each item is orthogonal in the unit circle, that is:

$$\int_{0}^{1} \int_{0}^{\pi} W_{n}^{k}(\rho, \theta) W_{n}^{q}(\rho, \theta) \rho d\rho d\theta = \begin{cases} \frac{\pi}{n+1} \delta, & (n=m, k=q) \\ 0, & (n \neq m, k \neq q) \end{cases}$$
(7.5)

where $W_n^k(\rho,\theta)$ and $W_n^q(\rho,\theta)$ are arbitrary two items of the Zernike polynomial; When k=0, $\delta=1$, and when $k\neq 0$, $\delta=0.5$. The orthogonality of the Zernike polynomial makes the coefficients of fitting polynomials independent of each other to avoid the interference of accidental factors.

- (3) The Zernike polynomial also has the unique rotational symmetry (Namely, the polynomial expression remains constant as it rotates around the origin), which makes it convergences well in the solving process of optical problems. Therefore, the Zernike polynomial is ideally suited for the error fitting of the surface deformation on the circular optical mirror.
- (4) When the Zernike polynomial is used as the data interface of programs, it can compress a large amount of data with good compatibility, and the expressed data is more intuitive.

3. Fitting Algorithm

It is the most crucial step for the deformation value fitting to solve the fitting coefficient of the Zernike polynomial. If the fitting coefficient a_k cannot be found out correctly, the subsequent deformation value fitting and aberration analysis will become meaningless. The methods commonly used to solve the fitting coefficient include: Gram-Schmidt orthogonalization method, Covariance matrix method, Householder transformation method, least squares method and so on [16].

(1) Gram-Schmidt Orthogonalization Method

A set of orthogonal base functions U can be expressed as follows:

$$U = BZ \tag{7.6}$$

where B is the coefficient matrix of the element b_{ij} ; Z is a Zernike polynomial; Elements in U satisfy the following conditions:

$$\sum_{\eta} U_{l_1} U_{l_2} = \begin{cases} 0, \ l_1 \neq l_2 \\ 1, \ l_1 = l_2 \end{cases}$$
 (7.7)

where η is the concentration of discrete data points.

 b_{ij} can be given by Gram-Schmidt orthogonalization, that is:

$$b_{ij} = \begin{cases} 0, & i < j \\ \left(\sum_{\eta} Z_i^2 - \sum_{l=1}^{i-1} \left(\sum_{\eta} Z_i U_l\right)^2\right)^{1/2} \right), & i = j \\ -\sum_{l=1}^{i-1} b_{ii} b_{lj} \left(\sum_{\eta} Z_i U_l\right), & i > j \end{cases}$$
(7.8)

From (7.4) and (7.6), we can get:

$$V(x, y) = \mathbf{A}^{\mathrm{T}} \mathbf{Z} = \mathbf{A}^{\mathrm{T}} \mathbf{B}^{-1} \mathbf{U} = \mathbf{C}^{\mathrm{T}} \mathbf{U}$$
(7.9)

where A is the Zernike coefficient matrix; $C^{T} = A^{T}B^{-1}$.

From (7.9) we can get:

$$\boldsymbol{U}^{\mathrm{T}}\boldsymbol{C} = \boldsymbol{V}^{\mathrm{T}} \tag{7.10}$$

Two sides of the above formulas left multiply by U:

$$UU^{\mathsf{T}}C = UV^{\mathsf{T}} \tag{7.11}$$

Since U is an orthogonal matrix, $UU^{T} = E$, then we can obtain $C = UV^{T}$. Combined with $C^{T} = A^{T}B^{-1}$, the fitting coefficient of the Zernike polynomial, $A = (VU^{T}B)^{T}$, can be obtained.

(2) Householder Transformation Method

Householder transformation is also known as reflection transformation or mirrorinjection, which is defined as follows:

$$\boldsymbol{H} = 1 - 2\boldsymbol{u}\boldsymbol{u}^{\mathrm{T}} \tag{7.12}$$

where u is a column vector, $u \in \mathbb{R}^n$. From the above definitions, we can see that the matrix H has three characteristics: orthogonality ($HH^{T} = E$), symmetry ($H = H^{T}$) and involutivity ($\mathbf{H}^2 = \mathbf{E}$).

The following two important theorems are often used in the Householder transformation method:

- (1) Set $u \neq 0$, let $\rho = 1/2||u||^2$, then $H = 1 \rho^{-1}uu^{\mathrm{T}}$ is a Householder matrix.
- (2) Set $x \in \mathbb{R}^n$, $\sigma = \pm ||x||$, and assume $x \neq -\sigma e$, then a Householder matrix H can be found to make $\mathbf{H}\mathbf{x} = -\sigma \mathbf{e_1}$, where $\mathbf{e_1} = (1, 0, ..., 0)^{\mathrm{T}}$.

With the help of two theorems above, corresponding algorithms can be programmed to orthogonalize the measurement matrix **Z** of the Zernike polynomial, and the ill-condition of the equations can be avoided to work out the coefficient matrix A of the Zernike polynomial.

(3) Covariance Matrix Method

Actually, the covariance matrix method is a simplified Gram-Schmidt method, which avoids the orthogonalization process, and the fitting coefficient a_i is worked out by a linear transformation of the covariance matrix of the Zernike polynomial Z.

 D_{ij} is defined as the covariance between Z_i and Z_j , set

$$D_{kl} = \frac{1}{n} \sum_{i=1}^{m} (Z_{ki} - \bar{Z}_k)(Z_{li} - \bar{Z}_l)$$
 (7.13)

where $\bar{Z}_j = \frac{1}{m} \sum_{i=1}^m Z_{ji} (j=1,2,...,n)$, and $D_{kl} = D_{lk}$. When the n items of the Zernike polynomial are fitted by using the Gram-Schmidt method, the matrix consisting of the first *n* rows in the covariance matrix is:

$$\begin{bmatrix} D_{11} & D_{12} & \cdots & D_{1n} & D_{1,n+1} \\ D_{21} & D_{22} & \cdots & D_{2n} & D_{2,n+1} \\ \vdots & \vdots & \ddots & \vdots & \vdots \\ D_{n1} & D_{n2} & \cdots & D_{nn} & D_{n,n+1} \end{bmatrix}$$

The following matrix equation can be constructed:

$$\begin{bmatrix} D_{11} & D_{12} & \cdots & D_{1n} \\ D_{21} & D_{22} & \cdots & D_{2n} \\ \vdots & \vdots & \ddots & \vdots \\ D_{n1} & D_{n2} & \cdots & D_{nn} \end{bmatrix} \begin{bmatrix} a_1 \\ a_2 \\ \vdots \\ a_n \end{bmatrix} = \begin{bmatrix} D_{1,n+1} \\ D_{2,n+1} \\ \vdots \\ D_{n,n+1} \end{bmatrix}$$
(7.14)

The fitting coefficient a_i of the Zernike polynomial can be obtained by solving the above equations. Furthermore, the smooth and continuous fitting function of the surface deformation can be worked out.

(4) Least Squares Method

Different from the above algorithms, the least squares method is more concise and faster. For example, the Householder transformation method, with larger computational complexity, is very complicated and cumbersome. In many references, the Gram-Schmidt orthogonalization method is recommended because serious ill-conditions of the coefficient matrix of the canonical equation in the least squares method can be avoided. In fact, the stability of the Gram-Schmidt orthogonalization method and that of the least squares method are consistent in solving the fitting coefficients of the Zernike polynomial. Namely, with the same order of the Zernike polynomial, the Gram-Schmidt orthogonalization method is also unable to work out the correct coefficients if the serious ill-condition of the canonical equation appears when using the least squares method. Therefore, the least squares method with a simple algorithm is used to fit the surface deformation in this paper.

7.3.2 Surface Fitting

1. Fitting Principle

After the static analysis on the prism by Ansys software, some information can be obtained by programming, such as coordinates of surface nodes and deformation values, which mainly includes: the coordinate of each node on the surface before deformation x_{1i} , y_{1i} , z_{1i} (i = 1, 2, 3, ..., m), the difference between the nodes before and after deformation Δx_{1i} , Δy_{1i} , Δz_{1i} (i = 1, 2, 3, ..., m). Where m is the number of surface nodes.

In the finite element model, Z axis is set as the optical axis of the prism, let

$$\begin{cases} x_i = x_{1i} + \Delta x_{1i} \\ y_i = y_{1i} + \Delta y_{1i} \\ \Delta z_i = \Delta z_{1i} \end{cases}$$
 (7.15)

 x_i , y_i , Δz_{1i} are substituted into the Zernike polynomial, to obtain the following equations:

$$\begin{cases} a_1 Z_1(x_1, y_1) + a_2 Z_2(x_1, y_1) + \dots + a_n Z_n(x_1, y_1) = \Delta Z_1 \\ a_1 Z_1(x_2, y_2) + a_2 Z_2(x_2, y_2) + \dots + a_n Z_n(x_2, y_2) = \Delta Z_2 \\ \vdots \\ a_1 Z_1(x_m, y_m) + a_2 Z_2(x_m, y_m) + \dots + a_n Z_n(x_m, y_m) = \Delta Z_m \end{cases}$$

$$(7.16)$$

Namely,

$$\begin{bmatrix} Z_{1}(x_{1}, y_{1}) & Z_{2}(x_{1}, y_{1}) & \cdots & Z_{n}(x_{1}, y_{1}) \\ Z_{1}(x_{2}, y_{2}) & Z_{2}(x_{2}, y_{2}) & \cdots & Z_{n}(x_{2}, y_{2}) \\ \vdots & \vdots & \ddots & \vdots \\ Z_{1}(x_{m}, y_{m}) & Z_{2}(x_{m}, y_{m}) & \cdots & Z_{n}(x_{m}, y_{m}) \end{bmatrix} \begin{bmatrix} a_{1} \\ a_{2} \\ \vdots \\ a_{n} \end{bmatrix} = \begin{bmatrix} \Delta Z_{1} \\ \Delta Z_{2} \\ \vdots \\ \Delta Z_{m} \end{bmatrix}$$
(7.17)

It can be further written into a matrix form:

$$\mathbf{Z}\mathbf{A} = \mathbf{Q} \tag{7.18}$$

where **Z** is a $m \times n$ matrix, the element $z_{ij} = Z_j(x_i, y_i)$, (i = 1, 2, 3, ..., m; j = 1, 2, 3, ..., n); $\mathbf{A} = (a_1, a_2, ..., a_n)^{\mathrm{T}}$; $\mathbf{Q} = (\Delta Z_1, \Delta Z_2, ..., \Delta Z_m)^{\mathrm{T}}$.

The matrix \mathbf{Z} in (7.18) represents the expression of each Zernike polynomial item of all the extracted nodes. \mathbf{Q} indicates the deformation of all nodes along the optical axis direction of the tracking prism, which can be obtained from results of the finite element analysis and it is a known quantity. The matrix \mathbf{A} is the coefficient of each Zernike polynomial item that needs to be solved, which is an unknown quantity. There are many ways to solve the matrix equations above, among them, a simple and fast method, the least squares method, is used to solve the matrix equation of (7.18). After finding the Zernike polynomial coefficients, the wavefront function of the surface fitting can be obtained by substituting these coefficients into (7.4).

2. Process of Deformation Value Fitting

Deformation value fitting of the prism surface mainly incorporates three aspects: calculation of Zernike Polynomial coefficients, construction of surface wavefront functions and mapping of fitting wavefront surfaces. Among them, the calculation of Zernike polynomial coefficients is most crucial.

The solving process of Zernike coefficients consists of two parts: data extraction and coefficient solving, respectively. In the part of data extraction, firstly the finite element model of the prism is established, and the solving and analysis are performed on it. Then data files of the surface deformation are output through APDL programming, including the node coordinates before deformation and the coordinate differences before and after deformation. In the part of coefficient solving, firstly the data in files is sorted into the data which serves for the Zernike polynomial fitting, then the matrix equation of fitting coefficients is constructed by using Matlab programming. Finally, fitting coefficients of the Zernike polynomial can be obtained.

The wavefront function of surface fitting can be constructed after solving the Zernike polynomial coefficients. Firstly, the fitting data region is selected according to the aperture size of the fitting surface. Then, aberration items of the Zernike polynomial are determined (In this chapter, the first 15 items of the Zernike polynomial are selected for the deformation value fitting), and the wavefront function of surface fitting can be obtained by substituting Zernike coefficients into the aberration items. Finally, according to the wavefront function, the cloud picture can be drawn, and

	Fitting coefficient of plane facet a_i	Fitting coefficient of wedge facet a_i	Corresponding Seidel aberration
1	-9.27525879	-9.01854778	Translation
2	0.00768386	0.00823912	X-axis tilting
3	-0.00705914	-0.00140176	Y-axis tilting
4	0.00004680	0.00004330	Defocusing
5	0.00000511	0.00000577	Astigmatism (0° or 90°)
6	0.00000446	-0.0000140	Astigmatism (45°)
7	0.00000002	0.00000002	X-axis coma
8	0.00000004	-0.00000003	Y-axis coma
9	0.00000001	0.00000001	Spherical aberration

Table 7.9 Fitting coefficients of Zernike polynomial (the first 9 items, 32.40° static working condition)

the PV and RMS values of the surface deformation fitting are worked out for the subsequent evaluation and comparison.

3. Fitting Examples of Surface Deformation

The surface deformation of the prism under static and dynamic conditions is fitted, respectively, which is compared and analyzed with the actual simulation cloud picture. Here we set D=400 mm as the fitting diameter of the surface. Deformation value fitting of the prism surface and precision evaluation are performed respectively, under 32.40° static working condition, 32.40° dynamic working condition, 159.84° dynamic working condition and 268.28° dynamic working condition [10].

(1) 32.40° Static Working Condition

The finite element model of the prism is established under static working conditions and the surface deformation data is output after meshing, adding constraints, loading and solving for the finite element model. After fitting surface deformation by the first 15 items of the Zernike polynomial, Table 7.9 lists fitting coefficients of the Zernike polynomial (the first 9 items), Fig. 7.33b shows the fitting wavefront on the plane facet, and Fig. 7.34b shows the fitting wavefront on the wedge facet.

From Figs. 7.33 and 7.34, on the plane facet of the prism, the fitting surface deformation value is PV = 9.2903 nm and RMS = 6.5421 nm, while the deformation value found by actual simulation is PV = 9.8235 nm and RMS = 6.6946 nm, the relative errors of which are 5.43 and 2.28%, respectively. on the wedge facet of the prism, the fitting surface deformation value is PV = 11.5088 nm and RMS = 5.4027 nm, while the deformation value found by actual simulation is PV = 12.6117 nm and RMS = 5.1205 nm, the relative errors of which are 8.75 and 5.51%, respectively. The results are shown in Table 7.10.

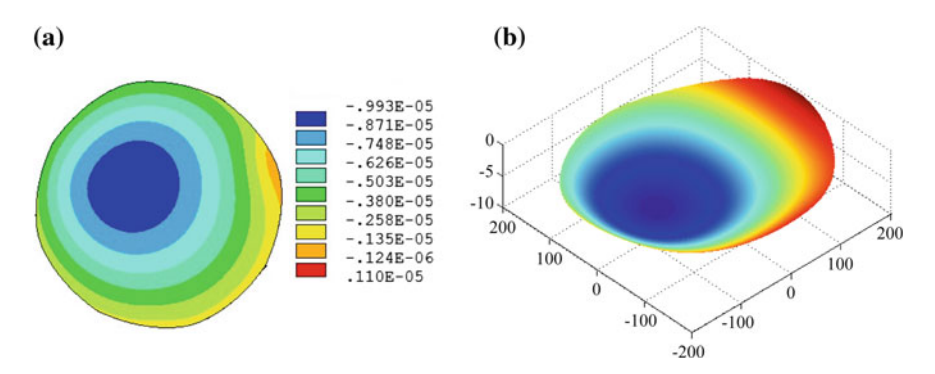


Fig. 7.33 Surface deformation comparison of the plane facet. a Actual simulation result; b Fitting result

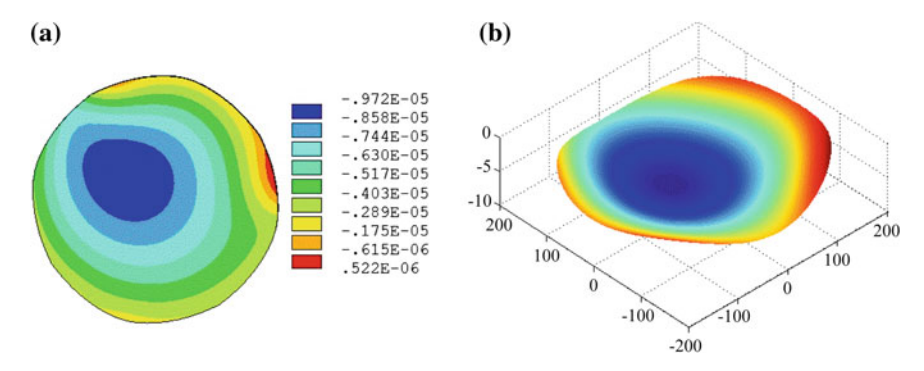


Fig. 7.34 Surface deformation comparison of the wedge facet. a Actual simulation result; b Fitting result

	Actual simulation result	Fitting result	Error (%)
PV value of plane facet/nm	9.8235	9.2903	5.43
RMS value of plane facet/nm	6.6946	6.5421	2.28
PV value of wedge facet/nm	12.6117	11.5088	8.75
RMS value of wedge facet/nm	5.1205	5.4027	5.51

Table 7.10 Comparison of surface deformation quality (32.40° static working condition)

(2) 32.40° Dynamic Working Condition

Adopting the same method as 32.40° static working condition, the surface deformation of the prism is fitted under 32.40° dynamic working condition. Table 7.11, which is the fitting coefficient of the Zernike polynomial (the first 9 items), Fig. 7.35b, the

	Fitting coefficient of plane facet a_i	Fitting coefficient of wedge facet a_i	Corresponding Seidel aberration
1	-11.72738175	-10.37480657	Translation
2	0.00602637	0.00962927	X-axis tilting
3	-0.01195571	-0.01327648	Y-axis tilting
4	0.00006018	0.00005777	Defocusing
5	0.00001311	0.00002028	Astigmatism (0° or 90°)
6	0.00000113	0.00001285	Astigmatism (45°)
7	0.00000004	0.00000004	X-axis coma
8	-0.00000002	-0.00000007	Y-axis coma
9	0.00000002	-0.00000001	Spherical aberration

Table 7.11 Fitting coefficients of Zernike polynomial (the first 9 items, 32.40° dynamic working condition)

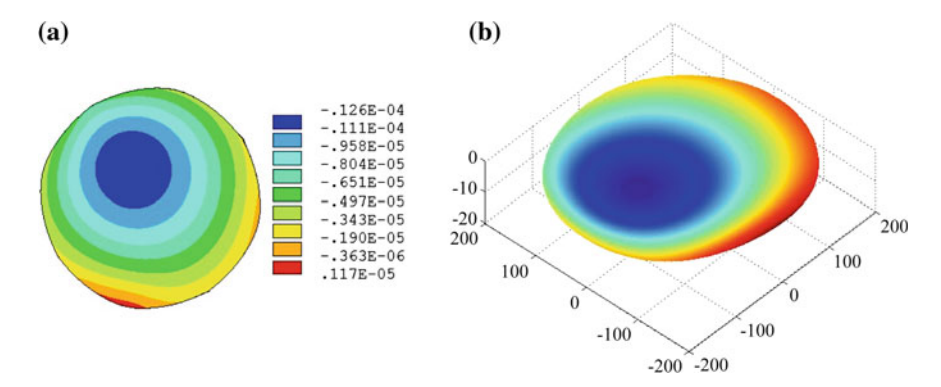


Fig. 7.35 Surface deformation comparison of the plane facet. a Actual simulation result; b Fitting result

fitting wavefront on the plane facet, and Fig. 7.36b, the fitting wavefront on the wedge facet, can be obtained respectively.

From Figs. 7.35 and 7.36, on the plane facet of the prism, the fitting surface deformation value is PV = 11.7735 nm and RMS = 8.2544 nm, while the deformation value found by actual simulation is PV = 12.6309 nm and RMS = 8.4458 nm, the relative errors of which are 6.79 and 2.27%, respectively. On the wedge facet of the prism, the fitting surface deformation value is PV = 13.0424 nm and RMS = 7.2463 nm, while the deformation value found by actual simulation is PV = 13.7399 nm and RMS = 7.4167 nm, the relative errors of which are 5.08 and 2.30%, respectively. The results are shown in Table 7.12.

(3) 159.84° Dynamic Working Condition

Adopting the same method as 32.40° static working condition, the surface deformation of the prism is fitted under 159.84° dynamic working condition. Table 7.13, which is the fitting coefficient of the Zernike polynomial (first 9 items), Fig. 7.37b,

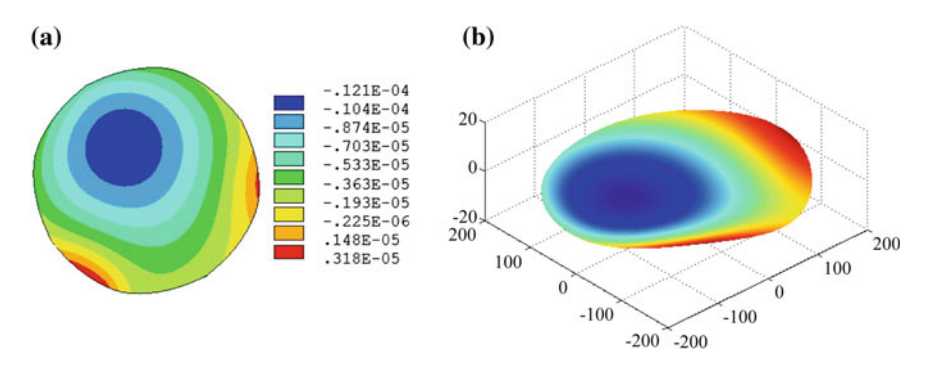


Fig. 7.36 Surface deformation comparison of the wedge facet. a Actual simulation result; b Fitting result

Table 7.12 Comparison of surface deformation quality (32.40° dynamic working condition)

	Actual simulation result	Fitting result	Error (%)
PV value of plane facet/nm	12.6309	11.7735	6.79
RMS value of plane facet/nm	8.4458	8.2544	2.27
PV value of wedge facet/nm	13.7399	13.0424	5.08
RMS value of wedge facet/nm	7.4167	7.2463	2.30

Table 7.13 Fitting coefficients of Zernike polynomial (the first 9 items, 159.84° dynamic working condition)

	Fitting coefficient of plane facet a_i	Fitting coefficient of wedge facet a_i	Corresponding Seidel aberration
1	15.04580574	14.74221763	Translation
2	-0.00685881	-0.00105213	X-axis tilting
3	-0.01675630	-0.01360338	Y-axis tilting
4	-0.00007801	-0.00007166	Defocusing
5	0.00000222	0.00002315	Astigmatism (0° or 90°)
6	-0.00001815	-0.00001014	Astigmatism (45°)
7	0.00000006	0.00000006	X-axis coma
8	0.00000001	0.00000002	Y-axis coma
9	-0.00000002	0.00000003	Spherical aberration

the fitting wavefront on the plane facet, and Fig. 7.38b, the fitting wavefront on the wedge facet, can be obtained respectively.

From Figs. 7.37 and 7.38, on the plane facet of the prism, the fitting surface deformation value is PV = 15.6704 nm and RMS = 10.5589 nm, while the deformation value found by actual simulation is PV = 16.4310 nm and RMS = 10.8092 nm,

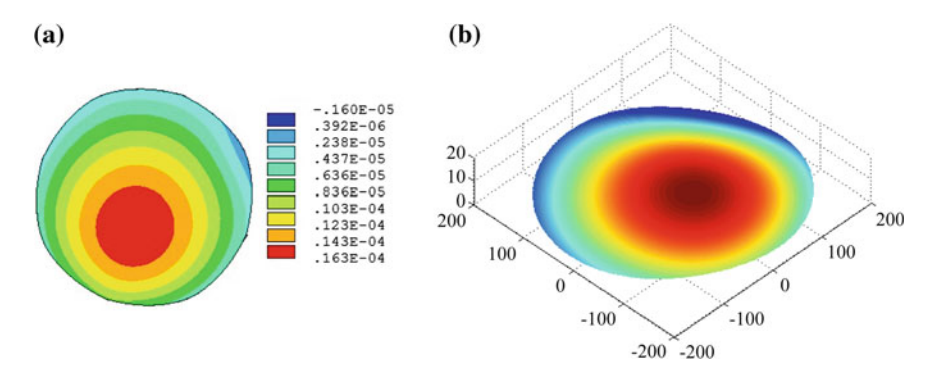


Fig. 7.37 Surface deformation comparison of the plane facet. a Actual simulation result; b Fitting result

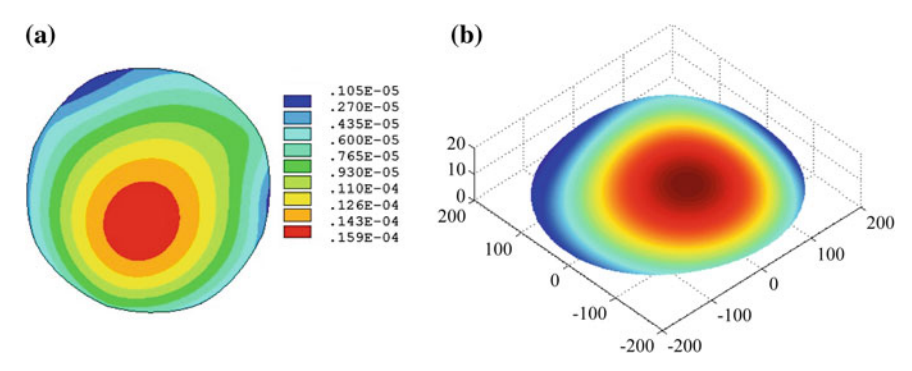


Fig. 7.38 Surface deformation comparison of the plane facet. a Actual simulation result; b Fitting result

the relative errors of which are 4.63 and 2.32%, respectively. On the wedge facet of the prism, the fitting surface deformation value is PV = 13.2356 nm and RMS = 10.4202 nm, while the deformation value found by actual simulation is PV = 13.5834 nm and RMS = 10.6675 nm, the relative errors of PV and PV are 2.56 and 2.32%, respectively. The results are shown in Table 7.14.

Table 7.14 Comparison of surface deformation quality (159.84° dynamic working condition)

	Actual simulation result	Fitting result	Error (%)
PV value of plane facet/nm	16.4310	15.6704	4.63
RMS value of plane facet/nm	10.8092	10.5589	2.32
PV value of wedge facet/nm	13.5834	13.2356	2.56
RMS value of wedge facet/nm	10.6675	10.4202	2.32

	Fitting coefficient of plane facet a_i	Fitting coefficient of wedge facet a_i	Corresponding Seidel aberration
1	1.45598043	3.32522588	Translation
2	0.00054062	-0.00146138	X-axis tilting
3	-0.00133654	-0.00499632	Y-axis tilting
4	-0.00001058	-0.00000976	Defocusing
5	-0.00000288	0.00001382	Astigmatism (0° or 90°)
6	-0.00000817	-0.00000162	Astigmatism (45°)
7	0.00000001	0.00000001	X-axis coma
8	0.00000002	-0.00000003	Y-axis coma
9	0.00000001	-0.00000001	Spherical aberration

Table 7.15 Fitting coefficients of Zernike polynomial (the first 9 items, 269.28° dynamic working condition)

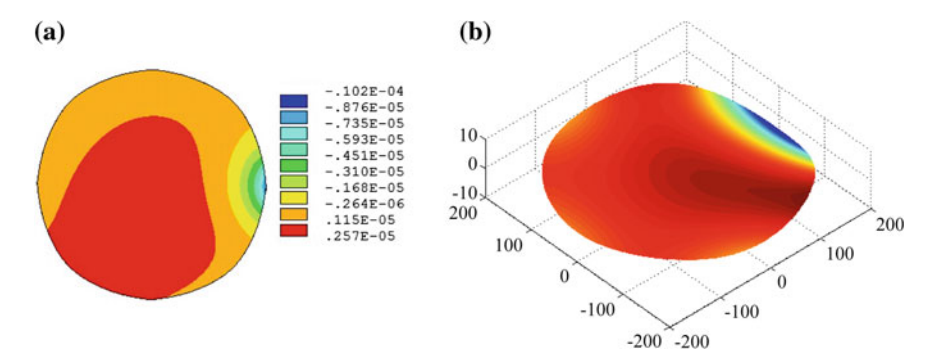


Fig. 7.39 Surface deformation comparison of the plane facet. a Actual simulation result; b Fitting result

(4) 269.28° Dynamic Working Condition

Adopting the same method, the surface deformation of prism is fitted under 269.28° dynamic working condition. Table 7.15, which is the fitting coefficient of the Zernike polynomial (first 9 items), Fig. 7.39b, the fitting wavefront on the plane facet, and Fig. 7.40b, the fitting wavefront on the wedge facet, can be obtained respectively.

From Figs. 7.39 and 7.40, on the plane facet of the prism, the fitting surface deformation value is PV = 7.0791 nm and RMS = 1.2069 nm, while the deformation value found by actual simulation is PV = 8.5197 nm and RMS = 1.1609 nm, the relative errors of which are 16.91 and 3.96%, respectively. On the wedge facet of the prism, the fitting surface deformation value is PV = 9.5505 nm and RMS = 2.8976 nm, while the deformation value found by actual simulation is PV = 10.7739 nm and RMS = 2.9376 nm, the relative errors of which are 11.36 and 1.37%, respectively. The results are shown in Table 7.16.

Whether the working condition is static or dynamic, since the surface deformation graph obtained by Ansys software tool is sharp, the cross linking is larger, while

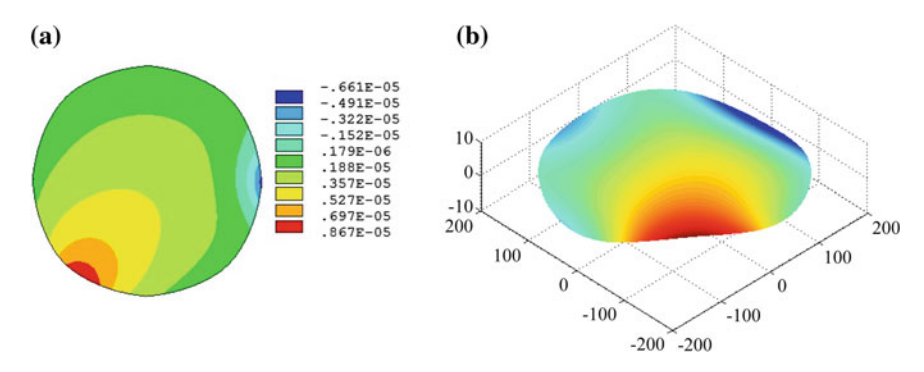


Fig. 7.40 Surface deformation comparison of the plane facet. a Actual simulation result; b Fitting result

surface deformation graphs of the Zernike polynomial fitting are relatively smooth, it inevitably results in the relative errors. However, the relative errors of PV and RMS values both are within the allowable range, and moreover the RMS values are small, which indicates that Zernike polynomial fitting by the first 15 items is feasible. The Zernike polynomial fitting data can be used to further study the wavefront aberration information.

4. Evaluation of Fitting Results

In this section, Zernike polynomials are used to fit the surface deformation of the prism. The maximum PV value error of the fitting wavefront is 16.91%, and the maximum RMS value error is 5.51%. The fitting result is within the allowable range, but the fitting error of PV values is still relatively large. The main reasons are:

- (1) Influenced by mesh generation and constraints of the prism model, the cross linking of data is larger, which is the main reason for low fitting precision.
- (2) The larger relative error is unavoidable because the surface deformation graph obtained by the actual simulation is sharp, and it is not a direct response to the actual form of aberration, compared with the wavefront surface deformation fitted by the Zernike Polynomial.

Table 7.16 Comparison of surface deformation quality (269.28° dynamic working condition)						
	Actual simulation result	Fitting result	Error (%)			
PV value of plane facet/nm	8.5197	7.0791	16.91			
RMS value of plane facet/nm	1.1609	1.2069	3.96			
PV value of wedge facet/nm	10.7739	9.5505	11.36			
RMS value of wedge facet/nm	2.9376	2.8976	1.37			

- (3) The least square method is simple and quick, but the fitting precision is not the highest, which is also a reason for the larger error.
- (4) The number of Zernike items is not proportional to the fitting precision, so it is necessary to select the number of fitting items reasonably.

7.4 Summary

According to the rotational motion requirements for the large-aperture scan prism, a radial multi-segmental support way, characterized by easy installation and radial fine adjustment, is proposed in this chapter. The three-segmental support way is analyzed under two cases of the thin end upward and downward, and it is found that the volatility of the surface deformation is least under the three-segmental support way, compared the support effects before and after optimization. Based on the analysis platforms of Adams software and Ansys software, the analysis method for dynamic performances of the optomechanical structure is proposed, which is suitable for the dynamic performance analysis on the optical system, and can provide references for the performance analysis on the similar optical system. The surface deformation of the prism is fitted by the first 15 items of the Zernike polynomial through Matlab programming. PV values and RMS values of the fitting wavefront are calculated and then compared with the surface deformation of actual simulation. The fitting errors of PV and RMS values are all within the allowable range, which can meet precision requirements for the surface figure.

References

- Cui XQ, Li XN, Zhang ZC et al (2005) Tentative fabrication test for large aperture thin astronomical mirror. Acta Optica Sinica 25(7):965–969
- Zhu B, Yang HB, Zhang JX et al (2010) Structure design and optimization of M3 in largeaperture telescope. J Eng Des 17(6):469–478
- 3. Salas L, Gutierrez L, Pedrayes MH (1997) Active primary mirror support for the 2.1 m telescope at the San Pedro Martir Observatory. Appl Opt 36(16):3708-3716
- Vukobratovich D, Richard RM (1991) Roller chain supports for large optics. Proc OE 1396:522–534
- Li AH, Wang W, Ding Y, Liang YC et al (2012) An overview of radial supporting ways for large-size movement mirror: a study case of a large-aperture rotating prism. Proc of SPIE 8487:84870T-84870T-11
- 6. Li AH, Li ZZ, Sun JF et al (2012) Optimization design of radial support for large-aperture rotating and tilting prism. Acta Optica Sinica 12(32):121205–121205-6
- Hu QQ (1983) Structure, support and gravity deformation calculation method for large-scale optical mirrors. Opt Mech 6(31):29–44
- 8. Ostaszewski M, Harford S, Doughty N et al (2006) Risley prism beam pointer. Proc SPIE 6304:630406–630406-10
- 9. Wang W (2014) Research on support optimization and dynamic analysis for large-aperture tracking rotating mirror. College of Mechanical Engineering, Tongji University, Shanghai

References 311

10. Li AH, Wang W, Bian YM et al (2014) Dynamic characteristics analysis of a large-aperture rotating prism with adjustable radial support. Appl Opt 53(10):2220–2228

- 11. Li AH, Jiang XC, Sun JF et al (2012) Radial support analysis for large-aperture rotating wedge prism. Opt Laser Technol 44:1881–1888
- 12. Jiang XC (2014) Research on the coarse-fine coupling scanning device based on double-prism. Tongji University, Shanghai
- Zhang YT, Cao XD, Kuang L et al (2012) Dynamic deformation analysis of light-weight mirror. Proc SPIE 8417:84172P–84172P-7
- 14. Xiao QJ, Jia HG, Han XF et al (2013) Performance analysis of a kind of moving reflector's mechanism with small coupling displacement. Infrared and Laser Eng 42(4):975–981
- Burns M (1994) Tracking performance simulation for the Gemini 8-M telescope. Proc SPIE 2199:805–816
- 16. Wang F, Wu X, Yang F et al (2008) Based on householder transform of the Zernike polynomial wavefront fitting method to solve active optics correction force. Proc SPIE 6835:683522–683522-5